Wind Pumping in a Snow Pack related to Atmospheric Turbulence

Martin J. Bell

A thesis presented for the degree of

Doctor of Philosophy in

Chemical and Process Engineering

University of Canterbury

1993

While some have a clear view of the mountains

others cannot see the forest for the trees

anon

To my parents, *Dorothy and Robin*

Whose unconditional support made the completion of this project possible.

Abstract

An extensive investigation has been carried out to evaluate the possible influence of wind pumping on snow metamorphism, and hence snow stability. Wind pumping refers to a pulsile forced flow of air in a snow pack due to surface pressure fluctuations.

❄ An extensive review of atmospheric turbulence from related disciplines was carried out in order to identify the characteristics of turbulence in mountain terrain. This was followed by an experimental programme to characterise and measure the pressure fluctuations on the snow surface in the mountain terrain of Arthur's Pass National Park. Frequencies between 0.0005 and 1 Hz were studied and power spectral / correlation function analysis was made. Gust exceedance statistics were also calculated.

The turbulence intensities and rms pressure fluctuations were found to be significantly larger than those reported in the literature. The spectral analysis showed similar form to other documented spectra, but was shifted substantially toward lower frequencies. The same low frequency components, and a semi-periodic component was evident in the autocorrelation analysis. It was suggested that these features arise from turbulent structures shedding off large upstream structures and/or gravity wave activity.

❄ Following this, laboratory tests on beds packed with granular materials were carried out to study wind pumping airflow dynamics and the influence of wind pumping airflow on diffusive mass transfer.

A mathematical basis for the dissipation of the surface pressure fluctuations in a permeable bed has been experimentally verified in the laboratory. Three one-dimensional models proposed were then applied to a wide variety of snow pack conditions. One model (finite-sealed) was found to be widely applicable to wind pumping modelling in the seasonal snow pack. A linear approximation to this model is applicable to most seasonal snow packs.

Sublimating naphthalene was used as a tracer in a set of laboratory experiments to measure the enhanced diffusive mass transfer rates in a packed column due to wind pumping. Compared to stagnant air diffusion rate, an *enhancement of one to two orders of magnitude* was measured in mass loss rates. The mass loss rate enhancement depended strongly on both the period and

magnitude of the applied wind pumping. The mass loss per cycle showed a large, linear dependence on cyclic displacement. This showed that *the naphthalene mass loss process was 1-D planar convective / diffusion controlled.* A slight dependence on peak velocity was also found. This indicated that the naphthalene mass loss process had a small dependence on boundary layer diffusion.

❄ Finally, cold laboratory experiments were carried out to directly study the effects of wind pumping in snow in a controlled environment. A number of strength tests were applied. The *cone penetrometer is recommended as the most useful strength testing tool* in this type of analysis.

Pressure fluctuations associated with gale force winds (60 to 90 km/hr) were used to provide strong wind pumping conditions. Two types of experiments were run, both in high density snow (≈350 kg/m^3):

- ❄ Initially bonded grains had moderate to high temperature gradients imposed on them to evaluate any enhancements in the faceting process.
- ❄ Grains without any initial bonding had low temperature gradients imposed upon them to evaluate any enhancements in the rounding process.

It was found that wind pumping enhanced the rate of the process in both cases.

There was a significant wind pumping enhancement of strength loss at high temperature gradients. *The influence of wind pumping on the growth rates of depth hoar appears to be almost as significant as the influence of the temperature gradient magnitude.* This wind pumping enhancement is most likely to occur when there is a large temperature difference near the surface of the snow pack between the air and snow or between two layers of snow.

There was a significant wind pumping enhancement of strength increase at low temperature gradients. *The effect of wind pumping on the development of snow strength appears to be more important than the effect of elapsed time.* The differences in enhancement with and without wind pumping appear to be larger at the beginning of the bonding process. It is conceivable that the wind pumping could play a major role in the initial bonding. It is therefore concluded that *wind pumping is possibly a major contributing mechanism in the development of wind slabs.*

Hence it can be concluded that wind pumping significantly enhances dry snow metamorphism.

Acknowledgments

I am very grateful to Dr John Abrahamson for this guidance and supervision of the work in this thesis. John's continual support and enthusiasm for this project have me truly indebted. His myriad of ideas and willingness to actively resolve the many problems that arose have impressed me. He waited patiently while I rejected, and some time later, took on board what he had to say. His efforts in obtaining funding and equipment for this project have been appreciated. I have always enjoyed working with John, his sense of humor, and his outlook on life.

The other academic staff of the Department of Chemical and Process Engineering have all contributed with their ideas and support, but in particular, Jim Stott for the use of his temperature control system which saved me a considerable amount of time, and Pat Jordan for his modelling ideas. This work would not have been possible without the assistance of the department's technical staff, who all have contributed in a major way to this project at one time or another.

There are many others who have contributed in some way to this project.

In the initial stages of the project I was grateful to Mt Cook National Park for the use of their alpine huts and village facilities, and to Mt Cook Airlines for their courtesy flights into Tasman Saddle.

I am very grateful to University of Canterbury and Temple Basin Ski Clubs for allowing the use of their facilities at Temple Basin for the research station that became home to me for several winters.

I am appreciative of the Mechanical Engineering Department for the use of DADiSP and their field instrument caravan. In particular I am grateful to Graham Harris for his support during the analysis of the atmospheric turbulence data, and Tony Bowen for his thoughts, advice and enthusiasm on the atmospheric turbulence work.

There are so many close friends to whom I owe a lot for their continual support. I would especially like to thank those who have helped through the final year. I hope one day I will get to return your gestures.

Finally I would like to acknowledge my parents, Dorothy and Robin, who offered both financial assistance and personal encouragement though this seemingly endless task. You two are just the best!

Table of Contents

Chapter 1: Perspective of this Work

Chapter 2: Review of Atmospheric Turbulence

Chapter 3: Measurements of Atmospheric Turbulence

Chapter 4: Packed Bed Airflow Dynamics

Chapter 5: Packed Bed Mass Transfer

Chapter 6: Wind Pumping in Snow

Chapter 7: Summary of Conclusions

Chapter 1
Perspective of this Work

The objective of Chapter 1 is to introduce the topics covered in this thesis, and to put the concept of wind pumping in context with avalanche safety operations and the science of snow metamorphism.

1.1. Table of Contents

1.2. List of Illustrations

1.3. Introduction

The objective of this chapter is to introduce the topics covered in this thesis, and to put the concept of wind pumping in context with avalanche safety operations and the science of snow metamorphism.

In section 1.4 some key terms are introduced. The relationship between wind pumping and snow and avalanche phenomena is developed in sections 1.4 and 1.5. Atmospheric turbulence is introduced in section 1.7. A historical and conceptual perspective on wind pumping is given in section 1.8.

The main points from sections 1.5 to 1.8 are summarised in section 1.9, and the need for this experimental programme identified. The experimental programme for this thesis is outlined in section 1.10.

The reader can assume that any information in this chapter that is not referenced is taken from the basic texts of Perla and Martinelli (1976) and CAA (1992).

1.4. Definitions of Snow Metamorphism and Wind Pumping

The snow crystals that form in the atmosphere and fall to the ground, may accumulate into what is termed the *snow pack*. From the time of formation in the atmosphere and settling on the ground, until sublimation back into the atmosphere, melting, or formation of glacial ice, the snow crystals, or *grains*, undergo continual changes. These changes are generally termed ***snow metamorphism***, and are controlled by the flow of heat and water vapour.

Wind pumping may be defined as the pulsile forced convection of air in a snow pack due to surface pressure fluctuations.

Wind pumping may be important to both:

* *Seasonal snow packs* - snow layers which accumulate during the winter season, and completely melt, or sublimate away during the summer season.
* *Glacial firn* - accumulated snow layers which are in the process of becoming glacial ice.

The seasonal snow pack is created from successive snowfalls. Each snowfall creates a new *layer* in the snow pack. Layers can remain identifiable in the stratum throughout the life of the seasonal snow pack. The strength of these layers, and the interfaces between them, are critical to the stability of the inclined snow pack.

1.5. Avalanche Phenomena

For a snow avalanche hazard to exist, three conditions are required; avalanche terrain, unstable snow and people and/or facilities. Commonly these are presented as the Avalanche Hazard Triangle shown in figure 1.1. This study is concerned with the influence wind pumping may have on the stability of the snow pack.

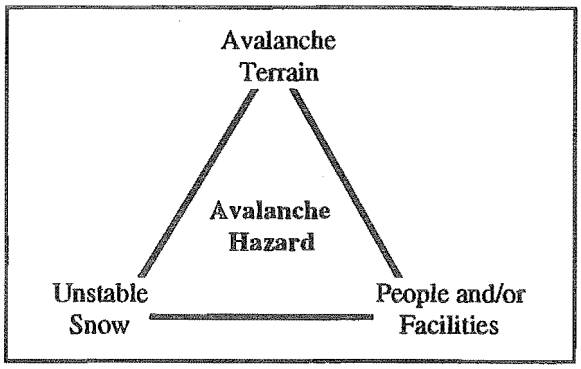

Figure 1.1. The Avalanche Hazard Triangle.

An *avalanche* occurs when some portion of an inclined snow pack is unable to support itself, fails, and the unstable snow flows down the slope until it comes to rest where the slope flattens out. This failure occurs in a relative weakness within or between layers in the snow pack. These weakness can originate from:

* New snow types which have few crystal to crystal contacts, or which slide easily over one another.
* Layers that do not bond well to one another.
* Faceted grains (see section 1.6.1), which have developed in the snow pack at the expense of grain to grain bonding.

Two types of avalanches are recognised:

* *Loose Snow Avalanches.* These are the release of cohesionless surface snow layers. Failure occurs because the cohesionless snow grains can no longer support each other. In new snow, this may occur before bonding has time to give the snow strength. In wet old snow it may occur when free water in the snow pack has melted sufficient bonds between grains to lose cohesion.
* *Slab Avalanches.* These occur when a relatively cohesive slab of snow, which may consist of many well bonded identifiably layers, fails as a unit on a relatively soft layer or plane of weakness. Failures and avalanches occur when the forces due to the weight of the snow layers, and forces from a trigger, exceed the strength of the snow.

When assessing the *snow stability*, knowledge of how the weaknesses in the snow pack are developing or stabilising is critical. The stability ratings that result from this assessment can be qualitative and/or quantitative.

In the snow safety industry, the avalanche forecaster generally makes a qualitative assessment of snow stability. This assessment is made after observation and consideration of a number of possible stability influences, for example:

1. *Primary Factors*: Evidence of natural avalanche activity and results of slope tests:
   - * Avalanche Activity
   - * Slope Tests by Ski, Foot or Explosives
2. *Secondary Factors*: Snow pack details, and historical information:
   - * Weak Layers
   - * Snow Overlying Weak Layers
   - * Snow Pack Settlement
   - * Penetration
   - * Snow Pack Temperatures
   - * Recent Action of Wind
   - * Previous Avalanche Activity
   - * Previous Slope Use
   - * Previous Snow Surface
   - * Likely Triggers
3. *Tertiary Factors*: Current and forecasted weather influences:
   - * Precipitation Type and Intensity
   - * Wind Strength and Direction
   - * Solar and Terrestrial Radiation
   - * Air Temperature and Trend
   - * Humidity and Trend
   - * Barometric Pressure and Trend

For definitions of these terms, refer to Perla and Martinelli (1976).

The question the avalanche forecaster might ask of this project is, *"how does wind pumping fit into these considerations?"* An attempt has been made to keep this fundamental thought in perspective throughout the research period.

Snow stability has been described quantitatively in terms of the *stability index* (see for example Conway and Abrahamson, 1984a, and Föhn, 1988). The stability index describes the stress / strength relationship of a weakness in the snow pack. Generally:

* A stability index of » 1 indicates a stable snow pack.
* A stability index of < 1 indicates an unstable snow pack.

In practical terms, a factor of safety might be applied to the slope before it is declared stable. For example, a safety factor of 6 might be applied to slopes used by skiers. The safety factor concept is common in many engineering applications. Note that because of spatial variability in snow pack strength, snow slopes with stability indices < 1 can exist (a trigger may initiate snow slope failure in this case).

The force balance in an inclined snow pack, and slope failure as a slab avalanche are illustrated in figure 1.2.

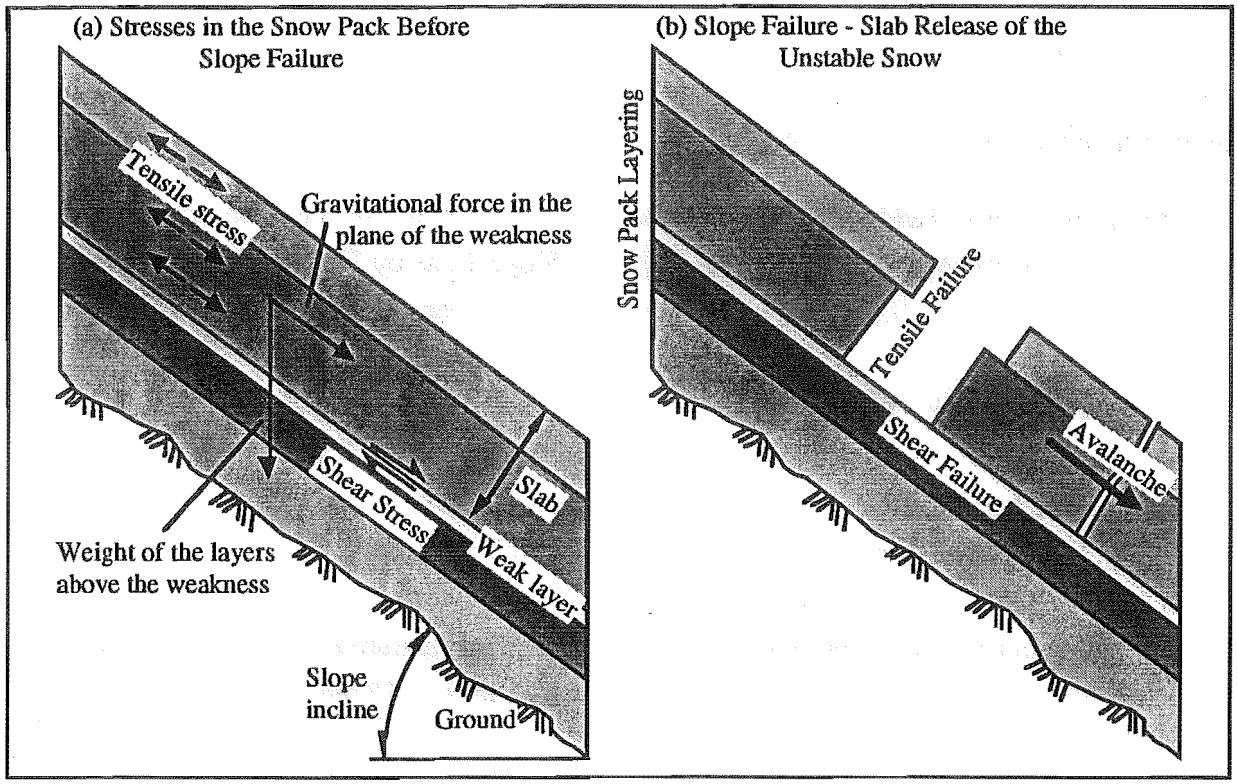

Figure 1.2. The Layered Inclined Snow Pack: (a) Stresses before Snow Slope Failure. (b) Snow Slope Failure.

The stability index changes with the continual metamorphic changes in the snow pack. Examples of factors which influence such changes in the stability index are shown in table 1.1. Factors which change the stability index sufficiently for the unstable snow to avalanche are termed *triggers*. For definitions of these influences, refer to Perla and Martinelli (1976).

To Lower the Stability Index (the snow pack becomes less stable)			
Increasing the Stress in the Snow Pack		Decreasing the Strength of Snow Pack	
Natural	Artificial	Natural	Artificial
• Precipitation • Wind redeposition • Solar radiation • Creep • Avalanching	• Skiers and climbers • Machinery • Explosives • Avalanching	• Faceting • Solar radiation • Creep and glide • Rain	• Road cuts
To Raise the Stability Index (the snow pack becomes more stable)			
Decreasing the Stress in the Snow Pack		Increasing the Strength of Snow Pack	
Natural	Artificial	Natural	Artificial
• Natural avalanches • Wind erosion	• Artificial release of unstable snow	• Rounding • Refreezing	• Skier compaction • Boot packing

Table 1.1. Examples of Factors which may Influence Changes in the Stability Index.

1.6. Overview of Snow Metamorphism in the Absence of Wind Pumping

Colbeck (1987a, 1982) has given excellent reviews on seasonal snow metamorphism. An historical perspective on snow cover research is also given by Colbeck (1987b). With such good published reviews, there is little point in reproducing material here as there have been few developments on metamorphism since 1987. Hence, in this section a number of points and terms relating to snow metamorphism are made, and the current state of the science reviewed where relevant to wind pumping effects on snow. Unless otherwise stated the material not referenced in this sections comes from these three papers.

According to Colbeck, the variation of snow types that are found in the snow pack develop because:

* Snow packs are generally subjected to varying environmental conditions.
* Snow is a finely dispersed aggregate of ice, water vapour, and/or water that is at, or close to its melting temperature. Therefore mass exchange between the phases readily occurs.

Accordingly, snow is constantly moving to reduce its surface free energy by densifying and eliminating smaller grains. At the same time it responds to different stimuli produced by its environment. The most important factors are free water and temperature gradients (see figure 1.3).

With few exceptions, the original form of the precipitated snow crystals have no lasting influence on grain form and processes in the snow pack.

Two scales need to be defined; *macro scale*, more than a few grain diameters, and *micro scale*, a single grain or pore space, or smaller.

The macro scale *temperature gradient* is generally considered to be the vertical distribution of temperature within part of snow pack. This is illustrated in figure 1.3. This differs from the micro scale temperature gradient defined in section 1.7.1.

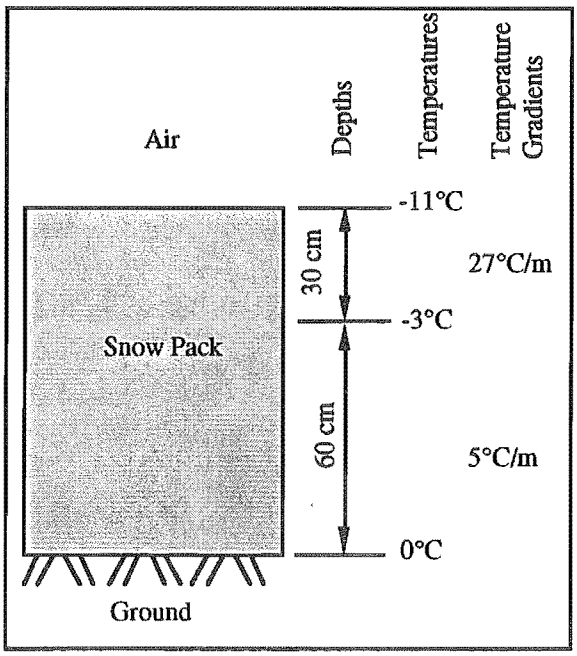

Figure 1.3. Macroscopic Temperature Gradient on a Snow Pack.

Snow form is characterised as either *wet* or *dry* depending on the presence of liquid water. Wet snow has markedly different form at *low* and

high liquid contents. Dry snow is characterised as having either a *faceted* or *rounded* form. These forms are derived through processes that occur according to the environmental conditions. As the environmental conditions change so do the processes action on the grains. Mixed form grains can result from such changes.

In dry snow mass transfer takes place in the vapour phase (Ramseier and Keeler, 1966) while in wet snow mass transfer takes place in the liquid phase. Wet phase processes are considerably faster than vapour phase processes. Consequently, the metamorphic processes in wet snow are not affected by the interstitial air. Note that close to the melting point, a mobile surface layer will blur between these.

Therefore wind pumping will not play any part in wet snow processes, and from this point only ***dry snow processes are considered.***

Other processes that occur on or in the snow pack, which do not fit into the categories of precipitation or snow metamorphism include:

* *Surface hoar* formation on the snow surface due to strong surface temperature gradients and calm, humid atmospheric conditions. Because the snow is a good emitter of long wavelength radiation, the snow surface temperature can be 10°C or more cooler than the atmospheric temperature. Radiation cooling requires clear skies, and low amounts of incoming solar radiation (shady slopes and night time).
* *Wind breakage* of surface crystals as they are picked up by the wind and rolled along the snow surface. This results in small fragmented crystals.
* *Sublimation of surface snow* into the atmosphere due to warm, windy, low humidity atmospheric conditions.
* *Riming and freezing rain* due to super cooled water vapour droplets in the atmosphere colliding and freezing to the snow surface.

For definitions of terms in this list, refer to Perla and Martinelli (1976).

Illustrations of new snow crystals and the various snow grains that develop in the snow pack are presented by Perla (1978a) and Colbeck (1982).

1.6.1. Dry Snow Metamorphism

Grain growth in dry snow is a process of continuous loss of mass by sublimation to the vapour phase from warmer and/or more curved (or convex) surfaces, and gain in mass by vapour deposition onto colder and/or less curved (or concave) surfaces. The warmer and/or more curved surfaces exhibit relatively high equilibrium vapour pressures, while colder and/or less curved surfaces exhibit relatively low equilibrium vapour pressures.

Two processes which depend on the temperature gradient in the snow pack, are important:

* The result of ***high vertical temperature gradients*** being imposed on a snow cover is the development of ***faceted grains***. The reason facets form is that surface kinetics control the placement and form of water vapour deposition onto the grain surfaces.

  There are degrees of faceting which depend on the stages in growth. On the imposition of a high temperature gradient, initial *squaring*, or development of sharp corners and faces, occurs on the warmer sides of the grains. If the high temperature gradient is maintained, this squaring is followed by the development of *striations*, or consecutive layers of faceting, until in the advanced stages a grain type commonly called *depth hoar* is formed.

  The large grains that result from prolonged faceting are mechanically strong within themselves, but intergranular strength is low because there is no mechanism for bonding between grains (Akitaya, 1974, Adams and Brown, 1982). Because of their size, large facets will maintain their form long after the temperature gradient is reduced, and so they present long term stability problems in the snow pack.

* The consequence of ***low temperature gradients*** is the development of ***rounded grains***. In this process, higher curvature surfaces are sacrificed in the formation of less curved surfaces. Also, the intergranular contacts *sinter* (form bonds), and the snow pack gains strength.

The transition between the rounding and faceting processes occurs at 10 to 20°C/m in snow that is warmer than -6°C (Colbeck, 1983b).

These processes are illustrated in figure 1 of Colbeck (1987a).

The rate of metamorphism increases with both:

* Magnitude of the imposed temperature gradient, even when only rounded crystals develop (Perla, 1978b, Colbeck, 1983b).
* Warmer snow temperature. Although temperature affects the equilibrium vapour pressure above an ice surface, the rise in rate with higher temperature is also due to the effect of temperature on crystal growth rates.

More technical details on these processes are given below in sections 1.6.1.1 to 1.6.1.3.

1.6.1.1. Faceting in Dry Snow

Given that a large macro scale temperature gradient is required for faceting, there appears to be a mechanism for vapour transport on a macro scale. However, there is strong evidence that the vapour transport takes place on a micro scale (Christon *et al*, 1987). Yosida (1955) was very close to today's *source and sink* grain concept with the idea of *hand to hand delivery of water vapour*; where the growth of one grain occurs with the simultaneous shrinking of a neighboring grain of higher temperature. This hand to hand transfer of water vapour is illustrated in figure 1.6(b).

To expand on this, from Colbeck (1982, 1983b, and 1987a), the temperature differences across the pore spaces are much greater than across the ice grains because ice has a thermal conductivity which is about 100 times that of air (Giddings and LaChapelle, 1962). Because of the tortuous nature of the heat flow paths, the temperature differences are greater for larger separations between ice surfaces. Hence, pairings of grains with greater separation will have higher temperature differences compared to other paired grains. Since the rate of metamorphism increases with the temperature difference, preferential paths for vapour diffusion between source and sink grains, and preferential sites for faceting on the sink grains, can be identified. Preferential sites may be enhanced by vertically elongated source and/or sink grains (or chains of grains) which are more effective heat flow paths into colder (or warmer) parts of the snow pack. In this way it is also understood why some grains grow, while others shrink and disappear. Figure 1.4 illustrates this source / sink concept.

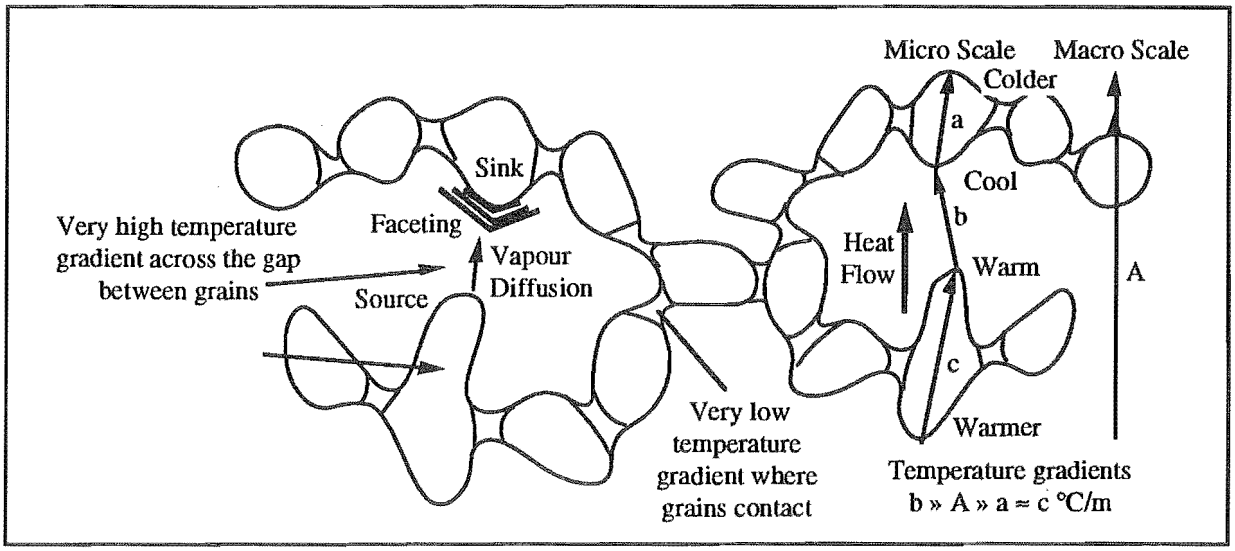

Figure 1.4. Illustration of the Mechanism of High Temperature Gradient Metamorphism in Dry Snow.

There is a need for a micro scale temperature gradient to be defined as the macro scale temperature gradient becomes too generalised. This is illustrated in figure 1.4. The micro scale temperature gradient will be dependant on heat flow through the ice grains, heat conduction

through the air, and latent heat transfer among a complicated geometrical distribution of ice grains.

From figure 1.4 it can be seen why faceting occurs only on the warmer side of the grains. If the process is allowed to continue for an extended period of time, complete recrystallisation can occur. Depth hoar is an extreme example of faceted crystals which grow when the snow is subjected to a large temperature gradient for a long time.

The growth rate of facets are high because of the strong temperature gradients. As with rounding there is also a rate dependence on absolute temperature (Giddings and LaChapelle, 1962). Distinct sharp corners on faces can appear within a day of the high temperature gradient application. Fully developed depth hoar can develop in as little as 10 days given the right conditions. There is also a rate dependence in the radius of curvature of the disappearing grains; higher curvature source grains give higher rates of faceting (Colbeck, 1980).

The growth of facets is limited in high density snow because facets require pore spaces to grow into (Marbouty, 1980, Akitaya, 1974).

1.6.1.2. Rounding in Dry Snow

At low temperature gradients, the rounded grains develop because it minimises their surface free energy. This shape is called the *equilibrium* form, although growth still occurs.

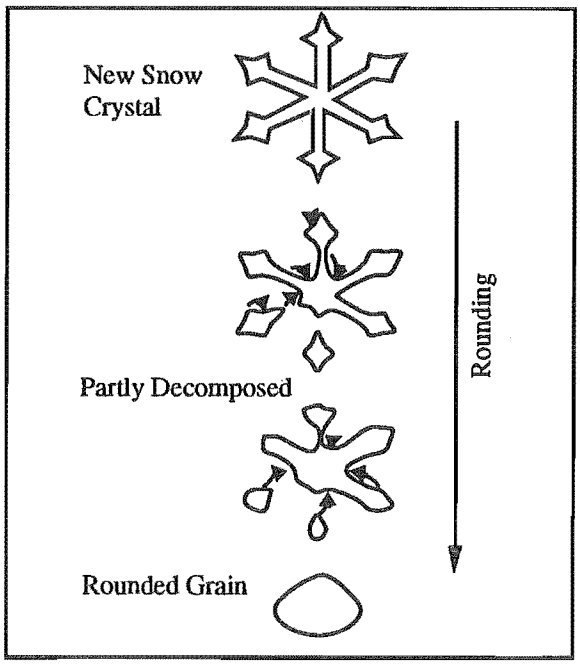

Figure 1.5. Illustration of the Rounding Process on an Individual Snow Grain.

It has been shown that the differences in radius of curvature does not control the rate of metamorphism except for very short periods in very fresh snow (Perla, 1978, Colbeck, 1980). However, at low temperature gradients, radius of curvature does control the direction of metamorphism towards rounding (Perla, 1978b, Colbeck, 1980, and 1982). The rounding process on an individual grain is illustrated in figure 1.5.

No equivalent source and sink mechanisms have been suggested for low temperature gradient metamorphism. This leaves an important question unanswered; how does the temperature gradient control growth.

Because the rate of metamorphism is dependant on the temperature gradient, and for rounding to occur the gradient must be low, the rate at which rounding occurs must be slow. Consequently equally sized rounded grains take a very long time to fully develop in the snow

pack. The new crystals loose their sharp forms relatively quickly (very high radii of curvature). In the same way the relatively small grains are quick to be consumed by the larger grains. This first stage of the rounding process may take around 3 to 5 days. The rate of low temperature gradient metamorphism slows down as the supply of relatively small grains is exhausted. This is because of the small differences in radius of curvature among the equal sized grains. The grains may not appear to be equal for 30 or more days.

1.6.1.3. Strength of Dry Snow

At low temperature gradients snow gains strength by *sintering*. This is the process by which the ice grains bond together by the movement of water molecules to the particle / particle contacts. Using concepts from equilibrium thermodynamics, the equilibrium vapour pressure is lowest over the concave surface of a particle / particle contact, or bond, and highest over sharp corners. Hence water molecules migrate to the particle / particle contacts, or bonds, by vapour diffusion. By the same principles it is also thought that migration in a quasi-liquid layer is important. Thus at low temperature gradients the rounding snow develops strength. This process is illustrated in figure 1.6(a).

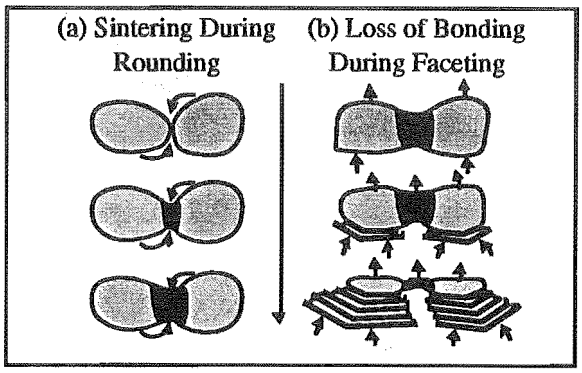

Figure 1.6. Metamorphic Effect on Bonding in Dry Snow. (a) Sintering During Rounding. (b) Loss of a Sintered Bond During Faceting.; The arrows indicate the direction of vapour flow.

At high temperature gradients sintering will not take place. This is because the supersaturation over the ice surfaces is high enough so that the shape of the crystal is no longer dictated by phase equilibrium principles, but by surface kinetics. Thus at high temperature gradients the faceting snow does not gain strength, in it fact loses strength because the recrystallisation process consumes the old grains, and the bonds between them. This process is illustrated in figure 1.6(b).

The main influences on strength (CAA, 1992) of dry snow, and hence the stability of the dry snow pack, are outlined in table 2.1.

Influence	Strong Snow	Weak Snow
Size and shape of the grains	Small	Large
Snow density	High	Low
Bonding between the grains	Rounding	Faceting
Snow temperature	Low	Close to 0°C

Table 1.2. General Influences on the Strength of Dry Snow.

1.6.1.4. Modelling Dry Snow Metamorphism

Because of the highly complex three-dimensional intergranular structure of the snow pack, one-dimensional modelling is inappropriate.

According to Colbeck (1987a), the modelling of dry snow metamorphism has grown beyond the stage of the one-dimensional diffusion equation, describing vapour flow between parallel ice plates. Diffusion among other multiple particle systems are now handled in more sophisticated ways, but in snow where the process is driven by an imposed temperature gradient, the approach of couple pairs is more attractive.

The state of the play in this field is in making the geometrical basis more realistic, and performing the laboratory testing of the model predictions. Stereology is being used to provide the information needed to characterise the geometry that controls the interactions between the grains. Unfortunately, the analysis of stereological results is not developed enough to be productive on this issue (Colbeck, 1987b). This is perhaps one reason why there have been few developments in modelling since the 1987 reviews of Colbeck.

1.6.1.5. Stagnant Air Assumption

The air in the pore spaces between ice grains is assumed to be stagnant, except in isolated cases where natural convection may occur . Most theories on metamorphism are based around this assumption, and the assumption that diffusion is the metamorphic rate limiting process in snow. **If pressure fluctuations at the snow surface, derived from atmospheric processes, create significant movements of air in the pore spaces, then the stagnant air diffusion assumptions clearly does not hold.** This is the primary purpose for looking into wind pumping in a snow pack.

With reference to dry snow metamorphism, Colbeck (1987a) states that:

> *"The rate limiting process in crystal growth in snow is the slow diffusion of water vapour among surfaces of different temperatures and curvatures. Thus, if air flow were to occur through the pores of snow, there would be a substantial effect on the transfer rate of vapour and possibly on the rate of metamorphism."*

Two processes have been recognised which can result in air flow:

* Natural convection due to interstitial air buoyancy differences in high temperature gradient, low density snow.
* Forced convection by wind pumping due to snow surface pressure fluctuations.

1.7. Atmospheric Processes

*It is supposed that **Atmospheric turbulence** is responsible for the **pressure fluctuations** which drive **wind pumping**.* Little has been studied on the connection between these topics and hence they become the focus of Chapters 2 and 3.

Atmospheric turbulence has several other well known effects on snow stability:

* *Wind erosion and redeposition* of the snow pack is by far the most important effect of turbulence. Winds of > 20 km/hr can pick up loose snow from the surface of the snow pack and transport it considerable distances. Most of the entrained snow travels in the air layer 1 to 1.5 m closest to the ground (Föhn, 1980). Fragmentation of the grains occurs through collisions with each other and with the ground during transport. The snow will remain in turbulent suspension until the wind speed lowers. The likely areas of erosion are on the upwind side of terrain features where wind speed up occurs. Unless the wind is very strong, redeposition usually occurs of the other side of the terrain feature. The redeposited, fine grained snow quickly gains strength because of its high number of particle to particle contacts. If the cohesive slab that results overlies a softer weaker snow layer, avalanching can result. Note that if the humidity is low during this process, much of the entrained mass of snow can sublimate back into the atmosphere (Schmidt, 1982).

* Light winds are sufficient to prevent the development of surface hoar. This is because mixing breaks down the very high temperature gradient which forms in a thin layer of air close to the snow surface, due to longwave radiation emission. Once surface hoar has formed, winds may be one of the components responsible for destroying it before it gets buried and creates a weak layer.

* Winds during snow fall that entrains newly formed snow in the atmosphere may cause the crystals to become *rimed* before they fall to the ground. Riming occurs when the crystals collide with relatively small super cooled water vapour droplets which freeze instantly on contact. In the extreme, the formation of spherical grains called graupel results. Large even size graupel form layers which are relatively weak.

1.8. Wind Pumping in Snow

1.8.1. A Brief Review

Wind pumping in snow was introduced by Reimer (1980), picking up on the earlier soil science work of Fukuda (1955), Farrell *et al* (1966), Scotter *et al* (1967) and Scotter and Raats (1969). Apart from establishing an order of magnitude increase in the thermal diffusivities in strong winds, most of Reimer's efforts were of an introductory nature.

Farrell *et al* (1966) go further into the theories relating the surface pressure fluctuations to the air movement in the permeable soil. In laboratory tests Scotter *et al* (1967) measured the mass flux enhancements due to wind pumping and find them to be at least 2 to 4 times those of molecular diffusion. They also found the mass fluxes to be greater for natural soils than less random bed materials. Scotter and Raats (1969) supported these results with theoretical calculations based on Farrell *et al's* (1966) equations. Scotter and Raats also looked at the effects of total soil depth, depth from the soil surface, particle size and period of fluctuation. All these measurements were made with regard to the movement of water vapour in the first few centimeters of the soil, and consequential loss of water vapour to the turbulent atmosphere.

Whilst mass losses are observed from deep glacial firn (Alley, 1988), this is not the case for seasonal snow packs. But to say that wind pumping does not affect the snow, on the basis that it does not lose mass in the same way wind pumping contributes to the drying of soils, would be dangerous. This is because of the very complex micro scale processes which are going on in the snow pack.

Colbeck (1989) on a theoretical basis, without reference to these earlier works, discounts any influence on snow metamorphism within the snow pack due to the pressure fluctuations created by atmospheric turbulence. To estimate the magnitude of the pressure fluctuations Colbeck used an experimental relation from Elliott (1972b), and data of Schols and Wartena (1986), which are both taken from flat terrain. This relation is not expected to hold over rough terrain, and certainly not in mountainous terrain. Also, neither include the static pressure contributions which will be felt at the snow surface.

Colbeck theoretically establishes that strong winds can alter the thermal regime in snow around snow surface topographical features. This is due to the spatial variation in surface pressure that is created by features. Clark et al (1987) and Clarke and Waddington (1991) have unsuccessfully attempted to match the differences in temperature profiles observed in firn near the surface of an ice sheet to wind pumping. These difference in temperature profiles appear to be related to location in the terrain.

More specific details of these papers are given where relevant through out the thesis.

1.8.2. Field Observations of Wind Pumping in Snow

The only specific field observation on wind pumping in snow was made by Reimer (1980) who measured an order of magnitude enhancement of thermal diffusivities in snow during strong winds.

It is still conjecture that the differences in temperature profiles observed by Clark et al (1987) and Clarke and Waddington (1991) in firn near the surface of an ice sheet, is due to wind pumping.

Several other conjectural observations have been made by technicians in the snow safety industry. For instance the penetration of the wind into the top layers of the snow pack is thought to be responsible for the formation of wind crusts, since wind crusts form in windy humid conditions. Some take this concept a step further, and tie the penetration of the wind to the very hard nature of cornices. Colbeck (1989) lays some theoretical foundation behind these observations.

Of very real interest is the link that has been made between very strong wind storms that last for 12 or more hours, and the unexplained speed at which previously unstable storm snow has settled and become remarkably stable. No known correlations have been attempted in this area.

1.8.3. Conceived Effects that Wind Pumping may have on the Seasonal Snow Pack

The vertical interstitial displacement of a parcel of air due to the surface pressure fluctuations at various points in the snow pack is of great interest to this project. It is likely that this displacement needs to be at least of the order of the snow grain or pore size for the wind pumping mechanism to have a strong affect on snow metamorphism.

It is assumed at this point that the primary effect wind pumping will have on snow metamorphism will be to enhance whatever process is prevalent at the time. One conceivable deviation from this, is loss of mass from the surface layers (Alley, 1988). In this case, rounding snow may lose some of its strength.

Effects on Rounding

It is expected that an enhancement of the strengthening process associated in rounding will occur in the upper snow pack layers. This will result in:

* More cohesive slabs.
* A strengthening of any weak layers.

During wind slab formation the ice grains are broken up. Given that wind slabs form during strong winds, the wind pumping would start immediately on the unbonded fragmented grains. The fact that these grains are on the surface means that the effect of the wind pumping will be maximised.

The link between high humidity and cohesive wind slab formation during strong winds made in stability assessment work, can be explained by wind pumping. Assuming that the wind slab is accumulating at the same temperature as the air, the surface layers may be losing mass to the atmosphere in the same way soil loses moisture under wind pumping conditions (Scotter *et al*, 1967). It is likely that this water vapour would have otherwise been destined for rounding and sintering, and hence the slab does not become as cohesive. At 100% humidity there will be no moisture lost from the snow pack, and the rounding and bonding will be enhanced by the wind pumping air flow.

Any enhancement in grain growth rate could be as a result of:

* An increase in the vapour pressure difference between the air above the growing grain, and the equilibrium vapour pressure of the grain ice surface. This difference is termed the *excess vapour density* and is equivalent to supersaturation. The excess vapour density controls the type of crystal that develops (Colbeck, 1983b).
* An increase in the difference of vapour pressure between source and sink grains. This is termed the *vapour density difference.*

As the pulsile airflow will increase the excess vapour density over a sink grain, it is conceivable that the transition to faceting will occur at a lower temperature gradient.

Effects on Faceting

Basal facets would probably require a three dimensional flow (see figure 4.2) to be influenced by wind pumping. This is because in one dimension there can be no vertical air movement in the bottom of the snow pack.

Faceted grains higher in the pack usually form just below impermeable crusts. Such crusts would prevent any wind pumping airflow from reaching them. In some cases faceted grains form near the surface. This is due to snow surface cooling through either surface radiation emission and/or cold air temperatures in comparison to the snow pack temperatures.

The mechanisms of wind pumping, created by strong winds, and high temperature gradients, created by surface cooling by radiation emission, are at odds. This is because the convective heat transfer coefficients at the snow surface are increased dramatically during strong winds.

This brings the snow surface closer to the air temperature, negating the effect of radiation cooling.

Thus, wind pumping enhancement of the faceting process is most likely to occur when there is a large temperature difference near the surface of the snow pack between :

* The air and snow.
* Two layers of snow.

1.9. Summary of Sections 1.5 to 1.8

The main reason for studying metamorphism is to enable potential avalanche conditions to be assessed and forecast. The main thrust of this investigation is to evaluate the potential influence of wind pumping as a stabilising or destabilising factor in snow stability assessments.

Faceting and rounding in dry snow are the only metamorphic processes likely to be affected by wind pumping airflows. The primary effect wind pumping will have on snow metamorphism will be enhancement of whatever process is prevalent at the time. Several potentially important influences have been suggested.

* Increase slab cohesiveness.
* Increasing the strength of relatively weak layers which have low temperature gradients.
* Transition to faceting at lower temperature gradients.
* Enhancement of faceting when there are high temperature gradients near the surface of the snow pack between:
    ** The air and snow.
    ** Two layers of snow.

There have been a several studies on the theory behind wind pumping, both in soils and in snow. The soil studies extended to water mass loss rates measurements from the soil surface. The experimental programme described next section results from the fact that no studies on wind pumping in snow have been performed on the laboratory scale, and it appears that it has significant influences on the stability of the seasonal snow pack.

1.10. A Guide to Chapters 2 to 7

This section presents an overview of the experimental programme carried out and the aims behind each component. Figure 1.7 illustrates the four distinct phases. More details on each of these stages are given in the following sections.

A summary of conclusions from Chapters 2 to 6 is made in Chapter 7.

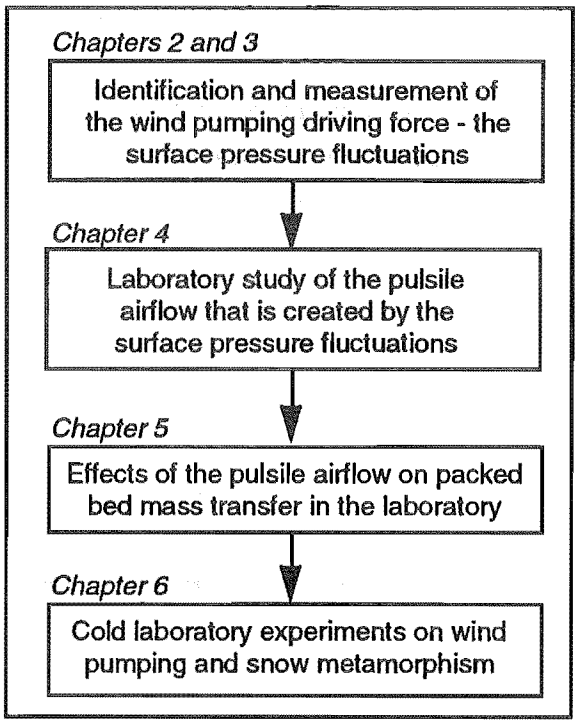

Figure 1.7. Progression of the Overall Experimental Programme.

1.10.1. Chapters 2 and 3 - Atmospheric Turbulence

Atmospheric turbulence, and the pressure fluctuations that result on the surface, is the driving force behind the wind pumping mechanism. To date, few measurements of fluctuating wind speed, and no measurements of fluctuating surface pressure have been made over mountain terrain.

Therefore it was the purpose of the work described in Chapters 2 and 3 to determine the amplitude and frequency characteristics of the surface pressure fluctuations, and to identify the likely characteristics of the atmospheric turbulence over alpine terrain during strong winds. This is done both from a literature review in Chapter 2, and a series of measurements in Chapter 3.

The characterisation of the driving forces is considered to be a critical component to the study of wind pumping. Consequently it receives considerable attention in this thesis. Let the reader beware; the review of atmospheric turbulence contained in Chapter 2 crosses many disciplines and is heavy reading. The complexity of the topic is perhaps one reason why it has been given such little attention to date.

1.10.2. Chapter 4 - Wind Pumping Airflow Dynamics

To make any inferences on the mass transfer effects of wind pumping, it is essential that the dynamics of the airflow within the snow pack, due to a fluctuating surface pressure, are known.

In the literature to date, the dissipation of the surface pressure fluctuations in a permeable bed, and the pulsile airflow that is created has mainly received theoretical attention. The mathematical theories of wind pumping airflow dynamics within a permeable bed have been experimentally examined and reported. Following this, the proposed models were applied over a wide range of snow pack conditions to give estimates of the possible air speeds and displacements in the snow pack due to wind pumping.

1.10.3. Chapter 5 - Packed Bed Mass Transfer

The purpose of taking such a careful look at wind pumping is to determine whether it has any effects on dry snow metamorphism. Since the base assumption of *water vapour diffusion rate limiting*[1] is behind the theory of dry snow metamorphism, it follows that the effects wind pumping airflow has on diffusion in a packed bed should be investigated.

Studies have been reported in the literature of diffusive mass transfer enhancement in a packed bed under pulsile airflow in connection with water vapour losses at a soil surface. A similar series of diffusion experiments in a packed bed have been carried out and reported. A conceptual discussion into the effects of wind pumping airflow on vapour transport in a porous medium follows these results.

1.10.4. Chapter 6 - Wind Pumping in Snow

No previous direct observations or measurements have been made on the effects of wind pumping in a controlled environment. The justification for such measurements are clear given the results of Chapter 3, 4 and 5.

The first objective of the work in Chapter 6 was to design and build an experimental apparatus capable of measuring the metamorphic effects of wind pumping on snow samples in a controlled cold laboratory environment. This was then used to determine the effects the pulsile airflow derived from wind pumping could have on the metamorphism of dry snow.

1.10.5. Chapter 7 - Summary of Conclusions

In Chapter 7 the key conclusions for the thesis are summarised. This includes some recommendations of further work.

---

[1] At very high excess vapour densities, surface kinetics can also have a controlling influence.

Chapter 2
Review of Atmospheric Turbulence

The primary objective of this review is to identify the likely characteristics of atmospheric turbulence over alpine terrain during strong winds, and to determine the amplitude and frequency characteristics of the driving forces behind wind pumping.

2.1. Table of Contents

2.2. List of Illustrations

2.3. Nomenclature

A_i	gust amplitude (Pa)
B	stream wise dimension (m)
b	separated shear layer thickness (m)
C_p	rms pressure coefficient
D	cross stream dimension (m)
f*	reduced frequency parameter
Fr	Froude number
Fr_b	Froude number for breaking gravity waves
Fr_c	critical Froude number
g	gravitational constant (m/s^2)
H, h	vertical relief or object height (m)
n	frequency (Hz)
N	Brunt-Väisälä (buoyancy) frequency (Hz)
p	dynamic pressure fluctuation (Pa)
p(t)	pressure fluctuations time series (Pa)
S_{tr}^r	Strouhal number based on the reattachment length
S_{tr}^h	Strouhal number based on the obstacle size h
S_{tr}^D	Strouhal number based on the cross stream dimension D
T	moving average period (s)
T_i	gust duration (s)
U	free stream velocity or mean ridge top wind speed (m/s)
u	wind speed fluctuation (m/s)
u(t)	wind speed fluctuations time series (m/s)
U_{sl}	average velocity in the separated shear layer (m/s)
v(t)	wind speed time series (m/s)
$\hat{v}(t,T)$	moving average wind speed time series (m/s)
$\overline{V}$	average wind speed (m/s)
X	stream wise separation (m)
X_r	reattachment length (m)
z	atmospheric height (altitude) (m)
λ	wavelength (m)
θ	potential temperature (K)
$\hat{\sigma}^2(t,T)$	short time period variance series (m^2/s^2)
σ_u^2	variance (m^2/s^2)
τ	time scale and period (s)

2.4. Introduction

Strong and gale wind storms are common occurrences over the Southern Alps of New Zealand, the area in which the turbulence measurements of Chapter 3 are made. It is the objective of this chapter to identify from the literature both a qualitative and quantitative understanding of the atmospheric turbulence associated with such winds.

Gustavsson and Linde (1979) comment that gusts in the *atmospheric boundary layer* (ABL) are coherent structures which have distinct features. The same kind of structures have been found in the well researched laboratory scale turbulent boundary layers. This leads to research in the following fields in the quest for possible associations between boundary layer flow and the wind pumping mechanism:

1. *Gust structure and statistics from interests in wind energy.* The same energy containing frequencies that are important in wind energy research (micrometeorological scale) is expected to be of importance in wind pumping. Colbeck (1989), in his initial study on the wind pumping mechanism, ignores frequencies lower than this (synoptic scale), an assumption that is not disputed in this thesis.

2. *Atmospheric turbulence from a meteorological and geophysical point of view.* Contributions in this area (mesometeorological scale) become important with terrain on the scale of the boundary layer thickness, as is the case in the mountainous terrain considered in this study.

3. *Extreme wind events and wind speed fluctuations from the point of view of structural design and forestry* (strength and excitation). Extreme events are of little interest, but the work field contains a lot of information on surface pressure sensing and bluff bodies.

4. *Structure of turbulence as a science itself.* This embodies all aspects up to the micrometeorological scale. The fact that snow acts as a low pass filter (dampens high frequency components) limits the usefulness of a large proportion of the material in this field (which tends to consider relatively high frequency phenomena) to this wind pumping study.

5. *Pollution dispersion through atmospheric turbulence.* This field deals mostly with problem areas associated with dispersion such as very stable stratification (inversions). Stable stratification becomes relevant for very large hills and so some of the work from this area is useful.

This represents a huge body of literature applicable to a wide range of scales and conditions. Only a small portion of these studies are relevant to the large scales of complex terrain

applicable to this wind pumping study. The search for pertinent information is narrowed by keeping two aspects of the wind pumping mechanism in mind:

1. The driving force necessitates repeating cycles of large amplitude.
2. High atmospheric turbulence frequencies (>1 Hz) are likely to be filtered out.

An appropriate approach to this task is to try to gain a physical understanding of the origin of the turbulence components in relation to the prevalent atmospheric conditions and terrain features. Whilst the work on turbulent boundary layers over simple flat and uniform geometries may offer some insights (see for example Raupach *et al*, 1991), this review concentrates on measurements from studies with less uniform geometries.

The review starts out on the less directly related, but more widely studied, wind phenomena. As the review develops, seemingly abstract topics, which relate more directly to this wind pumping study, are brought into perspective.

More specifically, to build a conceptual picture of the expected turbulence structure in mountainous terrain, a brief review is made of the *strong winds* work (average wind speed greater than about 10 m/s) over *flat terrain* (flat, uniform surfaces), *low hills* (where buoyancy forces are negligible) and *complex terrain* (changing terrain character). This sets the platform for looking at the more difficult, larger terrain scales, where buoyancy forces cannot be considered negligible.

Most ABL surface layer investigations are limited to wind speed measurements. To gain some idea of what pressures fluctuations are felt on the ground surface in mountainous terrain, some relevant work performed on tall buildings is reviewed. To fill in the gaps where measurements and/or knowledge are scarce, some work on laboratory scale turbulent boundary layers is also reviewed.

In Chapter 3 the experimental programme measuring the magnitude and extent of the wind pumping driving force is described. At the end of this chapter, in preparation for the experimental work, some background on the statistics required for the analysis of turbulence data is given.

The discussion at the end of Chapter 3 compares the conclusions of this chapter to the experimental measurements made in Chapter 3.

2.5. Overview of the Turbulent Atmospheric Boundary Layer (ABL)

Atmospheric flow is highly unpredictable and hence falls into the category of turbulent flow.

Pressure gradients and associated winds in the free atmosphere are generated by differential heating from solar radiation and the rotation of the earth. Above a certain height, 200 to 2000 m or more, surface friction forces can be ignored, so that the main forces controlling the horizontal mean motion are the large scale pressure forces, the forces due to the curvature and rotation of the earth, and the centripetal forces due to the curvature of the isobars. The wind resulting from the balance of these forces is called the *gradient* or *geostropic wind.* The height above the ground at which the gradient wind speed is first obtained is called the *gradient height.* Above the gradient height lies the *free atmosphere.*

The *Atmospheric Boundary Layer* (ABL) is located between the ground and the gradient height. The wind within the ABL is retarded by the effects of surface roughness transmitted upwards as Reynolds Stresses. *The process of momentum exchange between layers is the mechanism leading to the generation and decay of eddies, collectively known as turbulence.* The resulting mixture of air produces fluctuations in wind speed (*gusts*), temperature, pressure and humidity which vary in both time and space.

The atmosphere normally exhibits a stable vertical density stratification, being most dense at surface and thinning with elevation. Large scale vertical movements of air, caused by roughness elements on the scale of the ABL, convective cells, or horizontal shear forces, may in turn cause the vertical stratification to become distorted and gravity waves to be generated. These waves, which exist in the ABL, may dissipate, contributing to the total turbulence in the ABL.

The fundamental aspects of the ABL get excellent treatments from Plate (1982), Stull (1988) and Lesieur (1990). Note that in Lesieur, many of the fundamental turbulence ideas are applied to the atmosphere. Therefore this chapter only reviews those topics viewed as potential contributions to the wind pumping driving force.

2.6. Atmospheric Stability

In describing the atmospheric stability, distinction is made between local definitions and larger scale stability. On a local scale (within the *surface layer* - approximately the bottom 10% of the ABL), the stability can be dominated by surface generated turbulence, while on a larger scale stability is less influenced by the surface generated turbulence. The former description is common in wind engineering, while the latter is more relevant from a geophysical point of view.

On the local scale, the air is said to be *statically unstable,* if lighter air underlies more dense air (it wants to rise to equilibriate the imbalance resulting in convective turbulence) and *statically stable* if lighter air overlies the denser air. *Neutral static stability* exists at the interface between these cases.

In defining *dynamic stability* the effects of wind, surface roughness, and resulting mechanical turbulence need to be taken into account. Whereas *mechanical turbulence* rapidly increases in intensity with wind speed, the larger thermally derived convective motions tend to be dampened. When statically stable layers are mixed through the powerful action of mechanical turbulence, a state of *neutral dynamic stability* can be created. Cloud cover blocking radiation exchanges between earth and atmosphere allows this process to occur at less intense levels of mechanical turbulence.

In the surface layer for strong winds, surface roughness elements are not required (flat terrain and low hills) for a state of neutral dynamic stability to occur. Over ground, where the terrain features are large compared to the ABL depth (hilly terrain), the interaction between terrain and ABL can reduce a large portion of the atmosphere to a state of neutral dynamic stability (Davenport, 1961).

On a larger scale (large mountain ranges), the atmosphere's inherent strong stable stratification (buoyancy forces acting against vertical displacement) prevents surface generated turbulence from affecting the free atmosphere to the same extent. At this point some of the definitions become somewhat confused. For example, gravity waves generated in a stably stratified flow create buoyancy instabilities which may result in turbulence production.

This study investigates the typically turbulent strong mountain winds which are a feature of New Zealand's maritime climate. Neutral dynamic stability is expected from the wind engineering point of view, but given the terrain scale, the effects of stable stratification may also be of some importance. For example, Thompson *et al* (1991) find that, in an initially moderately stable flow over isolated three dimensional terrain, dynamic neutral stability is approached at the higher Froude number[1] of $Fr \approx 4$. This Froude number is well above an estimate of $0.5 < Fr < 2.0$ for the Arthur's Pass area made in section 2.8.3.1 (indicating stable stratification).

[1] Froude number is defined in section 2.8.3.1.

2.7. Atmospheric and Terrain Scales

The Van der Hoven spectrum for horizontal wind speed shown in figure 2.1 (Van der Hoven, 1957) identifies three spectral peaks in the frequency range 0.0007 to 900 cycles per hour (0.25 to 2×10^{-7} Hz). These peaks arise from natural meteorological scales described by Fiedler and Panofsky (1970), the precise limits of which are open to conjecture.

Period	Scale	Brief Description
> 48 hrs	Synoptic	Weather map scale systems
1 hr - 48 hrs	Mesoscale	Diurnal variations, frontal structures and long wavelength gravity waves
< 1 hr	Microscale	Mechanically driven eddies, convective cells and short wavelength gravity waves

The Van der Hoven spectrum shows a wide spectral gap between the micro and mesoscale peaks which he attributes to the lack of a physical process which could support wind speed fluctuations in this frequency range. This gap is discussed in more detail by Fiedler and Panofsky.

Gossard (1960) produced a similar spectra for atmospheric pressure fluctuations measured near the surface over the frequency range 0.006 to 720 cycles per hour (5 to 1.7×10^{-6} Hz). The spectra, shown in figure 2.2, does not show the same spectral gap observed in wind speed fluctuations. Possible mechanisms producing pressure fluctuations in this frequency range were identified as gravity wave activity at higher elevations (Herron et al, 1969) and convective cells in the unstable ABL. The high frequency end of the pressure spectrum must be considered with caution as full scale measurements of atmospheric pressure fluctuations were not accurately available until Elliott (1972a). Despite this, the spectral shape is not generally disputed by later work (Elliott, 1972b and Grachev and Mordukhovich, 1988). However, Elliott (1972b) does note some differences at low frequencies which may be due to contamination from mesoscale sources, presumably gravity wave activity. Gossard does not establish the microscale peak identified in the spectral representations (parallel with wind speed representations) of Elliott (1972b) and Schols and Wartena (1986).

Colbeck (1989) discusses the relative importance of differing scales of fluctuation to possible wind pumping affects on snow metamorphism. He effectively discounts synoptic and mesoscale contributions to wind pumping (this point is not disputed here), but does not recognise the existence of the pressure fluctuations in the spectral gap of wind speed fluctuations. The variety of possible contributions to the microscale fluctuations are discussed in detail in the next section.

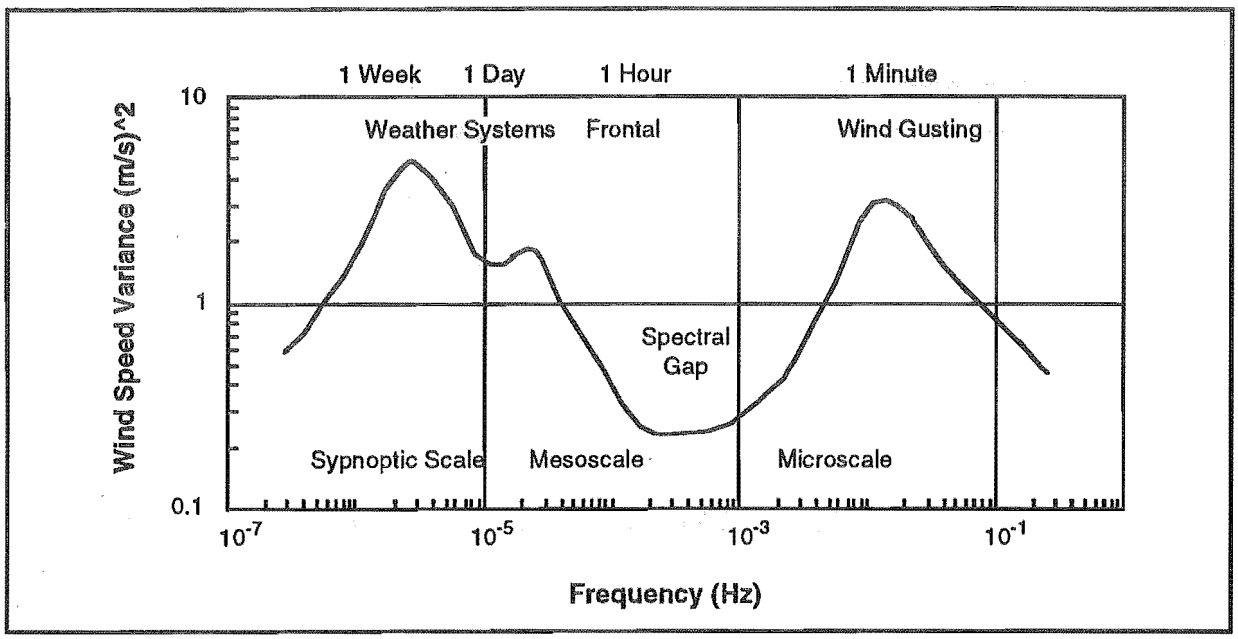

Figure 2.1. The Van der Hoven (1957) Spectrum for Wind Speed Fluctuations.

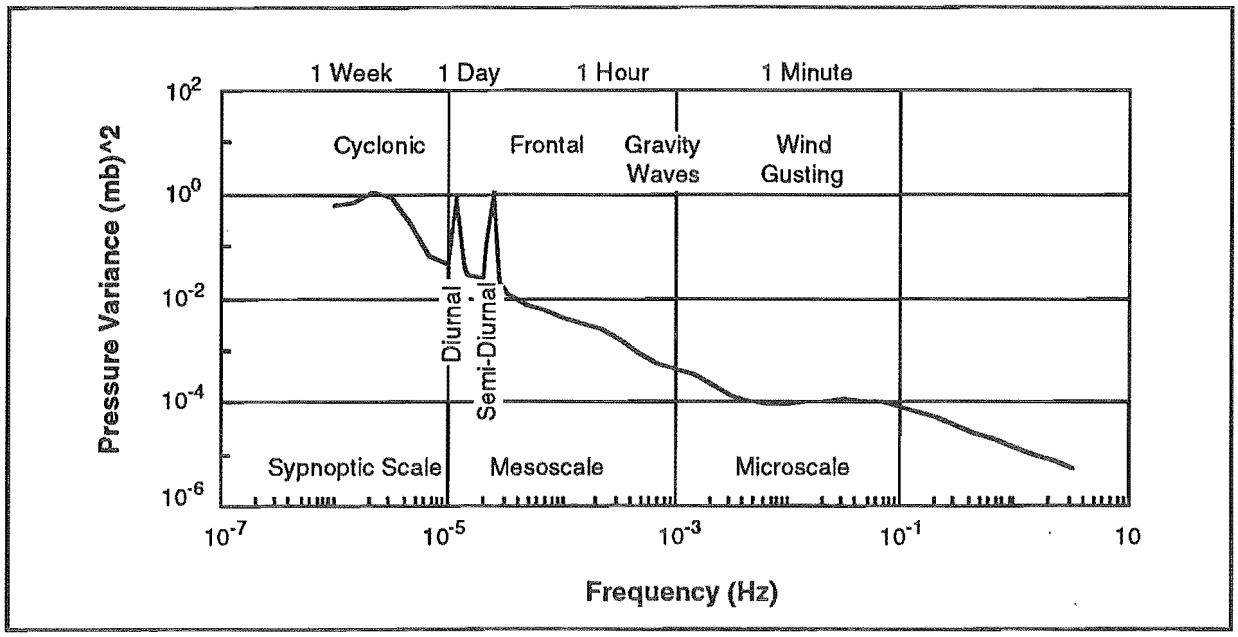

Figure 2.2. The Gossard (1960) Spectrum for Near Surface Atmospheric Pressure Fluctuations.

2.7.1. Microscale Fluctuations

The peak in the Van der Hoven spectrum at a period of about 1 minute may be due to many generation mechanisms; however Van der Hoven makes no attempt to distinguish between these. Bowen (1979) identifies many factors which may contribute to turbulence generation on this scale. Extending on Bowen's list, the following potential contributions to the generation of turbulence are likely to be relevant in large scale mountains:

1. Upwind velocity and temperature profiles
2. Extent of the mountain range
3. Geometry of individual mountains such as the length, height and overall shape
4. Scale of the the range and the mountains compared to ABL depth
5. 'Second order' surface features of the mountain slopes, such as the curvature at the ridge crest and the presence of gullies and minor ridges
6. Surface roughness of the mountain slopes
7. Three dimensional effects such as ridge length, nearby valley systems and shelter from upwind mountains
8. Angle of incidence between wind direction and ridge crest line
9. Flow separation behind terrain features and effect of the leeward slope
10. Thermal stability of the ABL
11. Local radiation heating and cooling of the flow by sunny and shaded slopes, and nocturnal cooling (in low wind conditions).

All contributions except 10 and 11 play a role in mountain turbulence during wind storms indicating the complexity of the problem presented in large scale mountains.

2.8. Wind Speed Fluctuations in the ABL

The approach of researchers to this topic has been evenly balanced between the accumulation of turbulence data, and the fitting of that data to the models developed. Only in this way has the understanding of the structure of atmospheric turbulence been understood.

Unfortunately, the models developed to date cannot be applied to the large scale, complex terrain under consideration in this wind pumping study. Consequently, the models themselves are not reviewed in the following discussion, rather the review is made to gain as much insight into the patterns and degree of expected turbulence from the various observations made to date.

An illustration of the applicable limit to the developed models was made by Reid (1983). Reid attempted a scale up of the wind speed up relation developed by Jackson and Hunt (1975) in various New Zealand mountains. He found it was limited to 1200m hills of moderate slope.

2.8.1. Uniform Surfaces and Low Hills

ESDU 74026, 74030 and 74031 (1974) summarises the statistical correlations used in turbulence analysis (turbulence intensity, autocorrelation, turbulence length scales and autospectral density) and field data for strong winds (where a neutral atmospheric stability is assumed) over a variety of surface roughness collated from global research prior to 1974. Much of the information in these documents cannot be used directly here. The mountain terrain scales studied in this thesis extend well beyond the range of scales covered by the data sets. Also, since its publication, new results have been obtained which modify the thinking of 1974. Harris (1990) for example points out the deficiencies in the spectral formulas used by ESDU.

Since ESDU, further turbulent statistics over uniform terrain have been collected. See, for example, Kaimal *et al* (1972), Kaimal (1973), Flay (1978) and Chen (1990). Basic to these studies is the assumption that the upper level flow does not directly sense the presence of the ground surface (Nieuwstadt, 1984, and Nappo and Chimonas, 1992). Einaudi and Finnigan (1981) and Finnigan and Einaudi (1981) clearly show that the presence of atmospheric gravity waves could cause erroneous conclusions under this assumption (these points are further discussed in section 2.8.3).

A great deal of work has been done on the effects of single, relatively smooth, low aspect hills since Jackson and Hunt (1975). See, for example, Bradley (1980), Smedman and Bergström (1984), Mason and King (1985), Mason (1986), a review by Taylor *et al* (1987) and Hunt *et al* (1988b). According to Smith (1979) and Taylor *et al* (1987), these studies have generally been restricted to small low aspect hills where the effects of buoyancy forces under topographic forcing can be neglected.

There are several recent departures from this trend. Hunt and Richards (1984) looked theoretically at the effects of hills on stratified flow, bringing together in a review paper ideas from fluid mechanics and microscale and mesoscale meteorology. Hunt *et al* (1988a) continue this work explaining theoretically much of the observed two and three dimensional behavior of strong stratification (when vertical accelerations are negligible) and for high Froude number ($Fr \gg 1$) over low hills where the buoyancy forces in the inner layer are considered weak. Taylor *et al* (1987) comment that data should be collected to compare against these models.

The low hill assumption is unlikely to be applicable for the mountainous terrain considered in this thesis; thus attention is turned toward treatments of complex and mountainous terrain, where less uniform surfaces are studied.

2.8.2. Complex Terrain

Panofsky *et al* (1982) brought together spectra over a variety of *complex terrain* cases (changing terrain character). Their paper represents a summary of much of the work carried out over the mid to late 70's and early 80's. Their findings conclude that the high frequency spectral densities of the longitudinal velocity depend on local surface features, while low frequency densities reflect the features further upstream. A recent review by Garratt (1990) concludes that the boundary layer response to multiple step changes in surface properties remains a major unsolved problem.

Little work appears to have been carried out over the different aspects of larger scale terrain, especially terrain exhibiting leeward separation. Gallagher *et al* (1988) did make observations over a long 655 m hill; however they were not concerned with any low frequency behavior. On a smaller scale, but with a three dimensional shape, Mason (1986) studied the flow at the summit of a 70 m conical hill and Jenkins *et al* (1981) made measurements over an isolated elliptical island roughly 1 km in diameter and 330 m high with flow reversal on the lee slope. Jenkins *et al* found that most of the down and cross wind component spectral energy on the leeward aspect is at very low frequencies (0.001 to 0.01 Hz). They related this to the time scale of the wake fluctuations. They did not observe shedding of vortices, but identified shifts in wind direction with periods of 5 to 6 minutes. This possibly indicates the large scale variations of the separated region.

Even less work has been published on two or more successive hills or full scale mountain terrain. Mason and King (1984) made measurements over a succession of 200 m approximately two dimensional ridges with marked flow separation. At the summit of the ridge they found the turbulent statistics to be broadly similar to those over level terrain. More importantly, they found the standard deviation of wind speed in the valley was much greater than the summit when the mean wind direction was perpendicular to the valley. Frequency spectra obtained in the valley suggest that eddies on the scale of the valley make a major contribution to this turbulent energy. With their short sample lengths (800 s), and linear trend removal, they could only obtain limited knowledge of the low frequency response to the terrain. Given that ABL has a 'long memory' to large perturbations (Panofsky *et al*, 1982) (the decay of large structures is very slow), one would expect some changes to the turbulence characteristics to be observed at the ridge top (Panofsky and Ming, 1983, Hunt and Richards, 1984 and Smedman and Bergström, 1984). It is also noted that the terrain scale is at the limit for buoyancy forces to be ignored (Smith, 1979), and so gravity waves may be expected.

Grant and Mason (1990) continued the work in and around the separated flows using the same location as Mason and King (1984). They calculated a 'regional' roughness length which accounted for the large scale terrain features and separation. Using this they found the

turbulence statistics and spectra to be very similar to results obtained over flat homogeneous terrain. Tieleman (1992) takes a similar approach, defining 'local' and 'regional' roughness lengths which account for the behavior observed by Panofsky *et al* (1982) discussed above. Grant and Mason emphasise that the calculation and use of the roughness length over complex terrain assumes logarithmic mean wind profile, and that a similar dependence of surface stress on wind shear exists over flat terrain. This assumption is not made in this thesis because no information is available on the velocity profile. Consequently, no attempt can made to base estimates off roughness lengths. This decision is supported by Föhn (1980), Mitsuta *et al* (1983) and Meister (1987) who show large deviations from the logarithmic profile at ridge top in mountain terrain and Patel *et al* (1991) who find that the logarithmic profile breaks down in the presence of separated flow and strong stream wise pressure gradients over wavy surfaces.

Smedman (1991) compares the turbulence statistics for seven sites with different terrain. The characteristic shapes of the spectral and co-spectral distributions were found to be site independent. In contrast, Tieleman (1992) finds that for increasingly complex upwind terrain, the spectral densities in the low reduced frequency range ($f_0 < 0.2$ Hz) are systematically larger than those observed over near uniform terrain. As well as increasing in magnitude, the spectral peaks also move to lower reduced frequencies.

In the most severe terrain application known to this author, Reid (1983) studied gust factors (highest wind speed compared to mean wind speed) at various mountain sites in New Zealand. He associated unusually high gust factors with wakes of steep upstream ridges, rather than the inner layer which develops over the promontory on which the anemometer is sited. These findings are in line with the observations of Panofsky *et al* (1982).

The most direct contributions to this thesis come from Mitsuta *et al* (1983), Meister (1987) and Antoniou *et al* (1992).

Mitsuta *et al* investigate the spatial distribution of wind gusts using 28 anemometer sites covering windward, ridge top and leeward aspects, in very rough terrain with a maximum vertical relief of 300m. They conclude that the mean wind speed, and to a lesser extent the wind speed fluctuations, are highly correlated to anemometer position relative to terrain features, and that the resulting power spectra are highly distorted.

Gallagher *et al* (1988) found greater turbulence levels and higher spectral levels at high frequencies closer to the edge of a summit on a 655 m two dimensional ridge where 'lip effects' were present. The spectra observed by Mason (1986), upstream and at the summit of a three dimensional 70 m conical hill, show larger spectral estimates at the summit at high frequencies with the difference being accentuated closer to the ground.

In a study of snow drifting over a ridge top at 2690 m ASL (above sea level), Meister (1987) measured a spectrum of horizontal wind speed fluctuations in a similar fashion to Van der Hoven (1957). He found the microscale peak occurred at about 0.08 Hz and the spectral gap at about 0.0003 Hz, the precise location of the spectral gap being dependent on the severity of the terrain.

The study by Antoniou *et al* (1992) over complex hilly terrain shows pronounced differences in wind spectra and turbulence length scales at the same site for different wind directions, reflecting the changes in wind structure due to terrain configuration.

It is worth noting one recent study by Andreas (1987) who investigates the boundary layer over a snow covered field. At low frequencies, the resulting spectra is dominated by upstream roughness elements (trees and 100 m hills), and possibly gravity waves. At high frequencies the resulting spectra is dominated by the local snow surface. Nappo and Chimonas (1992) would support the assertion that gravity waves could affect the spectra over terrain with 100 m vertical relief. Andreas concludes that the snow surface had little effect on the overall spectra.

2.8.3. Mountain Terrain

Smith (1979) reviews this topic from the geophysical point of view noting the atmosphere is extremely sensitive to vertical motion. Its inherent strong, stable stratification resists vertical displacement in such a way that buoyancy forces will try to return vertically displaced parcels of air to their equilibrium level, even if such restoration requires broad horizontal excursions or the generation of strong winds.

Such vertical displacements may be generated by:

1. Obstruction by terrain features forcing displacement from one environment to another
2. Horizontal wind shear destabilising a stratified flow
3. Heating or cooling of air parcels resulting in convective turbulence

The terrain scale of around 1000m studied in this thesis implies that the boundary layer thickness is small in relation to the scale of the flow. Consequently the buoyancy forces associated with the atmosphere's static stability are important, the flow outside the boundary layer cannot be considered irrotational, and internal gravity waves become possible (Smith, 1979). Indeed, over the Southern Alps of New Zealand in which the measurements in Chapter 3 are made, such mountain waves are a prominent feature of north westerly quarter storms, accompanied by downslope windstorms and indicative cloud forms.

It is assumed that the obstruction by terrain features is the dominant generation mechanism in this study. This is because the typically strong winds and cloud cover eliminate the development of convective cells, while the very large scale of terrain promotes topographic forcing. These waves are often described as mountain or lee waves. This view is supported by Peltier and Scinocca (1990) in their investigation of wave breaking (see below) as a mechanism for severe downslope windstorms.

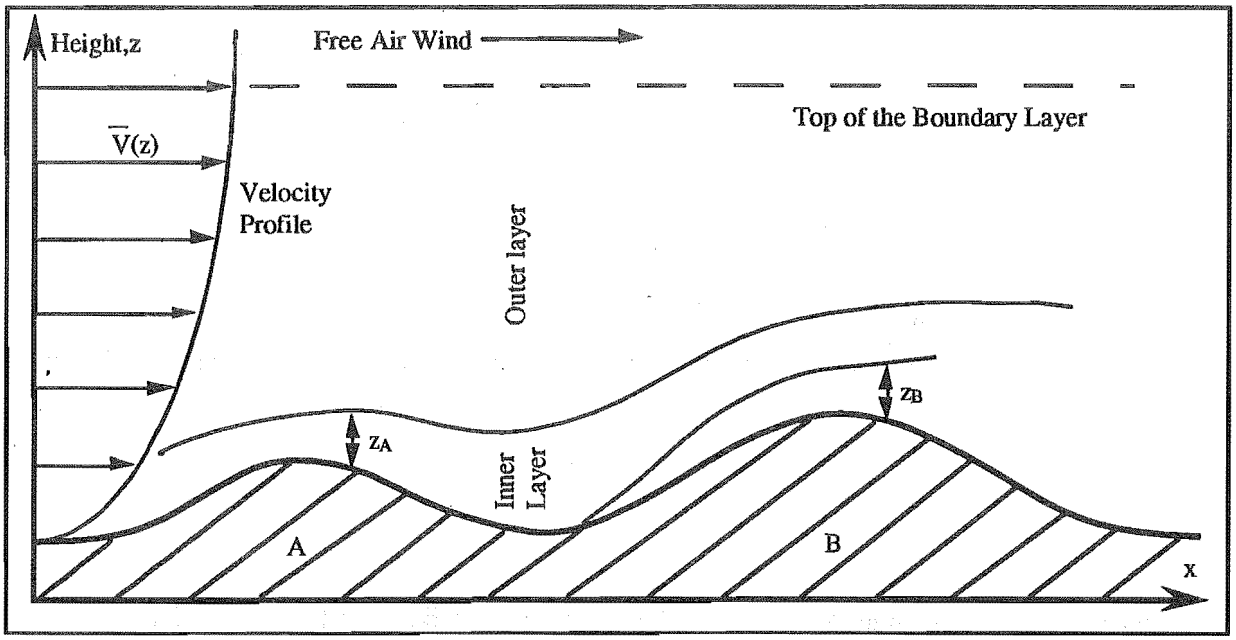

Figure 2.3. Schematic Diagram of Air Flow Over Two Hills from Hunt and Richards (1984) Showing the Inner and Outer Layers of the Boundary Layer. $\overline{V}(z)$ is the upwind mean velocity profile and z_A and z_B are the inner regions of hills A and B respectively. The inner region of hill B grows within the wake of the inner region of hill A.

A review on stratified flow over one or two (relatively low) hills by Hunt and Richards (1984) contains some useful definitions for this thesis (see figure 2.3), however, most of their discussion is rather too idealised to apply to the Arthur's Pass terrain. They define an inner region which develops over a second hill that is thickened by the inner region (which becomes the wake) of the first hill; a viewpoint which is strongly supported by Buckles *et al* (1984) in laboratory studies over wavy surfaces. According to Hunt and Richards, the turbulence in the inner region, which has a thickness of much less than the scale of the hill, results from the local surface conditions and the wake of any previous hill. They note that because the inner layer is thin, the hill displaces the flow above it, leading to accelerations and buoyancy forces in the outer region. If the scale of the terrain is large compared to the boundary layer thickness, this effect will go higher where internal waves are generated in the stratified flow.

2.8.3.1. Degree of Stratification and Consequences of Topographic Forcing

This portion of the review uses two key parameters which require definition. Firstly, the natural wavelength of the air, or Brunt-Väisälä (buoyancy) frequency N, is given by

$$N = \sqrt{\frac{g}{\theta}\frac{d\theta}{dz}} \qquad 2.1$$

where θ is the potential temperature, z height and g the gravitational constant. Typically $\theta \approx 283\,K$ and $d\theta/dz \approx 0.007\,K/m$ (the moist air adiabatic lapse rate). This gives $N \approx 0.016\,Hz$.

Secondly, the Froude number Fr, which compares the natural wavelength of the air to the terrain dimensions, is usually defined as

$$Fr = \frac{U}{NH} \qquad 2.2$$

where U is the mean ridge top wind speed and H is the vertical relief. For the Arthur's Pass area (see section 3.6.2), $H \approx 1000\,m$ and typically $10 < U < 30\,m/s$ which gives $0.5 < Fr < 2$ and typical length scales $600 < U/N < 2000\,m$.

The generalised patterns of lee wave activity around an isolated hill for different Froude numbers is illustrated in figure 2.4.

When the horizontal velocity component of a lee wave is equal and opposite to the background wind speed (the wave is 'standing'), the flow streamlines become vertical and a blocking condition exists (see figure 2.4 (a)). Baines (1987) presents a recent review of upstream blocking and air flow over mountains. Further increase in the wave amplitude results in a convective instability and wave breaking (Smith, 1977). Figure 2.5 shows a sketch of breaking gravity waves taken from a series of dye visualisation experiments by Castro *et al* (1983).

Numerical studies by Peltier and Clark (1979) and Clark and Peltier (1984) show that within such wave breaking regions a wave induced critical layer is generated and wave reflection rather than wave absorption occurs[2]. They predict the observations of Baines and Hoinka (1985), that wave amplitudes are large below the critical layer and very small above. However, the wave reflection is far from perfect as experiments by Rottman and Smith (1989) show.

---

[2] Critical levels occur whenever the component of the background wind in the plane of the wave vanishes, that is, where this component reverses direction.

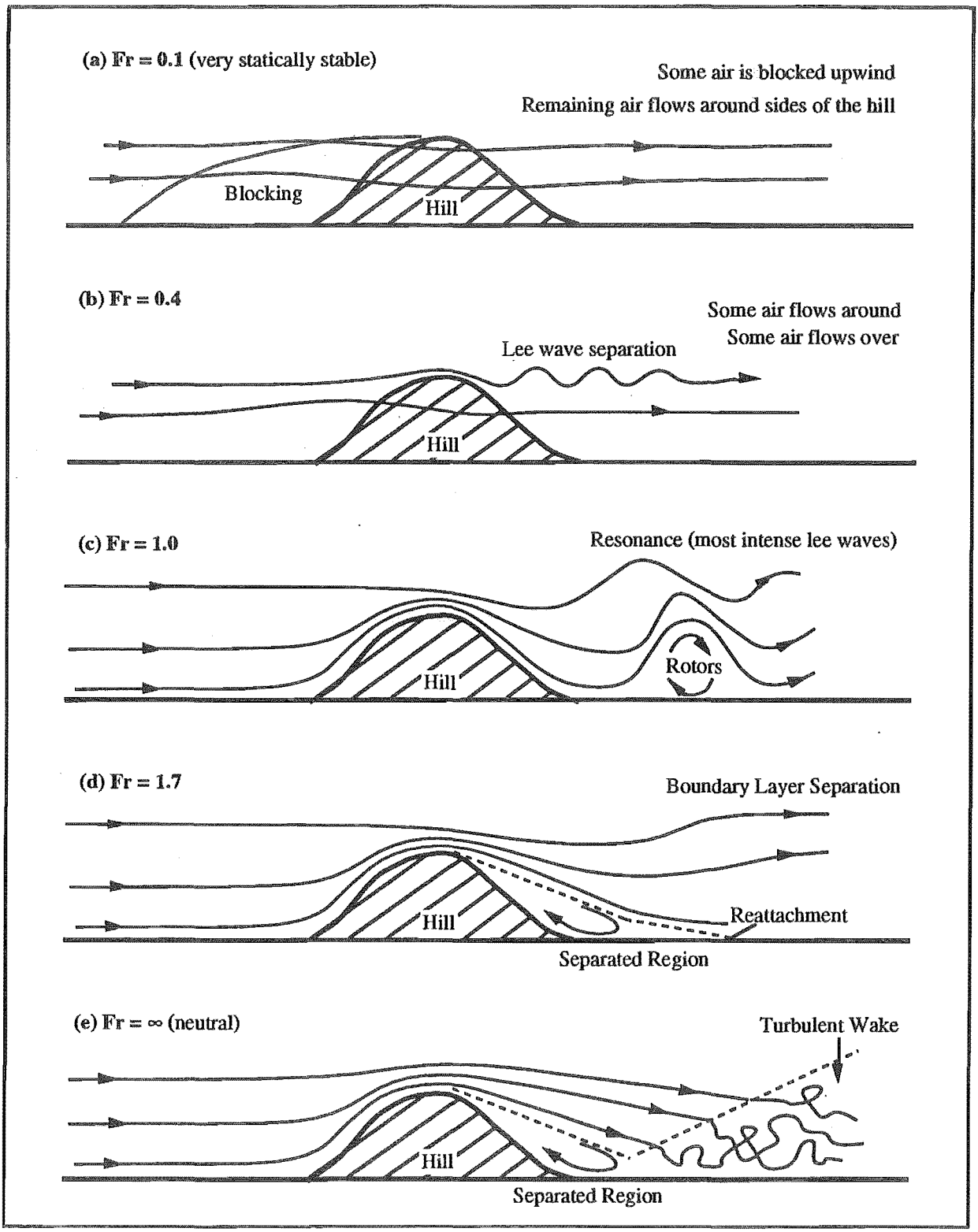

Figure 2.4. Generalised Separation Patterns Behind an Isolated Hill for Froude Number from Stull (1988).

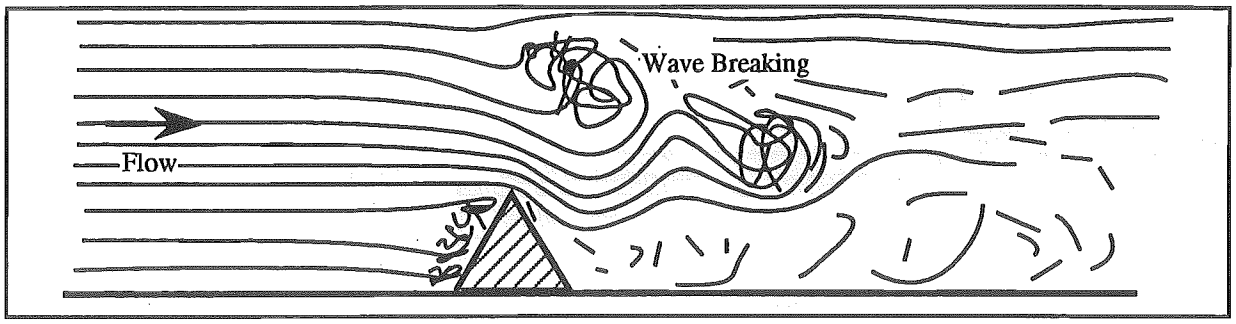

Figure 2.5. Breaking Gravity Waves Sketched from the Visualisation Experiments of Castro *et al* (1983) for a Froude Number Fr = 0.4 Flow about a Three Dimensional Triangular Ridge.

Strong downslope winds are linked to breaking waves, where low level air parcels experience permanent acceleration as they cross the mountains and do not return to their far upstream state. See, for example, Clark and Peltier (1977). Such strong winds are a feature of the northwest storms in the region where the measurements of Chapter 3 are made. Also, typical flow conditions on the valley floor in this area are relatively quiet (compared to higher on the mountains) indicating the occurrence of blocking and/or separated flow.

Gravity wave blocking and breaking occur at low Froude number, although the critical Froude number Fr_c which may indicate the onset of blocking has yet to be agreed upon. For breaking gravity waves, the Froude number Fr_b must be smaller than that for the onset of blocking. Tables 2.1 and 2.2 summarise the values obtained for Fr_c and Fr_b respectively. With the exception to the experiments by Castro *et al* (1983), all the data comes from two dimensional studies.

Two further features of breaking gravity waves; firstly, Rottman and Smith (1989) find that the region of mixed fluid produced by wave breaking is small for smaller Froude number, and becomes increasingly larger for increasing Froude number. Once the critical Froude number is reached, wave breaking ceases to occur; secondly, Castro *et al* (1983) observe that the wave breaking is relatively localised which significantly reduces the amplitudes of the remaining waves.

Topographic forcing and resulting mountain waves have been found to be a function of atmospheric flow, thermal profiles, terrain shape and terrain amplitude. More specifically, Baines and Hoinka (1985) and Lilly and Klemp (1979) found that blocking and wave breaking can occur at higher Fr for steeper terrain. It appears that the numerical models for smooth sinusoidal terrain will underestimate the extent of critical lee wave activity. The literature values of Froude number for blocking and wave breaking lie within the range estimated for these experiments (calculated as between $0.5 < Fr < 2$ for the Arthur's Pass area).

Fr_c	Source	Scale	Terrain	Author(s)
$Fr_c \approx 2.3$	measured	full scale	ridge	Kitabayashi (1977)
$Fr_c \approx 2.3$	measured	wind tunnel	" "	" "
$Fr_c \approx 1.3$	measured	wind tunnel	saw toothed valleys	Bell and Thompson (1980)
$Fr_c \approx 1.3$	numerical	-	" "	" "
$Fr_c \approx 0.5$	measured	wind tunnel	asymmetric ridge	Baines and Hoinka (1985)
$Fr_c \approx 0.9$	measured	wind tunnel	symmetric ridge	" "
$Fr_c \approx 2.8$	numerical	-	sinusoidal valleys	Kimura and Manins (1988)
$Fr_c \approx 1.5$	measured	wind tunnel	" "	" "

Table 2.1. Critical Froude Numbers from the Literature.

Fr_b	Source	Scale	Terrain	Author(s)
$Fr_b \approx 0.8$	numerical	-	ridge	Lilly and Klemp (1979)
$Fr_c \approx 0.4$	measured	towing tank	3D triangular ridge	Castro *et al* (1983)
$Fr_b \approx 1.3$	numerical	-	sinusoidal valleys	Kimura and Manins (1988)
$Fr_b \approx 1.0$	measured	towing tank	gentle ridge	Rottman and Smith (1989)
$Fr_b \approx 0.8$	measured	towing tank	steep ridge	" "

Table 2.2. Froude Numbers for the Onset of Wave Breaking from the Literature.

2.8.3.2. Breaking Waves and Turbulence

Other than the contribution of breaking waves to downslope wind speeds, little specific information is available on the effects breaking waves have on the structure of boundary layer turbulence near the ground. It is well known that turbulence is produced in the regions of wave breaking. See, for example, Finnigan (1988). This concept is reviewed by Itsweire *et al* (1986) and Lesieur (1990). Of interest here is whether the acknowledged wave generated turbulence is felt at ground level, or if other possible effects (derived from the wave activity) exist that could generate the turbulence at ground level.

Whilst there is a huge body of literature on gravity waves, very little has been directed to surface generated gravity waves in the boundary layer, and almost none to the role they play in the dynamics of the boundary layer mean flow. Nappo and Chimonas (1992) predict numerically that wave drag will act on the mean flow at a boundary layer critical level, generating discrete regions of turbulence. They find that, without critical levels, wave dissipation is quite weak. Thus, for waves to affect the boundary layer, critical levels are probably required. Critical levels occur whenever the component of the background wind in the plane of the wave vanishes, that is, where this component reverses direction.

Hunt and Snyder (1980) show lee vortices in a number of forms and orientations over three dimensional obstacles, for a wide range of Froude numbers, and in the presence of a viscous boundary layer. Recent developments with numerical models by Crook *et al* (1990),

Smolarkiewicz and Rotunno (1989, 1990) and Smith (1989) of low Froude number flow ($Fr < 1$) have suggested that lee vortices with vertically oriented axis can develop in the lee of three dimensional obstacles in the *absence* of viscous boundary layer forces. They suggest that the vortices are generated by the lee wave activity.

Since the lee vortex forms before the wave breaks, Rotunno and Smolarkiewicz (1991) find no link between the dissipative effects of breaking gravity waves and vertically oriented lee vortices in three dimensional stratified flow, as suggested above. Instead it is suggested that, although lee vortices and wave breaking can occur in the same range of Froude number, they are separate physical entities. Nappo and Chimonas (1992) support this assertion, finding that such wave generated vorticity may not be limited to low Froude number flow, provided that a critical level exists.

2.8.3.3. Separating the Wave and Turbulent Components of the Turbulence Records

Proper analysis of wave-turbulence interaction requires that the turbulence records be composed into mean, wave and turbulent components (Finnigan, 1988).

Caughey and Readings (1975) and Einaudi and Finnigan (1981) identify a very low frequency periodicity in all their turbulent spectra (most notably in Einaudi and Finnigan's pressure spectra) due to the wave activity in the stable nocturnal boundary layer. Finnigan and Einaudi (1981) and Finnigan (1988) determine that waves cannot be separated from turbulence using frequency spectra (attempted by Caughey and Readings, 1975). This is because waves are not monochromatic and their frequencies lie within the energy containing range of the turbulence.

Finnigan (1988) also observes that when the density stratification is approximately steady, little energy transfer takes place between the wave and turbulent fields. However, when the stratification is periodic, strong transfer takes place from wave to turbulence. Smith (1977) showed that the steepening of mountain waves is periodic with height, hence energy transfer is likely to be strong.

A method of phase averaging has been developed to separate the wave components from the turbulence where the turbulence data is taken in the time domain. In the work by Finnigan and Einaudi (1981) and Finnigan (1988) the surface pressure signal, which is least sensitive to the turbulent fluctuations, is used to give the period of the wave. Ensemble averages of other signal time series are then taken using this period, and finally the phase averaged wave form is modulated by a time dependent amplitude function to fit the total time series in some sense. Further details on this method are given in AppendixI of Finnigan (1988).

Einaudi and Finnigan (1981) show that erroneous conclusions could be reached in analysing the turbulence data if the presence of waves is ignored. The turbulence scales of gravity waves and wake flow experienced during the measurements detailed in Chapter 3 are likely to be

inseparable as they are both generated by the same terrain scale. This is supported by Einaudi and Finnigan who comment that the well defined single frequency reference signal related to the wave, required for phase averaging, is not often realised in atmospheric data. The turbulence measurements made in Chapter 3 do not contain such reference signal related to the wave, and hence application of the phase averaging technique to the data collected is not possible.

Unfortunately no studies similar to those of Caughey and Readings (1975) and Einaudi and Finnigan (1981), for boundary layer turbulence and gravity wave activity during strong winds, are known to the author; let alone over mountainous terrain.

Boundary layer turbulence in a stably stratified atmosphere may sometimes depend on the energy transfer from gravity waves; while at other times the turbulence may not depend on, but be strongly influenced by the waves (Finnigan, 1988, and references therein). Although it would be good to identify the origins of the pressure fluctuation at ground level, it is important to remember that the occurrence of the pressure fluctuations is the main priority to this wind pumping study.

2.8.3.4. Separation of Stratified Flows

Separated flows are defined in detail in section 2.10. This sections deals with some effects specific to stratified flows.

Suppression of separated flow regions (due to buoyancy recovery), and the formation *rotors* (a flow reversal which may be found close to the ground some distance downwind of the separated flow region), are both well known features of stratified flows forced by topography. Both are illustrated in figure 2.4(c).

Hunt and Snyder (1980), in a discussion on the effects of stratified flow on boundary layer turbulence, state that, when the length of the waves are of the same order as hill height, the boundary layer flow can begin to be controlled by the waves. That is; when $Fr \approx 1$ then $H \approx U/N$. Also, for $Fr \ll 1$ separation is controlled by the wave pattern; and for $Fr \gg 1$ it is controlled by the boundary layer flow. These generalised separation patterns are illustrated in figure 2.4.

Hunt and Snyder also note that for steep sided hills (>45°) separation always occurs; but for lesser slopes it can be totally suppressed. Also, when $Fr \ll 1$ and the terrain is three-dimensional, flow may be diverted horizontally around the obstacle where separation may then occur. These characteristics have been confirmed by Rottman and Smith (1989) and Castro *et al* (1983) in towing tank experiments and are discussed in more detail in Hunt and Richards (1984) review.

2.9. Pressure Fluctuations Beneath the ABL

To the knowledge of the author there have been no measurements made of surface pressure fluctuations over full scale terrain features. The closest related fields in this case are the surface pressure measurements made on full scale buildings (wind engineering) and the use made of pressure fluctuations in the general study of turbulence (particularly around bluff bodies).

Note that, while Clarke and Waddington (1991) illustrate the surface and subsurface fluctuating pressure spectra in their wind pumping study over (relatively flat) glacial firn, their results are at frequencies which are too high to be applicable to this thesis.

2.9.1. Flat Surfaces

Reviews on pressure fluctuations beneath turbulent flows for flat surfaces have been made by Willmarth (1975) and Eckelmann (1989).

Willmarth commented that the pressure field in a turbulent flow is produced by a summation of the turbulent velocity fluctuations. Also, larger eddies, which make the low frequency contributions, advect faster than smaller eddies. This is because they extend further from the wall layer, into regions of higher velocity. Typical advection velocities are 0.6 to 0.8 times the free stream velocity. On average, a pressure producing eddy of a given size travels ≈ 6 times its wavelength before decaying. However, some eddies retain their coherence for significantly longer periods. Doubling the surface roughness approximately doubled the surface pressure turbulence intensity.

Differences in the shapes of spectra are found between the wind tunnel measurements and those made in the ABL. Compare, for example, Blake's (1970) and Elliott's (1972b). Direct comparisons between the wind tunnel and ABL spectra are not possible because the scaling variables used in wind tunnel data are not available in the ABL case.

Contrary to Elliott (1972b), Eckelmann (1989) states that *no* reliable pressure fluctuation measurements had been made *within* the flow to date as the probe interferes with the flow of the typically small scale (laboratory) experiments. Eckelmann's main focus is to examine the role static wall pressure fluctuations play in the origin and development of turbulent structures.

An important observations to become apparent in the period between reviews is the high correlation velocity fluctuations maintain with the wall pressure fluctuations, the measurements suggesting at least two scales of wall pressure fluctuations, namely:

1. Large scale structures which originate from the outer part of the boundary layer.
2. Ordered small scale structures (sweep , ejection, burst) which are related to the wall region.

This suggests that the larger scale ABL structures, such as those generated through gravity wave activity, should be seen at the ground surface.

Similar works (not included in the review of Eckelmann) by Elliott (1972b), Schols (1984), Schols *et al* (1985) and Schols and Wartena (1986) on the ABL, support many of the conclusions from the earlier (laboratory) work. The distinction between scales remains with the large scale pressure fluctuations being approximately in phase with the downstream velocity fluctuations and the small scale being around 135° out of phase (Elliott, 1972b). On the small scale, the fluctuations are strongly correlated to the turbulent structures associated with the internal shear layer. On the large scale the turbulence is coupled to the passage of convective elements (Schols *et al*, 1985, Schols and Wartena, 1986). Schols *et al* (1986) found that, although the velocity patterns may have lost their identity, the static pressure patterns were more persistent as they propagate through the turbulence field.

Choi and Moin (1990) studied the flat plate surface pressure spectrum to investigate the appropriate scaling laws (using data collected since 1967). They found that the low frequency contributions were best scaled with outer variables, while the high frequency fluctuations were better scaled with inner variables. They also investigated the translation velocities determining that the large scale structures advect at about 0.8 times the free stream velocity and the small scale structures at about 0.6.

2.9.2. Wind Pressures Fluctuations around Buildings

The full scale measurement of surface wind pressures on buildings are surprisingly rare compared to the volume of wind tunnel tests. In wind engineering full scale measurements are required to confirm both theory and wind tunnel measurements. To this study, they represent the closest available comparable data to the pressure fluctuations that may be found over snow surfaces in mountainous terrain.

The Aylesbury experiment represents a benchmark study on full scale low rise buildings, see for example Eaton and Mayne (1975) and Apperley *et al* (1979). The windward spectra show one peak at 0.01 to 0.02 Hz, slightly higher than the spectral peak of the upstream 10m wind. Two peaks are prominent in the leeward spectra, the first peak from 0.01 to 0.02 Hz as above, and a second 0.1 to 0.3 Hz peak which they associate with structure generated turbulence. Some roof spectra show more dominant higher frequency components which they associate with flow reattachment. A future benchmark is likely to be the Texas Tech field experiments of Levitan *et al* (1991) and Levitan and Mehta (1992a, b), although the results of this study have not yet been fully analysed.

Milford and Waldeck (1988) study the fluctuating surface pressure statistics over a hanger and found two spectral peaks at 0.01 and 0.1 Hz in the separated flow. The low frequency peak corresponded to the peak of their wind speed spectrum and they related the high frequency peak to the formation of trailing vortices.

Recent full scale studies in Japan on high rise buildings are the most applicable to the sort of measurements made here because of the scale of the buildings, and the different building aspects studied. Kanda and Ohkuma (1990) reviewed these developments noting the general lack of understanding of turbulent flow around buildings and the consequential interest in spectral and coherence functions. Useful probability distributions according to building face aspect (windward and leeward) are regularly reported in the literature, although as Kanda and Ohkuma comment, extreme values of the probability distributions are of more interest to the structural engineer (see for example Kawabata *et al*, 1990, Dalgliesh *et al*, 1988, or Kristensen *et al*, 1991).

Also of some importance to the structural engineer, is the excitation of structures to natural wind frequencies. Associated with this, but only studied on the laboratory scale (see section 2.10.4.3), is the reattachment of separated shear layers, and/or the impingement of wakes from upstream buildings, onto the building in question.

Kanda and Ohkuma summarised spectra from windward and leeward surfaces. In general the leeward spectral peak lies between 0.06 and 0.15 Hz and the windward peak between 0.006 and 0.06 Hz (corresponding to the peak of the wind speed spectra). Ohkuma *et al* (1991) found a similar windward peak, but noted a sharper drop off at higher frequencies compared to the wind speed spectra. Matsui *et al* (1982) and Ohkuma *et al* (1991) found the wind pressure fluctuations at the edges of both the windward and leeward surfaces rather different to the centers. There is a greater high frequency component with no significant peak and higher root mean square (rms) pressure coefficients. Kawabata *et al* (1990) found a similar pattern and related it to the shedding of Karman vortices[3]. Matsui *et al* (1982) also found that the coherence between pressure and wind speed fluctuations is high on the windward surface, but low on the leeward surface, where the intensity of fluctuation is more moderate.

All of these studies are made over rectangular block shaped buildings of differing aspect ratios; shapes which are somewhat different to real terrain features. One recent exception to this trend comes from Ogawa *et al* (1991) who studied structures with a curved surface recording rms pressure coefficients and fluctuating pressure spectra over cylindrical and hemispherical domes.

---

[3] Karman vortices are defined as the flow instability where two shear layers separated from an obstacle interact with each other and roll up to form discrete vortices (see Lesieur, 1990).

2.10. Separation in Turbulent Flows

Flow separation and reversal were frequently observed during the research period, and it is obvious that such flow conditions are common during wind storms in mountainous terrain. Cloud motion and airborne snow particles provide a convenient tracer for these observations, as well as wind direction recordings at the measurement site.

Chang (1970) classifies two types of separated flow regions depending on their size with respect to the body. If the separation region is relatively small and enclosed by the separating stream line between the points of separation and reattachment, then it is referred to as *separated flow* (see figure 2.4 (d)). Conversely if the flow does not reattach, or the separated region is relatively large, then the separated region is termed *wake flow* (see figure 2.4 (e)).

In the mountains the terrain is highly three dimensional. Consequently the separated flows generated by the terrain will also be highly three dimensional. Both free and separated shear layers will contribute to the intensity and scales of upstream turbulence impinging on downstream terrain features. Not all separated shear layers will distinctly reattach before they become diffuse through interaction with other disturbances. Thus, both reattaching separated flows and wake flows are likely to be important. Note that, as the turbulence that is generated by separated shear flows associated with the terrain scale, the turbulence may become somewhat inhomogeneous. This latter point may be of importance to resonant effects in the mountains (see section 2.10.4).

It is obvious a great deal of intermittency is associated with turbulent boundary layer separation. Some separated flow has already been discussed with reference to full scale measurements in real terrain, around buildings, and in conjunction with buoyancy forces in a stratified flow. Many of the fundamental and more complex characteristics of separated flow are best revealed in smaller scale laboratory and numerical studies. Besides describing some key features of turbulent separated flow, it is the specific purpose of the following sections to characterise the scales, amplitude and frequencies of these intermittences.

Of primary interest to this study are the pressure fluctuations beneath separated flows. These should be similar those below wake flows.

A note of caution must be applied when scaling laboratory flows to full scale. Wilson *et al* (1979) discuss the sensitivity of separating flow to Reynolds number. They note that the influences seen at full scale are not easily reproduced in the laboratory, and that great care must be taken when interpreting laboratory results.

2.10.1. Pressure Fluctuations

It is well known that much larger pressure fluctuations and higher levels of acoustic noise are produced by separated flows in comparison to those produced by attached boundary layers. Turbulence in and around the separated region is inherently more rotational, and therefore surface pressure fluctuations of the same order as the local stagnation pressure may be expected. The largest fluctuations occur near reattachment of the separated shear layer. The nature of flow separation is highly dependent on both body surface (terrain) conditions and the nature of the turbulence in the impinging flow.

Farabee and Casarella (1984, 1986) find the rms wall pressure fluctuations near reattachment for a backward facing step, to be about five times those on a flat surface. For for a forward facing step, the rms wall pressure fluctuations are about ten times those on a flat surface. Businger (1981) suggests that the magnitude of the dynamic pressure fluctuations p in turbulent atmospheric flow over a flat surface may be given by

$$p \approx \pm\frac{1}{2}\rho\overline{V}u \qquad 2.3$$

where $\overline{V}$ is the mean wind speed and u the fluctuations of the wind. Typically $\overline{V} \approx 10$ m/s and $u \approx 2$ m/s (for a turbulence intensity of 20%) which gives $p \approx \pm 10$ Pa. From these rather basic observations the magnitude of the expected pressure fluctuations near reattachment over real terrain is estimated to be around ± 50 to ± 100 Pa. It has been identified that large, low frequency structures are associated with these fluctuations. These structures, which are shed from the shear layer, may remain coherent in the downstream wall pressure spectrum for up to 70 step heights. See, for example, Farabee and Casarella (1986).

2.10.2. Wavy Surfaces and Streamlined Bodies

Comprehensive studies on the influence of wave height and flow rate on steady turbulent separating and reattaching flows over sinusoidal surfaces were made by Zilker *et al* (1977), Zilker and Hanratty (1979) and Buckles *et al* (1984). These studies do not look at conditions where there is self induced unsteadiness of the flow in the cavities, and associated vortex shedding occurs (purging of the entire separated region). They are also limited to time averaged properties and their variances, and do not consider the frequency of any intermittences in the flow. However, some information apart from a physical understanding of the turbulence structure is useful.

Buckles *et al* (1984) note that, as opposed to laminar separation, nowhere in the flow field is the velocity reversed 100% of the time. Rather, the flow direction is intermittent and the velocity swings can be several times as great as the average velocity in and near the separated

region. Simpson's (1989) review concludes that the intermittent large eddy structure supplies most of the near wall back flow, opposing the traditional view that all of the back flow recirculate from far downstream. The forward flow element of the separated region is also supplied by these large eddies.

Logically, if reattachment occurs, the reattachment length will always be less than the terrain wavelength, otherwise wake flow is prevalent. For a wave amplitude (peak to trough) to wavelength (λ) ratio of 0.1 to 0.4 the separation occurs at about 0.1λ to 0.2λ from the peak and reattachment at about 0.6λ to 0.7λ. Simpson (1989) notes that the more curved the surface, the further upstream detachment occurs. The separation point shifts by $\pm 0.05\lambda$, and the reattachment point by $\pm 0.13\lambda$ (Zilker and Hanratty, 1979 and Buckles *et al*, 1984).

Buckles *et al* (1984) observe a very sharp maximum rms pressure coefficient ($C_p \approx 0.7$) just downstream of the reattachment point . This was due to the wandering of the reattachment location and velocity fluctuations in the fluid impinging on the wall caused by the passage of large scale structures produced by the separated shear layer. They also trace the upward movement of the shear layers from successive separations to give a similar structural impression to that of Hunt and Richards (1984) on stratified flow over one or two (relatively low) hills (see figure 2.3). Buckles *et al* note that the separated shear layer does not behave like a free shear layer. Unlike a large proportion of the shear layer in the backward facing step case where the surface is immediately distanced from the shear layer. The proximity of the wavy surface, which drops slowly away, results in a sharper downward bend and shorter reattachment length. This proximity influence is less for large amplitude terrain waves where separated region is thicker.

Patel *et al* (1991) show during numerical modelling of the flow, that the *law of the wall logarithmic velocity profile* breaks down in the strong alternating adverse and favorable surface pressure gradients associated with the alternating aspects in wavy terrain. This makes the calculation of the traditional aerodynamic roughness length difficult for wavy terrain.

2.10.3. Bluff Bodies

Bluff bodies are defined as those which generate separated flow over a substantial proportion of their surface. Buildings are obvious full scale examples of bluff bodies. Their contribution to this study has already been discussed in section 2.9.2. It is useful to look into laboratory (and numerical) studies to gain insight into the interaction between bluff bodies.

2.10.3.1. The Backward Facing Step

The two dimensional backward facing step is the most studied bluff body separation and has the simplest reattaching flow. Detachment occurs very near the sharp trailing edge of the step.

The first half of the resulting separated shear layer acts like a free shear layer, with only a slight curve to the mean flow streamline. This is because it is not affected by the presence of the wall. As the shear layer approaches the reattachment region it curves sharply downward. On impingement with the wall some of the flow is deflected upstream resulting in upstream velocities under the separated shear layer of up to 20% of the free stream velocity. The flow in this area is highly turbulent. Simpson (1989) indicates that the position of reattachment may vary by up to ±2 step heights about the normal mean reattachment length of approximately 6 step heights (Farabee and Casarella, 1986).

The flow in the separated shear layer is highly unsteady. Driver *et al* (1987) and Simpson (1989) identify two sources of intermittency from the surface pressure spectra near the reattachment zone.

1. Quasi-periodic vortical type motions passing through the reattachment region, which develop in the shear layer and have length scales at least as large as the step height. These structures have a convective speed of about 0.6 times the free stream velocity U and are characterised by a dimensionless frequency (or Strouhal number) S^r_{tr}, based on the reattachment length X_r, of

$$S^r_{tr} = \frac{nX_r}{U} \approx 0.6 \text{ to } 0.8 \qquad 2.4$$

where n is the frequency of the fluctuation. This is equivalent to a Strouhal number S^b_{tr}, based on the separated shear layer thickness b, similar to that of a free shear layer

$$S^b_{tr} = \frac{fb}{U_{sl}} \approx 0.2 \qquad 2.5$$

where $U_{sl} \approx 0.5U$ is the average velocity in the separated shear layer. Maximum energy content of the wall pressure fluctuations occurs at these frequencies, which also correspond to the frequencies associated with the roll up and pairing of vortices in free shear layers. For the Arthur's Pass area (see section 3.6.2) $X_r \approx$ 500 to 2000 m and typically $10 < U < 30$ m/s which gives $n \approx 0.01$ Hz.

2. Random flapping of the shear layer has been explained by particularly high momentum structures in the shear layer moving further down stream before attaching. The dimensionless frequency of this fluctuation is $nX_r/U \approx 0.1$ and is of relatively low energy compared to the above. For the Arthur's Pass area this gives $n \approx 0.001$ Hz. This frequency is also evident near the separation point (Cherry *et al*, 1984).

2.10.3.2. Other Geometries

The peak frequencies for steady turbulent separation over other types of two dimensional bluff bodies are essentially the same as that for the backward facing step, see for example Cherry *et al* (1983, 1984). However some observations by Mabey (1972) for flow over cavities are worth noting. Mabey found that the dimensionless frequency of the vortical fluctuations compares well to the peak frequency of the power spectra for a separated flow reattaching on the rear face of a shallow cavity. However, the peak power of a flow over a cavity is four times that of the backward facing step. For a deep cavity the pressure fluctuations are smaller, as bubbles form in the recirculation zone. Mabey also notes that such flows are highly three dimensional. Cherry *et al* (1984) explains that lateral coherence after two dimensional separation is relatively short lived which results in a three dimensional structure developing well before reattachment.

It is more common to base the Strouhal number (dimensionless frequency) on the obstacle size h

$$S_{tr}^{h} = \frac{nh}{U} \qquad 2.6$$

where n is the frequency of the fluctuation and U the mean free stream velocity. For example Nakagawa (1987) found the Strouhal number for alternating vortices shed from a two dimensional square cylinder was about $S_{tr}^{h} \approx 0.13$. Strouhal numbers for three dimensional bluff bodies appear to vary according to the angle of incidence of the flow. For example El-Sherbiny (1983) finds $0.05 < S_{tr}^{h} < 0.25$ (based on the projected cross stream dimension) for vortex shedding to occur around the sides of vertically standing triangular prism. For stratified flow Castro *et al* (1983) observed Karman vortex streets with $0.14 < S_{tr}^{h} < 0.18$ around the sides of a relatively long surface mounted triangular prism at low Froude number ($Fr < 0.4$).

In real terrain Jenkins *et al* (1981) estimated $S_{tr}^{h} \approx 0.2$ in the separated region behind a steep isolated three dimensional island and Kawabata *et al* (1990) found $S_{tr}^{h} \approx 0.1$ for a Karman vortex street around the sides of a very tall building.

2.10.4. Upstream Turbulence and Resonant Effects

Turbulence in separated flows can be influenced in several ways, namely:

* Intensity and scale of the upstream turbulence.
* Separated shear layer feedback.
* Bluff body / bluff body interaction.

Much of what is discussed here comes from the recent reviews by Hunt (1990) and Hunt *et al* (1990) and an earlier review by Bearman and Morel (1983).

The review by Hunt *et al* (1990) on wake turbulence around isolated bluff bodies identifies that little is understood of the interaction between the upstream turbulence and the velocity and pressure fluctuations in and outside the wake of a bluff body. The assumption of weak turbulence implies the scale of the upstream turbulence is much smaller that the scale of the bluff body. To satisfy the weak turbulence condition the bluff body may be in the wake of other bodies, but be at least several bluff body scales downstream. In terms of the Arthur's Pass terrain, where there are 2 to 4 valley to ridge top heights between ridge lines, the applicability of work with weak turbulence must be considered limited.

Ramsay (1990) states that when a fluid with inhomogeneous turbulence impinges on bluff body many complicated interactions occur. These include modification of the properties of the upstream turbulence, buffeting of the body and modification of the bluff body flow regime near the body. Some of the features of the interactions are similar to the effects obtained with homogeneous upstream turbulence. However the presence of coherent structures can lead to a wake resonance condition in which the quasi-periodic coherent structures force a quasi-resonant response of the wake of the downstream body.

2.10.4.1. Small Scale Upstream Turbulence

It is well established that higher levels of small scale (comparable to the shear layer thickness and small compared to the obstacle scale) free stream turbulence reduces the normal mean reattachment length. This is because the shear layer growth rate is enhanced through increased mixing. See for example Eaton and Johnston (1981), Hiller and Cherry (1981) and Nakamura and Ohya (1983, 1984). The effect of small scale turbulence appears to be the same for both two and three dimensional bluff bodies according to Nakamura and Ohya (1984).

Matsumoto *et al* (1988) used small sinusoidal pulsations of the flow past rectangular prism of varying slenderness ratio B/D, where B is the stream wise dimension and D the cross stream dimension. They found that vortex shedding from short prisms ($B/D < 2$) was not affected by the pulsations and the single peak in the wall pressure fluctuation spectrum occurred at the Karman vortex street frequency (Strouhal number based on the cross stream dimension) $S_{tr}^{D} \approx 0.2$. Over long cylinders ($B/D > 4$) the only peak in the pressure spectrum occurred at the pulsation frequency due to enhancement of the shear layer instability. At intermediate lengths ($B/D \approx 2$) two prominent frequencies in the pressure spectrum result from the hybrid flow patterns in which Karman vortex shedding competes with synchronised vortex shedding due to the flow pulsations.

2.10.4.2. Large Scale Upstream Turbulence

Equally well established is the strong interaction between *large scale* (comparable to the obstacle size) upstream turbulence and the vortex shedding from a bluff body. More specifically it weakens vortex shedding from two dimensional bluff bodies by reducing span wise coherence (Nakamura and Ohya, 1984). At the same time it strengthens vortex shedding from a three dimensional bluff bodies through resonant interaction by enhancing the roll up of the separated shear layers (Nakamura and Ohya, 1986).

For small slenderness ratio rectangular prisms (B/D<1, where B is the stream wise dimension and DxD the cross stream dimensions) Nakamura and Ohya (1986) obtain a Strouhal number of $S_{tr}^{D} \approx 0.12$ in both smooth flow and for large scale upstream turbulence. For the Arthur's Pass area (see section 3.6.2) $D \approx 100$ to 500 m and typically $10 < U < 30$ m/s which predicts frequencies $n \approx 0.04$ to 0.002 Hz. For longer prisms ($B/D \approx 2$), where shear layer reattachment occurs along the sides, the flow is dominated by the reattachment, the vortex shedding is of smaller scale and does not appear to be affected by large scale upstream turbulence.

Mullin *et al* (1980) found that strong sinusoidal pulsations of the flow lead to intermittences in the separation. Their work confirmed that of Lebouche and Martin (1976) who calculated a forcing Strouhal number they term a reduced frequency parameter f*

$$f^* = \frac{nh}{U} \qquad 2.7$$

for pulsating mean flow in a duct which had enlargements on both sides, where n is the frequency of pulsation, h the step height and U the mean free stream velocity. They found that when $f^* < 0.07$ the recirculation vortex associated with the separated flow region was periodically shed, when $f^* \approx 0.07$ the vortex was very unstable and when $f^* > 0.07$ the vortex was stable but smaller than for steady flow. From the measurements for the Arthur's Pass area in Chapter 3 the peak frequency is about $n \approx 0.005$ Hz, $10 < U < 30$ m/s and $100 < h < 1000$ m. This gives a reduced frequency in the range $0.5 < f^* < 0.02$ Hz which suggests that all three of these regimes are possible.

2.10.4.3. Wake Resonance

A review by Rockwell and Naudascher (1979), and later Rockwell (1983), describe how highly organised oscillations of an impinging flow can be sustained through a sequence of events, namely:

1. Feedback, or upstream propagation, of disturbances from the impingement region or detached shear layer unsteadiness to the sensitive area of the free shear layer near separation.
2. Inducement of localised vorticity fluctuations in this region by the arriving perturbations.
3. Amplification of these vorticity fluctuations in the shear layer between the separation and impingement or detached shear layer unsteadiness.
4. Production of organised disturbances at impingement or in the detached shear layer.

Whilst this phenomenon appears over a wide range of applications and scales, for example in aircraft components and velocity and pressure probes, the most applicable work here is the interaction of the flow between bluff bodies (with application to tall buildings).

Ramsay (1990) finds that the range of strong wake resonance interactions occurs for a narrow range of scales of upstream coherent structures approximately equal to the scale of the structures in the wake of the downstream bluff body wake. This will be the case for the tandem cylinders (discussed below) and possibly for some natural terrain configurations.

It is evident from wind tunnel experiments with two circular cylinders in tandem that interaction is highly dependent on spacing and stagger (Sun *et al*, 1992). Zhang and Melbourne (1992) conclude that vortex shedding plays a major role in the flow interference. They identify several interference regimes between circular cylinders in smooth flow according to the stream wise separation X.

* At X/D> 3.8 (where D is the cross stream dimension) the separated shear layer from the upstream cylinder does not reattach onto the downstream cylinder. A peak rms wall pressure coefficient ($C_p \approx$ 1.0 compared to 0.2 for an isolated cylinder) is evident on the upstream face of the downstream cylinder at X/D= 4 due to the vortex shedding from the upstream cylinder (C_p is defined in section 3.9.1.). Rms wall pressure coefficients in the wake area of the second cylinder remain approximately that of the isolated cylinder ($C_p \approx$ 0.2).

* At X/D< 3.2 the shear layer reattaches on the downstream cylinder and vortex shedding is suppressed from the upstream cylinder. The vortex shedding from the downstream cylinder synchronises with the fluctuations of the reattached shear layers. This produces large pressure fluctuations (rms wall pressure coefficient $C_p \approx$ 0.75) at $2*S_{tr}^{D}$ (Strouhal

number based on an isolated cylinder of diameter D) in the front region of the downstream cylinder.

* In the transition, $3.2 < X/D < 3.8$, the flow pattern interchanges between the above. Large fluctuations are observed during vortex shedding from the upstream cylinder, but they are reduced (by up to 70%) during reattaching phases. Vortex shedding from the downstream cylinder still continues, but at a much reduced strength and at a lower S_{tr}^{D} (reduced by up to 25%)

As the upstream turbulence intensity increases the vortex shedding is weakened and disorganised generally reducing interference. The results of Takeuchi and Matsumoto (1992) show similar regimes for interference between two rectangular cylinders One extra variable is added in this case, the slenderness ratio B/D, where B is the stream wise dimension and D the cross stream dimension. The response of the flow to low B/D cylinders is similar to that for circular cylinders. However, at high B/D observations by Nakamura and Ohya (1986) for long single cylinders, where shear layer reattachment occurs along the sides, the flow is dominated by the reattachment, the vortex shedding is of smaller scale and does not appear to be affected by large scale upstream turbulence, are relevant.

2.11. Statistical Descriptions of Atmospheric Turbulence

Two approaches have been taken in statistically analysing atmospheric turbulence data

1. Wind Speed Power Spectral and Coherence Functions
2. Gust Frequency and Amplitude Probabilities

The analysis of data in Chapter 3 requires that estimates of the expected gust size (amplitude), duration (period) and return period are found. Given that the approaches to this problem are generally accepted, only a brief review is provided here.

2.11.1. Spectral and Coherence Turbulence Descriptions

Atmospheric boundary layer turbulence is generally described by its spectral and coherence functions (Gustavsson and Linde, 1979). This has been the approach taken by almost all authors up to the present time, although the exact presentation varies according to author and application. The analysis used in this thesis is fully described in Chapter 3 and follows closely the methods used for wind speed fluctuations by Flay (1978), whose rigorous sensitivity testing provides useful insights as to the applicability of the data. For the pressure fluctuations the same methodology is used as seen in Choi and Moin (1990). The theory behind his work is extensively detailed in the excellent text of Bendat and Piersol (1986).

2.11.2. Amplitude Probability Descriptions - Gust Models

Gustavsson and Linde (1979) comment that the coherent wind structures (gusts) which appear randomly in the boundary layer are more or less concealed by spectral and coherence descriptions. This view is reiterated by Bergström (1987) who states that although spectral representation of the characteristic turbulence may be preferable from a scientific point of view, a more mechanistic gust model is sometimes preferred in engineering work. Consequently various gust models have been developed for use in relation to wind turbine systems.

1. Turbulent Model
2. $Gust_0$-Model
3. Velocity Difference or Gust Rise Model
4. Zero-Passage or Ramsdell Model
5. Conditional Sampling Model

These models are reviewed in detail by Powell and Connell (1980) and Linde (1983) who conclude that no one gust model has been universally accepted. A brief review of gust definitions for the various models is made below and the most appropriate model selected for this work. The chosen gust model will also be applied to the surface pressure fluctuations.

There is a distinction between discrete and turbulent gust models. Turbulent models are based on the standard statistical functions, spectra etc, while discrete models use other criteria to define the gust events. A discrete model can utilize turbulent statistics but there are also discrete models which only use the time-velocity function u(t).

Note that there are several new gust definitions for estimating extreme events which are not reviewed here. See for example Kawabata *et al* (1990), Dalgliesh *et al* (1988) and Kristensen *et al* (1991).

Definitions

Refer to section 3.9.1 for the definitions of the wind speed time series v(t) and its statistical properties used in the models described below.

2.11.2.1. Turbulence Model

The turbulent model is based on the power spectrum which assumes a stationary gaussian process. It defines a gust with amplitude x as when wind speed fluctuations time series u(t) exceeds x with a positive slope as shown in figure2.6.

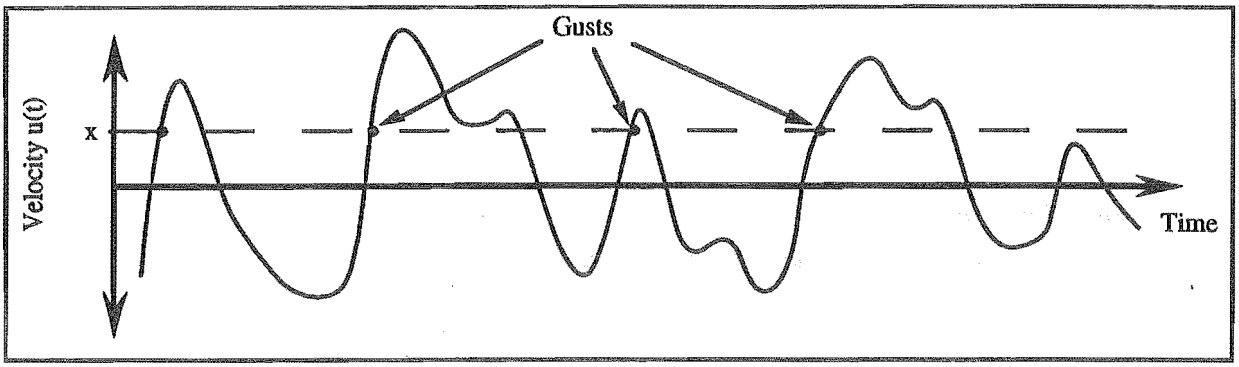

Figure 2.6. Turbulence Model.

2.11.2.2. Gust$_0$-Model

The Gust$_0$-Model is a discrete model that uses the power spectrum as input which also assumes a stationary gaussian process. In this model an interval between two zero crossings of u(t) is defined as a gust and the gust amplitude A_i as the maximum value of |u(t)| between the crossings. This is illustrated in figure 2.7.

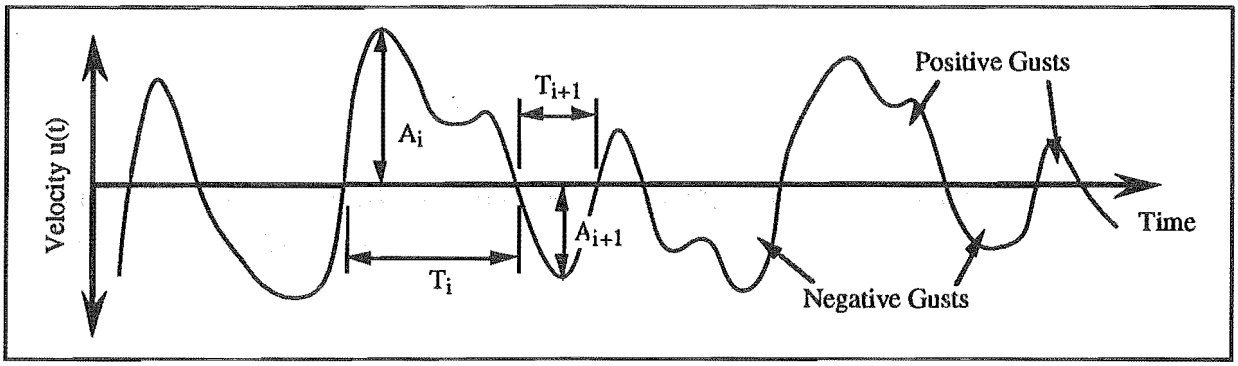

Figure 2.7. Gust$_0$-Model and Zero-Passage or Ramsdell Models.

2.11.2.3. Velocity Difference or Gust Rise Model

The Velocity Difference or Gust Rise Model used by Bergström (1987) is also a discrete model that uses the power spectrum as input and assumes a stationary gaussian process. In this model u(t) is substituted by a series of velocity differences Δu observed at equidistant time instances. The time interval τ is chosen as a typical gust time. The Δu series is given by

$$\Delta u_i = u(t_i+\tau) - u(t_i), \quad \Delta u_{i+1} = u(t_i+2\tau) - u(t_i+\tau) \ldots \qquad 2.8$$

Figure 2.8 illustrates this transform. The turbulence model described above is then applied to Δu. This model provides the possibility to study wind velocity fluctuations at different time scales by varying τ.

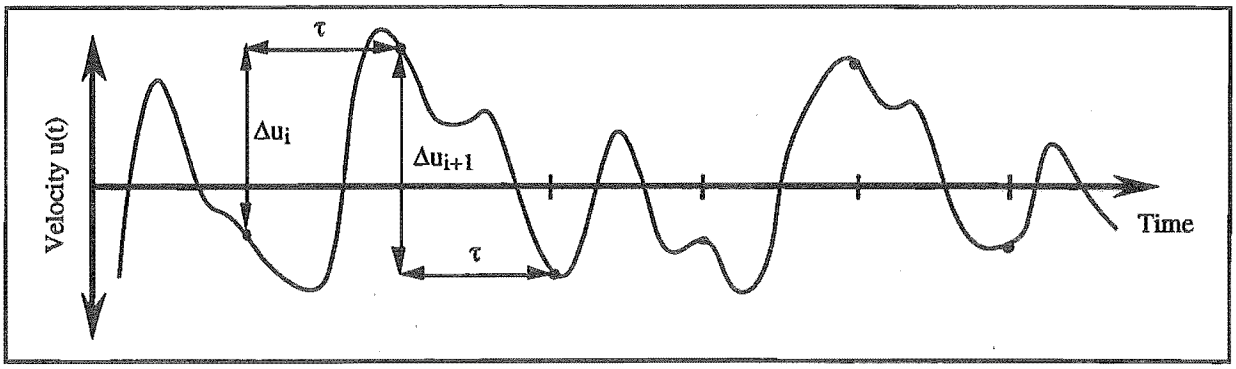

Figure 2.8. Obtaining the Transformed Δu(t) Series From u(t) for the Velocity Difference or Gust Rise Model.

2.11.2.4. Zero-Passage or Ramsdell Model

The same gust definition is used as for the $Gust_0$-Model but in addition it takes the time between the two crossings through the mean as the gust duration, T_i and the u(t) function is analysed rather than the spectrum. This is shown in figure 2.7.

Ramsdell (1978), Doran and Powell (1982), Linde (1983) and Bergström (1987) all use this model.

2.11.2.5. Conditional Sampling Model

The conditional sampling with variable time interval (moving) averaging technique described by Blackwelder and Kaplan (1976) utilizes the variance of the turbulent velocity, not u(t) itself for the detection of gusts. A gust is defined when the variance of u(t) after averaging exceeds a factor η times the variance of u(t), ie

$$\hat{\sigma}^2(t,T) > \eta\sigma_u^2 \qquad 2.9$$

where

$$\hat{\sigma}^2(t,T) = \frac{1}{T}\int_{t-\frac{T}{2}}^{t+\frac{T}{2}} |v(t)-\hat{v}(t,T)|^2 dt \qquad 2.10$$

and the moving average series $\hat{v}(t,T)$ is given by

$$\hat{v}(t,T) = \frac{1}{T}\int_{t-\frac{T}{2}}^{t+\frac{T}{2}} v(t)dt \qquad 2.11$$

This is illustrated in figure 2.9. Linde (1981 and 1983) uses the conditional sampling model, but comments that the technique does not constitute a complete gust model.

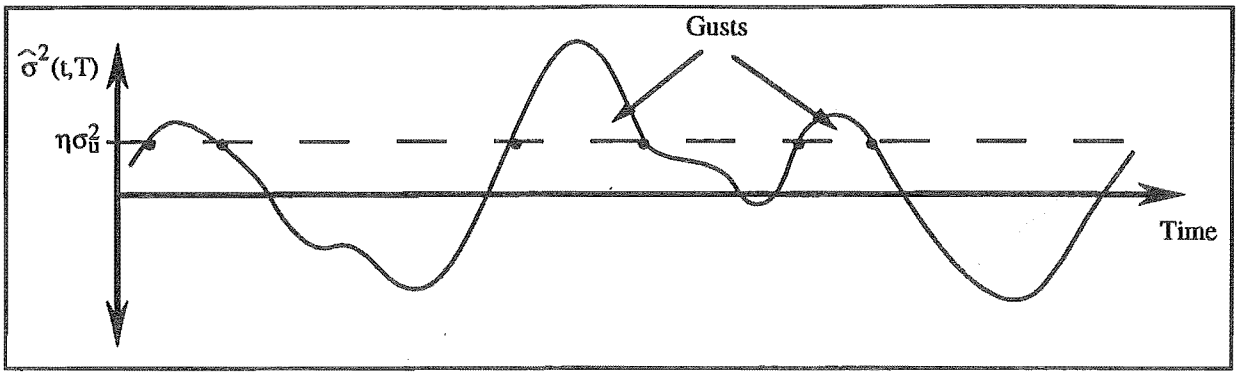

Figure 2.9. Conditional Sampling Model.

2.11.2.6. Choice of Gust Model

As the definition of a gust is somewhat arbitrary (Doran and Powell, 1982) the choice of model for the analysis of data here is made on the basis of the selected model giving the information required in the most useful way.

In this study of wind pumping the expected gust size (amplitude), duration (period) and return period all appear important. As spectral descriptions are be looked at in some detail in Chapter 3, a model which presents the data in an alternative way in the time domain, is sought.

This information can be obtained from both the $Gust_0$ and Zero-Passage Models. As the Zero-Passage Model has been used more frequently in the literature it is used here with some modifications. These modifications are described in detail with its implementation in sections 3.9.11 and 3.10.8.

2.12. Conclusions

2.12.1. Summary of Expected Influences in the Mountains

Fluctuations with periods longer than one hour are not expected to be an influence in the mechanisms of wind pumping. The origins of fluctuations shorter than one hour (microscale) are diverse and, importantly, the fluctuating atmospheric pressure field does not contain the spectral gap prevalent in the fluctuating wind speeds.

This study appears to lie somewhere within three distinct fields.

* Geophysical and meteorological applications of atmospheric turbulence over mountains.
* Structure of the atmospheric boundary layer for wind energy and environmental applications.
* Pressure fluctuations for structural design in wind engineering.

The purpose of this review was to gain both a qualitative and quantitative understanding of the expected flow patterns, keeping in mind that the wind pumping mechanism requires a driving force with repeating cycles of large amplitude and that the high frequency fluctuations (>1 Hz) are likely to be filtered out near the surface of the snow pack.

No surface pressure measurements have been made to date over rough real terrain features, hence measurements from the related fields were investigated to find estimates of the expected gust size (amplitude), duration (period) and return period.

Also, since no theoretical considerations extend to turbulence structure near the ground over such extreme terrain no theoretical estimations of the driving forces associated with wind pumping can be made. Note that the breakdown of the logarithmic wind speed profile close to the ground prevents the characterisation of the terrain with an aerodynamic roughness length, an important parameter in many of the theoretical models developed.

2.12.1.1. General Points

Over flat terrain local roughness elements determine the high frequency spectral characteristics while upstream terrain will determine the low frequency characteristics. To a certain extent this is likely to be true for hilly terrain, however the influences of flow separation and reattachment, intensity and scale of the upstream turbulence, separated shear layer feedback, bluff body interaction and atmospheric stratification become important considerations.

From previous measurements, for increasingly complex upstream terrain the spectral peaks are expected to both increase in magnitude and shift to lower frequencies. Smaller scale local terrain features, which disturb the flow in the inner layer (near the ground), result in increased spectral estimates at high frequencies (especially near the points of separation and reattachment). However, high frequency energy for a smooth snow cover is less than that for the bare ground.

While higher elevation turbulent structures may not be seen in the wind speed fluctuations they are likely to influence the surface pressure fluctuations as they propagate through the pressure field. This will result in a higher low frequency content in the spectrum of pressure fluctuations.

2.12.1.2. Separation and Reattachment

In the highly three dimensional terrain, flow separation will frequently occur. Usually when the flow separates, an area of low speed recirculation persists below the separated shear layer. Within the expanding shear layer, which generally reattaches at some point downstream, large coherent structures develop and are periodically shed resulting in a turbulent boundary layer with greater vorticity and larger turbulent fluctuations. These large turbulent structures advect downstream at about 0.6 to 0.8 times the free stream velocity and maintain a high degree of coherence for at least 6 times the wave length before beginning to decay. Some coherence in the pressure fields may remain for up to 70 step heights.

The level of turbulence is highly dependent on the exact location in the terrain the measurements are made. Highest turbulence is felt just downstream of reattachment, while the lowest is felt within the recirculating flow. Therefore measurements will be highly correlated to location within the terrain and the mean wind direction (which determines the turbulence characteristics resulting from upstream disturbances). Even with separation off two dimensional terrain, three dimensional turbulent structures develop within a few length scales and well before reattachment.

From fundamental studies the frequency of fluctuation expected from separated shear layers is estimated for the Arthur's Pass region to be $n \approx 0.01$ Hz. A second expected peak frequency due to the moving reattachment point lies at $n \approx 0.001$ Hz. These figures are unaffected by increases in the levels of small scale turbulence. From measured Strouhal numbers over three dimensional objects peak frequencies scaled up to mountain terrain lie in the range 0.005 to 0.08 Hz. Limited full scale measurements show frequencies of 0.003 to 0.005 Hz.

Atmospheric pressure fluctuations over flat terrain are of the order ±10 Pa. A first estimate of the wall pressure fluctuations in reattaching flows increases this to ±50 to 100 Pa. Over a

sharp ridge line (bluff body), for roughly periodic terrain, the point of separation will occur along the ridge itself, but for smooth ridges it will depend on the level of upstream turbulence and stratification and will fluctuate by up to 10% of the horizontal terrain scale. The reattachment point of the resulting shear layer will occur on the lower face of the next ridge and fluctuate by up to 25%. In real three dimensional terrain in the presence of fluctuating wind direction this is likely to be a gross underestimation.

Increased small scale turbulence acts to reduce the reattachment length while increased large scale turbulence strengthens the vortex shedding from three dimensional obstacles, increasing the fluctuations in the reattachment region (especially if the separation edge is not sharp).

Windward spectra around low rise buildings have a peak of 0.01 to 0.02 Hz, slightly higher than the wind speed spectra. Leeward spectra contain this and a second peak at 0.1 to 0.3 Hz due to the locally generated structure turbulence. Both of these peaks broaden and shift to lower frequencies for tall buildings (0.006 to 0.06 Hz and 0.06 to 0.15 Hz respectively). Spectra measured around separation points show a far larger content of higher frequency energy with broad peaks around 0.1 to 0.5 Hz.

2.12.1.3. Resonant Effects

In the terrain of Arthur's Pass the buffeting wind at the measurement site and the coherent structures produced off upstream terrain barriers may not be considered independent due to possible resonant effects. When interaction occurs the turbulence becomes quasi-periodic, especially when the two terrain features are of the same scale. If such a periodicity occurs then the separated flow region may be periodically shed. The magnitude of the rms pressure coefficients about and downstream of reattachment may be up to 0.7. If there exists an interaction between terrain features the magnitude of this may rise to 1.0 depending on the terrain shape.

2.12.1.4. Gravity Waves

Although topographic forcing by the terrain is expected to generate gravity waves in the stratified atmosphere, it is not known what influence these may have on the turbulence within the boundary layer.

Froude numbers and typical length scales estimated for stratified flow in the Arthur's Pass region during measurement conditions ($0.5 < Fr < 2$ and $600 < \lambda < 2000$ m respectively) lie within the critical range for gravity wave activity. Froude numbers calculated and measured for the onset of blocking and wave breaking vary according to author and terrain (obstacle shape). Vortex shedding at a scaled up frequency of 0.003 to 0.006 Hz may occur at low Froude

number (Fr< 0.4) in areas of highly three dimensional terrain (where the interaction between two separated shear layers is possible). The turbulence scales of gravity waves and wake flow experienced here are likely to be inseparable as they are both generated by the same terrain scale.

From observations within the environment it is difficult to determine whether the prime cause of flow stagnation in the valleys is due to blocking or pure flow separation. On the very large scale the former is more likely.

Although complete suppression of separation has been observed at the leeward end of the mountain range for slopes ≈45°, most likely due to stable stratification, no such observations were made in the middle of the mountain range (near the measurement site).

2.12.1.5. Return Period

No information has been gathered on the return periods of large amplitude fluctuations as the literature concerns itself with extreme events which tend to be isolated in time contrary to the requirements of the wind pumping mechanism. However, analytical techniques used for their estimation are used in the statistical analysis and are described in sections 3.9.11 and 3.10.8.

2.12.1.6. Upper Frequency Limit

The above discussion has identified the lower limit of the frequency band width of interest to this study. A possible upper limit can be identified according to the Van der Hoven (1957) and Gossard (1960) spectrums (shown in figures 2.1 and 2.2) where there appears to be little energy above 0.5 Hz. Although numerous authors have looked at frequencies as high as 10 Hz, Flay (1978) comments that the neutral ABL contains only small amounts of turbulent energy above 1 Hz.

The resistance of the snow pack to penetration by high frequency surface pressure fluctuations is such that frequencies above 1 Hz may be ignored given that the amplitude of such fluctuations are relatively small. Thus 1 Hz appears to be a convenient upper limit to the band width studied.

2.12.2. Choice of Analysis Procedures

The analysis procedures required for processing the data collected in Chapter 3 are generally well established and require little discussion.

2.12.2.1. Statistical Descriptions

This is not so much a matter of choice but the realisation of the accepted statistical procedures to follow. Flay (1978), Choi and Moin (1990) and Bendat and Piersol (1986) most clearly define the requirements.

2.12.2.2. Choice of Gust Model

It has been noted autocorrelation and autospectral functions do not give the amplitude composition of the wind speed and pressure fluctuations in a very useful way.

The Zero-Passage Model has been chosen over several other gust models. It was selected because it gives the expected gust size (amplitude), duration (period) and return period information in the time domain and has been used more frequently in the literature.

Chapter 3
Measurements of Atmospheric Turbulence

The primary objectives of these atmospheric turbulence measurements over alpine terrain during strong winds is to determine the amplitude and frequency characteristics of the driving forces behind wind pumping and compare them to the magnitudes and various possible origins discussed in Chapter 2 .

3.1. Table of Contents

3.2. List of Illustrations

3.3. Nomenclature

A_i	gust amplitude(m/s or Pa)
c	speed of sound (m/s)
$C_{ii}(\tau)$	autocovariance function (s^2/m^2 or Pa^2)
C_p	rms (root mean square) pressure coefficient
$C_{up}(\tau)$	Crosscorrelation Function (Pas/m)
d	degrees of freedom
f_0	dimensionless frequency
f_c	Nyquist frequency (Hz)
f_m	maximum frequency (Hz)
H	vertical relief (m)
h	dampening ratio
i	u or p
I(t)	time series (m/s or Pa)
i(t)	fluctuations of the time series I(t) (m/s or Pa)
i'(t)	time series with moving average trend removal (m/s or Pa)
$\hat{i}$	estimate of the true value of the variable i
$\overline{i^2}$	mean square of the time series (m^2/s^2 or Pa^2)
I_v	turbulence intensity
j	frequency bandwidth
L	tube length (m)
M	molar mass of air (kg/kmol)
m	number of spectral estimates
n	frequency (Hz)
N_{ij}	number of gust events
n_m	peak spectral frequency (Hz)
p	probability
p(t)	pressure fluctuations (Pa)
$p_t(t)$	pressure fluctuations at the transducer (Pa)
$\overline{p_s}$	average stagnation pressure (Pa)
q	number of records
R	gas constant (kJ/kmolK)
r	internal tube radius (m)
Re	Reynolds number
$S_{ii}(n)$	autospectral density function (s^2/m^2s or Pa^2/s)
s	standard deviation
T	air temperature (K)

t	time (s)
Δt	sampling interval (s)
T_0	record length or averaging length (s)
T_{Eul}	Eulerian time Scale (s)
T_{exp}	exponential time scale (s)
T_i	gust duration (s)
$u(t)$	wind speed fluctuations (m/s)
V	transducer volume or reference volume (m^3)
$V(t)$	instantaneous wind speed (m/s)
$\overline{V}$	average wind speed (m/s)
V_o	anemometer output voltage (volts)
var	variance
X	stream wise separation (m)
z	height above ground or snow surface or depth into the snow pack (m)

α	level of significance
ε_e	experimental error
ε_r	random error
ϕ	phase shift
Λ	integral length scale (m)
Λ_{Eul}	Eulerian integral length scale (m)
Λ_{exp}	exponential integral length scale (m)
Λ_{spec}	spectral integral length scale (m)
λ	wavelength (m)
λ_m	wavelength of the peak spectral frequency (m)
ν	kinematic viscosity of air (m^2/s)
ρ	density (kg/m^3)
$\rho_{ii}(\tau)$	normalised autocovariance function (s^{-1})
$\rho_{up}(\tau)$	normalised crosscorrelation function (s^{-1})
σ_i	standard deviation (m/s or Pa)
σ_p^2	pressure record variance (Pa^2)
σ_i^2	record variance (m^2/s^2 or Pa^2)
σ_u^2	wind speed record variance (m^2/s^2)
τ	time lag (s)
τ_{ref}	reference pressure time constant (s)
ω_n	natural frequency (Hz)
χ_2^2	chi-squared variable

3.4. Introduction

The primary objective of this chapter is to determine the amplitude and frequency characteristics of the driving forces behind wind pumping. This requires the measurement of fluctuating snow surface pressure over rough mountain terrain. To the knowledge of the author no such pressure measurements exist, and few measurements of fluctuating wind speed have been made in such mountainous terrain. Observation of winds are a requirement for snow safety work as in many other environmental and engineering applications. It is obvious that the fluctuating wind speed measurements be should made to accompany any fluctuating pressure measurements.

Several secondary objectives are also presented in this study:

* To examine the decay of the pressure fluctuations in the snow pack.
* To postulate the generation mechanisms behind the surface pressure fluctuations.

Section 3.5 describes the field experiments of this research programme. Sections 3.6 and 3.7 describe the research site at Temple Basin Ski Area Base in Arthur's Pass National Park and the measurement and data acquisition equipment used in the experiments.

Section 2.11 details the statistical procedures used in random data analysis as applied to atmospheric turbulence. Two complementary approaches are outlined:

1. Power spectral and correlation function analysis.
2. Gust amplitude probabilities and gust frequencies over finite frequency bandwidths.

These approaches require the data collected to be random and stationary; that is, data with statistical properties that are invariant with translations in time. Sections 3.8 and 3.9 fully describes the statistical procedures suggested in section 2.11. Included in this description are the results of the data verification tests and sensitivity analysis made on the various statistical variables.

Finally the results of the analysis are presented and discussed in sections 3.10 and 3.11.

3.5. Experimental Programme

To meet the primary objective of this study the following measurements were required:

1(a) Windward, ridge top and leeward surface pressure fluctuations about the average atmospheric pressure.
1(b) Ridge top wind speed for correlation with the 1(a).
1(c) Weather measurements during 1(a) and (b).

To meet the secondary objectives the following additional measurements were required:

2(a) Windward, ridge top and leeward sub-surface pressure fluctuations about the average atmospheric pressure.
2(b) Pressure fluctuations between two points beneath the snow surface.
2(c) Snow profile measurements including vertical snow permeability.

The wind speed and pressure measurement requirements were met by the use of wind and pressure sensors, chart recorder and digital data acquisition equipment described in detail in section 3.8 below. The snow pack and weather measurement requirements were met by using the blower permeometer described in Appendix III, and industry standard weather and snow pack observations.

These were the first full scale fluctuating pressure measurements over a snow cover in mountainous terrain. Hence extensive initial experiments using strip chart recorders were performed prior to the decision to make a more detailed digital analysis. These were combined with flow visualisation work to establish the basic flow patterns across the snow surface. These experiments are not detailed in this thesis due to the qualitative nature of the results.

3.6. Site Description

Given infinite resources, numerous locations with varying upstream terrain, at various altitudes in the vertical relief should be used. However practical, financial and time restrictions limited the measurements to one site. Two sites were considered.

3.6.1. General

3.6.1.1. Tasman Saddle, Mt Cook National Park

Tasman Saddle (2530 m), located at the top of the Tasman Glacier in Mt Cook National Park, has an abundance of storms but suffers significant disadvantages:

1. Maintenance of personal safety precludes working in extreme storms as the avalanche hazard and poor visibility severely limit movement. Working at night is almost totally barred, even in low intensity storms. This defeats the main purpose of being there.
2. With no mains (230 volt) power available at Tasman Saddle all instrumentation must be powered and kept warm by a transportable power source.
3. The scale of terrain features around Tasman Saddle Hut does not allow windward and leeward measurements to be made without considerable travel.
4. Access is by ski plane or helicopter. This limits both the timing of access (weather dependent) and the equipment that is able to be taken in.
5. Down time is high with periods of days waiting in Mt Cook Village for the weather to clear (to fly in), and similar periods confined to Tasman Saddle Hut.

3.6.1.2. Temple Basin, Arthur's Pass National Park

Temple Basin Ski Area is situated in Arthur's Pass National Park on the main divide in the Southern Alps of New Zealand. Access is off State Highway 73 at Arthur's Pass (970 m), 3.5 km north of Arthur's Pass Village (737 m), up a well graded walking track to the base area and accommodation huts (1370 m). Equipment is transported up the mountain on an aerial cable-way (the Goods Lift).

The general location of the ski area is shown in plate 3.1, and the layout of the base area, including the measurement site, in figure 3.2. Plate 3.2 shows the measurement site and upstream terrain looking northwest from Mt Cassidy. Figure 3.1 shows the profile of the key terrain features in this view in profile along with the north-south and east west profiles. Figure 3.3 shows a northwest-southeast profile through the measurement site.

Temple Basin overcomes all the disadvantages of the Tasman Saddle site described above. In particular the location of the huts, with national grid power, in relation to the terrain features allows data acquisition equipment to be operated in the dry warmth of indoors, leaving only the measurement systems to be weather proofed.

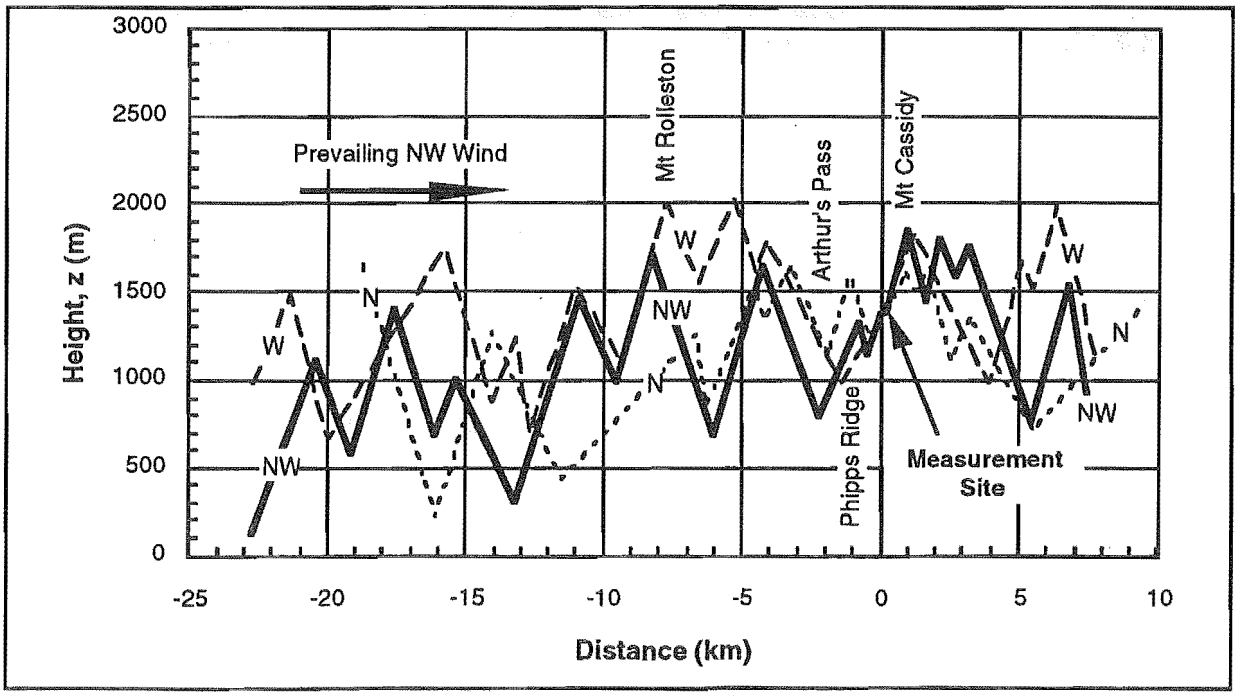

Figure 3.1. Profiles along West-East, Northwest-Southeast and North-South Axis Showing Major Terrain Features Near the Measurement Site.

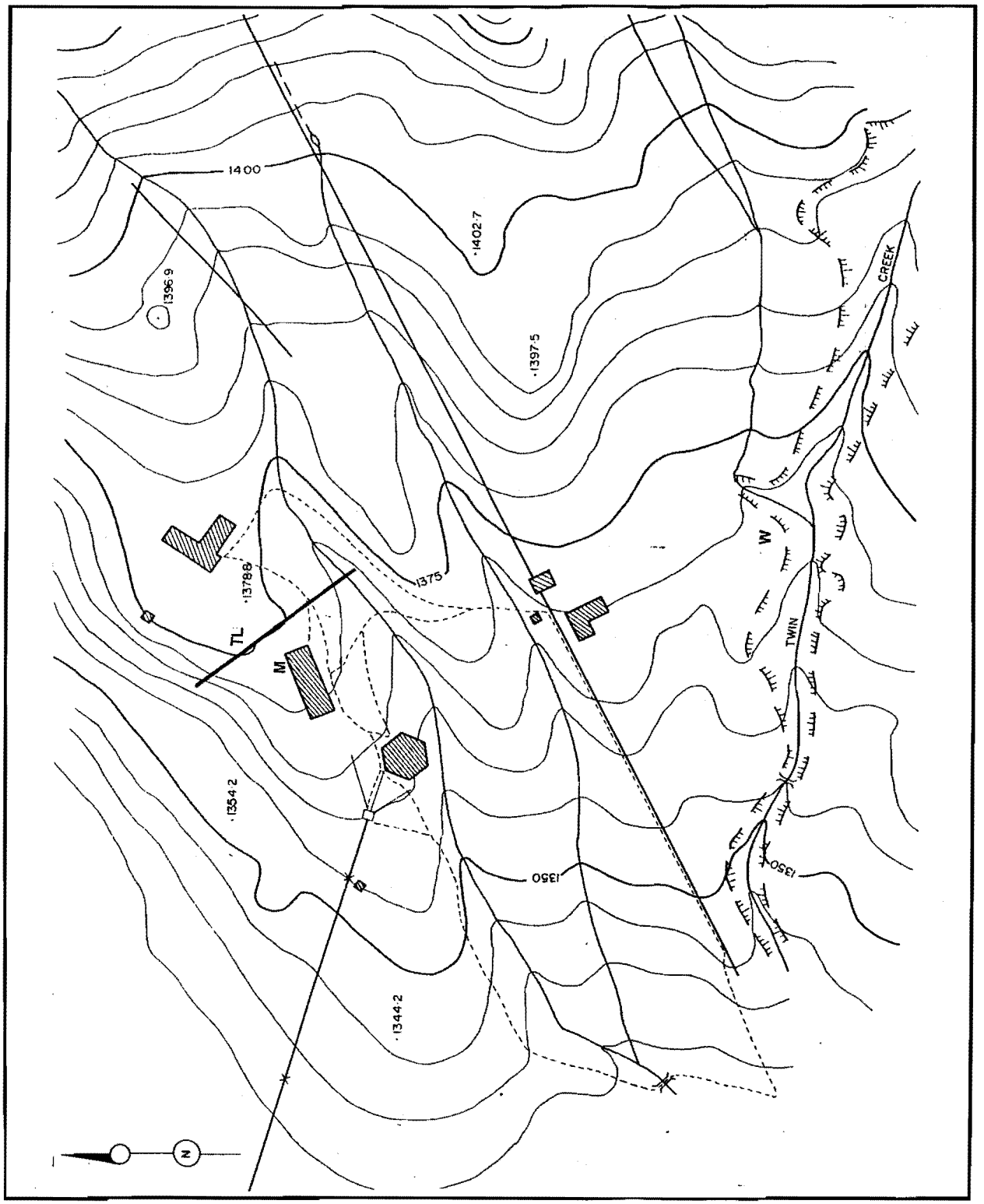

Figure 3.2. Temple Basin Base Area Layout. The Traverse Line over which Pressure Measurements were made is indicated 'TL', Wind Mast 'M' and Weather Observations 'W'. Approximate Scale 10 mm = 18 m. Contours at 5 m Intervals.

One distinct disadvantage of the Temple Basin site is its relatively low altitude. Precipitation, which fell mostly as wet snow or rain during the measurement period, was significantly harder to deal with (regarding instrumentation) compared to dry snow which could be brushed away.

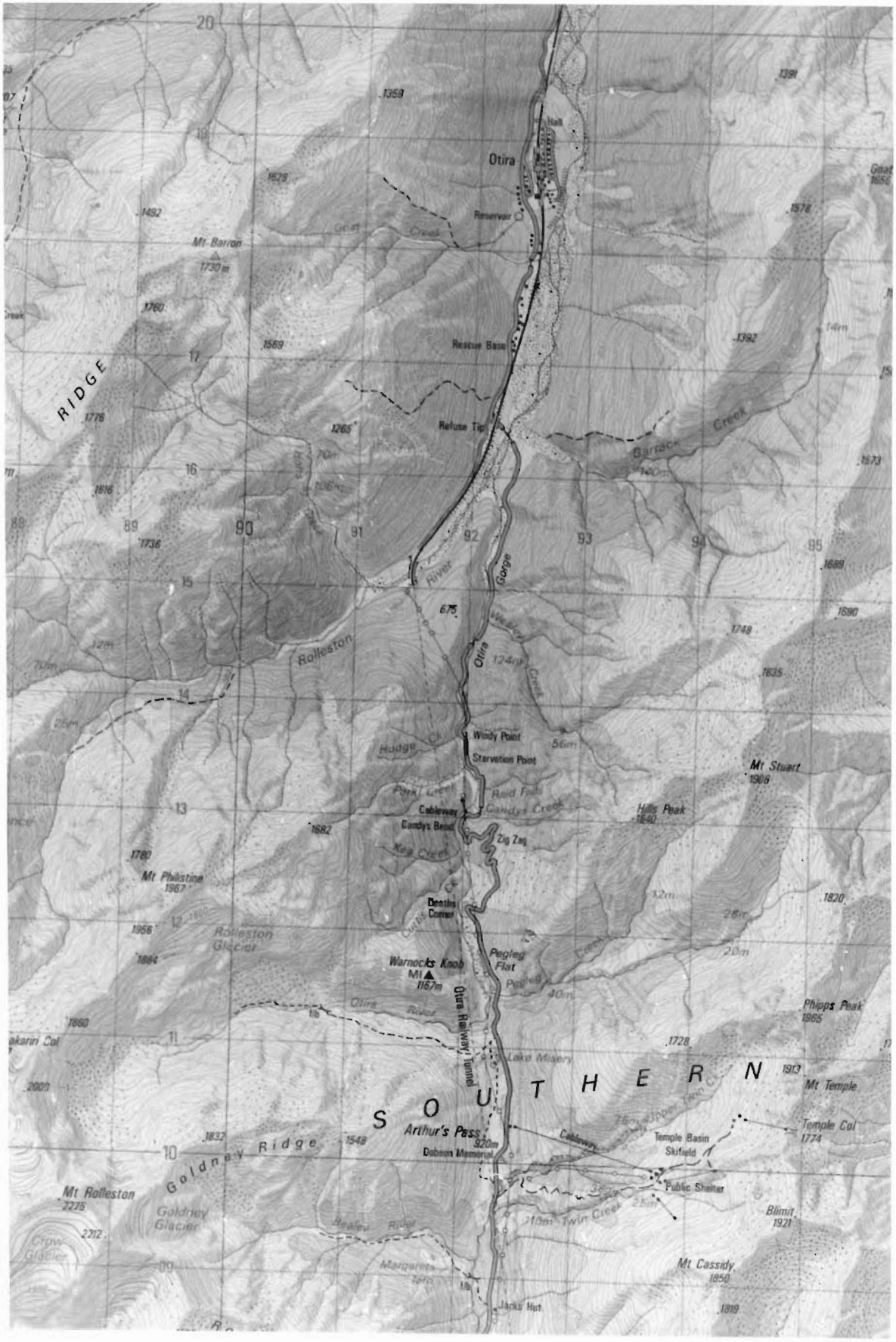

Plate 3.1. Terrain Map of Temple Basin and Ranges to the North and Northwest. Scale 1:50,000. Contours at 20 m intervals.

Plate 3.2. Measurement Site (between the huts in the foreground) and Upstream Terrain Looking Northwest from Mt Cassidy.

3.6.1.3. Inherent Problems of Both Sites

Cool alpine temperatures were typically below the minimum operating temperature of electronic equipment. Any instrument exposed to the elements were therefore heated.

Instruments also have to be protected from wind blown ice particles and water droplets.

3.6.1.4. Downstream Damming of the Flow (Blocking)

If the flow downstream of the measurement site is blocked by a terrain feature, then the wind will stagnate. Blocking occurs when, relative to the stable stratification, an approaching fluid parcel cannot overcome the potential energy deficit to surmount or find a way around a barrier (discussed in section 2.8.3.1). For the prevailing northwest wind Mt Cassidy lies directly downwind of the measurement site with 500 m vertical relief (see figure 3.1).

The wind was observed to both divert around the ridge to the west and/or climb over the ridge (with blowing snow as a tracer). The location of Mt Cassidy to the measurement site would be part of the overall dependence of the site on its specific location.

3.6.2. Terrain Analysis

In the study of atmospheric turbulence, the Arthur's Pass Terrain would have to be described as 'extremely complex'. Bell (1991b) and Waters (1980) give detailed descriptions of the local terrain. With a winter snow cover the terrain is described here in terms of four distinct scales, each an order of magnitude apart:

1. The mountain peaks and main ridge lines have 1,000 to 1,300 m vertical relief from the the main valley systems and ridge to ridge wave length of 4000 to 6000 m.
2. Sub ridges, spurs, ravines and side valleys have scales of about 100 to 500 m and horizontal scales of 500 to 1500 m.
3. Large rock outcrops, cliff bands and buildings have vertical scales of 4 to 10 m and horizontal scales of 4 to 40 m.
4. Snow surface, small rocks and alpine vegetation with vertical scales of up to 1 m and horizontal scales of up to 2 m.

The 'spectral gap' in terrain scales identified by Taylor *et al* (1987) does not exist here. The extent of the mountain range upwind according to wind direction is noted in table 3.1 and the most prominent upstream terrain feature in table 3.2.

Wind Direction	Extent (km)
North	110
Northwest	37
West	32

Table 3.1. Extent of the Mountain Range Upwind According to Wind Direction.

Wind Direction	Terrain Feature	Horizontal Distance (m)	Vertical Relief (m)
North	Phipps Ridge	1000	400
Northwest	Mt Philistine	4000	800
West	Mt Rolleston	5000	1300

Table 3.2. Most Prominent Upstream Terrain Feature According to Wind Direction.

3.6.3. Flow Visualisation

The choice of site was made, in part, according to the availability of windward slopes over which the flow was generally attached and leeward slopes over which the flow may become separated. Flow visualisation was used to identify features of the flow over the measurement site.

Two methods were used for flow visualisation:

1. Loose, dry snow was readily transported by the wind providing a convenient tracer. Observation of streamlined attached flow, separated flow and the point of separation were relatively easily identified by noting the differing ice particle concentrations. However a short distance after separation, the snow became more evenly dispersed with turbulent mixing and gravitational settling into the separated region.

2. 0.5 m long lightweight nylon streamers were attached to bamboo stakes 0.5m above the snow surface and placed along the traverse line giving the same information as above but with less dependence on the snow surface conditions.

These methods were used to characterise the flow patterns during north-westerly quarter winds only. The resulting trends are illustrated in figure3.3.

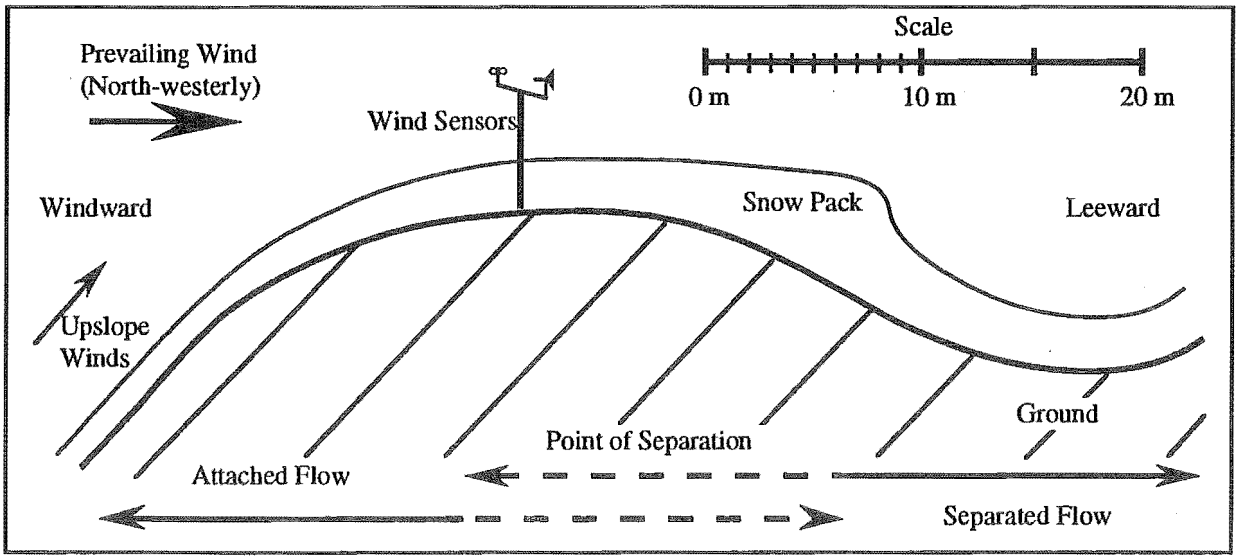

Figure 3.3. Profile of the Measurement Site Terrain on a Northwest to Southwest Axis (along the line 'TL' in figure 3.2) Showing General Areas of Attached and Separated Flow. (The vertical and horizontal scales are the same).

The flow usually separated on the lee slope unless a wind shift larger than 45° occurred. The point of separation varied greatly depending on the vertical component of the wind. Most notably it shifted further windward with upslope winds. Jenkins *et al* (1981) commented that local separation occurred at the summit of an isolated steep island. They concluded that the geostropic wind was a better reference velocity than the 4m summit velocity which was severely affected by the separation.

3.6.4. Measurement Site

The measurements were restricted to one northwest-southeast oriented traverse line located at 1370 m between the two lodges (huts) on a broad ridge leading from the main range to the valley floor. The extent of the traverse was limited to the reach of the 40m lead length that attached the pressure measurement unit to the data acquisition system (inside the north-western end of Temple Basin Ski Club lodge). Within reach was a windward slope up to 45° steep, a relatively flat ridge and a lee slope up to 35° steep, an ideal range for the measurements required. It was not thought that the huts would interfere with any turbulent patterns as they are of the same scale as the natural terrain features.

A sectional profile of the traverse line (indicated by the dark line in figure3.2) is shown in figure 3.3.

3.6.5. Weather Patterns

The NNE to SSW line of New Zealand's South Island, with a 3,000 to 4,000 m divide running down its length, intercepts the predominantly westerly flow which circumnavigates the mid to lower latitudes of the Southern Hemisphere. Few other land masses occupy these latitudes so a maritime climate predominates.

Bell (1991a) gives a general description of the type and intensity of the weather experienced at Temple Basin from six winters of weather observations by the ski patrol. Of interest to this work is the general description of westerly quarter storms when all measurements were made.

The most common meteorological condition that causes strong wind in the Arthur's Pass region is a deep depression passing eastwards across the southern part, or to the south of the South Island. As the depression approaches the South Island from the westerly quarter a strong moist flow from the northwest quarter develops over the area. This airflow usually changes to the southwest quarter as the depression passes to the east. Temperatures are relatively warm during the northwest phase of the cycle, but drop steadily, usually accompanied by frontal activity, as winds back to the south. Heaviest precipitation occurs during the northwest phase and can be in the form of rain even at higher elevations, or snow. Significant falls of drier snow can fall during the south-west phase of the storm.

These storms are generally more frequent and intense during the spring when the disturbed westerly flow oscillates between northwest and south-west. Associated fronts may pass on a daily basis. Figure 3.4 shows the South Island imbedded in a typical disturbed westerly flow.

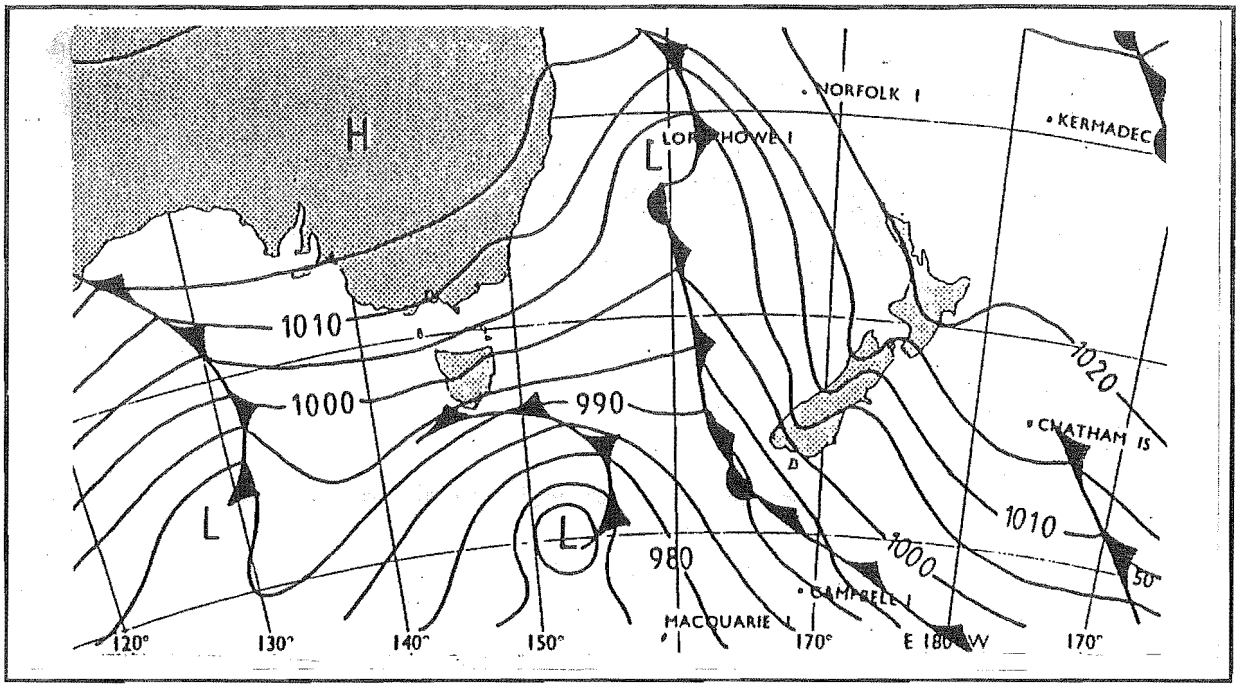

Figure 3.4. Example of a Typical Disturbed Westerly Flow.

These flows are accompanied by strong synoptic pressure gradients and the passage of fast moving frontal (mesoscale) activity which affects the stationarity of the data. Hence measurements were not attempted at the following times:

1. During northerly quarter storms. Such storms do not give consistent wind directions at the measurement site. 30% (or more) of the gusts can come from the reverse direction as they are deflected around by large terrain features.
2. During storms which are in the south east to south phases. During these phases atmospheric pressure and temperature are usually changing rapidly.

3.7. Experimental Set Up

The design of the apparatus was constrained by a number of factors:

* The dynamic response and accuracy of the instruments must be able to detect the expected fluctuations. From section 2.12.1 the important fluctuations for wind pumping should lie in the range of 0.001 and 1 Hz.
* Given that two more major apparati were required for the total research programme, funds limited the purchase of equipment to the minimum required to meet the primary objective.

* Equipment was not restricted by transport requirements to the base area of Temple Basin, but the pressure measurement system must be easily moved around the terrain during measurement.
* Ease of use as the weather conditions required for the measurements, made even simple procedures very frustrating to carry out, unless well designed.

Figure 3.5 shows a schematic of the wind speed and pressure measurement apparatus. The wind speed and pressure measurement systems are discussed below, the data acquisition system is discussed in section 3.8.5.

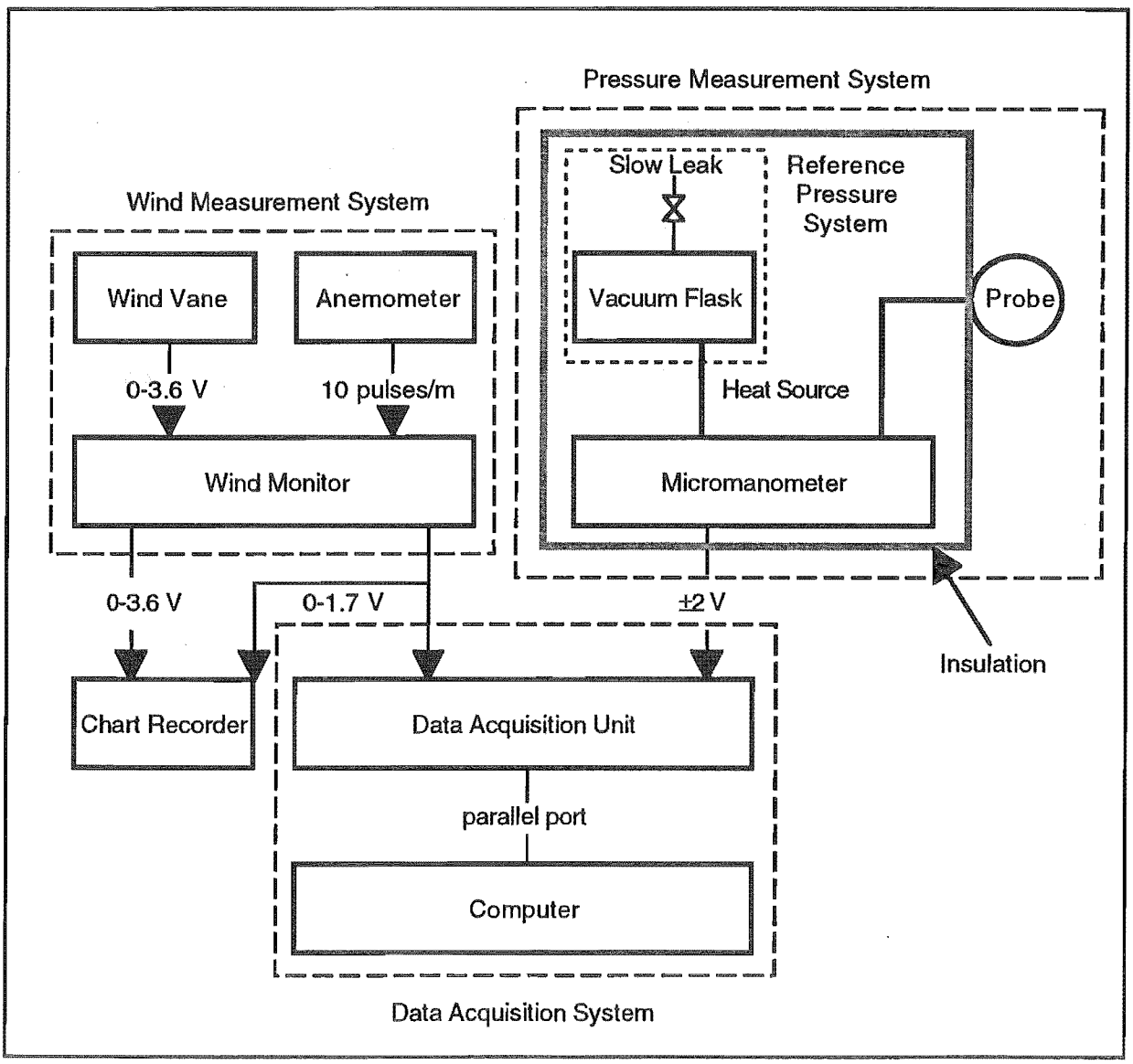

Figure 3.5. Apparatus Schematic for the Measurement of Wind Speed and Pressure Fluctuations.

3.7.1. Wind Speed Measurement System

It is well established that cup anemometers are not suited to accurate measurements of atmospheric turbulence, as they lack performance at the high frequency end of the spectrum. In a review of various anemometers used for turbulence research by Wyngaard (1981) two other comments were relevant. Firstly cup anemometers respond to horizontal wind speed regardless of the wind direction and thus the output only approximates the stream wise wind speed. Secondly, the mean wind speeds are slightly over estimated by approximately 10% in full scale measurements due to over speeding of the cups in fluctuating wind speeds.

Of the other options Bowen (1979), for example, explored the rationale behind using orthogonal arrays of propeller anemometers in place of cup anemometers. Combining the assumption that the pressure fluctuations would be closely related to wind speed fluctuations, and the snow pack would be likely filter out the high frequency fluctuations within the first few centimeters, there seemed to be insufficient justification in going to the complexity of such systems in this current investigation.

Strong lightweight materials mean cup anemometers have comparatively fast dynamic responses (down to length constants of 0.25 m for 6-cup versions). This work used Vector Instruments' (UK) 3-cup A110 Porton Anemometer installed on a 6.5 m[1] mast for general weather observations at Temple Basin. The mast was located on the ridge top, central to the measurement area, as indicated in figure 3.3.

A single anemometer, as opposed to more complex multi-component wind sensors, was used mainly from a cost perspective. This also seemed appropriate because near the ground (below 6 m) the horizontal component is by far the most significant. Vertical components will be deflected to the horizontal component as it nears the ground. However, as Colbeck (1989) comments, pressure fluctuations may be strongly correlated to the wind component normal to the snow surface (related to the stagnation pressure) and errors may arise in the crosscorrelation between the variables by the use of a cup anemometer. This mechanism for pressure fluctuations at the snow surface is supported in the results of Elliott (1972b).

The anemometer's electrical output of 10 pulses per meter wind run was converted and displayed as meters wind run and wind speed by the Wind Monitor described in Appendix II. The analog 0 to 1.7 volt output was converted to a digital signal and recorded by the data acquisition system described in section 3.8.5.

---

[1] This height changes according to accumulated snow pack depth HS during the season. For most measurements HS ≈ 3.0 m, leaving in an effective mast height of 3.5 m.

A wind vane connected to the Wind Monitor with a display of 0 to 360° (points of a compass) gave a mean wind direction and indicated the occurrence of back gusts. Wind direction was not digitally recorded but the 0 to 3.60 volt analog output was traced on a chart recorder.

3.7.1.1. Accuracy and Response Parameters of the Wind Speed Measurement

The specifications of the A100 Porton Anemometer are:

* Length Constant 3 m
* Threshold Velocity 0.2 m/s
* Wind run error ±0.1 m
* Steady state wind speed error is derived directly from the wind run error. For example, at 5 m/s the error is ±0.05 m/s.

The dynamic response of the anemometer can be derived from the length constant. Note that the instrument's time constant will be smaller at higher wind speeds.

3.7.2. Pressure Measurement System

Of interest here were atmospheric pressure fluctuations between 0.001 and 1 Hz which included stagnation pressure components. It is common practice to use differential pressure transducers for such applications (Waldeck, 1986), and hence a reference pressure must be supplied.

Ideally, several simultaneous pressure measurements should be taken at various terrain locations and snow pack depths, but in this first attempt at such measurements, the cost of such a set up was prohibitive. The following details each component of the system used.

3.7.2.1. Differential Pressure Transducer

Letchford *et al* (1992) found that using instruments with frequency responses below 10 Hz resulted in reduced peak amplitude readings (attenuation) in the separation and reattachment regions. At other points on windward and leeward faces of buildings, they found attenuation started with frequency responses below 2 to 4 Hz. However, they noted that it is the *relevant* data that must be collected. It has been assumed, and was demonstrated with the experimental program, that the high frequency information (above about 1 Hz) was not important in the wind pumping process.

The selected transducer, an Air Neotronics Digital Micromanometer MP6KSR, had the following applicable specifications:

* **Display Range** of ±199.9 Pa (the actual measurement range at the analog output is ±250 Pa).
* **Accuracy** of ±1% or ±0.1 Pa, which ever is greater. In the field with rapidly changing temperatures this accuracy reduced to ±2 Pa.
* **Frequency Response.** The unit is reported to respond to a maximum frequency of 2 Hz. This was an important variable to the overall study, so the dynamics of the pressure measurement system have been characterised experimentally.
* **Output.** LCD on unit and ±2.5 volt analog output (1 mv = 0.1 Pa).
* **Minimum Operational Temperature.** 0°C.
* **Power Source.** Internally fitted batteries (the wet environment prohibited mains power on the measurement site).

3.7.2.2. Probes

Two types of probes were required

1. **Surface Probe.** Wet snow posed the biggest design constraint on the surface probe, as it very quickly formed an impermeable cover over the probes ports. During dry snow conditions, problems arose with wind redistributed ice particles lodging inside the ports. These problems excluded the use of flat surface probes typically used in wind engineering (for example, see the review by Willmarth, 1975). Instead a hollow 30 mm diameter spherical probe with 20 x 3 mm diameter holes open to the atmosphere sitting on the snow surface was used. This is shown in figure 3.6 (a).

   A thin, dry, low density snow cover over the ports did not pose a significant problem as the permeability of the snow was sufficient to not dampen the pressure fluctuations.

   The dynamic contribution to the pressure fluctuations due to the probe interfering with the flow close to the ground must be minimised (Elliott, 1972a). Elliott's probe was deemed unsuitable for this task as very small dual ports would be easily blocked. Huey (1979), Blackmore (1987) and Kataoka *et al* (1989) developed spherical probes for measurements in the turbulent air flow which have static pressure errors of less than 2%. This gave a degree of confidence that the probe used here would be relatively unaffected by the flow.

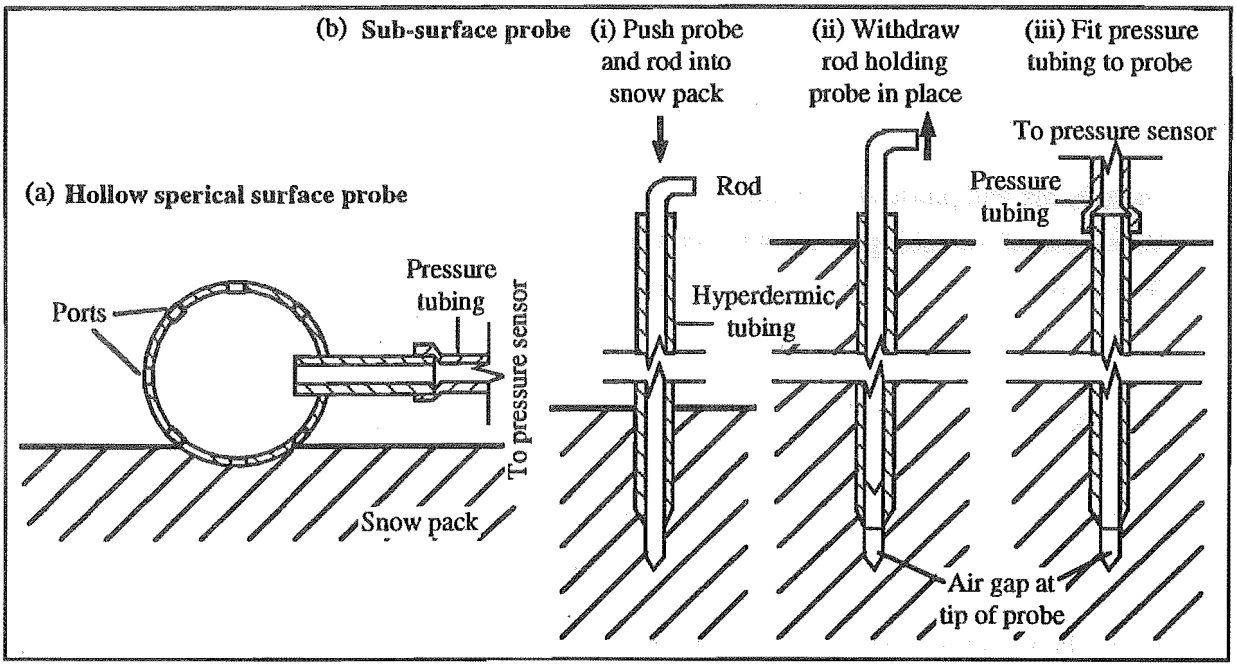

Figure 3.6. The Pressure Measurement Probes: (a) Surface Probe. (b) Sub-surface Probe.

2. **Sub-Surface Probe.** To measure pressure fluctuations beneath the snow surface a 2 mm diameter hypodermic tubing 1.2m in length was used. To allow easy insertion into the snow pack the end of the tube was bevelled to produce a sharp inner edge.

   Two problems arose with this design:

   1. A single ice particle is all that is required to block the end of the probe. This was overcome by placing a solid rod, slightly longer than the probe, inside the probe during the insertion into the snow pack. Once at the required depth the rod was withdrawn leaving a small air gap at the probe tip, thus overcoming the potential for the open end of the probe to rest on an ice particle. Finally the pressure tubing was attached. The probe and this procedure are illustrated in figure3.6 (b).

   2. The tube acts as a heat conductor so when the air temperature gets above 0°C the snow around the tube melts, creating a low resistance channel between the surface pressure fluctuations and the probe. This second problem was overcome by complete insertion of the probe beneath the snow surface. For depths of less than 1.2 m (the probe length) the probe can be inserted at an angle.

   Tests to check for channeling around the outside surface of the probe (a short circuit for the pressure fluctuations), showed no detectable differences in the pressure fluctuations. These tests were performed by using a 1.2 m probe connected to the reference port of the pressure transducer and inserted on an angle (to give a probe depth of 0.5 m) and a vertically inserted 0.5 m probe connected to the signal port.

3.7.2.3. Pressure Tubing

Factors influencing the pressure tubing design were:

* Dampening and phase shift of high frequency fluctuations.
* Vibrations of the tubing by the wind causing periodicities in the data.
* Ease of use in moving the probes and equipment around the measurement site.

Ease of use required the use of flexible tubing, which opened up the possibility of wind vibrating the tubing resulting in periodicities in the data. There was a choice between a long tubing system with the pressure sensor indoors out of the weather, and a short tubing system which required the protection of the sensor from the weather. To eliminate the chance of periodicities a 2 m long tube buried beneath the snow surface was used.

A check on the dynamic response of the tubing was made according to Holman (1978). This gave the pressure amplitude ratio

$$\left|\frac{p_t(t)}{p(t)}\right| = \frac{1}{\sqrt{\frac{1-f_m}{\omega_n} + 4\left(\frac{hf_m}{\omega_n}\right)^2}} \qquad 3.1$$

where $\omega_n = \sqrt{\frac{3\pi r^2 c^2}{4LV}}$ is the natural frequency, $h = \frac{2\nu}{cr^3}\sqrt{\frac{3LV}{\pi}}$ is the dampening ratio, and

$p(t)$ is the pressure fluctuations to be measured (Pa)
$p_t(t)$ is the pressure fluctuations at the transducer (Pa)
$r = 1.5\times10^{-3}$ m is the tubing internal radius
$V = 2\times10^{-7}$ m^3 is the transducer volume
$L = 2$ m is the tubing length
$f_m = 1$ Hz is the maximum frequency
ν is the air kinematic viscosity (m^2/s)
$c = 20.04\sqrt{T}$ is the speed of sound (m/s)
T is the air temperature (K)

The phase shift is given by

$$\phi = \tan^{-1}\frac{-2h(f/\omega_n)}{1-(f/\omega_n)^2} \qquad 3.2$$

The amplitude reduction was calculated as 7×10^{-4}% and phase shift -3.5×10^{-4}°, both well below significance. If the system was indoors, a 40 m tube was required and these became 1.1×10^{-2}% and 7.0×10^{-3}° respectfully. This was still negligible.

3.7.2.4. Low Frequency Filter - Reference Pressure System

Kataoka *et al* (1989) stated that the major difficulty, in the construction of the static pressure instruments, is the differentiation between synoptic and mesoscale pressure fluctuations from the turbulent (microscale) pressure fluctuations. The reference pressure system used here was conceptually the same as those developed by Elliott (1972a), Schols and Wartena (1986) and Kataoka *et al* (1989). The reference port of the differential pressure transducer is connected to a very rigid and thermally stable volume (usually a vacuum flask) which was in turn open to the atmosphere through a high resistance constriction. A vacuum flask with volume V = 1000 ml was used for the reference volume.

Experience through trial and error was used to determine the maximum reference pressure leakage resistance to balance the transient average pressure[2]. This did not include the fast changing atmospheric pressure associated with the passage of fronts, during which the wind shifts to the southerly quarter. This resistance was found by using a 0.406 mm diameter hypodermic tube 0.48 m long and inserting 0.225 and 0.345 mm wires varying distances into the tube. To *just* maintain the pressure fluctuations on scale, a fully inserted 0.225 mm wire functions best.

Since the flow in the annulus forming the restriction is laminar ($Re_{annulus} = 0.014 \ll 2100$) the dynamic response of the system will be indicated by its time constant. Kataoka *et al* (1989) calculated the reference pressure time constant τ_{ref} for a similar system using

$$\tau_{ref} = \frac{8MV\nu L}{\pi RTr^4} \qquad 3.3$$

where

ν, L, T, and r are defined as in equation 3.1 above
$V = 1 \times 10^{-3}$ m^3 is the reference volume
R is the gas constant (kJ/kmolK)
M is the molar mass of air (kg/kmol)

Using this to calculate the time constant for varying diameters, an estimate of the dynamics of the annulus may be made. To check the validity of these equations, the time constant for the empty tube was measured assuming first order dynamics. The resulting time constants are shown in table 3.3.

---

[2]This resistance will be particular to the conditions during which measurements are made; in this case with the northwest phase of the weather systems.

internal radius, r (mm)	0.203	0.153	0.102
$\tau_{ref,theo}$ (minutes)	1.7	7	27
$\tau_{ref,expt}$ (minutes)	1.5±0.3	-	-

Table 3.3. Time Constants for the Reference Pressure System for Varying Leakage Tubing Radius.

The time constant measured for the fully inserted wire was τ_{ref}= 7.5±0.6 minutes. This related to an equivalent diameter of 0.15mm. This time constant was lower than the 27 minutes for the system used by Kataoka *et al.* This is to be expected as the measurements made here were during active storms cycles where the average atmospheric pressure drifted relatively quickly.

To examine the effect of the reference pressure system on the frequency response of the pressure measurement system, equations 3.1 to 3.3 above are evaluated and plotted in figures 3.7 and 3.8 for r= 0.15 mm and the reference volume, V= 1000 ml.

3.7.2.5. High Frequency Response

In a similar fashion to Elliott (1972a) and Schols and Wartena (1986) the high frequency characteristics of the micromanometer were investigated using the sinusoidal pressure fluctuations delivered by the apparatus described in section 4.6. The amplitude and phase responses of the Air Neotronics Micromanometer and Reference Pressure system are plotted in figures 3.7 and 3.8 respectively, with an accuracy of 5% in amplitude, and 5° in phase.

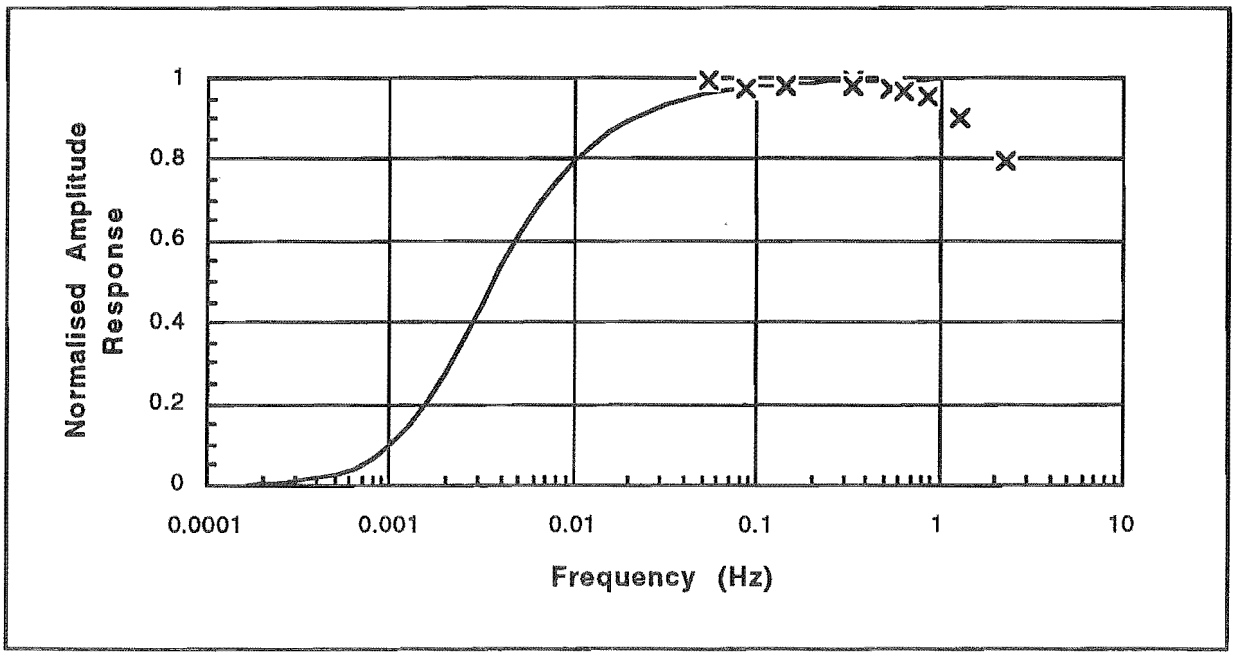

Figure 3.7. Measured Values of the Amplitude Response at High Frequencies and Predicted Response at Low Frequencies for the Air Neotronics Micromanometer and Reference Pressure Measurement System.

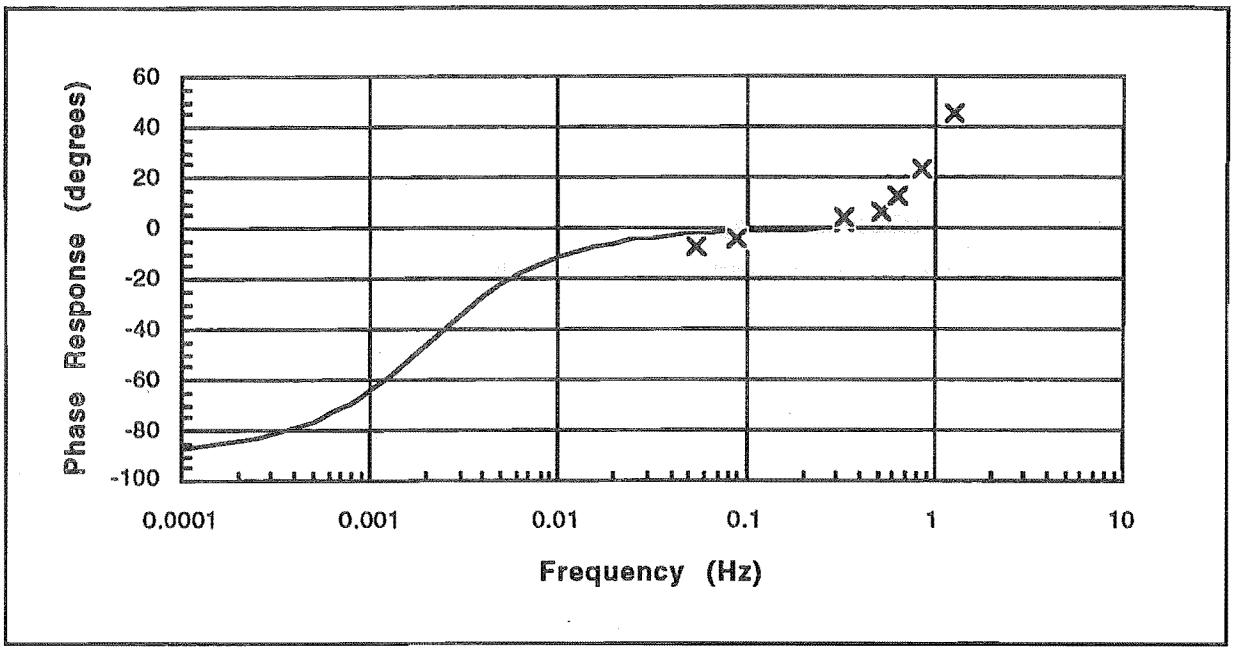

Figure 3.8. Measured Values of the Phase Response at High Frequencies and Predicted Response at Low Frequencies for the Air Neotronics Micromanometer and Reference Pressure Measurement System.

In summary, the pressure measurement system should give better than a 80% amplitude response between $0.01 \geq n \geq 2$ Hz and better than 95% between $0.04 \geq n \geq 1$ Hz. Except where stated, the results obtained in the following experiments were not corrected for attenuation in the pressure of wind speed signals due to limiting instrument response.

3.7.2.6. Weather Proofing

The pressure measurement system was enclosed in an insulated weatherproof container, designed to cope with the weather experienced during storm periods at Temple Basin. Two features of this container were:

* Exclusion of water and blowing snow from the container. This was important for two reasons; the instruments in the container must remain dry, and the finest of ice particles or water droplets is sufficient to block the 0.4 mm diameter hypodermic tubing that provided the resistance for the reference pressure system.
* An ability to maintain the container temperature to within the operational temperature range of the micromanometer. This was achieved in two ways; the container was insulated with polystyrene foam, and heated to above 5°C by a frequently replaced 2 liter hot water container. The thermal stability of the vacuum flask required that the box be opened as little as possible.

3.7.3. Weather Measurements from the Temple Base Study Plot

The base study plot at Temple Basin is located about 150m south of the anemometer mast beside Twin Creek at 1370m above sea level. The following observations of snow and weather conditions were taken according to NZMSC (1987) at least once during each run, and more frequently if the overall weather pattern appeared to be changing.

* Weather - Cloud cover and precipitation type and intensity
* Temperature - Maximum, minimum and present or dry bulb
* Thermohydrograph - Temperature and relative humidity and trends
* Snow depths - Interval, new, 24hour and storm snow boards and total snow stake
* Precipitation - New snow density and water equivalent or rain gauge reading
* Snow surface and foot penetration
* Wind - Strength and direction at the plot and ridge top
* Atmospheric pressure and trend

3.7.4. Snow Pack Measurements

Periodically snow profiles were made near the measurement site which included, in addition to the standard observations outlined in NZMSC (1987), permeability profiles of the snow pack. The Blower Permeometer used for these measurements is detailed in Appendix III.

3.8. Digital Data Collection and Pre-Processing

3.8.1. Sampling

Flay (1978) performs a very comprehensive study of the parameters associated with sampling. According to Flay, careful consideration must be given to each of the following as the requirements on storage space and processing time need to be minimised while maintaining the statistical accuracy of the results:

1. Sample Rate
2. Sample Averaging
3. Record Size

3.8.2. Choice of Sampling Rate

Sample rates were chosen according to the recorded signal's frequency characteristics. For example, sampling too fast will result in unnecessarily large data files, while sampling too slow may result in important information being lost and misleading information appearing in spectral analysis due to digital aliasing.

To avoid digital aliasing, the sample frequency needs to be at least twice that of the highest frequency of interest. The highest frequency will be determined by the fastest of the physical process being measured, the dynamic response of the instruments, and the setting of any low pass filters. The causes and effects of digital aliasing are well documented and are not discussed further here.

Although the measurement systems were designed to have a limit to their high frequency response of about 1 Hz (refer to section 3.7.2.5), the micromanometer responds to signals around 5 Hz with a much reduced amplitude. Sampling at 10 Hz resulted in some aliasing still being present in very high winds (>25 m/s), while at 20 Hz, the next available sampling frequency in the data acquisition unit (Strobes Macquisition, New Zealand) no aliasing occurred. Quite possibly, the aliasing occurred due to the sharp pulse created by the micromanometer zero (refer to section 3.8.7). Hence 20 Hz was used in these experiments. The data acquisition unit required that both channels be sampled at the same rate.

The Nyquist Frequency associated with this sampling rate is

$$f_c = \frac{1}{2\Delta t} = 10 \text{ Hz} \qquad 3.4$$

where Δt is the sampling interval.

3.8.3. Sample Averaging

Although 20 Hz was required to avoid aliasing, the anemometer and micromanometer do not respond accurately above about 1 Hz.

Averaging the discrete samples integrates the fluctuations over the period of averaging. This in effect is a low pass filter with its first zero at 1/(Averaging Time) and is beneficial from the point of aliasing (Flay, 1978).

As long as the averaging time does not remove high frequency information from the spectral analysis, this is an appropriate method of reducing the number of data points and subsequent processing time.

A series of sensitivity tests over averaging times of 0.1 to 2.0 s for the wind speed and pressure fluctuations, using the moving average technique (Levitan *et al*, 1991b), showed that no information was lost up to a 0.5 s averaging period from the readings given by the instruments detailed in section 3.7. Thus the sample frequency of 20 Hz was effectively reduced to 2 Hz by averaging over 10 samples and consequently no aliasing was observed in the 2 Hz data.

The sample frequency choice of other authors depended largely on application. Sampling frequencies both lower and higher than this have been used in the literature.

3.8.4. Record Length (duration)

With the condition that the data remain stationary, the longer the record the better the resolution of the correlation and spectral density function. Resolution could also be gained by averaging the results of an ensemble, or collection of records.

ESDU 72026 (1974) commented that the 10 minute mean wind speed fluctuates widely from one 10 minute period to the next, and that due to changing weather patterns the 2 hour mean wind speed will also change from one period to the next. Flay (1978) determined that for his data, collected over relatively flat rural terrain, the minimum sampling period to achieve representative turbulent statistics was 30 minutes, with better spectral estimate at low frequencies found with longer records.

Considering the extreme terrain by comparison to other work, a similar sensitivity analysis is carried out for this analysis, the results of which are summarised below.

The runs selected for presentation here represent the character of most sample records. Deviations from typical character are bourne out in the lack of record stationarity (see section 3.9.3) and generally require some sort of trend removal (see section 3.9.3.2).

3.8.4.1. Dependence of Statistical Properties on Record Length

Mean wind speed, and the turbulent intensities of both the wind speed and pressure fluctuations, were plotted against increasing record length for Runs 33 to 43 and 88 to 98 (both 130 minutes), 99 to 106 (90 minutes) and 125 and 127 (30 minutes) in figures 3.9, 3.10 and 3.11 respectively. The statistics were evaluated at discrete elapsed times on the records so that time varying trends could be observed. All statistics used in this section are fully described in sections 3.9.1 to 3.9.6.

Using the standards of consistency set by Flay (1978), it appeared that the mean wind speed became reasonably steady after 20 minutes for low wind speeds. The mean for runs at high wind speeds, limited to 30 minutes due to the harsher experimental conditions (see section 3.8.4.2), did not become constant within the record length. Wind speed standard deviation appeared to become constant after 40 minutes, although the results were quite variable. There appeared to be considerably more variability in the standard deviations of the pressure fluctuations. This variability did not appear to settle until 70 minutes had elapsed. Much of this variability in the mean and standard deviation was treated successfully with trend

removal (section 3.9.3.2) and hence was not so apparent in the autocorrelation and auto spectral functions.

The assessment of drift in mean and/or standard deviation in *every* sample was important to the assumption of stationarity, and is treated in detail in section 3.9.3. Also, note that mean pressure was not measured as a variable in this thesis due to the necessity to filter out the low frequency (synoptic) fluctuations.

The autospectral density, autocorrelation and cross correlation functions were plotted after moving average trend removal (section 3.9.3.2) in figures 3.12 to 3.16 for both the pressure and wind speed fluctuations of Runs 33 to 43 for sampling periods of 136, 68, 34, 17 and 8.5 minutes.

Both the autocorrelation and autospectral functions showed consistent results for wind speed fluctuation record lengths of ≥ 17 minutes, and ≥ 34 minutes for the pressure fluctuations. According to the autospectral functions, the longer the record length the more consistent the results were at lower frequencies.

The crosscorrelation function showed no definitive record length at which the results became consistent. Such inconsistent features of the crosscorrelation function are discussed in section 3.10.6.

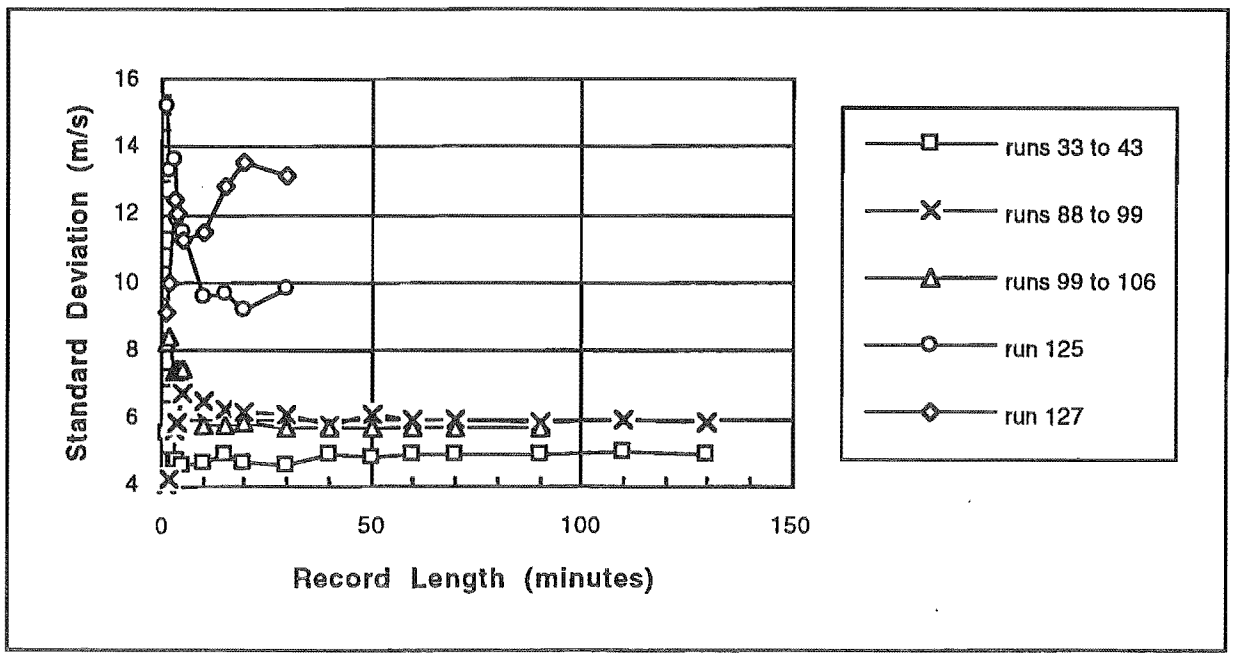

Figure 3.9. Mean Wind Speed for Varying Record Lengths (no trend removal).

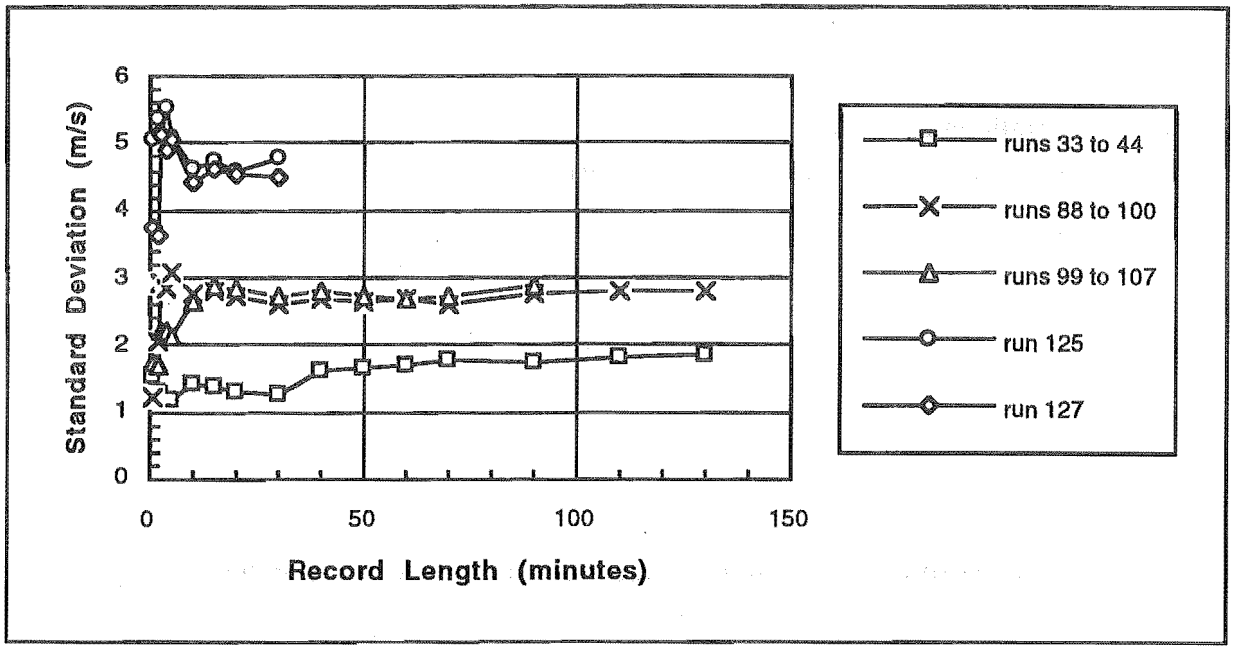

Figure 3.10. Standard Deviations of the Wind Speed Fluctuations for Varying Record Lengths (no trend removal).

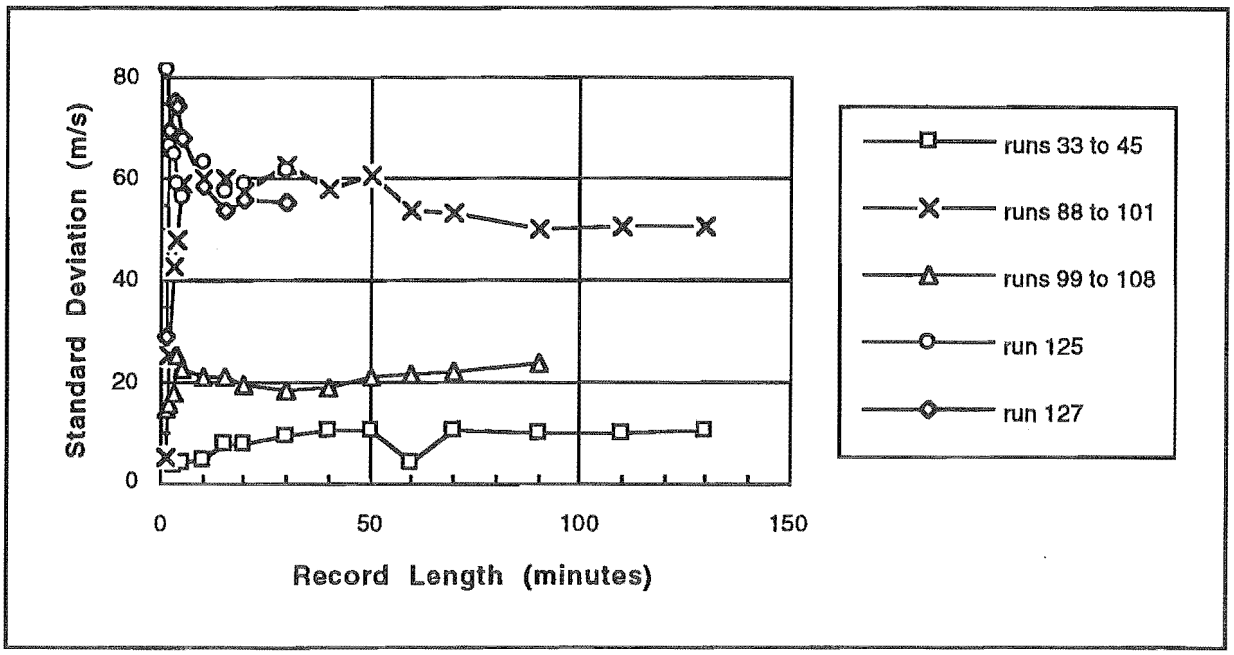

Figure 3.11. Standard Deviations of the Pressure Fluctuations for Varying Record Lengths (no trend removal).

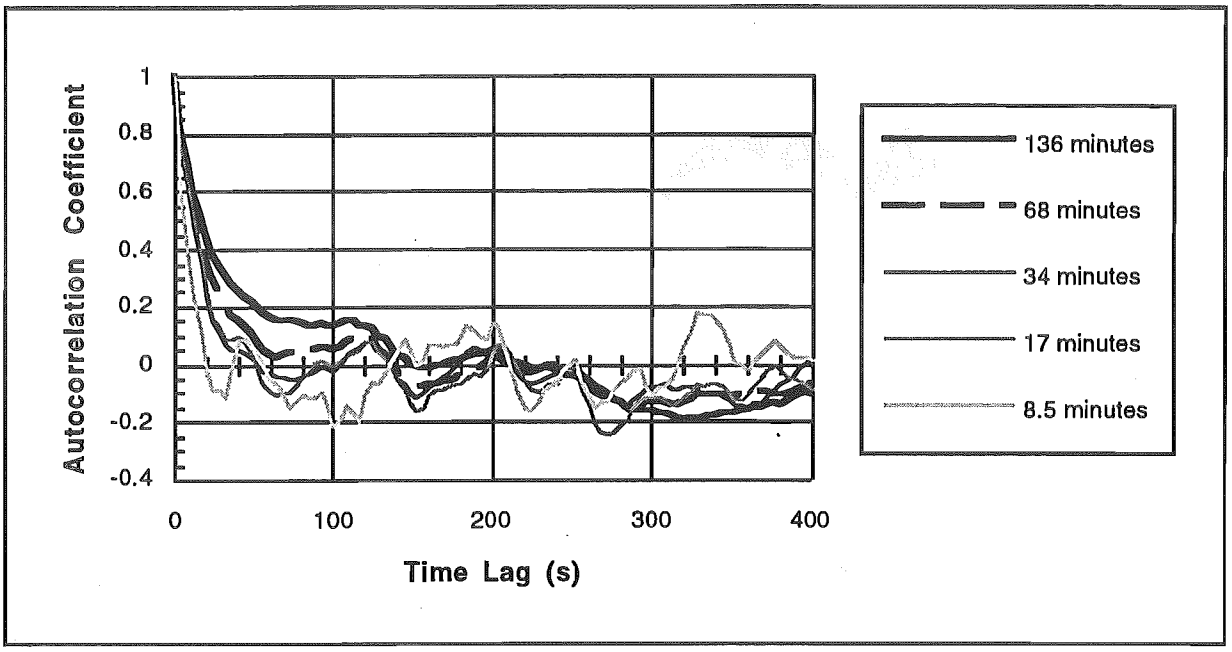

Figure 3.12. Autocorrelation Functions of the Wind Speed Fluctuations from Runs 33 to 43 for Varying Record Lengths (after trend removal).

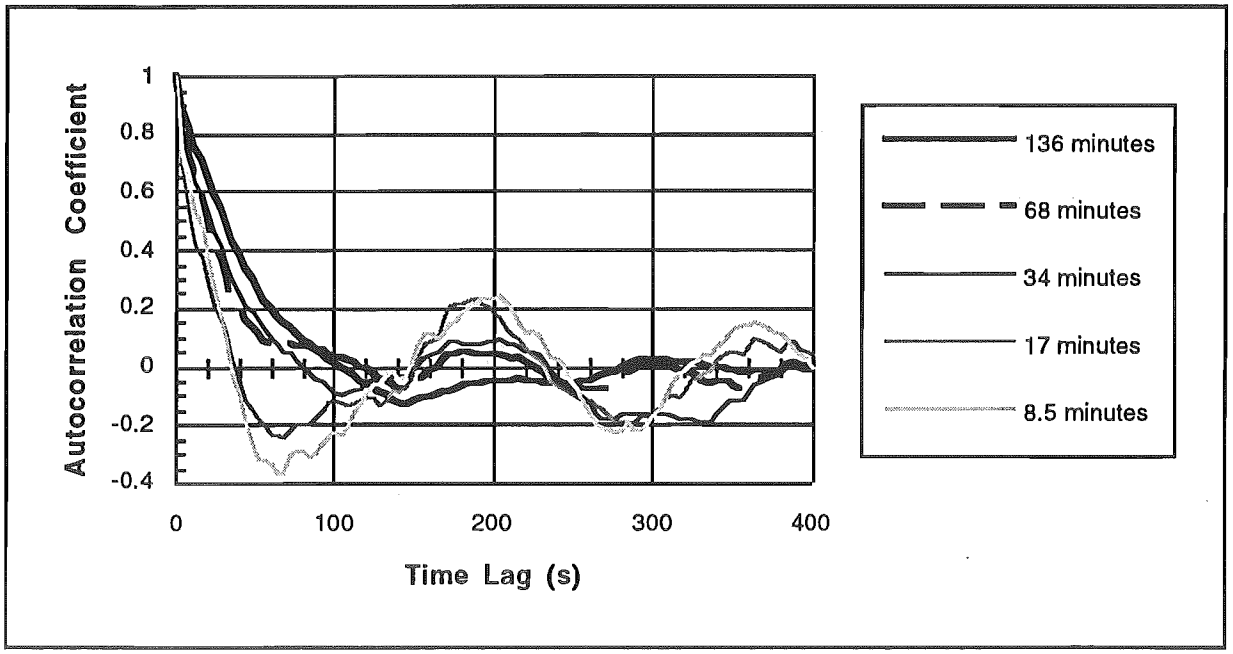

Figure 3.13. Autocorrelation Functions of the Pressure Fluctuations from Runs 33 to 43 for Varying Record Lengths (after trend removal).

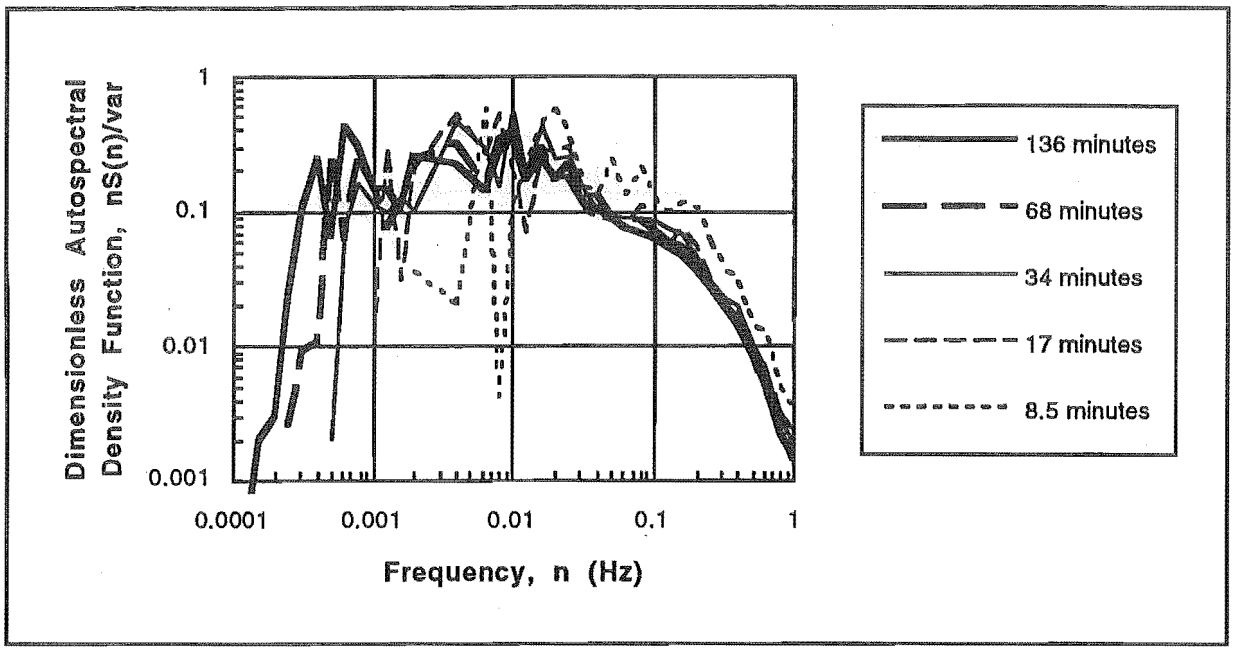

Figure 3.14. Smoothed Autospectral Density Functions of the Wind Speed Fluctuations from Runs 33 to 43 for Varying Record Lengths (after trend removal).

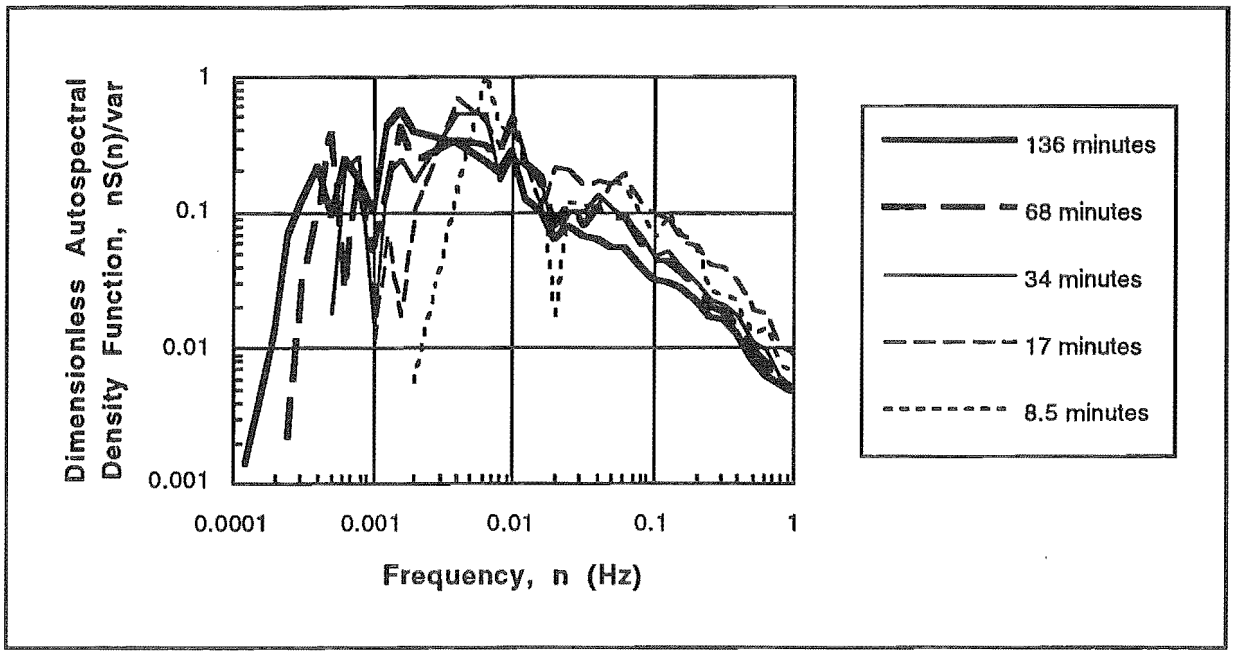

Figure 3.15. Smoothed Autospectral Density Functions of the Pressure Fluctuations from Runs 33 to 43 for Varying Record Lengths (after trend removal).

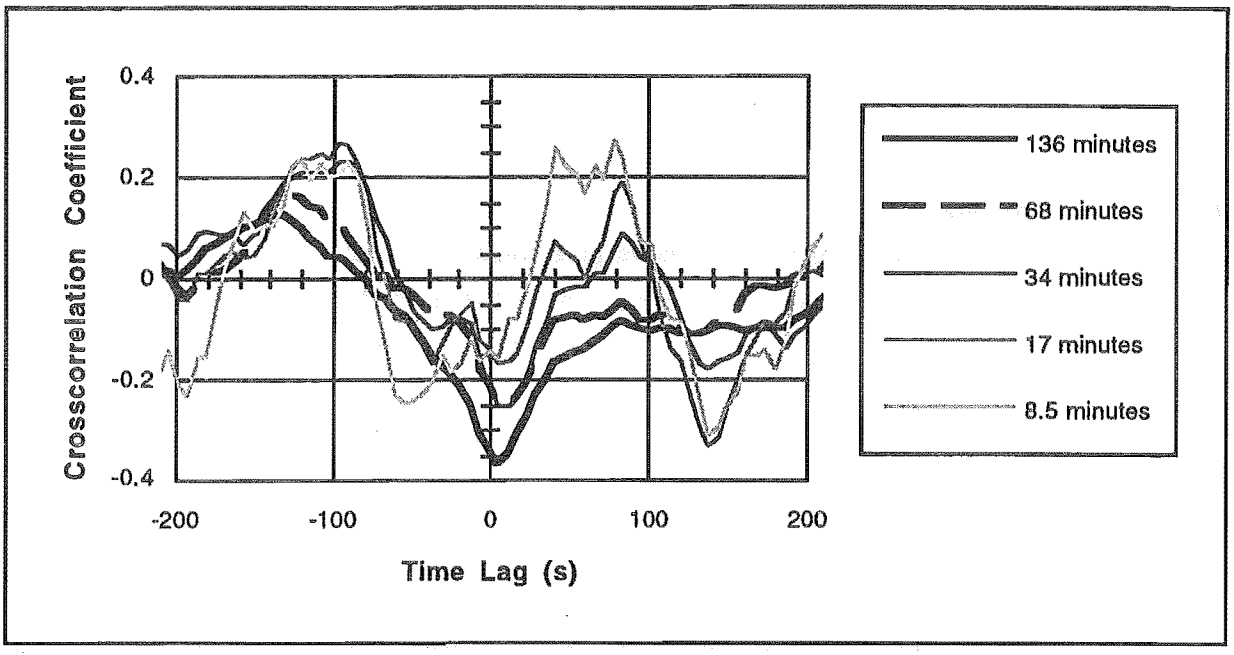

Figure 3.16. Crosscorrelation Functions Between the Pressure and Wind Speed Fluctuations from Runs 33 to 43 for Varying Record Lengths (after trend removal).

3.8.4.2. Environmental Factors and Record Length

The weather conditions during sampling imposed two limiting sample duration conditions:

1. *The presence of non-stationary conditions*, as changes in wind patterns occurred and frontal systems passed. Most measurements were made during active westerly quarter storms which, in the South Alps of New Zealand, are characterised by the frequent passage of frontal activity. Some of this activity is obvious, accompanied by distinct atmospheric pressure changes and more intense precipitation, while other activity is obscured by the inherent strength of the westerly flow and associated orographic effect.

2. *Fouling or failure of the pressure measurement system.* Although designed to reduce such occurrences, the extreme weather in which measurements were made resulted in frequent early termination of a run.

    * Heavy rain (up to 300mm in one 24hr period) made it very difficult to keep moisture out of the instruments.
    * Blowing snow blocking and/or burying the pressure probe.
    * Wind eroding snow covering the pressure tubing and eventually moving the probe and in one case the entire instrument box.
    * Heat source unable to maintain the instrument box above 5°C, the minimum instrument operating temperature.

3.8.4.3. Accepted Record Length

From the above results and discussion it appears that, without trend removal, wind speed record statistics are reasonably consistent for record lengths longer than about 40 minutes. There is inherently more variability in the pressure fluctuation record statistics, and it appears that records of around 70 minutes are required to give consistent results. After trend removal, sample records 34 minutes or longer give consistent statistics for both the fluctuating wind speed and pressure data. This compares to 30 minutes selected as a minimum by Flay (1978).

The major limitation on achieving the minimum desired record length was equipment reliability in the typically harsh experimental conditions. This was borne out in the fact that no records longer than 27 minutes could be obtained during very strong wind conditions (>10m/s) due to equipment failure.

Provided that the conditions remain stationary, more information can be gathered with longer record lengths. This is important to the accuracy of the low frequency end of the autospectral function. Note that a maximum record length of 151 minutes was set by hardware limitations (see section 3.8.5).

Over some record lengths the memory limitations of DADiSP Worksheet on the DECpc 433 Workstation required truncation of the record length to 2^a samples as discussed in Appendix I.

3.8.5. Data Collection by an Apple Mac Plus and Macquisition

The outputs of the anemometer and micromanometer were sampled by the Strobes Acquisition Unit 901A, a two channel digital storage oscilloscope and spectrum analyser. An Apple Mac Plus with 1MB of RAM provided the interface with the data acquisition unit running the Macquisition V1.4. The maximum file length or frame size available in Macquisition is 16384 samples (128 minimum), and although consecutive files may be made and saved to disk automatically a four second segment of data is missed between each file. In this case the storage device was a single density external floppy disk drive which limited the number of consecutive files to eleven before the disk must be swapped and Macquisition reset. All files were saved in Macquisition format, which uses 20% of the file space Text files occupy.

Procedures are discussed below to interpolate for the missing four seconds between files. No attempt was made to estimate the data missed during the time between disks and thus a disk determined the maximum length of the record. With a sampling frequency of 20Hz this related to eleven 13:39 minute samples and a total maximum record length of 150 minutes.

Although samples were saved in the time domain, as data was collected it could be inspected in the frequency domain for aliasing using the spectrum analyser.

3.8.6. Translation from Apple Macquisition Format to IBM Text Format

On returning from the field station, files were opened up in Macquisition and re-saved as text files. These text files were then translated to IBM format using Apple File Exchange 1.1.4 and loaded onto a 486 DECpc 433 Workstation (8 MB of RAM) where all subsequent processing took place using Microsoft Excel 4.0 spread sheets and macros.

3.8.7. Micromanometer 'Zero' Removal

At approximately two minute intervals the micromanometer corrected itself for changing ambient pressure and temperature. This was achieved by two solenoid valves opening a line between the two sides of the pressure transducer, and closing both the reference and signal ports. This state was maintained for approximately three seconds before returning to the measurement. This switching was accompanied by a voltage surge at the start of the 'zeroing' cycle.

The plumbing could be arranged to bypass the solenoid switching, but the voltage surge was imbedded in the internal electronics and could not be avoided. Hence this glitch in the output voltage had to be dealt with in software. The four approaches that were investigated to deal with the glitches are illustrated in figures 3.17 and 3.18 and described below:

1. **Leaving the glitches** in the records. This would have the effect of adding two components to the autospectral density function:

    1. A very powerful high frequency component due to the voltage surges associated with the onset of the 'zero'.
    2. Addition of square wave components whose power depends on the average pressure of the data stream at the time of the 'zero'.

2. **Deleting the affected samples.** This would add a high frequency component to the autospectral density function as a step is created in the time series between the start and end of the 'zero'. It would also require the removal of equivalent samples from the time series of the wind speed fluctuations to keep the two in phase and avoid errors in the crosscorrelation function.

3. **Linear interpolation** over-writing the data between the start and end of the 'zero' is far better than the two options above, but still results in two sharp changes in slope at the end point of interpolation. This again would add some high frequency components to the autospectral density function.

4. **Cubic Lagrangian interpolation** over-writing the data between the start and end of the 'zero'. As the slopes at the end points were taken into account no high frequency components were added. *This was chosen as it appeared to closely follow the natural pattern of the data.* Note that the noise in the data was smoothed over in the evaluation of the slopes at the start and end of the 'zero' to prevent the accentuation of a random error in the interpolation.

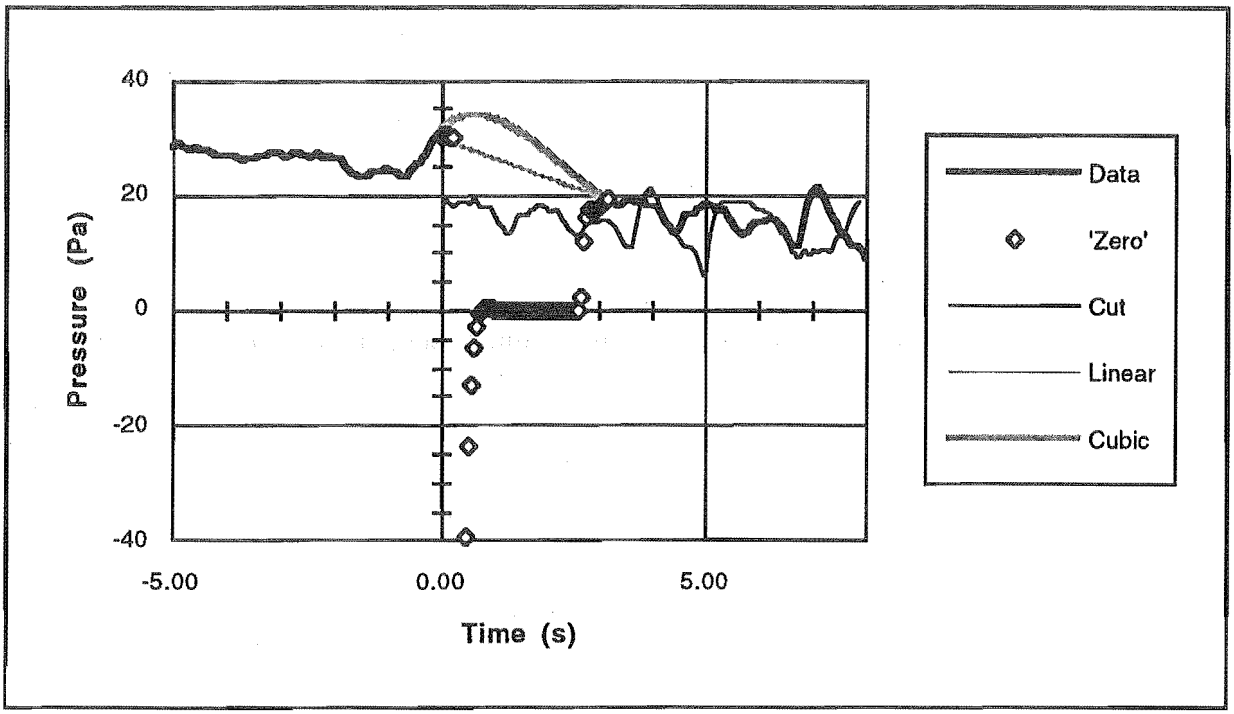

Figure 3.17. Options in Dealing With the Micromanometer 'Zero'. Example from Run 92.

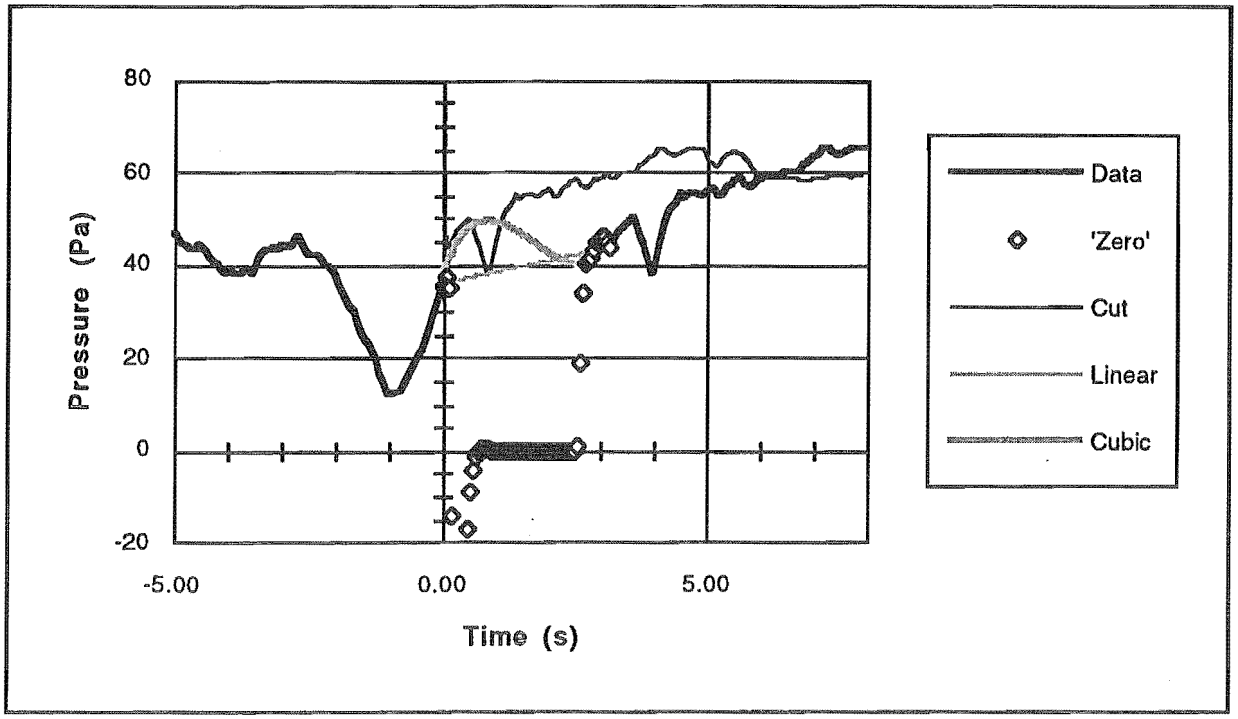

Figure 3.18. Options in Dealing With the Micromanometer 'Zero'. Example from Run 94.

At this point the calibration equation

$$\text{Wind Speed} = -4.53 + 7.36*V_0 - 0.104*V_0^2 + 0.00799*V_0^3 \qquad 3.5$$

derived in Appendix III for converting the anemometer measurements from output voltage V_0 (volts) to wind speed (m/s), and the micromanometer measurements conversion from output voltage to pressure (linear conversion of 10 mV = 1 Pa) were applied to the records.

3.8.8. Joining 'Runs' to form a 'Record'

Joining consecutively saved runs was done with cubic Lagrangian interpolation in the same manner as smoothing over the micromanometer 'zeroing', only this time there were four seconds of missing data from both the wind speed and pressure data. Up to a maximum of 11 runs were joined to give sufficient record lengths to examine the low frequency fluctuations (0.01 to 0.001 Hz).

3.9. Statistical Analysis

The method of analysis of individual records used here followed closely the principles outlined in Bendat and Piersol (1986) and used by Flay (1978) and later Bowen (1979). Figure 3.19 outlines the steps in this analysis. Each step was performed for both the wind speed and pressure fluctuations except for the crosscorrelation analysis which was done between the variables.

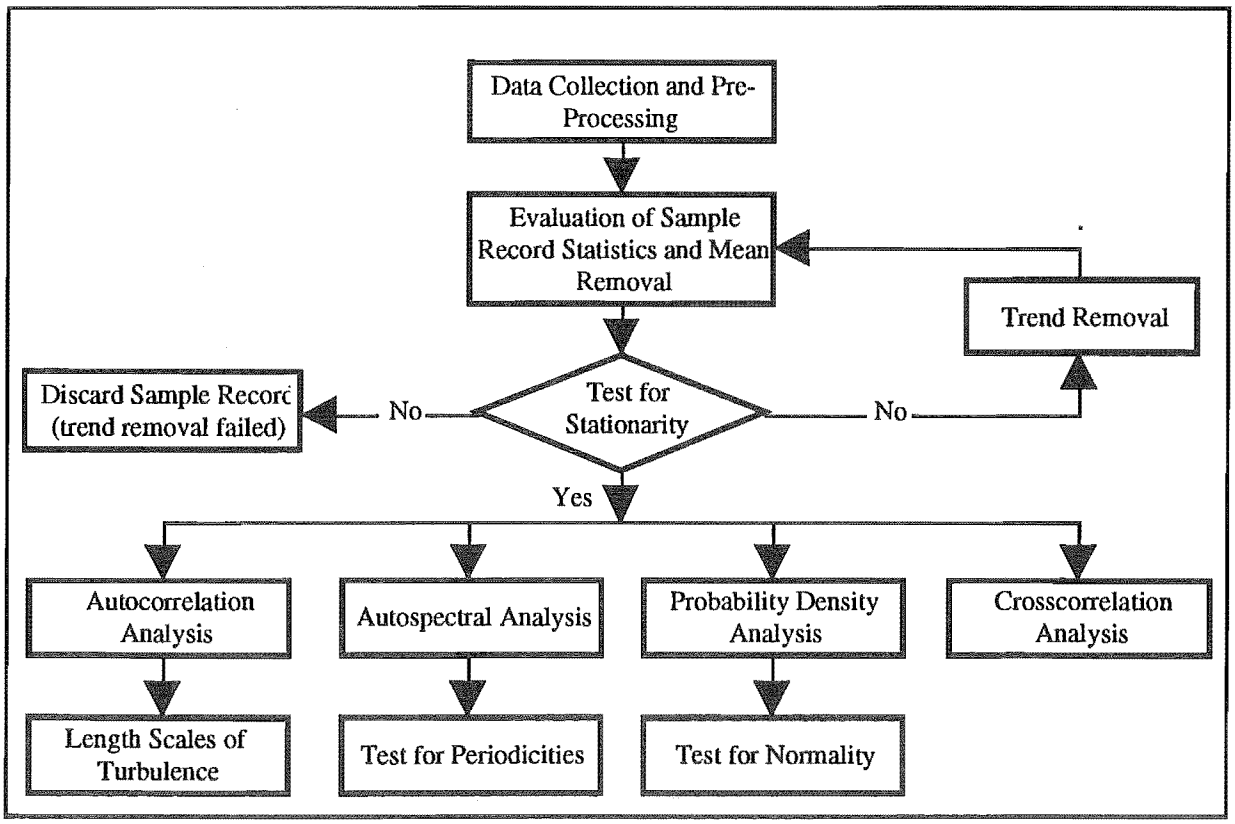

Figure 3.19. Procedure Used to Analyse Individual Records.

As a very large volume of information was generated by the statistical analysis of individual records, the data was collated into averages for similar sampling conditions. This averaging over an ensemble (collection) of records was also used as an important step in the reduction of random errors (see section 3.9.6.2). The results of this analysis are summarised and discussed in section 3.10 and summaries of the individual record statistics included in Appendix IV.

3.9.1. Record Variance Statistics

ESDU 72026 (1974) defines that at height z (3.5 m in this study) the instantaneous wind speed V(t) and wind speed fluctuation u(t) are related by

$$v(t) = u(t) + \overline{V} \qquad 3.6$$

where $\overline{V}$ is the average wind speed over the record of length T_0, given by

$$\overline{V} = \frac{1}{T_0}\int_0^{T_0} V(t)dt \qquad 3.7$$

T_0 is an averaging time of at least 15 minutes fixed by the Van der Hoven spectrum (figure 2.1), although Flay (1978) and Bowen (1979) use a period of at least 30 minutes. For this application an averaging time of 34 minutes was an appropriate minimum (see section 3.8.4.3). Note that

$$\overline{u} = \frac{1}{T_0}\int_0^{T_0} u(t)dt = 0 \qquad 3.8$$

The wind speed record variance σ_u^2 is given by

$$\overline{u^2} = \sigma_u^2 = \frac{1}{T_0}\int_0^{T_0} u(t)^2 dt \qquad 3.9$$

and is used to measure the turbulence intensity

$$I_v = \frac{\sigma_u}{\overline{V}} \qquad 3.10$$

σ_u may be thought of as the standard deviation of the total turbulence V(t), or the rms amplitude of the fluctuating component u(t).

According to Papesch (1984), the averaging technique used here for turbulence estimates becomes suspect over high surface roughness where accelerations and pressure changes occur.

Also rapid changes in wind direction, caused by deflections of the wind off large terrain features, and the constant changing weather patterns experienced during the measurements, must add to this suspicion.

Although the results of this analysis must be treated with caution from the point of view of the atmospheric scientist, they do still give some very useful information on the driving forces involved in the wind pumping through a snow pack.

For the pressure fluctuations the mean has no meaning and is removed from the record leaving the pressure fluctuations p(t). Again note that

$$\overline{p} = \frac{1}{T_0}\int_0^{T_0} p(t)dt = 0 \qquad 3.11$$

and the pressure record variance σ_p^2 is given by

$$\overline{p^2} = \sigma_p^2 = \frac{1}{T_0}\int_0^{T_0} p(t)^2 dt \qquad 3.12$$

The turbulence intensity for the pressure fluctuations is evaluated using the average stagnation pressure $\overline{p_s}$

$$\overline{p_s} = \frac{1}{2}\rho\overline{V}^2 \qquad 3.13$$

where ρ is the air density and $\overline{V}$ the average wind speed of the record defined in equation 3.7 (only available at $z = 3.5$ m). The pressure turbulent intensity is otherwise called the rms pressure coefficient C_p (Plate, 1982)

$$C_p = \frac{\sigma_p}{\overline{p_s}} \qquad 3.14$$

Note that caution is required when making comparisons between rms pressure coefficients as the exact definition for average velocity varies from author to author.

3.9.2. Peak Gusts

As the mechanism of wind pumping requires many cycles to be effective there seems little point in any extreme value analysis of the records.

3.9.3. Stationarity

The statistical procedures discussed here assume that the data is *random* and *stationary*; that is, *data with statistical properties which are invariant with translations in time.* However, it is generally accepted that atmospheric turbulence is a non-stationary process (as are most natural processes). None the less, in order to use the following statistics it was sometimes considered stationary over relatively short record lengths (10 to 120 minutes). Non stationary data can be analysed as in Bendat and Piersol (1986), but the procedures for doing so are substantially more complex.

The statistical analysis at least requires the records to be *weakly stationary.* An ensemble (collection) of records of a random process is said to be *strongly stationary* if all possible moments and joint moments computed from it are time invariant. An ensemble of records of a random process is said to be *weakly stationary* if the mean and autocorrelation functions are time invariant. However, in practice the individual records were assessed as stationary if the variation of its properties, computed over short time intervals, did not vary more than normal statistical sampling variations from one interval to the next.

According to Bendat and Piersol, the simplest way to evaluate the stationarity of sampled random data is to consider the physical processes involved in producing the data. There are two key considerations here:

1. ESDU 72026 (1974) suggests that the synoptic scale pressure systems will cause changes in the levels of atmospheric turbulence over periods greater than about two hours. Experience with the weather patterns at Temple Basin suggested that with the frequent passage of frontal activity, the mesoscale fluctuations are a more important consideration here.

2. An additional factor affecting the measurement of the pressure fluctuations, is the interaction of the relatively slow mesoscale and synoptic pressure changes with the reference pressure system as described in section 3.7.2.4. This results in uncorrelated drifts in the mean pressure reading.

Therefore the stationarity of the data must be looked at in more detail, and the likelihood that trend removal be required is high.

3.9.3.1. Test for Stationarity

Levitan and Mehta (1992) comment that stationarity testing is one of the most important statistics in current Texas Tech field experiments where they are making every effort to ensure the quality of their data. The method used here (and by Levitan and Mehta), to evaluate the

stationarity of the records, follows Bendat and Piersol (1986) and Flay (1978), and has two basic assumptions. The given record must:

1. Properly reflect the non-stationarity character of the random process in question.
2. Be long compared to the lowest frequency component in the data excluding a non-stationary mean. This allows the non-stationary trends to be differentiated from the random fluctuations in the time history.

Flay makes a third assumption, that any non-stationarity of interest will be revealed by time trends in the mean square value of the data. This assumption will not strictly be made here, as some records in which trends are not revealed are still regarded as non-stationary after visual inspection of the time history and autocorrelation function.

Bendat and Piersol suggest the following procedure, the *Run Test* to detect underlying trends in the data.

1. Divide the original sample record i(t) into N equal time intervals, or averaging periods, of length T_0. The data in each period may be considered time independent.
2. Compute the mean square for each interval using

$$\overline{i^2} = \frac{1}{T_0}\int_0^{T_0} i(t)^2 dt \qquad (i = u \text{ or } p) \qquad 3.15$$

3. Test the sequence of mean squares for the presence of underlying trends or variations other than those expected due to normal sampling variations.

Flay used an averaging period of 2.28 minutes as the autocorrelation function fell to zero generally after about 1 minute, inferring that the mean squares could be considered independent. On that basis, the averaging period used here was 5 minutes, except for the two 41 minute records where 2.5 minutes was used (to maintain a statistical significance in the test).

The results were plotted, as the example in figure 3.20 shows, and the number of *runs* counted for the Run Test. In the Run Test, a run is defined as a continuous sequence of mean squares, above or below the average of the mean squares, that is followed and preceded by a sequence on the opposite side of the average, or by no observations at all. In this case there are r = 15 runs in the sequence of N = 26 observations. Table A6 of Bendat and Piersol gives the number of runs which are acceptable for several levels of significance, for different numbers of observations. The hypothesis tested here is that the trend is zero. Choosing a α level of significance, if the number of runs falls outside the intervals between $\Gamma_{N/2:1-\alpha/2}$ and $\Gamma_{N/2:\alpha/2}$ the hypothesis is rejected and there is an underlying trend. Otherwise any trend is ignored.

In the example above, at the α level of significance, the number of runs should lie in the range 8 to 19. Thus in this case the hypothesis is not rejected and any trend uncovered is ignored.

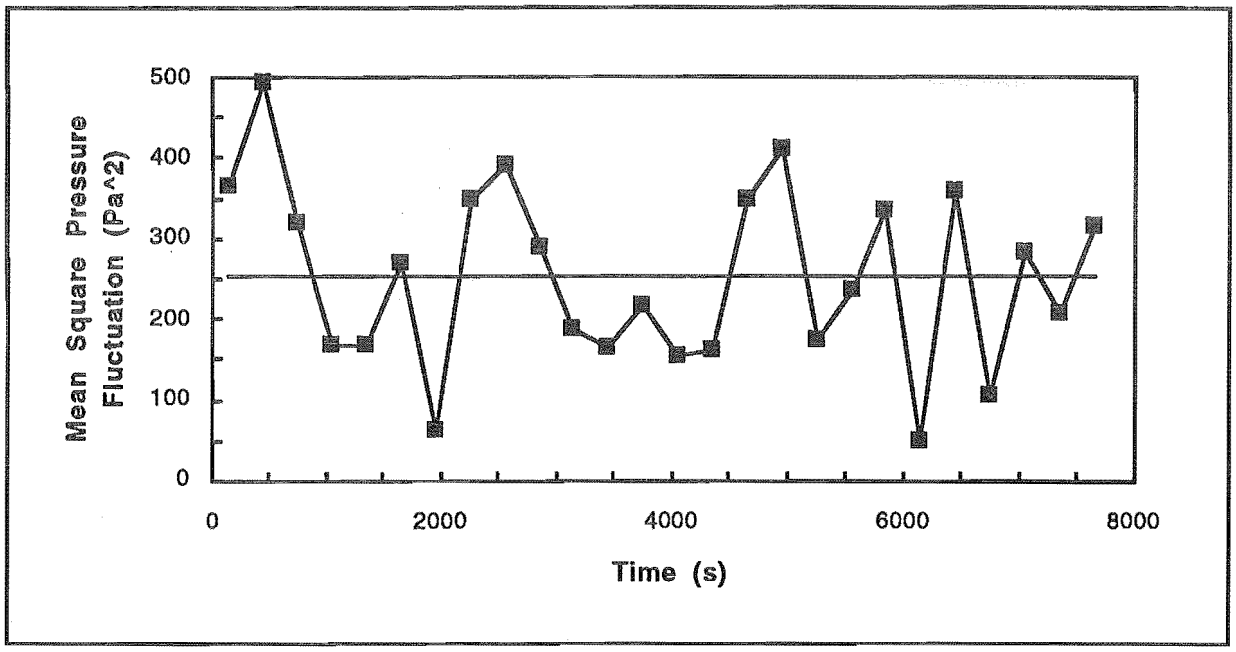

Figure 3.20. Run Test Example: Variation of the Mean Square Pressure Fluctuations Averaged Over 5 Minutes After a 20 Minute Moving Average Trend Removal.

In records which failed the Run Test (null hypothesis rejected) the time lag for the autocorrelation to tend to zero was very large (>10 minutes). Those that passed were (not rejected) had autocorrelations that tended to zero between about one and three minutes. The former records were not regarded as stationary.

A few records which passed the run test also had autocorrelation functions which did not converge to zero until large time lags. Upon visual inspection of the records' time histories these too were regarded as non-stationary.

Records classed as non-stationary were then processed with a trend removal, detailed in section 3.9.3.2, and re-evaluated for stationarity. In only one record, Runs 121 to 124, did trend removal not force the data to become stationary. This record was not discarded as it is unique, but the results of the statistical analysis were treated with caution.

3.9.3.2. Trend Removal

A trend in the record can be thought of as a low frequency component with a wave length longer than the record length (Bendat and Piersol, 1986). If such trends are not removed from the data large distortions can occur in the later statistical analysis.

In the measurement of wind speed fluctuations trends may be the result of synoptic and/or mesoscale changes in the weather pattern, such as a strengthening or weakening in the mean

wind speed or a change in direction. Trends in the data may be expected in any of the records, as most measurements are made during the passage of cold fronts in a disturbed Westerly air stream, during which the weather can change significantly in a few minutes.

In addition to the above, the measurement of pressure fluctuations will reflect the balance of synoptic and mesoscale pressure changes, and the reference pressure system (described in section 3.7.2.4). This balance will result in uncorrelated low frequency fluctuations below about 0.001 Hz which should be removed.

The Linear and Quadratic Trend Removals used here are discussed in detail by Flay (1978). These involved the fitting of a least squares polynomial to the record (of order 1 and 2 respectively) and subtracting the result from the record.

Also used here was a *low frequency moving average trend removal* or high pass filter defining a new record, i′(t) as

$$i'(t) = I(t) - \frac{1}{T_0}\int_{-T_0/2}^{T_0/2} i(t)dt \qquad (I \text{ and } i = u \text{ or } p) \qquad 3.16$$

where I(t) is the original time series. The averaging period (T_0) was chosen from the following sensitivity analysis and the physical considerations of the system.

Figures 3.21 to 3.24 show the autocorrelation and autospectral functions of the wind speed and pressure fluctuations for moving average periods from 5 to 30 minutes. The 30 minute averaging period stood out from the other periods tested in all plots. Most obvious is the very slow convergence in the autocorrelation function of the pressure fluctuations (figure 3.23). This period was too long to filter out trends in the pressure fluctuations data caused by the balancing of the slow synoptic pressure changes and reference pressure system (see section 3.7.2.4 for a full description). This was further supported by the very low frequency component of both autospectral functions (figures 3.22 and 3.24).

It was difficult to tell the remaining periods apart. It might appear that the 5 minute averaging period was filtering out too much of the low frequency fluctuations, as indicated by the fastest lag time for both autocorrelation functions to converge to zero. However, this was not demonstrated by the autocorrelation functions as would be expected.

Therefore, to offer the least interference while providing the desired effect, a T_0 of 20 minutes was used when moving average trend removal was required. This compared to a T_0 of 10 minutes used by Bergström (1987) and 3.3 minutes used by McMillen (1988) to achieve the same effect.

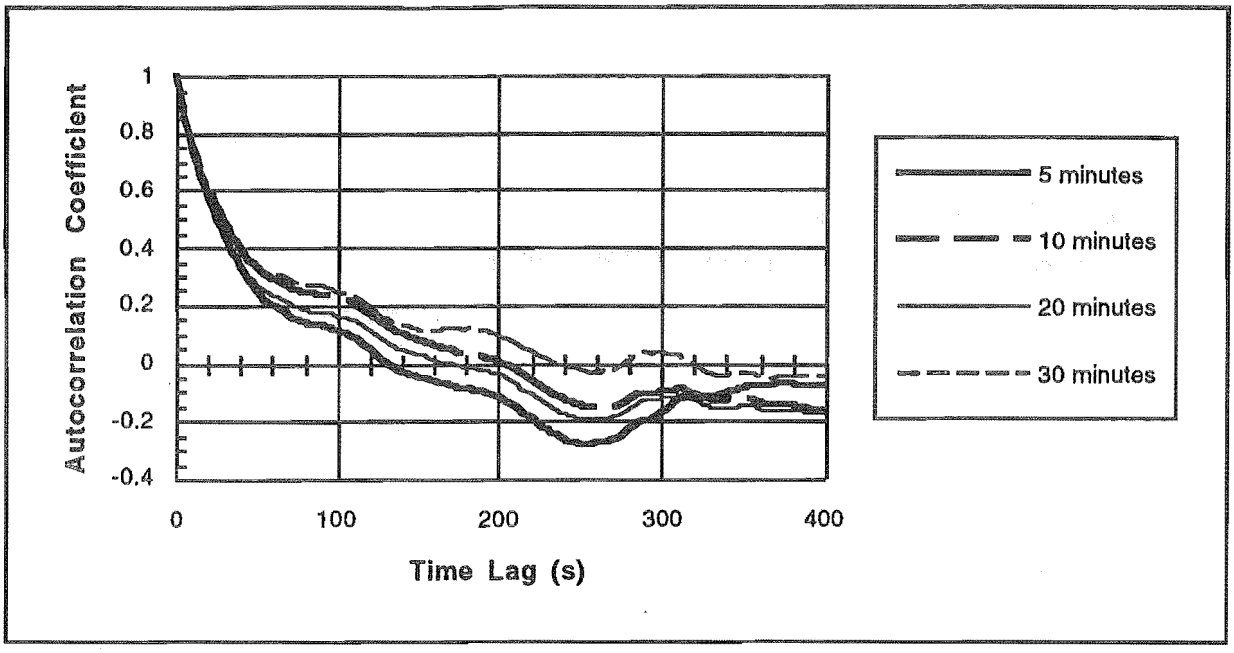

Figure 3.21. Autocorrelation Functions of the Wind Speed Fluctuations from Runs 110 to 120 for Varying Periods of Moving Average Trend Removal.

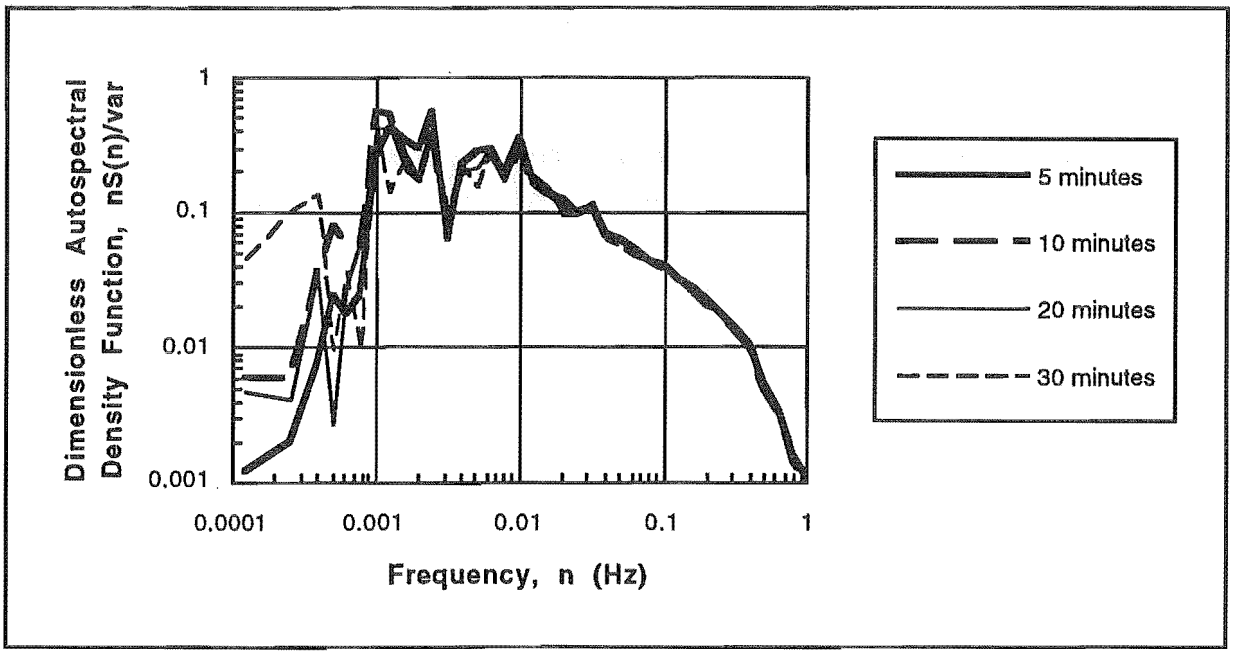

Figure 3.22. Smoothed Autospectral Density Functions of the Wind Speed Fluctuations from Runs 110 to 120 for Varying Periods of Moving Average Trend Removal.

To decide upon the type of trend removal that should be applied to each record the time series, autocorrelation and autospectral density functions and run test were all analysed with different trend removals applied. The simplest trend removal procedure which satisfied the stationarity criteria was then used. The trend removals in order of simplicity were:

1. No Trend Removal
2. Linear Trend Removal
3. Quadratic Trend Removal
4. Moving Average Trend Removal

Both the pressure and wind speed data were treated with the same trend removal, regardless of whether one of the variables did not require it. This was to ensure that any low frequency trends in both variables got the same treatment.

Figures 3.25, 3.26 and 3.27 show examples of linear, quadratic and 20 minute moving average trend removals and their associated Run Tests.

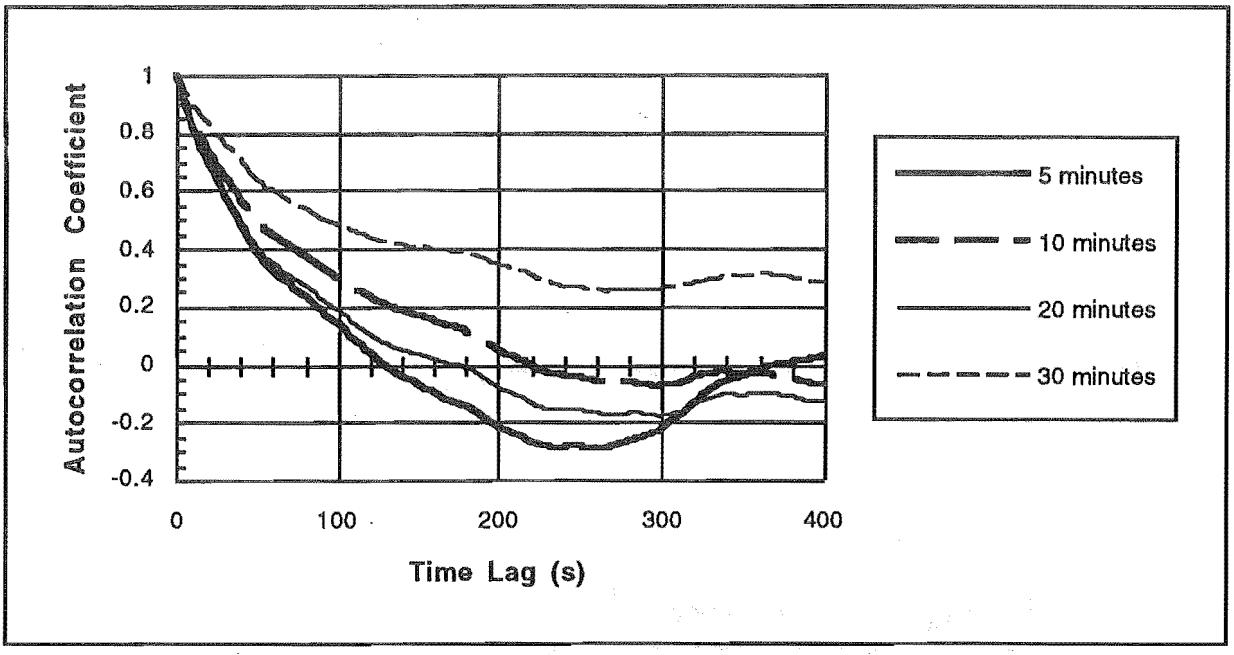

Figure 3.23. Autocorrelation Functions of the Pressure Fluctuations from Runs 110 to 120 for Varying Periods of Moving Average Trend Removal.

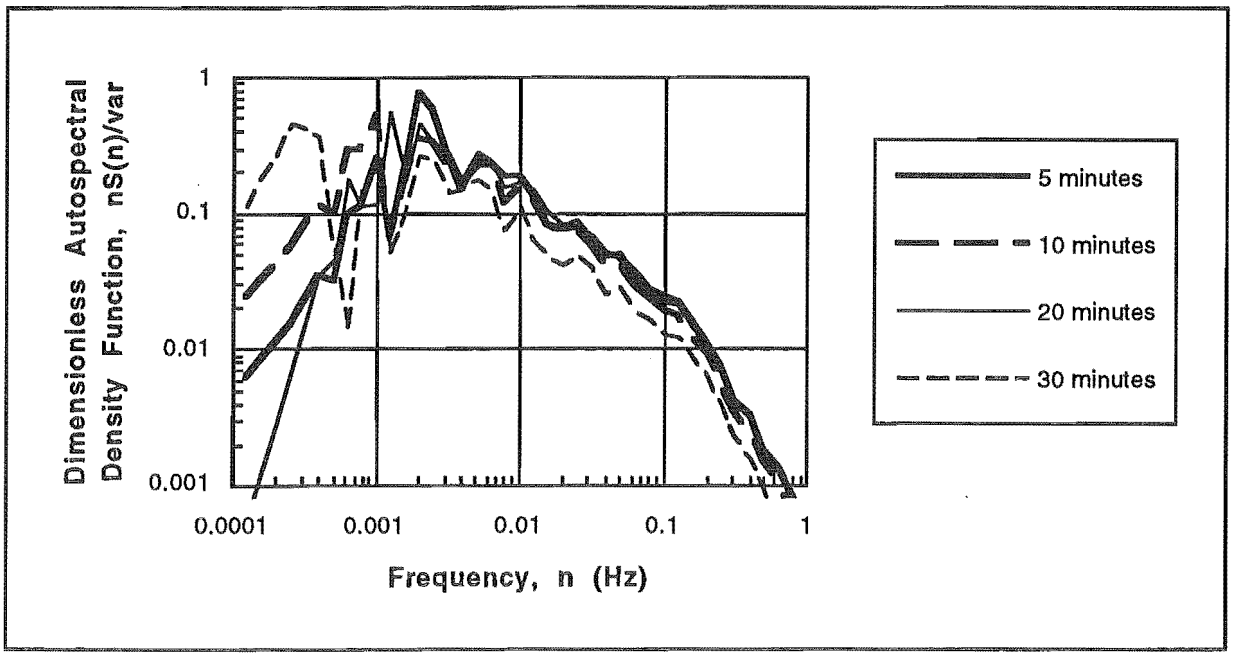

Figure 3.24. Smoothed Autospectral Density Functions of the Pressure Fluctuations from Runs 110 to 120 for Varying Periods of Moving Average Trend Removal.

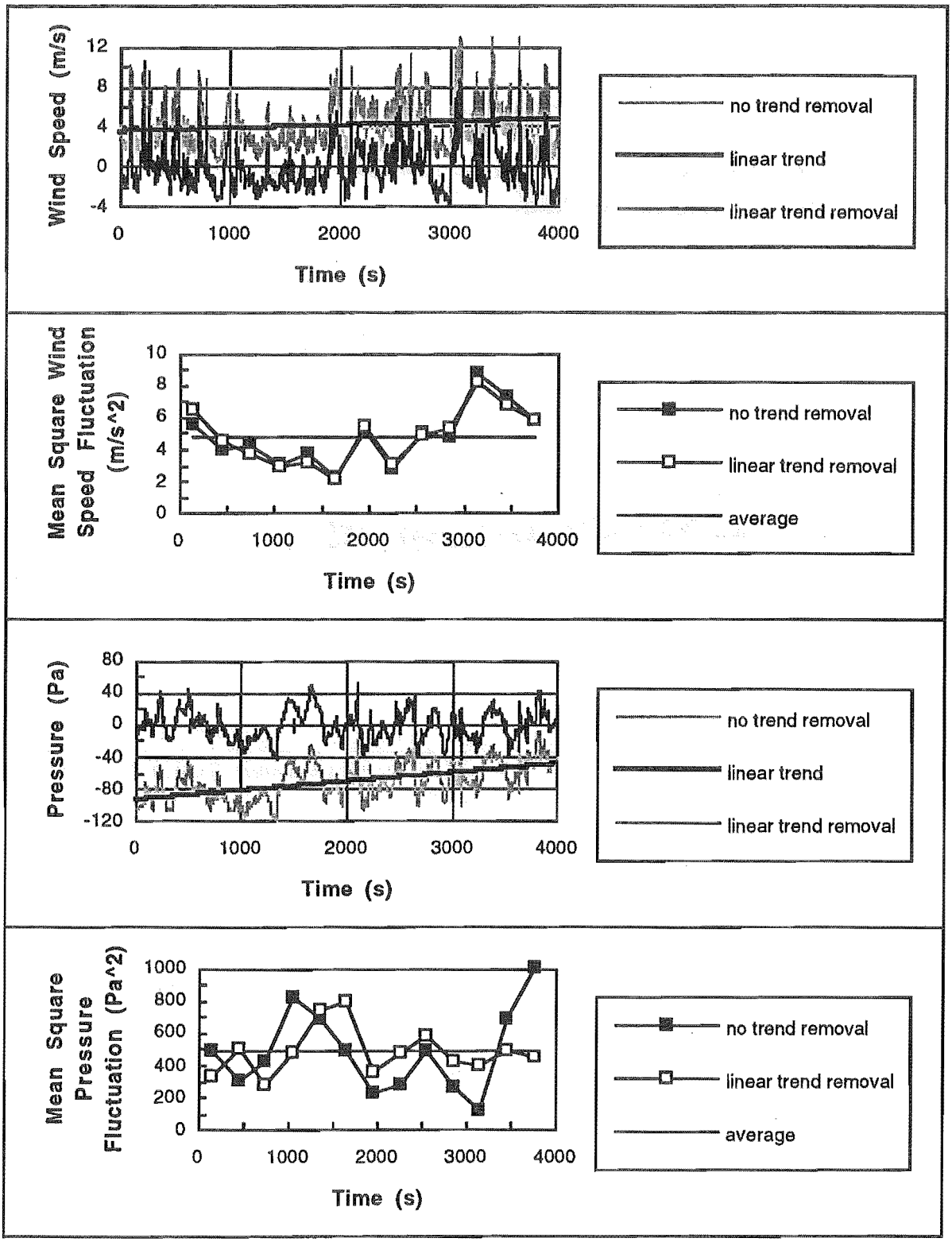

Figure 3.25. An example of Linear Trend and Mean Removal from the Wind Speed and Pressure Fluctuations (using Runs 77 to 81). Also shown are the Run Tests for the Variations in Successive 5 Minute Average Mean Square Wind Speed and Pressure Fluctuations for the Raw Data and after Linear Trend Removal.

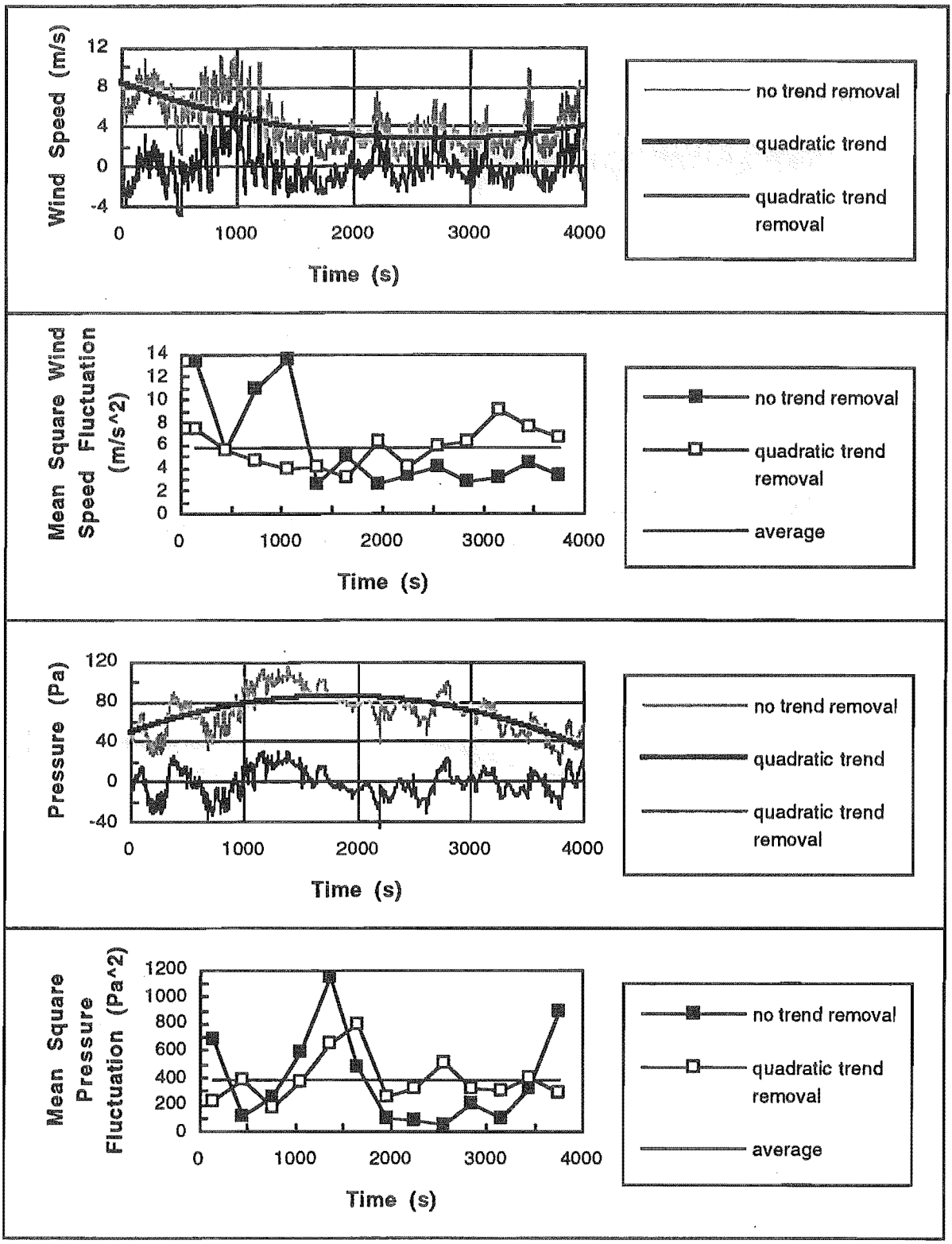

Figure 3.26. An example of Quadratic Trend and Mean Removal from the Wind Speed and Pressure Fluctuations (using Runs 23 to 27). Also shown are the Run Tests for the Variations in Successive 5 Minute Average Mean Square Wind Speed and Pressure Fluctuations for the Raw Data and after Quadratic Trend Removal.

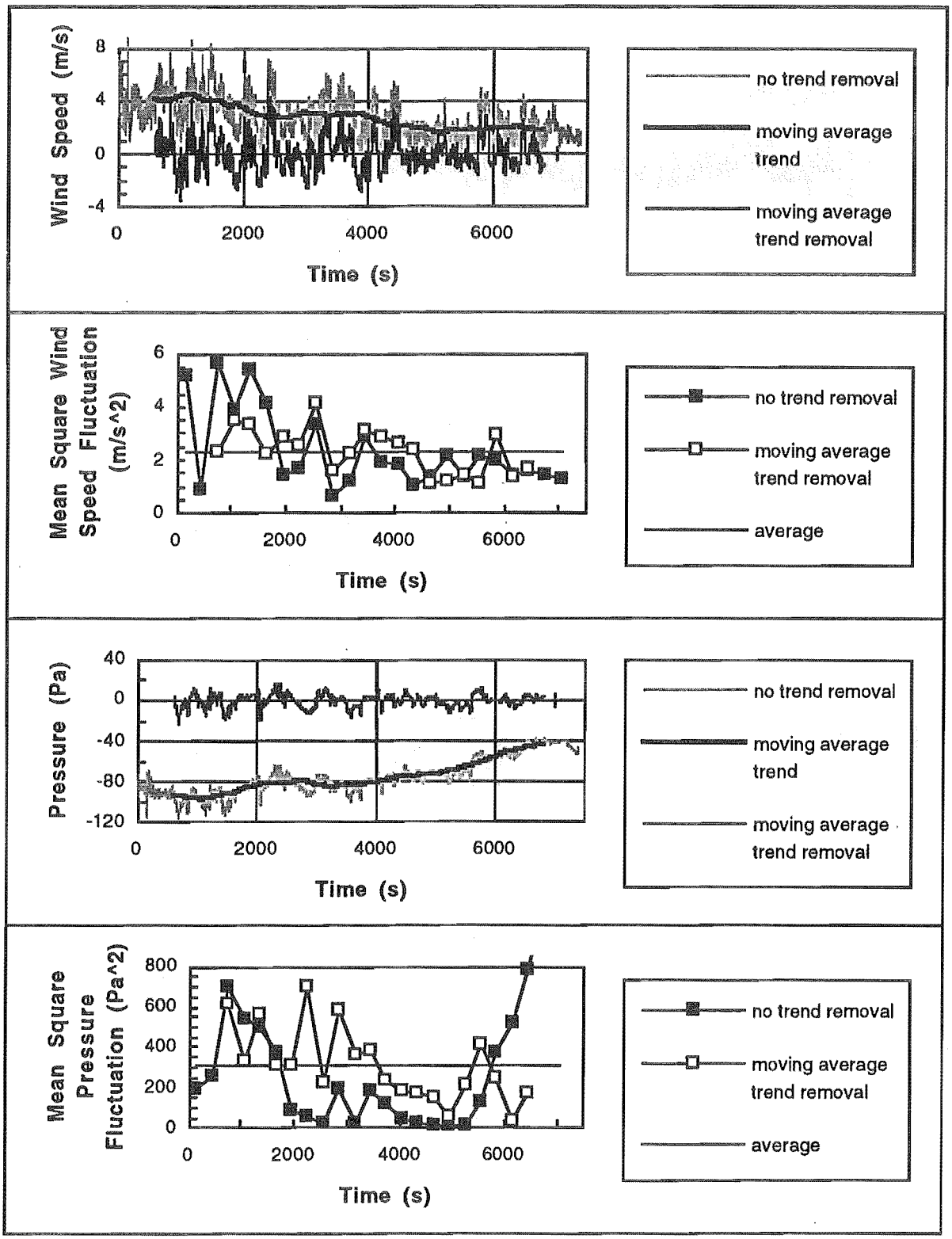

Figure 3.27. An example of a 20 Minute Moving Average Trend and Mean Removal from the Wind Speed and Pressure Fluctuations (using Runs 1 to 10). Also shown are the Run Tests for the Variations in Successive 5 Minute Average Mean Square Wind Speed and Pressure Fluctuations for the Raw Data and after Moving Average Trend Removal.

3.9.4. Autocorrelation Functions

The autocorrelation function shows how well a random stationary variable is correlated with itself offset by varying time periods. Thus when the autocorrelation function is obtained from wind speed data in the atmospheric surface layer, it gives an indication of the extent in time of the large scale eddies. The same information is gained from the autocorrelation function as the autospectral density function, only it is delivered in the time domain rather than the frequency domain.

ESDU 74030 (1974) defines the covariance function as the mean product of the fluctuating velocity components measured at one or more points in space either simultaneously or with a time lag between them. For measurements made at a single location the autocovariance function $C_{uu}(\tau)$ is defined the mean product of the fluctuations measured at times t and t+ τ, where τ is the time lag. For the wind speed fluctuations

$$C_{uu}(\tau) = \overline{u(t).u(t+\tau)} = \lim_{T_0 \to \infty} \int_0^{T_0} u(t).u(t+\tau)dt \qquad 3.17$$

Note that at $\tau = 0$, $C_{uu}(0) = \sigma_u^2$, the record variance. It is usual to normalise the autocovariance function by σ_u^2, ie

$$\rho_{uu}(\tau) = \frac{C_{uu}(\tau)}{\sigma_u^2} \qquad 3.18$$

The plot of $\rho_{uu}(\tau)$ against τ should exponentially decay from a maximum of $\rho_{uu}(\tau) = 1$ at $\tau = 0$ to $\rho_{uu}(\tau) = 0$ as $\tau \to \infty$. Periodicities in the data can be identified if the autocorrelation function oscillates about rather than decaying to zero.

Similarly, for the pressure fluctuations a $C_{pp}(\tau)$ may be defined as

$$C_{pp}(\tau) = \overline{p(t).p(t+\tau)} = \lim_{T_0 \to \infty} \int_0^{T_0} p(t).p(t+\tau)dt \qquad 3.19$$

and

$$\rho_{pp}(\tau) = \frac{C_{pp}(\tau)}{\sigma_p^2} \qquad 3.20$$

To implement these on the discrete data DADiSP Worksheet, a data analysis and digital signal processing software package was used. For computational efficiency the one sided

autocorrelation function is evaluated using Fast Fourier Transform techniques. Specific details of DADiSP and its library functions used are included as Appendix I.

Practically, autocorrelation functions are regarded as unreliable for time lags greater than 10% of the record length, so the graphic presentation is for no more than $\tau = \pm 1200\,s$.

3.9.5. Length Scales of Turbulence

The length scale of turbulence is a measure of the largest spatial separation of correlated wind speeds. Three ways of obtaining the length scales from wind speed data are described by Kaimal (1973) and Flay (1978).

1. Integration of the area under the autocorrelation function yields the *Eulerian* Time Scale of Turbulence, T_{Eul}

$$T_{Eul} = \int_0^\infty \rho_{uu}(\tau)d\tau \qquad 3.21$$

In practice however the upper limit of the integration is taken as the first time the autocorrelation function passes through zero, or falls to a correlation coefficient of 0.05. Assuming that Taylor's (1938) hypothesis of equivalence between Eulerian space and time spectra is true (see section 3.9.5.1) the turbulence field can be considered as frozen in space and convected past a point with velocity $\overline{V}$. The integral length scale Λ_{Eul} is therefore

$$\Lambda_{Eul} = \overline{V}\, T_{Eul} \qquad 3.22$$

Difficulties often occur with this calculation when the autocorrelation function does not converge to, or oscillates about, zero due to trends or very low frequencies in the data.

2. If the decay of $\rho_{uu(\tau)}$ is assumed *exponential* T_{exp} is given by the time for $\rho_{uu(\tau)}$ to drop to 1/e and Λ_{exp} is found as above.

3. Again assuming Taylor's hypothesis the wavelength λ_m may be obtained from the *spectral* peak frequency of the autospectral density function n_m by

$$\lambda_m = \frac{\overline{V}}{n_m} \qquad 3.23$$

The wavelength is related to the integral length scale Λ_{spec} for an exponentially decaying autocorrelation function by

$$\Lambda_{spec} = \frac{\lambda_m}{2\pi} \qquad 3.24$$

Note that if the spectral peak is broad, choice of n_m becomes difficult, and errors result.

It is assumed that the integral length scales of the pressure fluctuations can be calculated in the same way. Discussion on this assumption is made in section 3.10.4.3.

The autocorrelation function and length scales of turbulence are derived though the inverse Fast Fourier Transform of the autospectral function. Hence, the same cautionary notes, discussed in section 3.9.6, apply to their accuracy.

3.9.5.1. Validity of Taylor's Hypothesis

To be confident in the legitimacy of the integral length scale results, Taylor's hypothesis needs to be examined in more detail. Briefly, Taylor's hypothesis states that if turbulence can be considered frozen as it advects past a point in space, the wind speed can be used to translate turbulence measurements as a function of time, to their corresponding measurements in space. Kaimal (1973) examines the two considerations which must hold for the application of Taylor's hypothesis.

1. It can only be expected to hold for eddies small enough so that wind shear (cross stream wind) is negligible compared to the convective (streamwise) wind speed, ie

$$\overline{V} \gg \frac{\lambda_m d\overline{V}}{2\pi\, dz} \qquad 3.25$$

where, z is perpendicular to $\overline{V}$. For base area mean winds of $\overline{V} \approx 5$ m/s (at 1350 m) the 2000 m wind is approximately 20 m/s giving $d\overline{V}/dz \approx 0.02$ (m/s)/m (this is estimated from local knowledge of the 2000 m wind in relation to base area winds). The wave length at the peak spectral frequency is determined in section 3.10.4 as $\lambda_m = 2\pi\Lambda_{spec} \approx 1000$ m. If » is taken to mean an order of magnitude greater, then the inequality (estimated to be $\overline{V} \gg 3$) holds only weakly.

2. The change in eddy shape may be considered small according to Lumley (1965) when

$$\overline{V} > \sqrt{nS_{uu}(n)} \qquad 3.26$$

From spectral peak (see section 3.10.5.2) $nS_{uu}(n) = 0.005\sigma_u^2$ and the inequality becomes

$$I_v = \frac{\sigma_u}{\overline{V}} < 2.8 \qquad 3.27$$

where I_v is the turbulence intensity. For Temple Basin $0.27 < I_v < 0.63$ (see section 3.10.3.1) and so the inequality holds reasonably well.

From the above analysis it was shown that Taylor's hypothesis is observed only weakly. Hence caution must be taken when interpreting integral length scale results.

3.9.6. Autospectral Density Function

The autospectral density function (also called the power spectral density function) for a stationary record represents the rate of change of mean square value with frequency, and thus defines the frequency composition of the data.

The one dimensional autospectral density function can be defined that so that the total energy, or variance, associated with each gust over the frequency range $0 \leq n < \infty$ can be represented by

$$\sigma_i^2 = \int_0^\infty nS_{ii}(n)dn \qquad (i = u \text{ or } p) \tag{3.28}$$

where

$$S_{ii}(n) = \lim_{T_0 \to \infty, \delta n \to 0} \frac{1}{T_0 \delta n} \int_0^{T_0} i^2(t;n,\delta n)dt \tag{3.29}$$

The filtered signal i(t;n,δn) was obtained by putting the original signal i(t) through a narrow band-pass filter. Consequently, only those parts of the signal i(t), corresponding to a frequency bandwidth of δn, centered about frequency n, remain.

As with the autocorrelation function, DADiSP Worksheet was used to evaluate the autospectral density function, the specific details of which are included in Appendix I. The normalisation

$$1 = \frac{1}{\sigma_i^2} \int_{-\infty}^{\infty} nS_{ii}(n)d(\log_e n) \tag{3.30}$$

is a used as check in the computations performed by DADiSP.

Presentation of Autospectral Density Functions

The parameters by which autospectral density functions are non-dimensionalised, to bring results for different terrain and atmospheric conditions to a single curve, have received much attention in the literature. See for example Kaimal *et al* (1972) or McBean (1971) on wind speed spectra and Elliott (1972b) on pressure spectra. The most commonly used method is to divide the function by σ_i^2 as suggested by Bendat and Piersol (1986) and used by Flay (1978) and many others for the wind speed spectra, Elliott (1972b), Schols and Wartena (1986) and Kanda and Ohkuma (1990) for the pressure spectra.

As the dimensional values of the spectral peaks are of most interest in this thesis the dimensionless frequency f_0

$$f_0 = \frac{nz}{\overline{V}} \qquad 3.31$$

is used only in the comparison of the Temple Basin wind speed spectra with those of other authors ($\overline{V}$ is mean wind speed and z the measurement height).

To avoid the peak giving misleading information about the scales of turbulence autospectral density functions are plotted on a log-log scale (Zangvil, 1981), ie

$$\log \frac{nS_{ii}(n)}{\sigma_i^2} \text{ vs } \log n \qquad (i = u \text{ or } p)$$

3.9.6.1. Statistical Errors in Spectral Estimates

The statistical errors in the calculation of autospectral density functions are discussed here as they are significantly larger that any of the other turbulence parameter estimates. Bendat and Piersol (1986) show that each autospectral density estimate has a sampling distribution given by

$$\frac{\widehat{S_{ii}}(n)}{S_{ii}(n)} = \frac{\chi_2^2}{2} \qquad (i = u \text{ or } p) \qquad 3.32$$

Where $\widehat{S_{ii}}(n)$ is the estimate of the true value $S_{ii}(n)$ and χ_2^2 is the chi-squared variable with d = 2 degrees of freedom. The random error of this estimate is substantial. The normalised standard error, which defines the random portion of the estimation error is

$$\varepsilon_r[S_{ii}(n)] = \frac{\sigma[\widehat{S_{ii}}(n)]}{S_{ii}(n)} = \sqrt{\frac{2}{d}} \qquad (i = u \text{ or } p) \qquad 3.33$$

In this case $\varepsilon_r[S_{ii}(n)] = 1$, which means that the standard deviation is as great as the quantity being estimated. This was unacceptable and so was reduced in two ways:

1. Averaging the spectral estimates over an ensemble of q records.
2. Averaging m spectral estimates over bandwidths of the frequency domain for each record.

Since each spectral estimate adds two statistical degrees of freedom to the estimate d=2qm and the normalised random error becomes

$$\varepsilon_r = \frac{1}{\sqrt{qm}} \qquad 3.34$$

The influence of q and m on the random error is illustrated in figure 3.28 (a) to (c). Comparing the random errors for the different length records in (a), and between (b) and (c), a decrease in random error is observed for the longer record length. Looking at the random errors resulting from single record, the reduction in random error by averaging over an ensemble of records can be seen.

3.9.6.2. Smoothing and Grouping of Spectral Estimates

For a variety of reasons the records are generally of different lengths. Consequently, so are the resolution bandwidths of the computed autospectral density functions. To produce average autospectral density functions over an ensemble of records, the spectral estimates need to be made at identical frequencies and bandwidths.

To overcome this problem, and the statistical errors discussed above, m spectral estimates are averaged over frequency.

The number of spectral estimates that are averaged over each bandwidth will vary for different records according to record length. Also, as there is a small number of low frequency events the number of spectral estimates per bandwidth is minimised at the low frequency end of the spectrum. The opposite is the case at the high frequency end. This change in the bandwidth is achieved by taking uniform $\log_{10}(n)$ steps .

The result of this procedure is an increase in the number of spectral estimates, m per bandwidth as frequency, n increases, and each frequency is identical between records allowing smoothing over an ensemble of estimates. Flay (1978) performed a similar but less tidy bandwidth smoothing operation.

In this analysis, data over the four decades in the frequency domain below 1 Hz is gathered. Each decade is split into 10, 20 and 50 bandwidths for presentation. The resulting $\log_{10}(n)$ bandwidths are $\Delta\log_{10}(n) = 0.1$, 0.05 and 0.02. Note that in some bandwidths at the low frequency end of the spectrum, there will be no spectral estimates. For subsequent work these empty bandwidths are ignored as they do not represent zeros in the spectrum.

Figure 3.29 shows the effect of various smoothing bandwidths on the autospectral density function on Runs 99 to 106. The trade off for bandwidth choice is between lower random noise in the spectra and loss of information from the spectra. In most cases $\Delta\log_{10}(n) = 0.1$ is chosen for the presentation of spectra. This is much finer than McBean (1971) who takes $\Delta\log_{10}(n) = 0.5$.

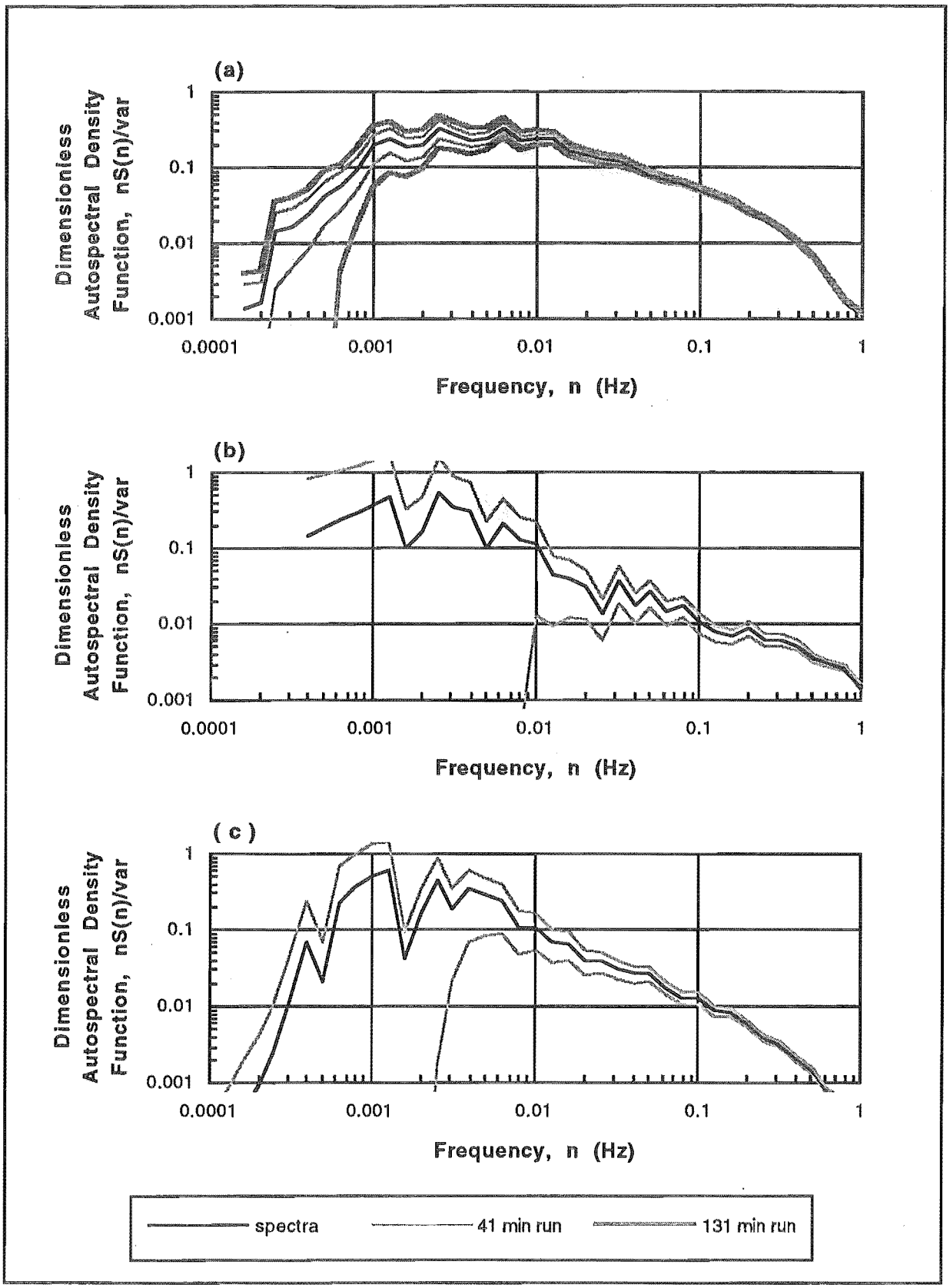

Figure 3.28. Statistical Error in Spectral Estimates (all with a $\log_{10}(n)$ smoothing bandwidth = 0.1): (a) Errors for 41 and 131 Minutes of 2 Hz Data imposed on the Average of All (15) Wind Speed Records. (b) Errors for 41 Minutes of 2 Hz Data Imposed on a Single Pressure Record (Runs 14 to 16). (c) Errors for 131 Minutes of 2 Hz Data Imposed on a Single Pressure Record (Runs 44 to 54).

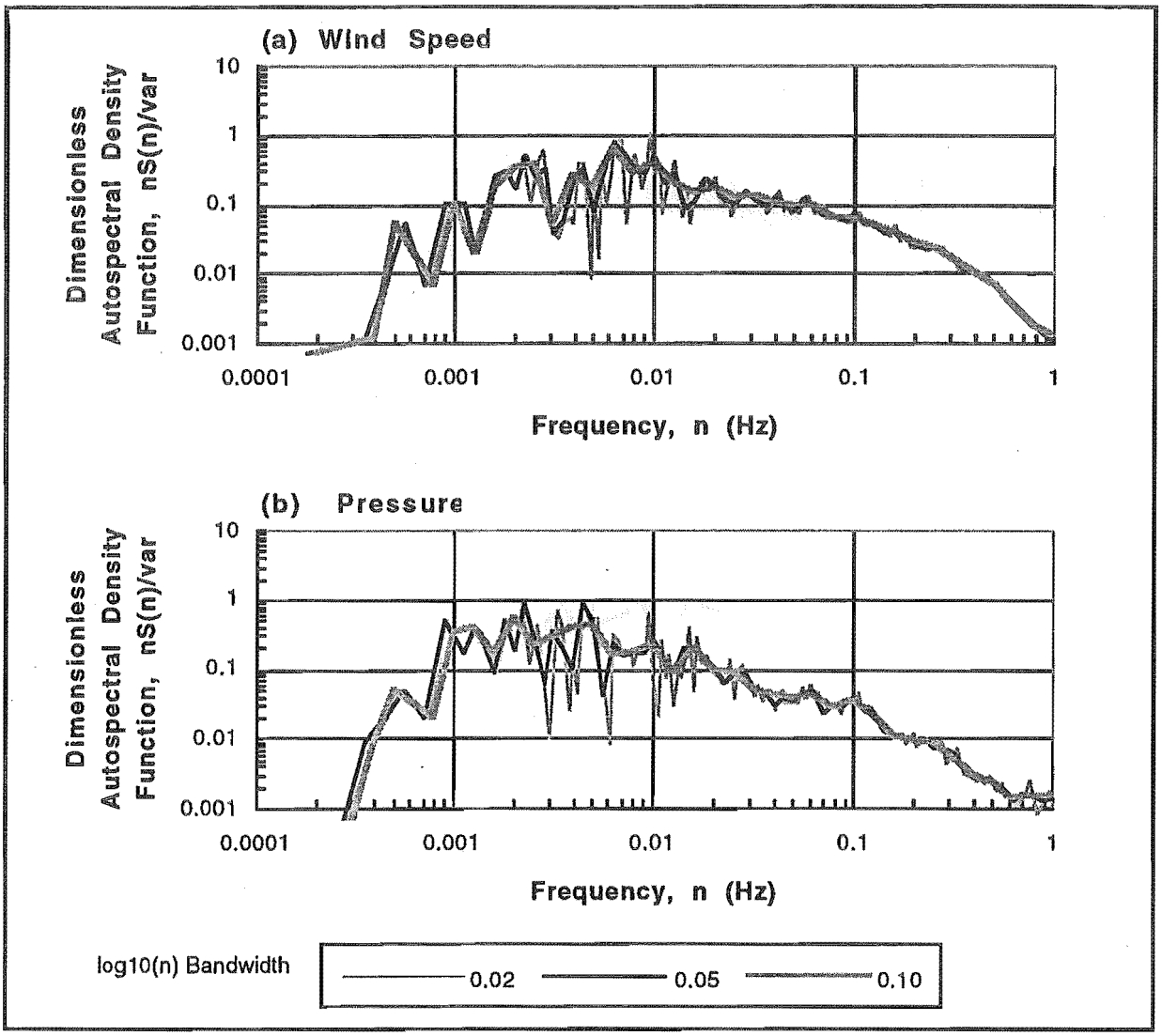

Figure 3.29. Dimensionless Autospectral Density Functions from Runs 99 to 106 for Varying $\log_{10}(n)$ Smoothing Bandwidths: (a) Wind Speed Fluctuations. (b) Pressure Fluctuations.

Note that the smoothing operation introduces numerical errors, as within each bandwidth the spectral estimate frequencies are displaced slightly to the bandwidth's frequency. Hence at this stage in the calculations the integration in equation 3.30 (repeated below) is evaluated both before and after smoothing.

$$1 = \frac{1}{\sigma_i^2}\int_{-\infty}^{\infty} nS_{ii}(n)d(\log_e n)$$

The deviations from unity are less that 1% prior to smoothing and up to 4% after.

3.9.7. Cosine Tapering of Records

Autospectral density functions are calculated here for simple 'box-car' truncations of the record. Flay (1978) examines the effect of using a cosine taper for the first and last 10% of the data to reduce leakage from one frequency component to another. Flay shows no significant variations between the autospectral density functions for the two windows, except at very low frequencies. Because the low frequency end of the spectrum is subject to a large amount of random error (see section 3.9.6.1), Flay did not consider cosine tapering necessary.

Some trials with cosine tapering on records were made here. As with Flay no significant changes occur and hence it is not used in the general analysis.

3.9.8. Test for Periodicities

Periodic noise, which may contaminate the data through physical or electronic process in the data acquisition stage, is likely to be consistent from record to record. The autospectral density function of each record is usually inspected for periodic components which should appear as sharp peaks with size proportional to the resolution bandwidth, regardless of what resolution bandwidth is used (Bendat and Piersol, 1986).

Periodic components were neither expected or observed.

3.9.9. Wind Speed / Pressure Crosscorrelation Function

It was expected that there would be a strong correlation between the fluctuations in wind speed and surface pressure. To investigate this expectation the crosscorrelation function between the two variables can be evaluated. The crosscorrelation function $C_{up}(\tau)$ is defined in a similar way to the autocorrelation function

$$C_{up}(\tau) = \overline{u(t).p(t+\tau)} = \lim_{T_0 \to \infty} \int_0^{T_0} u(t).p(t+\tau)dt \qquad 3.35$$

or in normalised form

$$\rho_{up}(\tau) = \frac{C_{up}(\tau)}{\sigma_u \sigma_p} \qquad 3.36$$

Again the computations were performed in DADiSP as detailed in AppendixI.

As with the autocorrelation functions graphic presentation of crosscorrelation functions are made for no more than $\tau = \pm 1200$ s.

3.9.10. Probability Density Analysis and Test for Normality

Viewing the record probability density functions may help to gain an understanding of the physical processes involved. In particular, with regard to comparisons between wind speed and pressure fluctuations, and between aspects for the pressure fluctuations.

It is often assumed that wind speed fluctuations over periods of between 10 minutes and 2 hours have normal probability distributions (Flay, 1978). Whilst it is recognised that this is not the case, Flay (1978), Bowen (1979) and Matsui *et al* (1982) show that deviations are not large for horizontal wind speed fluctuations. Mayne (1979) describes the Weibull and extreme value distributions which account for the deviations from normality. However, as the assumption of normality is not required for the statistics used to process the records a discussion of other possibilities is not entered into here.

The probability density distribution was evaluated to test its equivalence with the normal distribution using the Chi-Squared Goodness-of-Fit Test. The procedure is applied as in Bendat and Piersol (1986).

Two other statistics were calculated for the record as a check on the degree of normality.

1. Kurtosis, which characterises the relative peakedness or flatness of a distribution compared to the normal distribution. A positive kurtosis indicates a relatively peaked distribution and vice versa for a negative value.

2. Skewness, which characterises the degree of asymmetry of a distribution about its mean. A positive skewness indicates an asymmetric distribution with a longer tail extending towards more positive values and vice versa for a negative value.

3.9.11. Gust Exceedance Statistics

The Zero-Passage Wind Speed Gust Model described in section 2.11.2.4, is a discrete model in which the time series u(t) is analysed rather than the spectrum. In the model an interval between two zero crossings of u(t) is defined as a gust event. The gust amplitude A_u is defined as the maximum value of |u(t)| between the crossings and the gust duration T_u as the time between the two crossings through the sample record mean (u(t) = 0). This is illustrated in figure 2.7. Here the same model is applied to both the fluctuating pressure data as well as the wind speed data[3].

---

[3] A generalised subscript i is used to refer to either the wind speed (subscript u) or pressure fluctuations (subscript p).

Gust statistics are traditionally investigated between the frequency bandwidth limits n_1 and n_2 which are of importance to wind turbines. Typically the ratio $n_1/n_2 \approx 10$. In this case it was more appropriate to look at the full range of frequencies, split up into discrete frequency bandwidths, so that the amplitude exceedance probabilities in each bandwidth can be investigated. A $n_j/n_{j+1} = 5$ was chosen in this analysis. At an upper limit of 2 Hz, this results in bandwidths of:

j = 1	2 to 0.4 Hz
j = 2	0.4 to 0.08 Hz
j = 3	0.08 to 0.016 Hz
j = 4	0.016 to 0.0032 Hz
j = 5	0.0032 to 0.00064 Hz

The upper and lower frequency limits of the above ranges lie at the extremes of the sensor's sensitivity ranges. Note that the lowest frequency bandwidth may be severely affected by reference pressure system attenuation (see sections 3.7.4.2 and 3.7.4.5).

To divide the data into these bandwidths, filters are applied to the record at the cut off frequencies, n_j and n_{j+1}:

* n_j: The sampling rate is reduced to n_j by averaging consecutive groups of samples. The result is a low pass filter with its first zero at 1/(AveragingTime) = n_j.
* n_{j+1}: A moving average subtraction described by equation 3.16 is performed on the data by setting the averaging period (T_0) equal to n_{j+1}. The result is a high pass filter.

Over each bandwidth j, the number of gust events N_{ij} are counted for both wind speed and pressure. The standard deviation σ_{ij} (for both wind speed and pressure), wind turbulence intensity $I_{v,j}$ and rms pressure coefficient $C_{p,j}$ for each j are also calculated using equations 3.9, 3.10 and 3.14 respectively. For each gust event the maximum absolute amplitude A_i, is made dimensionless by σ_i, as given by

$$\frac{A_i}{\sigma_i} = \frac{\max(|i(t)|)}{\sigma_i} \qquad (i = u \text{ or } p, j = 1 \text{ to } 5) \qquad 3.37$$

In this calculation positive gusts and negative gusts are treated in the same way. Gust *exceedance* (cumulative) probability for each bandwidth is then given by the number of events with dimensionless amplitudes greater than x, divided by the total number of events in the bandwidth.

Mathematically for each bandwidth j this probability is given by

$$p\left(\frac{A_i}{\sigma_i}>x\right) = \frac{\sum_{k=x}^{\infty} f_{A_{ik}}}{\sum_{0}^{\infty} f_{A_{ik}}} \qquad (i = u \text{ or } p,\ j = 1 \text{ to } 5) \qquad 3.38$$

The results are presented here as

$$\frac{A_i}{\sigma_i} \text{ vs } p\left(\frac{A_i}{\sigma_i}>x\right) \qquad (i = u \text{ or } p,\ j = 1 \text{ to } 5) \qquad 3.39$$

If extreme events were of interest, a logarithmic vertical axis could be used to enlarge the detail of the high amplitude end of the plot.

Bergström (1987) uses this model to study the turbulent time scales using the gust duration T_i as well as gust amplitude. Given the detailed spectral analysis performed, this is surplus to requirements here.

3.10. Results

Of the runs made, about two thirds were prematurely terminated or corrupted by some failure in the apparatus, through either the adverse weather conditions, operator error or physical equipment failure. In accordance with the discussion in sections 3.8.4 and 3.9.3 all stationary records longer than 34 minutes were fully analysed. As none of these were during gale wind conditions, several 27 minute records during such conditions were also partially analysed.

3.10.1. Weather and Snow Pack Conditions During Measurements

3.10.1.1. Weather Conditions

All runs were made during the reasonably stable northwest phase of the storms, usually prior to the (cold) frontal activity associated with a rapid change in atmospheric pressure, cooling and a shift to the south in wind direction. Table 3.4 outlines the average weather conditions for each group of runs.

Runs in Group	Date	Start Time (hrs)	Temp-erature (°C)	Atmos. Pressure (mbar)	Cloud Cover	Precipitation	Wind Direction	Wind Strength
1 to 10	10/09/91	20:30	-1.0	1000	Overcast	Light Snow	Northwest	Moderate
14 to 16	13/10/91	12:35	0.0	994	Overcast	Light Snow	Northwest	Strong
17 to 19	13/10/91	14:06	0.0	994	Obscured	Moderate Snow	Northwest	Moderate
23 to 27	14/10/91	22:44	1.0	1006	Scattered	Light Snow	Northwest	Moderate
33 to 43	15/10/91	00:13	1.0	1006	Scattered	Light Snow	Northwest	Moderate
44 to 54	15/10/91	08:25	2.5	1008	Overcast	Light Rain	Northwest	Moderate
55 to 60	15/10/91	14:41	3.0	1008	Overcast	Light Rain	Northwest	Moderate
61 to 65	15/10/91	16:33	3.0	1008	Overcast	Light Rain	Northwest	Moderate
66 to 76	15/10/91	19:17	2.5	1009	Overcast	Light Rain	Northwest	Moderate
77 to 81	15/10/91	21:53	3.0	1011	Obscured	Light Rain	Northwest	Moderate
82 to 87	16/10/91	00:01	3.0	1011	Obscured	Light Rain	Northwest	Moderate
88 to 98	16/10/91	01:25	3.0	1008	Obscured	Moderate Rain	Northwest	Strong
99 to 109	16/10/91	04:20	4.0	1008	Overcast	Moderate Rain	Northwest	Strong
110 to 120	16/10/91	09:01	4.0	1008	Overcast	Moderate Rain	Northwest	Strong
121 to 124	16/10/91	12:34	4.0	1012	Broken	Nil	Northwest	Moderate
125 to 133	12/09/91	10:30	2.0	1006	Obscured	Rain and Snow	Northwest	Gale

Table 3.4. Summary of Weather Conditions for the Runs Analysed. Observations are made at the beginning of each run. With the exception of Runs 125 to 133 (which are each individual runs) the runs in each group are joined to form longer records.

3.10.1.2. Snow Pack Conditions

Table 3.5 summarises the snow pack properties that existed during the measurements. The relatively low elevation of the measurement site is evident in the type of precipitation (rain) that fell during the spring of 1991.

Date	Total Depth (cm)	Depth (cm)	Permeability ($x10^4$ m^2/Pas)	Density (kg/m^3)	Snow Form
10/09/91	250	10	1.32	500	very wet 2-3 mm graupel
		20	1.55	410	wet clustered 1-2 mm melt freeze
		100	0.64	315	wet clustered 0.5-1 mm melt freeze
		150	0.82	340	wet 0.25 mm melt freeze
		175	-	430	very wet clustered 1 mm melt freeze
		225	-	-	wet 0.25 mm melt freeze
14/10/91	260	10	1.09	150	dry 0.25 mm partially settled
		30	0.63	225	dry 0.5 mm rounds
		50	0.45	240	dry 1 mm rounds
		80	0.40	310	dry clustered 3 mm melt freeze
		100	0.57	305	dry clustered 2 mm melt freeze
15/10/91	280	10	0.27	-	wet clustered 2 mm melt freeze
		50	0.34	-	wet clustered 3 mm melt freeze
16/10/91	270	15	0.36	360	wet clustered 2 mm melt freeze
		30	0.19	450	wet clustered 2 mm melt freeze
		50	0.59	370	moist clustered 3 mm melt freeze

Table 3.5. Summary of Snow Pack Properties During Measurements. For definitions of snow form terms, refer to NZMSC (1987). Depth is measured from the snow surface.

3.10.1.3. Other Observations

From the author's experience in the Arthur's Pass region (five winters), the storms during which digital recordings of atmospheric turbulence were made were fairly moderate. In other words, *these measurements were not made during severe storm periods.*

The observed patterns of atmospheric turbulence during storms varies a great deal with slight changes in mean wind direction. This knowledge was gained from the lee loading characteristics of wind blown and redeposited snow associated with different wind directions. The variability in storm character is reflected in the results, particularly the crosscorrelation results.

During some strong wind conditions there was a dominance of upslope winds (from the direction of the valley floor) at the measurement site. During other storms the wind tended to buffet the windward slope (large vertical component). This behavior is consistent with the

concepts of reattachment of a separated flow (from Phipps Ridge) discussed in section 2.10.3. Higher rms pressure coefficients would be expected during buffeting wind conditions. Unfortunately this visual observation was not made during the digitally recorded runs, and hence the records cannot be divided into buffeting and upslope wind-storms.

On clear windy days, observations of shedding vortices off ridges containing entrained snow were made. These vortices had scales of 100 to 500m. Their visual dissipation was likely to be significantly faster than observed as the snow drops out of the air and/or sublimes back into vapour.

3.10.1.4. Atmospheric Stability

ESDU 72026 (1974) and Doran and Powell (1982) state that in strong winds (10 minute average greater than 10m/s), there is enough mechanical stirring to eliminate thermally driven convective currents. This average wind speed stated by ESDU is arrived at from measurement made over flat open terrain to urban and hilly terrain, but not to the extent of the mountainous terrain of the current measurements.

While the mean wind speeds of the fully analysed data, typically 4 to 6m/s (see table IV.2), are not as high 10m/s, the measurement height of 3.5m is somewhat lower than the 10m referred to by ESDU 72026. From wind speed-up studies over hills of moderate slope, the 10 m mean wind speed is greater than that below. However, the wind speed profile results of Mitsuta *et al* (1983) and Föhn (1980), on mountainous ridge crests, show a maximum wind speed near the ground ($2 < z < 4$ m) and falls off above that.

The comparison between the turbulent intensities (I_v) measured at Temple Basin ($I_v = 0.49$), and those measured during neutral conditions in other published works, gives a strong indication that neutral stability (from a wind engineering viewpoint) existed during sampling at Temple Basin. Turbulent intensities found in other works include; $I_v = 0.26$ from Matsui *et al* (1982) around tall buildings, $I_v = 0.19$ from Flay (1978) over flat rural terrain, and $I_v = 0.19$ and 0.30 from Bowen (1979) downwind of sloping and cliff escarpments respectively. This assumes that an indication of the degree of mixing (and hence dynamic neutral stability) can be gained from turbulent intensities.

All measurements were made during overcast conditions, which would minimise any radiation heat transfer and consequential development of convective instabilities. No diurnal differences in the spectral characteristics of either the wind speed or pressure fluctuations are observed, indicating the absence of large scale convective cells.

The temperature difference between the Arthur's Pass National Park weather station at 800 m in the valley, and the temperature at the Temple Basin weather plot during strong northwest

storms is generally -0.6 °C per 100 m, about equivalent to the saturated air adiabatic lapse rate. This is to be expected for neutral conditions.

From a wind engineering point of view, it is reasonable to assume that neutral stability existed during measurements, an assertion which is also made by Jenkins *et al* (1981) who assume neutral stability exists at >5 m/s over a steep isolated island.

These factors do not negate possible effects of the larger scale stable stratification discussed in section 2.12.1.4.

3.10.2. Time Series Examples

Figures 3.30 and 3.31 show two 131 minute records of the synchronous wind speed and pressure fluctuations in the time domain sampled at 0.2 Hz after mean and trend removal. The large scale structures are clearly visible in both variables as is the relative difference between the scales.

Figure 3.32 shows a sample of data from figure 3.30 at 2 Hz. This sample was selected on the basis that it illustrates the reversal of correlation between the two variables. For example, the wind gust between 210 and 260 s is positively correlated with the pressure gust during the same time interval, whilst the wind gust between 310 and 370 s is negatively correlated to the corresponding pressure gust. This feature of the correlation between variables is further discussed in section 3.10.6.

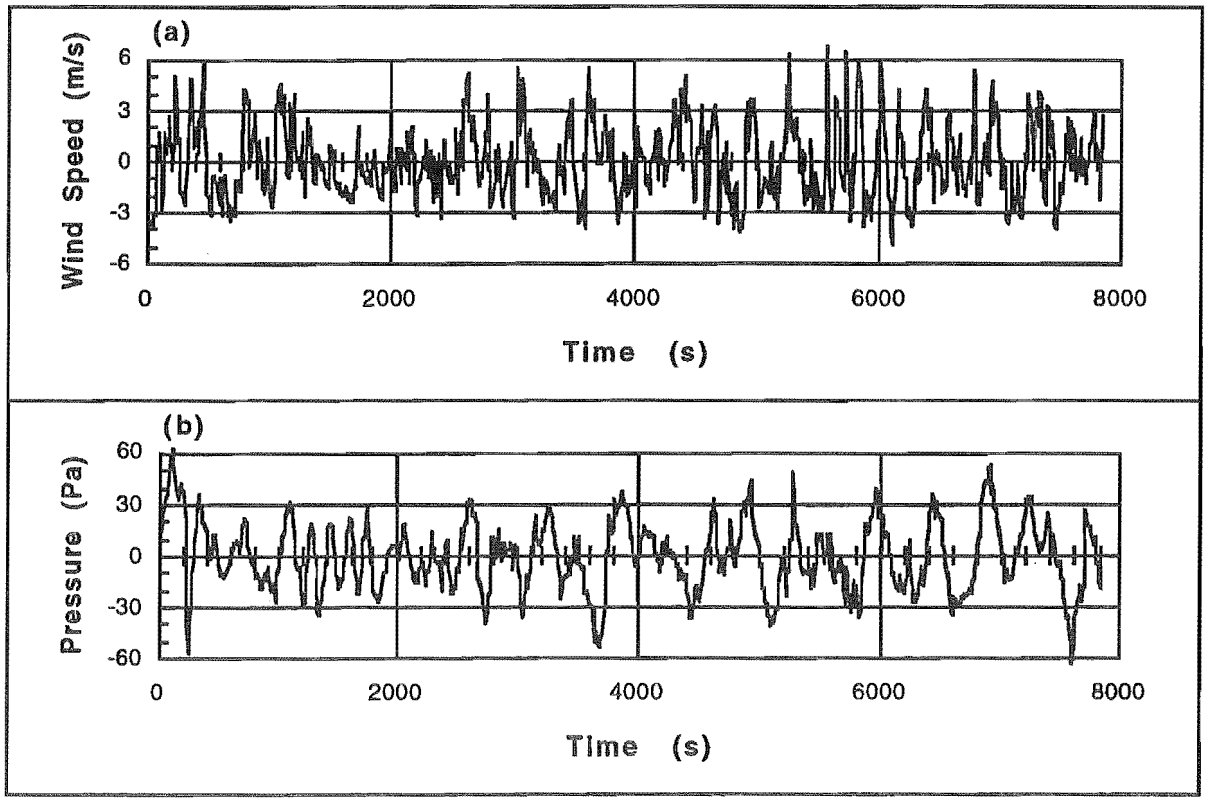

Figure 3.30. Synchronous Fluctuating (a) Wind Speed and (b) Pressure Time Series from Runs 66 to 76 at 0.2 Hz after Mean and Moving Average Trend Removal.

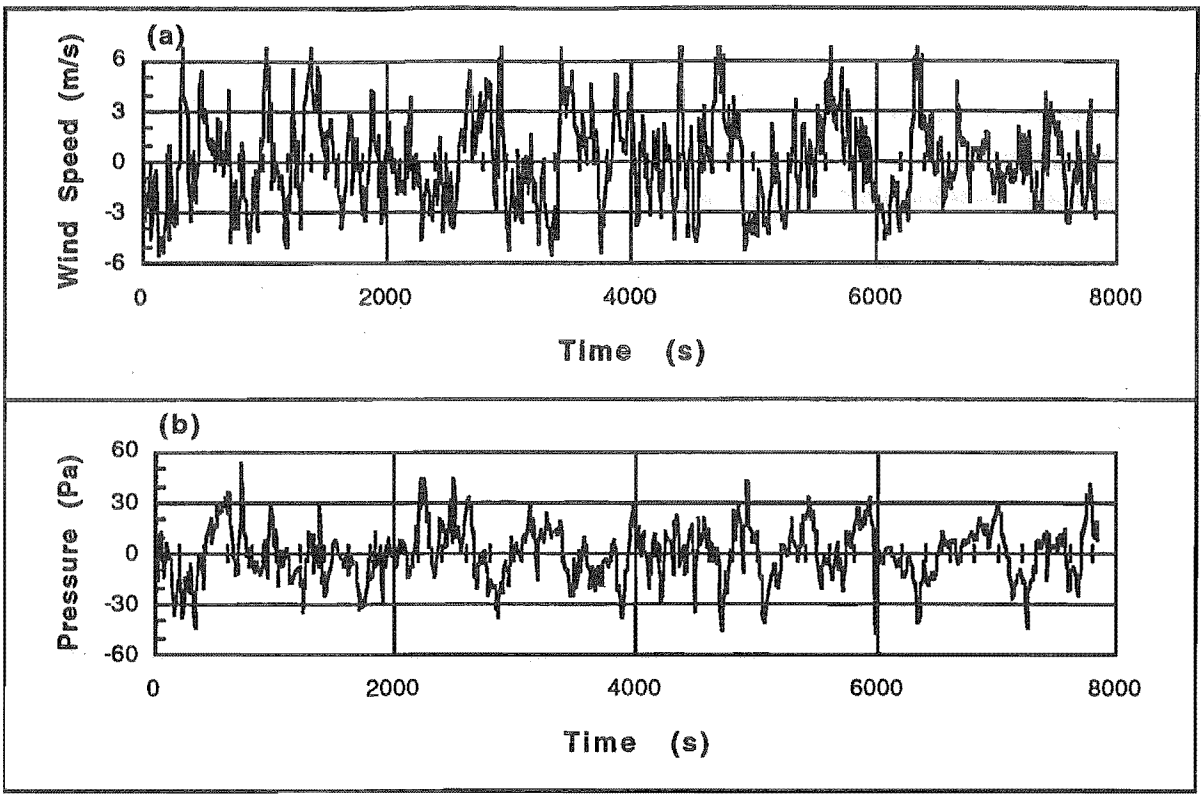

Figure 3.31. Synchronous Fluctuating (a) Wind Speed and (b) Pressure Time Series from Runs 110 to 120 at 0.2 Hz after Mean and Moving Average Trend Removal.

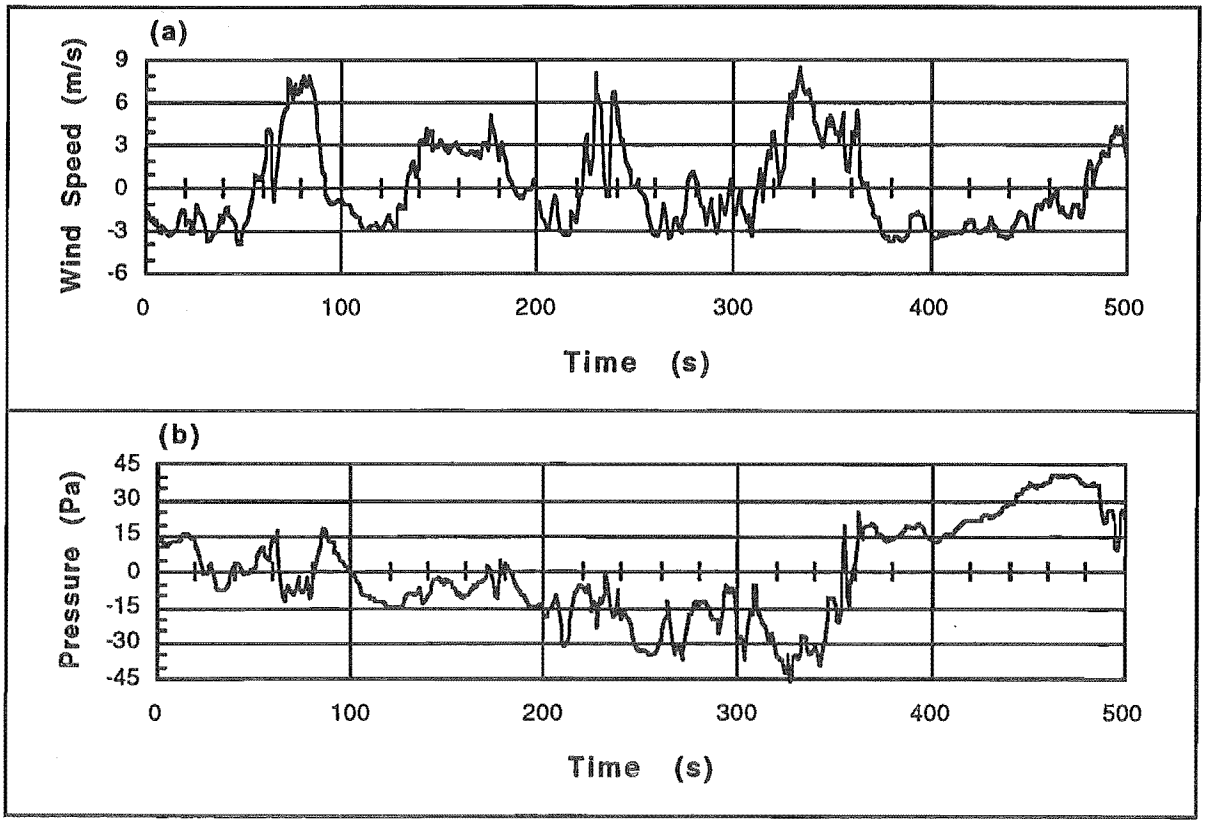

Figure 3.32. Synchronous Fluctuating (a) Wind Speed and (b) Pressure Time Series from Run 72 at 2 Hz after Mean and Moving Average Trend Removal.

3.10.3. Record Variance Statistics

Table IV.2 details the means, standard deviations and turbulence intensities for the fluctuating wind speed records and standard deviations and rms pressure coefficients for the fluctuating pressure records, before and after trend removal.

3.10.3.1. Wind Speed Turbulence Intensities

Figure 3.33 shows the wind speed turbulence intensities before and after trend removal, during northwesterly conditions plotted against the mean wind speeds of all records. As expected the effect of trend removal is to reduce the variance, and hence the turbulence intensity of the records.

Approximately 27 minutes of data were extraneously collected during southwesterly winds (the details of which are not included in Appendix IV). This occurred after a rapid wind shift from the northwesterly phase of a storm cycle. The substantially lower turbulence intensity for the southwesterly portion of the record is plotted alongside the northwesterly runs in figure 3.33. The author considers that this lower level of turbulence is typical for southwesterly storms, and that it is primarily due to the distance upstream of the nearest terrain feature (Phipps Ridge lies 1.0 km northwest and Avalanche Peak 5.1 km southwest). Reid (1983) makes a similar conclusion by associating high gust factors (highest wind speed compared to mean wind speed), with wakes of steep upstream ridges, rather than to the inner layer which develops over the promontory on which the anemometer is sited.

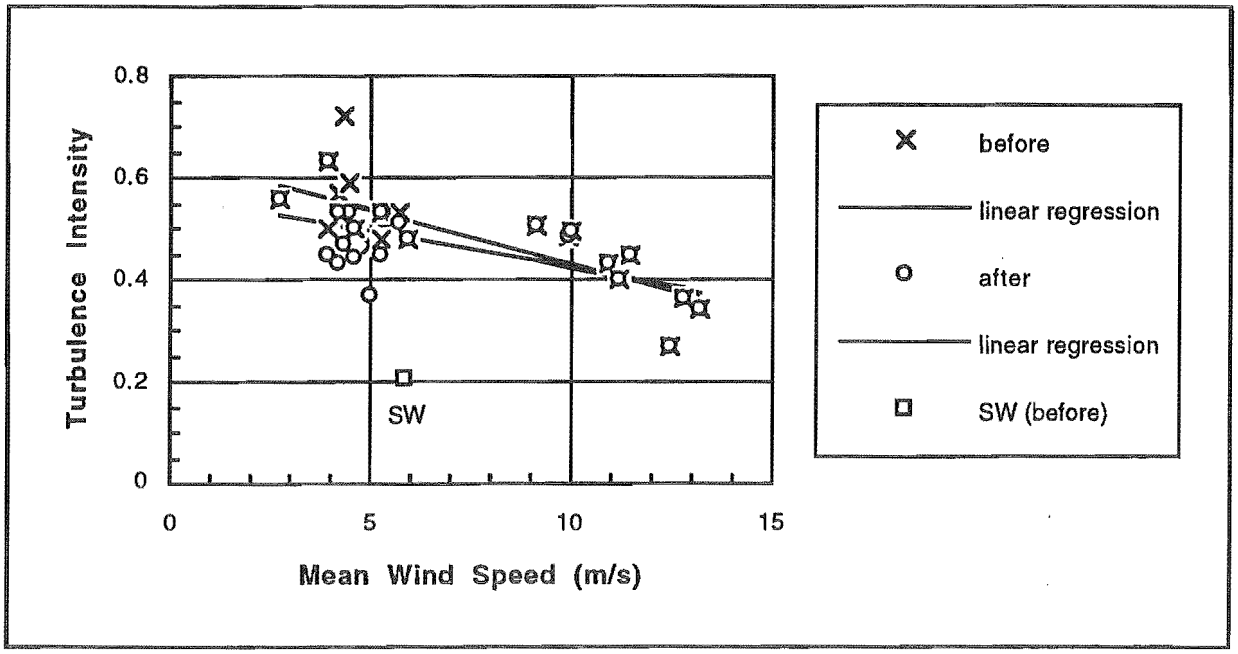

Figure 3.33. Variation of Wind Speed Turbulence Intensity Before and After Trend Removal in Northwesterly Conditions for Various Mean Wind Speeds. A Linear Regression is Fitted to Both Data Sets to Summarise the Effect of the Trend Removal. The Turbulence Intensity for One Record Made During Southwesterly Winds is Also Potted.

Several examples of measured turbulence intensities in real terrain are documented alongside the Temple Basin Data in table 3.6. There is no doubt that these turbulence intensities are significantly larger than expected. The results of Mitsuta *et al* (1983) and Bowen (1979) indicate that this is likely to be a product of the turbulent structures associated with separation off upstream terrain features.

It can be inferred from the x = 0.5H and 4H (x is horizontal distance and H the vertical relief) cliff escarpment results of Bowen, that it is not the immediate terrain feature, but one further upwind, that is important. Phipps Ridge, the terrain feature in question for a northwesterly flow at Temple Basin, lies 2.5H upstream. The sharpness of the upstream feature also appears to be important from Bowen's results (Phipps Ridge is very steep on both sides).

Author(s)	Terrain Description	Vertical Relief (m)	Range of Turbulent Intensities
Temple Basin Data	rough mountainous terrain	1000	0.27 - 0.63
Mitsuta *et al* (1983)	rough mountainous terrain - windward	300	0.14 - 0.32
" "	" " - leeward	300	0.27 - 0.55
Botta *et al* (1992)	various locations in rough hilly terrain	700	0.13 - 0.22
Antoniou *et al* (1992)	top of a steep hill	180	0.16 - 0.23
Matsui *et al* (1982)	top of a high rise building	70	0.19 - 0.33
Bowen (1979)	escarpments - sloping	13	0.14 - 0.22
" "	" " - vertical (0.5 H downstream)	H = 12	0.13 - 0.28
" "	" " - vertical (4 H downstream)	H = 12	0.29 - 0.49
Flay (1978)	flat rural terrain	0	0.17 - 0.21

Table 3.6. Examples of Wind Speed Turbulence Intensities Measured in Various Kinds of Terrain.

Some further results of Mitsuta *et al* (1983) are worth noting in order to highlight the degree of complexity of wind flow in complex mountain terrain. At any one ridge site the maximum wind speed occurs at the ridge top, and decreases with height above the ridge. Along the ridge line, the maximums in wind speed occur both in dips in the ridge line through which the flow is channelled and over high spots where speed up is experienced. The minimum wind speeds are experienced on the leeward side, although the magnitudes of the fluctuations remains about the same.

3.10.3.2. RMS Pressure Coefficients

Figure 3.34 shows the variation of the ridge top and leeward rms pressure coefficient for varying mean wind speeds. There appears to be little significant difference between the two sets of northwest data. This supports the conclusions about the location of flow separation over the ridge from visualisation results in section 3.6.3.

As with the wind speed fluctuations the southwesterly record shows a substantially lower rms pressure coefficient, further supporting the comments made above.

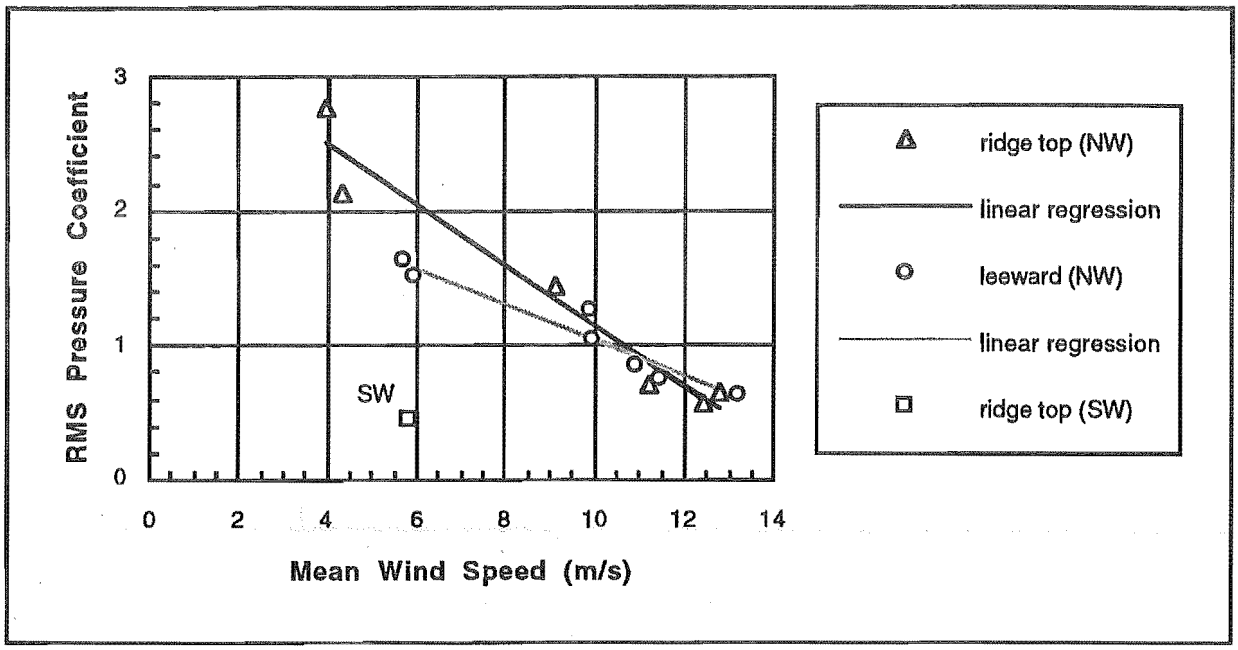

Figure 3.34. Variation of RMS Pressure Coefficient After Trend Removal in Northwesterly Conditions for Various Mean Wind Speeds. A linear regression is fitted to both data sets to summarise the effect of the aspect. The turbulence intensity for one record made during southwesterly winds is also plotted.

Figure 3.35 (a) and (b) shows the record rms pressure coefficients before and after trend removal, during northwesterly conditions. The coefficients are grouped according to aspect and probe depth. Note that the leeward 0.3 m run has been plotted as 0.5 m for ease of presentation.

The primary objective of trend removal for the pressure fluctuations is to ensure that the pressure measurement system's reference pressure leakage (detailed in section 3.7.4.2) does not impose extraneous low frequency components on the data. Given the way in which the trend removal has brought consistency to the rms pressure coefficient data, it appears that this technique is appropriate. The choice of type of trend removal *was not* made on the basis of achieving expected trends in the rms pressure coefficient results. Also, as with the wind speed fluctuations, the effect of trend removal is to reduce the variance and consequently the turbulence intensity of the records.

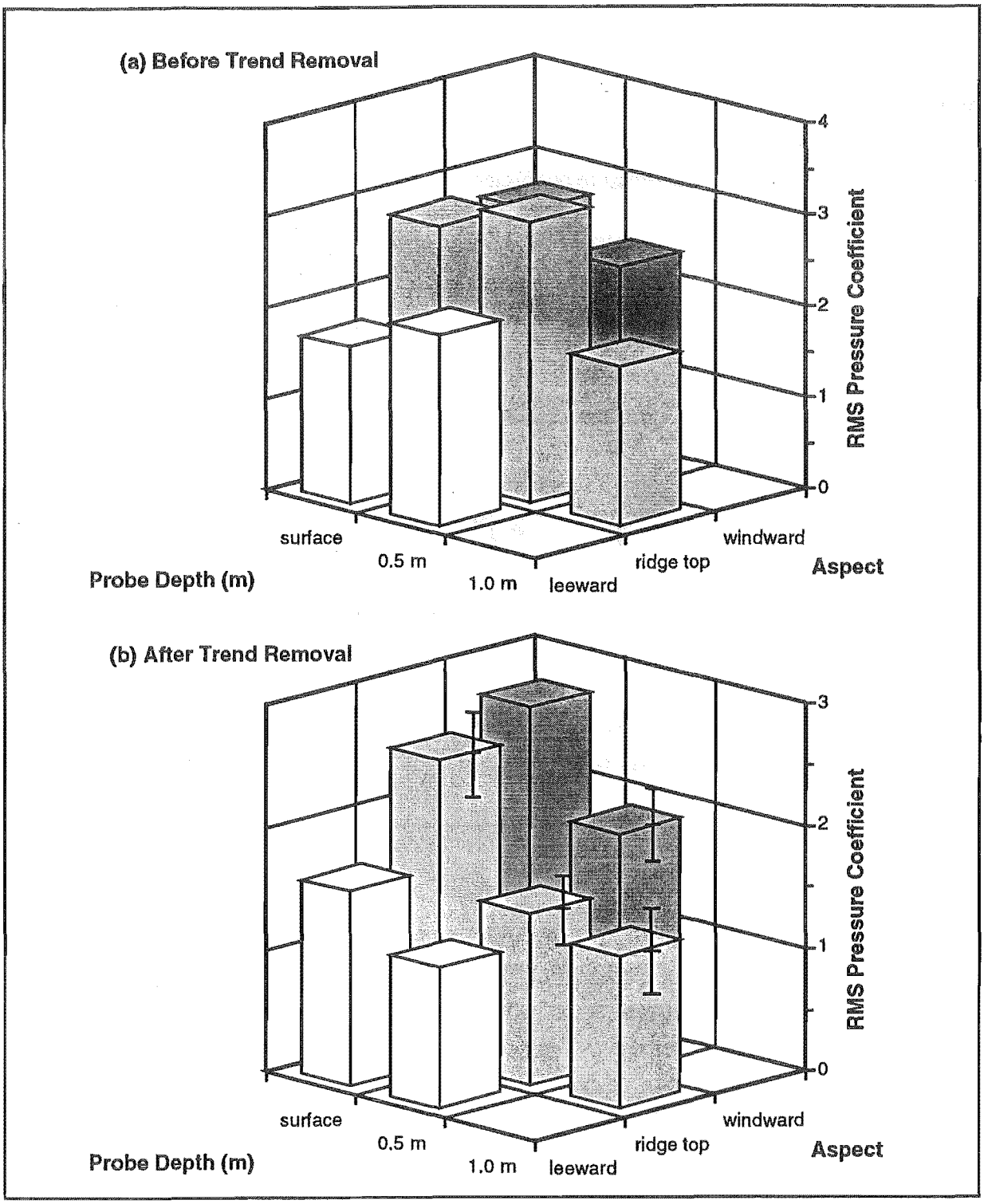

Figure 3.35. Variation of RMS Pressure Coefficients (a) Before and (b) After Trend Removal in Northwesterly Conditions According to Aspect and Probe Depth. The Records Used in This Comparison all Have Mean Wind Speeds of About 5 m/s and an Average Snow Pack Depth of Around 2 m. Where possible the errors are shown in (b) as $\pm 2\sigma/\sqrt{q}$ (σ is the standard deviation of the q grouped records). No readings were taken at the 1.0 m level for the windward or leeward aspects.

The windward to leeward distribution of surface rms pressure coefficients over the relatively gentle ridge of the measurement site are consistent with those of Ogawa *et al* (1991), Sun *et al* (1992) and Zhang and Melbourne (1992) over curved surfaces. Milford and Waldeck (1988), Kawabata *et al* (1990) and Ohkuma *et al* (1991) show that for more abrupt changes in curvature (ie a 90° corner) the largest rms pressure coefficients occur on the side faces or roof top.

Figure 3.36 shows the strong correlation between rms pressure coefficient and wind speed turbulence intensity.

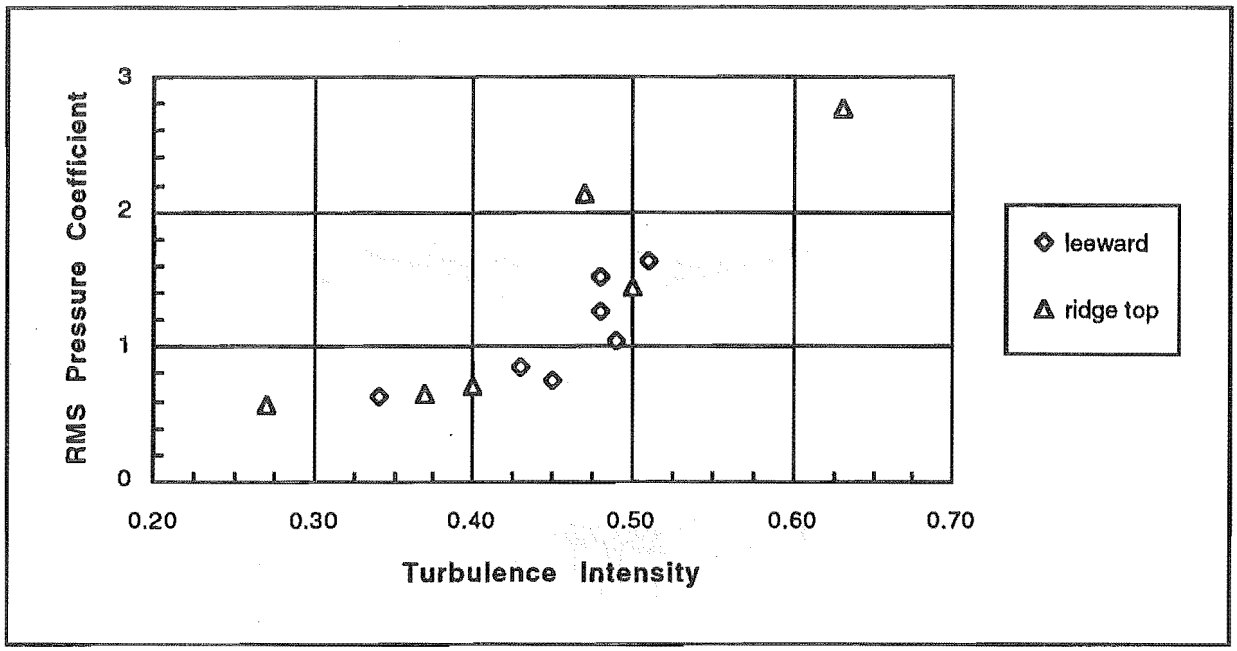

Figure 3.36. Variation of Leeward and Ridge Top Surface RMS Pressure Coefficients with Turbulence Intensity.

Although the Temple Basin rms pressure coefficients appear to be much larger than most published data, comparisons of the observed rms pressure coefficients with data from other experiments is complicated because the velocity scales used in the definition are not directly comparable. Table 3.7 illustrates the resulting variability in the published data.

Author(s)	Bluff Body Type	Leeward	Windward
Temple Basin Data	rough mountainous terrain	1.6	2.7
Ogawa *et al* (1991)	domes and cylinders - wind tunnel	0.05	0.4
Buckles *et al* (1984)	wavy surface - wind tunnel	0.06	0.68
Zhang and Melbourne (1992)	tandem cylinders - wind tunnel	0.2	1.0
Ohkuma *et al* (1991)	high rise building	0.2	0.5
Matsui *et al* (1982)	high rise building	0.1	0.45
Milford and Waldeck (1988)	roof of a hanger	-	0.25 to 2.5

Table 3.7. Examples of Leeward and Windward RMS Pressure Coefficients from the Literature for Various Bluff Body Types.

3.10.4. Autocorrelation Functions and Integral Length Scales

Table 3.8 summarises the integral length scales for the wind speed and pressure data using the three methods outlined in section 3.9.5. The results from individual records are included in table IV.4.

Length Scale, Λ	Wind Speed (m)	Pressure (m)	Difference (m)	Spread Derived From;
Eulerian Λ_{Eul}	161 ± 88	286 ± 140	125	± 2 standard deviations over all runs
Exponential Λ_{exp}	150 ± 80	303 ± 60	153	± 2 standard deviations over all surface runs
Spectral Λ_{spec}	152^{+228}_{-57}	316^{+414}_{-129}	194	locating the peak of the autospectral density functions

Table 3.8. Integral Length Scales Averaged over All Wind Speed Records and All Surface Pressure Records for the Three Methods Outlined in Section 3.9.5.

3.10.4.1. Fluctuating Wind Speed Results

The autocorrelation functions have been reported in the results of full scale measurements less frequently than their corresponding autospectral density functions. However, they generally provide better integral length scale estimates (see section 3.9.5).

Integral Length Scales

At height[4] z = 3.5 m, the fluctuating wind speed integral length scales measured at Temple Basin range from 60 to 269 m. These appear significantly larger that most integral length scales reported in the literature. For example, Flay (1978) reports integral length scales $\Lambda = 45$ to 145 m at z = 5.3 m over flat rural terrain.

Flay (1978) and Antoniou *et al* (1992) show that the integral length scales increase substantially with height. This observation is important to avoid confusion between the conclusions made below and the results of higher elevation length scales. For example, Flay at z = 20 m measured $\Lambda = 65$ to 245 m and Matsui *et al* (1982) in a city at z = 73 m (on top of a high rise building) measured $\Lambda = 38$ to 287 m.

In measurements made by Antoniou *et al* (1992) over hilly complex terrain at z = 8.1 and 31 m, the length scales were found to lie between $\Lambda = 80$ to 700 m and $\Lambda = 150$ to 900 m

[4] The mast height is 6.5 m, however this is reduced to about 3.5 m during the measurements due to the accumulated snow pack.

respectively. Antoniou *et al* found the length scale to be highly dependent on the upwind terrain. Their z= 8.1 data is summarised in table 3.9.

Direction	Integral Length Scale (m)	Approximate Terrain Scales (m)	
		ridge to ridge	total vertical relief
355° - 005°	600 - 700	800	180
010° - 020°	80 - 200	400	120

Table 3.9. Integral Length Scale Data from Antoniou *et al* (1992) at z= 8.1 According to Upwind Terrain.

Flay's (1978) comments on the accuracy of these length scale measurements are acknowledged but not reiterated here.

Autocorrelation Functions

The autocorrelation functions of the Temple Basin measurements do not follow the expected exponential decay shown in the results of Antoniou *et al* (1992) and Flay (1978). Instead, as can be seen in examples of figure 3.37(a), a definitive decay is not apparent below a correlation coefficient of about 0.2, and in some cases a strong oscillation about zero remains. Such oscillations indicate periodic or semi-periodic components to the data.

3.10.4.2. Fluctuating Pressure Reressure data have not been reported in the literature like those for wind speed measurements. This would be due in part to the lack of microscale peak in some of the published fluctuating pressure spectra (see figure 2.2). As with Elliott (1972b) and Schols and Wartena (1986), spectral peaks do appear in the Temple Basin fluctuating pressure spectra (see section 3.10.5), and so the integral length scales can be evaluated.

Like the wind speed results, the fluctuating pressure autocorrelation functions show varying degrees of periodicity as illustrated in figure 3.37.

3.10.4.3. Comparing Wind Speed and Pressure Results

It can be seen from table 3.8 that the fluctuating pressure integral length scales are somewhat larger than those for wind speed. Two psults

Integral length scales for fluctuating possible explanations are put forward:

1. It is not appropriate to use the 3.5 m mean wind speed for calculation of the fluctuating pressure integral length scale.
2. Transmission of pressure through the lower ABL to the snow surface from higher layers where larger structures are likely to be prevalent.

The latter would seem more likely given that distance between the wind speed and pressure measurements were much less than the length scales.

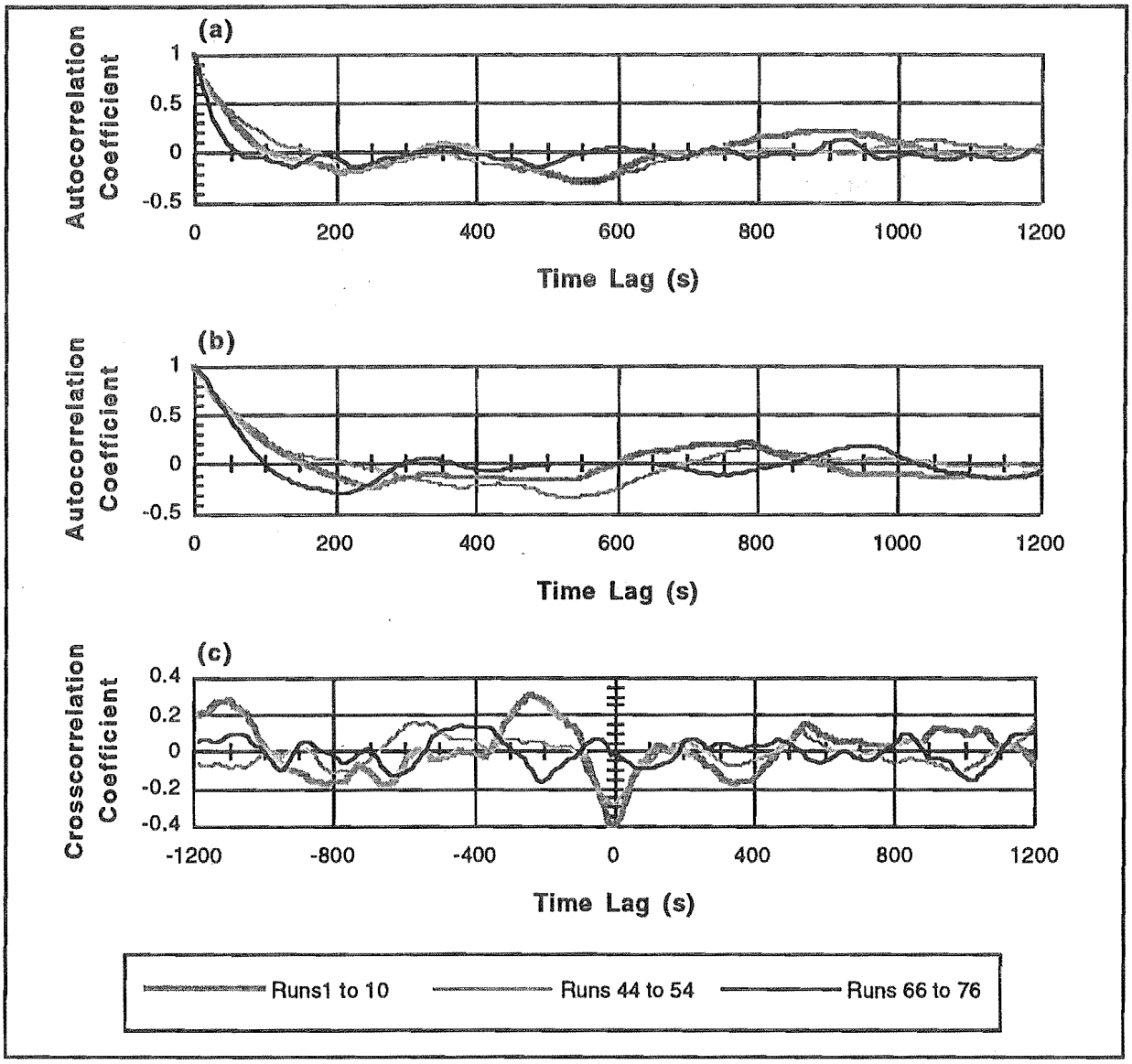

Figure 3.37. Examples of (a) Fluctuating Wind Speed and (b) Pressure Autocorrelation Functions with Varying Degrees of Periodicity (oscillations about zero). (c) Shows Examples of the Cross Correlation Functions between Wind Speed and Pressure Fluctuations.

While higher elevation turbulent structures may not be seen in the wind speed fluctuations, they are likely to influence the surface pressure fluctuations as they propagate through the pressure field. Larger high elevation structures could be derived from two mechanisms:

1. Panofsky and Ming (1983) show that the upper layers of the boundary layer are affected by roughness elements further upstream by comparison to the lower layers. This should show in larger integral length scales.
2. From the discussion in section 2.12.1.4, it was concluded that it is likely that the measurement site lies in the region of internal gravity wave generation. While detection of standing waves (wave speed equal to the mean wind speed) is not expected, travelling or breaking waves might occur. As these waves travel above ridge top it is expected that

they will have less influence on the wind speed fluctuations than on the surface pressure fluctuations.

The supposition that the Temple Basin fluctuating pressure data contain gravity wave components is well supported, see for example Gossard (1960), Herron *et al* (1969), Elliott (1972b), Andreas (1987) and Nappo and Chimonas (1992).

A final note of caution on the validity of these results should be made, as it is shown in section 3.9.5.1 that Taylor's hypothesis, used to derive the integral length scales, is only weakly observed.

3.10.4.4. Previous Surface Measurements of Gravity Waves

In a study of wave phenomenon in the first 200m of the nocturnal atmospheric boundary layer, Caughey and Readings (1975) measure a peak frequency in their velocity and temperature data with periods between 5 to 8 minutes.

Einaudi and Finnigan (1981) and Finnigan (1988) detected gravity waves in the nocturnal ABL with a variety of sensors near Boulder, Colorado (USA). Einaudi and Finnigan (1981) measured waves with amplitudes $\approx \pm 10$ Pa, periods ≈ 4 minutes, phase velocities ≈ 12 m/s and wavelengths ≈ 2.8 km. Later Finnigan (1988) recorded amplitudes of ± 5 to ± 10 Pa and periods of 3.5 to 9.5 minutes in a variety of conditions including those in which there was substantial reinforcement of turbulent kinetic energy from the wave field. The source of these waves is not documented.

The detection of gravity waves with periods of about 10 minutes by surface pressure measurements have been made by Monserrat *et al* (1992) and Monserrat and Thorpe (1992) in relation to sea level fluctuations in the Mediterranean. Amplitudes of ± 150Pa have been detected for waves with periods of 8 to 50 minutes, wavelengths 2 to 60km and phase speeds of 18 to 30m/s. The source of these waves, whilst discussed, are not determined.

There are no measurements of wave activity during strong wind conditions or over rough complex terrain (known to this author).

In the cases above, where the waves themselves are determinant, they are likely to be relatively large scale events. In the mountainous region of Arthur's Pass, where lee mountain waves are likely to be generated, one would expect waves on the scales of the terrain producing them. Interactions between terrain, waves and turbulence are likely to be extremely complex and no attempt is made here to propose any direct links other than to present the results at hand.

3.10.5. Autospectral Density Functions

In this section similarities between the wind speed and pressure autospectral density functions are discussed before the individual properties of each are looked at in detail. Finally, spectral differences between the variables are examined.

3.10.5.1. Similarities in Fluctuating Wind Speed and Pressure Spectra

The similarities between the wind speed and pressure spectra shown in figures 3.38 and 3.39 raises several points.

Three key features, which may illustrate different turbulence mechanisms, are observed in figures 3.38(b) and (c) and 3.39(a) and (b):

1. Similar variability between wind speed and pressure below ≈ 0.015 Hz (about a period of 1 minute) indicating that the large scale turbulent structures are independent of terrain location and probe depth.
2. The relatively high variability of the pressure spectra above ≈ 0.015 Hz, possibly due to the influence of terrain and snow depth on the high frequency pressure fluctuations.
3. The spectral peaks at n = 0.0013 and 0.0025 Hz (12.8 and 6.4 minutes) in both the wind speed and pressure spectra.

These spectral peaks are clearly evident in all aspect and depth spectra (shown in figure 3.43), and in the two sub-surface probe spectra (shown in figure 3.44). To investigate the statistical significance of the peaks (from the trough between them) a single sided t-test was used to test equivalence between the spectral estimate for the peak frequency, and the spectral estimate for the adjacent trough frequency (both are mean spectral estimates over all runs). The results from this analysis are summarised in table 3.10.

	Spectral Peak		Spectral Trough		Conclusion
	Frequency	Estimate	Frequency	Estimate	
Wind Speed	0.0013	0.24	0.0016	0.18	ns
	0.0025	0.33	0.0016	0.18	**
Pressure	0.0013	0.40	0.0016	0.24	*
	0.0025	0.47	0.0016	0.24	**

Table 3.10. Results of a Single Sided t-Test Between the Spectral Estimates of Adjacent Peaks and Troughs in the Averaged Wind Speed and Pressure Dimensionless Autospectral Density Spectra Shown in Figure 3.38 (b) and (c). The conclusions for each test are indicated by ** - significantly different at $\alpha = 0.025$, * - significantly different at $\alpha = 0.05$, ns - not significantly different at $\alpha = 0.05$.

The peaks in the wind speed spectra are weaker compared to the pressure spectra. These peaks appear to be significant, with the exception of the lower frequency wind speed peak. Note that data at the low frequencies of these peaks will be attenuated by the reference pressure system detailed in section 3.7.2.4. This may be the sole cause for the smaller low frequency peaks compared to the higher frequency peaks.

A connection between the two peaks may be linked with:

1. Terrain scales.
2 Harmonics of gravity wave activity.
3. Coalescence of turbulent structures.

The doubling of frequency from one peak to the next suggests that the second or third mechanisms may be occurring, as the terrain scales are discrete, and appear to vary in order of magnitude between scales (see section 3.6.2).

The spectral peaks of both variables lie in the range of frequencies predicted for mountain terrain in Chapter 2 ($0.001 < n < 0.08$ Hz) related to fluctuations in and around a separated flow (separated shear layer, shedding vortices and moving reattachment point). High frequency peaks in the range $0.1 < n < 0.5$ Hz due to flow separation, are not observed in either spectra. The peak frequencies also lie in the region where gravity wave activity may be detected.

Reliability

An impression of the variability in experimental estimates can be gained from figure 3.39 which shows the individual dimensionless autospectral functions of all fully analysed records. In more complete terms figure 3.38 (b) and (c) shows the experimental error $\varepsilon_e[\widehat{S_{ii}}(n)]$, in each spectral estimate $\widehat{S_{ii}}(n)$, given by

$$\varepsilon_e[\widehat{S_{ii}}(n)] = \pm\frac{2\sigma[\widehat{S_{ii}}(n)]}{\sqrt{q}} \qquad (i = u \text{ or } p) \qquad 3.40$$

where $\widehat{S_{ii}}(n)$ is the estimate of the true value $S_{ii}(n)$, $\sigma[\widehat{S_{ii}}(n)]$ is the standard deviation of the estimate and q is the number of records in the estimate. This is an appropriate error to consider at mid to high frequencies. However, at low frequencies the random error in spectral estimates should be considered. This topic is treated in detail in section 3.9.6.1 and illustrated in figure 3.28 (a).

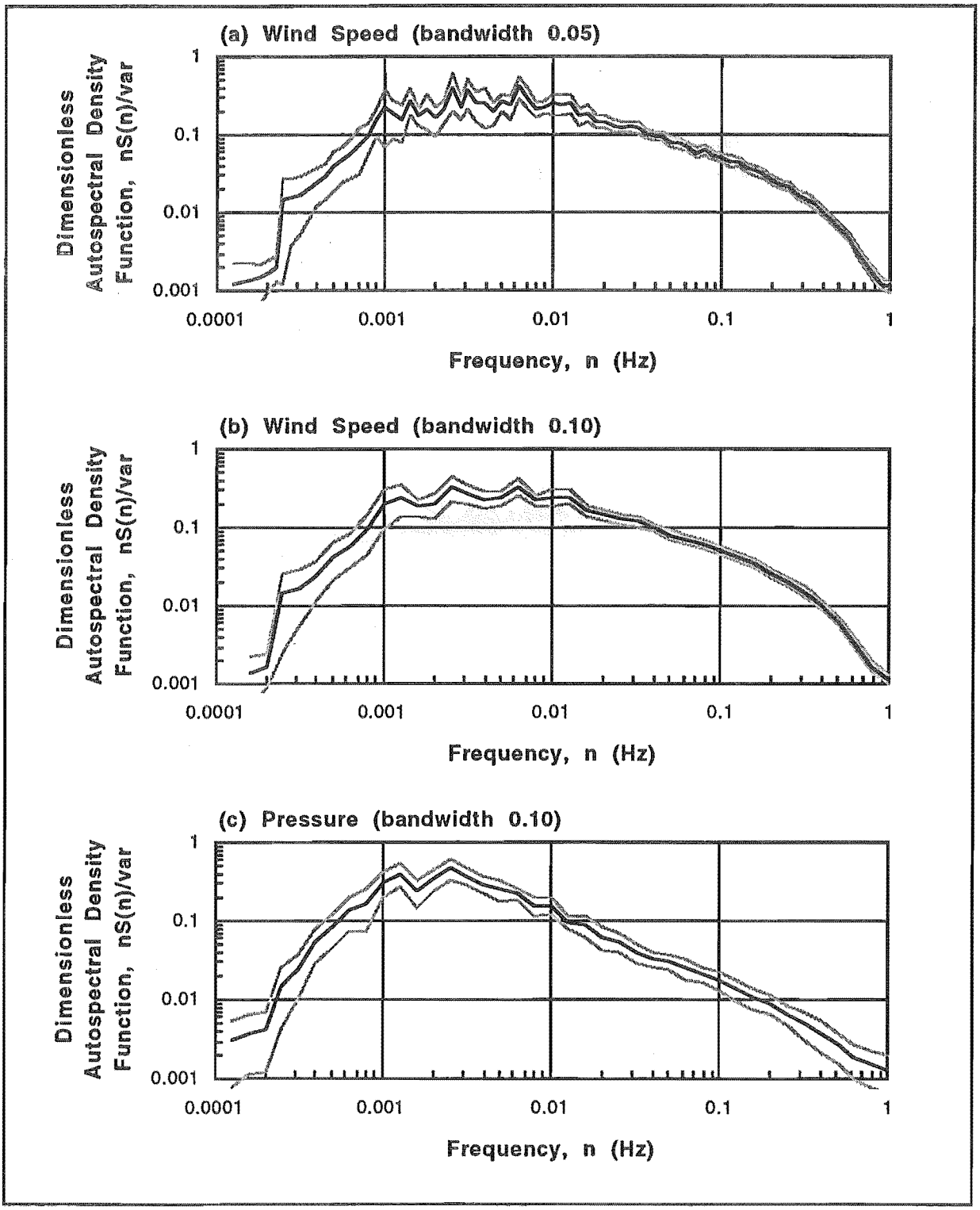

Figure 3.38. Averaged Dimensionless Autospectral Density Functions of the Fully Analysed Records (not including pressure records with two sub-surface probes): (a) Wind Speed ($\Delta \log_{10}(n) = 0.05$). (b) Wind Speed ($\Delta \log_{10}(n) = 0.10$). (c) Pressure ($\Delta \log_{10}(n) = 0.10$). The experimental errors for the spectral estimates (calculated using equation 3.40) are shown with the light lines above and below the average spectra.

The shape of the spectra is influenced by the low frequency trends in the data and trend removal. To meet record stationarity requirements, the analysis approach with the Temple Basin data was to remove the smallest amount of low frequency information possible (see section 3.9.3 for full details). The effect of a trend on the autospectral density function is to increase the apparent energy of the lowest frequencies, at the expense of the energy levels of the rest of the spectra. Although removing the trend idealistically corrects this imbalance, it also makes the form of the spectra seem somewhat arbitrary. It is not thought that trends and trend removal sufficiently effect the data to the degree of negating the extent of the lateral shift in the spectra (see the discussion in section 3.10.5.2).

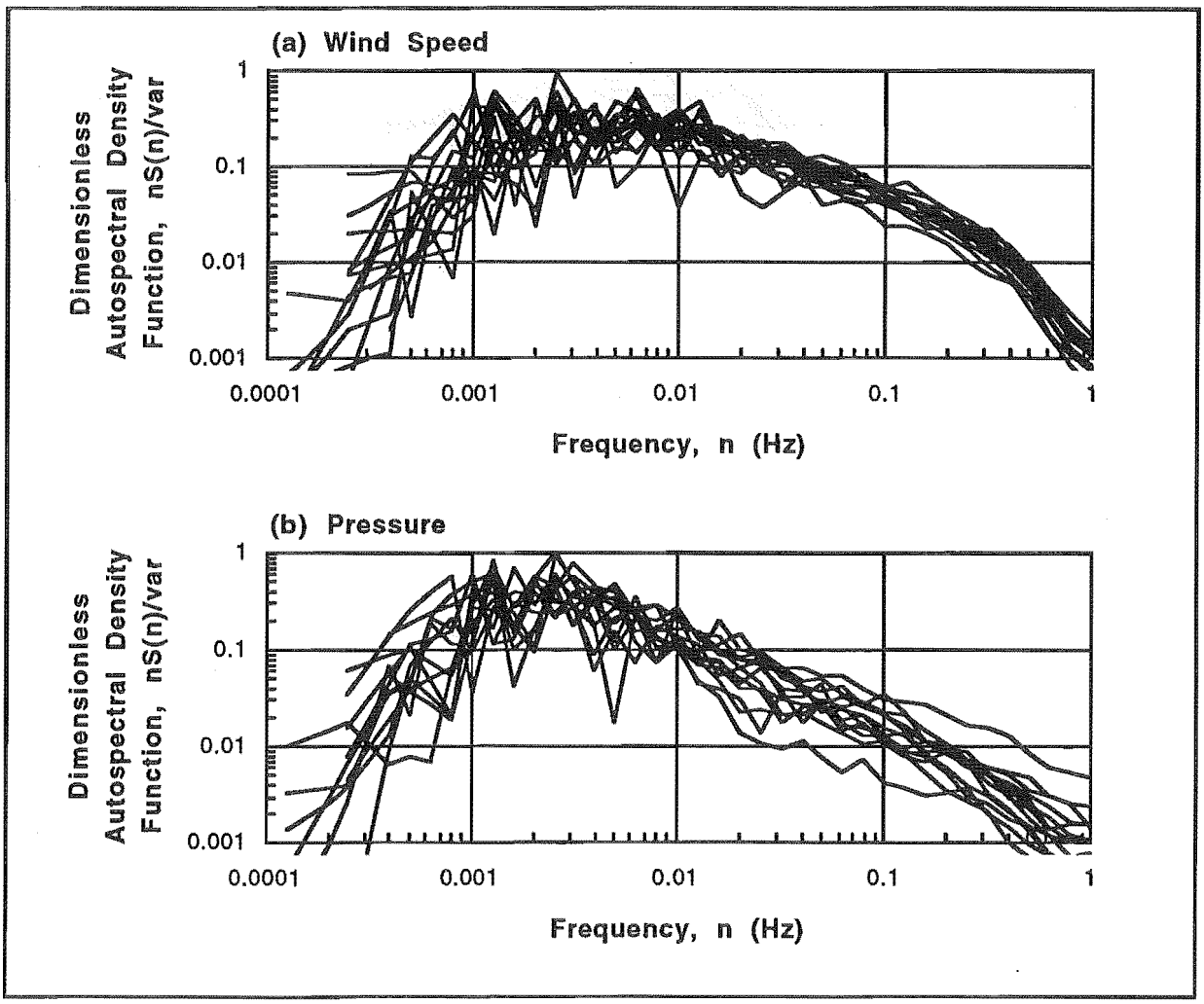

Figure 3.39. Dimensionless Autospectral Density Functions of the Fully Analysed Records (not including pressure records with two sub-surface probes) for a Smoothing Bandwidth of $\Delta \log_{10}(n) = 0.10$: (a) Wind Speed. (b) Pressure.

3.10.5.2. Fluctuating Wind Speed Spectra

The dimensionless autospectral density function for Temple Basin is plotted against dimensionless frequency alongside two previously reported spectra in figure 3.40. The vertical scaling varies considerably in the literature. The unavailability of several key scaling variables in the Temple Basin data limits peak height comparisons. Conversely, the dimensionless frequency used in figure 3.40 is common throughout the literature, and therefore the position of the spectral peak can be easily compared.

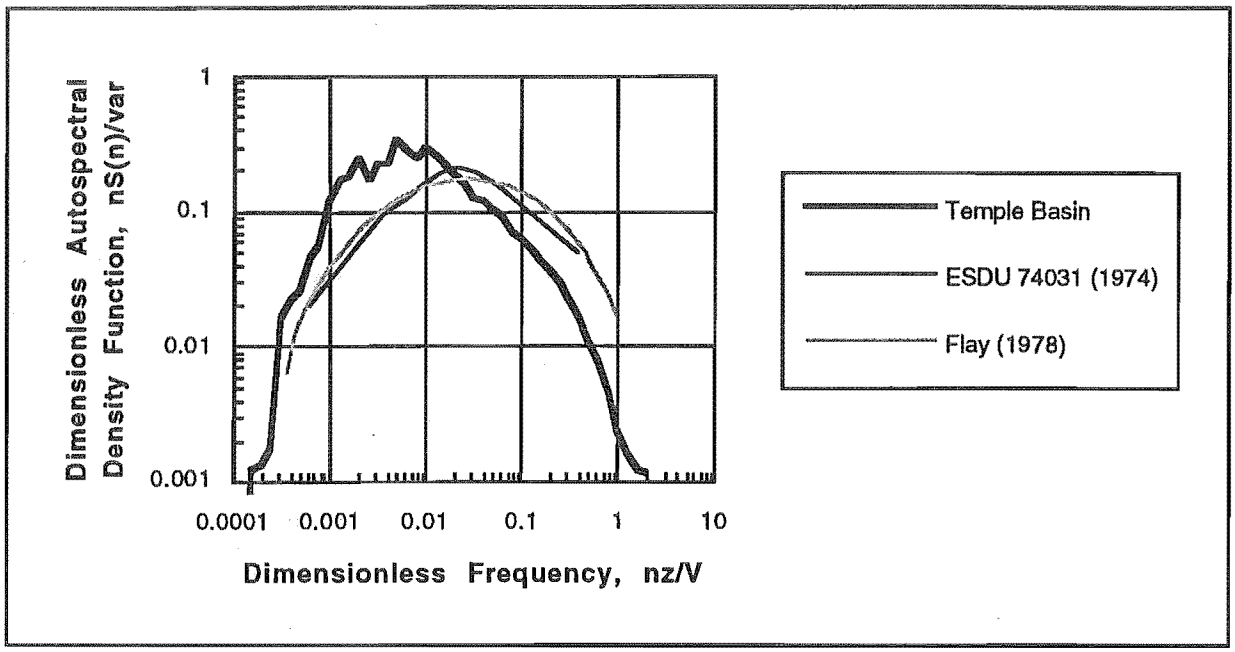

Figure 3.40. Averaged Autospectral Density Function for the Temple Basin Wind Speed Fluctuations Compared to ESDU 74031 (1974) and Flay (1978).

The Temple Basin spectra has similar form to other documented spectra, but is shifted substantially toward lower frequencies. The differences between the Temple Basin spectra, and other reported spectra are very large compared to the differences within the reported spectra. There are some notable exceptions to this:

* Mitsuta *et al* (1983) show a similar scale departure and find the spectra are highly correlated to local topography. Their terrain is only slightly smaller in scale and slightly less complex compared to the terrain around Temple Basin.
* Antoniou *et al* (1992) find pronounced differences among the spectra from different wind directions over complex hilly terrain.
* Smedman (1991) finds a site dependence which is related to surface roughness in a comparison of spectra over seven less rugged sites with different kinds of terrain.

Thus it appears that terrain is largely responsible for the peak shifting to lower frequencies. However, it could also be due to more low frequency energy being included in the Temple Basin measurements.

Examining the Temple Basin spectra in more detail, between the dimensionless frequencies $0.013 < nz/\overline{V} < 0.13$ $(0.01 < n < 0.1)$ the spectra falls off according to a power of -0.66 ± 0.08. This is consistent with the -2/3 power law predicted by dimensional arguments for an inertial subrange (see for example Elliott, 1972b). The minimum frequencies of the inertial subrange from Elliott ($nz/\overline{V} = 0.2$) for open grasslands and Matsui *et al* (1982) ($nz/\overline{V} = 0.14$) on top of a high rise building, are far higher than those found here. Above $nz/\overline{V} = 0.13$ $(n = 0.1)$ the slowly increasing negative slope of the Temple Basin data is likely to be due to the response characteristics of the anemometer. There are no apparent spectral peaks above $nz/\overline{V} = 0.13$ $(n = 0.01$ Hz).

A broad peak occurs at $0.001 < n < 0.01$, consistent with the observations of Jenkins *et al* (1981) in measurements over an isolated elliptical island roughly 1 km in diameter, and 330 m high, with flow reversal on the lee slope. Surprisingly this is somewhat lower than the peak at 0.08 Hz recorded by Meister (1987) in similar terrain. Jenkins *et al* relate their results to the time scale of the wake fluctuations, and possibly to gravity wave recovery. Over this broad peak lie several small peaks, the significance of which are discussed in section 3.10.4.2 above. At low frequency $(n < 0.001)$ the spectra drops away into the spectral gap as expected from Van der Hoven (1957).

For comparative purposes figure 3.38(a) and (b) show the average wind speed autospectral density functions for smoothing bandwidths of $\Delta \log_{10}(n) = 0.05$ and 0.10 respectively. The same essential features discussed above (for $\Delta \log_{10}(n) = 0.1$), are prevalent in the $\Delta \log_{10}(n) = 0.05$ spectra.

3.10.5.3. Fluctuating Pressure Spectra

Spectra of pressure fluctuations have been made much less frequently in the literature. Unfortunately for comparative reasons, there is little consistency in the dimensionality of the frequency axis. There is little purpose in making frequency dimensionless as done with the velocity fluctuations (equation 3.31). This is because mean wind speed and measurement height are site dependent and remote from the fluctuating surface pressure measurements. The scaling of wind tunnel wall pressure data using boundary layer thickness and free stream velocity (Blake, 1970) prevent direct comparison with atmospheric data as such variables are not easily defined for the ABL. Efforts by Elliott (1972b) to group pressure spectra from different elevations and surface roughness, by non-dimensionalising using typical atmospheric scaling variables, were unsuccessful.

In the range $0.003 < n < 1$ Hz the Temple Basin spectra follows a similar power law to the Gossard's (1960) spectrum (shown in figure 2.2). However, the spectral energies appear lower. This is possibly due to more low frequency energy being included in the Temple Basin measurements.

A broad spectral peak lies in the range $0.001 < n < 0.003$ Hz. However, making conclusions about the shape of the spectra at frequencies much lower than the peak is dangerous, considering the magnitude of the statistical and experimental errors (illustrated in figures 3.28(a) and 3.38(c) respectively). As there is no microscale peak in the Gossard spectrum, the peak and low frequency drop off in the Temple Basin spectra may solely be the result of the reference pressure system attenuation (described in section 3.7.2.4). Both Elliott (1972b) and Schols and Wartena (1986) show microscale peaks, but it is unclear whether they corrected for low frequency attenuation.

Figure 3.41 shows the dimensionless spectra corrected for measurement system attenuation. Very little high frequency attenuation of the spectra due to the micromanometer's response is evident. However, attenuation of the spectra by the reference pressure system below 0.002 Hz ($\approx 1/\tau_{ref}$ where τ_{ref} is the reference pressure system leakage time constant) is clearly significant. The peak, shifted to the left to lie between $0.0004 < n < 0.0015$ Hz, is still evident in the corrected spectrum. Caution must be applied in commenting on the new peak's significance as the random errors are much larger at these lower frequencies.

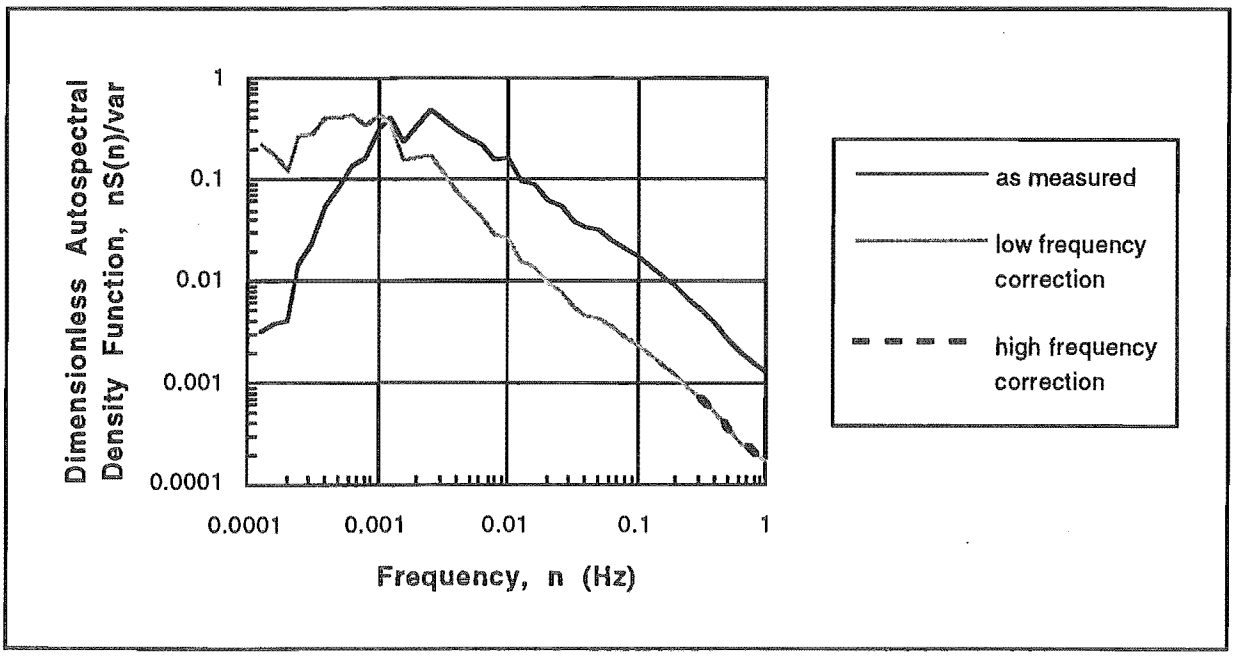

Figure 3.41. Attenuated and Corrected Averaged Autospectral Density Functions for the Temple Basin Pressure Fluctuations. The low frequency correction makes a significant difference to the spectra, while insignificant change to the spectra is seen with the high frequency correction

As the peak of the uncorrected spectrum is in the same range as $1/\tau_{ref}$, this attenuation results in a severe underestimation of the fluctuating pressure integral length scale. Recalculating from the corrected spectra using only the spectral method (refer to section 3.9.5), Λ_{spec} increases from 316 to 1330 m.

Kanda and Ohkuma (1990) summarise spectra from windward and leeward faces of high rise buildings. Unfortunately, a direct comparison with their results is difficult due to the location of their wind speed measurement and its use in presenting the spectra as a function of wave number ($n/\overline{V}$). One result of Kanda and Ohkuma is worth noting; that is, a frequency peak on the leeward aspect which is approximately double in frequency than on the windward aspect. It is possible that the peaks in the Temple Basin spectra are derived from these sources.

Due to the effects of separation, one would expect an increase in the high frequency pressure fluctuations on the lee slope. Conversely, the filtering of high frequency components by the snow pack should cause attenuation of the high frequency end of the spectra in sub-surface pressure measurements. Within the errors illustrated in figure 3.38 (b) the pressure spectra averaged according to aspect and probe depth in figure 3.42 do not show any of these expected variations.

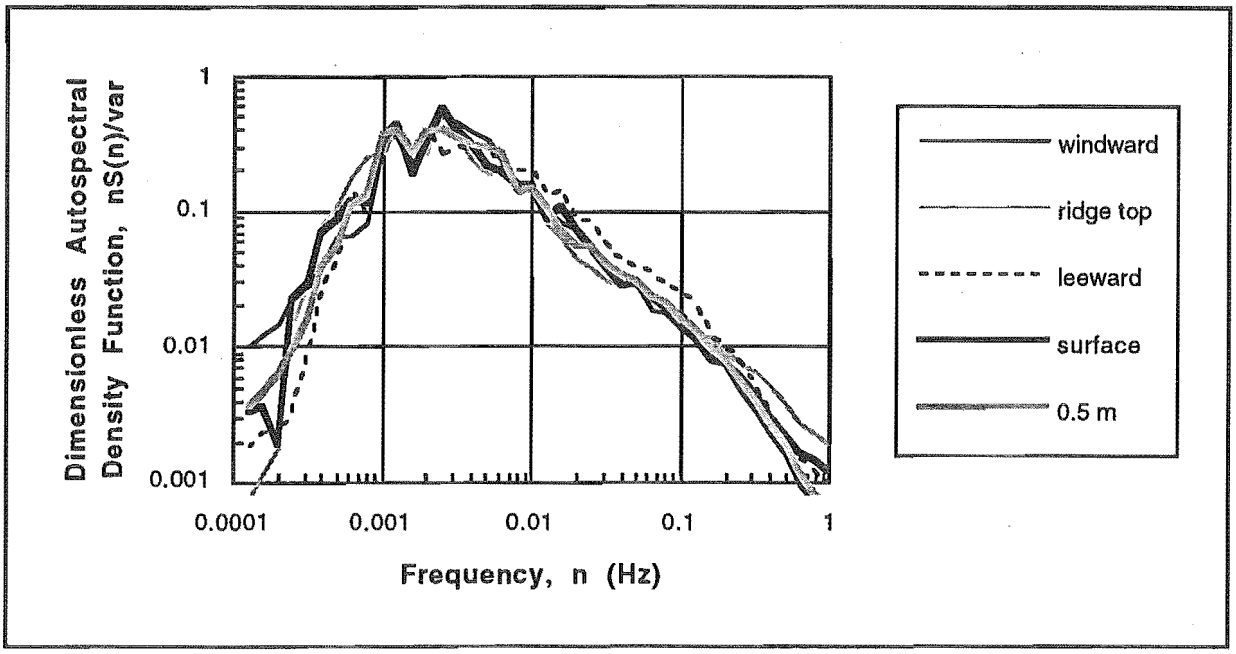

Figure 3.42. Averaged Dimensionless Autospectral Density Functions of the Pressure Records for a Smoothing Bandwidth of 0.10 According to Aspect and Probe Depth.

The spectra for the runs using two sub-surface 0.5 m deep probes, separated by X = 4.5 m, are plotted in figure 3.43. They both show the expected frequency peak at about 0.1 Hz ($= \overline{V}/2\pi X$). However, there is more low frequency energy than might be expected, possibly due to the oscillation of quasi-stationary high and low pressure zones (illustrated in figure 4.2(b)).

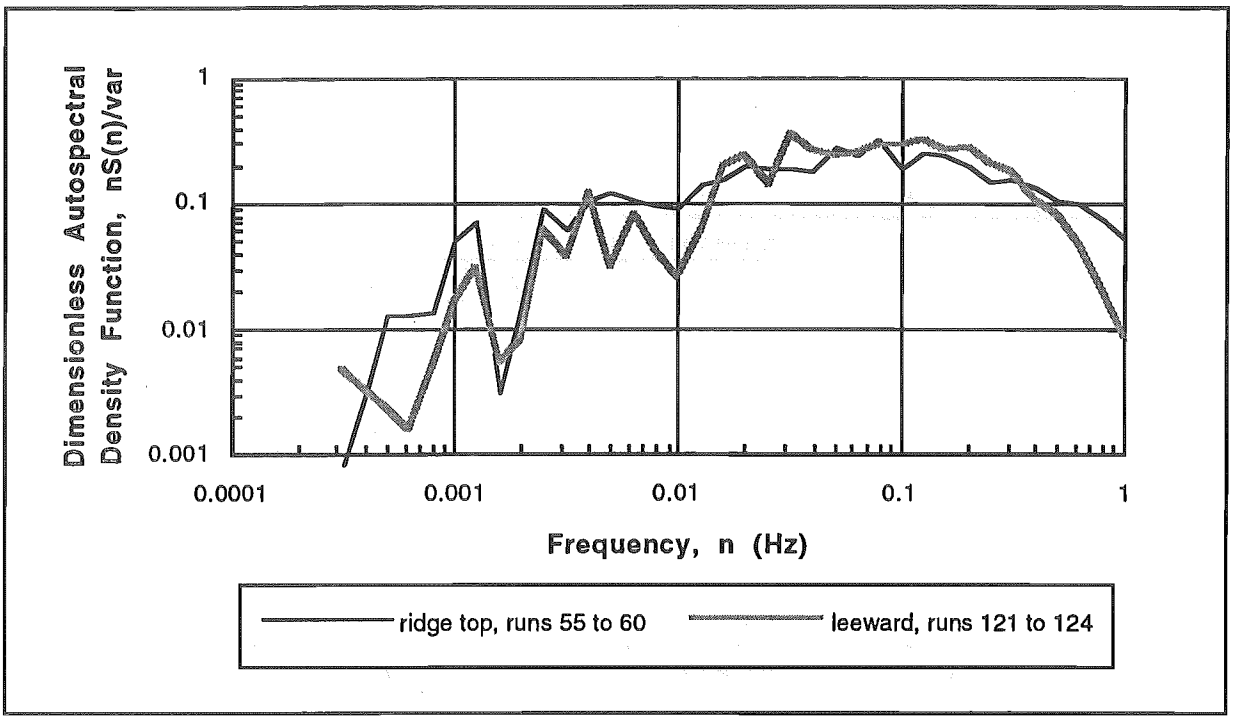

Figure 3.43. Dimensionless Autospectral Density Functions of the Pressure Records with two Sub-Surface Pressure Probes Separated by X = 4.5 m at the Same Snow Pack Depth of d = 0.5 m (Smoothing Bandwidth = 0.10).

Reliability

Unfortunately insufficient records were obtained to study the detailed effects of probe depth and aspect. At most three successful records were taken for any one combination of aspect and probe depth, and in some cases only one record was made. The random error in the presentation of a single record is very large at the mid to low frequency end of the spectra, a problem accentuated by short record lengths. These errors are illustrated in figures 3.28(b) and (c).

3.10.5.4. Differences Between Fluctuating Wind Speed and Pressure Spectra

The observed fluctuating wind speed spectral peak is both broader, and at a higher frequency compared to the fluctuation pressure spectral peak. Schols and Wartena (1986) also note a lower frequency spectral peak for the pressure fluctuations. This aspect of the spectra is examined in detail in the discussion of integral length scales (section 3.10.4.3).

3.10.6. Wind Speed / Pressure Crosscorrelation Functions

The wind speed / pressure crosscorrelation functions obtained in this analysis can only be described as irregular. Several examples are included in figure 3.37(c) (in section 3.10.4). Table 3.11 shows the crosscorrelation coefficients of all fully analysed runs for the peak closest to time lag $\tau = 0$.

Runs	Length (min)	Position	Probe Depth (m)	Crosscorrelation Coefficient
88 to 98	130.8	leeward	0.0	0.2
99 to 109	109.7	leeward	0.0	0.12
110 to 120	130.8	leeward	0.3	-0.18
14 to 16	41.1	ridge top	0.0	-0.29
17 to 19	41.1	ridge top	0.0	-0.63
1 to 10	103.4	ridge top	0.5	-0.41
44 to 54	130.8	ridge top	0.5	-0.3
23 to 27	68.3	ridge top	1.0	-0.27
33 to 43	136.5	ridge top	1.0	-0.37
61 to 65	68.3	windward	0.0	-0.11
66 to 76	130.7	windward	0.5	0.08
77 to 81	68.5	windward	0.5	0.2
82 to 87	62.2	windward	0.5	0.2
55 to 60	62.2	ridge top	†	0.06
121 to 124	54.8	leeward	†	0.2

Table 3.11. Wind Speed / Pressure Crosscorrelation Coefficients for the Peak Closest to Time Lag $\tau = 0$. Probe Depth † refers to a pressure probe configuration of two sub-surface probes separated by X = 4.5 m at the same snow pack depth of d = 0.5 m.

If the probe is on the lee side of a predominant terrain feature, behind which separation of the flow is likely to occur, then a strongly negative correlation is expected between the two variables (in line with the venturi effect). For the probe on the windward side a strong positive correlation is expected, associated with buffeting of the impinging flow. If the probe is near the point of separation or reattachment of a separated flow then the degree of correlation may be less defined. These expectations are derived from the surface pressure coefficient observations of Wells and Hoxey (1980), Buckles *et al* (1984) and Patel *et al* (1991) over successive triangular or wavy ridges. Of particular note are the conclusions of Buckles *et al* (1984), that over the windward surface of a high-rise building, the pressure fluctuations follow the wind speed fluctuations. In contrast, over the leeward surface they hardly follow the wind speed fluctuations.

These trends, which should have been easily observed in the crosscorrelation functions, are not readily apparent. The most consistent result is the moderate negative correlation on the ridge top, otherwise it appears the two variables are only weakly correlated. Variations appear to be strongly storm dependent.

Two characteristic storm factors (discussed in section 3.10.1.3) are thought to contribute to this lack of correlation:

1. Changing wind direction, or in the extreme case, back gusts.
2. Changing vertical component of the wind, which in turn changes the points of separation and reattachment (if reattachment occurs).

Both may result in the probe being sometimes in the lee of the prevailing run wind direction, and at other times windward. In turn this may cause the wind speed and pressure fluctuations to switch between *in phase* and *180° out of phase* in association with impinging and separated flows respectively.

It is concluded that the crosscorrelation analysis is an *inappropriate assessment* of the correlation between the wind speed and surface pressure fluctuations, unless run conditions are unusually steady. However, it is still thought that the wind speed fluctuations of *individual gusts* are strongly correlated to the surface pressure fluctuations. Some discussion of the wind speed / pressure correlation between individual gusts is made in section 3.10.2.

To investigate this further, a sample record is divided into many short segments and the cross correlation coefficient evaluated for each segment. The probability distribution of cross-correlation coefficients from the segments are then plotted. Figure 3.44 and 3.45 show the results of this analysis for segment lengths of 5, 20 and 80s.

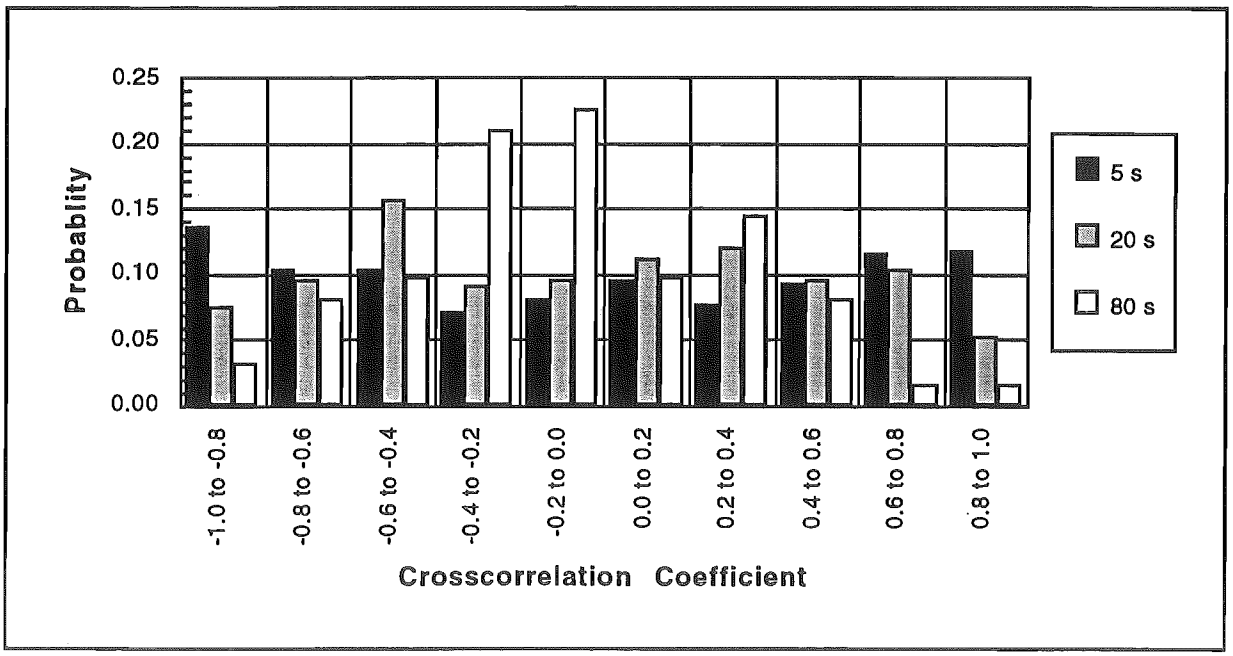

Figure 3.44. Probability Distribution of Crosscorrelation Coefficients from Runs 88 to 91 for Varying Segment Lengths.

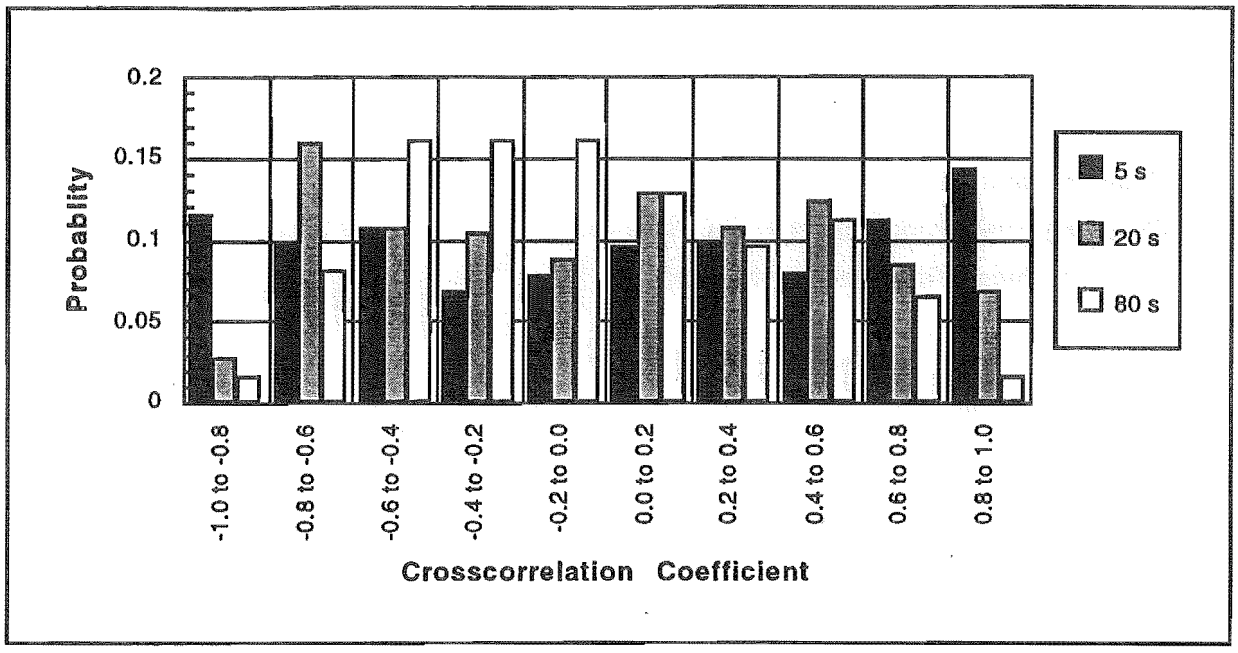

Figure 3.45. Probability Distribution of Crosscorrelation Coefficients from Runs 99 to 101 for Varying Segment Lengths.

It can be seen from these charts that for smaller segment lengths there is a higher probability of negative and positive correlation between the wind speed and pressure fluctuations. However, the correlation is still not particularly strong. Further investigations could be made into looking at the crosscorrelation for different scale turbulent structures. To do this a conditional sampling approach would be more appropriate so that the targeted structures are clearly identified. This is not attempted here.

The crosscorrelation coefficient is the value of the crosscorrelation function at time lag $\tau = 0$. The maximum crosscorrelation coefficient may not occur at $\tau = 0$ due to the spatial separation and different phase responses of the wind speed and pressure sensors. Adjusting for spatial separation would require both horizontal components of wind speed which cannot be obtained from the cup anemometer without digitally recording the wind direction. Whilst these corrections may marginally improve the data, such procedures would not add to the overall picture.

The above mechanisms assume that the pressure structures result directly from the interaction of the wind with the ground. In Chapter 2 it was pointed out that while higher elevation turbulent structures may not be seen in the wind speed fluctuations, they are likely to influence the surface pressure fluctuations as they propagate through the pressure field. This may be what is observed in the crosscorrelations between the variables. Such disturbances may be either large scale turbulent structure shed off upstream terrain features or gravity wave activity. For a more detailed discussion on these point refer to section 2.12.1.

3.10.7. Probability Distributions

The probability distributions obtained for the fluctuating wind speed and pressure data are plotted alongside the normal distribution in figure 3.46. The wind speed distribution is the average of all the fully analysed runs, and the two pressure distributions are for all the fully analysed leeward and ridge top surface runs.

The Temple Basin wind speed probability distribution is skewed to the right, with a peak similar to that of the normal distribution. This data, which could be fitted to a Weibull distribution (Mayne, 1979), is typical of wind speed fluctuations.

The leeward surface pressure probability distribution appears to be skewed slightly to the left. An ill-defined secondary peak is noted which matches the position of the main peak mirrored about the vertical axis. This is consistent with the idea that the leeward probe is not always in a separated flow region.

The ridge top surface pressure probability distribution does not deviate very much from the normal distribution. Although quite possibly just noise in the plot, two vague peaks occur either side of the normal distribution peak.

These results are also reflected in the skewness and kurtosis statistics summarised in table 3.12 (the full set of statistics is included in Appendix IV). The errors in the accumulated wind speed data are small enough to confirm that the distribution is skewed to the right, but it is not peaked compared to the normal distribution. The errors in the pressure fluctuation distributions are too large to make any conclusions about departures from normality.

	Wind Speed (all runs)		Pressure (leeward surface runs)		Pressure (ridge top surface runs)	
	average	error	average	error	average	error
Skewness	0.45	0.16	-0.35	0.26	-0.17	0.27
Kurtosis	0.08	0.24	0.82	0.60	0.15	0.29

Table 3.12. Summary of the Skewness and Kurtosis Statistics. The errors shown are two standard deviations divided by the square root of the number of records the data represents.

Note that there are insufficient windward runs to present alongside these results.

In no case, for either the fluctuating wind speed or pressure data, was the hypothesis of normality accepted at any levels of significance. Two reasons are cited for the complete lack of fit:

1. Noise in the probability distribution as illustrated in figure 3.38(b) and (c).
2. Deviations from normality in the tails of the distribution as shown in figure 3.38(a).

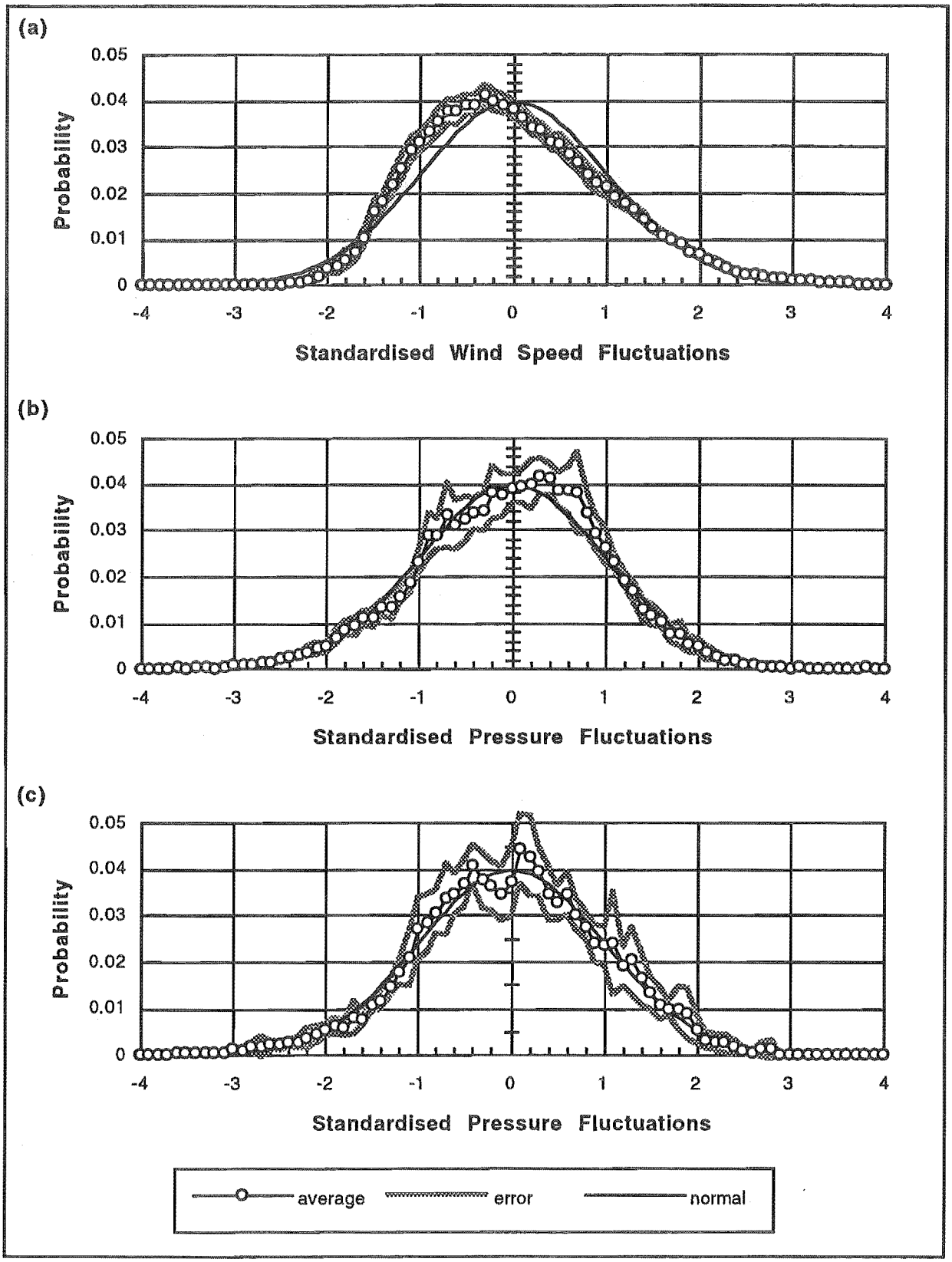

Figure 3.46. The Normal Probability Distribution Compared to the Probability Distributions for: (a) Wind Speed Fluctuations of All Runs. (b) Pressure Fluctuations of All Leeward Surface Runs. (c) Pressure Fluctuations of All Ridge Top Surface Runs. The errors shown are two standard deviations divided by the square root of the number of records the data represents.

The probability distribution for wind speed fluctuations of Matsui *et al* (1982) on top of a high rise building (70 m) appears to be slightly skewed in the opposite direction to the Temple Basin distribution. They did not make a statistical decision on whether their wind speed data is normally distributed. Their probability distributions for surface pressure fluctuations on the leeward and windward faces of the building clearly show positive and negative skewness respectively, consistent with the Temple Basin data. Unlike the Temple Basin data both faces show positive kurtosis.

The same leeward face behavior is found by Ribeiro and Blessmann (1992) in wind tunnel tests on a three dimensional square cylinder. However, they find a normal distribution on the front (windward) face. Ribeiro and Blessmann relate the non-normal leeward and lateral (equivalent to ridge top) distributions to the effect of Karman vortices.

3.10.8. Gust Exceedance Statistics

Table IV.3 summarises the gust amplitude standard deviation and gust rate results for all fully analysed records. Unfortunately, as the gust exceedance presentation made below is unique to this work, no comparisons can be made to other work on gust statistics.

3.10.8.1. Wind Speed Fluctuations

Figure 3.47 shows the number of wind gusts per second (gust rate), and standard deviation of gust magnitudes about the mean wind speed for each bandwidth There is a power law relationship (slope = 0.21) between gust rate and bandwidth frequency.

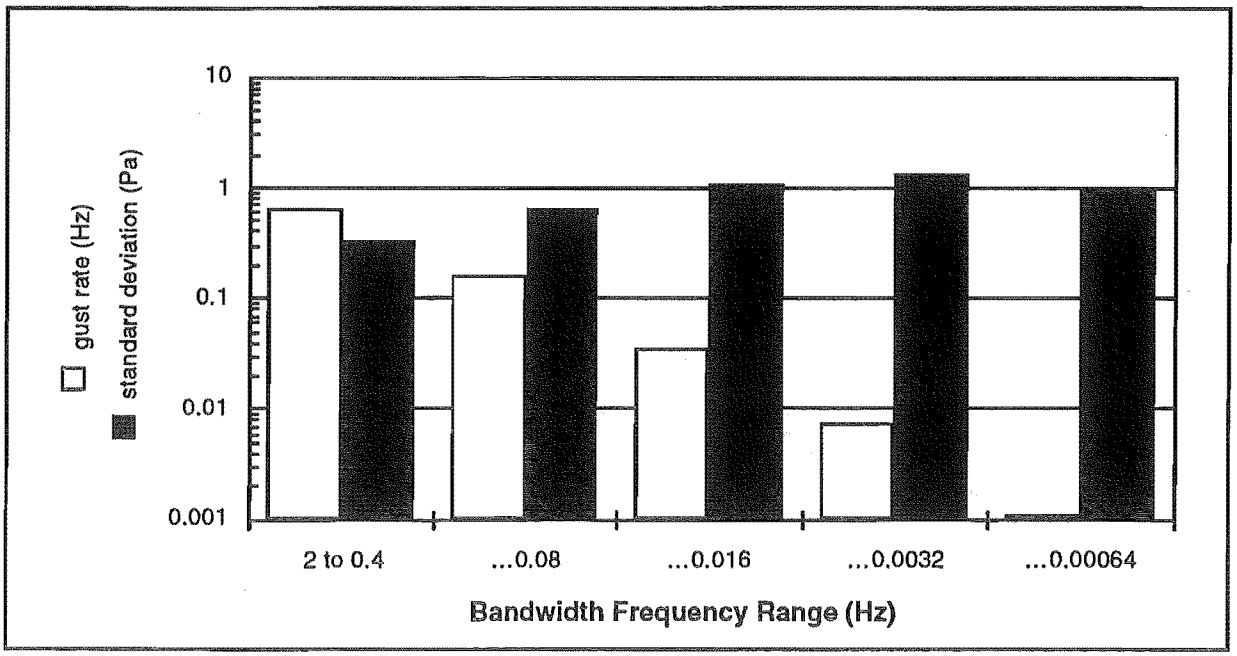

Figure 3.47. Gust Rate and Standard Deviation of Wind Gust Magnitudes About the Mean Wind Speed for Each Bandwidth.

The dimensionless wind gust exceedance probabilities for each frequency bandwidth are shown in figure 3.48. The degree by which the results come together through non-dimensionalising by the record standard deviation is very good, except in the lowest frequency bandwidth where there are only a small number of gusts. This agreement is shown in figure 3.48 as the light lines either side of each probability curve defined b

$$\varepsilon_{\sigma}[\hat{p}] = \pm\frac{2\sigma[\hat{p}]}{\sqrt{q}} \qquad 3.41$$

where the $\hat{p}$ exceedance probability estimate (p is defined in equation 3.38) and $\sigma[\hat{p}]$ is the standard deviation of the estimate over the q records used to compute the estimate.

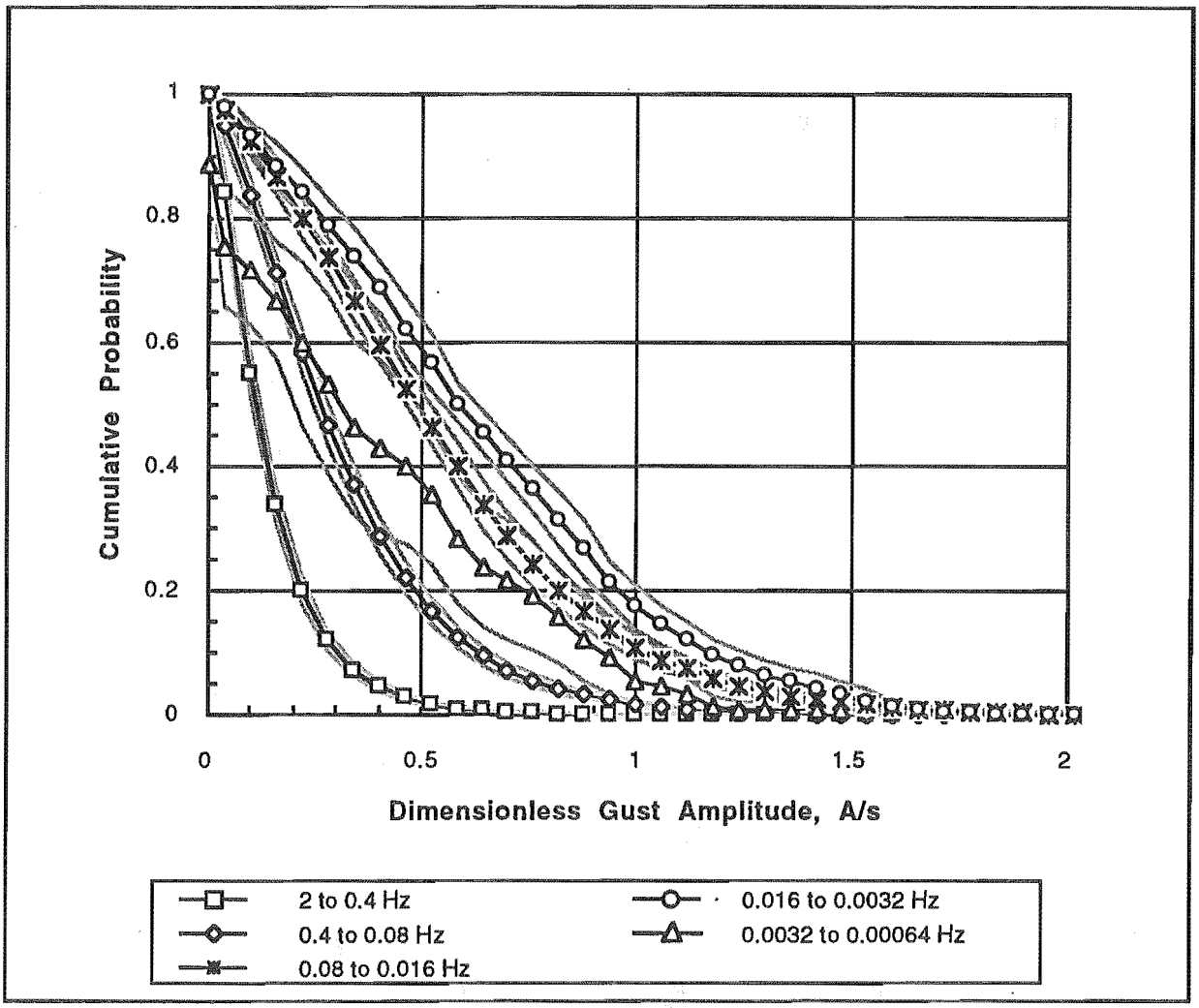

Figure 3.48. Dimensionless Wind Gust Exceedance Probabilities for Various Frequency Bandwidths. The errors are shown as the light lines either side of the probability curves.

3.10.8.2. Pressure Fluctuations

Figure 3.49 shows the pressure gust rate and standard deviations of the surface pressure gust magnitudes for each bandwidth. As with the wind gusts the pressure gust rate shows the same power law relationship (slope = 0.21) with frequency bandwidth.

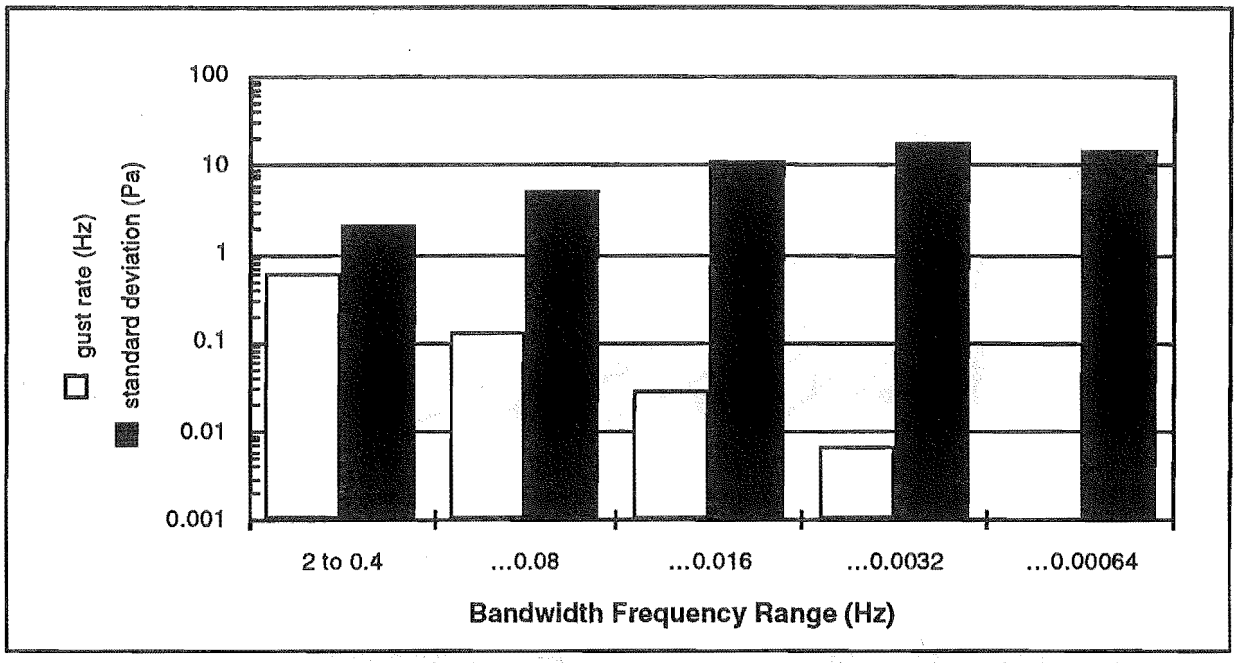

Figure 3.49. Gust Rate and Standard Deviation of Surface Pressure Gusts Magnitudes (all aspects combined) About the Average Pressure for Each Bandwidth.

The dimensionless pressure gust exceedance probabilities for the four highest frequency bandwidths are shown in figure 3.50. The variability in the gust exceedance probability for lowest frequency bandwidth is very high and is therefore not plotted. This is because there are only few gusts of this length recorded (see table IV.3).

The degree by which the results come together through non-dimensionalising by the record standard deviation, is not as good as the wind gust case. This agreement is shown in figure 3.50 as the light lines either side of each probability curve defined in a parallel fashion to the wind gusts (see equation 3.41).

With knowledge of the rms pressure coefficient and mean wind speed the approximate amplitude and occurrence frequency of the pressure gusts can be estimated from these two plots.

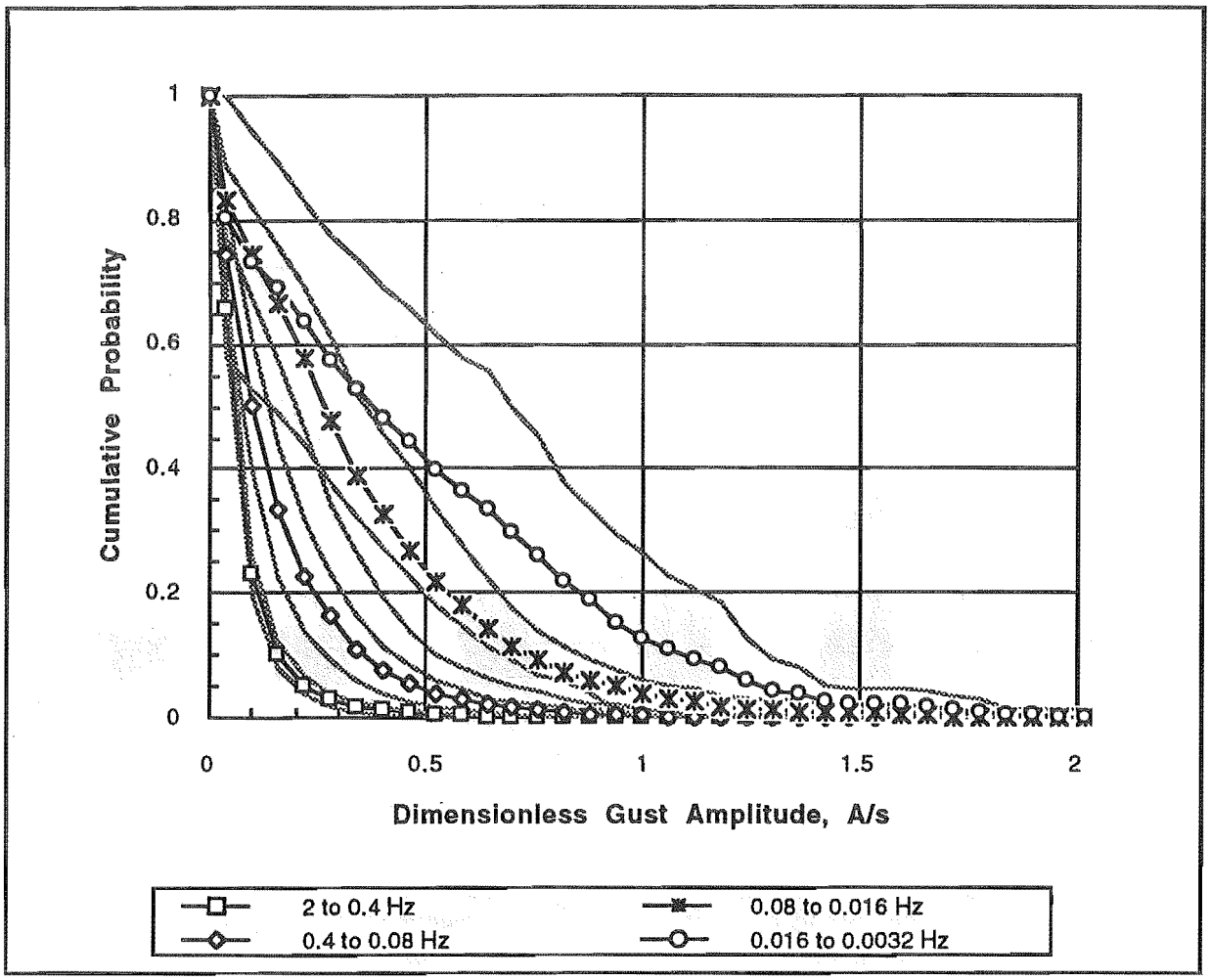

Figure 3.50. Dimensionless Surface Pressure Gust Exceedance Probabilities (all aspects combined) for Various Frequency Bandwidths. The errors are shown as the light lines either side of the probability curves.

3.11. Conclusions

The main objective of this chapter was to determine the amplitude and frequency characteristics of the driving forces behind wind pumping over rough mountain terrain. Also of interest was the decay of the pressure fluctuations in the snow pack, and the generation mechanisms behind the surface pressure fluctuations.

3.11.1. Record Measurement

Both the fluctuating snow surface pressure fluctuations and accompanying wind speed fluctuations have been measured and analysed. The two statistical methods used were power spectral and correlation function analysis, and gust exceedance analysis.

While the spectral presentations may be more difficult to interpret, it appears that much more information on the character of the turbulence can be obtained from such presentations in comparison with gust exceedance statistics.

Funding, time and logistical considerations limited the measurements to the one site at Temple Basin Ski Area's base in Arthur's Pass National Park. At this site both windward and leeward aspects are easily accessed.

Measurements were made only during the northwest phase of the storm cycles. During this phase winds tend to be strong to gale force, and the barometric pressure steady.

A 3-cup anemometer and a digital micromanometer were used for the measurements. Sufficient detail and accuracy was obtained from these instruments to both quantify and assess the characteristics of the turbulence experienced at the measurement site. However, the quality of results would be improved using a anemometer array and a collection of micromanometers.

It has been concluded that the fast pressure fluctuations generally have small amplitudes and are filtered out in the first few centimeters of the snow pack. Consequently, results are not presented for frequencies greater than $n = 1$ Hz. The lowest frequency of interest was defined in Chapter 2 at $n = 0.001$ Hz.

Records were made up of consecutive 13.5 minute runs sampled at 20 Hz. It is apparent that the low frequency fluctuations are important in wind pumping. More information about these low frequencies is obtained with a longer record. The maximum record length, from computer hardware limitations, was 131 minutes. Few runs of this length could be collected due to several equipment and environmental factors.

The shortest record length recommended for consistent statistical properties at lower average wind speeds ($\overline{V}$ = 5 m/s) is 34 minutes. The record length required to meet these conditions during strong winds ($\overline{V}$ = 10 m/s) was not determined. This was because equipment failure limited the length of all such runs to 27 minutes.

To satisfy the required condition of stationarity, various trend removal techniques were used. No runs were rejected on the basis of non-stationarity.

3.11.2. Results

General Weather Observations

The storms during which the measurements were made are considered to be moderate by comparison to many in the Arthur's Pass area.

The patterns of turbulence observed at the measurement site varied considerably with slight changes in mean wind direction. This had considerable effects on the wind speed / pressure crosscorrelation results.

From a wind engineering point of view, it is reasonable to assume that neutral dynamic stability existed during measurements. This does not negate possible effects of the larger scale stable stratification.

Turbulence Intensities and RMS Pressure Fluctuations

There is no doubt that the recorded turbulence intensities and rms pressure fluctuations are significantly larger than those reported in the literature. This is likely to be associated with the turbulent structures associated with separation off upstream terrain features.

The windward to leeward distribution of surface rms pressure coefficients follow the patterns expected around a separated region (higher within the separated region).

A strong correlation is apparent between rms pressure coefficient and wind speed turbulence intensity.

Autocorrelation Functions

Neither the fluctuating wind speed nor pressure autocorrelation functions of the measurements completely follow the expected exponential decay. Rather, below a correlation coefficient of about 0.2, a strong oscillation about zero remains. Such oscillations indicate periodic or semi-periodic components to the data. These periodicities are thought to be in the turbulence, and not a product of the measurement system.

Integral Length Scales

The fluctuating wind speed integral length scales measured at Temple Basin are significantly larger than most integral length scales reported in the literature.

The fluctuating pressure integral length scales are significantly larger than those for wind speed. This difference is accentuated when the pressure signal is corrected for low frequency measurement attenuation.

The differences between the fluctuating wind speed and pressure integral length scales are possibly explained by gravity wave activity. While higher elevation turbulent structures may not be seen in the wind speed fluctuations, they are likely to influence the surface pressure fluctuations as they propagate through the pressure field. The Southern Alps terrain is known to produce gravity wave activity. However, the interactions between terrain, waves and turbulence are likely to be extremely complex and no attempt is made here to propose any direct links.

Integral length scale results should be approached with some caution as Taylor's hypothesis is only weakly observed. This is not thought to be a strong enough reason to completely invalidate the results.

Autospectral Functions

The Temple Basin spectra has a similar form to other documented spectra, but is shifted substantially toward lower frequencies It appears that terrain is largely responsible for this shift. However, it could also be due to more low frequency energy being included in the Temple Basin measurements than in the other work.

The spectral peaks of both variables (wind speed and pressure) lie in the range of frequencies predicted for mountain terrain in Chapter 2. High frequency peaks, due to flow separation, are not observed in either spectra.

Similar variability between wind speed and pressure spectra below about 0.015 Hz indicates that the large scale turbulent structures are independent of probe location in the terrain, and probe depth into the snow pack.

The relatively high variability of the pressure spectra above about 0.015 Hz is possibly due to the influence of terrain.

The spectral peaks at n = 0.0013 and 0.0025 Hz in both the wind speed and pressure spectra are possibly linked with terrain scales, harmonics of gravity wave activity and coalescence of turbulent structures. No firm conclusion is drawn on this.

The peak frequencies also lie in the region where gravity wave activity may be expected.

Below around 0.001 Hz the statistical errors in the data become significant. Below this frequency care must be made in interpreting the spectral results and trends.

Crosscorrelation Functions

The wind speed / pressure crosscorrelation functions obtained can only be described as irregular.

The lack of correlation is explained by the changing wind approach angles, shifting the point of separation around the measurement site, and periodic back gusts.

Unless run conditions are unusually steady, it is concluded that the crosscorrelation analysis is an inappropriate assessment of the correlation between the wind speed and surface pressure fluctuations. However, it is still thought that the wind speed fluctuations of *individual gusts* are strongly correlated to the surface pressure fluctuations.

Gust Exceedance Statistics

There is a similar power law relationship between gust rate and bandwidth frequency for both the wind speed and pressure gusts.

The degree by which the pressure gust exceedance probabilities come together through non-dimensionalising by the record standard deviation is not as good as it is for the wind gusts.

With knowledge of the rms pressure coefficient and mean wind speed, the approximate amplitude and occurrence frequency of the pressure gusts can be estimated from the gust exceedance charts.

3.11.3. Further Work

The results obtained at Temple Basin are not thought to be deficient in any critical way. However, there are several observations that would create a more complete picture of the turbulence characteristics:

* Pressure measurements could be made with two or more pressure sensors so that vertical profiles of the pressure fluctuations could be made within the snow pack.
* Wind speed measurements should be made at the exact location of the pressure measurements. From this more accurate information a better crosscorrelation could be obtained between the wind speed and pressure fluctuations. This sort of information would then be useful where only wind speed is measured.

* A variety of terrains could be studied, especially where well defined separation occurs. Also sites with a variety of *upstream* terrain could be studied so that the generating mechanisms of the fluctuations could be further investigated.
* Pressure measurements could be made in the specific snow pack conditions where changes in the snow grain structure are expected to be influenced by the wind pumping.

Chapter 4
Packed Bed Airflow Dynamics

The primary objective of Chapter 4 is to compare the theoretical and experimental decays of a fluctuating surface pressure signal down a permeable bed.

4.1. Table of Contents

4.2. List of Illustrations

4.3. Nomenclature

A	cross sectional or unit area (m^2)
a	length dimension of a rectangular panel (m)
a_{sv}	surface area per unit volume (m^2/m^3)
b	width dimension of a rectangular panel (m)
C_v	water vapour concentration (kg/m^3)
c	thickness dimension of a rectangular panel (m)
$\overline{D}_{p2}^2$	particle diameter of a hypothetical sphere with the same volume as S_0 (m)
d	depth of the bed or snow pack (m)
E	modulus of elasticity (Pa)
K	bed permeability (m^2/Pas)
k	bed permeability (m^2)
m	time steps
n	frequency (Hz)
$\overline{P}$	average (barometric) pressure (Pa)
P_z	maximum pressure swing at depth z (Pa)
p	pressure (Pa)
P_c	amplitude of pressure fluctuation (Pa)
R	leak resistance (Pas/m^3)
Re_b	bed Reynolds number
r_{sv}	mass generation rate per unit volume (kg/m^3)
S_z	distance a parcel of air is displaced or cyclic displacement at depth z (m)
S_0	ratio of *internal surface of packing* to *volume of solids in packing* (m^2/m^3)
T	temperature (°C)
t	time (s)
t_z	time for a pressure wave to reach a depth z (s)
V_z	maximum superficial velocity at depth z (m/s)
v	superficial air velocity (m/s)
V_{box}	box volume (m^3)
V_d	volume of air displaced into or out of the bed (m^3)
V_{stroke}	stroke volume (m^3)
x	surface dimension (m)
y	surface dimension (m)
z	depth in to bed or snow pack (m)

α	thermal diffusivity (m^2/s)
Δ_f	deflections in the centre of a rectangular panel with fixed edges (m)
Δ_s	deflections in the centre of a rectangular panel with supported edges (m)
ε	bed voidage
Φ_d	diameter of sphere having the same volume as the particle (m)
Φ_s	ratio of *surface area of a sphere of equal volume to the particle* to *surface area of the particle* (m^2/m^2)
$\varnothing$	particle diameter (m)
Λ	integral length scale (m)
μ	viscosity (Pas)
ρ	density (kg/m^3)
τ	period of fluctuation or time constant (s)

4.4. Introduction

In Chapter 2 it has been established that significant pressure fluctuations exist on the snow surface, even during only moderately windy conditions. These fluctuations appear to result from highly three dimensional turbulent structures generated off upstream terrain features, which are advected downwind in the turbulent atmospheric boundary layer at close to the free stream wind speed. Despite the observations being made at a single location it is obvious that the snow surface pressure field is a two dimensional transient function, $p_{z=0} = f(x,y,t)$. It is hypothesized that this surface pressure fluctuation is able to penetrate the permeable snow pack resulting in interstitial air movements as the air below compresses and expands. The resistance to this flow results in the decay of the pressure and velocity swings with depth z. This concept is illustrated in figure 4.1(a).

Thermal waves have been of interest in heat transfer for a very long time. One example of this is in the burial depth determination of water pipes in cold climates to avoid freezing. This can be done by prediction of the diurnal and annual temperature fluctuations in soil. As a result of this type of work, relatively simple mathematical solutions exist for periodic heat waves.

Analogies to these heat wave solutions were applied to wind pumping in soils by Fukuda (1965), Farrell *et al* (1966) and Scotter and Raats (1969). It is the purpose of this chapter to reformulate their periodic pressure wave analogy, and to justify the basic assumptions behind the resulting dissipating forced convection equations. This is achieved by measuring the decay of the pressure fluctuations down a permeable bed. Once the analogy has been justified, the models are applied over a wide range of snow pack conditions. Accurate estimates of the possible air speeds and displacements in the snow pack due to wind pumping can then be made. Finally some simplifications for seasonal snow packs are proposed which reasonably cover the range of surface (driving force) conditions indicated in Chapter 3.

Some debate arises over the dimensionality of wind pumping airflow dynamics modelling. Clarke and Waddington (1991) find it necessary to extend Clarke *et al*'s (1987) *one dimensional* approach to *three dimensional.* Clarke *et al*'s wind pumping energy dissipation mechanism, due to viscous friction, requires significantly higher frequencies ($0.1 \leq n \leq 10$ Hz) than those that are thought to create forced (convective) air movements in a seasonal snow pack (from Chapter 3 $0.001 \leq n \leq 0.1$ Hz). Clarke and Waddington envisaged length scales (size of the fluctuating pressure producing eddy) of $\Lambda \sim 0.5$ m. The length scales associated with the major energy of the atmospheric pressure fluctuations measured in the mountains lie in the range $150 \leq \Lambda \leq 700$ m (see table 3.8). Clearly these integral length scales are much greater than seasonal total snow pack depths d ($\Lambda \gg d$). Hence the original assumption behind Clarke *et al*'s *one dimensional* approach remains applicable here and the models formulated in this chapter are restricted to one dimension.

Presented in section 4.5 are models for the dissipation of sinusoidal surface pressure fluctuations within a packed bed. In section 4.8 the numerical experiments to determine the vertical air velocities and displacements resulting from surface pressure swings for varying snow pack properties are described. Sections 4.6 and 4.7 describe the laboratory experiments carried out to test the validity of the models in a finite depth packed bed under controlled laboratory conditions. The laboratory and numerical results are presented and discussed together in section 4.9 together with the proposed simplifications.

4.4.1. One Dimensional Wind Pumping Concept

To evaluate the crude effects of wind pumping, the surface pressure was assumed to fluctuate with time identically at all points on the snow surface. In this case the surface pressure may be termed as a planar transient boundary condition function, $p_{z=0} = f(t)$. The one dimensional dissipation of the surface pressure can then be examined according to snow pack depth z, that is $p = f(z,t)$.

With a planar transient boundary condition the fluctuating pressure can create only vertical movements of air as it compresses and expands in response to the surface forcing (illustrated in figure 4.1(a)). Note that there can be no nett vertical or horizontal flow. The planar transient boundary condition was briefly investigated by Colbeck (1989) who models the snow pack as a finite bed with an impermeable lower boundary.

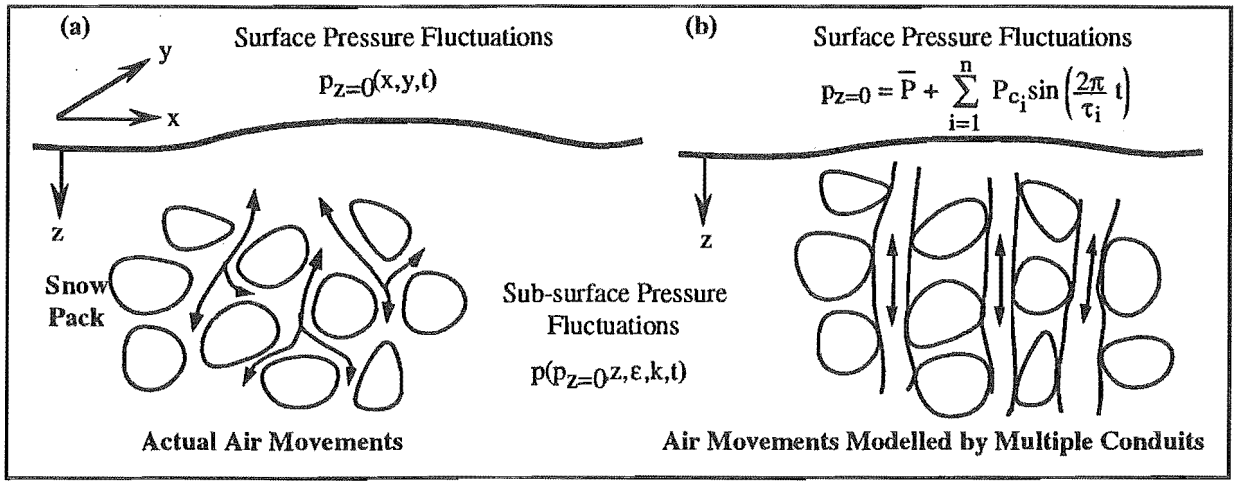

Figure 4.1. Interstitial Air Movements in a Snow Pack due to Surface Pressure Fluctuations: (a) Real Case. (b) Modelled Case.

Two theories, drag and channel, may be used to approach the modelling. Drag theory on particles may be considered appropriate given that a typical snow pack has a very high voidage. However, because the porous snow system is assumed to be a bundle of tiny channels with non-circular cross sections, channel theory is used. In this case the pressure drop of the

system is identical with that for one of the channels (Kanaoka, 1991). This concept is demonstrated in figure 4.1(b).

A few conceptual observations are worth noting at this point:

* As the surface pressure increases, air will be pushed into the permeable snow pack and the air below will be compressed (and vice versa).
* Therefore the deeper the snow cover the greater the flow
* The greater the pressure fluctuation, the greater the compression, and hence the greater the flow.
* The less dense the snow pack (higher permeability) the greater the flow.
* The lower the frequency of fluctuation, the greater the flow. This is because the air in the slow pack is allowed to closer reach a steady pressure.
* Air will be stagnant at the base of the snow pack (assuming no base leakage) and maximum flow will be at the surface.
* The higher the frequency and/or the deeper the snow pack, the more out of phase the flow in the snow pack will become with the surface pressure fluctuation.

4.4.2. Nett Flow Scenarios

If the surface pressure fluctuation is not planar transient it is possible to have adjacent areas of low and high pressures. The horizontal pressure gradients that result may produce significant horizontal flow. Possible mechanisms behind such boundary conditions include:

* A fully three dimensional turbulent boundary layer. In this case the proximities of highs and lows would be dependent on the turbulent length scales (the highs and lows would advect in the mean wind direction reducing this affect). This is illustrated in figure 4.2(a). Clarke and Waddington (1991) use this concept in their three dimensional theory of wind pumping.

* Quasi-stationary centers of high and low pressure near terrain and/or snow surface features, for example, around separated flow regions. This is illustrated in figure 4.2(b). Colbeck (1989) considers this case. He looks theoretically at the flow through surface features, such as dunes with horizontal and vertical scales of up to 10 m and 0.25 m respectively, and concludes that such air flow is possible. Stronger flows are expected for small scale snow features, although the flow at depth can be greater for larger features. Colbeck does not consider larger scale terrain oriented snow pack features such as cornices.

Neither of these cases are developed any further here.

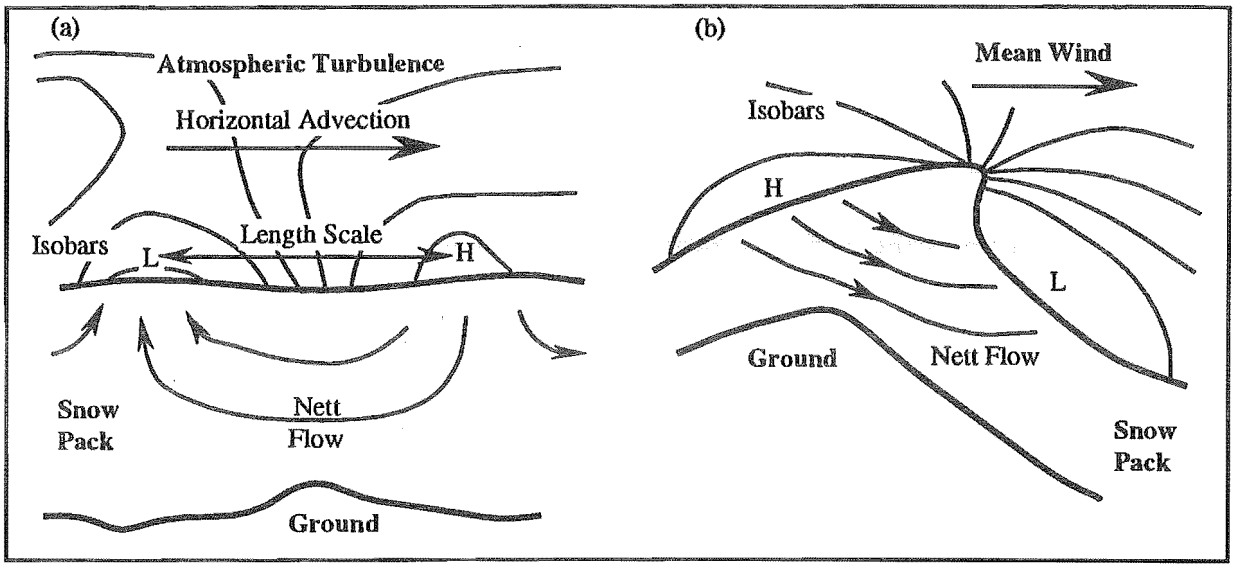

Figure 4.2. Two Possible Scenarios for a Nett Flow Between High and Low Pressure Centers: (a) Varying Pressures Associated with Advected Turbulent Structures. (b) Quasi-Stationary Centers Near Terrain and/or Snow Surface Features.

4.5. One Dimensional Wind Pumping Equations

4.5.1. Governing Equations

Assuming laminar flow, from Darcy's Law the superficial air velocity v through a packed bed is given by

$$v = \frac{k\partial p}{\mu \partial z} \qquad 4.1$$

where p is pressure, k (m^2) is the bed permeability in the z direction (perpendicular to the surface). In this work, K (m^2/Pas) is also taken as the permeability.

$$K = \frac{k}{\mu} \qquad 4.2$$

According to Bear (1972) Darcy's Law is applicable until the bed Reynolds number Re_b exceeds some value between 1 and 10. The bed Reynolds number is defined by Fayed and Otten (1984) as

$$Re_b = \frac{\rho v \left(\Phi_s \Phi_d\right)}{\mu(1-\varepsilon)} \qquad 4.3$$

where Φ_s is the ratio of *surface area of a sphere of equal volume to the particle* to *surface area of the particle*, Φ_d is the *diameter of sphere having the same volume as the particle*, ρ the fluid density, v the superficial velocity, μ the fluid viscosity and ε the bed voidage.

The water vapour concentration C_v may vary with temperature, given a vertical temperature gradient dT/dz. However, any temperature gradient is assumed to be small enough so that the bulk air properties can be assumed constant.

The unsteady state mass balance per unit area A for the gas phase about a slice, shown in figure 4.3, is therefore given by

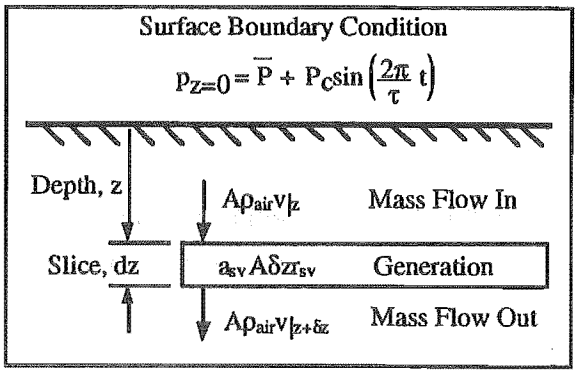

Figure 4.3. One Dimensional Mass Balance Terms About a Slice at Depth z.

$$A\delta z\varepsilon\frac{\partial \rho_{air}}{\partial t} = A\rho_{air}v|_z - A\rho_{air}v|_{z+\delta z} + a_{sv}A\delta z r_{sv} \qquad 4.4$$

where ρ_{air} is the density of air, a_{sv} the surface area per unit volume, r_{sv} the mass generation rate per unit surface area, ε the voidage and t time. For an ice/air system the voidage may be approximated by

$$\varepsilon \approx 1 - \frac{\rho_s}{\rho_{ice}} \qquad 4.5$$

where ρ_s is the bulk snow density and ρ_{ice} the density of ice. Assuming constant air density permeability and viscosity with depth, negligible generation, constant temperature with time and the ideal gas law 4.1 and 4.4 give

$$\frac{\partial p}{\partial t} = \frac{\bar{P}K}{\varepsilon}\frac{\partial^2 p}{\partial z^2} \qquad 4.6$$

where $\bar{P}$ is the average barometric pressure. This is also derived by Fukuda (1965), Farrell *et al* (1966), Scotter and Raats (1969), Clarke *et al* (1987) and Colbeck (1989).

This is analogous to the one dimensional Fourier conduction equation

$$\frac{\partial T}{\partial t} = \alpha\frac{\partial^2 T}{\partial z^2} \qquad 4.7$$

where T is temperature and α is thermal diffusivity.

Debate arises over the forcing function for equation 4.6. The solutions of Clarke *et al* (1987) and Clark and Waddington (1991) use the power spectrum of the measured pressure fluctuations, while Fukuda (1965), Farrell *et al* (1966), Scotter and Raats (1969) and Colbeck (1989) all assume a periodic surface pressure fluctuation. Despite having measured the power spectrum in Chapter 3, the periodic approach is used in this thesis.

There are two reasons for using Colbeck's approach:

* A primary objective of this thesis is to experimentally determine the effects wind pumping has on snow metamorphism. To do this in a controlled laboratory environment, a well defined surface forcing pressure fluctuation is required.
* To test the assumptions behind equation 4.6, particularly the levels of particle bed turbulence. This is of interest because turbulence has a large influence on the mechanics of mass transfer.

The design of the experiment to achieve this purpose uses a mathematically well defined upper sinusoidal surface boundary condition, to which relatively simple analogous solutions exist in heat transfer.

4.5.1.1. Upper (Surface) Boundary Conditions - the Forcing Function

In general, for three dimensional turbulence above the snow pack, the pressure at the snow surface should be described as a function of the surface coordinates x and y and time t. Here, in the one dimensional case, the surface pressure will be a function of t only.

Assuming linearity (laminar flow), the wind pumping driving force may be considered as the sum of m contributing periodic pressure fluctuations. The snow surface boundary condition is taken as

$$p_{z=0} = \overline{P} + \sum_{i=1}^{m} P_{c_i} \sin\left(\frac{2\pi}{\tau_i} t\right) \qquad 4.8$$

where $p_{z=0}$ is the fluctuating pressure at depth z = 0 m (surface), $\overline{P}$ the average (barometric) pressure and P_{c_i} and τ_i the amplitude and period of the i^{th} fluctuations respectively. Hence for any one of these (with the subscript *i* dropped)

$$p_{z=0} = \overline{P} + P_c \sin\left(\frac{2\pi}{\tau} t\right) \qquad 4.9$$

4.5.1.2. Lower Boundary Conditions

Three rather idealised scenarios are worth developing, each with its unique lower boundary condition to equation 4.6.

1. Relatively deep snow pack or glacier of constant density and permeability - ***infinite lower boundary condition.***

   $$\text{at } z \to \infty,\ p \to \overline{P} \text{ and as } z \to \infty,\ v \to 0 \qquad 4.10$$

   Clarke *et al* (1987) and Clarke and Waddington (1991) use this type of boundary condition in their studies of wind pumping in glacial firn.

2. Relatively shallow snow pack of consistent density and permeability - *finite-sealed lower boundary condition.*

$$\text{at } z = d,\ v = 0 \text{ and as } d \to \infty,\ p \to \overline{P} \qquad 4.11$$

Where d is the snow pack depth or depth to an impermeable layer. This is the boundary condition used by Colbeck (1989) in his seasonal snow pack study. It is envisaged that this will remain the most important case in this thesis.

3. Relatively shallow snow pack with higher density snow overlying considerably less dense snow (there is no restriction to the air pulsation below the interface between densities) - *finite-free lower boundary condition.*

$$\text{at } z = d,\ p = \overline{P} \text{ and as } d \to \infty,\ p \to \overline{P} \qquad 4.12$$

Where d is the depth of the higher density snow. This boundary condition may be applicable in a seasonal snow pack where substantially lighter snow underlies dense snow. It is also the boundary condition pertinent to the napthalene experiments in Chapter 5, and the laboratory wind pumping experiments on snow samples in Chapter 6.

Analytical and numerical solutions to each of these are presented in turn.

The major limitation of this development lies in the assumption of constant bed properties throughout the bed depth. Composite bed solutions are used in heat transfer, however at this early stage of wind pumping research, focus is kept on the three relatively simple cases described above.

4.5.2. Infinite Bed Solution

This case is equivalent to the semi-infinite insulated rod case in heat transfer. From Ingersoll *et al* (1954) the solution to equation 4.8 for boundary condition 4.10 is

$$p = \overline{P} + P_c e^{-z\beta} \sin\left(\gamma t - z\beta\right) \qquad 4.13$$

where

$$\beta = \sqrt{\frac{\pi\varepsilon}{\tau\overline{P}K}} \qquad 4.14$$

$$\gamma = \frac{2\pi}{\tau} \qquad 4.15$$

The superficial velocity is evaluated using equation 4.1

$$v = \chi e^{-z\beta}\left[\sin(\gamma t - z\beta) + \cos(\gamma t - z\beta)\right] \qquad 4.16$$

where

$$\chi = P_c K\beta = P_c\sqrt{\frac{\pi\varepsilon K}{\bar{P}\tau}}$$

The time for a pressure wave to reach a depth z is given by t_z

$$t_z = \frac{z}{2}\sqrt{\frac{\varepsilon\tau}{\pi K\bar{P}}} \qquad 4.17$$

The maximum pressure swing P_z and superficial velocity V_z at depth z are given by

$$P_z = \pm P_c e^{-z\beta} \qquad 4.18$$

$$V_z = \pm\sqrt{2}\chi e^{-z\beta} \qquad 4.19$$

Using the maximum velocity at z = 0 (surface), the laminar flow assumption can be checked by evaluation of the bed Reynolds number (equation 4.3).

Assuming a tortuosity factor of 1, the *interstitial displacement* or *cyclic displacement* S_z of a parcel of air should be calculated using Lagrangian coordinates. An approximation can be using Eulerian coordinates if the velocity does not change rapidly with distance. In Eulerian coordinates, the interstitial displacement is obtained by integrating the velocity equation (equation 4.16) at constant z between adjacent times of zero velocity.

$$S_z \approx \int_{\gamma t-\beta z=\frac{7\pi}{4}}^{\gamma t-\beta z=\frac{3\pi}{4}} \frac{\chi}{\varepsilon} e^{-z\beta}\left[\sin(\gamma t - z\beta) + \cos(\gamma t - z\beta)\right] dt \qquad 4.20$$

which gives

$$S_z \approx \frac{2\sqrt{2}\chi}{\varepsilon\gamma} e^{-z\beta} \qquad 4.21$$

The discrepancy in cyclic displacements between the two coordinate systems is discussed further in section 4.8.1.3.

The depth at which P_z, V_z and S_z fall to X% of their surface values is given by

$$z = -\frac{\ln\left(\frac{X}{100}\right)}{\beta} \qquad 4.22$$

4.5.3. Finite-Sealed Bed Solution

Solving equation 4.6 for boundary condition 4.11 is analogous in heat transfer to a slab with periodic surface temperature fluctuations on both sides. In this thesis half the slab depth is taken as being equivalent to the total snow pack depth d, which is the same approach as used by Colbeck (1989). The solution from Carslaw and Jaeger (1959) gives

$$p = \overline{P} + P_c \eta \sin\left(\gamma t + \phi\right) \qquad 4.23$$

where

$$\eta = \sqrt{\frac{\cosh 2\beta(d-z) + \cos 2\beta(d-z)}{\cosh 2\beta d + \cos 2\beta d}} \quad \text{and} \quad \phi = \text{Arg}\left[\frac{\cosh \beta(d-z)(1+i)}{\cosh \beta d(1+i)}\right]$$

and β and γ are as before in equations 4.14 and 4.15. Note as $d \rightarrow \infty$ equation 4.23 reduces to equation 4.13.

Due to the difficulty of obtaining analytical expressions for dp/dz (the interstitial velocity), and $\int(dp/dz)dt$ (the distance a parcel of air is displaced), they are evaluated numerically. The procedure used for this is described in section 4.8.1.3.

4.5.4. Finite-Free Bed Solution

Solving equation 4.6 for boundary condition 4.12 is analogous in heat transfer to a slab with periodic surface temperature fluctuations on one side, and the other side held at the mean value T. In this thesis the slab depth is taken as being equivalent to the total snow pack depth d. The solution from Carslaw and Jaeger (1959) gives

$$p = \overline{P} + P_c \eta \sin\left(\gamma t + \phi\right) \qquad 4.24$$

where

$$\eta = \sqrt{\frac{\cosh 2\beta(d-z) - \cos 2\beta(d-z)}{\cosh 2\beta d - \cos 2\beta d}} \quad \text{and} \quad \phi = \text{Arg}\left[\frac{\sinh \beta(d-z)(1+i)}{\sinh \beta d(1+i)}\right]$$

and β and γ are as before in equations 4.14 and 4.15. Note as $d \rightarrow \infty$ equation 4.24 also reduces to equation 4.13. Again the interstitial velocity and displacement are evaluated numerically using the procedure described in section 4.8.1.

4.6. Experimental Apparatus

A schematic of the essential experimental apparatus, located on the south wall in the Denham Laboratory, is shown in figure 4.4. Plate 4.1 shows the main components of the apparatus. The following sections describe the features of the design in detail.

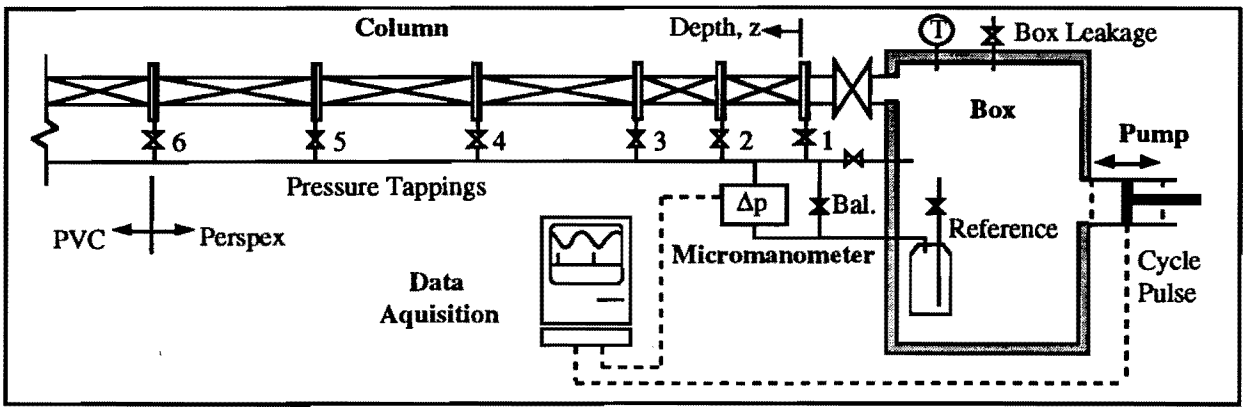

Figure 4.4. Schematic of the Bed Dynamics Experiment. PVC and Perspex refer to the type of material the column was constructed of (see section 4.6.4.1).

4.6.1. General

4.6.1.1. Design Criteria

The apparatus was built to produce sinusoidal pressure fluctuations with an amplitude range between ±10 and ±100 Pa over a frequency range of 0.05 to 2 Hz. Although this does not cover the very low frequency range of the measured field pressure fluctuations (see Chapter 2), low frequency bed dynamics would be strictly laminar in this range, and can be extrapolated from the lower end of the data collected here with reasonable confidence.

The pump mechanism was expected to operate for no more than 4000 hours over three years in a dry environment.

Particulate material for packing the column was chosen such that the particle bed Reynolds number was of the same order to that expected in snow.

Maximum uncertainties of ±2% were targeted for all calibrations and measurements.

(a)

(b)

(c)

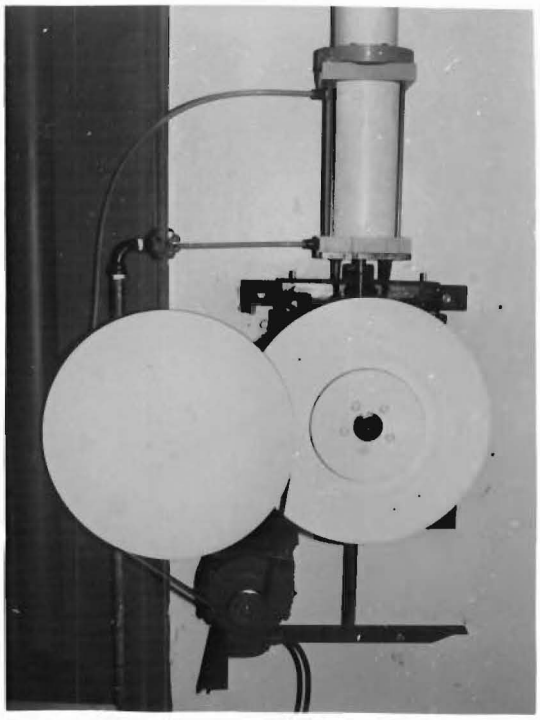

(d)

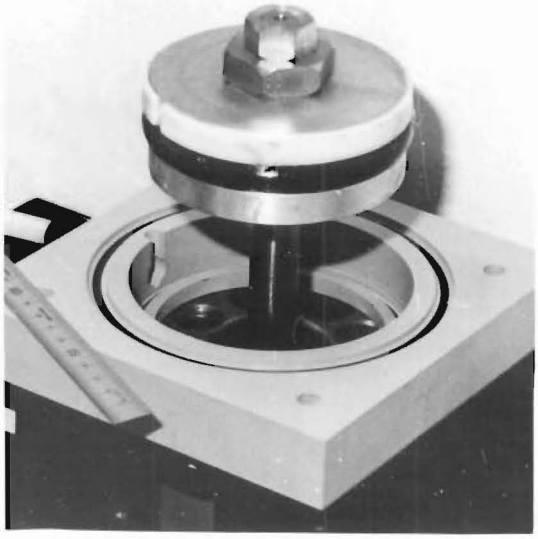

Plate 4.1. Components of the Experimental Apparatus: (a) Overview Showing the Sinusoidal Drive, Cylinder, Box and Perspex Sections of the Column (including the Pressure Tappings). (b) Box, Stiffening and Insulation. (c) Sinusoidal Drive and Cylinder (note the cooling water tappings). (d) Piston Attached to the Sinusoidal Drive.

4.6.1.2. Location

Initially a 15 m vertical column and associated apparatus was erected in the four storey 'well' of the department's Siemon Block. However the thermal gradient and ambient pressure noise caused too much interference with the very small pressure fluctuation measurements required. Such noise was generated by the opening and closing of doors or windows, and through atmospheric wind conditions buffeting the five story block.

To overcome these problems the apparatus was relocated horizontally onto the south (glass) wall of the departments Semi-Scale Laboratory. This laboratory has much fewer doors and is not as exposed to wind. However in this location, during clear periods (no cloud cover), the long wave radiation losses at night and incoming solar radiation during the late afternoon causes the box to act as a gas thermometer. This latter factor created special problems in the mass transfer experiment described in Chapter 5. For this experiment these effects were minimised by insulating the apparatus, and by making all runs on still cloudy nights, during stable weather (steady atmospheric pressure and laboratory temperature). At this time of day there was very little activity in the department.

4.6.1.3. Box and Stroke Volume

As the pressure in the box increases air was pushed into the bed. If a large proportion of the stroke volume is pushed into the bed the form of the sinusoidal pressure signal will be affected. To account for this the box must be sufficiently large so that the volume pushed into the bed is small compared to the stroke volume.

From equation 4.21 the volume V_d of air displaced into or out of the bed is given by

$$V_{d,z=0} \approx \pm\frac{\sqrt{2}\alpha A}{\gamma} \qquad 4.25$$

where A is the cross sectional area of the column. For the plastic beads $V_d = \pm 0.018$ litres when $P_c = \pm 100$ Pa and $\tau = 10$ s. To keep within the required 2% design error limit, a minimum stroke volume $V_{stroke} = \pm 0.9$ litres is required. Assuming an ideal gas the minimum box volume is given by

$$V_{box} = \frac{V_{stroke}(\overline{P} + P_c)}{P_c} \qquad 4.26$$

Given $\overline{P} = 101325$ Pa, $V_{box} = 0.91$ m^3. After construction, P_c, V_{stroke} and V_{box} were measured at ± 125 Pa, ± 1.2 litres and 0.97 m^3 respectively. The resulting form of the sinusoid shown in figure 4.14, is almost indistinguishable from the true sinusoid. This also includes box leakage and reference pressure balancing effects.

4.6.2. Sinusoidal Pump

The sinusoidal drive is the key element of the apparatus. The limit in the drive's ability to produce an accurate sinusoidal pressure fluctuation sets the limit for a comparison between the theoretical and experimental results. Therefore great care was taken in the design and construction to obtain that accuracy. Figure 4.5 shows a schematic of the cylinder and sinusoidal drive unit, and the sections below detail any special design features.

4.6.2.1. Cylinder

An aluminium cylinder (bore = 100 mm and stroke = 225 mm), aluminium piston and rubberised ring seal from an industrial pneumatic ram was used to create the ±1.2 litres air displacement. The piston is shown in plate 4.1(d).

Substantial friction between the piston and the cylinder produces enough heat to warm the air in the box, hence increasing the pressure. After long periods at high frequency, this heat production was sufficient to damage the rubberised seal. To overcome both of these problems a flooded water cooling jacket was fitted around the cylinder.

4.6.2.2. Sinusoidal Drive Mechanism

The mild steel mechanism was designed to handle frequencies of up to 15 Hz, although the limiting frequency response of the pressure sensor restricts operation to 0.5 Hz (see section 3.7.2.5).

Grease rather than oil was used to lubricate the slot and guides as there was plenty of power delivered by the motor. Depending on frequency, greasing was required about every 120 hours of operation.

The slot in the cross head has a tolerance of 0.05 mm on either side of the roller. Any less than this and the lubricant was squeezed out and the mechanism rapidly runs dry. Any greater than this and hammer was introduced. Also, with a greater tolerance, a step and flat spot develops in the resulting sinusoid.

Vibration from the heavy duty pump mechanism rotating at 0.5 Hz required the equipment to be very well fixed so that it did not produce noise in the pressure measurement. This was achieved by anchoring it to the concrete wall at the western end of the laboratory.

4.6.2.3. Mechanical Gearing

Gearing was achieved using one or two 6:1 v-belt reductions between the motor and the sinusoidal drive. The belt arrangement can be seen in plate 4.1(c).

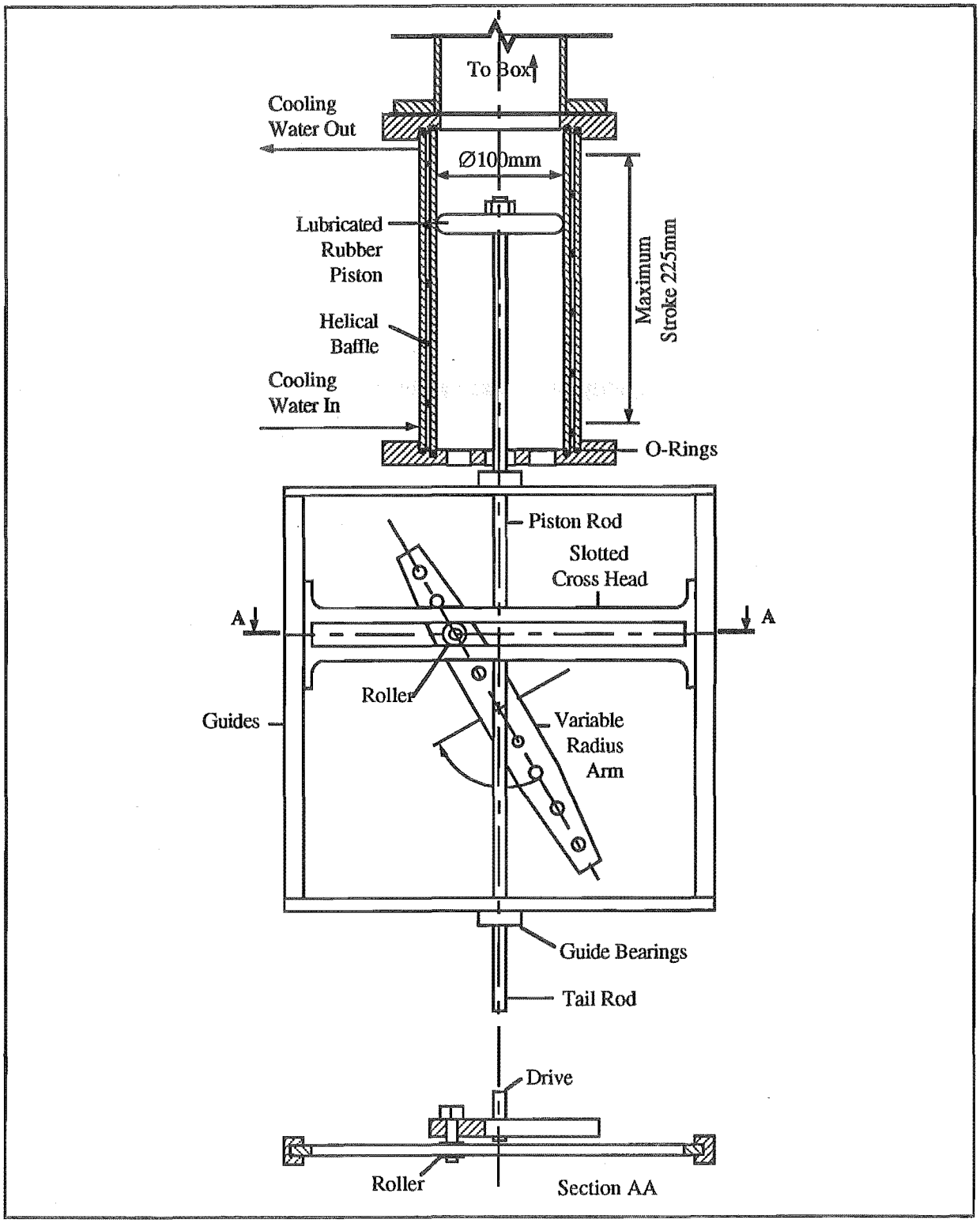

Figure 4.5. Schematic of Pump and Sinusoidal Drive Unit.

4.6.2.4. Electric Motor and Variable Speed Controller

The pump and mechanical drive was driven by a 1.1 kW 240 V 3 phase induction motor with a maximum speed of 15 Hz which was in turn powered by a 1.5 kW Zoner MSC-S7 variable speed drive.

The low end cut off to the available frequency range was determined by the motor overheating rather than the limit of the variable controller. Heat production over the period required to perform the experiment prohibits runs being made at below 0.05 Hz. This was despite a fan for additional air cooling being fitted.

4.6.3. Box

The box shell material selection of 19 mm custom board was influenced largely by cost with little foresight into consequential rigidity and leakage problems.

As relatively small pressure swings were being measured in this experiment, close attention was made to the thermal stability of the apparatus. Since the box represents most of the surface area of the apparatus, controlling the stability was most easily achieved by controlling the box temperature.

4.6.3.1. Rigidity

From Vallance and Doughtie (1951) the deflections in the centre of a rectangular panel with supported and fixed edges are given by

$$\Delta_s = \frac{0.1422 b^4 P_c}{Et^3\left(1+2.21\frac{b^3}{a^3}\right)} \qquad 4.27$$

$$\Delta_f = \frac{0.0284 b^4 P_c}{Et^3\left(1+1.056\frac{b^5}{a^5}\right)} \qquad 4.28$$

where E is the modulus of elasticity (= 3000 MPa for custom board) and a, b and c are the length, width and thickness dimensions respectively. The volume displaced in the deflection was estimated for each panel in the box using volume of a square pyramid where deflection equals height, and summed over all panels to give the total volume displaced.

Prior to stiffening, for a $P_c = \pm 100$ Pa the volume associated with movement in the walls was estimated to be 0.39 litres. After the vertical and horizontal stiffening shown in plate 4.1(b) was added, this reduced to 0.018 litres, or 1.8% of the stroke volume.

4.6.3.2. Leakage

Custom board is highly permeable, and despite coating with a sanding sealer the time constant for the box leakage remained well under 60 s. A leakage of this rate would severely affect the slow pressure fluctuation experiments ($\tau = 20$ s). Leakage through the custom board was virtually eliminated with three coats of Decktred®, an impermeable rubberised marine coating, over the internal surface. The resulting closed system (box, pump, column and ducting) time constant was lifted to $\tau \approx 3 \pm 1$ min.

Note that the reference pressure resistance outlet is open to the box and closed to the outside environment as shown in figure 4.4. The time constant of the reference pressure leakage must be smaller than that of the box leakage whilst not attenuating the signal. This is so that it serves its purpose of balancing the slow pressure changes over the two sides of the pressure transducer.

4.6.3.3. Thermal Stability

Disregarding the reference pressure and other small leakages, the pump, box, column and pressure measurement tubes represent a closed system. An increase or decrease in box temperature, and consequential change in mean pressure, caused a base line drift in the pressure measurement. This made the results difficult to interpret without some form of post processing to eliminate the trend.

The temperature in the box responded to both a change in the ambient laboratory temperature and, during clear periods, radiation exchange with the outside atmosphere. The radiation component comprised of long wave radiation losses at night, and incoming solar radiation during the late afternoon. These effects were

reduced by insulating the box and timing the experiments away from unsuitable weather conditions.

The pressure drift in the box needed to be kept below 2.8 Pa/min over the period the measurement was made to maintain a pressure measurement error of below 2%. 100 mm of polystyrene foam insulation was required to prevent an envisaged laboratory temperature drift of 0.5 K/hr from creating a pressure drift greater than 2.8 Pa/min. In addition, to minimise radiation effects, the insulation was covered with aluminium coated building paper.

4.6.4. Column

The column was made up of discrete units which were joined using closed cell foam gaskets as illustrated in figure 4.6. Each section had a pressure tapping at its bottom end. The packing material was contained by wire mesh with a similar grid size to the particle dimensions.

An initial leakage check on the fully assembled column, box and pump system indicated no increase in the box leakage time constant. It seems from the results (see section 4.9) that it might have been wise to check for leakages in the system each time the column length was altered.

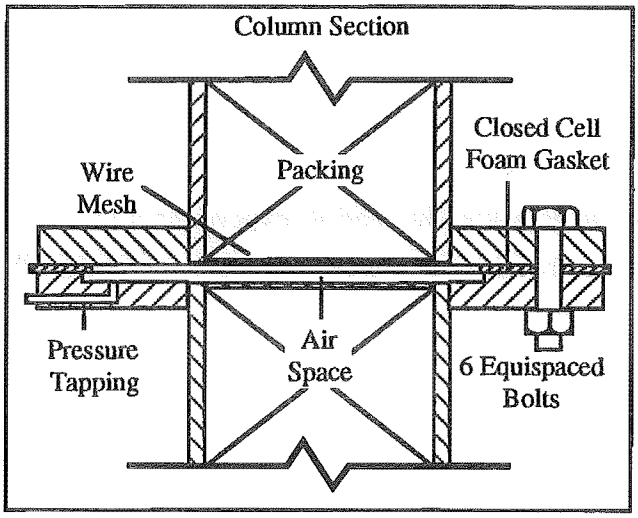

Figure 4.6. Joint Between Column Sections.

4.6.4.1. Length

Practical considerations limited the length of the column to 25 m. Equation 4.22 is plotted in figure 4.7 for the plastic beads to show at what period the 25 m column can be approximated by an infinite bed.

The lengths of individual column sections are detailed in table 4.3.

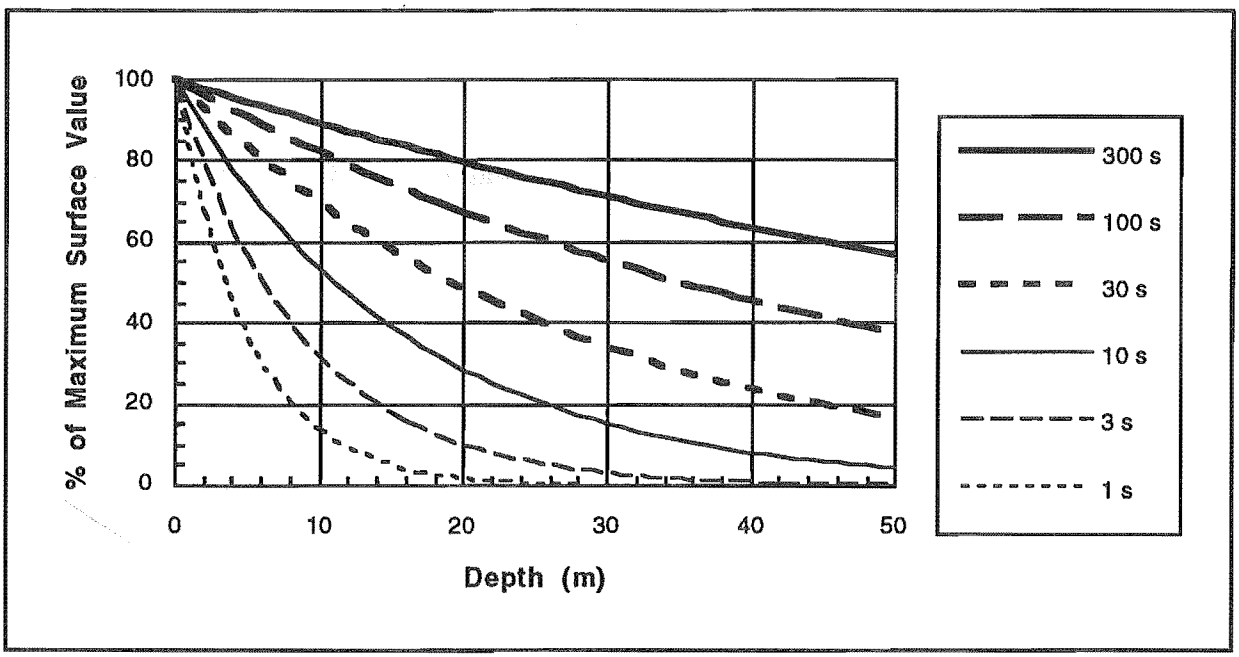

Figure 4.7. Decay of the Maximum Surface Pressure, Velocity, or Displacement Values with Depth for Varying Periods in the Bed of Plastic Beads using Infinite Bed Theory.

4.6.4.2. Diameter

Wall channelling effects become insignificant if the column diameter is greater than 12 x particle diameter ($\varnothing_{\text{plastic beads}} \approx 3.5$ mm). The diameters of the perspex sections were 57 mm and PVC sections 53 mm, both much greater than the size given by this criteria.

Perspex was used in the 2 m of column closest to the box as some initial flow visualisation trials were made with coloured gas. Visibility was also useful to check on the pack (degree of settlement and channel formation along the upper wall). Cost considerations did not allow the entire column to be constructed from perspex. Unfortunately this resulted in a 13% narrowing in cross sectional area at z = 2.0 m. The contribution of this reduction to the packing properties is discussed in section 4.6.7.4. Note also that the basis of the theory assumes a constant cross sectional area (equation 4.4).

4.6.5. Pressure Measurement System

The pressure measurement system used in the atmospheric turbulence measurements (described in section 3.7.2) was used in these column experiments.

To maintain a stable system, it was important that the reference pressure system time constant (7.5±0.6 min) be significantly less than the pump, box and column leakage time constant (13±1 min). These values meet this requirement.

4.6.5.1. Pressure Tappings

Pressure tappings were positioned at the break points in the column. As shown in figure 4.6 there was a 1.5 mm air gap between the packings of each column. This was to allow the pressure to equilibriate across the column section, thus avoiding any possible error due to wall effects. This volume of the air space and the pressure tapping was kept as small as possible to reduce the introduction of errors. This was because any empty air space would have the effect of increasing the overall voidage. The maximum errors that this may introduce into the column permeability and voidage estimations would be less than 0.5%.

4.6.5.2. Tubing System

Using the relations given in section 3.7.2.3 for attenuation and phase shift of the pressure signal due to the pressure measurement tubing system, the amplitude reduction was calculated as $1.5\text{x}10^{-5}$% and phase shift $-1.5\text{x}10^{-4}$°, both well below error significance.

4.6.6. Phase Shift Measurement

Phase shift was measured using the amplified signal of a Slotted Opto Switch. The switch was positioned so that a pointer on the last drive pulley cuts through the switch once per cycle (when the piston was at its midpoint or when $\sin(2\pi f/\tau) = 0$).

The Slotted Opto Switch's response characteristics limit the phase shift measurements at high pump frequencies. This limitation is shown in figure 4.8 where the phase lag is presented as a percentage of the period. The drop off in performance below a period of about $\tau = 1.5$ s must be considered when comparing the accuracy of the experimental results with any theory.

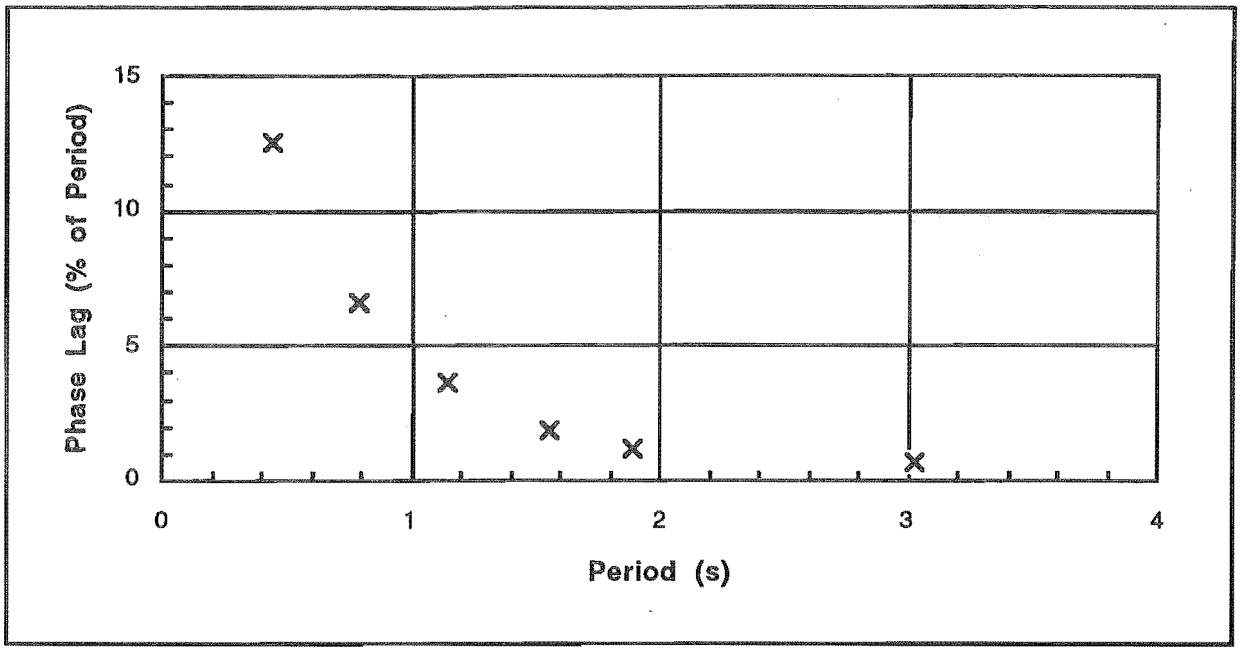

Figure 4.8. Phase Lag Measurements of the Slotted Opto Switch.

4.6.7. Bed Packings

Two materials of differing size, shape, voidage and permeability were investigated. The properties of these materials are summarised with a range of snow pack values in table 4.1. Plate 4.2 shows the bed materials on a 2 mm grid. The determination of the packed bed properties is detailed further in section 4.6.7.

Property	Plastic Beads	Mustard Seeds	Seasonal Snow
Density (kg/m^3)	920	1100	100 - 400
Permeability (x10^4 m^2/Pas)	2.84	1.04	0.2 - 5
Voidage	0.359	0.329	0.9 - 0.6
Shape	cylindrical	spherical	new and old
Dimensions (mm)	ø ≈ 3.5 h ≈ 2.5	ø ≈ 2.1	0.5 - 3
Reynolds Number (max)	0.3	0.2	0.7

Table 4.1. Summary of Typical Packed Bed Material and Snow Pack Properties. h and ø are the approximate particle heights and diameters respectively.

4.6.7.1. Packing Technique

It was of primary importance to the experiment that the column be packed to give consistent bed properties which would not alter during later handling. In particular this meant avoiding a channel forming along the top of the horizontal-axis bed through further settling. This would undesirably have allowed the pressure field to short circuit the bed resistance.

(a)

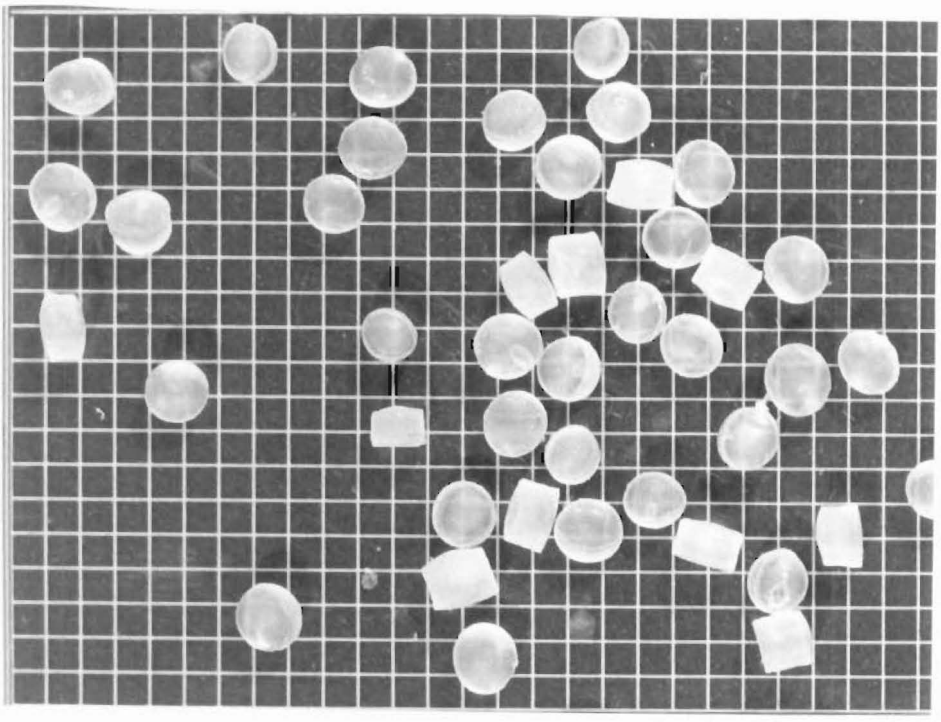

(b)

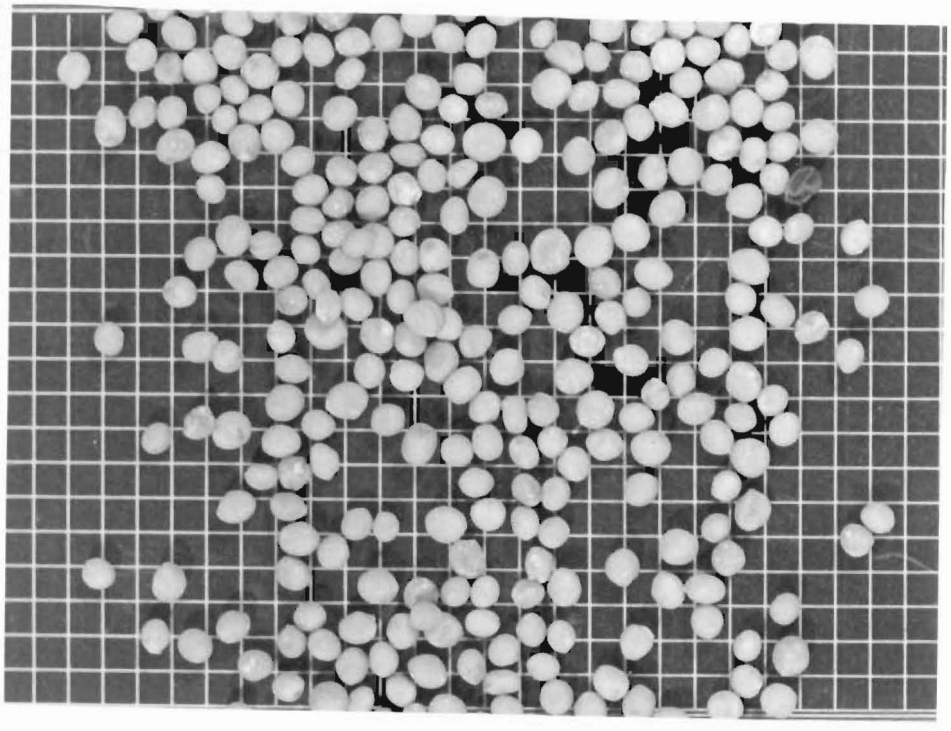

Plate 4.2. The Packed Bed Materials on a 2 mm Grid: (a) Plastic Beads. (b) Mustard Seeds.

The fundamental approach to packing is to target a certain voidage, calculate the amount of packing material to be packed into each section and pack or repack until the required material just filled the section. Once full the column was sealed with a steel mesh to prevent beads escaping. To obtain an even voidage throughout each section's length, the beads were poured into the section at 0.3 m/min whilst secured to the bed of a Fritsch 03.502 vibrator set at 2/3 full power. Figure 4.9 shows a schematic of the technique.

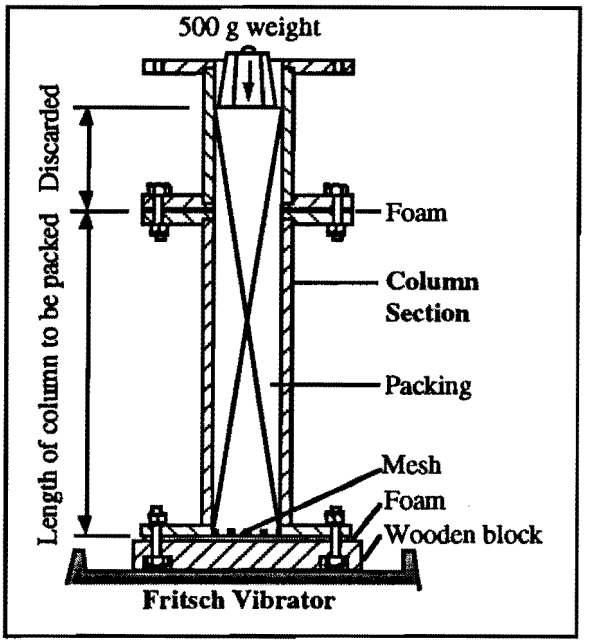

Figure 4.9. Column Packing Technique.

It proved difficult to obtain packings in the longer PVC sections which were as tight as those required in the Perspex sections to avoid channel formation, even with repeated attempts this could not be done. The following sections show how this difference in degrees of packing affected the bed properties (voidage and permeability).

4.6.7.2. Voidage

Assuming $\rho_{material} \gg \rho_{air}$ and $\rho_{material}$ is known, the bed voidage ε is given by

$$\varepsilon = 1 - \frac{\rho_{bulk}}{\rho_{material}} \qquad 4.29$$

* $\rho_{plastic\ beads} = 920\ kg/m^3$.
* $\rho_{mustard\ seeds}$ was determined by immersing of a known mass of seeds into a liquid and measuring the displaced volume. The concern that the seeds swelled as a result of liquid adsorption in this procedure was alleviated through immersion in several different liquids. Measurements of seed diameter were made before and after immersion but no changes were noted. The volume measurement could be made within a few seconds of immersion. From this technique $\rho_{mustard\ seeds} = 1100\ kg/m^3$.

ρ_{bulk} was easily and accurately measured, but was highly dependent on the degree of packing. As the column was oriented horizontally the material must be sufficiently well packed to prevent a channel from developing along the top side of the column through further settling. With particular reference to the plastic beads, the column could not be over packed as the beads tended to become oriented with each other and the wall, and hence the bed lost its randomness.

Considering the perspex sections alone, although the voidage measurement error of 3% was higher than the prescribed design error (of 2%), the discrepancy between sections was lower than 1%. The same result was found for PVC sections which were used with the plastic bead packing only. However, a 3% discrepancy in the average voidage between the perspex and PVC portions of the column was found. These results are summarised for the plastic beads in table 4.2 and shown in more detail in table 4.3. This was likely to be due to the packing requirements described above.

	Errors in Voidage, ε		Errors in Permeability, K	
	Measurement	Spread	Measurement	Spread
Perspex Sections (2 to 6)	±3%	±0.9%	±2%	±7%
PVC Sections (7 to 12)	±3%	±1%	±4%	±9%
Between Perspex and PVC Portions	-	3% increase	-	20% increase

Table 4.2. Measurement Errors in Plastic Bead Packed Bed Parameter Estimation and the Parameter Spread Between Column Sections and Types. Table 4.5 has the data these errors are drawn from.

4.6.7.3. Permeability

The permeability was calculated for each section using Darcy's Law (equation 4.1). The pressure drop was measured for various flows delivered by a stainless steel bell gasometer as illustrated in figure 4.11.

As summarised for the plastic beads in table 4.2, although the measurement errors (2 to 4%) were similar to those found in the voidage measurements, the variation between sections (7 to 9%), and between the perspex and PVC portions (20%) was much greater.

Consequently this variation, the largest error in the system, limited what could be expected of the fit between theoretical and experimental results. The source of the variation is further discussed below.

4.6.7.4. Variability in the Plastic Bead Packing Parameters

Although the measurement error in permeability was similar to that of voidage, the spread among sections was significantly higher as shown in table 4.2.

Also, the longer PVC sections of the column (7 to 12) have systematically lower voidage and larger permeability compared with the shorter perspex sections (2 to 6). This has to do with the packing requirements (see section 4.6.7.1 above), and was encountered only for the beads as

the PVC sections were not used for the seed runs. The measurement errors and spread between sections for the plastic bead packing parameters are summarised in table 4.2. Figures 4.12 and 4.13 shows the systematic dependence of permeability on voidage.

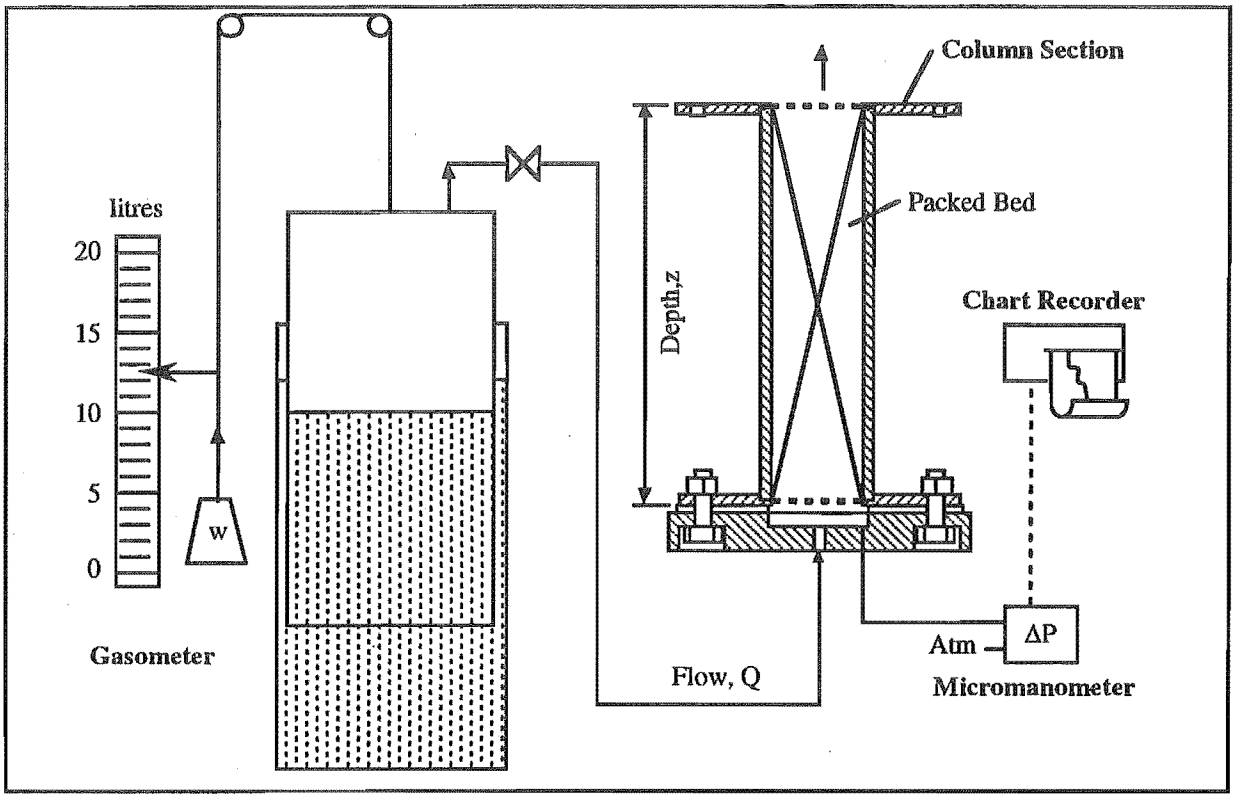

Figure 4.11. Experimental Schematic for Measuring the Permeability of the Materials in the Packed Column Sections.

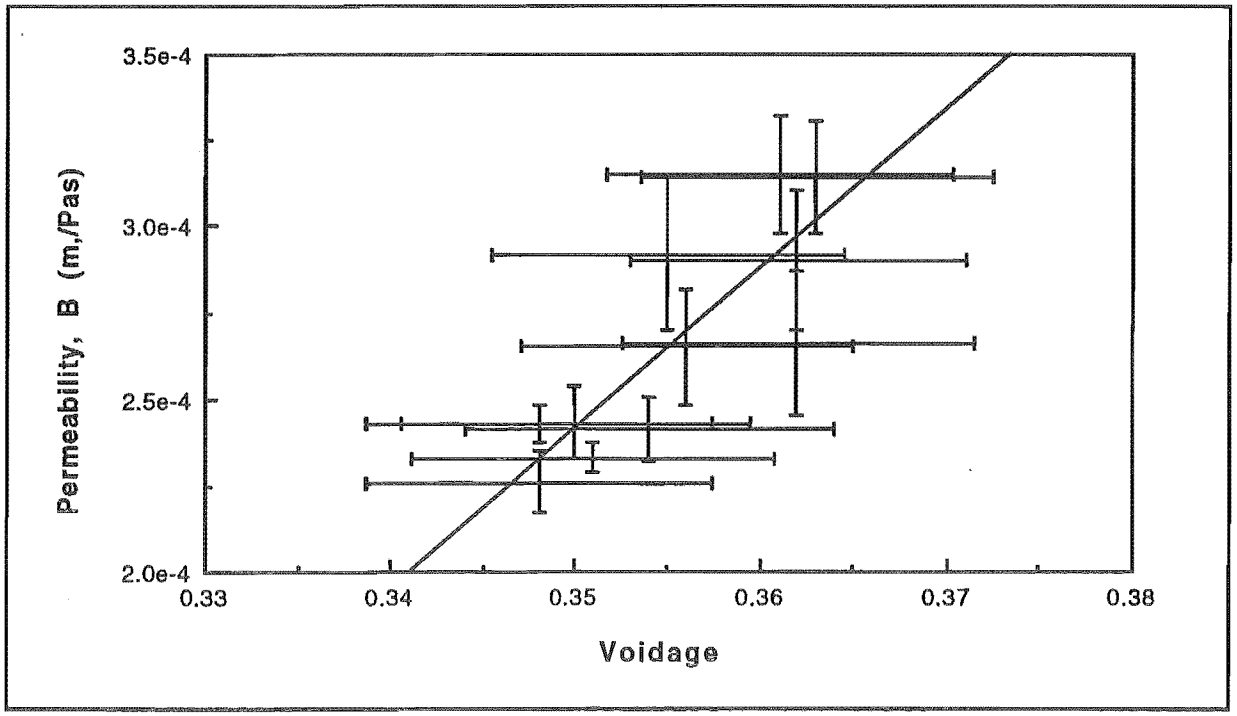

Figure 4.12. Relationship Between Permeability on Voidage for the Plastic Beads in Different Column Sections Showing the Measurement Errors and a Linear Fit to the Data.

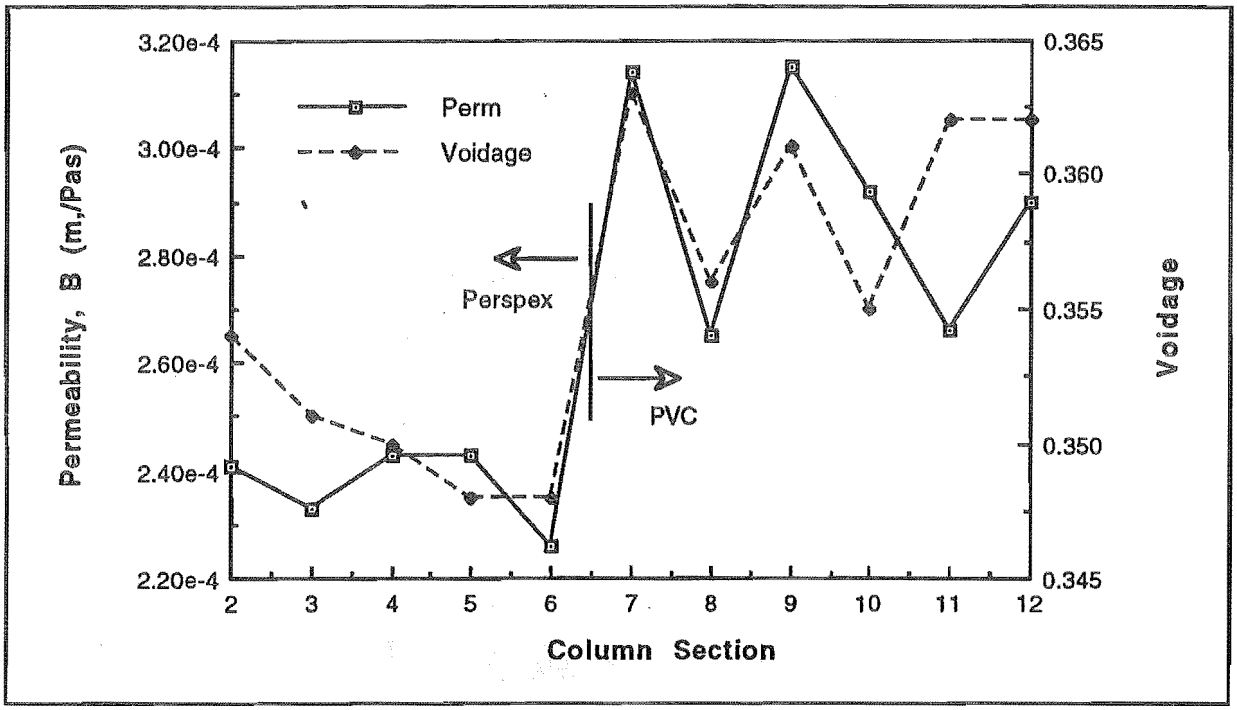

Figure 4.13. Dependence of Section Permeability on Voidage for the Plastic Beads.

After several attempts at packing, a 20% increase in the permeability, coinciding with a 3% increase in the voidage, remained in moving from the shorter perspex sections, to the longer PVC sections. From the Carmen-Kozeny equation and the laminar term of the Ergun equation (Fayed and Otten, 1984) the permeability K (m^2/Pas) is given by

$$K=\frac{\overline{D}_{p2}^2\varepsilon^3}{180\mu(1-\varepsilon)^2} \qquad 4.30$$

where $\overline{D}_{p2}^2 = 6/S_0$ is the mean particle diameter of a hypothetical sphere with the same volume as S_0, and S_0 is the ratio of *particle surface of packing* to *volume of solids in packing*. Consequently, for a 3% increase in voidage (at $\varepsilon \approx 0.35$), K is increased by 13%. This dependance is illustrated by the linear fit to the data in figure 4.12. Although less defined, there is also some dependence of ε on $\overline{D}_{p2}^2$.

There may also be some dependence on the slight narrowing of the column in the PVC sections (column sections 7 to 12) as the permeability may increase with channelling of the flow near the wall. Tests for this effect on voidage resulted in no measurable change for column diameters of 25 to 200 mm. The effect on permeability was not tested.

To minimise the effect of the variable packing in the experimental comparisons, the bed parameters were calculated as the average over the bed depth and weighted according to section length. The resulting parameters are displayed in table 4.3.

Section or Tapping	Section length (m)	Column length (m)	Voidage	Cumulative Voidage (±3%)	Permeability x10^4 (m^2/Pas)	Cumulative Permeability x10^4 (m^2/Pas) (±5%)
1	(box)	-	-	-	-	-
2	0.25	0.25	0.354	0.354	2.41	2.41
3	0.25	0.5	0.351	0.353	2.33	2.37
4	0.5	1.0	0.350	0.351	2.43	2.40
5	0.5	1.5	0.348	0.350	2.43	2.41
6	0.5	2.0	0.348	0.349	2.26	2.37
7	4.2	6.2	0.363	0.358	3.14	2.87
8	5.8	12.0	0.356	0.357	2.65	2.77
9	2.9	14.9	0.361	0.358	3.15	2.84
10	1.5	16.4	0.355	0.358	2.92	2.85
11	2.9	19.3	0.362	0.358	2.66	2.82
12	5.8	25.1	0.362	0.359	2.90	2.84

Table 4.3. Plastic Bead Packed Bed Parameters.

4.7. Laboratory Experiments

The following section describes the data collected for the packed bed airflow dynamics experiment, and compares the results to the infinite and finite-sealed bed theories where appropriate. Discrepancies between experimental and theoretical amplitude and phase are used as direct measures of this comparison.

4.7.1. Data Collection

The outputs of the micromanometer and Slotted Opto Switch were sampled by the Strobes Acquisition Unit 901A, a two channel digital storage oscilloscope and spectrum analyser. An Apple Mac Plus with 1MB of RAM provides the interface with the data acquisition unit running the Macquisition V1.4. This was the same system as used for the atmospheric turbulence measurements in Chapter 3. Unlike the turbulence measurements the full capacity of the system was not required in this application.

Amplitude and period were evaluated from pressure measurements made at 600 samples per cycle for 10 cycles. This gives good clarity as to the location of maxima and minima, whilst eliminating the significance of measurement errors. The affects of drifting box temperature (and hence pressure) did not appear in any results over the duration of sampling.

Periodic steady state was observed to occur after approximately 30 seconds that the motor requires to settle into its speed setting. This time frame is supported by the numerical one dimensional model detailed in appendix XI.

4.7.2. Data Processing

Obtaining the amplitude, frequency and phase data from the Macquisition output was a straight forward task which was inexpensive in computer time. Obtaining the comparative curves from the theory was also straight forward, requiring only the computation of the analytical solutions for pressure and none of the numerical work that is outlined in section 4.8.

4.7.3. Laboratory Measurements

In all laboratory experiments reported in this chapter, the bottom of the column was closed off to create a sealed lower boundary condition. This limits the experimental programme to direct testing of the *finite-sealed* and bed theory only. This was unfortunate as later the mass transfer and cold room experiments of Chapters 5 and 6 respectively had to be made with an open *finite-free* lower boundary condition, the pressure decay theory for which cannot be fully justified with these results. However, the 25 m bed should behave as infinitely deep during runs of relatively high frequency, and provide a relatively good basis to compare the *infinite* bed theory.

The pressure measurements were made over 10 cycles for each of the column tappings. This gives a profile of the pressure swing decay down the column. Amplitude was measured as half the height between the maximum and minimum pressures of the cycle, and period was the time from peak to peak. Phase shift was given by the time between the Slotted Opto Switch pulse and the midpoint crossing of each cycle.

The following details the imposed experimental conditions.

4.7.3.1. Generated Surface Pressure Fluctuations

The apparatus was built to produce the pressure fluctuations given by the equation 4.9. Knowledge of the experimental sinusoidal wave form's accuracy is important. Any fit to the proposed models is meaningless without this mathematically well defined surface forcing function. Tests were performed to compare the wave form produced with equation 4.9 in the absence of the column, that is, with the main valve closed.

4.7.3.2. Effect of Amplitude and Repeatability

If the flow is strictly laminar, then the effects of amplitude should be directly proportional. To test this hypothesis runs were made for amplitudes of ±70 and ±124 Pa with a period of 3.2 s in 2.0 and 25.1 m columns of plastic beads and 1.0 and 2.0 m columns of mustard seeds. Duplicates were made of these runs to check repeatability.

4.7.3.3. Effect of Total Depth

As the total depth $d \rightarrow \infty$ the pressure decay in the column should approach that given by the infinite bed theory. To evaluate how soon the approach was made a series of runs were made for total depths of 1.0, 2.0, 6.2, 12.0, 19.3 and 25.1 m columns of plastic beads with a period of 3.2 s.

4.7.3.4. Effect of Cycle Frequency

Runs were made for periods of 0.5, 1.1, 3.2, 8.2 and 17.7 s with an amplitude of ±124 Pa in 2.0 and 25.1 m columns of plastic beads and a 2.0 m column of mustard seeds.

4.7.3.5. Other Recordings

Recordings of general laboratory conditions and weather observations were made during runs to ensure conditions were stable enough to get the best possible data from the equipment. These include:

* Internal box temperature to monitor the drift in mean box pressure.
* Ambient laboratory temperature to monitor the potential for drift in the mean box pressure.
* Atmospheric pressure to monitor the drift in mean ambient pressure.
* Wind strength and gustiness to check against any unexpected pressure spikes in the data.
* Cloud cover to monitor exposure to night time radiation losses and incoming day time radiation.
* Activity in the department, such as use of doors in the laboratory, to check against any unexpected pressure spikes in the data.

Although this information is not specifically documented in this thesis, it should be noted that all measurements were made during periods when laboratory conditions were at their most stable, that is during calm cloudy nights.

4.8. Numerical Experiments on Snow

A comprehensive array of numerical experiments, using the infinite, finite-sealed and finite-free lower boundary condition theories, have been computed for snow packs with varying properties, and over the range of atmospheric turbulence frequency scales. In particular:

* Snow pack permeability ranging between $0.00002 < K < 0.002$ m^2/Pas.
* Snow pack voidage ranging between $0.6 < \varepsilon < 0.9$.
* Surface forcing function periods ranging between $0.001 < \tau < 10$ s.
* Range of total snow pack depths between $0.1 < d < 100$ m.

Barometric (mean) pressures varied only a small amount compared to these inputs. It was therefore taken as the constant value $\overline{P}$ = 100,000 Pa. The full array of results are included in appendix IX. Some examples are also presented in the discussion (section 4.9.2).

4.8.1. Numerical Methods

The following is a very brief description of the theory behind the numerical computations. A series of User Defined Macros and Functions in Microsoft Excel 4.0 running on a 486 DECpc 433 Workstation were used to perform the computations. The same approach was taken for all three bed theories (infinite, finite-sealed and finite-free). Listings of the macros used are not included in this thesis.

4.8.1.1. Pressure Swing Profiles

The maximum pressure swing at depth z from the surface was computed at intervals Δz apart using the analytical solutions for pressure (equations 4.13, 4.23 and 4.24) to give the pressure swing profile.

4.8.1.2. Peak Velocity Profiles

The peak velocity is the maximum superficial velocity v_z experienced at depth z. Using Darcy's law (equation 4.1) instantaneous velocity v is approximated by

$$v \approx -\frac{K}{\delta z}(p_z - p_{z-\delta z}) \qquad 4.31$$

where $\delta z \ll \Delta z$ and p is evaluated using the analytical solutions for pressure (equations 4.13, 4.23 and 4.24). The peak velocity values in the profile were computed by finding the maximum value of equation 4.31 over any one period at intervals Δz apart.

The analytical solution for velocity from the infinite bed theory (equation 4.19) is used as a check on the numerical method.

4.8.1.3. Eulerian and Lagrangian Cyclic Displacement Profiles

The vertical interstitial displacement of a parcel of air at various points in the snow pack, due to the surface pressure fluctuations, is of great interest to this project (see section 5.9.3).

Numerically the displacement S_z is estimated by dividing the period into m time steps of length τ/m and summing the successive displacement estimates. Hence S_z is given by

$$S_z \approx \frac{\tau}{2\varepsilon m} \sum_{i=0}^{m} |v_i| \qquad 4.32$$

where v is evaluated using equation 4.31. This gives the full displacement to the extremes on both sides of the mean position.

Eulerian vs Lagrangian Displacement

In Eulerian coordinates v_i is calculated at constant z for all i. This gives the *length of air that passes* the fixed point z. In Lagrangian coordinates the distance the *same element of air is displaced* is evaluated by adjusting the depth for each successive displacement estimation by using

$$z_i \approx z_{i-1} + \frac{\tau v_{i-1}}{m} \qquad 4.33$$

in equation 4.31. Whereas the cyclic displacement is even about the rest point in Lagrangian coordinates, the displacement in Eulerian coordinates is greater above the rest position, closer to the snow surface, than below the rest position.

In terms of mass transfer, a decision on what coordinate system is appropriate depends on whether the point of view of the air or the ice grain is taken. For example, if looking at the mass transfer about a grain it is the Eulerian displacement which is of interest because knowledge of the amount of air and how quickly it passes a certain fixed point is important. However, the condition of the air passing must also be known, so knowledge of where each element of air has been is of importance as well.

In comparing the two estimates over the range of typical snow pack and turbulence parameters, less than 0.5% discrepancy was found. Considering that this is smaller than the accepted numerical error discussed below, and that the estimate using Lagrangian coordinates requires more computation, the estimate using Eulerian coordinates was used for the cyclic displacement profiles.

4.8.1.4. Numerical Errors

The following numerical variables influence the accuracy of the estimations:

* The discrete depth increments (Δz in equation 4.31) over which the profiles were made (all calculations).
* The depth interval (δz in equation 4.31) over which pressure was calculated to estimate the velocity (velocity and displacement calculations).
* The discrete time increments (τ/m in equation 4.32) over which the displacement were estimated.

Through sensitivity tests these variables were adjusted to produce results with less than 1% numerical error. Note that the subtraction error in the velocity calculation (equation 4.31) limits the accuracy of these numerical methods when the velocity was very low. This was beyond the control of the above numerical variables.

4.9. Results

4.9.1. Laboratory Experiments

4.9.1.1. Generated Surface Pressure Fluctuations

Typical examples of the resulting experimental sinusoids (shown in figure 4.14) are almost indistinguishable from the theoretical surface sinusoids. The maximum positive and negative deviations from the true sinusoid for $P_c = \pm 127.0 \pm 0.1$ Pa and $\tau = 18.3 \pm 1$ s were 0.3% and 1.1% respectively.

Both amplitude and phase errors were observed to increase with frequency. The limits of phase accuracy are illustrated in figure 4.8. Figure 3.8 gives the amplitude response of the pressure measurement system. Despite the attenuation of the amplitude at high frequencies the form of the sinusoid measured still met the accuracy requirements as seen in figure 4.14. As there was no attenuation of the low frequency (0.057 Hz) sinusoids, it is reasonable to conclude that the *box* leakage had no significance.

4.9.1.2. Comparisons with Theory and the Column Leakage Problem

A great deal of effort was made to suppress leaks in the packed bed apparatus. Leakage tests were performed on the full 25 m column packed with plastic beads. Any leaks found were traced and eliminated. This was done until attenuation of the sinusoidal pressure signal was found to be negligible. A major flaw in this approach was discovered some 18 months after the experimental period during the analysis of shorter and faster fluctuation column results. These

experimental results seemed to lie inexplicably between the results given by the substantially different infinite and finite-sealed theories. This is best illustrated in figures 4.17, 4.18, 4.20 and 4.23[1].

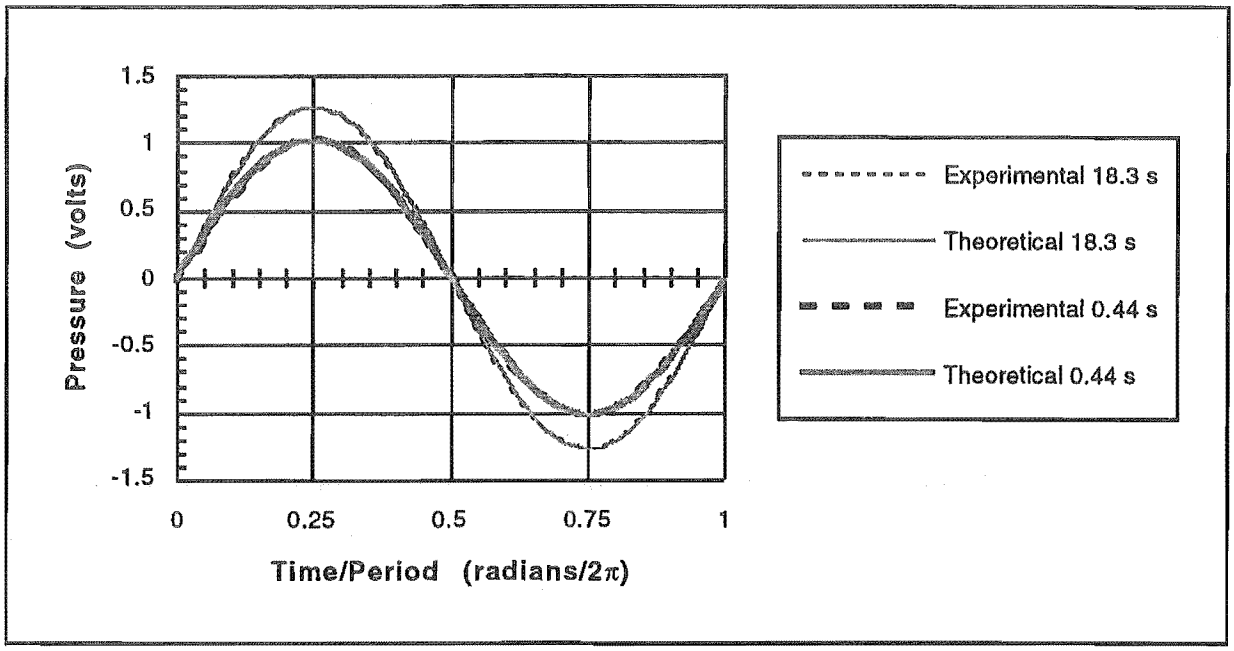

Figure 4.14. Two Examples of the Resulting Surface Pressure Fluctuation Superimposed onto the True Sinusoid: (a) Amplitude = ±127 Pa, Period = 8.3 s. (b) Amplitude = ±99 Pa, Period = 0.44 s.

Several possibilities were considered in the search for the likely cause.

* Column wall effects.
* Particle boundary layer effects.
* Fluid acceleration / deceleration effects.
* Sampling system volume, including the 1.5 mm spacing between column sections (at the sampling ports) and the sampling tube volume, of around 3 ml.
* Leakage at various points along the column.
* Leakage at end of column.

Only the last possibility is consistent with the nature of the discrepancy, that is that the effect seems to stem from the bottom of the column. This is best seen in the longer column results of figure 4.20.

As this problem was discovered 18 months after the experiment had been dismantled, the full column could not be retested for leaks. So to investigate this further, a *finite-leak model* was

[1]These figures can be found in the ordered presentation of the experimental data.

developed in Appendix XI to find the effective resistance of the leak. This was then compared to the measured resistance of the permeable fiberboard bottom sealing plate.

Figures 4.15 and 4.16 show the finite-leak model results plotted alongside the finite-sealed and finite-free bed models and the plastic bead experimental data (period of $\tau = 3.185$ s) for 25.1 and 2.0 m columns respectively. For each column length, the same resistance found to fit the amplitude data for period $\tau = 3.185$ s is applied to the other amplitude and phase data presented. The discrepancies between experimental data and finite-leak model fit is a result of using the same resistance for each set of data.

The resistances estimated from the finite-leak model of $R = 4.5 \times 10^7$ Pas/m^3 (25.1 m column of plastic beads), and $R = 3.9 \times 10^7$ Pas/m^3 (2.0 m column of plastic beads), compare well to the resistance $R = 5.3 \times 10^7$ Pas/m^3 measured for the fibreboard.

The finite-leak model uses the same heat conduction theory used in the infinite, finite-sealed and finite-free theories. As there appears to be a very good fit of the finite-leak model to the experimental data, and because the cause for this leak appears to have been identified, any confidence lost in the applicability of infinite, finite-sealed and finite-free models was regained, and their underlying assumptions vindicated.

4.9.1.3. Effect of Amplitude and Repeatability

The results of repetitions made for two column lengths illustrated in figure 4.17 and 4.18 show low random measurement errors compared to the difference between experimental and theoretical results. Note that the measurement errors are at their most significant for small phase shift measurements The experimental phase shift results shown in figure 4.16(b) have maximum measurement errors of around ±0.04 radians, which account for the apparent scatter.

The surface forcing amplitudes of these runs varied between 70 and 125 Pa. No trend is observed in either the reduced amplitude[2], or phase results. This implies laminar flow conditions prevail in the pack bed, and consequently, surface forcing amplitude does not need to be regarded as a variable in further analysis.

---

[2] Amplitude plots are scaled (reduced) according to the forcing surface amplitude. This results in a maximum column amplitude of 1 Pa/Pa at the bed surface.

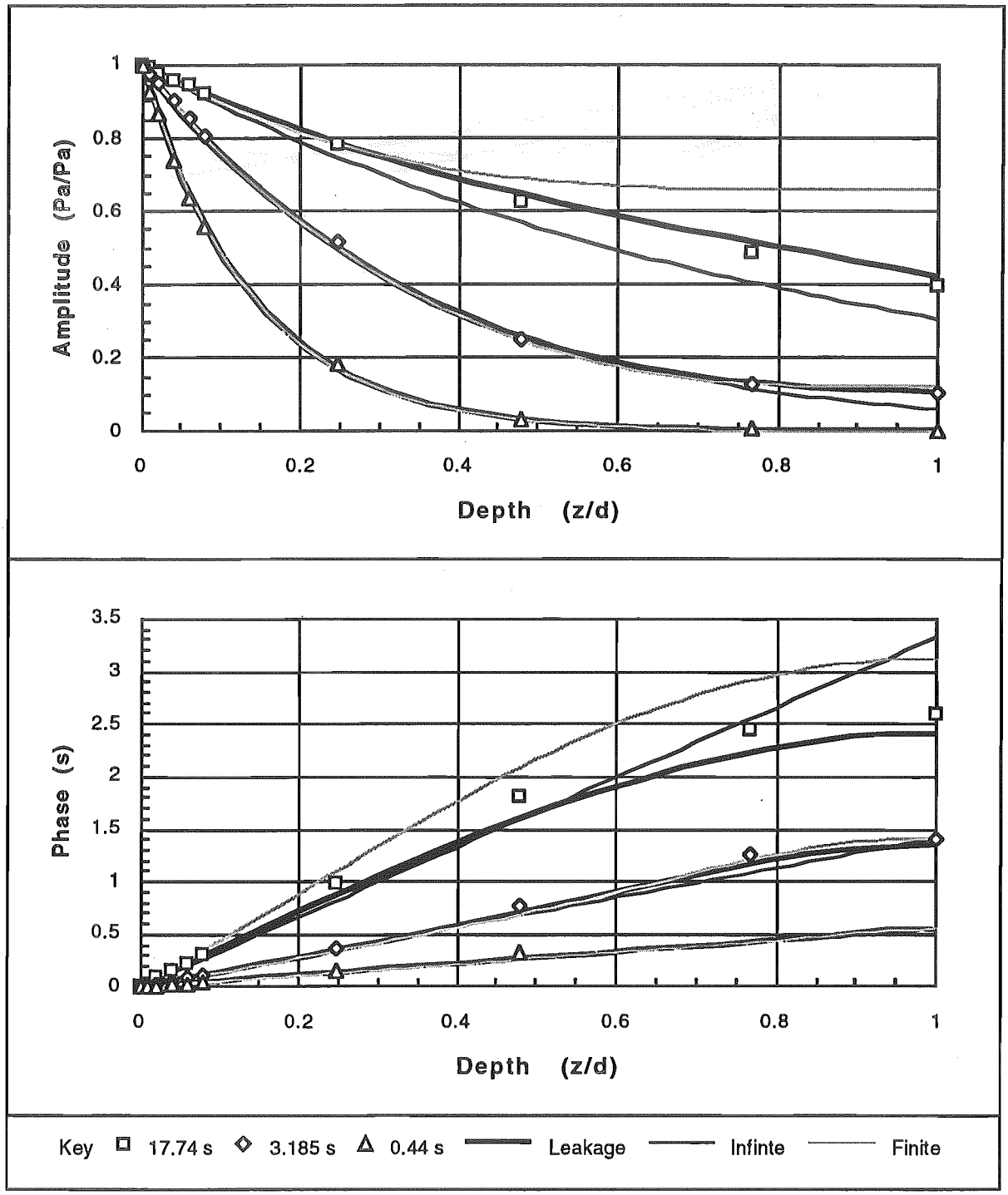

Figure 4.15. Finite-Leak Model Maximum Pressure Swings Plotted Alongside the Experimental Data and the Infinite and Finite-Sealed Theories for a 25.1 m Column of Plastic Beads. The same resistance ($R = 4.5 \times 10^7$ Pas/m^3) found to fit the amplitude data for period $\tau = 3.185$ s is applied to the other data presented above. This is the cause for the discrepancies between experimental data and finite-leak model fit.

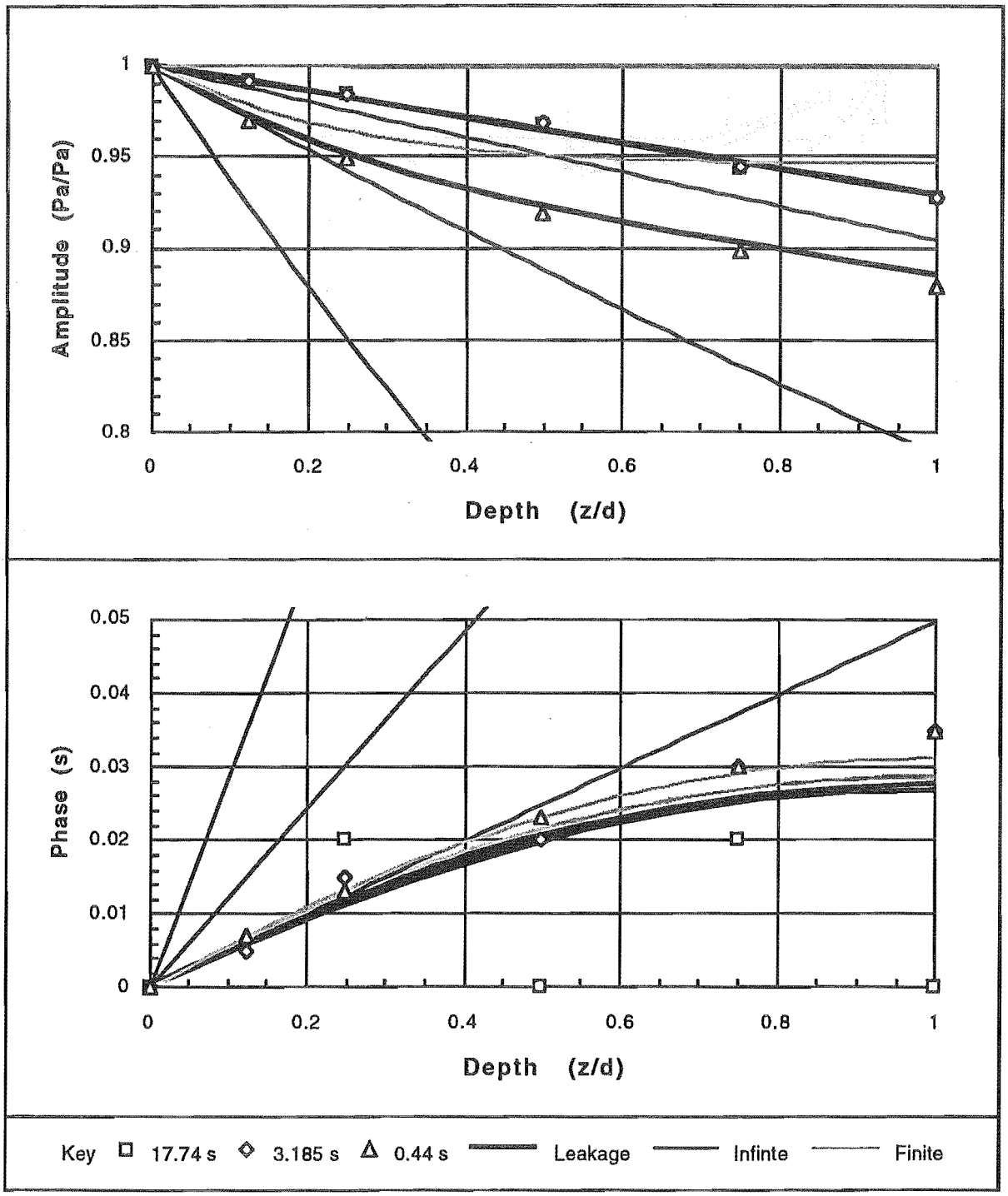

Figure 4.16. Finite-Leak Model Maximum Pressure Swings Plotted Alongside the Experimental Data and the Infinite and Finite-Sealed Theories for a 2.0 m Column of Plastic Beads. The same resistance ($R = 3.9 \times 10^7$ Pas/m^3) found to fit the amplitude data for period $\tau = 3.185$ s is applied to the other data presented above. This is the cause for the discrepancies between experimental data and finite-leak model fit.

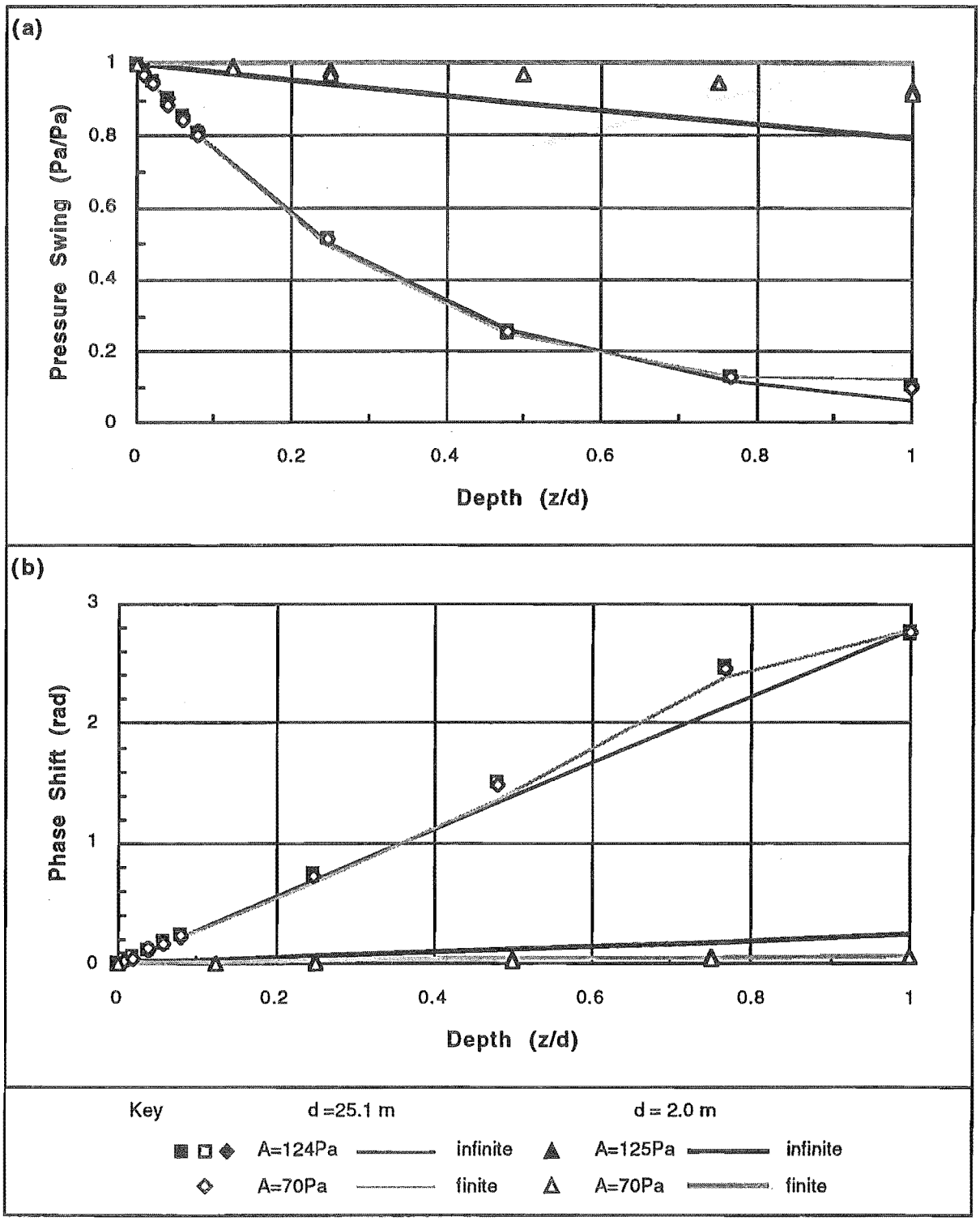

Figure 4.17. Theoretical Maximum Pressure Swings Plotted Alongside the Experimental Results for the Plastic Beads with Period $\tau = 3.18$ s and Column Length $d = 25.1$ m: (a) Amplitude. (b) Phase Lag.

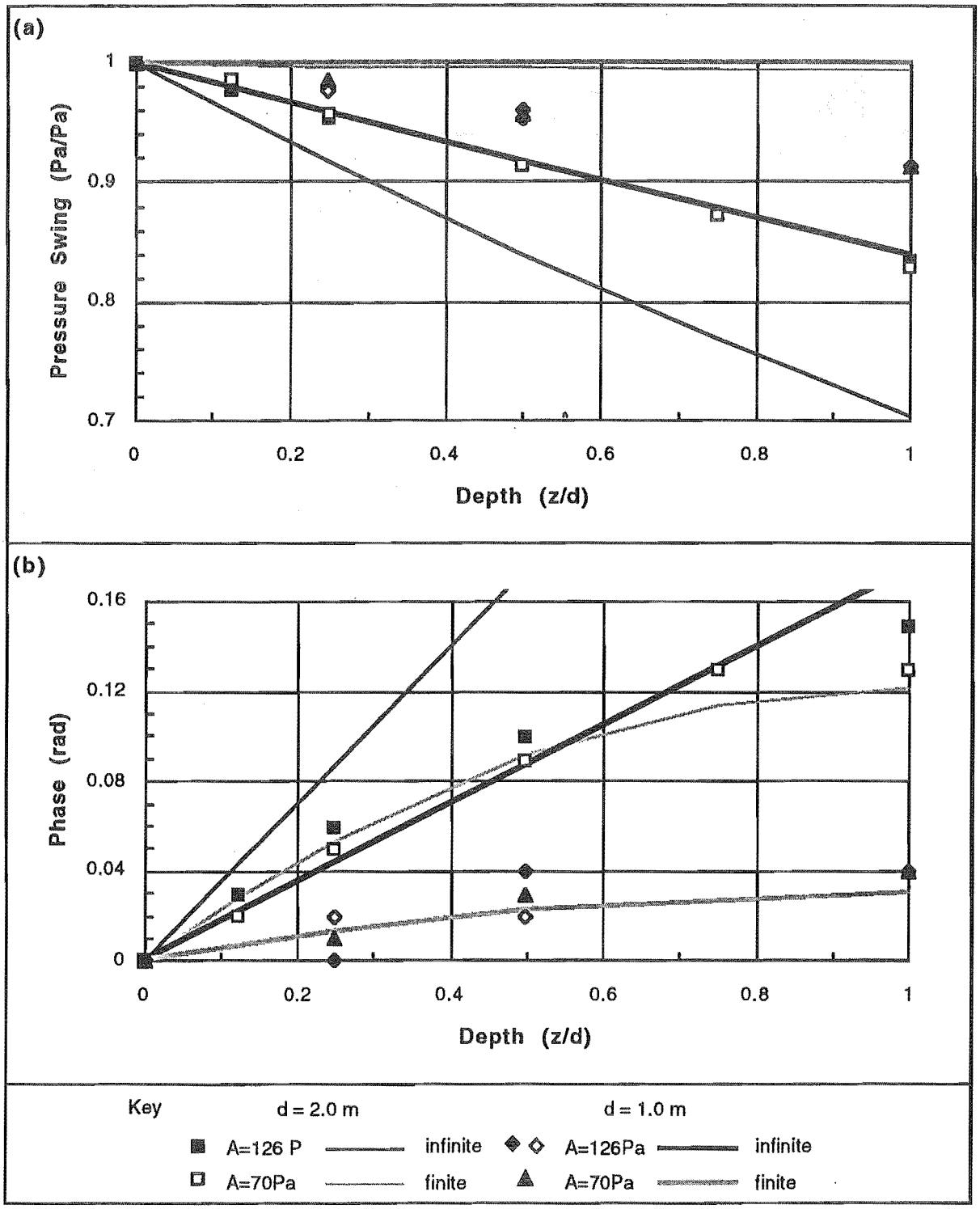

Figure 4.18. Theoretical Maximum Pressure Swings Plotted Alongside the Experimental Results for the Mustard Seeds with Period $\tau = 3.18$ s and Column Length $d = 2.0$ m: (a) Amplitude. (b) Phase Lag.

4.9.1.4. Effect of Total Depth

Length effects were examined for plastic bead and mustard seed bed packings at a period of $\tau = 3.18$ s. The results are plotted in figure 4.19 for $1.0 \leq d \leq 25.1$ m columns packed with plastic beads, and $1.0 \leq d \leq 2.0$ m columns packed with mustard seeds. The decay in amplitude and increase in phase shift follow the expected trends, specifically:

* For a particular location beneath the surface (depth), the deeper the bed, the greater the amplitude attenuation and phase shift.
* For the bottom of the column, the deeper the total bed depth, the greater the amplitude attenuation and phase shift.

The very small attenuations of the shortest total bed depths ($d = 1$ m) were too small to measure accurately given the ±0.02 Pa/Pa measurement error. Similar limits are imposed on the presentation of small phase shifts where measurement accuracy is ±0.04 radians.

The longer column length plastic bead data is re-plotted alongside the infinite and finite-sealed bed theories in figure 4.20. At a period of $\tau = 3.18$ s, for a total bed depth of greater than around 12 m, the upper portion of the bed (upper 2 m for the 12 m column), behaves in a similar manner to the infinite length column. In this case the experimental results and infinite and finite-sealed bed theories merge onto the same decay curve. This is observed despite the bottom plate leakage problem discussed in section 4.9.1.2 as the leakage only affects the bottom portion of the longer beds.

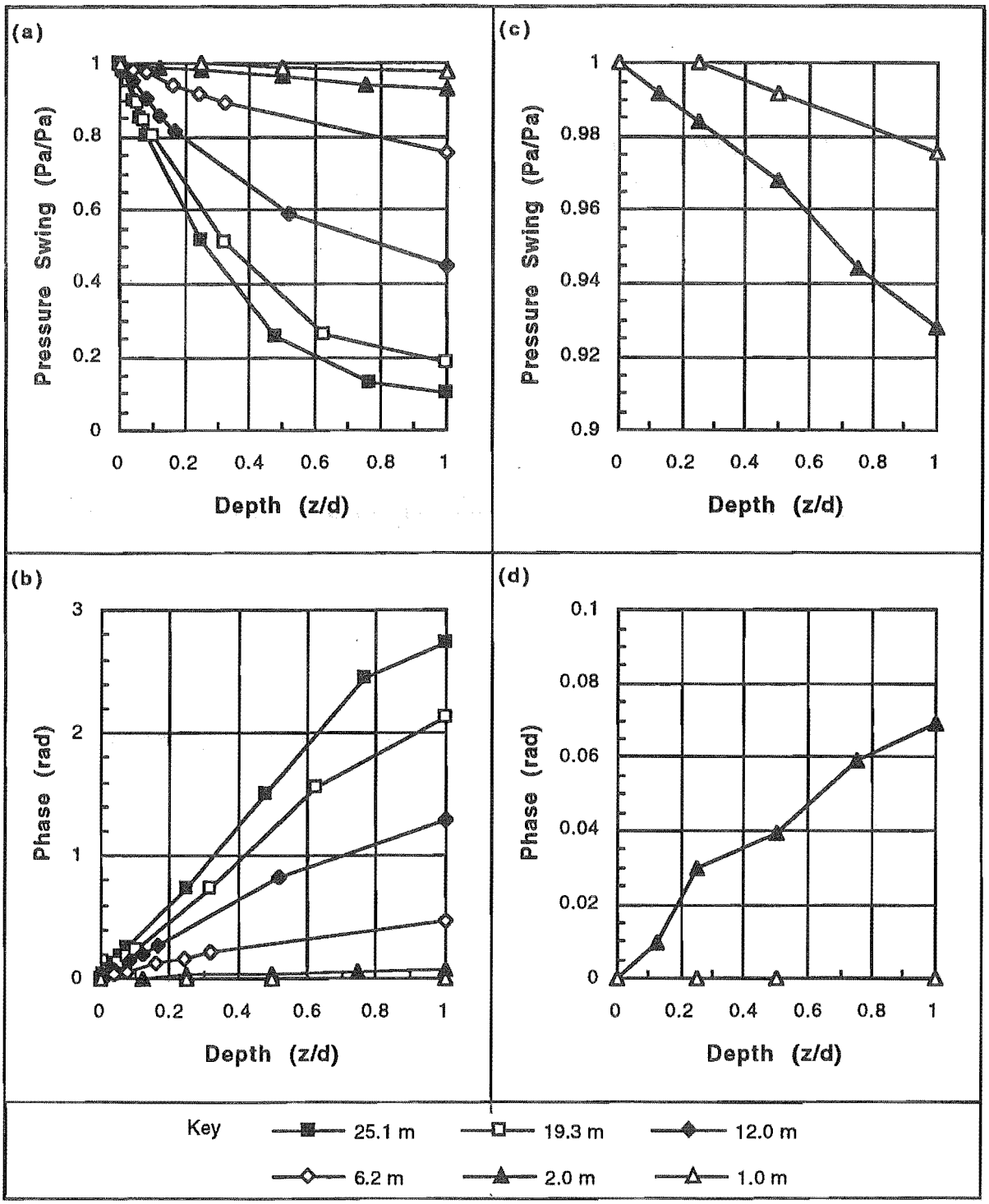

Figure 4.19. Experimental Maximum Pressure Swings for the Plastic Beads with Period $\tau = 3.18$ s and Varying Column Length: (a) Plastic Beads: Amplitude. (b) Plastic Beads: Phase Lag. (c) Mustard Seeds: Amplitude. (d) Mustard Seeds: Phase Lag.

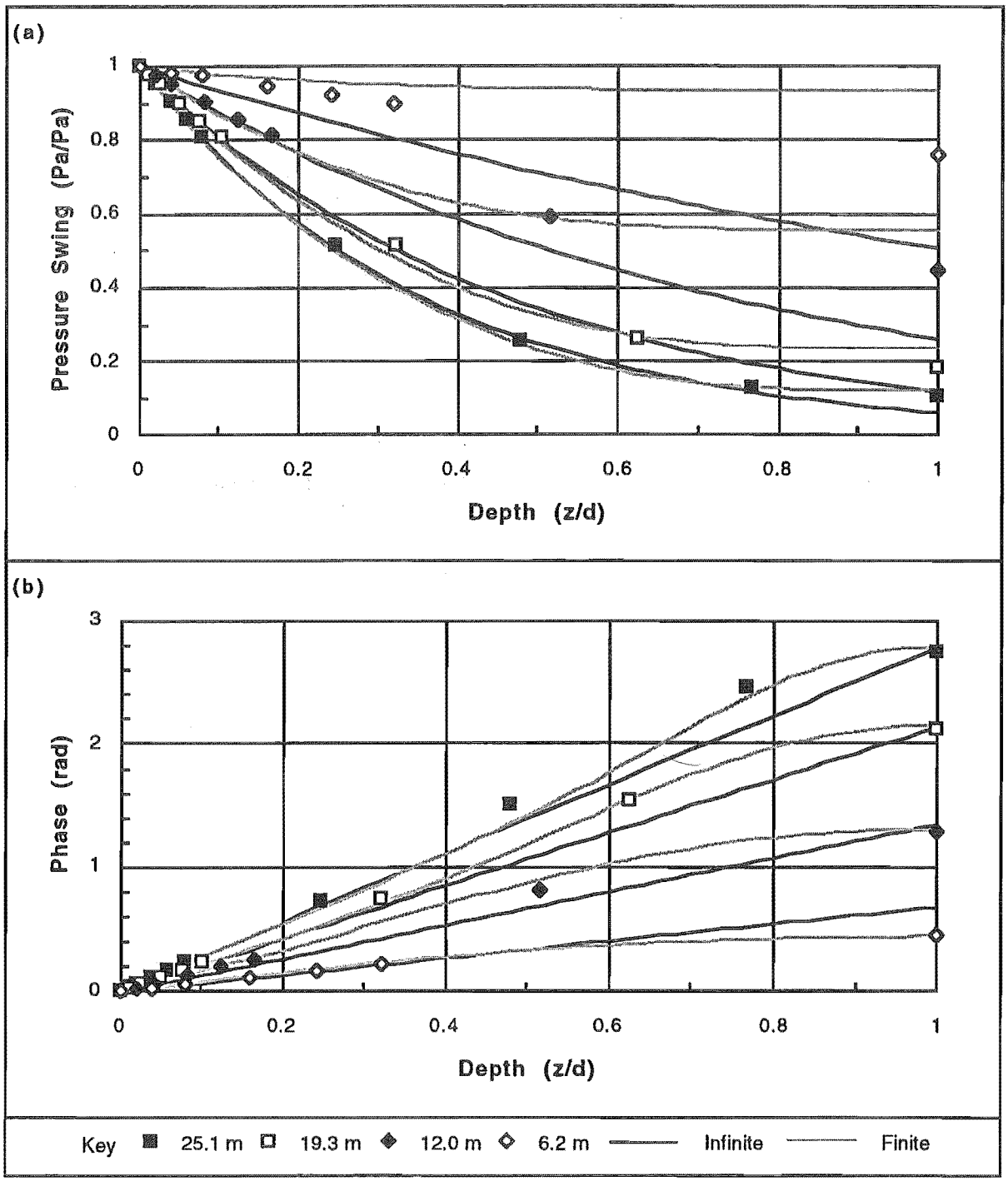

Figure 4.20. Theoretical Maximum Pressure Swings Plotted Alongside the Experimental Results for the Plastic Beads with Period $\tau = 3.18$ s and Varying (longer) Column Lengths: (a) Amplitude. (b) Phase Lag. Due to the column leakage problems discussed in section 4.9.1.1 there is some difficulty in matching the appropriate infinite and finite-sealed model lines to the appropriate experimental data, especially for the shorter column length and higher frequency data.

4.9.1.5. Effect of Cycle Frequency

Frequency effects were examined for 2.0 and 25.1 m columns packed with plastic beads, and a 2.0 m column packed with mustard seeds. The mustard seed results are plotted in figure 4.21 and plastic bead results in figure 4.22.

The decay in amplitudes, and increase in phase shift, follow the expected trend with wind pumping cycle period. Specifically, for a particular location beneath the surface (depth), the faster the fluctuation, the greater the amplitude attenuation and the greater the phase shift. The degree of amplitude attenuation was measurable for all periods used. However, the phase shift measurements in the 2.0 m columns at the largest period (τ = 17.74 s) were limited by the ±0.04 radian measurement error.

The plastic bead period data for the 25.1 m column is re-plotted alongside the infinite and finite-sealed bed theories in figure 4.23. For all the results, bar those for a period of τ = 17.74 s, the upper portion of the column behaves in a similar manner as the infinite length column. In this case the experimental results and infinite and finite-sealed bed theories merge onto the same decay curve. This is observed despite the bottom plate leakage problem discussed in section 4.9.1.2 as the leakage affects only the bottom portion of the longer beds. For periods of τ = 17.74 s, and presumably greater, there is a poor match over a large portion of the bed.

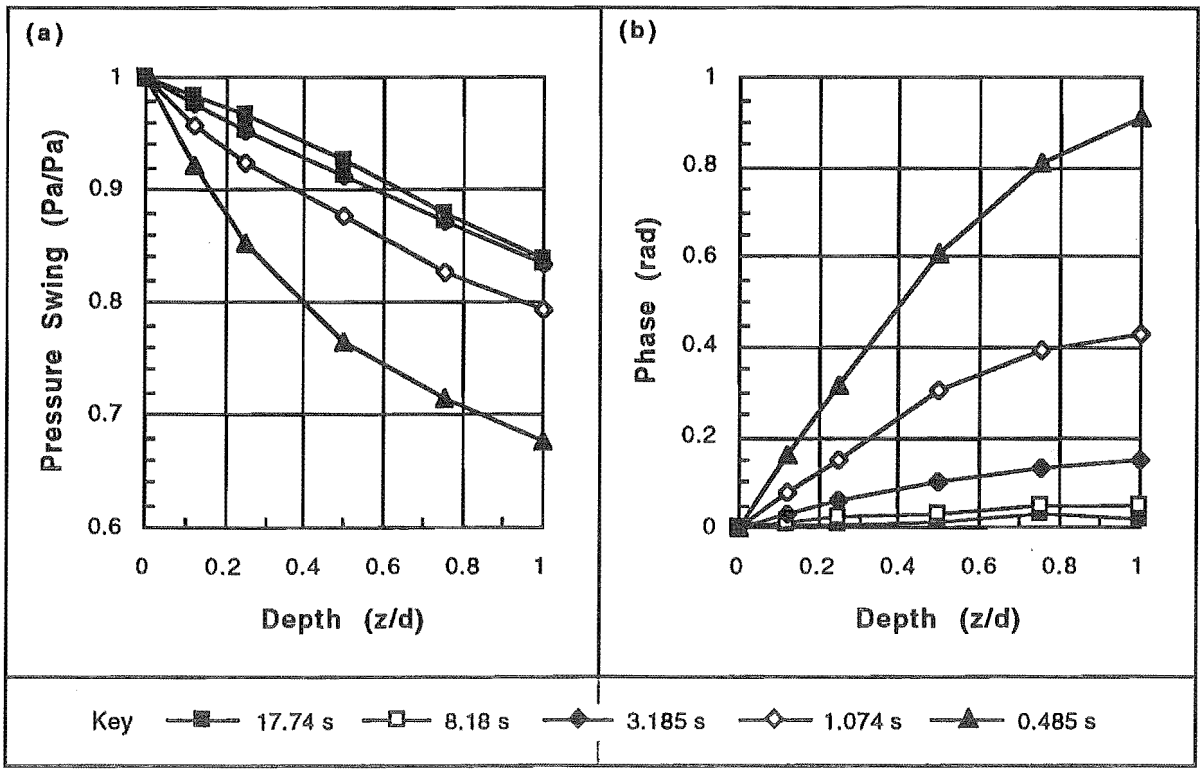

Figure 4.21. Experimental Maximum Pressure Swings for the Mustard Seeds for Varying Period and Column Length d = 2.0 m: (a) Amplitude. (b) Phase Lag.

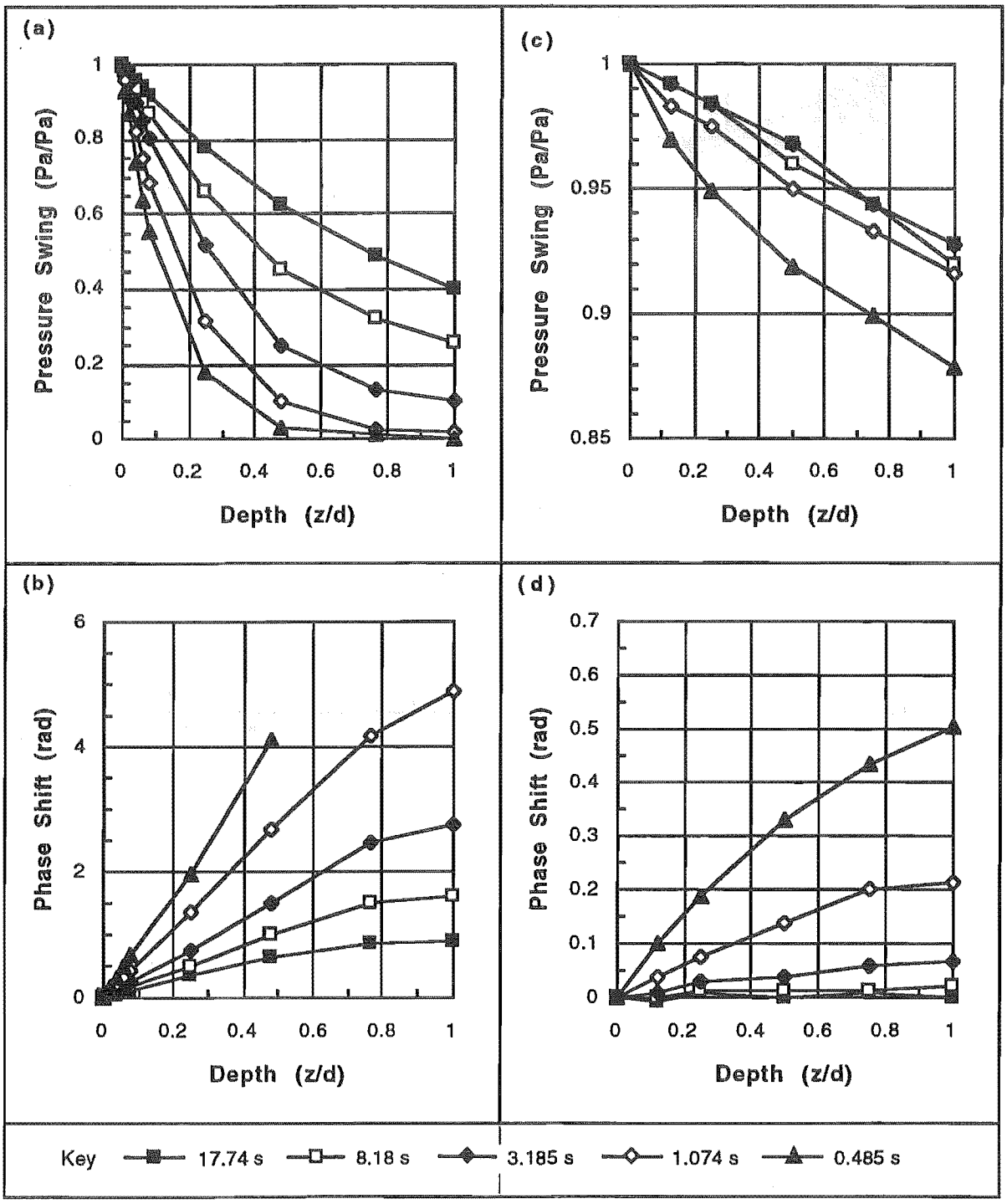

Figure 4.22. Experimental Maximum Pressure Swings for the Plastic Beads for Varying Period and Column Length: (a) d = 25.1 m: Amplitude. (b) d = 25.1 m: Phase Lag. (c) d = 2.0 m: Amplitude. (d) d = 2.0 m: Phase Lag.

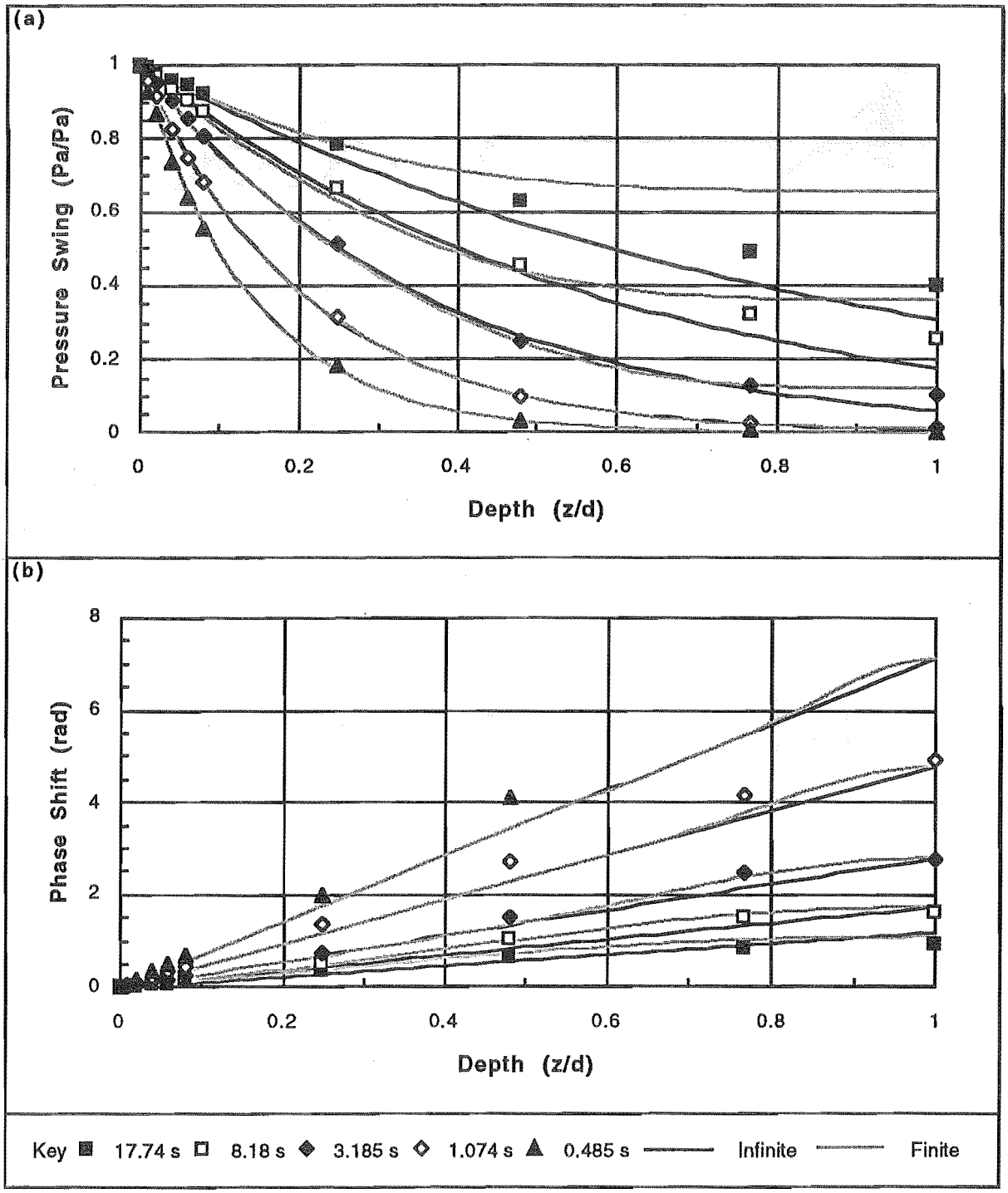

Figure 4.23. Theoretical Maximum Pressure Swings Plotted Alongside the Experimental Results for the Plastic Beads with Varying Period and Column Length d = 25.1 m: (a) Amplitude. (b) Phase Lag. Due to the column leakage problems discussed in section 4.9.1.1 there is some difficulty in matching the appropriate infinite and finite-sealed model lines to the appropriate experimental data, especially for the shorter column length and higher frequency data.

4.9.2. Numerical Experiments

The full array of results computed for the three bed theories is included in Appendix IX. Some of this information is reproduced here for the purposes of discussion.

No discussion is made on the finite-free bed theory, as it seems unlikely that this lower boundary condition would occur in nature. However, the theory is used as a tool in the experiments of Chapter's 5 and 6.

Note that profiles calculated from infinite bed theory for a bed of finite depth d were obtained by setting $z_{finite} = z_{infinite}$ for $0 \leq z \leq d$. This the allows the infinite theory to be plotted as functions of z/d, and for a visual check to be made on the approach of the infinite bed numerical result to finite bed results.

4.9.2.1. Finite-Sealed Bed Theory

Examples of pressure swing, maximum velocity, and cyclic displacement profiles are shown in figures 4.24, 4.25 and 4.26 for the finite-sealed bed theory. A distinct feature of the velocity and displacement profiles is their simplicity in shape. This is derived from the nearly full depth penetration of the pressure fluctuation. Note the expanded scale in figure 4.24. This "breathing as a unit" feature of the seasonal snow pack was also noted by Colbeck (1989).

A particularly interesting result (shown in figure 4.27), is the indistinguishable variation of cyclic displacement in a 1 m snow pack for widely varying periods. This shows that the trends in the above three plots (figures 4.24 to 4.26), hold for the turbulence frequencies expected in the mountains.

Recognition of these distinct, apparently linear trends, leads to the finite-sealed bed approximations which are proposed in section 4.9.2.2.

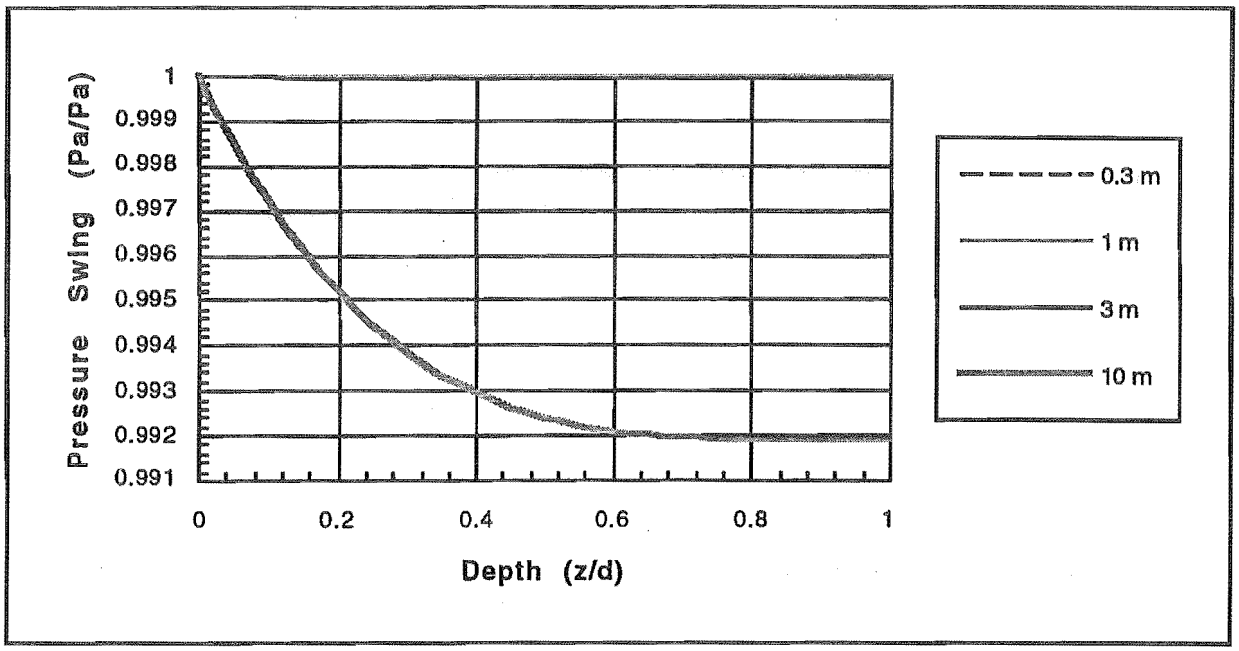

Figure 4.24. Snow Pack Profiles of the Maximum Pressure Swing for Varying Snow Pack Depth Using the Finite-Sealed Bed Theory and Period $\tau = 100$ s. The snow pack permeability and voidage were taken as $K = 2 \times 10^{-4}$ m^2/Pas and $\varepsilon = 0.75$ respectively and mean atmospheric pressure as $\overline{P} = 100{,}000$ Pa.

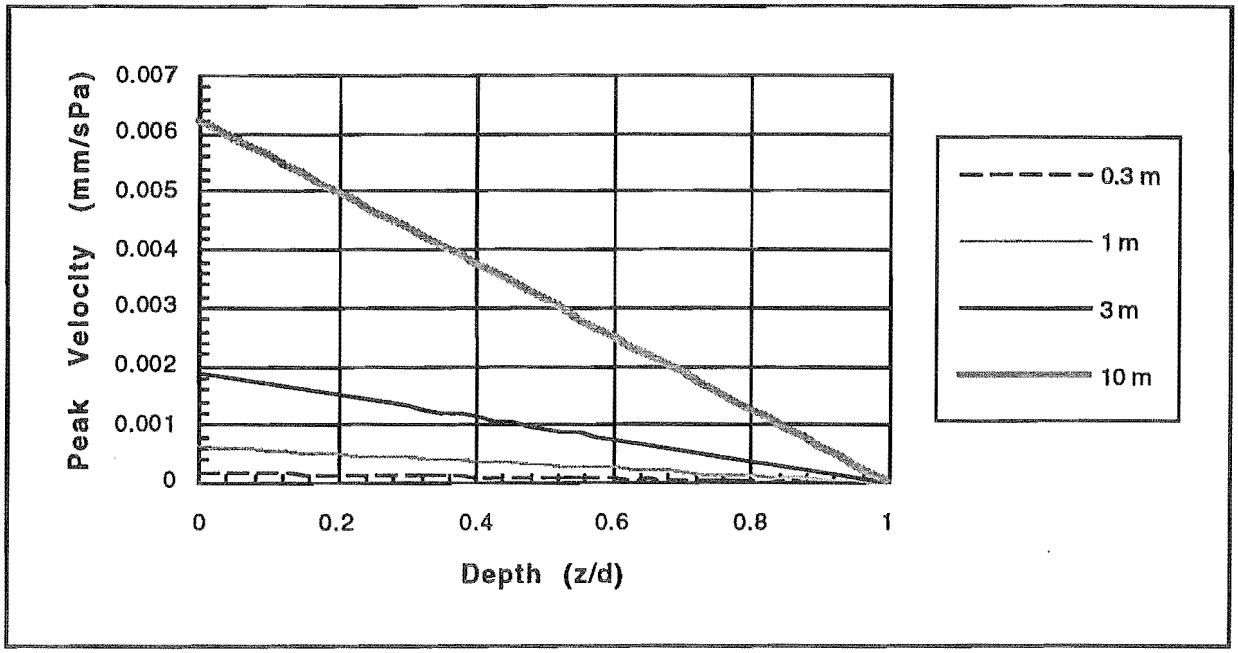

Figure 4.25. Snow Pack Profiles of the Peak Velocity for Varying Snow Pack Depth Using the Finite-Sealed Bed Theory and Period $\tau = 100$ s. The snow pack permeability and voidage were taken as $K = 2 \times 10^{-4}$ m^2/Pas and $\varepsilon = 0.75$ respectively and mean atmospheric pressure as $\overline{P} = 100{,}000$ Pa.

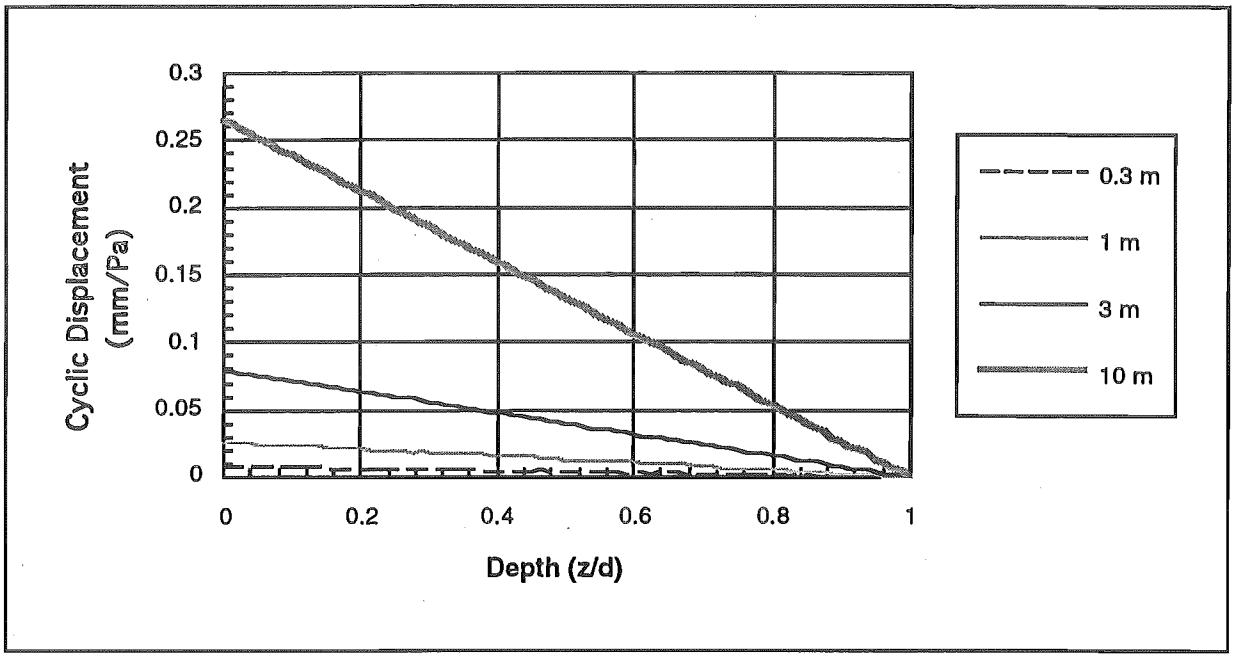

Figure 4.26. Snow Pack Profiles of the Cyclic Displacement for Varying Snow Pack Depth Using the Finite-Sealed Bed Theory and Period τ = 100 s. The snow pack permeability and voidage were taken as K = 2x10^{-4} m^2/Pas and ε = 0.75 respectively and mean atmospheric pressure as $\overline{P}$ = 100,000 Pa.

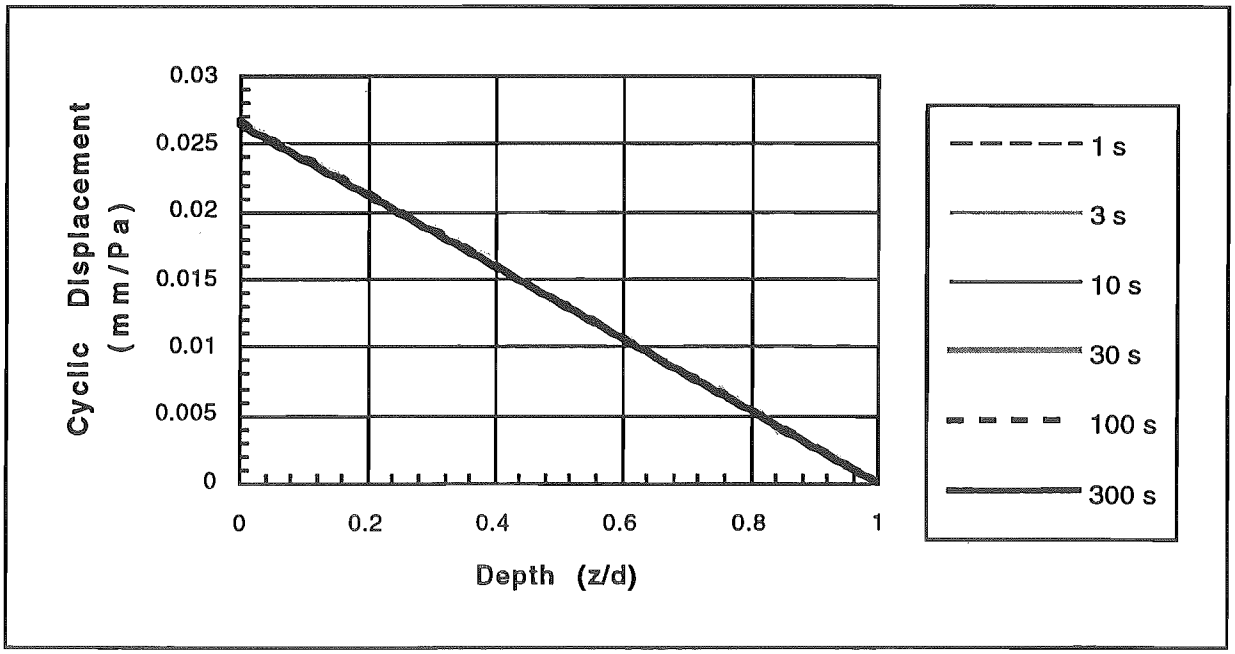

Figure 4.27. Snow Pack Profiles of the Cyclic Displacement in a 1 m Snow Pack for Varying Period Using the Finite-Sealed Bed Theory. The snow pack permeability and voidage were taken as K = 2x10^{-4} m^2/Pas and ε = 0.75 respectively and mean atmospheric pressure as $\overline{P}$ = 100,000 Pa.

4.9.2.2. Linear Approximations to the Finite-Sealed Bed Theory

Given the high degree of regularity in the finite-sealed bed dynamic observed in section 4.9.2.1 above, the following approximations for profiles of pressure swing P_z, maximum velocity V_z and cyclic displacement S_z are proposed:

$$P_z = \pm P_c \qquad \text{for } \beta d \leq 1 \qquad 4.34$$

$$V_z = \pm \frac{2P_c \pi \varepsilon (d-z)}{\tau \overline{P}} \qquad \text{for } \beta d \leq 1 \qquad 4.35$$

$$S_z = \frac{2P_c (d-z)}{\overline{P}} \qquad \text{for } \beta d \leq 1 \qquad 4.36$$

where P_c is the surface amplitude of the sinusoidal pressure fluctuations, τ the period of the sinusoidal pressure fluctuations, ε the voidage, d the total snow pack depth, z depth into pack and $\overline{P}$ is the average (barometric) pressure.

It should be noted that the snow pack parameters play only a minor role in these equations. There is no dependence on permeability in these relations, and voidage, which varies between $0.7 \leq \varepsilon \leq 0.9$ in most dry snow packs, appears only in the velocity equation. Consequently the equations should hold well over several different layers in a snow pack until an impermeable boundary occurs in the form of either the ground or an ice layer.

Rapid departures from these approximations occurs for $\beta d > 1$. A combination of atmospheric conditions and seasonal snow pack, with βd exceeding this limit of 1, is difficult to conceive. Taking permeability $K = 0.00002$ m^2/Pas, voidage $\varepsilon = 0.6$, period of fluctuation $\tau = 10$ s and $\overline{P} = 100{,}000$ Pa as an extreme example, the snow pack would have to be $d = 2.8$ m deep to exceed the limit of $\beta d = 1$.

Therefore the above relations should hold over most natural seasonal snow pack conditions.

4.9.2.3. Infinite Bed Theory

Results from the infinite bed theory appear to have little use in seasonal snow pack flow prediction. Even for the relatively high frequency fluctuations illustrated in figure 4.28, only the top 20% of a 10 m snow pack can accurately be modelled as infinite. In more complete terms the comparison breaks down for $\beta d < 3$.

Whilst it may appear to be applicable to glacial firn scenarios, rapidly decreasing voidage with depth to the pore close off density ($\varepsilon \approx 0.15$) at $d \approx 40$ m limits this aspect of its use.

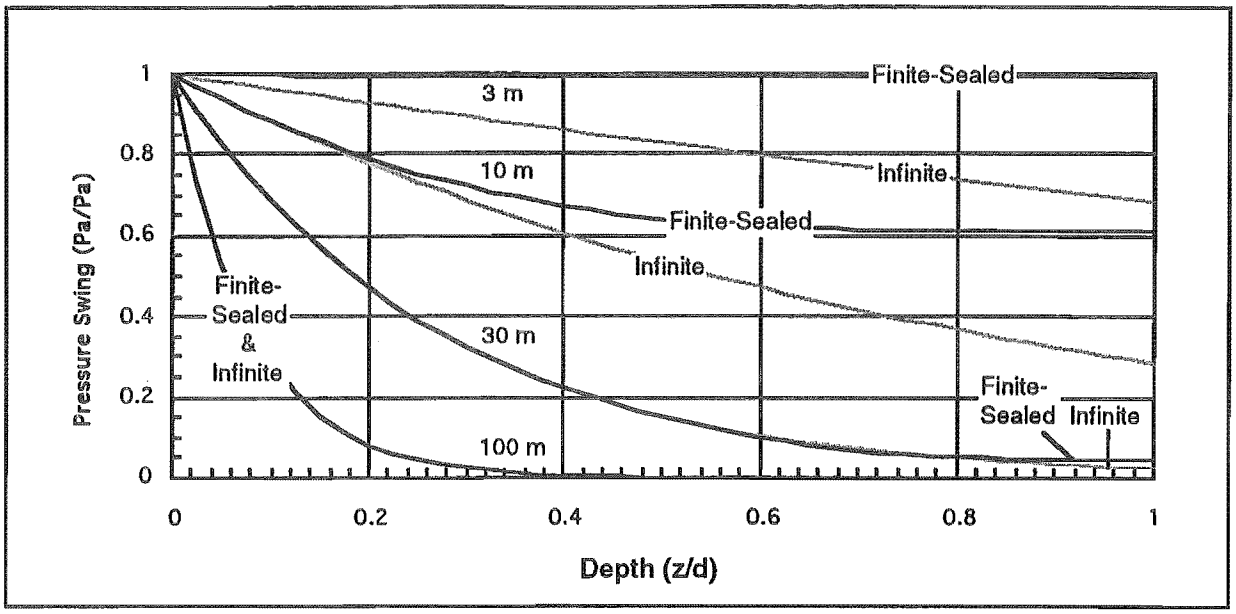

Figure 4.28. Comparison of the Snow Pack Profiles of the Pressure Swing Calculated Using the Infinite and Finite-Sealed Bed Theories for Varying Snow Pack Depths. The snow pack permeability and voidage were taken as $K = 2 \times 10^{-4}$ m^2/Pas and $\varepsilon = 0.75$ respectively, period as $\tau = 10$ s and mean atmospheric pressure as $\overline{P} = 100{,}000$ Pa.

4.10. Conclusions

It was the purpose of this chapter to compare the theoretical and experimental decay of fluctuating surface pressure down a permeable bed. Having achieved this, the models developed in the process were then to be applied over a wide range of snow pack conditions in a set of numerical experiments. This gave a range of air speeds and displacement estimates in the snow pack due to wind pumping.

4.10.1. Proposed Models

The length scales associated with the atmospheric pressure fluctuations measured in the mountains, determine that a one dimensional modelling approach is applicable.

Three models are proposed from analogies with periodic heat transfer problems, with each model relating to a differing lower boundary condition.

1. Relatively deep snow pack or glacier of constant density and permeability - **infinite** lower boundary condition.
2. Relatively shallow snow pack of consistent density and permeability - **finite-sealed** lower boundary condition.
3. Relatively shallow snow pack with higher density snow overlying considerably less dense snow, where there is no restriction to the air pulsation below the change in density interface - **finite-free** lower boundary condition.

To make the required comparisons between the models and laboratory experiments, a mathematically well defined periodic upper surface boundary condition was chosen to represent the turbulent atmospheric pressure fluctuations.

4.10.2. Laboratory Experiments

The wind pumping apparatus provided sinusoidal pressure fluctuations which were almost indistinguishable from the comparative theoretical sinusoid. This laid the platform for the required model tests to be made.

The experiments determined that the bed flow was directly proportional to the magnitude of the surface pressure fluctuation. This implies laminar flow conditions prevailed and that the use of Darcy's Law is valid (equation 4.1).

The decay in amplitude and increase in phase shift, compared to the surface sinusoid, followed the expected trends. Specifically, the amplitude attenuations and phase shifts are increased by:

* Increasing measurement depth into the bed.
* Deeper total bed depth.
* Lower bed voidage.
* Lower bed permeability.
* Higher frequency of fluctuation.

Unfortunately a leakage at the end of the column prevented any close experimental matches with the proposed models. The leak was discovered some time after the dismantling of the apparatus. This problem was surmounted by formulating a fourth model which allowed for the leakage. The new model gave a good fit to the experimental data. The resistance of the leak determined by the model closely matched the measured leak resistance.

It is concluded that, as all four models have the same underlying assumptions, they are all vindicated by this experiment and subsequent analysis.

4.10.3. Numerical Experiments

A comprehensive array of numerical results was produced for all three original theories. *The finite- sealed model was thought to most closely represent most snow pack situations.*

Distinct, apparently linear trends in the *finite-sealed bed model* results were recognised over a wide range of seasonal snow pack and atmospheric turbulence conditions. Consequently linear finite-sealed bed theory approximations are proposed for the maximum velocity V_z and cyclic displacement S_z profiles for $\beta d < 1$. These are given by equations 4.35 and 4.36. Restating

$$V_z = \pm\frac{2P_c\pi\varepsilon(d-z)}{\tau\overline{P}} \qquad\qquad S_z = \frac{2P_c(d-z)}{\overline{P}}$$

These approximations are independent of snow pack permeability and should therefore hold reasonably well over several layers in a snow pack until an impermeable boundary occurs (either the ground or an ice layer). Note that although most conceivable seasonal snow pack and atmospheric conditions prevail below $\beta d = 1$, rapid departures from these approximations occurs for $\beta d > 1$.

Results from the *infinite bed theory* appear to have little use in seasonal snow pack flow prediction.

The results concluded here meet all the objective requirements of this chapter, and hence it is considered that no further work is required for the present purpose on one dimensional laminar pulsile flow modelling in a packed bed.

Chapter 5
Wind Pumping Mass Transfer

The primary objective of Chapter 5 is to compare the relative mass transfer rates in a packed bed due to varying magnitudes and intensities of wind pumping.

5.1. Table of Contents

5.2. List of Illustrations

5.3. Nomenclature

d	snow pack depth (m)
$\dot{m}$	mass loss rate (g/hr)
P_c	pressure fluctuation amplitude (Pa)
$\overline{P}$	average (barometric) pressure (Pa)
S_z	interstitial displacement (mm)
T	ambient temperature (K)
V	volume (ml)
W	weight (g)
ε	voidage
ρ	density (kg/m^3 or g/ml)
σ	standard deviation
τ	period (s)

5.4. Introduction

A controlled set of laboratory experiments was required to detect and measure any enhancement (or retardation) of the *diffusive mass transfer rates* in a packed bed due to the wind pumping mechanism.

To achieve this an inert diffusing tracer was required. Naphthalene was ideal for this purpose because it sublimes at measurable rates from the solid to gas phase at room temperature and it has a similar diffusivity to water vapour ($D_{AB\ naphthalene} = 6.6 \times 10^{-6}\ m^2/s$ and $D_{AB\ water} = 22 \times 10^{-6}\ m^2/s$). The naphthalene sublimation technique has found its place in the measurement of mass and heat transfer rates when the effects of a flow over a particular surface configuration in ambient laboratory conditions was of interest. See for example Sogin and Providence (1958), Sparrow and Kalejs (1977), Molki and Sparrow (1983) and Wilson (1985).

By measuring the mass loss rates of solid naphthalene through a packed bed with varying degrees of wind pumping, the effects of wind pumping on the water vapour diffusion process can be investigated. The wind pumping flow conditions imposed on the column need to be compares to those in the natural snow pack and to the wind pumping metamorphism experiments of Chapter 6.

Scotter *et al* (1967) performed a similar set of experiments to detect enhancements of water vapour losses from the top few centimetres of soils. They monitored the diffusion of atmospheric oxygen back into a column which had been flushed with nitrogen.

In sections 5.5 and 5.6 the experiment designed to facilitate the measurement of diffusive mass transfer rates is described. Several problems experienced with experimentation and analysis are described in section 5.7. In section 5.8 the measurement programme is described and in section 5.9 the results are detailed and discussed. Also in section 5.9 is a conceptual discussion of the effects of a wind pumping airflow on vapour transport.

5.4.1. Mechanisms of Mass Transfer Control

Three mechanisms, illustrated in figure 5.2, may be responsible for the control on mass transfer rates in a packed bed with pulsile flow.

(a) **Kinetic Control:** If the diffusion rate is sufficiently high, then the mass transfer might be dependent on the rate at which naphthalene can sublimate from the surface. Such a kinetically controlled processes would be unique to the naphthalene beads, and of no relevance to water vapour transport in a snow pack. Kinetic control should be distinguished by the mass transfer rates dependence on surface area. Because of this, there is a requirement to test for surface area dependence (see section 5.7.1).

(b) **Local Film Diffusion Control:** It is possible that a high interstitial velocity could create a mass transfer boundary layer around the surface of the beads. If this is the case a local film diffusion control might exist. If film diffusion control is evident, then one might expect to see surface area and velocity dependencies on the mass transfer rates.

(c) **Planar 1-D Convective Diffusion:** For the mass loss rates to be governed by the convective diffusion rate in the axial direction, the wind pumping airflow velocity must be sufficiently low so that the interstitial air in the layer of the naphthalene beads is saturated with naphthalene vapour. Planar convective diffusion controlled mass transfer should have a wind pumping cyclic displacement dependence.

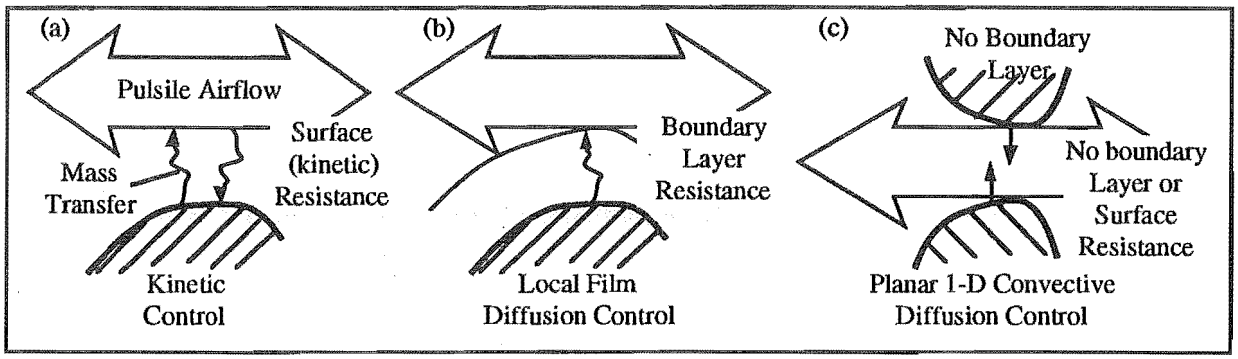

Figure 5.1. Illustration of the types of Mass Transfer Control Mechanisms: (a) Kinetic. (b) Local Film Diffusion. (c) Planar 1-D Convective Diffusion. Although in this experiment micro-scale naphthalene concentration gradients may exist in any direction, the macro-scale gradient is horizontal.

5.5. Apparatus

The experimental apparatus used to measure the mass loss rates under the influence of the wind pumping mechanism is illustrated in figure 5.2.

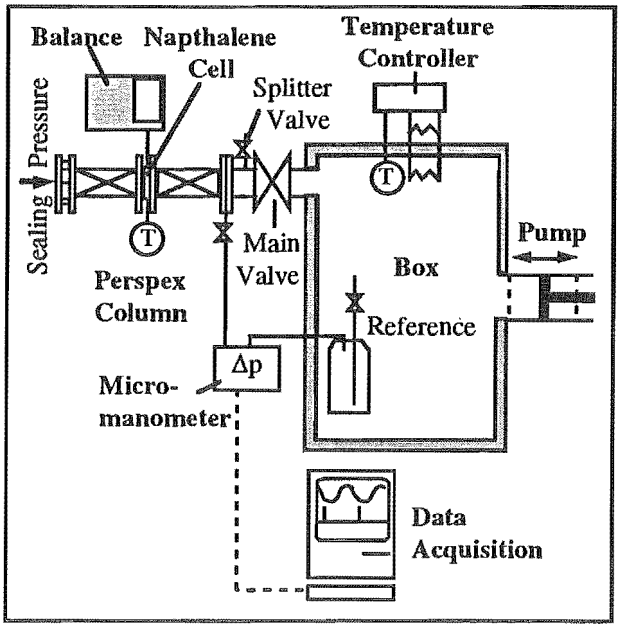

Figure 5.2. Schematic of the Wind Pumping Mass Transfer Apparatus.

5.5.1. Design Concept

In the experiment a layer of naphthalene beads is placed into the centre of a packed column. This layer may be one to several bead diameters thick and extended across the full column cross sectional area. This is aimed at reducing the problem to one dimension. When surface pressure fluctuations were applied to the end of the packed bed to simulate wind pumping, a pulsile airflow occurred. It is proposed that this pulsile airflow would *accelerate the diffusion of*

naphthalene vapour away from the layer of naphthalene beads, towards both ends of the column.

The naphthalene vapour concentration is assumed to zero at both ends of the packed bed. The bottom end of the packed bed was open to the laboratory. This represents the *free lower boundary condition* as described in section 4.5.1.2.

The column must be constructed and packed with a material that is inert to naphthalene. The plastic beads used in the experiments of Chapter 4 are thought to be ideal. To allow the development of the wind pumping flow regime to be independent of the bed material, the naphthalene must be cast into beads of the same dimensions as the plastic beads.

To prevent naphthalene vapour short circuiting the resistance of the packed bed there must be no leaks over the packed column sections and naphthalene cell portion of the apparatus. This means that some disturbance must be made on the sample, preventing fully *in situ* measurement of mass loss rates. This in turn necessitates a careful mass loss monitoring procedure.

5.5.2. Box and Wind Pumping Apparatus

Apart from the two modifications to suppress gas thermometer effects described in section 5.7.1, the wind pumping apparatus was the same as used in the experiments of Chapter 4 and described in detail in section 4.6.

5.5.3. Column Sections

The two short 0.25 m sections of perspex column used in the experiments of Chapter 4 were used again for these experiments. A full description of the column sections can be found in section 4.6.4. The column sections were modified to provide a dry flat sealing surface for the sealing surface of the naphthalene cell to bed against. This sealing arrangement is described in section 5.5.6.

A steady state concentration profile must be established in the column before steady mass loss rates can be measured. The short sections were used in preference to longer sections because they result in a faster approach to this steady state.

The column was oriented horizontally to allow the mass loss rate measurements to made as much *in situ* as possible

5.5.4. Column Packing

The same plastic beads as used in the experiments of Chapter 4 were used as the inert packing in this series of experiments. The bead properties and packing procedures are described in section 4.6.7. The bed voidage obtained was $\varepsilon = 0.35$.

5.5.5. Naphthalene Cell

The layer of naphthalene beads was contained in the cell illustrated in figure 5.3. The beads were retained in position by wire mesh screens and the cell in turn was clamped tightly between the two column sections.

As the beads lose weight and shrink, they will eventually settle and leave an air gap at the top of the cell. Once an air gap was established the wind pumping flow would short circuit the bed and the mass loss rates fell away. To maximise the time it takes for this to occur, the two mesh retaining screens were pulled together with thin wire. This compresses the naphthalene bed packing and restricts any settling movement.

The weight of the cell was kept below 100 g to enable the use of the sensitive balance (±0.1 mg) to measure the naphthalene mass losses.

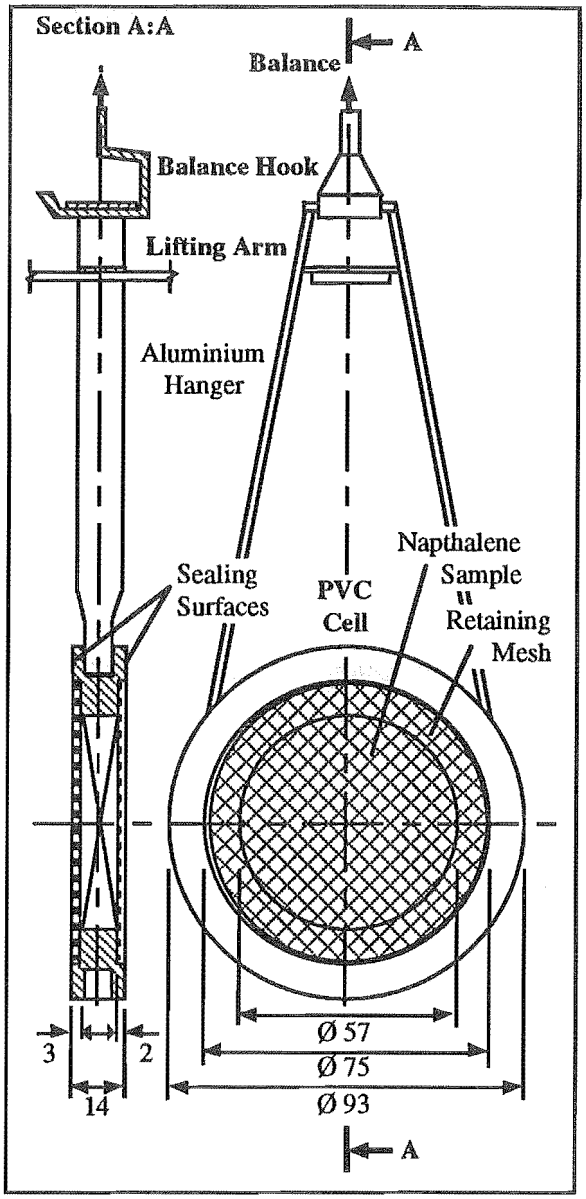

Figure 5.3. Naphthalene Cell and Hanger Details. Scale 1:2. Dimensions in mm.

5.5.6. Cell / Column Sealing Mechanism

The column / cell sealing arrangement developed for accuracy and ease of mass loss measurements is illustrated in figure 5.4.

The column sections were modified to provide a flat dry sealing surface for the naphthalene cell to bed against. The dry seal was designed so that the cell falls free for weight measurement upon the release of the sealing pressure.

A layer of soft 3 mm closed cell foam was glued between the old column sealing surface and the new perspex sealing ring. To align the sealing surfaces, the floating section of the column

was sufficiently mobile to adjust itself into position as the sealing pressure was applied. Any misalignment between the sealing surfaces was adsorbed by the give in the closed cell foam.

The seal was pressurised by a screwing a thread and squeezing the column components between the ends of a rigid frame. All sealing surfaces were polished flat by rubbing the surface down to 1200 grit on a very flat surface and finishing with a rubbing compound.

The maximum gap between the naphthalene beads and plastic beads was about 3 mm, or one bead dimension. This space was required for the wire meshes to hold both the plastic and naphthalene beads in place.

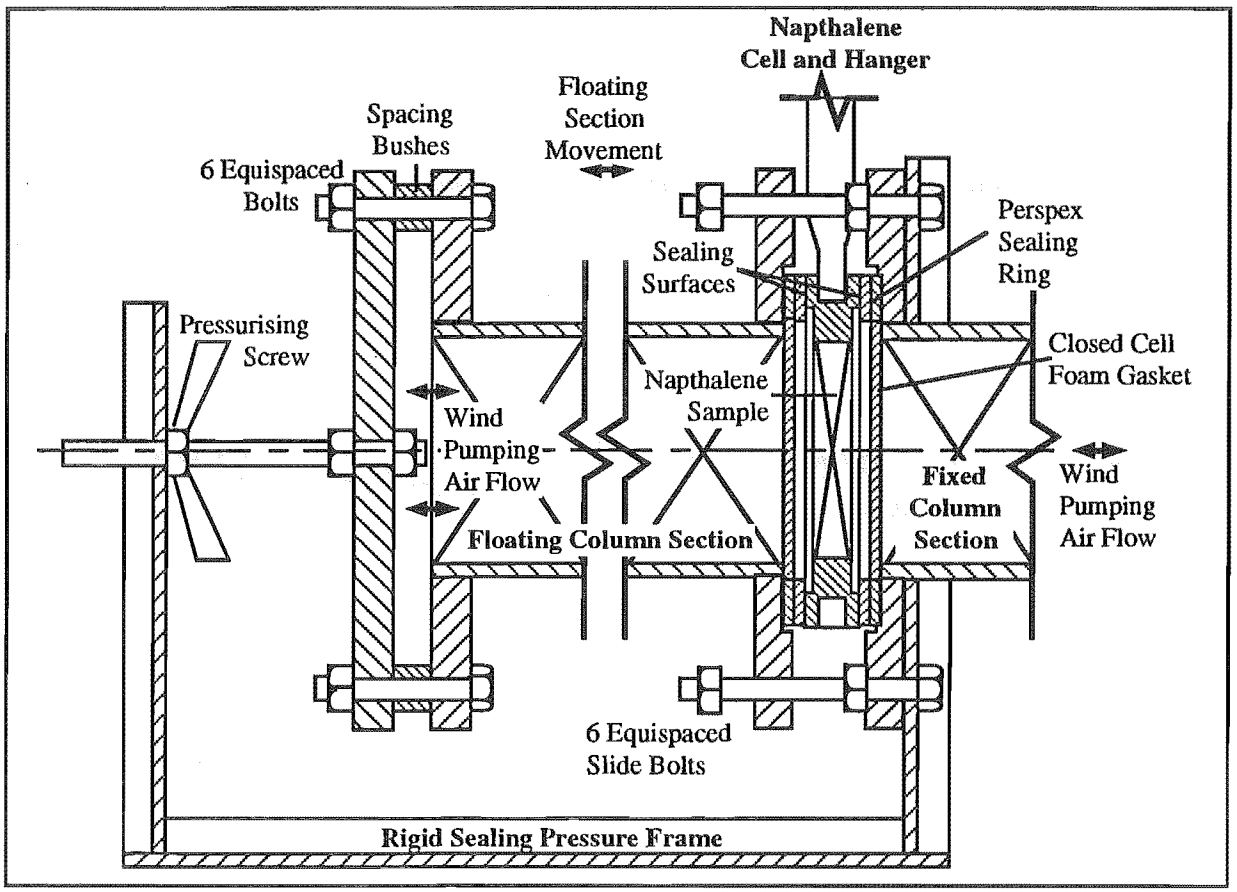

Figure 5.4. Schematic of the Naphthalene Cell Seal and Sealing Pressure Mechanism. An air current shield was fitted over the naphthalene cell using clamps over the two nearby column section flanges. Neither the plastic or naphthalene bead retaining meshes are shown. Approximate scale 1:2.

5.5.7. Radiation Protection

Given the location of the apparatus on the south window wall of the department's Semi-Scale laboratory, all of the box, column and balance were shielded from radiation exchange with the outside environment (day time gains and night time losses). As these mass transfer experiments extended over several weeks, no time-tabling to avoid intense radiation periods (as in Chapter 4) could be made.

5.5.8. Mass Loss Measurement

The naphthalene cell was weighed with a Mettler AE200 electronic balance. The balance is quoted to be accurate to ±0.1 mg, but under the laboratory conditions experienced during the experiments it proved reliable to only ±1 mg. The balance will measure weights of up to 205 g.

5.6. Experimental Procedure

5.6.1. Naphthalene Bead Casting

The naphthalene beads were cast in a 3 mm aluminum plate with a series of Ø3 mm holes drilled through. The resulting 3 mm high by 3 mm diameter beads were close to the average size of the cylindrical beads packed into the column and described in section 4.6.7. Note that the holes were drilled and reamed to give the beads a smooth finish.

The following steps describe the bead casting procedure illustrated in figure 5.5.

1. Cover the bottom end of the casting holes with aluminium foil tape. This must be done in such a way that no tape glue is left exposed to the naphthalene (to the bottom of the holes). If exposed, the glue tends to end up on the bottom surface of the beads, reducing the effective surface area for mass transfer.
2. Heat casting plate to slightly above the naphthalene melting point.
3. Pour liquid naphthalene over the casting plate, filling the holes and leaving a thick excess over the plate.
4. Remove any trapped air bubbles with a hot soldering iron before the naphthalene begins to solidify.
5. As it solidifies the naphthalene tends to

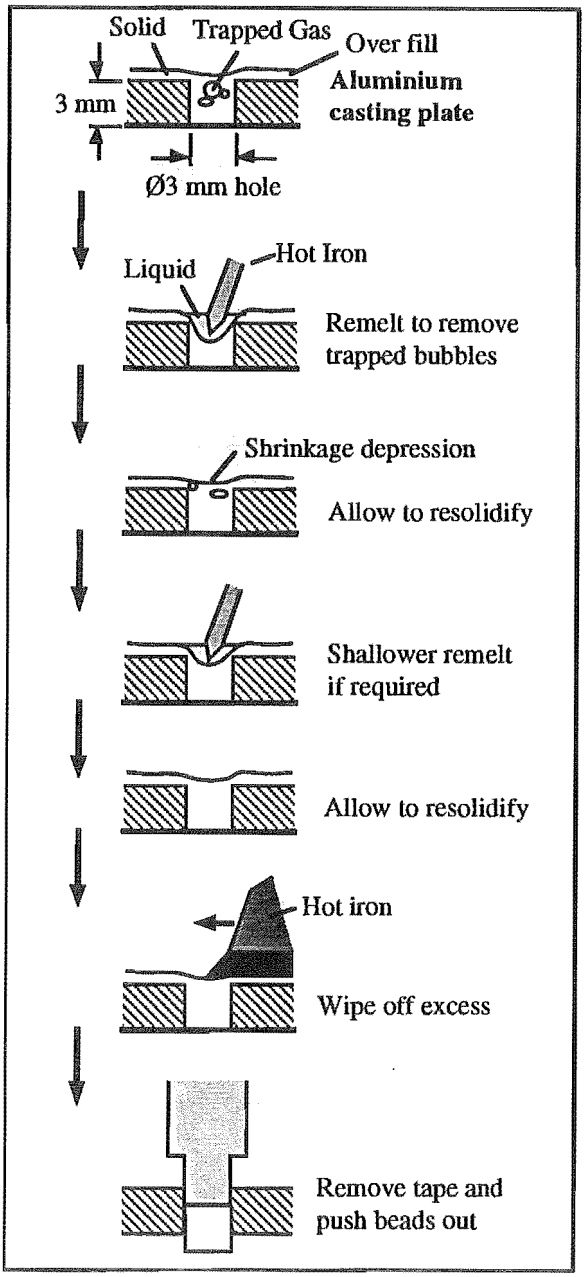

Figure 5.5. Naphthalene Bead Casting Procedure.

degas and shrink resulting in trapped gas bubbles in the holes. Remelt the naphthalene around trapped gas bubbles with hot soldering iron to bring the bubbles to surface and then allow to resolidify. This part of the procedure may be repeated several times.

6. Once the holes are sufficiently degassed and fully solidified the excess naphthalene is wiped away with a hot flat iron, without remelting the naphthalene in the holes. It is important to over fill (step 3) as this use of the hot iron produces the best finish.
7. Allow the plate to cool. Note that the slower the cooling process the better bead surface finish attained.
8. Finally the backing tap is removed and the beads carefully pushed out of the holes.

The casting plate used to produce the beads for this experiment produced 30 beads per fill. Around 300 beads were required to fill the naphthalene cell.

The surface finish on the cast beads was fairly rough, generally as a result of pushing them out of the casting plate. Consequently new beads were left for several days before use to allow the small asperities (fragments attached to the beads) to sublime away. Although the diffusion process proved to be surface area independent (see section 5.7.2) this was still done as a precautionary measure.

5.6.2. Mass Loss Rate Measurement

Mass loss rates were calculated by periodic measurement of the amount of naphthalene remaining in the naphthalene cell. The mass loss between measurements was generally very small. requiring the use of a very sensitive balance.

The naphthalene cell was clamped into place between the packed column sections to effect the required seal. To measure the weight of the cell, this seal must broken. It was found in tests that removal of the cell from the apparatus for weighing destroys the concentration profile established in the cell itself, and in the column close to the cell. Given the time period required for steady state to be established (see section 5.7.3) a less disruptive *in situ* method was developed.

This procedure, described below, takes around 15 seconds to complete.

1. Quickly close the main valve, *then* turn off the pump if required.
2. Unscrew the pressurising screw and slide floating section away from the cell.
3. Drop the cell with the lever onto the balance hook. In doing this the cell swings away from the other sealing surface - no part of the cell can be touching anything other than the balance hook.
4. Wait for the weight measurement to stabilise, then take the reading.
5. Lift the cell back into the sealing position with the lever.

6. Push the floating column section closed and pressurise seals with the screw mechanism.
7. Quickly open the main valve (turn pump on *first* if turned off in step 1).
8. Note laboratory temperature and pressure for buoyancy corrections.

Additional Notes

* The measured mass loss rates are not relevant until the column attains a steady state concentration profile.
* To minimise disruption to the column concentration profile, the air in the column must be still when the seal is broken .
* If the pump is turned off without first closing the main valve, and the box left pressurised, sufficient air could flow from the box replacing the air in the column and completely destroy the concentration profile.
* The distance the two column sections are separated when making a weight measurement is the minimum amount required to get the cell free hanging on the balance hook. This is minimised by the ease of separation of the dry sealing surfaces.
* As an additional precaution against mass loss, the inside of the air current shield is coated with naphthalene to create a high concentration naphthalene atmosphere in the vicinity of the cell.

5.7. Experimental Problems

This section details several key extensions to the basic experimental concept aimed at overcoming some very inconsistent initial mass loss rate measurements. However, the resulting modifications do not completely nullify the apparent variability seen in the final results. This is further discussed in section 5.9.2.

5.7.1. Suppression of Gas Thermometer Effects

A relatively small change in box temperature, compared to temperature changes seen in the laboratory, created significant movement of air in or out of the box through the column. As illustrated in figure 5.7, the resulting flow severely effected the mass transfer rates as the steady state concentration profile in the column was disrupted.

Gas thermometer flows were suppressed in two ways:

1. Box temperature control.
2. A wind pumping flow splitter.

Each of these is described below.

5.7.1.1. Box Temperature Control

The box was controlled to within ±0.5°C with a Mark I Proportional Thermistor Bridge Temperature Controller and 22 kΩ Thermistor Probe. The output of the controller powered two 150 W lamps connected in parallel. Only one was required for the heating duty within the box. The second lamp provided the load that was required by the controller to function and was positioned outside the box. The control circuit is illustrated in figure 5.6.

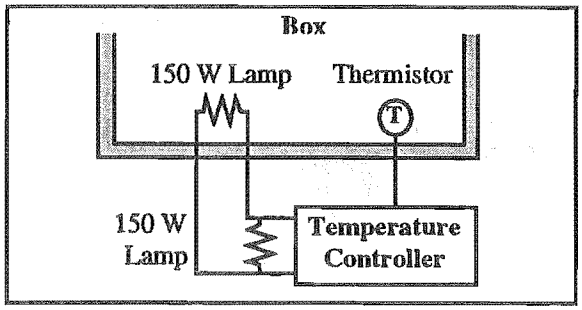

Figure 5.6. Box Temperature Control Circuit.

No cooling was provided in the box so the controller was set to maintain the maximum envisaged box temperature of 31.0°C attained by heat exchange with ambient laboratory conditions.

5.7.1.2. Flow Splitting

The wind pumping flow was split approximately 50% / 50% between the column and a fast leak to the laboratory. This fast leak, fitted to the apparatus specifically for these mass transfer experiments, operated at all times during the mass transfer experiments. The position of the valve controlling the fast leak (splitter) is illustrated in figure 5.2.

The effect of the fast leakage was to balance the long term average pressure on both sides of the column thus preventing any nett flow. As 95% of the temperature fluctuation amplitude after the temperature control is applied is diurnal, the flow splitter should prevent any net flow.

5.7.1.3. Resulting Changes in the Diurnal Mass Transfer Rates

The mass transfer rates from tests before and after the suppression of gas thermometer flows are shown in figure 5.7 and 5.8 respectively. Both sets of data have also been corrected for buoyancy effects. The improvement in mass loss rate stability was resounding.

5.7.2. Mass Transfer Rate Dependence on Surface Area

From the discussion in section 5.4.1, if the rate of mass transfer has a surface area dependence, it is likely to be kinetically or film controlled.

In tests with varying naphthalene cell depths (1, 2, 3 + layers of naphthalene beads) mass loss rates were measured for various wind pumping conditions. Two examples from these tests are outlined in table 5.1.

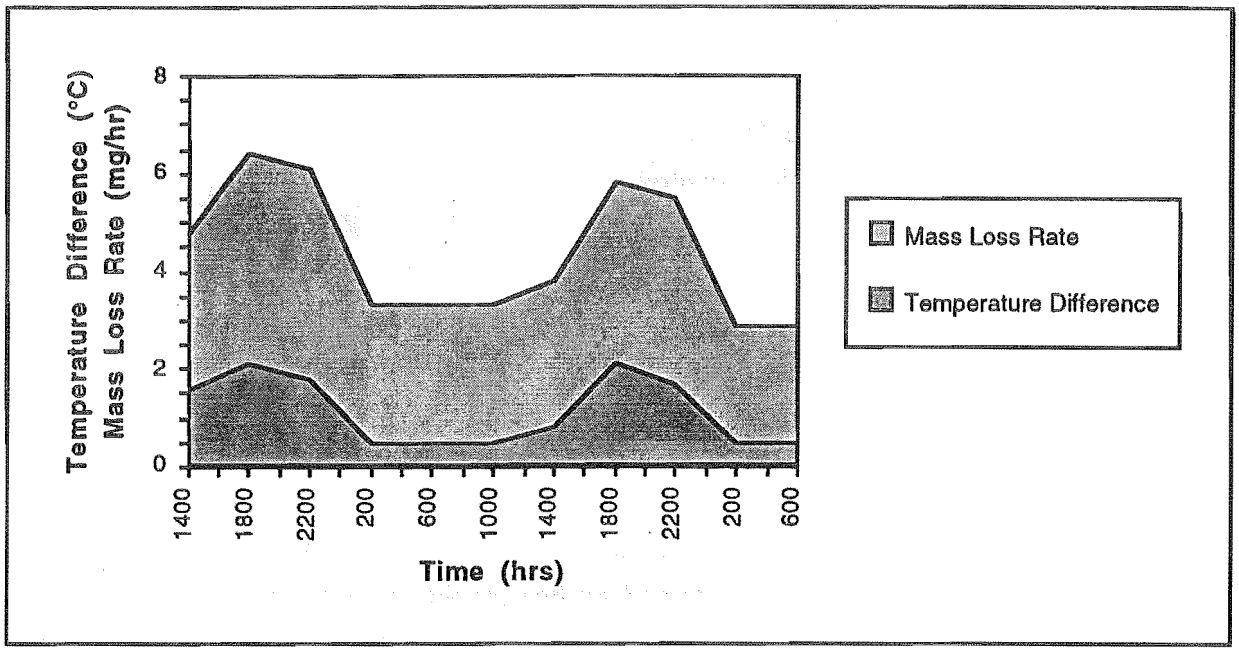

Figure 5.7. Trends in Diurnal Naphthalene Mass Loss Rates from the Cell and Absolute Differences in Temperature Between Measurements Over 2 Days *Without* Gas Thermometer Flow Suppression.

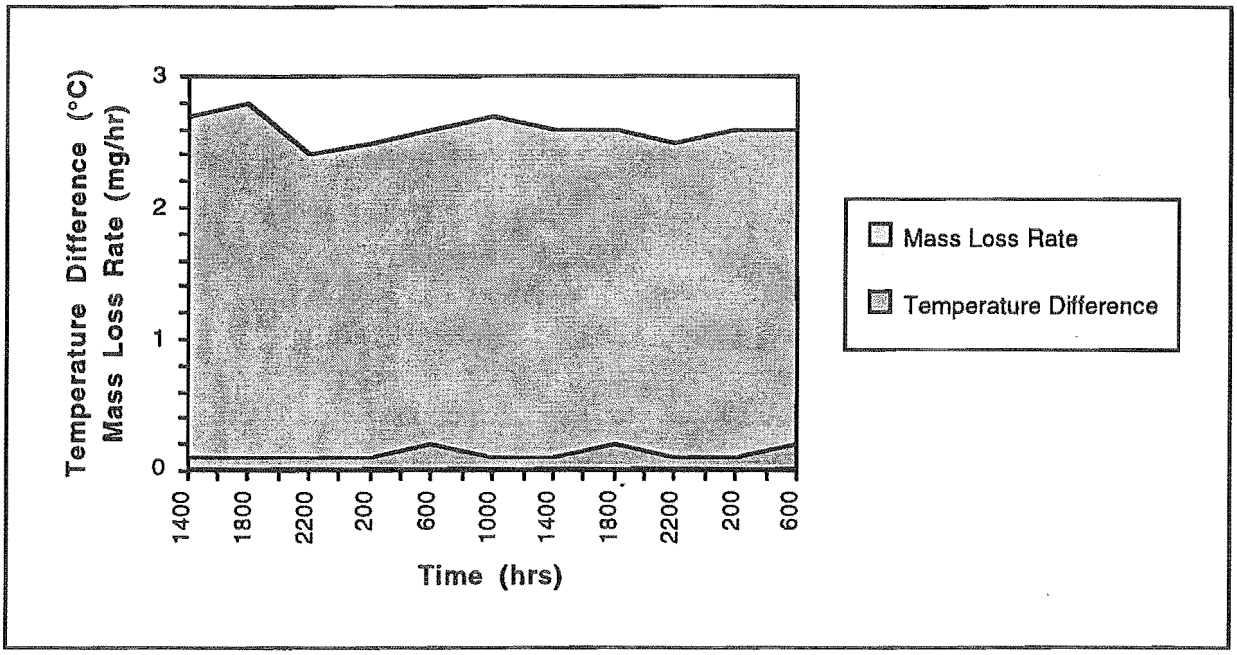

Figure 5.8. Trends in Diurnal Naphthalene Mass Loss Rates from the Cell and Absolute Differences in Temperature Between Measurements Over 2 Days *With* Gas Thermometer Flow Suppression.

The surface area was directly proportional to the mass of beads in the cell as all beads were approximately the same dimensions. It can be seen from this table that the *ratios of relative mass loss rates were inversely proportional to the ratios of initial masses of naphthalene beads, and therefore surface area.* Also the absolute mass loss rates appear independent of the total surface area. It can therefore be concluded that the *sublimation rate was high enough for the process not to be controlled by surface kinetics, nor by local film diffusion.*

Test	Layers (approx.)	Initial Total Mass (g)	Change in Mass (g)	Time Elapsed (hrs)	Mass Loss Rate Relative (%/hr)	Mass Loss Rate Absolute (g/hr)
1a	3	15.4388	0.362	20:50	0.113	0.0174
1b	1	6.2469	0.313	17:50	0.281	0.0176
		ratio			1 / ratio	discrepancy
		2.47			2.49	1.1%
2a	2	9.3700	0.139	16:00	0.092	0.0087
2b	1	5.3894	0.184	20:00	0.171	0.0092
		ratio			1 / ratio	discrepancy
		1.74			1.86	5.4%

Table 5.1. Tests on the Influence of Naphthalene Surface Area on Mass Loss Rates. Both runs in each pair were made at identical wind pumping frequencies and amplitudes, and consequently have identical peak velocities and cyclic displacements. Note that the 'Layers' are layers of naphthalene beads.

5.7.3. Steady State

Mass loss rates were not recorded until reasonable steady state was reached. For the column which had been flushed with fresh air and high degrees of wind pumping, this took around 24 hours. For the same initially flushed column and low intensity wind pumping, 48 hours was required. An example of the former case is illustrated in figure 5.9.

Note that the data for figure 5.9 was recorded prior to the installation of the flow splitter described in section 5.7.1. It was presumed that the continuing slow fall off in mass transfer rate seen in figure 5.9 was due to the slow build up of naphthalene vapour in the area above the column on the wind pumping side. This is further discussed in section 5.7.4.

In most cases the experimental conditions were changed between runs without removing the naphthalene cell and disrupting the previously established concentration profile. The cell had to be removed if more naphthalene was required in the cell. Despite this precaution the time to steady state was not seen to differ.

The short length of the column used in the experiment reduces the time it takes to reach a steady state concentration profile and consequently the time to reach steady mass loss rates.

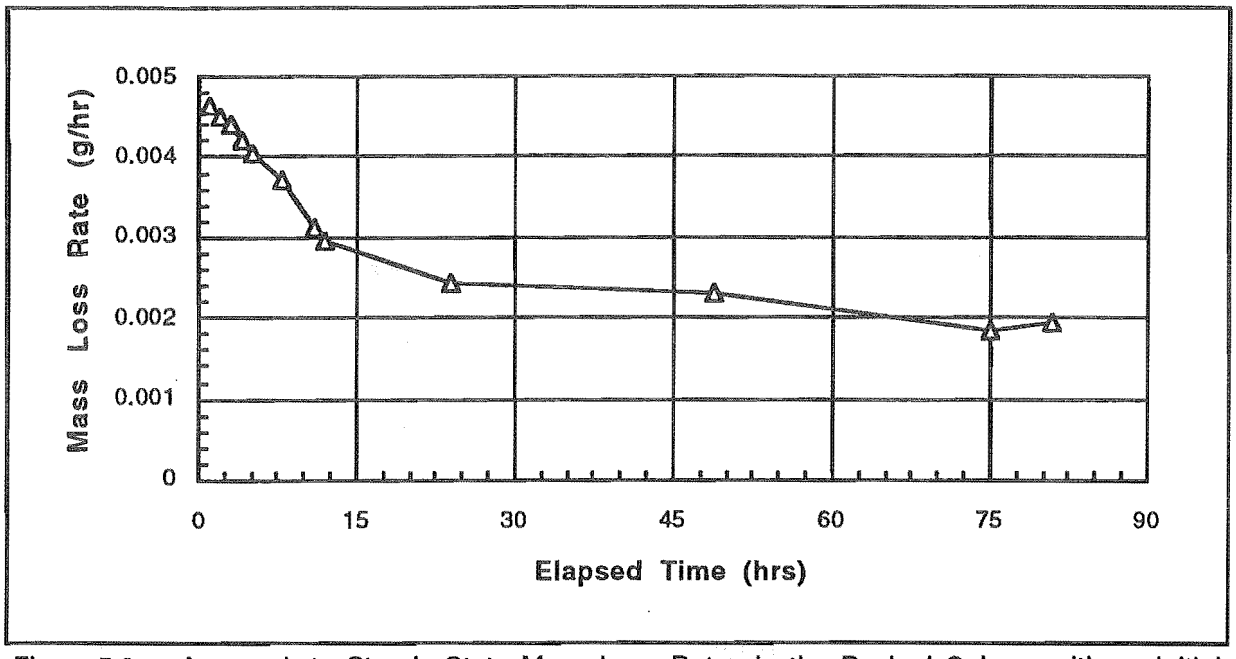

Figure 5.9. Approach to Steady State Mass Loss Rates in the Packed Column with an Initial Naphthalene Vapour Concentration Profile from a Previous Run. A period of $\tau = 3.2$ s and amplitude of $P_c = \pm 40$ Pa were used.

5.7.4. Build Up of the Naphthalene Vapour Concentration in the Box

The flow splitter used to suppress gas thermometer effects (see section 5.7.1) serves a second purpose; namely to minimise the build up of naphthalene vapour on the wind pumping box side of the packed column. The flow splitting valve continually flushes air in and out of the ducting on the box side of the column, thus preventing any naphthalene vapour concentration build up at this point.

5.7.5. Corrections for Buoyancy

Given the following points, fluctuations in the measured weights were expected due to buoyancy effects.

* The volume of the naphthalene cell, hanger and naphthalene beads was around 100 ml.
* Mass losses were measured in micrograms.
* Air density fluctuates between about 1.15 and 1.20 kg/m^3 in the ambient laboratory conditions.

The relationship between the measured weight W_a, and density of the laboratory air ρ_{air}, can be written as

$$W_a = W_v - (V_{ns} + V_{nb})\rho_{air} \qquad 5.1$$

where W_v is the weight in a vacuum, V_{ns} is the volume of the naphthalene cell and hanger and V_{nb} is the volume of the naphthalene beads. From the expected air density fluctuations, the measured weight was expected to vary by about ± 2.5 mg. Given that the hourly loss rate of

naphthalene was generally less than 3 mg/hr, and may be as low as 0.2 mg/hr, a calibration was made for buoyancy effects. An alternative to buoyancy corrections is to make mass loss measurements over longer periods.

5.7.5.1. Buoyancy Correction Tests

Weight measurement tests were performed on the empty naphthalene cell over 9 days. During this period diurnal temperature fluctuations, and two synoptic scale weather systems with the associated pressure changes, were experienced in the laboratory. Using the ideal gas law ρ_{air} is calculated from

$$\rho_{air} = 0.00348 \frac{\overline{P}}{T_{air}} \qquad 5.2$$

where $\overline{P}$ is the atmospheric pressure and T_{air} the ambient temperature. The temperature was measured inside the air current shield with a Fluke 52 J/K digital thermometer and the atmospheric pressure with a Casella 4898 barometer.

Figure 5.10 shows the relative changes in air density along side the relative changes of naphthalene cell weight. The two scales of change (diurnal and synoptic) are both evident with the two variables appearing moderately correlated (correlation coefficient of 0.5).

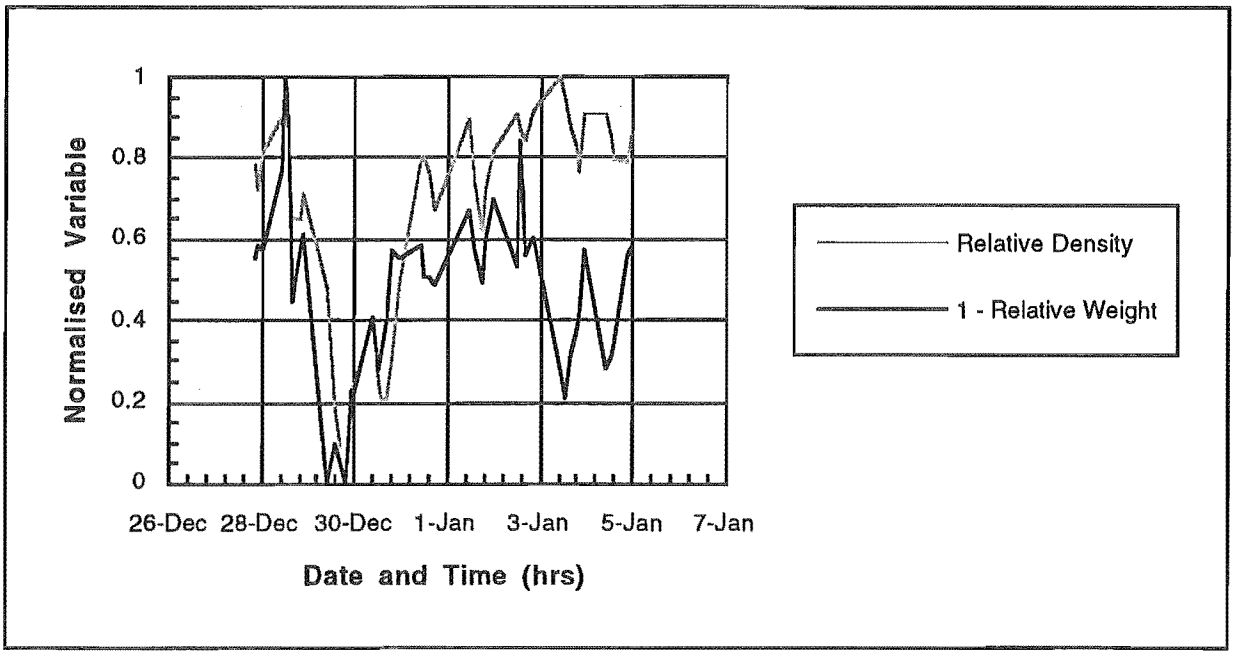

Figure 5.10. Inverse Relation between Relative Air Density Changes and Relative Naphthalene Cell Weight Changes Over a 9 Day Period. The range of 0 to 1 represents 0.057 kg/m^3 for density and 0.0069 g for cell weight.

Figure 5.11 shows the measured weight plotted against air density. The linear regression has a slope of -51 ml which is very close to the measured volume of the empty naphthalene cell (52±3 ml), which is predicted as the slope from equation 5.1. This apparent accuracy must be treated with caution given the scatter in the results.

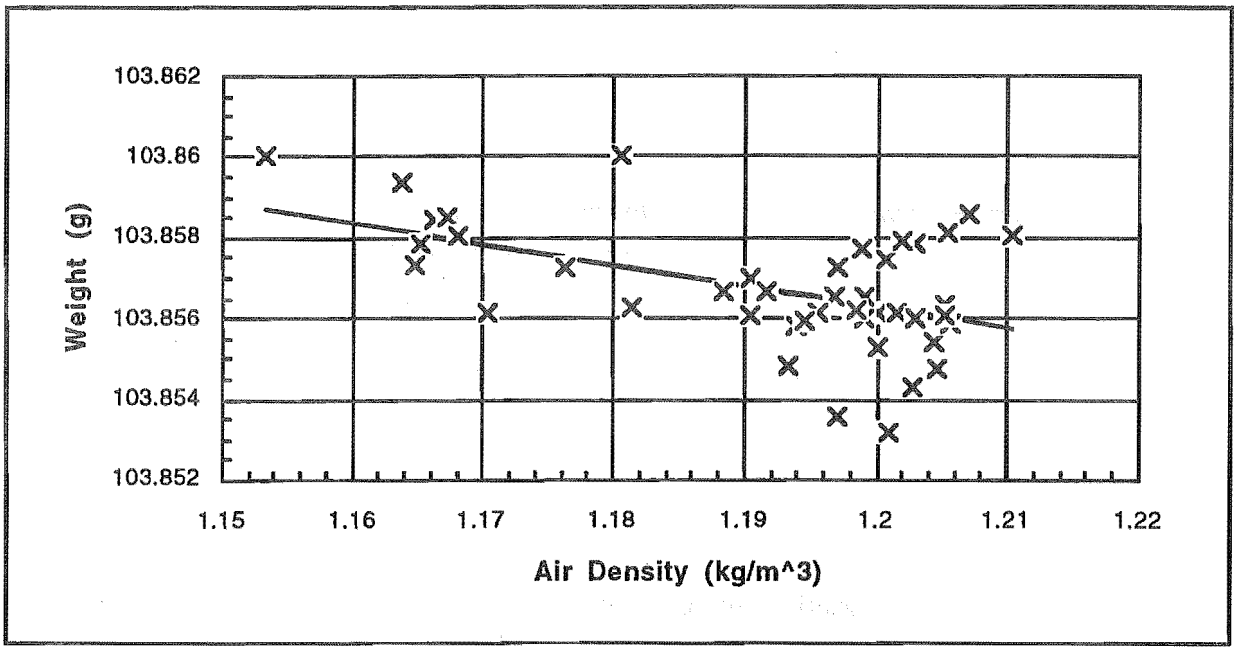

Figure 5.11. Measured Weights of the Empty Naphthalene Cell Plotted Against Air Density Over a 9 Day Period. The linear regression fitted has a slope of -51 ml.

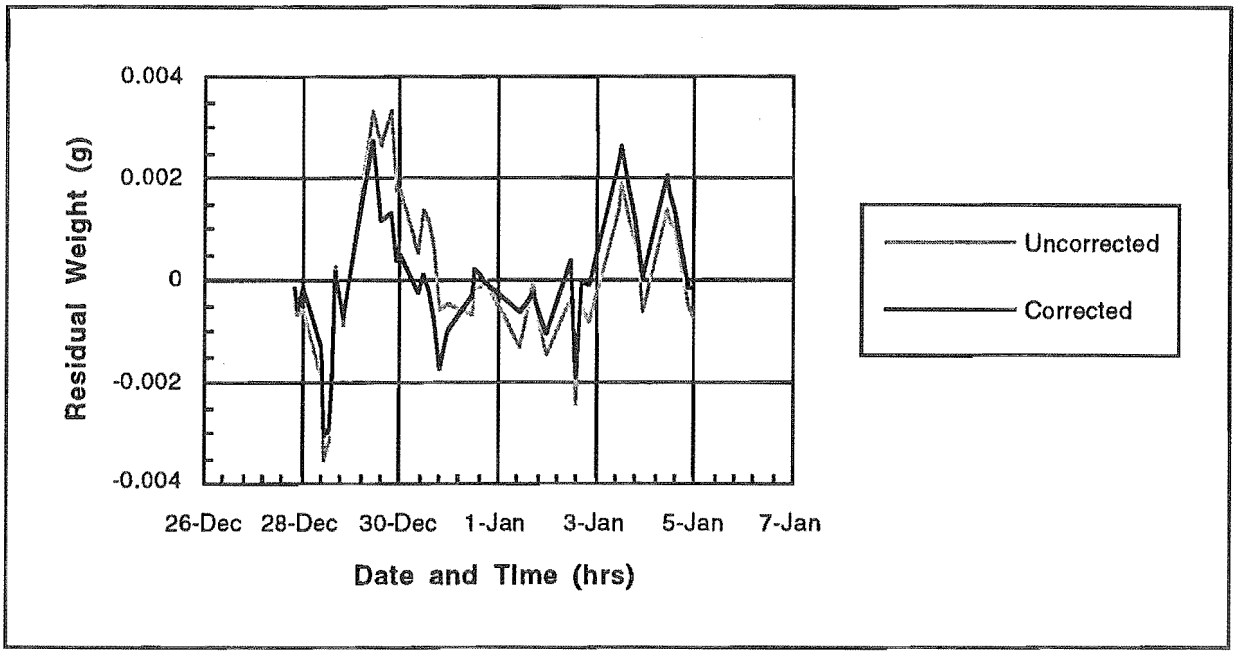

Figure 5.12. Naphthalene Cell Residual Weight (weight less the mean weight) Over a 9 Day Period Before and After Buoyancy Correction.

Figure 5.12 shows the weight measurements less the mean weight (residual weight) before and after buoyancy correction. The improvement in the results is only slight; $\sigma_{Uncorrected} = 1.5$ mg and $\sigma_{Corrected} = 1.3$ mg.

5.7.6. Errors in Mass Loss Measurements

Figure 5.12 gives a good estimate of the variability in weight measurements, as the 9 day period over which the empty naphthalene cell was monitored included the whole range of laboratory atmosphere conditions experienced during the experimental period (990 to 1020 mbar and 17 to 25°C). For a single measurement, the error was taken as ±3 mg. This determined the length of time any one weight loss measurement had to be made over to get a significant result.

5.8. Experimental Programme

To examine the effects wind pumping has on the diffusive mass transfer rates in a packed bed, the wind pumping airflow conditions imposed on the bed should approximate those expected in a natural snow pack. To achieve this, the number of grains the air passes by in each cycle was made equivalent between the natural snow and laboratory configurations. This should also make the Reynolds numbers of the two configurations approximately equal.

Unfortunately the wind pumping mechanism designed for the air flow dynamics experiments of Chapter 4 was not capable of the low frequency pulsations observed in the field (see Chapter 3). Consequently only a small range of relatively high frequencies could be investigated. Three periods of fluctuation were chosen; $\tau = 3.2$ s, 6.7 s and 10.3 s.

In section 4.9.2.2 it was decided that the finite-sealed bed theory was most likely to represent the seasonal snow pack. From Figures IX.2 and IX.3, for a period of $\tau = 10$ s, surface amplitude of $P_c = \pm 30$ Pa (strong winds) and d = 3 m snow pack (seasonal), an interstitial displacement of around $S_z = 2$ mm is likely to result near the snow surface. This is around 4 ice grains of diameter 0.5 mm. To give a *passage of air past the **same number of grains*** in the column packed with 3 mm plastic beads, an interstitial displacement of around $S_z = 12$ mm was required. From the free bed theory (see equation 4.36, section 4.5), the pressure fluctuation amplitude that gives this displacement was approximately ±40 Pa. Pressure fluctuation amplitudes ranging between $\pm 15 < P_c < \pm 120$ Pa were chosen for investigation.

The mass loss rates measured for the above wind pumping conditions could then be compared to runs in which there was no wind pumping (stagnant air).

Note that the accumulation of mass transfer data is a very slow process. To get the accuracy indicated by section 5.7.6, each measurement requires at least two days to make. For runs with no wind pumping the measurement error remains very high, even after four days. Consequently the results presented in the following section took about five months of almost continuous operation to accumulate.

5.9. Results

5.9.1. Mass Loss Rate Comparisons

The mass loss rate results are presented in six ways:

1-3 In the first three ways; the loss rate (g/hr) is plotted as a function of the applied surface pressure swing ($\pm P_c$) in figure 5.13, the peak velocity in the naphthalene bed in figure 5.14, and the cyclic displacement in the naphthalene bed in figure 5.15. All of these are plotted for various periods.

4 In figure 5.16 the mass loss per wind pumping cycle is compared to the cyclic displacement in the naphthalene bed, again for various periods.

5-6 Figures 5.17 and 5.18 isolate peak velocity and cyclic displacement dependencies in an attempt to identify the mechanism of diffusion control. In section 5.7.2, kinetic control and local film diffusion were ruled out as controlling mechanisms. A check on the latter is in order here.

Whilst the relationships between mass loss rates and wind pumping variables were not assumed to be linear given the scatter in the data, the linear trends are illustrated in these figures. In all cases these linear trends are forced through the mass loss rate obtained for no wind pumping in the column. This stagnant air mass loss rate measurement was replicated six times during the five month experimental programme. The results did not have the variability evident in the wind pumping results because the main valve was closed, isolating the column from the box and pump. The resulting mass loss average over the runs was $\dot{m} = 0.10 \pm 0.01$ mg/hr).

The most obvious and important result from these experiments is the very large (one to two orders of magnitude) enhancement in naphthalene mass loss rates under imposed sinusoidal wind pumping conditions compared to stagnant air diffusion. This enhancement increases almost linearly with an increase of wind pumping intensity. The enhancements found here are significantly larger than the enhancements factors of 2 to 4 found by Scotter *et al* (1967) and Scotter and Raats (1969) in the soil studies ($Re_p \ll 1$).

Figure 5.12 to 5.15 all illustrate the dependence the mass loss rate has on both intensity and magnitude of the applied wind pumping. Figure 5.16 shows that the dependence on period is approximately linear. This supports the distance equivalence (number of grain diameters) used to choose the range the variables were to be investigated over.

For constant peak velocities, both figures 5.17 and 5.18 show strong cyclic displacement dependent trends. The greater the cyclic displacement, the greater the mass loss rate per cycle. For constant cyclic displacements, both figures 5.17 and 5.18 exhibit weak peak velocity dependent trends. At higher peak velocities, the mass loss rates per cycle are slightly lower.

These features indicate that the *mass transfer rates are controlled by planar 1-D convective diffusion*, and that *2nd order boundary layer or local film effects are evident.* This smaller effect of velocity supports the finding in section 5.7.2 that neither the boundary layer film, or the surface kinetics control the rate.

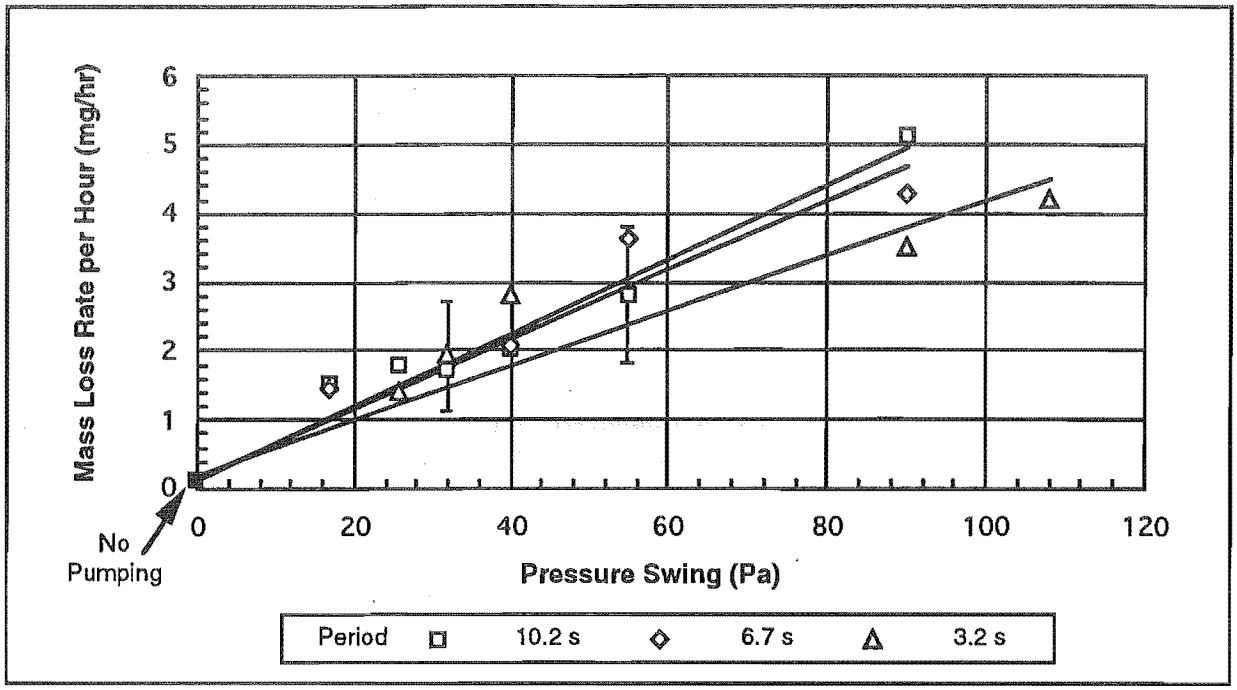

Figure 5.13. Mass Loss Rates per Hour from the Naphthalene Bed vs Surface Pressure Swing for Various Periods. The two example error bars shown are ±2 replicate standard deviations. The "no pumping" result has an error of ±0.01 mg/hr.

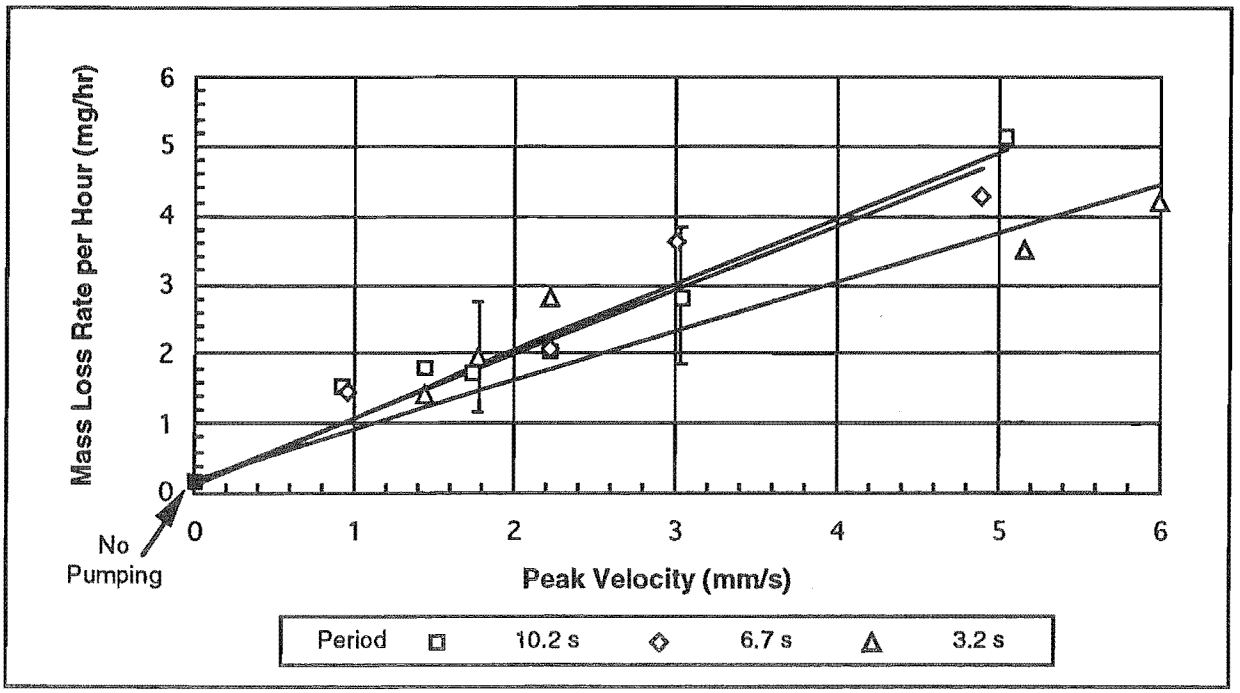

Figure 5.14. Mass Loss Rates per Hour from the Naphthalene Bed vs Peak Velocity for Various Periods. The two example error bars shown are ±2 replicate standard deviations. The "no pumping" result has an error of ±0.01 mg/hr.

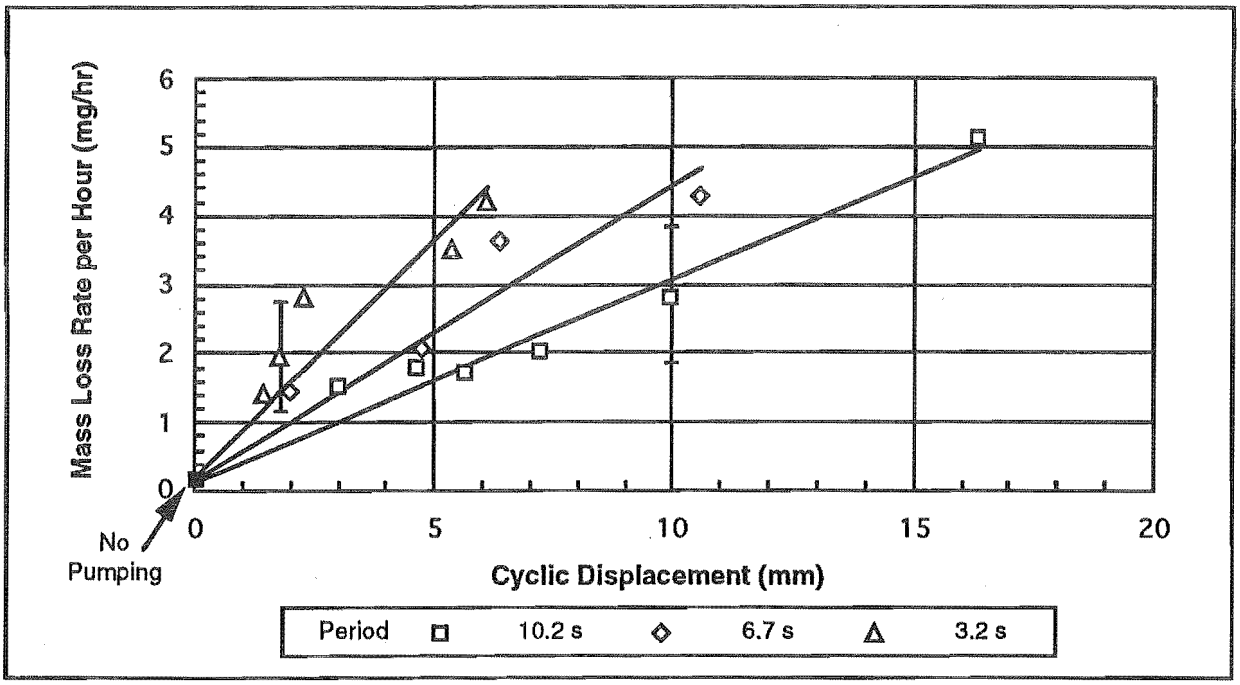

Figure 5.15. Mass Loss Rates per Hour from the Naphthalene Bed vs Cyclic Displacement for Various Periods. The two example error bars shown are ±2 replicate standard deviations. The "no pumping" result has an error of ±0.01 mg/hr.

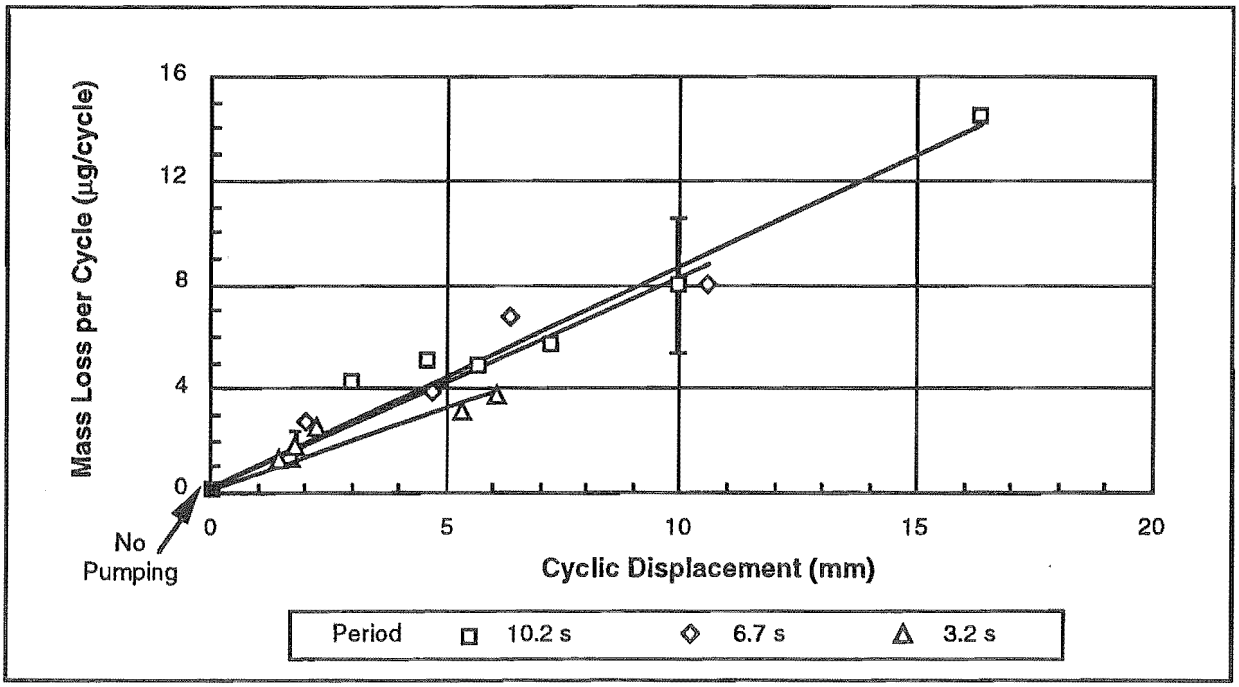

Figure 5.16. Mass Loss per Wind Pumping Cycle from the Naphthalene Bed vs Cyclic Displacement for Various Periods. The two example error bars shown are ±2 replicate standard deviations. The "no pumping" result is a little arbitrary here because it has no period. An approximate was taken by using a period of 10.2 s, so $\dot{m} = 0.003 \pm 0.0003$ µg/hr.

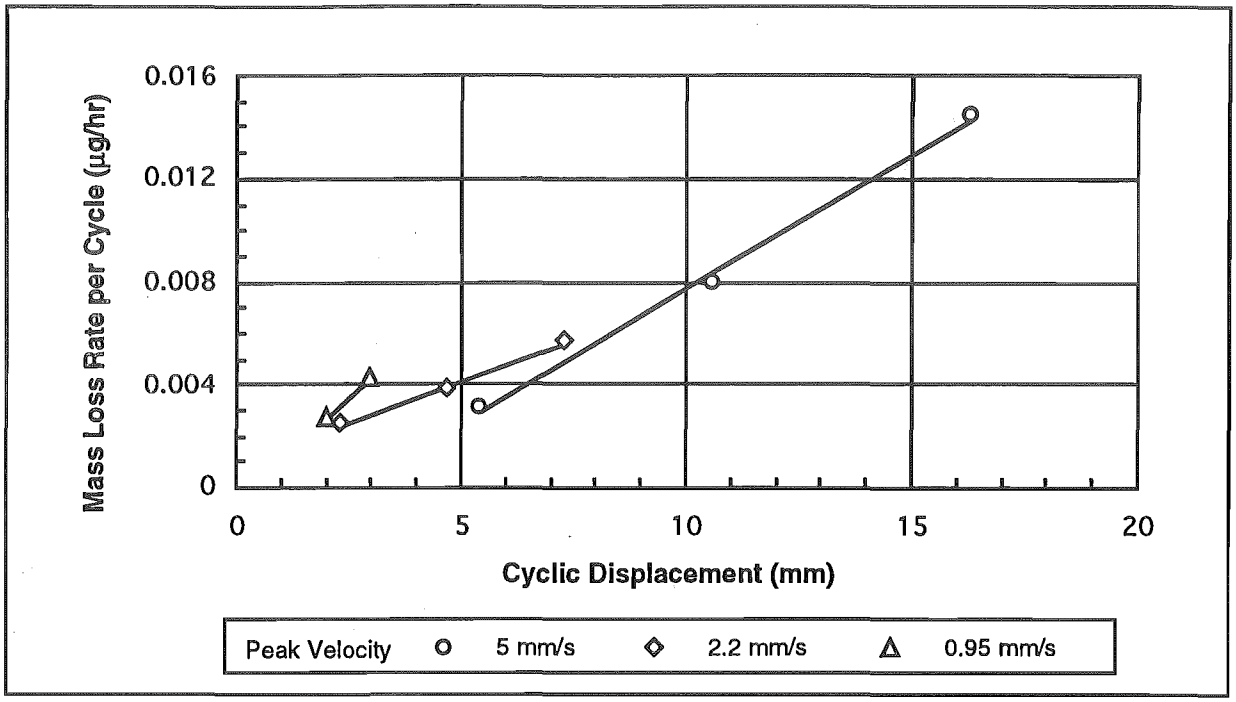

Figure 5.17. Mass Loss Rates per Cycle from the Naphthalene Bed vs Cyclic Displacement for Various Peak Velocities.

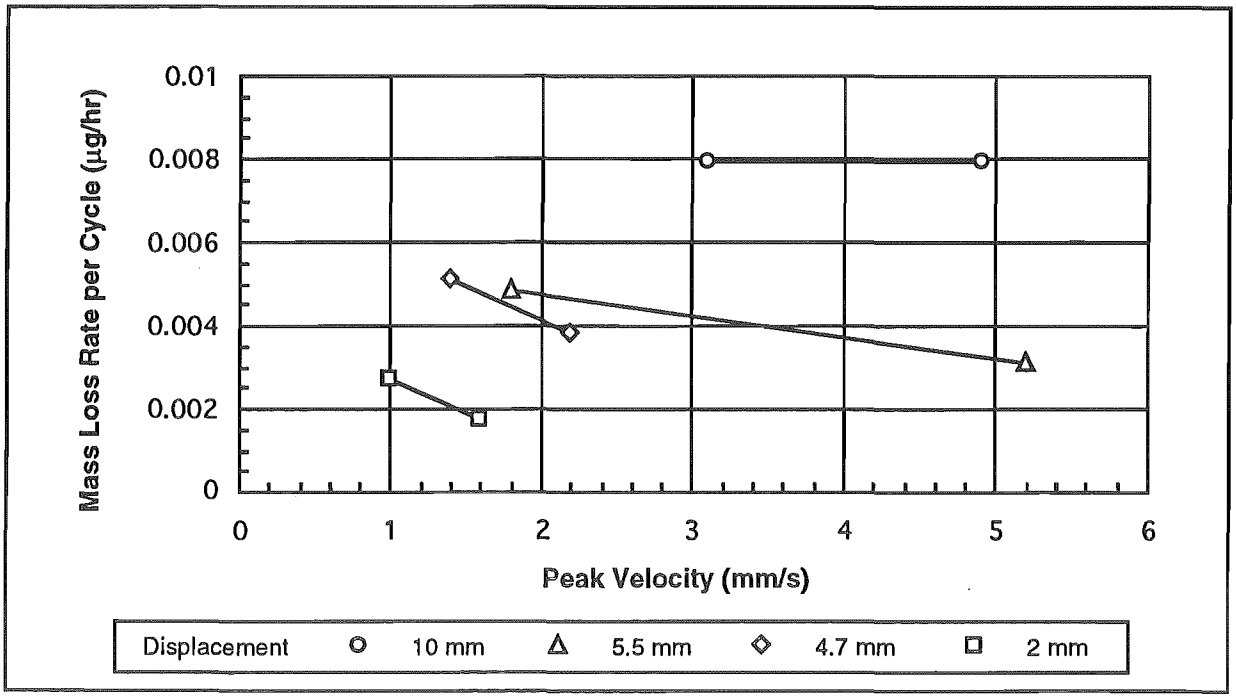

Figure 5.18. Mass Loss Rates per Cycle from the Naphthalene Bed vs Peak Velocity for Various Cyclic Displacements.

5.9.2. Measurement Variability and Errors

The results from this experiment exhibit considerable inconsistencies.

Most of the data points in the figures 5.13 to 5.16 were at least replicated. Error bars, representing ±2 replicate standard deviations, for two points with four replicates are shown in these figures. The variability illustrated by these error bars stems from the lack of repeatability between independent measurements. For example, the variation of successive weight readings, which go to make up a mass loss rate measurement for a particular wind pumping setting, have a variability of up to ±100% in some cases.

Although no trends are observed between the individual weight measurements and any other recorded variables (box temperature, naphthalene cell temperature, ambient pressure or time of day), there does appear to be some underlying source of variability which has not yet been isolated[1]. The effect of this unknown factor was however observed to be random, and did not introduce a time trend.

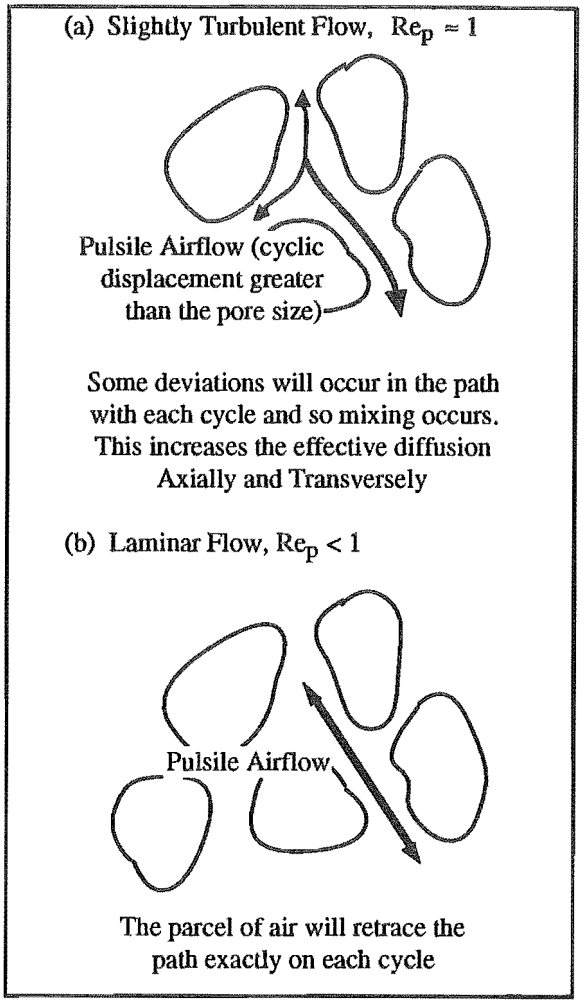

Figure 5.19. The Dependence of Mixing on Bed Reynolds Number.
(a) Laminar Flow, $Re_p < 1$.
(b) Slightly Turbulent Flow, $Re_p > 1$.

5.9.3. Relating These Results to Snow Metamorphism

Several terms associated with the changes of snow grains and snow pack structure are used in this section. For background explanations of these terms, refer to Chapter 1.

---

[1]The time consuming nature of this experiment, performed in the latter stages of this PhD programme, precluded any further experimental design refinements beyond those detailed in section 5.7 being made.

Two scales need to be considered; *macro scale*, more than a few grain diameters, and *micro scale*, a single grain, or pore space, or smaller. Mass transfer processes occurring on either scale will be influenced by any interstitial air mixing.

It is worth noting at this point the mechanics of interstitial air mixing in the bed. Figure 5.19(a) illustrates how slightly turbulent flow will cause some deviations in the cyclic movement of a parcel of air. The result of this is an increase in the effective diffusion both axially and transversely. Note that for this turbulent mixing to exist, the cyclic displacement must be greater than the pore size. As illustrated in figure 5.19(b), if the flow was strictly laminar, the parcel of air would follow exactly the same path on each cycle.

The bed Reynolds number limits on laminar flow in a packed bed occur at about $Re_p = 1$ (Bear, 1972). It has been established that the bed Reynolds numbers for wind pumping airflows were close to, but not greater than 1 (see table 4.1). It is quite possible, that in some smaller than average interstitial channels in the bed, the bed Reynolds is greater than 1. Hence this mixing mechanism is possible.

5.9.3.1. Dependence of Bed Reynolds Number on Interstitial Air Mixing

Even at low Re_p enhance mass transfer will occur provided the path length is larger than the stagnant air diffusion length. This is because the effective diffusion will increase by movement of material from one surface to another.

5.9.3.2. Snow Grain Growth

The parcel of air that sweeps through a common path in each wind pumping cycle should have a vapour concentration that is approximately the average of the vapour sources and sinks that it passes by. This must reduce the mean time a water vapour molecule takes to travel from its source to relevant sink, thus increasing the mass transfer rate.

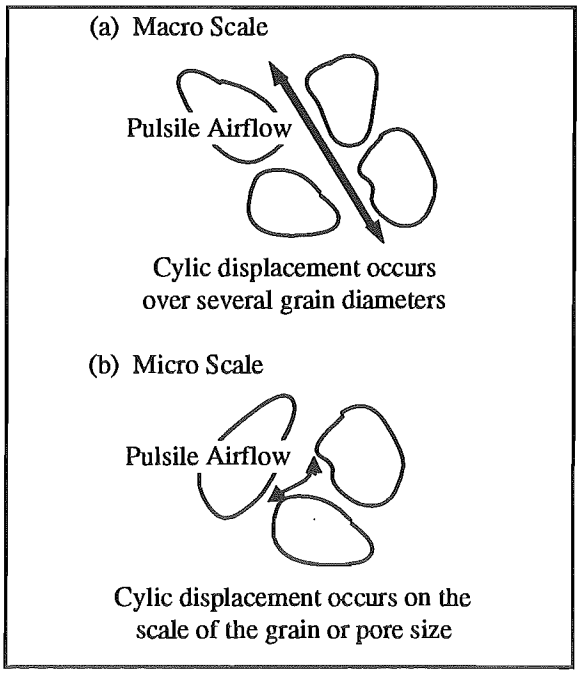

Figure 5.20. Illustration of Macro and Micro Scale Cyclic Displacements.

Although both faceting and rounding processes occur on the micro scale, the temperature gradients that control their growth rates exist on the macro scale. This establishes the possibility that *wind pumping could change the scale of the faceting and rounding processes*, provided that the cyclic displacement is greater than the grain size. Macro and micro scale cyclic

displacements are illustrated in figure 5.20. In nature, these temperature gradients nearly always exist (Colbeck, 1987a).

How wind pumping on low temperature gradient snow would affect metamorphism cannot be estimated. This is because the *mechanism* relating these low temperature gradients to the rate of metamorphism *without* wind pumping has not yet been described in the literature[2].

The imposed naphthalene vapour pressure gradient is on a macro scale and therefore should most closely relate to water vapour transport in high temperature gradient metamorphism, although this will be complicated by the source / sink component of vapour transport.

In this case a comparison between a stagnant air diffusion length and a wind pumping convective length seems an appropriate parameter to relate to the mass transfer enhancement. The ratio between these two parameters for a particular wind pumping condition should plot strongly against the ratio between the measured stagnant air diffusive and wind pumped mass loss rates.

In the extreme, if diffusion no longer controls the grain growth rates, enhancement will be limited by the kinetics of growth.

5.10. Conclusions

A set of laboratory experiments using the naphthalene sublimation technique was carried out to measure the enhancement of diffusive mass transfer rates in a packed bed, under various magnitudes and intensities of wind pumping.

5.10.1. Experimental

The wind pumping conditions were set so that the air flow conditions in the packed bed approximated those expected in a natural snow pack in strong winds. The mass loss rates obtained were then compared to that for stagnant air in a packed bed.

A one to two orders of magnitude enhancement in naphthalene mass loss rates under the imposed sinusoidal wind pumping conditions (compared to stagnant air diffusion) was found. This enhancement increased almost linearly with increase wind pumping intensity.

The mass loss rate depended strongly on both the intensity and magnitude of the applied wind pumping. The dependence on period was approximately linear. The naphthalene mass loss

---

[2]Colbeck's (1983) theory does give the rate, but does not give the direction of metamorphism.

process has been shown to be essentially 1-D planar convective diffusion controlled, although a small dependence on boundary layer diffusion is apparent.

The results of this experiment exhibit considerable random variation from sources not yet identified. Given the consistency of the runs without wind pumping, when the column was isolated from the rest of the apparatus, it appears that the problem stems from the box and/or pump.

It may be inferred from the results of this experiment that such air movements must increase the vapour transport in the snow pack. In fact it is possible that *wind pumping could change the scale of the processes from micro to macro scale*. This is because large enhancement of water vapour transport on a macro scale, rather than on the micro scale, should take place under wind pumping conditions when vapour density gradients are imposed on the snow pack. In nature this latter is nearly always the case.

5.10.2. Recommendations on Further Work

These results indicate a strong enhancement of the mass transfer rates. However, confirmation of the results should be made once the source of the variability in the data is detected and removed.

Once this is achieved, results should be obtained at the lower frequencies indicated by Chapter 3.

The enhancements of mass transfer rates by the pulsile airflow mechanism has ramifications well beyond the scope of wind pumping in snow. It certainly deserves some further attention from an industrial perspective. For example, enhancement of mass transfer in pulsed columns has been noted in industry, but not given the attention it deserves.

Chapter 6
Wind Pumping in Snow

The objectives of Chapter 6 are to design and build an experimental apparatus capable of measuring the metamorphic effects of wind pumping, and to experimentally determine the effects a pulsile airflow derived from wind pumping could have on the metamorphism of dry snow.

6.1. Table of Contents

6.2. List of Illustrations

6.3. Nomenclature

D	penetration depth (mm)
dog	degrees of freedom
F	force (N)
Φ	grain diameter (mm)
f_c	unconfined compressive strength (Pa)
n	repetitions
s	standard deviation
s^2	variance
t_{exp}	experimental t statistic
$\bar{x}$	means
α	level of significant difference
ρ	density (kg/m^3)

6.4. Introduction

No direct observations or measurements have been made on the the effects of wind pumping in snow in a controlled environment. The requirement for such measurements are clear given the results of Chapter 3, 4 and 5.

Two objectives are met in this chapter:

1. To design and build an experimental apparatus capable of measuring the metamorphic effects of wind pumping on snow samples in a controlled cold laboratory environment.
2. To determine the effect a pulsile airflow derived from wind pumping could have on the metamorphism of dry snow. The pressure fluctuations envisaged from gale force winds (60 to 90 km/hr) are used to provide strong wind pumping.

The range of variables (see for example Bader, 1939, and Colbeck, 1987a) contributing to snow metamorphism and the resulting inherent spatial variability of snow (see for example Conway and Abrahamson, 1988, and Fohn, 1988) prohibits *in situ* field observation of snow metamorphism due to wind pumping. It is therefore common practice to monitor metamorphism on an isolated snow sample in the controlled environment of a cold laboratory (Akitaya, 1974, Bradley *et al*, 1977, Marbouty, 1980, and Sommerfeld 1983) .

The cold laboratory used for these wind pumping metamorphism experiments was based on those developed to investigate metamorphism under imposed temperature gradients (see for example, Akitaya, 1974, and Marbouty, 1980), with the addition of wind pumping capabilities. This addition introduced many difficulties into the experimental design. Given that each experimental run was expected to take several days or more, refining the experimental design was a slow process. Consequently results from the experimental runs and the experimental development are reported chronologically.

In section 6.5 the requirements of the wind pumping apparatus and experimental programme are detailed. Descriptions of the apparatus, and the analysis techniques are included in sections 6.6 and 6.7 respectively. In section 6.8 the results are described in chronological order to aid the explanation of developments to the experimental design. The important features of the apparatus, analysis tools and results are brought together in discussion contained in section 6.9. Finally, in section 6.10 conclusions in the effects of wind pumping in snow covers are drawn.

6.5. Cold Room Metamorphism Experiments

This section identifies the experimental programme required to investigate the wind pumping concept in a cold laboratory. Time was a key limiting factor to these experiments, as the cold laboratory was rented on weekly basis.

6.5.1. Experimental Expectations, Requirements and Programme

As a result of wind pumping one might expect to see *changes* in

* Ice Grain Form and Structure
* Permeability
* Density
* Mechanical Strength
* Temperature Profile

6.5.1.1. Ice Grain Form

It is well known that the number and area of bonds are far more important for strength than ice grain form. Photographic techniques have been used by others to observe snow structure. Stereological (thin section) analysis, as used for example by Bader (1939), Kry (1975a,b), Perla (1982) and Good (1987), give a more detailed picture. Perla (1982) describes in detail the methods behind the preparation of section planes in snow specimens. However, thin section analysis does not appear to easily produce the basic information on direction and speed of metamorphism desired in this initial detailed wind pumping study. Also, as there was already a large development component to the wind pumping experiments, and as the analysis of thin section results have not been fully developed for snow (see Good, 1987, Buser and Good, 1987, and Colbeck, 1987b) the time and effort involved would be misdirected. Only a very small amount of snow was extracted for photographic work.

6.5.1.2. Permeability

Permeability appears to be a sensitive indicator of snow structure and strength. Conway and Abrahamson (1984) found that snow permeability varies with both position and direction in the snow pack, and varied with time as metamorphic changes occurred. The thin section analysis of Buser and Good (1987) showed relationships between permeability and different geometric parameters, and between permeability and strength parameters. Permeability is also a nondestructive test and hence does not exclude the use of other tests. Therefore permeability measurements have been made routinely both before and after the experimental period.

6.5.1.3. Density

Density increases are observed to occur in new snow with low temperature gradient metamorphism (as the snow settles). In high temperature gradient metamorphism, densification is not so apparent (Akitaya, 1974). Sample densities were taken for comparison before and after the experimental period.

6.5.1.4. Mechanical Strength

Mechanical strength tests are highly destructive on the sample, but are an important component in determining if wind pumping has any effect on snow metamorphism. This is because snow pack strength is one step closer in applicability to avalanche prediction compared to ice grain structure[1]. A selection of small scale tensile and shear tests have been made in such a way to maximise the amount of information gained from the sample.

6.5.1.5. Temperature Profile

Clarke *et al* (1987) and Clarke and Waddington (1991) attempted to relate the differing temperature profiles in glacial firn at different terrain locations to wind pumping. As the experiments performed for this thesis were with imposed temperature profiles over small depths for relatively short time periods, it was unlikely that changes in temperature profile with the samples would be observed due to wind pumping. Three temperature probes were placed in the initial samples, however later sample preparation techniques excluded this option. A check on the temperature gradients was made with these initial experiments.

6.5.2. Variables Investigated and Central Apparatus Requirements

By keeping all other factors constant, the aim was to investigate two variables per experimental run. In all cases one of these variables was wind pumping, with other variable being one of the following:

* Varying intensity and/or magnitude of wind pumping.
* Imposed temperature gradient.
* Snow types with differing properties (for example grain structure, strength, densities and permeabilities).
* Varying elapsed experimental period before analysing the samples.

---

[1]For an avalanche to occur a weakness is required. Assessment of that weakness is made more directly with strength measurements than snow crystal observations.

To provide the necessary controls for the two variables four experiments using identical snow samples were required. Given that stored snow samples would continue to undergo metamorphic changes, these experiments were run simultaneously to ensure that all other variables were identical between samples. This necessitated the construction of *four sample apparati* , two with wind pumping capabilities.

At the end of the experimental period the four samples were analysed and results compared with each other, and with the initial snow sample properties. The snow was loaded into the sample tubes and placed into the sample apparati which took up to 9 hours to reach a thermal steady state (see section X.3). Therefore care had to be taken in the timing of the initial snow analysis. The most reliable method to achieve this was to use a *fifth sample apparatus* and analyse it at the time when steady state was reached and the wind pumping was started. This fifth sample apparatus did not require wind pumping capabilities. Note that all five sample apparati required temperature gradient and control capabilities.

6.5.3. Subsidiary Apparatus Requirements

Apart from the five sample apparati, the following equipment were developed for use as part of the experimental programme:

* Cold Room (laboratory).
* Snow Making Apparatus.
* Temperature Control Equipment.
* Mechanical Strength Testing Equipment, including:
  * Hardness Test Rig.
  * Tensile Test Rig.
  * Shear Test Rig.
* Wind Pumping Apparatus.
* Ice Grain Photography Equipment.
* Permeability Testing Device.

Figure 6.1 shows the peripheral components of the sample apparati and figures 6.2 and 6.3 the sample apparatus detail. Sections 6.6 to 6.7 describe each of these components in context with the experimental procedure.

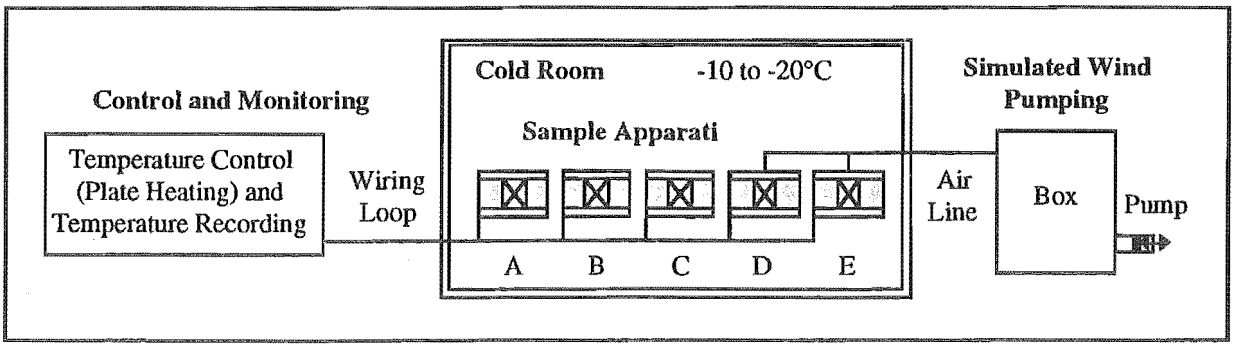

Figure 6.1. Overview of the Wind Pumping Experimental Set Up.

6.5.4. Planned Experimental Runs

The apparatus was designed so that two variables could be investigated during any one run. The purpose of this project is such that one of those variables had to be wind pumping. There is a myriad of possibilities for the other variable, some of which are listed in section 6.5.2. Most of the preconceived plan was abandoned during the research period. This was because a large proportion of the available experimental time was dedicated to the development of the apparatus. The aim of the actual investigations carried out are summarised below.

Run 1. To get an indication of the consistency the results might offer at low temperature gradients.

Run 2. To get an indication of the consistency the results might offer at high temperature gradients.

Run 3. Considering the problems exposed by Runs 1 and 2, to apply a high and moderate temperature gradient over the samples and obtain some meaningful results.

Run 4. To examine the progression of metamorphism from an initial state of no bonding between ice grains at low temperature gradients. This was done to investigate the effect wind pumping may have during wind slab formation.

Run 5. As with Run 4, but over a shorter time frame.

Run 6. To confirm the low temperature gradient results and investigate the effects sieving the samples had on the results.

In all runs, the wind pumping imposed represented gale force winds (60 to 90 km/hr).

6.6. Experimental Apparatus Details

This section details the final experimental design of both the central (sample apparati) and peripheral equipment used in the cold laboratory experiments. The analysis tools are described in section 6.7.

6.6.1. Cold Laboratory

A portable 3x3x3 m freezer with 150 mm aluminium clad polystyrene walls, roof and floor was rented and set up at the university as the cold laboratory[2]. The cooling was provided with a 1.5 kW refrigeration unit capable of maintaining the room at -20°C. Cold room temperature was controlled to within ±2°C with an on/off thermostat.

---

[2]The cold laboratory was set up outside the south wall of the department's Semi-Scale Laboratory near the sinusoidal pump used in the experiments of Chapters 4 and 5 to provide the wind pumping pressure fluctuations.

6.6.2. Wind Pumping Apparatus

The wind pumping apparatus used for these experiments was the same as that used in the experiments of Chapters 4 and 5. A detailed description of the wind pumping apparatus is given in section 4.6.

6.6.2.1. Wind Pumping Monitoring

The period and amplitude of wind pumping pressure fluctuations imposed over the top of the snow sample were measured by the differential pressure transducer (Air Neotronics Micromanometer) described in section 3.7.2.1. The ports of the transducer were connected to the two tappings shown in figure 6.2 on either side of the sample. These fluctuations were recorded as required using the data acquisition system detailed in section 4.7.1.

6.6.2.2. Magnitude of Wind Pumping Within the Sample

The practical restrictions on sample apparatus depth meant it cannot truly represent a seasonal snow pack. To examine what may occur in a portion of the snow pack, the bottom of the sample was open[3] to the ambient cold laboratory pressure. This implies a finite free lower boundary condition (see section 4.5.1.2 for an explanation of this term). From the numerical packed bed results in Appendix IX it can be seen that, for the dimensions and conditions prevalent in the sample apparati, the air velocities and displacements are nearly identical through the length of the sample. In other words the entire sample was exposed to the same degree of wind pumping.

Note that rigidly sealing the bottom of the sample equates to the finite sealed lower boundary condition. This is undesirable over such a short sample depth because the air displacements derived from the wind pumping surface pressure fluctuations will vary from a maximum at the top of the sample, to nothing at the bottom. This makes the results of the analysis highly dependent on location in the sample.

The air flow dynamics can be estimated using the analytical and numerical theory from Chapter 4. The size of the air movement in the finite free snow sample was set so that it was equivalent to what may be expected in a seasonal snow pack. This was achieved by adjusting the surface pressure fluctuation amplitude.

---

[3]Note that the flexible diaphragm offers negligible restriction to the wind pumping pressure fluctuations at either end of the sample.

6.6.3. Sample Apparatus

The final design, after several modifications through the experimental runs, is illustrated in figures 6.2 and 6.3 for the two apparati with wind pumping capabilities. For the three apparati that do not require wind pumping, the diaphragms and casings were omitted, and the space left was filled with polystyrene. Several views of the sample apparatus are illustrated in plate 6.1, and plate 6.2 shows several snow sample illustrations which are discussed at various stages further on in this chapter. The key features of the design are described below.

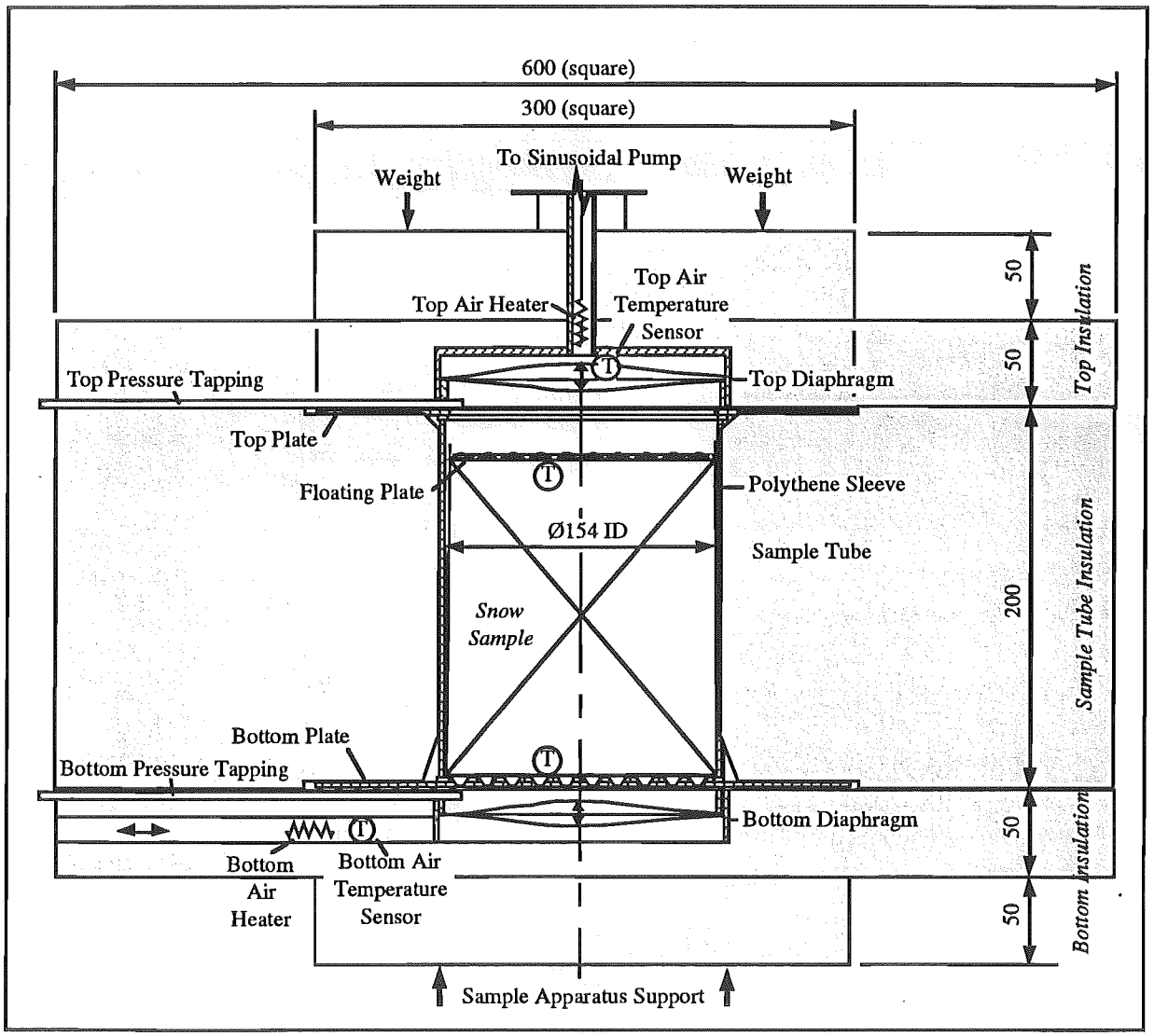

Figure 6.2. Scale Drawing of the Sample Apparatus with Wind Pumping Capability. Dimensions in mm. Scale 1:4. T = temperatue sensor.

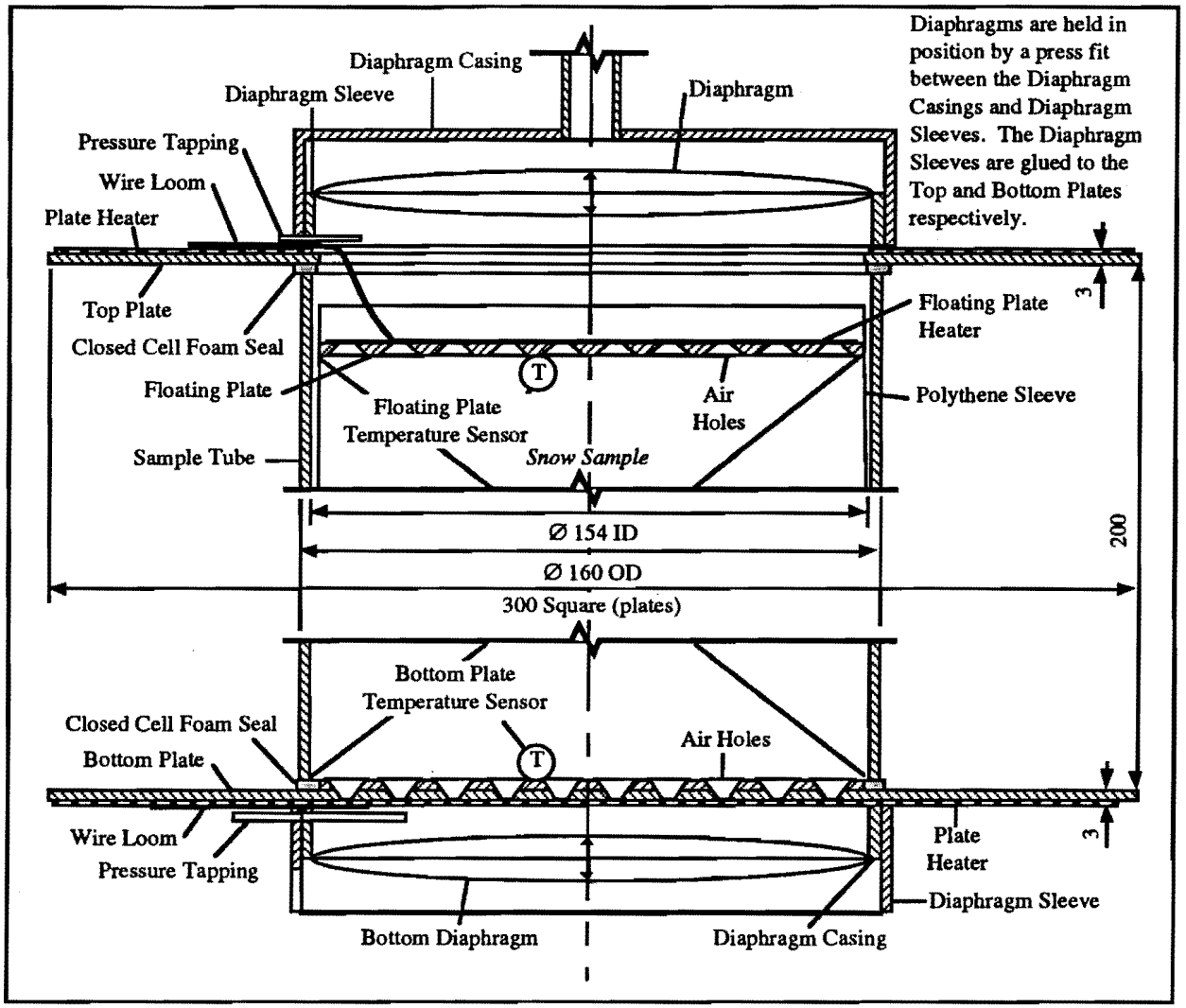

Figure 6.3. Top and Bottom End Details of the Sample Sample Apparatus with Wind Pumping Capability. Dimensions in mm. Scale 1:2.

6.6.3.1. Design Criteria

The key rationale behind the design are:

* Accurate control on the vertical macroscopic temperature gradient - to within ±1°C/m.
* Minimise lateral macroscopic temperature gradients - to less than 1% of the vertical temperature gradient.
* Preventing the pumping pressure fluctuations from short circuiting around the sides of the snow sample (between the snow sample and the sample tube).
* Sealing of the snow sample against vapour transport, due to vapour pressure gradients between the sample and other parts of the apparatus and/or cold laboratory.
* The above sample vapour seals could not be allowed to restrict the pressure fluctuations, and consequently the pulsile airflow.
* Ability to easily pull the apparatus apart, remove the sample and divide into test portions.

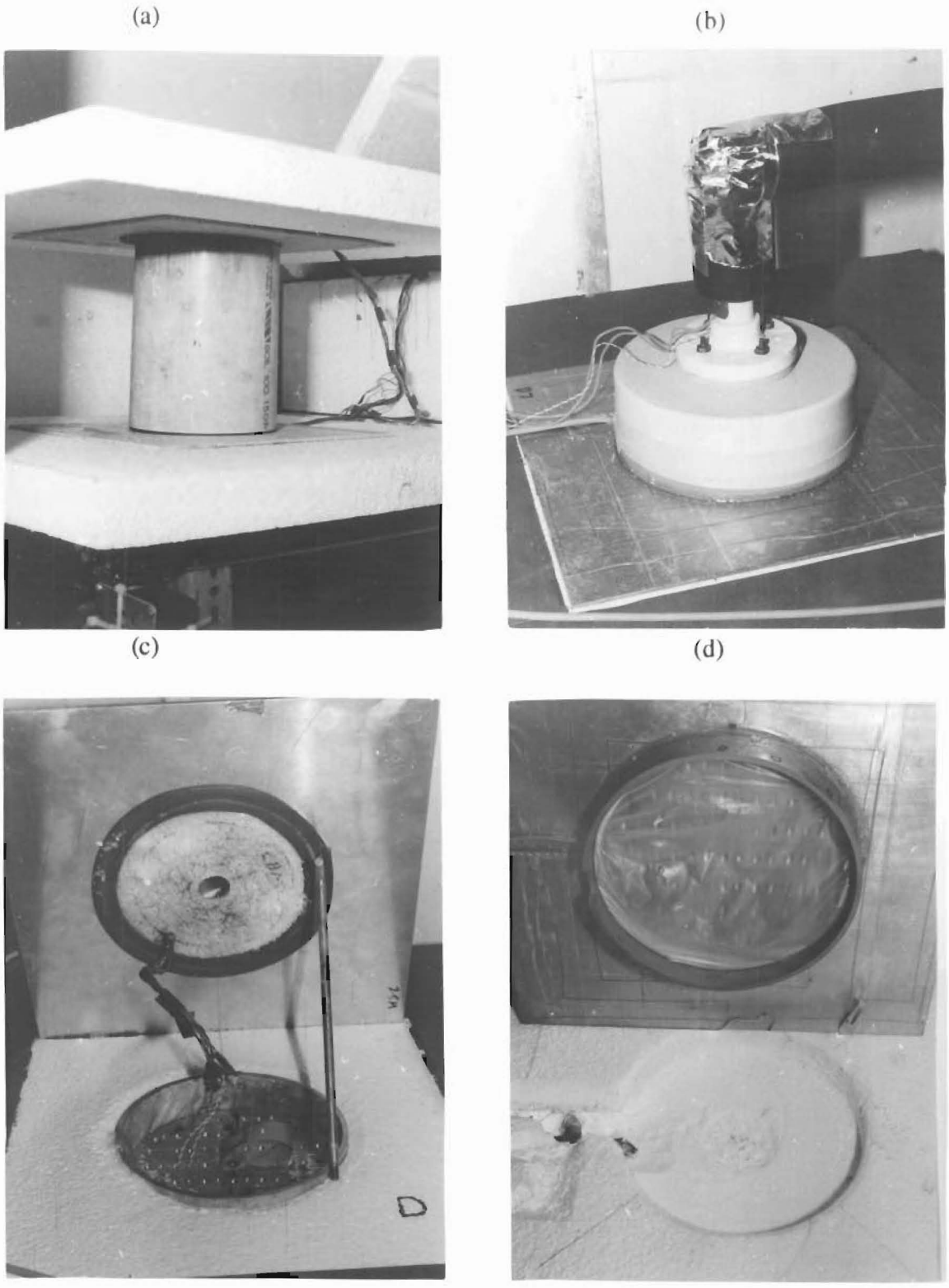

Plate 6.1. Sample Apparatus: (a) Assembled view without the Sample Insulation. The Top and Bottom Insulation, and Heating Plates are separated by the Sample Tube. (b) Top Plate and Diaphragm Casing sitting on the Sample Insulation. (c) View into the top of the Sample Insulation, Sample Tube and Floating Plate with the Top Plate opened up. (d) Bottom Plate, Diaphragm and Diaphragm Casing opened up and sitting on the Bottom Insulation.

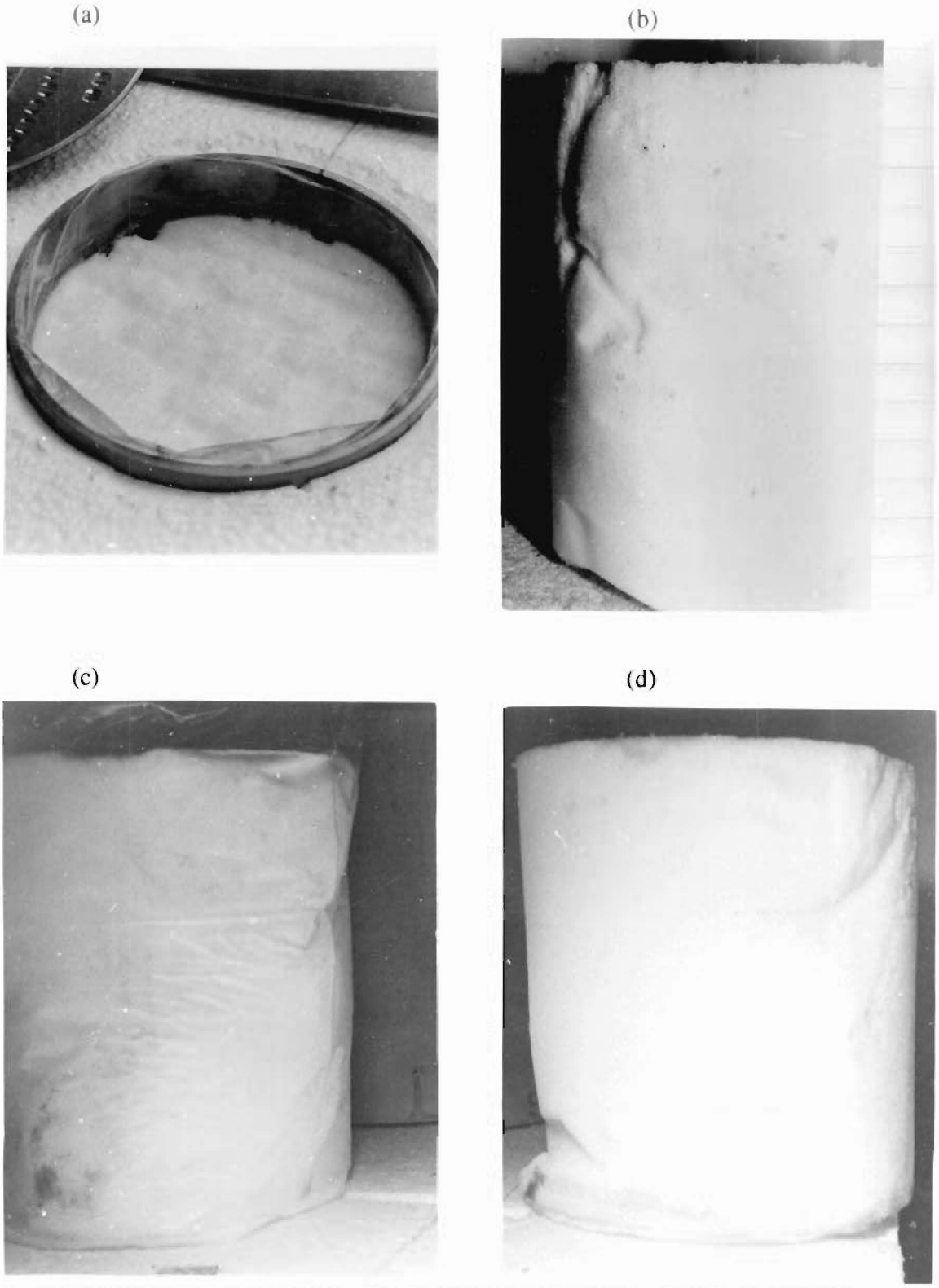

Plate 6.2. Snow Sample Illustrations: (a) Top view into a Sample Tube showing the etching from the wind pumping airflow, and the top ends of three channels which have formed between the Sample and Polythene Sleeve. (b) Side view of a channel which had formed between the Sample and Polythene Sleeve. (c) Sample with a crease covered by the Polythene Sleeve (shortly after removal from the Sample Tube). (d) Sample showing several creases after the Polythene Sleeve had been removed.

6.6.3.2. Sample Tubes

Cylindrically shaped samples enclosed in a 160 mm OD by 200 mm high tube (termed the *sample tube*) were used for ease of sealing and construction. The sample dimensions were chosen as a compromise between a sufficient volume of snow to analyse, the cost of collecting or making larger snow samples and the cost of providing larger scale equipment to run the experiment.

6.6.3.3. Sample Tube Insulation

The sample tube insulation lateral thickness was determined using the three dimensional steady state design model described in Appendix X. To reduce the lateral temperature gradients to below 1% of the vertical temperature gradient the model showed that a lateral thickness of about 200 mm was required. It was convenient to cut the 200 mm thick polystyrene sheet (1200x1800 mm) into 600x600 mm portions. With the 160 mm OD sample tube this gives a minimum lateral thickness of 270 mm.

6.6.3.4. Top and Bottom Insulation

The top and bottom insulation thicknesses were chosen to give good control of the heat delivered to the sample. From Appendix X, 50 mm was more than adequate for the bottom insulation given a -10 to -20°C cold room temperature and plate temperatures of -1 to -11°C. A problem arose with the top insulation thickness when a large temperature gradient was imposed on the sample. If the insulation thickness is too great, the heat flow from the warmer (bottom) plate, through the sample, to the colder (top) plate becomes more than the heat loss from the colder plate to the cold laboratory (see figure X.9). This results in the plate warming up beyond its set point and the imposed temperature gradient becomes smaller than intended. To get around this, as little as 3 mm closed cell foam insulation had to be used in some runs as the cooling control was provided by the ambient cold laboratory temperature.

6.6.3.5. Heating Plates

The heating plates were constructed from 3 mm aluminium plate with 3.5 mm 20 Ω/m resistance heating ribbon distributed over the surface away from the sample. Cost prohibited the plates from covering the entire insulation surface as indicated by the models in Appendix X. The chosen size of 300 x 300 mm (square) was sufficient as a larger than minimum sample tube insulation thickness was used.

The length of resistance ribbon was calculated using the estimated maximum heat loads from the models in Appendix X.

Bottom Plate

From figure X.8 it can be seen that the load over the sample portion of the bottom plate was significantly higher than the insulated portion. To accommodate this, the density of heating ribbon laid down over the sample portion was twice that over the insulation portion.

Top and Floating Plate

Due to snow settlement the sample was not always level with the top of the sample tube. Any air gap that resulted between the top of the sample and top plate would form a major undesired resistance to the heat flow. The top plate was split into two portions to overcome this. A Ø150 mm disk was cut from the centre of the top plate and allowed to rest on top of the sample. This portion of the top plate is labelled the *floating plate*. The resistance ribbon was evenly distributed over the top and floating plates.

Air Holes (sample tubes D and E only)

In the sample apparati that required wind pumping capabilities air had to be allowed to pass through the heating plates. To achieve this Ø3 mm holes were drilled through the floating plate tube portion of the bottom plate. To prevent air jetting through the holes and etching the sample (see plate 6.2(a)) these holes were bevelled and partly covered with aluminium tape to create a flow splitter as illustrated in figure 6.4.

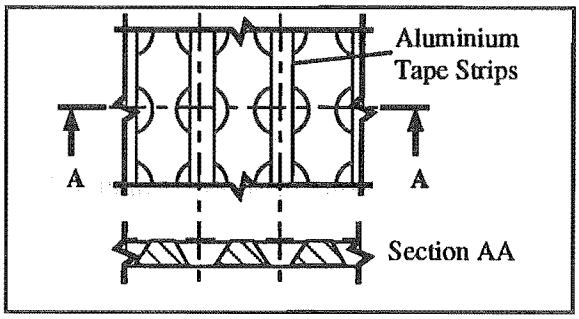

Figure 6.4. Air Hole Design for the Floating and Tube Plates.

6.6.3.6. Sealing Snow Samples

The sample tubes had to be sealed so that the pressure fluctuations were forced through the samples. Also, since the water vapour in the sample tube would be strongly attracted by the relatively cold laboratory, the snow samples had to be enclosed in a vapour barrier. For the most part both of these criteria were met by the impermeable PVC sample tubes and aluminium plates. Attention was required on the sealing details between the sample tubes and heating plates and, for sample tubes D and E, at each wind pumping pulsile airflow port.

Sample Tubes

Ease of sample removal was maintained through the use of closed cell foam gaskets between the ends of the sample tubes and the top and bottom plates. Pressure on the seal was

maintained by applying weights in the positions indicated in figure 6.2 between the top and bottom of the apparatus. The sample tube insulation depth needed to be slightly undersized to effect a seal.

Diaphragms (sample tubes D and E only)

The air had to be allowed to pulsate in the wind pumped apparati. To achieve a vapour barrier at each end of the samples a flexible diaphragm was placed over each wind pumping airflow port. Using a diaphragm of equal diameter to the sample tube, the maximum vertical displacement of ±3 mm in the centre of the diaphragm was estimated from the theory in Chapter 4. The diaphragm used was a thin polythene sheet held into position by a press fit between the diaphragm casing and diaphragm sleeve. The diaphragm was pre-stretched so that it offered negligible resistance to the air movement imposed by the wind pumping. This is illustrated in figure 6.3 and plate 6.1(d).

6.6.3.7. Temperature Balance Heaters (sample tubes D and E only)

The air line between the wind pumping apparatus and the two sample apparati passed through several environments. Consequently the air inside the sample apparatus was at a different temperature to the top plate temperatures, and there was an opportunity for a temperature gradient to form. As any migrating vapour was blocked at the diaphragm, it was deposited onto the diaphragm as faceted ice crystals. A similar scenario existed for the air between the bottom plate and the cold laboratory.

To eliminate this problem, coiled resistance wire heaters and a thermocouple were fitted on the laboratory side of the diaphragms. The heaters were controlled to equilibriate the temperature difference. The position of these heaters and thermocouples are shown in figure 6.2.

6.6.3.8. Modifications Between Initial and Final Sample Apparatus Design

Most modifications revolved around the selection, preparation and loading of the samples. This is discussed in detail in section 6.8.1.4 in conjunction with the development of the internal polythene sleeve.

Initially the air holes in the floating and bottom plates (sample tubes D and E only) did not have bevelled edges or flow splitters, causing the impinging air to etch holes in the sample. The modification alleviating this, and the addition of the balance heaters (sample tubes D and E only), were made after *Run 1*.

6.6.4. Temperature Control and Monitoring Equipment

The control and monitoring hardware described below were housed in the Mechanical Engineering Department's field instrument caravan parked adjacent to the cold laboratory.

6.6.4.1. Plate Temperature Control

Computerised control was used to maintain the temperature gradient over the five snow samples by heating the top, floating and bottom plates to *temperature set points* (TSP) *which had to be above the ambient cold laboratory temperature*. No other provision was made for cooling the plates. The equipment and programming concepts were developed from the works of Hanson (1985), Harris (1986) and Livingstone (1987) who had similar tasks on a vertical column of coal.

The plate temperature control system developed for this task is illustrated in figure 6.5 and further described below.

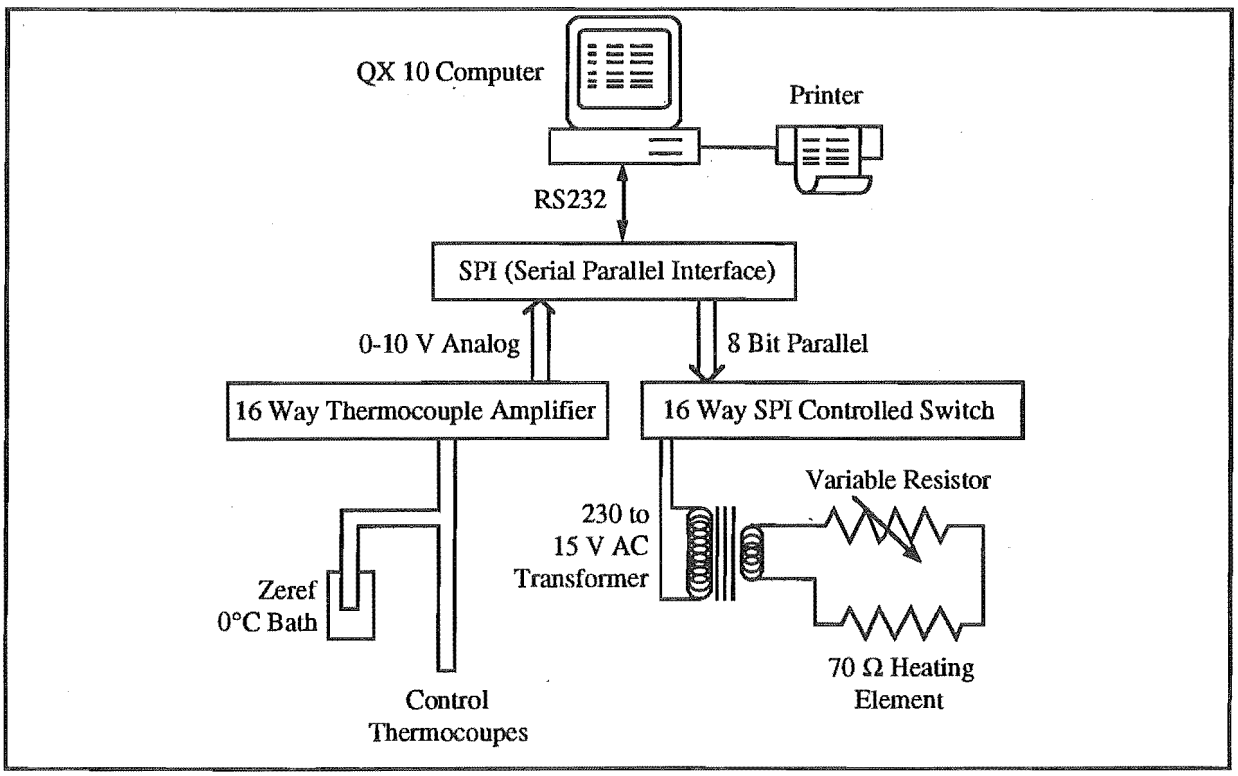

Figure 6.5. Temperature Control Hardware Diagram.

Temperature Measurement

Ten differential copper / constantan thermocouples were used to sense the plate temperatures. The plate thermocouples were taped to the sample side of the aluminium plate and the reference thermocouples placed in a Mectron 136 B Zeref Ice Point Reference. The thermocouple

signals were amplified about 24,000 times in a 16 Way Thermocouple Amplifier converting this signal from 0 to 440 μV to 0 to 10 V (equating to 0.0 to -11.0°C).

The amplified signal was then converted by 12 bit analog to digital (A/D) converters in a Serial Parallel Interface (SPI) to digital signals of 1 to 4095. These were then read by software running on a Epson QX-10 computer.

Thermocouple Calibration

Each thermocouple was calibrated by insertion in a glycol constant temperature (±0.1°C) bath over a period of 258 minutes. The outputs averaged over 1000 readings, using portions of the software outline below, were accurate to within ±1% or ±0.1°C.

Control Routines

The thermocouple readings for each plate were read from the SPI by the QX-10 computer. The heat requirements for each plate were determined by the software and appropriate heater instructions were sent back to the SPI. Figure 6.6 outlines the control aspects of the software used to achieve this.

The thermocouple amplification results in a very noisy signal (about ±0.5°C). The design criteria on the vertical temperature gradient was ±1°C/m or ±0.2°C over the length of the sample. The accuracy of the plate control was improved to ±0.1°C by averaging 1000 thermocouple readings (number of samples, NOS) before evaluating if any control was required. Each run through the control loop takes about 3 minutes. This was a sufficient control period considering the speed of the system.

Although strictly speaking the control was

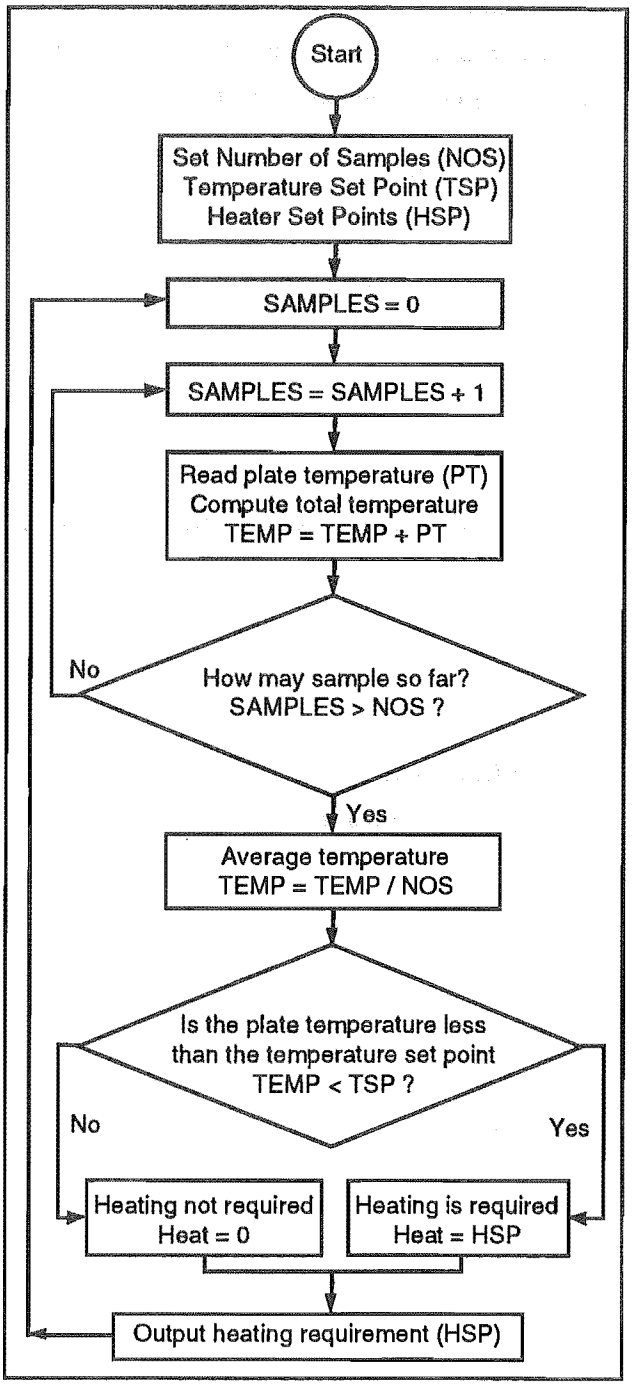

Figure 6.6. Software Flow Diagram for the Central Control Segments. Each step was performed for each plate before progressing to the next step. Programme execution is terminated with a keystroke.

on / off, some software and hardware proportional control was available. In the software this was through adjustment of the maximum heater set point (HSP) which determined the proportion of the *space to mark controller period* (see figure 6.7) the plate heater is turned on if heat is required. In the hardware a potentiometer was used to reduce the power output of the space to mark controller. Both of these controls were available for each plate.

The SPI to QX-10 data acquisition and QX-10 to SPI data export routines written in Macro-80 Assembly Language were the same as those used by Harris (1986) for control of the lateral temperature gradients in a column of coal. The data processing and control routines within the QX-10 were written in Fortran-80. Listings for these programmes are not presented in this thesis.

Control Implementation

At the end of a control loop the heating instructions for each plate were sent by the QX-10 computer to the SPI. These were passed on in digital form to the 16 Way SPI Controlled Switch which contains 16 space to mark controllers with outputs of 0 or 230 V AC. The space to mark refers to the high (on) and low (off) proportions of the fixed controller period as illustrated in figure 6.7. This proportion was adjustable in the software by the heater set point (HSP). For example, a HSP of 255 means the heater would be on for 100% of the controller period, 127 for 50%, etc. The controller period was about 2 s for these experiments. Once the HSP's have been accepted the switches operate for successive controller periods with the given HSP's until new instructions are received from the QX-10 (another control loop is completed).

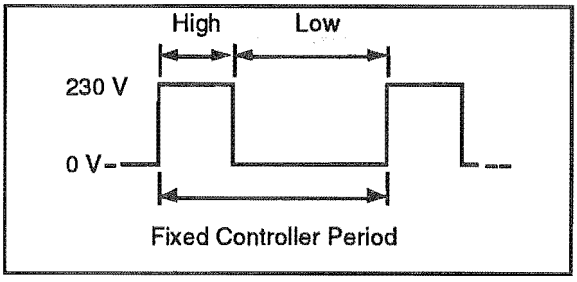

Figure 6.7. Example of a Space to Mark Controller Output.

As the load on the plates had a maximum of 3 W (estimate by the steady state models in Appendix X) the 230 V AC outputs of the space to mark controller were reduced to 15 V AC with a transformer and optionally further reduced using a potentiometer. This plate load was insufficient to trip the switches (which require a load to operate), so a 40 W light bulb was placed in parallel with the switches.

Tuning the Controller

The proportional aspects of the control could be manually set at any time. Software control was adjusted by terminating the control program, adjusting the desired set points and restarting the programme. The most stable steady state control was obtained when the heating was

required for around 90% of the control loops. The average control (giving this percentage) was monitored by the software for each heater.

Steady state tests on the control system indicated that the plate temperature control was to within ±0.04°C of the temperature set point. Thus the limit of the control accuracy lies within the thermocouple calibration accuracy of ±0.1°C.

6.6.4.2. Diaphragm Differential Temperature Control

Ideally the control of the diaphragm balance air heaters would be made by setting the difference between the plate and balance air heater thermocouple signals to zero. This would have required major reprogramming as the balance air heaters were late additions to the circuit. Hence heater / thermocouple setups similar to those for the plates were used, along with the same control routines. The balance air heater temperature set points were set to the same temperature set point of their respective plates. This appeared to be sufficient as it solved the problem of ice formation on the diaphragms.

6.6.4.3. Temperature Monitoring

With the exception of sample apparatus 'A', Platinum Resistance Thermometers (PRT's) were placed adjacent to each plate thermocouple and three were inserted into the sample.

The output of the plate PRT's were read by a Fluke 52 J/K Digital Thermometer and were installed to check against the plate thermocouple readings. The output of the sample PRT's were charted directly on a 12 channel Phillips Transkomp 250 Recorder to investigate the imposed temperature gradients in the samples.

The tested accuracy of the PRT's showed that they were all within ±0.2°C. This was the expected limit in accuracy for such instruments. Subsequent measurements during initial testing of the apparatus confirmed the estimated times for steady state to be established. These initial estimates were made in the design phase using the one dimensional unsteady state model described in section X.3.

The lack in accuracy of these PRT measurements, the difficulty in positioning the PRT's, and the limitations the PRT's imposed on the sample loading methods meant that they were not used after the initial tests (prior to *Run 1*). Some of these measurements were replaced with more direct temperature measurements at the beginning of the analysis.

6.7. Sample Analysis and Analysis Tools

This section describes the analysis tools and some of the analysis techniques (in approximate order of performance) carried out on each sample. Many of the specific details on the design of the analysis tools are described in the appendices.

6.7.1. Permeability Measurement

Permeability measurements were made both before and after the run, using the blower permeometer described in Appendix III.

6.7.1.1. Test Procedure

Up until *Run 4* measurements were made prior to inserting the sample tube into the foam insulation, before the run, and at the end of the run after removing the sample tube from the insulation. It was suspected that this procedure disturbed the snow sufficiently to create a channel between the snow sample and the wall of the tube. Measurements from *Run 4* onwards were made with the sample tube in the foam as illustrated in figure 6.8.

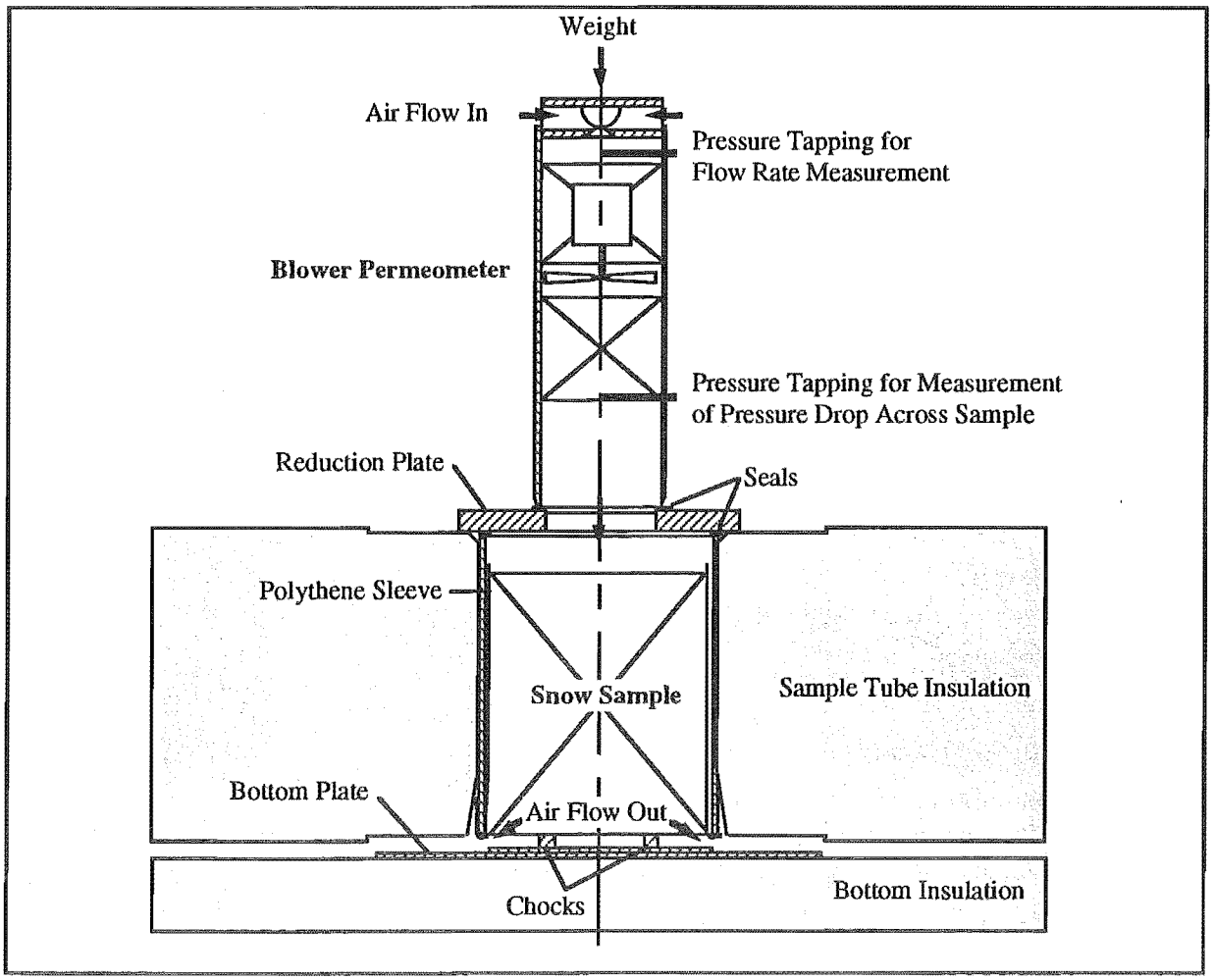

Figure 6.8. *In Situ* Permeability Measurement using the Blower Permeometer.

6.7.2. Density Measurement

Snow density was measured both before and after the run by measuring the height of the loaded sample and its weight.

6.7.3. Division of the Sample Into Test Pieces

In light of the mechanical destructive strength test requirements the sample was divided into the sections illustrated in figure 6.9. Using various modified saw blades, the sample was cut into test sections and analysed in the following order:

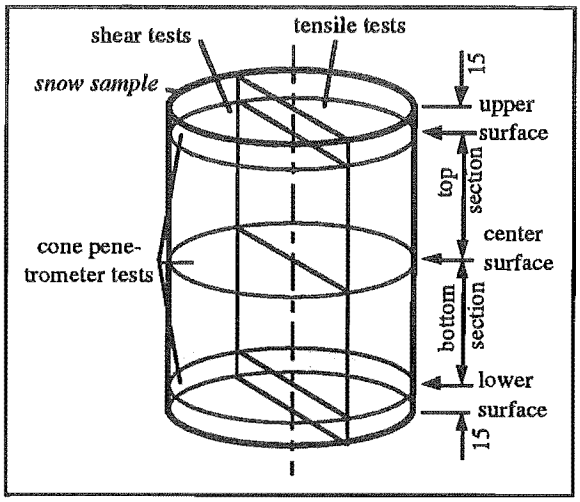

Figure 6.9. Snow Sample After Removal from the Sample Tube and Polythene Showing the Division into Test Pieces. Scale 1:5.

1. To reduce possible end effects on the mechanical tests 15 mm was cut off each end of the sample and discarded. Such end effects may arise from uneven contact between the sample and heating plates, or the discrete nature of wind pumping air flow through the holes in the heating plates.
2. Cone penetrometer tests were performed on the top and bottom surface (into the bulk of the sample and not into the discarded ends).
3. The sample was then split horizontally in two (upper and lower) sections and cone penetrometer tests performed on one of the central surfaces.
4. The penetrometer holes were removed from the surfaces to ensure there were no discontinuities that could affect the shear and tensile tests.
5. Finally the upper and lower sections were split vertically in two and the tensile tests performed on one side and shear tests on the other side.

The comparison of test results between samples was made, keeping in mind the temperature of the portion of the sample the test was made in[4].

[4]It is important to note the rate dependance snow metamorphism has on temperature. Specifically, metamorphic rates will be higher at the bottom (warmer) end of the sample in the temperature gradient cases.

6.7.4. Ice Grain Photography

To observe general grain form, samples were taken from the top, centre and bottom surfaces (locations illustrated in figure 6.9) and photographed with a high power macro lens and ring flash setup. This did not prove to be a useful tool as no visible differences in the grain structure was observed due to the wind pumping. Consequently, the photography work is not detailed with the results. Note that the expected generalised observations of the rounding and faceting processes according to temperature gradient were made.

6.7.5. Mechanical Strength Testing

Destructive mechanical tests were made on the areas of the sample defined above. They were performed to give ice grain bonding comparisons between experiments.

6.7.5.1. Hardness Testing

A cone penetrometer was used to test the hardness of the top, centre and bottom snow sample surfaces. Whilst still a destructive test, it was primarily used because it required less sample than the tensile and shear tests, and was simple to perform. Note that the hardness tests were made using a static load in the sample's axial direction.

In Appendix VI Knight and Johnson (1988) give the relationship between the unconfined compressive strength f_c and penetration depth D as

$$f_c \propto \frac{F}{D^2} \qquad 6.4$$

where F is the force applied. Thus, where there are significant differences in hardness, the fractional change in unconfined compressive strength can be estimated.

6.7.5.2. Tensile and Shear Strength Testing

The more traditional tensile and shear tests were used to give an indication of absolute snow strength. The shear strength tests performed were not aligned to any specific plane of weakness as was usually the case in snow slope stability studies.

Shear tests were done with the shear stress acting in the horizontal plane of the sample, and tensile tests with the tensile stress acting in the vertical plane.

The hand-held cone penetrometer, tensile test rig and shear test rig and their use is further detailed and illustrated in Appendices VI, VII and VIII respectively.

6.7.6. Statistical Analysis of the Results

6.7.6.1. Permeability Tests

Repetitions of permeability measurements were made on several occasions. The spread in measurements was consistently between ±2.5% and ±3.5%.

6.7.6.2. Strength Tests

The high degree of variability in the strength measurement results demanded a more rigorous approach than with permeability tests.

In each run there were two variables (treatments) under investigation. At each location in each sample, several repetitions of the measurements were made. t-tests were used to examine if there was any difference in the mean strengths between treatments.

The variability of each type of strength test appears to be consistent from sample to sample, and from run to run. This allows a pooled variance s^2_{pool} to be calculated over j groups of measurements using

$$s^2_{pool} = \frac{\sum_{k=1}^{j} (n_k-1)s_k^2}{\sum_{k=1}^{j} (n_k-1)} \qquad 6.2$$

where s^2 is the variance of n_k repetitions. Taking the null hypothesis of *no difference in the means between treatments*, the t_{exp} statistic is calculated using

$$t_{exp} = \frac{\bar{x}_1 - \bar{x}_2 - 0}{s_{pool}\sqrt{\frac{1}{n_1} + \frac{1}{n_2}}} \qquad 6.3$$

where the subscripts 1 and 2 refer to the two samples being tested and the $\bar{x}$'s are the means of the samples. Because s_{pool} is being used, the number of degrees of freedom is given by

$$dof = \sum_{k=1}^{j} (n_k-1) \qquad 6.4$$

6.8. Experimental Runs and Development

The first part of this section describes the sourcing and preparation of the snow samples and the second part details the results of the experimental runs. There was a considerable development component to these aspects of the experimental work. The runs are described in chronological order to aid the explanation of the developments.

6.8.1. Snow Sample Preparation

6.8.1.1. Source of Snow Samples

Two approaches were made:

* Collection of natural snow.
* Making of artificial (laboratory) snow.

There were several key philosophies behind the use of artificial snow over natural snow

* Remoteness of sources of natural dry snow (100 to 150 km).
* Restriction of experimentation to winter time if natural snow was to be used.
* Cost considerations in obtaining natural snow in an experimental programme that was in a development phase
* Consistency of laboratory snow (Sommerfeld and Freeman, 1988).

The sources used for each experimental run were as follows:

Run 1. Temple Basin - Light New Snow.
Run 2. Laboratory Snow.
Run 3. Laboratory Snow.
Run 4. Mt Lyford - Wind Packed, Partially Settled New Snow.
Run 5. Mt Lyford - Wind Packed, Partially Settled New Snow.
Run 6. Temple Basin - Wind Packed, Partially Settled New Snow.

6.8.1.2. Natural Snow Collection

There were two choices of when to load the sample tubes:

* At the Collection Site
* In the Cold Laboratory

In both cases the snow was packed into large chilly bins (ice boxes) with dry ice and very carefully transported by vehicle to the cold laboratory in Christchurch.

New snow is easily damaged. In particular vibration of snow after it had been loaded into the sample tubes at the collection site resulted in air gaps developing between the snow and sample tube, a short circuit for any subsequent wind pumping air flow.

Ideally the loading of transported natural snow into sample tubes in the laboratory would simply follow the technique outlined in section 6.7.4.2. Unfortunately the travel disturbances fractured the blocks in the chilly bins. Using such samples would give meaningless strength testing results. Consequently such samples were sieved and loaded in the same way as the laboratory snow. Whilst this destroys any of the original snow bonding structure and to some extent fragments the ice grains, it should not affect the experimental comparisons between the control samples and samples with the imposed wind pumping.

6.8.1.3. Laboratory Snow Making

The laboratory snow making procedure used here follows closely the principles used by Sommerfeld and Freeman (1988) and is described in detail in Appendix V.

When natural dry snow forms in the atmosphere it usually grows into highly spatial forms (see Perla, 1978a) and, unless it is severely smashed up by wind action, it settles with a very high voidage ($0.90 < \varepsilon < 0.97$). These spatial forms are thermodynamically unstable and rapidly metamorphose to reduce their surface area. Under low temperature gradient conditions this *rounding* and consequential densification process continues through the season so that by spring the isothermal snow pack consists of large rounded grains with bulk densities as high as $\rho_s = 500\ kg/m^3$ ($\varepsilon = 0.5$). This *rounding* process is illustrated by the bottom series of ice grain photographs in figure 1 of Colbeck (1987a) and is described in more detail in section 1.6.1. Typical winter time dry settled snow pack densities range from $150 < \rho_s < 300\ kg/m^3$.

The densities of the packed laboratory snow ($\rho_l \approx 500\ kg/m^3$), which was comprised of spheres in a narrow size range ($0.25 < \Phi_l < 0.75$ mm), were considerably higher than those of settled dry natural snow of around the same grain sizes.

The reason for the difference lies in the initial bonding of the natural snow. The initial spatial forms reduce the possible contacts between ice grains which usually then become the bonds between grains (in the low temperature gradient case). The characteristics of the bridged structure remain in the snow pack until the bonds are degraded through either high temperature gradient or wet snow processes. The laboratory snow does not have these initial contact restrictions and higher densities result.

To have the laboratory made snow simulate a well settled snow pack the density should be kept as low as possible. This was best achieved by leaving the freshly sieved snow as undisturbed

as possible while the initial bonding (sintering) was in process. After a short time (≈ 1 hr) at above -10°C bonding in the laboratory snow had progressed sufficiently for the sample to be quite robust.

Discussion may arise regarding the validity of such a different starting material. Assuming that adequate controls are provided (and they were), then the comparison between results with and without wind pumping are just as valuable for laboratory snow as they are for natural snow.

6.8.1.4. Loading Sample Tubes

The loading process varied for each experimental run as techniques and requirements developed. Below are details of each packing leading to the development of the final technique (for *Run 6*) illustrated in figure 6.12.

Run 1 - Natural New Snow

The light new snow from Temple Basin was loaded directly into sample tubes as illustrated in figure 6.10. Note that, to hold the sample in place, a mesh screen had been glued to the bottom of the sample tube. This meant that the sample had to be collected by pushing the sample tube into the snow, resulting in an inverted snow sample for the experiment. The samples were placed in chilly bins and packed with dry ice (solid carbon dioxide) for transportation to Christchurch.

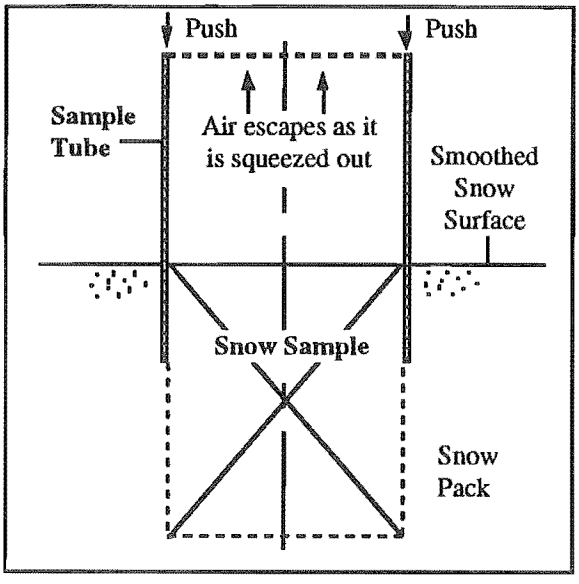

Figure 6.10. Illustration of the Sample Tube Loading Procedure Used for Run 1.

Once in the cold laboratory the sample tubes were removed from the chilly bins and any carbon dioxide vapour in the samples flushed with cold air. It was assumed that this would have a negligible affect on the results as about 9 hours was required for the experiment to come to a thermal steady state (see section X.3), which should have been sufficient time for the vapour phase in the voids to return to equilibrium with the solid phase.

Sample preparation was completed after permeability and density measurements, whereby the sample tubes were loaded into the sample apparati.

Any vibration or jolting of the samples could cause an air gap to develop between the sample and sample tube walls. This was evident in the inconsistent bridging and permeability results.

To get around this problem an internal flexible sleeve was used that allowed slip between the sample and tube wall, and remained 'tight' against the sample so that air could not channel around the sample. One end of the internal sleeve had to be attached and sealed against the tube wall to meet this second requirement.

Runs 2 and 3 - Laboratory Snow

For *Run 2* the larger end of a tapered polythene sleeve (cut from a plastic glove) was wrapped around the top end of the sample tubes so the narrow end hung just above the wire mesh. The dried (of liquid nitrogen) laboratory snow was then sieved directly into the sample tubes with 710 μm mesh screen. To allow the air trapped between the polythene sleeve and tube wall to escape, the sleeve had several slits cut in the sleeve near the top of the tube. Once the sample was loaded the slit portion of the tube was then pulled up and over the top of the tube to provide the seal between the sample and tube. This loading procedure is illustrated in figure 6.11.

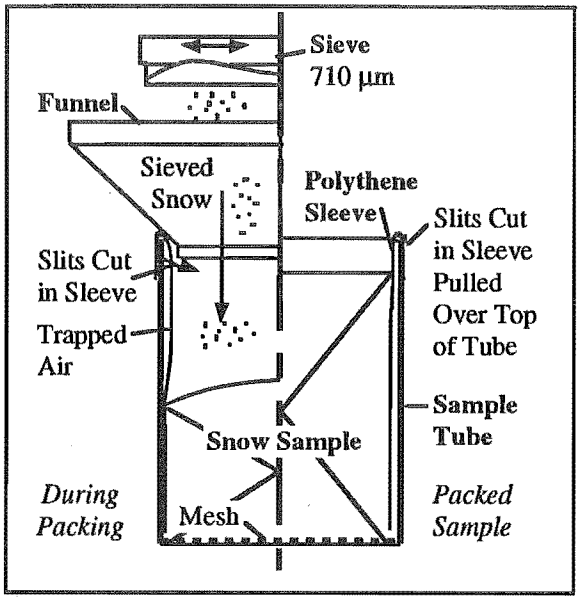

Figure 6.11. Illustration of the Sample Tube Loading Procedure Used for Run 2.

A photo of the top of the polythene sleeve wrapped over the top of the sample tube in an assembled state is shown in plate 6.2(a). The polythene sleeve covering the removed sample is illustrated in plate 6.2(c).

This technique still did not fully solve the problems of *Run 1*. Whilst there appeared to be no bridging, the gentle folds in the polythene sieve that were not flattened out by the weight of the sample resulted in air gaps. The folds flattened out when the sleeve was pulled tight to move the cut slits over the top of the sample tube. This resulted in spaces between the polythene sleeve and the sample, and an increased chance of channel development. An example of a resulting channel is shown in plate 6.2(b).

To get around this for *Run 3* the sleeve was not moved once the sample was loaded. To achieve this and allow the trapped air to escape pieces of thick string were laid over the rim creating an air gap either side of the string for the air to escape. Once loaded, the string could be pulled out to provide the seal between the sample and tube.

Run 4 - Natural Partially Settled Snow

The wind packed, partially settled new snow was transported from Mt Lyford in sealed plastic bags to exclude carbon dioxide vapour (dry ice was used to cool the sample for travel). Upon arrival at the cold laboratory the snow was coarsely sieved with a 1000 μm screen directly into the sample tube which had already been inserted into the sample tube insulation. This was to further reduce the possible disturbances on the sample. The polythene tube technique was the same as that used for *Run 3*. Adams and Brown (1982) used a similar sieving method in their laboratory temperature gradient experiments.

Run 5 - Natural Partially Settled Snow

In *Run 4* there was no detectable settlement so no polythene sleeve was used for *Run 5*. Otherwise the snow source and packing technique were the same as for *Run 4*.

Run 6 - Natural Partially Settled Snow

The collection and transportation of the snow from Temple Basin used for this run utilized the same method used for *Runs 4 and 5*.

Up until this point the mesh screen glued to the bottom of the sample tubes to hold the sample in place had restricted techniques to top loading only. For *Run 6* the mesh screens were removed and the tubes loaded as described below and shown in figure 6.12(a).

1. After transportation to the cold laboratory, the snow was sieved with two mesh sizes into two chilly bins and allowed to settle for 18 hours (by which time it could be tipped out as a robust block).
   * Through 1000 μm into a bin from which three samples were taken (for sample tubes A, B and E).
   * Through 2800 μm into a bin from which two samples were taken (for sample tubes C and D).
2. The blocks from the chilly bins were then cut into smaller blocks (slightly larger than the sample tube).
3. The polythene tube was wrapped tightly about both ends of the sample tube so that the narrow end was at the top and there were no creases in the polythene.
4. Slits were cut near the top of the sleeve to allow the trapped air to escape.
5. The tube was pushed down over the prepared block of snow, self cutting to the correct shape (the polythene sleeve was tough enough to withstand the abrasion by the snow around the bottom rim of the sample tube).
6. The polythene sleeve above the slits was cut off and discarded (the seal between the polythene tube and the sample was gained at the bottom end of the tube).

Two concepts were behind this method:

* More pressure would be exerted on the snow sample by the polythene sleeve.

* No creases could occur in the polythene sleeve.

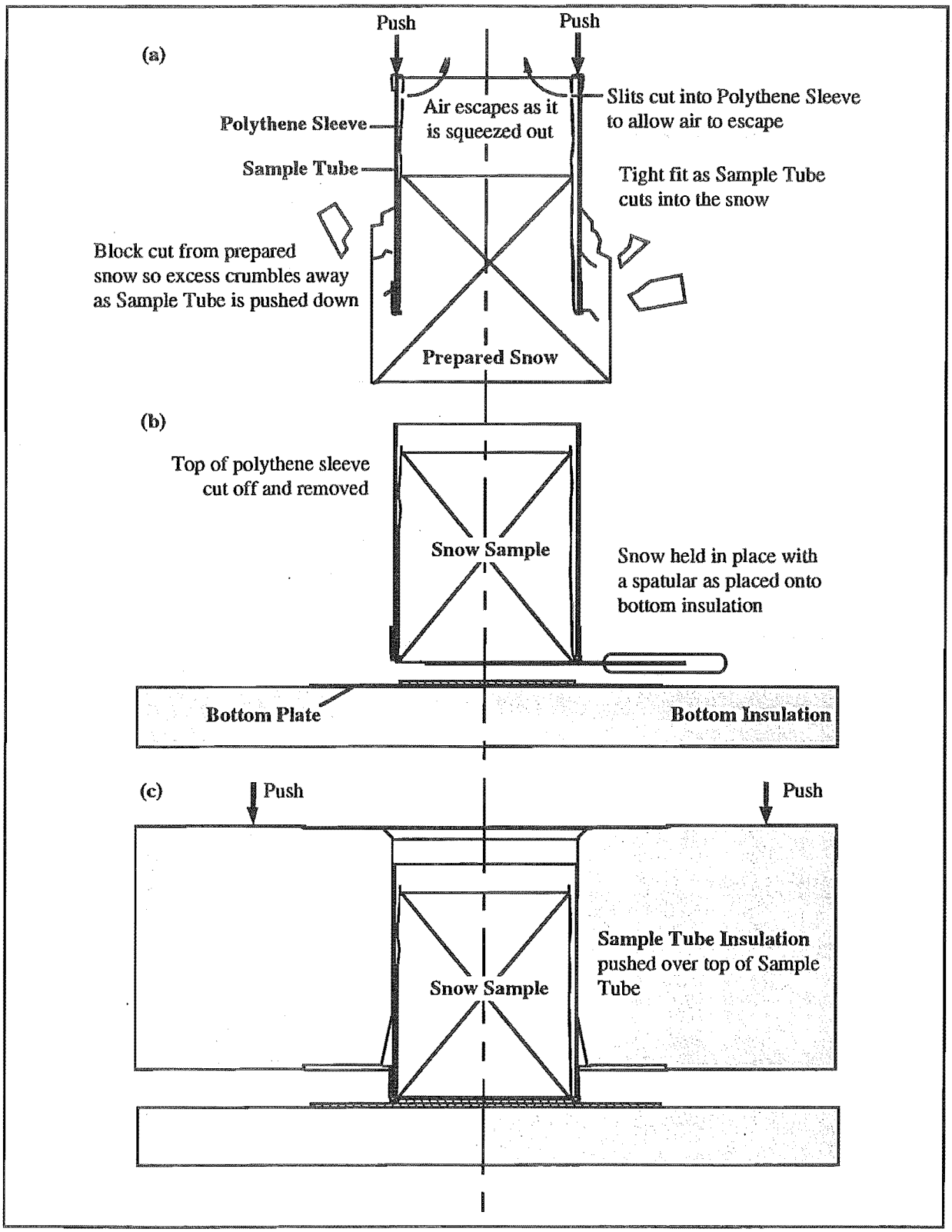

Figure 6.12. Illustration Showing the Final Method Used to load Snow into the Sample Tubes and the Sample Tubes into the Sample Apparatus.

6.8.2. Results

The following details the results of the six runs made. These developments in the apparatus and in experimental technique are noted chronologically through the documentation of the runs.

Prior to these six runs, numerous test runs were made using laboratory snow in an attempt to remove the major problems from the snow making, sample loading, experimental control, and sample analysis procedures. No results from these test runs are presented here.

The sample loading methods used for each run are detailed in section 6.8.1.4, and the tools used in the analysis detailed in section 6.7.

In most cases, the strength tests are presented as statistical comparisons. Summaries of the data used for these comparisons are included in Appendix XII.

6.8.2.1. Applied Wind Pumping

The applied wind pumping was set to equate to the gale force wind (60 to 90 km/hr) conditions that are likely to be experienced in the mountains during storms. It was concluded in Chapter 5 that the number of *grain diameters* the wind pumping airflow travels through in each cycle is the controlling influence on vapour transport enhancement. The imposed conditions, and grain diameters are summarised in table 6.1.

Run	Period (s)	Amplitude (Pa)	Maximum Velocity (mm/s)	Cyclic Displacement (mm)	Grain Size (mm)	Number of Grain Diameters
3	3.2	100	1.1	1.2	0.3	4
4	3.2	100	2.1	3.5	0.3	12
5	3.2	100	1.1	1.8	0.2	9
6	3.2	80	1.4	2.4	0.25	10

Table 6.1. Applied Wind Pumping for Runs 3 to 6. The maximum velocity and cyclic displacement were calculated using the numerical methods detailed in section 4.8.1.

6.8.2.2. Run 1 - Low Temperature Gradients on Natural New Snow

Objectives

To get an indication of the consistency the results might offer, all sample apparati were run at low temperature gradients (plates all set at the same temperature).

Results and Experimental Developments

Permeabilities and the results of the strength testing for *Run 1* are not reported. This was due to several factors:

* In some of the sample tubes the snow at the top of the sample stuck to the tube walls and bridged. Subsequent settlement of the un-bridged snow below left large air spaces within the sample. This allowed air to be channelled though lower resistance paths, thus bypassing the sample.
* Substantial ice buildup was noted on the sample side of both diaphragms (sample tubes D and E only). It was assumed that this was a result of the temperature gradient between the snow sample and cold laboratory. This ice build up is illustrated in plate 6.1(c).
* The wind pumping airflow through the top and bottom plates etched holes up to 30 mm deep in the top and bottom surfaces of the sample (sample tubes D and E only). These holes can be seen in plate 6.2(a).

Several modifications were made to the apparatus to alleviate these problems. These included:

* Addition of the polythene sleeve to prevent bridging, whilst allowing for settlement. This is fully described in section 6.8.1.4.
* Fitting of the diaphragm balance heaters to remove any temperature gradient forming over the diaphragm (sample tubes D and E only). Section 6.6.4.2 fully details this modification.
* Addition of airflow splitters to the holes in the top and bottom plates to better distribute the wind pumping air movements (sample tubes D and E only). This modified air hole configuration is described in section 6.6.3.5 and illustrated in figure 6.4.

The accumulation of ice on the diaphragm clearly showed that the vapour barriers were required. Without them, the mass of ice accumulated would have been lost to the cold laboratory.

6.8.2.3. Run 2 - High Temperature Gradients on Laboratory Snow

Objectives

To get an indication of the consistency the results might offer, all sample apparati were run at similar high temperature gradients.

Results and Experimental Developments

As with *Run 1*, the results for *Run 2* are not reported. This was because:

1. Some of the slits cut into the polythene sleeve were not pulled completely over the top of the sample tube.
2. The action of pulling up the sleeve left hollows around the sample where folds existed during pouring of the sample. The result of such folds are illustrated in plates 6.2(c) and 6.2(d).
3. Wind pumping channels formed around the outside of the sample (sample tubes D and E only). One of the resulting channels is illustrated in plate 6.2(b). The top end of three channels can be seen in plate 6.2(a).

These all allowed air to be channelled though lower resistance paths, thus bypassing the sample. To get over the problems experienced in this run, modifications were required in the way the polythene sleeve was used. These modifications are fully described in section 6.8.1.4.

No specific problems were experienced due to the application of the high temperature gradient

6.8.2.4. Run 3 - Moderate and High Temperature Gradients on Laboratory Snow

Objectives

To apply moderate and high temperature gradients over the samples, and obtain some meaningful results.

Experimental Procedure

The procedures and settings used for *Run 3* are detailed in tables 6.2 and 6.3 respectively. Note that samples A and E were paired, and samples C and D were paired. One of each pair (sample D and E) were exposed to the wind pumping. Sample B was used for the initial (control) analysis.

Date	Time (hrs)	Task
08/05/92	0900 - 2000	Laboratory Snow Making.
	1400 - 1500	Tubes packed and placed into the sample apparati according to the method described in section 6.8.1.
09/05/92	1130	Heaters turned on.
	2100	Wind pumping turned on.
10/05/92	1000	Wind pumping and heaters turned off sample B. Elapsed time 13 hours.
	1000 - 1100	Sample B analysed.
18/05/92	0930	Wind pumping and heaters turned off samples A, C, D and E. Elapsed time 8 days and 12.5 hours.
	0930 - 1400	Samples A, C, D and E analysed.

Table 6.2. Time Details for Run 3.

Sample Apparatus	Sample Specific Details	Top Plate Temperature (°C)	Bottom Plate Temperature (°C)	Temperature Gradient (°C/m)	Sample Density (kg/m^3)
A	moderate temperature gradient	-6.0	-4.0	11	315
B	analysed after 13 hours	-6.0	-4.0	11	320
C	high temperature gradient	-9.0	-1.0	49	330
D	high temperature gradient	-9.0	-1.0	45	325
E	moderate temperature gradient	-6.0	-4.0	11	330

Table 6.3. Sample Details for Run 3.

Results

In all cases solid type depth hoar (Akitaya, 1974) formed thought out the sample.

Sample Apparatus	Permeabilities (x10^5 m^2/Pas) Initial	Final	Change
A	0.8	2.1	↗62%
B	1.1	1.6	↗33%
C	0.8	1.1	↗29%
D	0.8	1.7	↗52%
E	0.9	3.8	↗78%

Table 6.4. Permeabilities from Run 3.

As can be seen in table 6.4 permeability has risen substantially in all samples, as was expected with the faceting process (Conway and Abrahamson, 1984b). In both the high and moderate temperature gradient cases, this rise was greater in samples which have the wind pumping imposed (D and E). These changes are all greater than the inherent variability of the permeability measurement (about ±3%). Note that sample B had a large crease in its polythene sleeve. It was assumed that this was the cause of the higher recorded permeability.

The growth of faceted grains is expected with the applied temperature gradients. The growth rates should be dependent on both absolute temperature and temperature gradient. The faceting process should be accompanied by a loss in strength in the samples (Adams and Brown, 1982, Colbeck, 1987a). The results of the cone penetrometer tests for *Run 3* are shown in table 6.5. Several trends, all consistent with the faceting process, are apparent in both sets of results:

* All samples exhibited the expected weakening. This can be seen in comparisons with sample B which was analysed after 9 hours (the other samples were analysed after 200 hours).
* The high temperature gradients samples have become significantly weaker (at the $\alpha = 0.025$ level) compared to the moderate temperature gradient samples (with and without wind pumping).
* There was a significant enhancement (at the $\alpha = 0.025$ level) in the loss of strength process in the high temperature gradient sample with wind pumping.

* There was no significant difference (at the $\alpha = 0.05$ level) between the moderate temperature gradient samples with or without wind pumping.

If an indication of the high temperature gradient grain growth rates can be drawn from the intergranular strength[5], then it appears that the influence of wind pumping is almost as important as the magnitude of the temperature gradient. From the discussion in section 1.8.3, the higher temperature gradient enhancement through wind pumping is most likely to occur when there is a large temperature difference between :

* The air and snow near the surface of the snow pack
* Two layers of snow near the surface of a permeable snow pack.

Cone Weight	2150 g			5150 g		
Temp. Grad.	Mod. 11°C/m		High 47°C/m	Mod. 11°C/m		High 47°C/m
No	A = 3.2	↘47% **	C = 4.4	A = 5.9	↘59% **	C = 9.0
Wind Pumping ?	↘26% ns		↘37% **	↗7% ns		↘26% **
Yes	E = 3.7	↘55% **	D = 5.5	E = 5.7	↘71% **	D = 10.6

Table 6.5. Cone Penetration Results for Run 3 - Moderate and High Temperature Gradients on Laboratory Snow. Each quoted result is an average of the upper, centre and lower measurements taken from table XII.1. The percentages are comparisons of strength calculated using equation 6.4 (the arrows showing the direction of change). To illustrate the direction of the comparison, E is 26% weaker that A, and C is 47% weaker than A. The conclusions for each test are indicated by ** - significantly different at $\alpha = 0.025$, * - significantly different at $\alpha = 0.05$, ns - not significantly different at $\alpha = 0.05$.

The vertical distribution of hardness varied according to the applied temperature gradient. Two trends are evident from table XII.1 (in Appendix XII):

* At moderate temperature gradients there is a significant trend (at the $\alpha = 0.025$ level) of stronger snow at the top of the sample to weaker at the bottom. This is explained by the metamorphic rate dependence on temperature (Perla and Martinelli, 1976).
* The trend appears to be inverted at high temperature gradients, although it is not significant at the $\alpha = 0.05$ level. In this case a neutral trend may be expected as the metamorphic rate is strongly dependent on the temperature gradient (Colbeck, 1983b).

---

[5]During high temperature gradient metamorphism (faceting) the bonds between the grains are consumed by the recystallisation. This is covered in more detail in section 1.6.1.1.

All of the trends observed in the cone penetrometer tests are apparent in the tensile results shown in table 6.6. However, there are insufficient results to make any statistical conclusions on these results.

No significant changes were observed in the densities. No shear tests were performed in this run.

Sample Apparatus	Tensile Strength ($\times 10^{-5}$ Pa) Reps.	Mean	s
A top	2	1.3	0.4
bottom	2	0.74	0.06
B all tests	4	1.4	0.5
C top	2	0.74	0.01
bottom	3	0.79	0.61
D top	2	1.4	0.3
bottom	3	1.9	0.6
E top	2	3.0	1.2
bottom	2	2.1	0.1

Table 6.6. Tensile Strength Results for Run 3. s is the standard deviation of the replications made in each sample.

Experimental Developments

Some problems with the sample packing and wind pumping airflow were still apparent in this run, namely:

1. The action of pulling up the sleeve left hollows around the sample where folds existed during pouring of the sample. The result of such folds are illustrated in plate 6.2(c) and 6.2(d).
2. Some channels resulting from the wind pumping were still around the outside of the sample (sample tubes D and E only).

The persistence of depressions around the wind pumping airflow holes showed that most of the air was indeed going through the sample, and not tracking around it. Continued modifications were made on the use of the polythene sleeve in an attempt to improve the seal between the sample and polythene.

6.8.2.5. Run 4 - Low Temperature Gradients on Wind Packed Snow

Objectives

In this run the progression of metamorphism at low temperature gradients was examined from an initial state of no bonding between ice grains. This was done to investigate the effect wind pumping may have in wind slab formation.

Experimental Procedure

To achieve this objective the wind pumping was applied from the time the samples were packed, a low temperature gradient was applied to all sample apparati, and the samples analysed after 19 and 43 hours. To avoid any extraneous effects the application of temperature gradients may have had on the samples while they were being brought to the required plate temperature, the heater set points were set at the snow temperature at the time it was loaded.

The procedures and settings used for *Run 4* are detailed in tables 6.7 and 6.8 respectively. Note that samples A and D were paired, and samples B, C and E were grouped. One of each pair (sample D and E) was exposed to the wind pumping. Apart from permeabilities, no initial (control) analysis was made.

Date	Time (hrs)	Task
23/05/92	1600	Natural snow collected from Mt Lyford Ski Area, North Canterbury.
24/05/92	1400 - 1500	Tubes packed and placed into the sample apparati according to the method described in section 6.8.1.
	1500	Wind pumping and heaters turned on.
25/05/92	1000	Wind pumping and heaters turned off sample apparati B and D. Elapsed time 19 hours.
	1000 - 1400	Samples A and D analysed.
26/05/92	1000	Wind pumping and heaters turned off sample apparati B, C and E. Elapsed time 43 hours.
	1000 - 1400	Samples B, C and E analysed.

Table 6.7. Time Details for Run 4.

Sample Apparatus	Sample Specific Details	Top Plate Temperature (°C)	Bottom Plate Temperature (°C)	Temperature Gradient (°C/m)	Sample Density (kg/m^3)
A	analysed after 43 hours	-4.0	-4.0	0.0	315
B	analysed after 19 hours	-4.0	-4.0	0.0	320
C	analysed after 19 hours	-4.0	-4.0	0.0	330
D	analysed after 43 hours	-4.0	-4.0	0.0	325
E	analysed after 19 hours	-4.0	-4.0	0.0	330

Table 6.8. Sample Details for Run 4.

Results

In all cases rounding and sintering occurred throughout the samples.

Table 6.9 shows the changes in permeability found in *Run 4*. It is surprising to find that the permeability has risen in 4 of the 5 samples. This is against the expected trend for settlement of snow under low temperature gradient metamorphism (Conway and Abrahamson, 1984b).

Sample	Permeabilities (x10^5 m^2/Pas)		
Apparatus	Initial	Final	Change
A	5.9	7.0	↗18%
B	6.1	6.7	↗10%
C	6.1	5.7	↘ 7%
D	5.5	6.8	↗22%
E	6.1	8.9	↗47%

Table 6.9. Permeabilities from Run 4.

Although more subtle, it appeared that the air was still tracking around the sample in the snow close to the polythene sleeve. By comparison to the samples without wind pumping, the snow adjacent to the sleeve looked thinner, or eaten away, leaving a more skeletal like structure. This skeletal layer appeared to be around 3 grain diameters thick. The substantially higher wind pumping sample permeabilities can probably be explained by this.

If channeling was occurring, then the airflow through the rest of the sample will have been less. Hence any significant results obtained from the statistical tests would have been more so than if no channeling had occurred. The etching (illustrated in plate 6.2(a)) around the holes in the heating plates in the top and bottom surfaces of the sample are evidence that some of air was moving through the sample.

The results of the shear and tensile tests are shown in table 6.10. Considerable variation is observed in the measurements. Although not significant (at the $\alpha = 0.05$ level), two trends are apparent in the results:

* At both analysis times, a trend towards stronger snow is found in the samples with wind pumping compared to those without.
* A sample *weakening* trend with time is observed with and without wind pumping. This is not expected under a low temperature gradient. No reason can be offered for this peculiar result.

Test	Shear			Tensile		
Time Elapsed	19 hours		43 hours	19 hours		43 hours
No Wind Pumping ?	B & C =40	↘43% *	A = 23	B & C = 24	↘67% ns	A = 8
	↗5% ns		↗57% ns	↗26% ns		↗25% ns
Yes	E = 42	↘14% ns	D = 36	E = 33	↘60% ns	D = 10

Table 6.10. Shear and Tensile Strength Results for Run 4 - Low Temperature Gradients on Wind Packed Snow. The percentages are strength comparisons between variables. To illustrate the direction of the comparison, E is 5% stronger that B & C, and A is 43% weaker than B & C. The conclusions for each test are indicated by ** - significantly different at $\alpha = 0.025$, * - significantly different at $\alpha = 0.05$, ns - not significantly different at $\alpha = 0.05$.

It is possible that with the 0.0°C/m temperature gradient imposed on the plates, the micro scale temperature gradients within the sample were in fact not being controlled. This would mean that differing small temperature gradients could exist in each sample. From section 6.6.4.1 the limit on control accuracy is governed by the ±0.1°C error in the thermocouple calibrations. Thus the maximum uncontrolled temperature may be as high as 1°C/m The uncontrolled radial gradients, which are estimated to be a maximum of 0.3°C/m in section X.1.6.2, might also

have some influence. From Colbeck (1882) such low temperature gradients control the rate (but not the direction) of metamorphism. Further, Perla (1978b) showed that an imposed temperature gradient is necessary to get the commonly observed rates of grain growth, even when only rounded grains develop.

Another possibility was that the strength of the snow had plateaued out by the time of the analysis at 19 hours. Consequently, only a small gain in strength was observed between 19 and 43 hours, and also between no wind pumping and wind pumping. This is consistent with the higher initial rounding growth rates of new and wind redeposited snow (Colbeck, 1987b).

No significant changes were observed in the densities. No cone penetrometer tests were performed for *Run 4*.

Experimental Developments

As no notable settlement occurred with the density of snow that was being examined, the next run was performed without the polythene sleeve.

6.8.2.6. Run 5 - Low Temperature Gradients on Wind Packed Snow

Objectives

The progression of metamorphism at low temperature gradients was examined from an initial state of no bonding between ice grains in this run. This was done to investigate the effect wind pumping may have in wind slab formation (as in *Run 4*). The analysis of the sample for this run was performed in a reduced time frame compared to *Run 4* so that the period where the processes occur at a higher metamorphic rate could be investigated.

Experimental Procedure

The wind pumping was applied from the time the samples were packed, a low temperature gradient applied to all sample apparati, and the samples analysed after 4 and 9 hours. To avoid any extraneous effects the application of temperature gradients may have had on the samples while they were being brought to the required plate temperature, the heater set points were set at the snow temperature at the time it was loaded.

The procedures and settings used for *Run 5* are detailed in tables 6.11 and 6.12 respectively. Note that samples B and D were paired, and samples A, C and E were grouped. One of each pair (sample D and E) was exposed to the wind pumping. Apart from permeabilities, no initial (control) analysis was made.

Date	Time (hrs)	Task
24/05/92	1600	Natural snow collected from Mt Lyford Ski Area, North Canterbury.
29/05/92	0900 - 1030	Tubes packed and placed into the sample apparati according to the method described in section 6.8.1.
	1030	Wind pumping and heaters turned on.
	1430	Wind pumping and heaters turned off sample apparati B and D. Elapsed time 4.0 hours.
	1430 - 1730	Samples B and D analysed.
	1930	Wind pumping and heaters turned off sample apparati A, C and E. Elapsed time 9.0 hours.
	1930 - 2230	Samples A, C and E analysed.

Table 6.11. Time Details for Run 5.

Sample Apparatus	Sample Specific Details	Top Plate Temperature (°C)	Bottom Plate Temperature (°C)	Temperature Gradient (°C/m)	Sample Density (kg/m^3)
A	analysed after 9 hours	-4.5	-4.5	0.0	375
B	analysed after 4 hours	-4.5	-4.5	0.0	365
C	analysed after 9 hours	-4.5	-4.5	0.0	365
D	analysed after 4 hours	-4.5	-4.5	0.0	365
E	analysed after 9 hours	-4.5	-4.5	0.0	360

Table 6.12. Sample Details for Run 5.

Results

In all cases rounding and sintering occurred throughout the samples.

Sample Apparatus	Permeabilities ($x10^5$ m^2/Pas) Initial	Final	Change
A	2.7	3.0	↗10%
B	3.0	3.2	↗7%
C	3.0	3.3	↗10%
D	3.0	3.1	↗3%
E	3.3	3.2	↘ 3%

Table 6.13. Permeabilities from Run 5.

The permeability results are shown in table 6.13. The opposite trend was apparent compared to *Run 4*. There was no evidence of the airflow channelling between the sample and the walls of the sample tubes. It is therefore more likely that a true bulk permeability was measured. The permeabilities of the samples with wind pumping did not change significantly, while the samples without wind pumping all have increased permeability. There was no apparent difference between the 4 and 9 hour results. This indicates that all permeability results to this point are functions of the deficiency of the experiment itself, and not of the wind pumping mechanism.

The results of the shear and tensile tests are shown in table 6.14. The results are more consistent than those in *Run 4*. However the apparent trends (below) are still not significant at the $\alpha = 0.05$ level.

* At both analysis times, a trend towards stronger snow was found in the samples with wind pumping compared to those without.
* The samples analysed at 9 hours appear stronger than their counterparts at 4 hours.

No significant changes in the densities were observed in these results.

Test	Shear			Tensile		
Time Elapsed	4 hours		9 hours	4 hours		9 hours
No Wind Pumping ?	B = 11	↗45% **ns**	C = 16	B = 11	↗36% **ns**	C = 15
	↗18% **ns**		↗56% **ns**	↗55% **ns**		↗33% **ns**
Yes	D = 13	↗15% **ns**	E = 25	D = 17	↗15% **ns**	E = 20

Table 6.14. Shear and Tensile Strength Results for Run 5 - Low Temperature Gradients on Wind Packed Snow. The percentages are strength comparisons between variables. To illustrate the direction of the comparison, D is 18% stronger that B, and C is 45% stronger than B. The conclusions for each test are indicated by ** - significantly different at $\alpha = 0.025$, * - significantly different at $\alpha = 0.05$, **ns** - not significantly different at $\alpha = 0.05$. Sample A was damaged during removal from the apparatus and could not analysed.

In terms of wind slab, the affect of wind pumping appears to be more important to the development of the slab cohesiveness (strength) than the stagnant diffusive metamorphism over the time scales used in this experiment. If the time scale is extrapolated back to when the wind slab is gaining in thickness (fragmented snow is being added to the snow surface), it is conceivable that the wind pumping could be playing a major role in the initial bonding. Caution should be applied to this extrapolation because the conditions in the sample tubes are not quite the same as what occurs at the top of a wind slab (where there can be different atmospheric humidities).

The enhancement of bonding created by wind pumping may go some way to explaining the stabilisation of storm snow weakness after very strong prolonged windstorms (see section 1.8.2), where the magnitude of wind pumping may be greater than that imposed in these experiments.

Experimental Development

To this point the method of loading the tubes had been severely limited by the holding mesh at the bottom of the sample tubes. For *Run 6* this was removed and a loading technique used

which eliminated the problems associated with top loading. This modification is fully described in section 6.8.1.4 and illustrated in figure 6.12.

6.8.2.7. Run 6 - Low Temperature Gradients on Partially Settled Snow

Objectives

As this was the last possible run that could be made in the cold laboratory time, due to rental costs, it was decided that another set of low temperature gradient results be obtained. In this run the effect of sieving the sample with two different mesh sizes was also examined.

Experimental Procedure

To achieve this objective the samples were prepared by sieving with mesh sizes of 1000 μm and 2800 μm, and all samples analysed after 66.5 hours. To avoid any extraneous effects the application of temperature gradients may have had on the samples while they were being brought to the required plate temperature, the heater set points were set at the snow temperature at the time it was loaded.

The procedures and settings used for *Run 6* are detailed in tables 6.15 and 6.16 respectively. Note that samples C and D were paired, and samples A, B and E were grouped. One of each pair (sample D and E) was exposed to the wind pumping. In an attempt to extract some statistical significance from the strength tests only cone penetration tests were performed on the samples. Some initial cone penetrations were made on excess snow.

Date	Time (hrs)	Task
27/06/92	1600	Natural snow collected from Temple Basin Ski Area Base, Arthur's Pass National Park.
	2200	Chilly bins packed in the cold laboratory.
28/07/92	1600 - 1700	Tubes packed and placed into the sample apparati according to the method described in section 6.8.1.
	1730	Wind pumping and heaters turned on.
01/07/92	1200	Wind pumping and heaters turned off. Elapsed time 66.5 hours.
	1200 - 1400	Samples analysed.

Table 6.15. Time Details for Run 6.

Sample Apparatus	Sample Specific Details	Top Plate Temperature (°C)	Bottom Plate Temperature (°C)	Temperature Gradient (°C/m)	Sample Density (kg/m^3)
A	sieved with 1000 μm mesh	-6.0	-6.0	0.0	340
B	sieved with 1000 μm mesh	-6.0	-6.0	0.0	370
C	sieved with 2800 μm mesh	-6.0	-6.0	0.0	320
D	sieved with 2800 μm mesh	-6.0	-6.0	0.0	320
E	sieved with 1000 μm mesh	-6.0	-6.0	0.0	330

Table 6.16. Sample Details for Run 6.

Results

In all cases rounding and sintering occurred throughout the samples.

Changes in density were negligible. No reason can be offered as to why sample B had a higher density compared to samples A and E, which were sieved in the same manner. The pattern of differing results for sample B is also consistent through the cone penetrometer tests shown in table 6.18. Therefore it would seem prudent to leave sample B out of the comparisons of other samples.

The densities resulting from sieving through a mesh of 1000 μm were not very different from those sieved through a 2800 μm mesh. This suggests that the results should be reasonably independent of the packing methods used.

The permeabilities changes shown in table 6.17 are consistent with those found in *Run 5*. In all samples the permeability has increased. For both sieve sizes the permeabilities of samples with wind pumping appear to have changed less than those samples without. This indicates that the sample loading method developed does not interfere with the wind pumping processes, as any inadequacies tend to increase the apparent permeability.

Sample	Permeabilities (x10^5 m^2/Pas)		
Apparatus	Initial	Final	Change
A	4.7	5.3	↗11%
B	3.4	3.8	↗11%
C	5.8	6.2	↗6%
D	6.1	6.4	↗5%
E	4.9	5.3	↗8%

Table 6.17. Permeabilities from Run 6.

Some cone penetrometer tests were performed on some excess initial sample sieved with the larger mesh. With a cone weight of 150 g, a mean penetration of 12.7 mm with a standard deviation of 4.0 was found from 10 tests. All the 150 g results shown in table 6.18 indicate a hardening of the samples. Several trends are evident in the results:

* With both sieve sizes the samples with wind pumping appear stronger than the samples without. This trend appears to be significant at the $\alpha = 0.05$ level.
* The samples sieved with the 1000 μm mesh are stronger than their counterparts sieved with the 2800 μm mesh. This is not statistically significant at the $\alpha = 0.05$ level.

Cone Weight	150 g			650 g		
Mesh Size	1000 μm		2800 μm	1000 μm		2800 μm
No Wind Pumping ?	A = 9.2	↘5% ns	C = 9.1	A = 16.8	↗9% ns	C = 17.8
	↗69% **		↗33% **	↗9% ns		↗9% *
Yes	E = 7.0	↗25% *	D = 8.0	E = 16.2	↗9% ns	D = 16.9

Table 6.18. Cone Penetration Results for Run 6 - Low Temperature Gradients on Partially Settled Snow. The percentages are comparisons of strength calculated using equation 6.4 (the arrows showing the direction of change). To illustrate the direction of the comparison, E is 69% stronger that A, and C is 5% weaker than A. The conclusions for each test are indicated by ** - significantly different at $\alpha = 0.025$, * - significantly different at $\alpha = 0.05$, ns - not significantly different at $\alpha = 0.05$.

Experimental Development

No problems were experienced as a result of the experimental techniques used for this run.

Unfortunately it had taken the duration of the time allotted to this portion of the overall experimental programme to get to a point where the apparatus and techniques were developed sufficiently to get trouble free results.

6.9. Discussion on the Experimental Design

Points pertaining directly to the results have been discussed with the presentation of the results in the previous section. There is a need for some discussion on the experiment itself prior to drawing conclusions on this chapter.

6.9.1. Experimental Apparatus

A few concluding comments on the demands placed on apparatus by the wind pumping requirement are appropriate.

The most prominent difficulty was getting the air to flow through the sample, and not around the walls, whilst not inhibiting settlement. The solution to this revolved around the sample loading techniques. Although the earlier techniques all essentially worked, it was felt that the final method used was by far the most successful. This was because the sample pressed out against the polythene sleeve, making it wrinkle free, and more difficult for channels to form.

Stopping the migration of sample water vapour to the colder diaphragms was effectively achieved by the diaphragm balance heaters.

For the effect of the low temperature gradients on the growth rates to be controlled, greater accuracy is required on the temperature control. The limiting factor on the control used here was the calibration of the thermocouples. With better calibration equipment it is thought that this control could be improved by an order of magnitude to ±0.1°C/m.

There is some concern about the effect the sample selection, preparation and packing techniques may have had on the results. Given the location of the cold laboratory, far from sources of natural snow, few other options were available. Ideally this work needs to be done in a location where consistent snow samples are readily available.

6.9.2. Variables Analysed

Only one strong wind pumping condition resulting from gale force winds (60 to 90 km/hr) was imposed. This condition is not thought cover storm force winds (>90 km/hr), and so on isolated occasions the strength of the wind pumping could be greater than that used here. There is a need to look at a variety of wind pumping intensities. The results could then be related to the number of grain diameters the cyclic displacement passes through. Longer period fluctuations also need to be examined.

In these experiments only a few snow pack variables have been examined. Although the results show some strong trends, there is still a need to investigate a number of parameters not studied here. These are detailed in section 6.10.2.

6.9.3. Comments on the Strength Tests

The inherent variability of the shear and tensile tests is significantly larger than the cone penetration tests which appeared to be independent of the experimental difficulties. Also, many more cone penetration tests can be made in the same volume of sample by comparison to the shear and tensile tests. As a result the cone penetrometer gave statistically significant results, whereas the shear and tensile tests did not. The cone penetrometer must therefore be recommended at the best strength testing tool in such analysis.

The reasons why the cone penetrometer is the more reliable test lies in the greater complexity of the shear and tensile tests. The source of variability for each test are thought to be:

Tensile Test — Handling involved with the test piece preparation, and the final quality of the test piece. The result is likely to be very sensitive to any stress concentrations in the test piece. These stress

	concentrations may result from the shape and finish of the test piece and/or any misalignment in the axial load.
Shear Test	Applied bending moments on the sample during testing. These arise when the test piece begins to crush on its back face allowing the upper shear block (see figure VIII.1) to tilt.
Cone Penetrometer Test	From the load rate. The two sides to this variability are; shock loading at load rates which are too high, and viscoelastic deformation at load rates which are too low.

Increasing the weight on the cone in the penetration tests does not appear to improve the results, and serves to destroy larger amounts of the sample. Therefore the lighter weights are preferred.

6.10. Conclusions

The purposes of this chapter were to design and build an experimental apparatus capable of measuring the metamorphic effects of wind pumping, and to experimentally determine the effects the wind pumping airflow has on the metamorphism of dry snow.

6.10.1. Laboratory Metamorphism Experiments

No direct observations or measurements had previously been published on the the effects of wind pumping in a controlled environment. The number of uncontrollable variables in the natural snow pack prohibited in *situ* field observations of snow metamorphism due to wind pumping, and so cold laboratory studies were required.

The major difficulties in the design of the experimental apparatus that required wind pumping capabilities were resolved.

Pressure fluctuations associated with gale force winds (60 to 90 km/hr) were used to provide strong wind pumping conditions. Two types of experiments were run, both in high density snow ($\approx$350 kg/m^3):

* Initially bonded grains had moderate to high temperature gradient imposed on them to evaluate any enhancements in the faceting process.
* Grains without any initial bonding had low temperature gradients imposed upon them to evaluate any enhancements in the rounding process.

Elapsed time to sample analysis varied from 4 hours to 8.5 days. The conclusions are mainly drawn from the strength tests performed. The successful application of strength tests varied:

* The cone penetration tests, which appeared to be independent of the experimental difficulties, produced statistically significant results.

* The variability of the shear and tensile tests made it difficult to extract statistically significant conclusions from the data. However, the trends in the shear and tensile tests followed those of the cone penetrometer.

The cone penetrometer is therefore recommended as the best strength testing tool in this type of analysis.

Photographical work did not prove to be a useful tool in the analysis of the results. Stereology is probably required to quantify the structural changes geometrically.

6.10.1.1. Enhancement of the Faceting Process

Moderate (11°C/m) and high (47°C/m) temperature gradients were placed over the initially well rounded samples for 8.5 days. In all cases solid type depth hoar formation was observed. The strength tests on the samples were consistent with the development of facets:

* All samples exhibited the expected weakening.
* At moderate temperature gradients there was a significant trend of stronger snow at the top of the sample to weaker at the bottom. At high temperature gradients, this trend was not apparent.
* The high temperature gradient samples became significantly weaker compared to the moderate temperature gradient samples.

There was a significant enhancement in the loss of strength process in the high temperature gradient sample with wind pumping. *The influence of wind pumping on the growth rates of depth hoar appears to be almost as significant as the influence of the temperature gradient magnitude.* This wind pumping enhancement is most likely to occur when there is a large temperature difference near the surface of the snow pack between:

* The air and snow.
* Two layers of snow.

Wind pumping is unlikely to enhance the development of facets at the bottom of the snow pack, or below ice crusts.

As expected, the sample permeabilities increased during the faceting process.

6.10.1.2. Enhancement of the Rounding Process

Zero temperature gradients were placed over initially unbonded fragmented partially settled samples for varying periods. In all cases rounding occurred. In all but one case, the strength tests on the samples were consistent with sintering. That is, all the samples gained strength with time.

In all cases, this development of strength appeared to be larger with wind pumping. *The effect of wind pumping on the development of snow strength appears to be more important than the effect of elapsed time.* In the rounding process, the growth rates (without wind pumping) are dependant on the magnitude of the low temperature gradient. It is possible that with the temperature gradient set at 0.0°C/m, the real temperature gradient in the sample could have been as high as ±1°C/m. In retrospect, to increase the reliability in the results, the low temperature gradients needed to be controllable to a greater precision.

The differences in enhancement, between the samples with wind pumping and those without, appear to be larger at the beginning of the bonding process (the earliest measurement was after 4 hours had elapsed). If this early behaviour applies when a wind slab is gaining in thickness (fragmented snow is being added to the snow surface), it is conceivable that wind pumping could be playing a major role in initial bonding. This thought does not take into account the possible influences of atmospheric humidity.

The enhancement of bonding created by wind pumping may go some way towards explaining the stabilisation of weak layers in storm snow after very strong, prolonged windstorms.

As the pulsile airflow will increase the excess vapour density over sink grains, it is conceivable that the transition to faceting will occur at a lower temperature gradient.

The permeabilities of the samples generally dropped with time. This was not expected and no reason could be found for the observation.

6.10.2. Further Work

In these experiments only a few snow pack variables have been examined. Although the results show some strong trends, there is still a need to investigate a number of parameters not studied here. In particular it is recommended to investigate:

* Repition of tests with new and partially settled snow undisturbed by either wind or sieving. This would give some important information on the effects of wind pumping where there is higher curvature. Conclusions may then be drawn on the possible enhanced settlement of rounding low density snow layers. Such layers may be weaknesses in the snow pack.
* Under low temperature gradient conditions, shorter elapsed times to the analysis on initially fragmented (wind damaged or sieved) snow. This would allow fuller conclusions to be drawn about the early effect wind pumping has on the stiffness of wind slabs.
* Varying degrees of temperature gradient. This would give information on:
  ** Any shift in the transition gradient between rounding and faceting due to macro scale vapour diffusion under wind pumping.
  ** The growth rate effects of varying low temperature gradients.

Chapter 7
Summary of Conclusions

In this chapter the most important conclusions from each chapter are brought together and summarised.

7.1. Table of Contents

7.2. Summary of Chapters 1 to 6

7.2.1. Chapter 1 - Perspective of this Work

In Chapter 1 the topic of wind pumping in snow was put into perspective with avalanche safety operations, and the science of snow metamorphism. Many of the terms used throughout the thesis were defined. No conclusions were drawn from this chapter.

7.2.2. Chapters 2 and 3 - Atmospheric Turbulence

Objectives Met

The wind pumping surface pressure fluctuations over mountain terrain were characterised, and measured, on windward, ridge top and leeward aspects. This included an extensive review of atmospheric turbulence from related fields.

Experimental Conclusions

The fluctuating snow surface and sub-snow surface pressure fluctuations and accompanying wind speed fluctuations (at 3.5 m height) were measured. Measurements were made in strong to gale conditions on windward, ridge top and leeward aspects at Temple Basin Ski Area in Arthur's Pass National Park. The leeward and ridge top locations both exhibited flow separation. The storms during which the measurements were made were considered to be moderate by comparison with many storms experienced in the Arthur's Pass area.

Two statistical methods were used in the analysis of the data. They were power spectral / correlation function analysis, and gust exceedance analysis. More information on the character of the turbulence could be obtained from spectral presentations.

It was concluded that the fast pressure fluctuations generally have small amplitudes, and are filtered out in the top few centimeters of the snow pack. On that basis the highest frequency of interest was 1 Hz. From the review, the lowest frequency of interest was defined at 0.001 Hz. This equated well to the lowest frequencies measured.

Turbulence Intensities and RMS Pressure Fluctuations

The recorded turbulence intensities and rms pressure fluctuations were found to be significantly larger than those reported in the literature for any type of terrain. This was considered to be connected with the turbulent structures separating off large upstream terrain features. The windward to leeward distribution of surface rms pressure coefficients followed the patterns expected around a separated region (higher within the separated region). A strong

correlation between rms pressure coefficient and wind speed turbulence intensity was apparent on all terrain aspects.

Autocorrelation Functions, Integral Length Scales and Autospectral Functions

A strong oscillation about zero occurred in most autocorrelation functions. This indicated that the data contained low frequency periodic or semi-periodic components. These periodicities were thought to originate from the atmospheric turbulence and/or gravity wave activity.

The integral length scales of the fluctuating wind speeds measured at Temple Basin were significantly larger than most integral length scales reported in the literature. The fluctuating pressure integral length scales were significantly larger than those for wind speed. The differences between the fluctuating wind speed and pressure integral length scales could possibly be explained by gravity wave activity. There is strong evidence from the literature that gravity waves exist in the atmospheric turbulence over the mountains at Arthur's Pass.

The Temple Basin power spectra showed form similar to other documented spectra, but it was shifted substantially toward lower frequencies. This supported the information given by the autocorrelation functions.

Crosscorrelation Functions

The wind speed / pressure crosscorrelation functions obtained for the Temple Basin data were very irregular. The lack of correlation was explained by the distance between the pressure and wind speed measurements, and changing wind approach angles, shifting the point of separation, and periodic back gusts.

7.2.3. Chapter 4 - Wind Pumping Airflow Dynamics

Objectives Met

A mathematical basis for the dissipation of the surface pressure fluctuations in a permeable bed was experimentally verified in the laboratory. The models proposed were then applied to a wide variety of snow pack conditions.

Modelling and Experimental Conclusions

Given the large turbulent length scales, it was concluded that a one dimensional modelling approach was applicable for a local snow pack. Three models with differing lower boundary conditions were proposed, and then tested in the laboratory on a packed column with a well defined surface pressure fluctuation. These tests showed that the assumptions behind the

models were valid, and that the models gave accurate predictions to beds with appropriate lower boundary conditions.

A comprehensive array of numerical results were produced for all three theories. Of the three models proposed, only the finite depth bed with no leakage at the bottom (finite-sealed) was found to be widely applicable to wind pumping modelling in the seasonal snow pack.

Numerical Experiments with the Finite-Sealed Model

Distinct, apparently linear trends in the finite-sealed bed model results were recognised over a wide range of seasonal snow pack and atmospheric turbulence conditions. Consequently linear finite-sealed bed theory approximations were proposed for the maximum velocity V_z and cyclic displacement S_z profiles for $\beta d < 1$.

$$V_z = \pm\frac{2P_c\pi\varepsilon(d-z)}{\tau\overline{P}} \qquad S_z = \frac{2P_c(d-z)}{\overline{P}} \qquad \beta d = \left(\frac{\pi\varepsilon}{\tau\overline{P}K}\right)^{1/2} d$$

βd is a dimensionless function of the snow pack properties, d is the depth of the snow pack, z the distance into the pack, ε the voidage, K the permeability, and $\overline{P}$ the average (barometric) pressure. These approximations are independent of snow pack permeability and should therefore hold reasonably well over several layers in a snow pack, down to either the ground or an impermeable ice layer. Note that although most conceivable seasonal snow pack and atmospheric conditions prevail below $\beta d = 1$, rapid departures from the above approximations occur for $\beta d > 1$.

7.2.4. Chapter 5 - Packed Bed Mass Transfer

Objectives Met

The effects of the wind pumping pulsile airflow on the diffusion processes in a permeable bed were experimentally determined. A conceptual discussion into the mechanisms of these effects followed from this.

Experimental Conclusions

Sublimating naphthalene was used as a tracer in a set of laboratory experiments to measure the enhanced diffusive mass transfer rates in a packed column due to wind pumping. This was achieved by recording the steady state mass loss rates from the naphthalene. The wind pumping conditions applied approximated those expected in a natural snow pack during strong winds. Scaling of the wind pumping magnitude was required because of the difference in particle sizes between the column and snow pack. This scaling was performed at a constant *cyclic displacement / grain diameter* ratio.

Compared to stagnant air diffusion rate, an *enhancement of one to two orders of magnitude* was measured in mass loss rates. This enhancement increased almost linearly with increased wind pumping intensity. The mass loss rate depended strongly on both the period and magnitude of the applied wind pumping. A large, linear dependence on cyclic displacement was found. This showed the naphthalene mass loss *process was 1-D planar convective diffusion controlled.* A slight dependance on peak velocity was also found. This indicated that the naphthalene mass loss process had a small dependence on boundary layer diffusion.

It may be inferred from the results of this experiment that wind pumping air movements will increase the vapour transport in the snow pack. It is also possible that wind pumping could change the scale of the processes from micro (less than the grain size) to macro (greater than the grain size). This is because the enhancement mechanism occurs on the scale of the cyclic displacement. The scale ratio *cyclic displacement / grain diameter* is considered to be important.

7.2.5. Chapter 6 - Wind Pumping in Snow

Objective Met

A cold laboratory experimental apparatus was designed, constructed and used to measure the effects of wind pumping on snow samples.

Experimental Conclusions

Pressure fluctuations associated with gale force winds (60 to 90 km/hr) were used to provide strong wind pumping conditions. Two types of experiments were run, both in high density snow ($\approx$350 kg/m^3):

* Initially bonded grains had moderate to high temperature gradient imposed on them to evaluate any enhancements in the faceting process.
* Grains without any initial bonding had low temperature gradients imposed upon them to evaluate any enhancements in the rounding process.

Elapsed time to sample analysis varied from 4 hours to 8.5 days. The conclusions on the results are mainly drawn from the strength tests performed. The *cone penetrometer is recommended as the most useful strength testing tool* in this type of analysis. It produced statistically significant results, while shear and tensile tests did not.

Photographical work did not prove to be a useful tool in the analysis. Stereology is probably required to quantify the structural changes geometrically.

Enhancement of the Faceting Process

Moderate (11°C/m) and high (47°C/m) temperature gradients were placed over the initially well rounded samples for 8.5 days. In all cases solid type depth hoar formed. The strength testing results were consistent with recognised facet development rate dependant variables.

There was a significant wind pumping enhancement in the loss of strength process at high temperature gradients. *The influence of wind pumping on the growth rates of depth hoar appears to be almost as significant as the influence of the temperature gradient magnitude.* This wind pumping enhancement is most likely to occur when there is a large temperature difference near the surface of the snow pack between the air and snow or between two layers of snow.

Wind pumping is unlikely to enhance the development of facets at the bottom of the snow pack, or below ice crusts.

Enhancement of the Rounding Process

Zero temperature gradients were placed over initially unbonded fragmented partially settled samples for varying periods. In all cases rounding occurred. In all but one case, the strength tests on the samples were consistent with sintering.

In all cases, this development of strength appeared to be larger with wind pumping. *The effect of wind pumping on the development of snow strength appears to be more important than the effect of elapsed time.*

The differences in enhancement with and without wind pumping appear to be larger at the beginning of the bonding process. It is conceivable that the wind pumping could play a major role in the initial bonding. It is therefore concluded that *wind pumping is possibly a major contributing mechanism in the development of wind slabs.*

Further,the enhancement of bonding created by wind pumping may go some way towards explaining the stabilisation of weak layers in storm snow after very strong, prolonged windstorms.

As the pulsile airflow will increase the excess vapour density over sink grains, it is conceivable that the transition to faceting will occur at a lower temperature gradient.

7.3. Recommendations for Further Work

Measurements of Wind Pressure Fluctuations and Atmospheric Turbulence

The results obtained at Temple Basin are not thought to be deficient in any critical way. However, there are several observations that would create a more complete picture of the turbulence characteristics:

* Pressure measurements could be made with two or more pressure sensors so that vertical profiles of the pressure fluctuations could be made within the snow pack.
* Wind speed measurement should be made at the exact location of the pressure measurements. From this more accurate information a better crosscorrelation could be obtained between the wind speed and pressure fluctuations. This sort of information would then be useful where only wind speed is measured.
* A variety of terrains could be studied, especially where well defined separation occurs. Also sites with a variety of *upstream* terrain could be studied so that the generating mechanisms of the fluctuations could be further investigated.
* Pressure measurements could be made in the specific snow pack conditions where changes in the snow grain structure are expected to be influenced by the wind pumping.

Measurements of Diffusive Mass Transfer Enhancement

The source of the variability in the naphthalene evaporation rates should be investigated.

Cold Laboratory Work

With reference to the wind pumping experiments, some further work may be beneficial:

* Repetition of tests with new and partially settled snow undisturbed by either wind or sieving. This would give some important information on the effects of wind pumping where there is higher curvature. Conclusions could then be drawn on the possible enhanced settlement of rounding low density snow layers.
* Under low temperature gradient conditions, shorter elapsed times to the analysis on initially fragmented (wind damaged or sieved) snow. This would allow fuller conclusions to be drawn about the early effect wind pumping has on the stiffness of wind slabs.
* Varying degrees of temperature gradient. This would give information on:
  ** Any shift in the transition gradient between rounding and faceting due to macro scale vapour diffusion under wind pumping.
  ** The growth rate effects of varying low temperature gradients.

References

Adams, E. E., and R. L. Brown, (1982), "A Model for Crystal Development in Dry Snow", Geophys. Res. Lett., 9(11), 1287 - 1289.

Akitaya, E., (1974), "Studies on Depth Hoar", Low Temp. Sci., Ser. A (26), 1 - 67.

Alley, R. B., (1988), "Concerning the Deposition and Diagenesis of Strata in Polar Firn", J. Glaciol., 34(118), 283 - 290.

Andreas, E, L., (1987), "Spectral Measurements in a Disturbed Boundary Layer over Snow", J. Atmos. Sci., 44(15), 1912 - 1939.

Antoniou, I., D. Asimakopoulos, A Fragoulis, A. Kotronaros, D. P. Lalas and I. Panourgias, (1992), "Turbulence Measurements on Top of a Steep Hill", J. Wind Eng. and Ind. Aerodynamics, 39, 343 - 355.

Apperley, L., D. Surry, T. Stathopoulos and A. G. Davenport, (1979), "Comparative Measurements of Wind Pressure on a Model of the Full-Scale Experimental House at Aylesbury, England", J. Wind Eng. and Ind. Aerodynamics, 4, 207 - 228.

Bader, H., (1939), "Chapter I. Mineralogical and Structural Charachterisation of Snow and of its Metamorphism", in Snow and its Metamorphism, Bader, H., R Haefeli, E. Buchker, J. Neher, O. Eckel and C. Thams (eds), Beitr. Geol. Schweiz, Geotech. Ser., Hydrol., 3, 2 - 65.

Baines, P. G., (1987), "Upstream Blocking and Airflow Over Mountains", Ann. Rev. Fluid Mech., 19, 75 - 97.

Baines, P. G., and K. P. Hoinka, (1985), "Stratified Flow over Two-Dimensional Topography in Fluid of Infinite Depth: A Laboratory Simulation", J. Atmos. Sci., 42(15), 1614 - 1631.

Bear, J. (ed), (1972), Dynamics of Fluids in Porous Media, Elsevier

Bearman, P. W., and T. Morel, (1983), "Effect of Free Stream Turbulence on the Flow Around Bluff Bodies", Prog. Aerospace Sci, 20(2-3), 97 - 123.

Bell, M. J., (1991a), Avalanche Atlas of the Temple Basin Ski Area. Part 1: Avalanche Safety Plan, New Zealand Mountain Safety Council

Bell, M. J., (1991b), Avalanche Atlas of the Temple Basin Ski Area. Part 2: Slide Path Inventory, New Zealand Mountain Safety Council

Bell, R. C., and R. O. R. Y. Thompson, (1980), "Valley Ventilation by Cross Winds", J. Fluid Mech., 94(4), 757 - 767.

Bendat, J. S., and A. G. Piersol (eds), (1986), Random Data: Analysis and Measurement Procedures, 2nd edition, Wiley

Bergström, H., (1987), "A Statistical Analysis of Gust Characteristics", Boundary-Layer Meteorol., 39, 153 - 173.

Blackmore, P. A., (1987), "A Static Pressure Probe for Use in Turbulent Three-Dimensional Flows", J. Wind. Eng. and Ind. Aerodynamics, 25, 207 - 218.

Blackwelder, R. F., and R. E. Kaplan, (1976), "On the Wall Structure of the Turbulent Boundary Layer", J. Fluid Mech., 76(1), 89 - 113.

Blake, W. K., (1970), "Turbulent Boundary-Layer Wall Pressure Fluctuations on Smooth and Rough Walls", J. Fluid Mech., 44(4), 637 - 660.

Botta, G., R. Castagna, M. Borgehetti and D. Mantegna, (1992), "Wind Analysis on Complex Terrain - The Case of Acqua Spruzza", J. Wind Eng. and Ind. Aerodynamics, 39, 357 - 366.

Bowen, A. J., (1979), "Some Effects of Escarpments on the Atmospheric Boundary Layer", Ph.d Thesis, Mech. Eng. Dept., University of Canterbury

Bradley, C. C., R. L. Brown and T. R. Williams, (1977), "Gradient Metamorphism, Zonal Weakening of the Snow-Pack and Avalanche Initiation", J. Glaciol., 19(81), 335 - 342.

Bradley, E. F., (1980), "An Experimental Study of the Profiles of Wind Speed, Shearing Stress and Turbulence at the Crest of a Large Hill", Quart. J. R. Meteorol. Soc., 106, 101 - 123.

Buckles, J., T. J. Hanratty and R. J. Adrian, (1984), "Turbulent Flow Over Large-Amplitude Wavy Surfaces", J. Fluid Mech., 140, 27 - 44.

Buser, O., and W. Good, (1987), "Acoustic, Geometric and Mechanical Parameters of Snow", Int. Symp. on Avalanche Formation, Movements and Effects, Davos, Switz., Int. Ass. Hydrological Sci. Publ. no. 162, 61 - 71.

Businger, J. A., (1981), "Equations and Concepts", in Atmospheric Turbulence and Air Pollution Modelling, F. T. M. Nieuwstadt and H. Van Dop (eds), D. Reidel Pub. Co., 1 - 36.

CAA, (1992), Avalanche Programme, Course Manual, New Zealand Version of the Canadian Avalanche Association Training Schools Course Manual, Otago Polytechnic

Carslaw, H. S., and S. C. Jaeger (eds), (1959), Conduction of Heat in Solids, 2nd Ed., 92 - 106.

Castro, I. P., W. H. Snyder and G. L. Marsh, (1983), "Stratified Flow Over Three-Dimensional Ridges", J. Fluid Mech., 135, 261 - 282.

Caughey, S. J., and C. J. Readings, (1975), "An Observation of Waves and Turbulence in the Earths Boundary Layer", Boundary-Layer Meteorol., 9, 279 - 296.

Chang, P. K. (ed), (1970), Separation of Flow, Pergamon Press

Chen, F., (1990), "Turbulent Characteristics Over a Rough Natural Surface. Part I: Turbulent Structures", Boundary-Layer Meteorol., 52, 151 - 175.

Cherry, N. J., R. Hiller and M. E. M. P. Latour, (1983), "The Unsteady State Nature of Two-Dimensional Separated-and-Reattaching Flows", J. Wind Eng. and Ind. Aerodynamics, 11, 95 - 105.

Cherry, N. J., R. Hiller and M. E. M. P. Latour, (1984), "Unsteady Measurements in a Separated and Reattaching Flow", J. Fluid. Mech, 144, 13 - 46.

Choi, H., and P. Moin, (1990), "On the Space-Time Characteristics of Wall-Pressure Fluctuations", Phys. Fluids A, 2(8), 1450 - 1460.

Christon, M., P. Burns, E. Thompson and R. Sommerfeld, (1987), "Water Vapour Transport in Snow: A 2-D Simulation of Temperature Gradient Metamorphism", Seasonal Snowcovers: Physics, Chemistry, Hydrology, H. G. Jones and W. J. Orville Thomas (eds.), D. Reidel Pub. Co., 37 - 62.

Clark, T. L.,and W. R. Peltier, (1977), "On the Evolution and Stability of Finite-Amplitude Mountain Waves", J. Atmos. Sci., 34, 1715 - 1730.

Clark, T. L., and W. R. Peltier, (1984), "Critical Level Reflection and the Resonant Growth of Nonlinear Mountain Waves", J. Atmos. Sci., 41(21), 3122 - 3134.

Clarke, G. K. C., and E. D. Waddington, (1991), "A Three Dimensional Theory of Wind Pumping", J. Glaciol., 37(125), 89 - 96.

Clarke, G. K. C., D. A. Fisher and E. D. Waddington, (1987), "Wind Pumping: A Potentially Significant Heat Source in Ice Sheets", The Physical Shape of Ice Sheet Modelling, Vancouver Symposium, Int. Assoc. Hydrological Sciences Publ. no. 170, 169 - 180.

Colbeck, S. C., (1980), "Thermodynamics of Snow Metamorphism Due to Variations in Curvature", J. Glaciol., 26(94), 291 - 301.

Colbeck, S. C., (1982), "An Overview of Seasonal Snow Metamorphism", Rev. Geophys. and Space Phys., 20(1), 45 - 61.

Colbeck, S. C., (1983a), "Ice Crystal Morphology and Growth Rates at Low Supersaturations and High Temperatures", J. Appl. Phys., 54(5), 2677 - 2682.

Colbeck, S. C., (1983b), "Theory of Metamorphism of Dry Snow", J. Geophys. Res., 88(C9), 5475 - 5482.

Colbeck, S. C., (1987a), "Snow Metamorphism and Classification", Seasonal Snowcovers: Physics, Chemistry, Hydrology, H. G. Jones and W. J. Orville Thomas (eds.), D. Reidel Pub. Co., 1 - 35.

Colbeck, S. C., (1987b), "History of Snow-Cover Research", J. Glaciol., Special Issue, 60 - 65.

Colbeck, S. C., (1989), "Air Movements in Snow Due to Windpumping", J. Glaciol., 35(120), 209 - 213.

Conway, H., and J. Abrahamson, (1984a), "Snow Stability Index", J. Glaciol., 30(106), 321 - 327.

Conway, H., and J. Abrahamson, (1984b), "Air Permeability as a Textural Indicator of Snow", J. Glaciol., 30(106), 328 - 333.

Conway, H., and J. Abrahamson, (1988), "Snow Slope Stability - A Probabilistic Approach", J. Glaciol., 34(117)

Crook, N. A., T. L. Clark and M. W. Moncrieff, (1990), "The Denver Cyclone. Part I: Generation of Low Froude Number Flow", J. Atmos. Sci., 47(23), 2725 - 2742.

DADiSP Worksheet, (1990), User Manual, DSP Development Corporation.

Dalgliesh, W. A., J. T. Templin and K. R. Cooper, (1979), "Comparisons of Wind Tunnel and Full Scale Building Surface Pressures with Emphasis on Peaks", Wind Eng., Proceedings 5th Int. Conf., Fort Collins, Colorado, 1, 553 - 565.

Davenport, A. G., (1961), "The Spectrum of Horizontal Gustiness Near the Ground in High Winds", Quart. J. R. Meteorol. Soc., 87, 194 - 211.

de Montmollin, V., (1982), "Shear Tests on Snow Explained by Fast Metamorphism", J. Glaciol., 28(98), 187 - 198.

Doran, J. C., and D. C. Powell, (1982), "Gust Structure in the Neutral Surface Boundary Layer", J. Appl. Meteorol., 21, 14 - 17.

Dowd, T., and R. L. Brown, (1986), "A New Instrument for Determining Strength Profiles in Snow Cover", J. Glaciol., 32(111), 299 - 301.

Driver, D. M., H. L. Seebmiller and J. G. Marvin, (1987), "Time-Dependent Behavior of a Reattaching Shear Layer", AIAA J., 25(7), 914 - 919.

Eaton, J. K., and J. P. Johnston, (1981), "A Review of Research on Subsonic Turbulent Flow Reattachment", AIAA J., 19(9), 1093 - 1100.

Eaton, K. J., and J. R. Mayne, (1975), "The Measurement of Wind Pressure on Two Story Houses at Aylesbury", J. Ind. Aerodynamics, 1, 67 - 109.

Eckelmann, H., (1989), "A Review of Knowledge on Pressure Fluctuations", in Near Wall Turbulence, S. J. Kline and N. H. Afgan (eds), Hemisphere, New York, 328 - 347.

Einaudi, F., and J. J. Finnigan, (1981), "The Interaction Between ann Internal Gravity Wave and the Planetary Boundary Layer. Part I: The Linear Analysis", Quart. J. R. Meteorol. Soc., 107, 793 - 806.

El-Sherbiny, S., (1983), "Flow Separation and Reattachment Over the Sides of a 90° Triangular Prism", J. Wind Eng. and Ind. Aerodynamics, 11, 393 - 403.

Elliott, J. A., (1972a), "Instrumentation for Measuring Static Pressure Fluctuations Within the Atmospheric Boundary Layer", Boundary-Layer Meteorol., 2, 476 - 495.

Elliott, J. A., (1972b), "Microscale Pressure Fluctuations Measured Within the Lower Atmospheric Boundary Layer", J. Fluid Mech., 53(2), 351 - 383.

ESDU 74026, (1974), "Characteristics of Wind Speed in the Lower Layers of the Atmospheric Near the Ground: Strong Winds (Neutral Atmosphere)", Engineering Science Data Unit, London

ESDU 74030, (1974), "Characteristics of Atmospheric Turbulence Near the Ground. Part I: Definitions and General Information", Engineering Science Data Unit, London

ESDU 74031, (1974), "Characteristics of Atmospheric Turbulence Near the Gound. Part II: Single Point Data for Strong Winds", Engineering Science Data Unit, London

Farabee, T. M., and M. J. Casarella, (1984), "Effects of Surface Irregularity on Turbulent Boundary Layer Wall Pressure Fluctuations", J. Vib., Acoustics, Stress, and Reliability in Design, 106, 343 - 350.

Farabee, T. M., and M. J. Casarella, (1986), "Measurements of Fluctuating Wall Pressure for Separated/Reattached Boundary Layer Flows", J. Vib., Acoustics, Stress, and Reliability in Design, 108, 301 - 307.

Farrell, D. A., E. L. Greacen and C. G. Gurr, (1966), "Vapour Transfer in Soil Due to Air Turbulence", Soil Sci., 102, 305 - 313.

Fayed, M. E., and L. Otten (eds), (1984), Handbook of Powder Science and Technology

Fiedler, F, and H. A. Panofsky, (1970), "Atmospheric Scales and Spectral Gaps", Am. Meteorol. Soc. Bull., 51(12), 1114 - 1119.

Finnigan, J. J., (1988), "Kinetic Energy Transfer between Internal Gravity Waves and Turbulence", J. Atmos. Sci., 45(3), 486 - 505.

Finnigan J. J., and F. Einaudi, (1981), "The Interaction Between ann Internal Gravity Wave and the Planetary Boundary Layer. Part II: Effect of the Wave on the Turbulence Structure.", Quart. J. R. Meteorol. Soc., 107, 807 - 832.

Flay, R. G. J., (1978), "Structure of a Rural Atmospheric Boundary Layer Near the Ground", Ph.d Thesis, Mech. Eng. Dept., University of Canterbury

Föhn, P. M. B., (1980), "Snow Transport Over Mountain Crests", J. Glaciol., 26(94), 469 - 480.

Föhn, P. M. B., (1988), "Snowcover Stability Tests and the Areal Variability of Snow Strength", Int. Snow Sci. Workshop, Whistler, BC, 1 - 12.

Fukuda, H., (1955), "Air and Vapour Movement in Soil Due to Wind Gustiness", Soil Sci., 79, 249 - 256.

Gallagher, M. W., T. W. Choularton and M. K. Hill, (1988), "Some Observations of Airflow Over a Large Hill of Moderate Slope", Boundary-Layer Meteorol., 42, 229 - 250.

Garratt, J. R., (1990), "The Internal Boundary Layer - A Review", Boundary-Layer Meteorol., 50, 171 - 203.

Giddings, J. C. and E. R. LaChapelle, (1962), "The Formation Rate of Depth Hoar", J. Geophys. Res., 67(6), 2377 - 2383.

Good, W., (1987), "Thin Sections, Serial Cuts and 3-D Analysis of Snow", Int. Symp. on Avalanche Formation, Movements and Effects, Davos, Switz., Int. Ass. Hydrological Sci. Publ. no. 162, 35 - 48.

Gossard, E. E., (1960), "Spectra of Atmospheric Scalars", J. Geophys. Res., 65(10), 3339 - 3351.

Grachev, A. I., and M. I. Mordukhovich, (1988), "Spectrum of Pressure Fluctuations in the Atmospheric Ground Layer", Izv., Atmos. Oceanic Phys., 24(2), 159 - 161.

Grant, A. L. M., and P. J. Mason, (1990), "Observations of Boundary-Layer Structure Over Complex Terrain", Quart. J. R. Meteorol. Soc., 116, 159 - 186.

Gustavsson, H., and M. Linde, (1979), "The Gust as a Coherent Structure in the Turbulent Boundary Layer", Aeronautical Res. Inst. Sweden, FFA AU-1499, Pt. 5, 1 - 19.

Hanson, P. J., (1985), "The Spontaneous Heating of Coal", BE Project Report, Chem. Eng., University of Canterbury

Harris, B. J., (1986), "The Spontaneous Heating of Coal", BE Project Report, Chem. Eng., University of Canterbury

Harris, R. I., (1990), "Some Further Thoughts on the Spectrum of Gustiness in Strong Winds", J. Wind Eng. and Ind. Aerodynamics, 33, 461 - 477.

Herron, T. J., I. Tolstoy and D. W. Kraft, (1969), "Atmospheric Pressure Background Fluctuations in the Mesoscale Range", J. Geophys. Res., 74(6), 1321 - 1329.

Hiller, R., and Cherry, N. J., (1981), "The Effects of Stream Turbulence on Separation Bubbles", J. Wind Eng. and Ind. Aerodynamics, 8, 49 - 58.

Holman, J. P. (ed), (1978), Experimental Methods for Engineers, 3rd Ed., McGraw Hill, Japan, 191 - 211.

Huey, L. J., (1978), "A Yaw-Insensitive Static Pressure Probe", J. Fluids Eng., 100, 229 - 231.

Hunt, J. C. R., (1990), "The Structure of Velocity and Pressure Fields in Turbulent Flows Over Bluff Bodies, Hills and Waves", J. Wind Eng. and Ind. Aerodynamics, 39, 245 - 253.

Hunt, J. C. R. and K. J. Richards, (1984), "Stratified Airflow Over One or Two Hills", Boundary-Layer Meteorol., 30, 223 - 259.

Hunt, J. C. R., and W. H. Snyder, (1980), "Experiments on Stably and Neutrally Stratified Flow over a Model Three-Dimensional Hill", J. Fluid Mech., 96(4), 671 - 704.

Hunt, J. C. R., H. Kawai, S. R. Ramsey, G. Pedrizetti and R. J. Perkins, (1990), "A Review of Velocity and Pressure Fluctuations in Turbulent Flows Around Bluff Bodies", J. Wind Eng. and Ind. Aerodynamics, 35, 49 - 85.

Hunt, J. C. R., K. J. Richards and P. W. M. Brighton, (1988a), "Stably Stratified Air over Low Hills", Quart. J. R. Meteorol. Soc., 114, 859 - 886.

Hunt, J. C. R., S, Leibovich and K. J. Richards, (1988b), "Turbulent Shear Flow over Low Hills", Quart. J. R. Meteorol. Soc., 114, 1425 - 1470.

Ingersoll, L. R., O. J. Zobel and A. C. Ingersoll (eds), (1954), Heat Conduction, Univ. Wisconsin Press, Madison

Itsweire, E. C., K. N. Helland and C. W. Van Atta, (1986), "The Evolution of Grid-Generated Turbulence in a Stratified Flow", J. Fluid Mech., 162, 299 - 338.

Ivanov, V. N., and A. E. Ordanovich, (1967), "Spectra of Wind Velocity for Unstable Stratification in the Low Frequency Range", Izv., Atmos. Oceanic Phys., 3(8), 827 - 835.

Jackson, P. S., and J. C. R. Hunt, (1975), "Turbulent Wind Flow Over a Low Hill", Quart. J. R. Meteorol. Soc., 101, 929 - 955.

Janna, W. S. (ed), (1986), Engineering Heat Transfer, PWS Publishers

Jenkins, G. J., P. J. Manson, W. H. Moores and R. I. Sykes, (1981), "Measurements of the Flow Structure Around Ailsa Crag, a Steep, Three-Dimensional, Isolated Hill", Quart. J. R. Meteorol. Soc., 107, 833 - 851.

Kaimal, J. C., (1973), "Turbulence Spectra, Length Scales and Structure Parameters in the Stable Surface Layer", Boundary-Layer Meteorol., 4, 289 - 309.

Kaimal, J. C., J. C. Wyngaard, Y. Izumi and O. R. Coté, (1972), "Spectral Characteristics of Surface-Layer Turbulence", Quart. J. R. Meteorol. Soc., 98, 563 - 589.

Kanaoka, C, (1991), "Permeation (Flow Through Porous Medium)", Powder Technology Handbook, Iinoya, K, K. Gotoh and K. Higashitani (eds), Dekker, 139 - 149.

Kanda, J., and T. Ohkuma, (1990), "Recent Developments in Full-Scale Wind Pressure Measurements in Japan", J. Wind Eng. and Ind. Aerodynamics, 33, 243 - 252.

Kataoka, T., Y. Mitsuta and O. Tsukamoto, (1989), "The Development of a Fast Response Static Pressure Instrument for Field Use", J. Meteorol. Soc. Japan, 67(3), 351 - 356.

Kawabata, S., T. Ohkuma, J. Kanda, H. Kitamura and K. Ohtake, (1990), "Chiba Port Tower: Full-Scale Measurement of Wind Actions. Part 2. Basic Properties of Fluctuating Wind Pressures", J. Wind Eng. and Ind. Aerodynamics, 33, 253 - 262.

Kimura, F., and P. Manins, (1988), "Blocking in Periodic Valleys", Boundary-Layer Meteorol., 44, 137 - 169.

Kitabayashi, K., (1977), "Wind Tunnel and Field Studies of Stagnant Flow Upstream of a Ridge", J. Meteorol. Soc. Japan, 55(2), 193 - 203.

Knight, P. C., and. S. H. Johnson, (1988), "Measurement of Powder Cohesive Strength with a Penetration Test", Powder Tech., 54, 279 - 283.

Kristensen, L., M. Casanova, M. S. Courtney and I. Troen, (1991), "In Search of a Gust Definition", Boundary-Layer Meteorol., 55, 91 - 107.

Kry, P. R., (1975a), "Quantitative Stereological Analysis of Grain Bonds in Snow", J. Glaciol., 14(72), 467 - 477.

Kry, P. R., (1975b), "The Relationship Bewteen the Visco-Elastic and Structural Properties of Fine-Grained Snow", J. Glaciol., 14(72), 479 - 500.

Lebouche, M., and Martin, M., (1976), Lecture given in the 73rd Euromech Colloquim on "Oscillatory Flows in Ducts" held in Aix-en-Provence, France. Reported in Brocher, E., (1977), "Oscillatory Flows in Ducts: A Report on Euromech 73", J. Fluid Mech., 79

Lesieur, M. (ed), (1990), Turbulence in Fluids, 2nd Ed, Kluwer Academic Press

Letchford, C. W., P. Sandri, M. L. Levitan and K. C. Mehta, (1992), "Frequency Response Requirements for Fluctuating Wind Pressure Measurements", J. Wind Eng. and Ind. Aerodynamics, 40, 263 - 276.

Levitan, M. L., and K. C. Mehta, (1992a), "Texas Tech Field Experiments for Wind Loads Part 1: Building and Pressure Measuring System", J. Wind Eng. and Ind. Aerodynamics, 41 - 44, 1565 - 1576.

Levitan, M. L., and K. C. Mehta, (1992b), "Texas Tech Field Experiments for Wind Loads Part II: Meteorological Instrumentation and Terrain Parameters", J. Wind Eng. and Ind. Aerodynamics, 41-44, 1577 - 1588.

Levitan, M. L., K. C. Mehta, W. P. Vann, and J. D. Holmes, (1991), "Field Measurements of Pressure on the Texas Tech Building", J. Wind Eng. and Ind. Aerodynamics, 38, 227 - 234.

Lilly, D. K. and J. B. Klemp, (1979), "The Effects of Terrain Shape on Nonlinear Mountain Waves", J. Fluid Mech., 95(2), 241 - 261.

Linde, M., (1981), "Analysis of Gust Structure in the Atmospheric Boundary Layer by Using Conditional Sampling", Aeronautical Res. Inst. Sweden, FFA HU-2262, Pt. 1, 1 - 22.

Linde, M., (1983), "Gust Structure and Gust Statistics. Results Form an Analysis of Atmospheric Turbulence Measurements by use of Conditional Sampling Technique", Aeronautical Res. Inst. Sweden, FFA TN 1983-28, 1 - 44.

Livingstone, M. I., (1987), "The Spontaneous Heating of Coal", BE Project Report, Chem. Eng., University of Canterbury

Lumley, J. L., (1965), "Interpretation of Time Spectra Measured in High Intensity Shear Flows", Phys. Fluids, 8(6), 1056 - 1062.

Mabey, D. G., (1972), "Analysis and Correction of Data on Pressure Fluctuations in Separated Flow", J. Aircraft, 9(9), 642 - 645.

Marbouty, D., (1980), "An Experimental Study of Temperature Gradient Metamorphism", J. Glaciol., 26(94), 303 - 312.

Mason, P. J., (1986), "Flow Over the Summit of an Isolated Hill", Boundary-Layer Meteorol., 37, 385 - 405.

Mason, P. J. and J. C. King, (1984), "Atmospheric Flow Over a Succession of Nearly Two-Dimensional Ridges and Valleys", Quart. J. R. Meteorol. Soc., 110, 821 - 845.

Mason, P. J., and J. C. King, (1985), "Measurements and Predictions of Flow and Turbulence over an Isolated Hill of Moderate Slope", Quart. J. R. Meteorol. Soc., 111, 617 - 640.

Matsui, G., K. Suda and K. Higuchi, (1982), "Full-Scale Measurements of Wind Pressures Acting on a High-Rise Building of Rectangular Plan", J. Wind Eng. and Ind. Aerodynamics, 10, 267 - 286.

Matsumoto, M., N. Shiraishi and H. Shirato, (1988), "Bluff Body Aerodynamics in Pulsating Flow", J. Wind Eng. and Ind. Aerodynamics, 28, 261 - 270.

Mayne, J. R., (1979), "The Estimation of Extreme Winds", J. Wind Eng. and Ind. Aerodynamics, 5, 109 - 137.

McBean, G. A., (1971), "The Variations of the Statistics of Wind, Temperature and Humidity Varitions with Stability", Boundary-Layer Meteorol., 1, 438 - 457.

McMillen, R. T., (1988), "An Eddy Correlation Technique with Extended Applicability to Non-Simple Terrain", Boundary-Layer Meteorol., 43, 231 - 245.

Meister, R., (1987), "Wind Systems and Snow Transport in Alpine Topography", Int. Symp. on Avalanche Formation, Movements and Effects, Davos, Switz., Int. Ass. Hydrological Sci. Publ. no. 162, 265 - 279.

Milford, R. V., and J. L. Waldeck, (1988), "Statistics of Full-Scale Surface Pressures", J. Wind Eng. and Ind. Aerodynamics, 30, 35 - 44.

Mitsuta, Y., O. Tsukamoto and M. Nenoi, (1983), "Wind Characteristics Over Complex Terrain", J. Wind Eng. and Ind. Aerodynamics, 15, 185 - 196.

Molki, M., and Sparrow, E. M., (1983), "In-Tube Heat Transfer for Skewed Inlet Flow Caused By Competition Among Tubes Fed by the Same Plenum", J. Heat Transfer, 105, 870 - 877.

Monserrat, S., A. Ibbetson and A. J. Thorpe, (1991), "Atmospheric Gravity Waves and the 'Rissaga' Phenomenon", Quart. J. R. Meteorol. Soc., 117, 553 - 570.

Monserrat, S., and A. J. Thorpe, (1992), "Gravity Wave Observations Using an Array of Microbarographs in the Balearic Islands", Quart. J. R. Meteorol. Soc., 118, 259 - 282.

Mullin, T., C. A. Greated and I. Grant, (1980), "Pulsating Flow Over a Step", Phys. Fluids, 23(4), 669 - 674.

Nakagawa, T., (1987), "Vortex Shedding Behind a Square Cylinder in Transonic Flows", J. Fluid Mech., 178, 303 - 323.

Nakamura, Y., and Y. Ohya, (1983), "The Effects of Turbulence on the Mean Flow Past Square Rods", J. Fluid Mech., 137, 331 - 345.

Nakamura, Y., and Y. Ohya, (1984), "The Effect of Turbulence on the Mean Flow Pat Two-Dimensional Cylinders", J. Fluid Mech., 149, 255 - 273.

Nakamura, Y., and Y. Ohya, (1986), "Vortex Shedding from Square Prisms in Smooth and Turbulent Flow", J. Fluid Mech., 164, 77 - 89.

Nappo, C. J., and G. Chimonas, (1991), "Wave Exchange Between the Ground Surface and a Boundary-Layer Critical Level", J. Atmos. Sci., 49(13), 1075 - 1091.

Narita, H., (1980), "Mechanical Behavoiur and Structure of Snow Under Uniaxial Tensile Stress", J. Glaciol., 26(94), 275 - 282.

Nieuwstadt, F. T. M., (1984), "Some Aspects of the Turbulent Stable Boundary Layer", Boundary-Layer Meteorol., 30, 31 - 55.

NZMSC, (1987), New Zealand Guidelines to Weather, Snowpack and Avalanche Observations, New Zealand Mountain Safety Council

Ogawa, T., M. Nakayama, S. Murayama and Y. Sasaki, (1991), "Characteristics of Wind Pressures on Basic Structures with Curved Surfaces and their Response to Turbulent Flow", J. Wind Eng. and Ind. Aerodynamics, 38, 427 - 438.

Ohkuma, T., Marukawa, H., Y, Niihori and N. Kato, (1991), "Full-Scale Measurement of Wind Pressure and Response Accelerations of a High-Rise Building", J. Wind Eng. and Ind. Aerodynamics, 38, 185 - 196.

Panofsky, H. A., and Z. Ming, (1983), "Characteristics of Wind Profiles Over Complex Terrain", J. Wind Eng. and Ind. Aerodynamics, 15, 177 - 183.

Panofsky, H. A., D. Larkom, R. Lipschutz, G. Stone, E. F. Bradley, A. J. Bowen and J. Højstrup, (1982), "Spectra of Velocity Components over Complex Terrain", Quart. J. R. Meteorol. Soc., 108, 215 - 230.

Papesch, A. J. G., (1984), "Wind and its Affects on (Canterbury) Forests", Ph.d Thesis, Mech. Eng. Dept., University of Canterbury

Patel, V. C., J. Tyndall Chon and J. Y. Yoon, (1991), "Turbulent Flow in a Channel with a Wavy Wall", ASME J. Fluids Eng., 113, 579 - 586.

Peltier, W. A., and J. F. Scinocca, (1990), "The Origin of Severe Downslope Windstorm Pulsations", J. Atmos. Sci., 47(24), 2853 - 2870.

Peltier W. R., and T. L. Clark, (1979), "The Evolution and Stability of Finite Amplitude Mountain Waves. Part II: Surface Wave Drag and Severe Downslope Windstorms", J. Atmos. Sci., 36

Perla, R. I., (1969), "Strength Tests on Newly Fallen Snow", J. Glaciol., 8(54), 427 - 440.

Perla, R. I., (1977), "Slab Avalanche Measurements", Canadian Geotechnical J., 14(2), 206 - 213.

Perla, R. I., (1978a), "Snow Crystals", Nat. Hydrology Res. Inst., Canada, Paper No. 1, IWD Sci. Ser. (No. 96)

Perla, R. I., (1978b), "Temperature-Gradient and Equi-Temperature Metamorphism of Dry Snow", 2nd Int. Meeting on Snow and Avalanches, Grenoble, France

Perla, R. I., (1982), "Preparation of Section Planes in Snow Specimens", J. Glaciol., 28(98), 199 - 204.

Perla, R. I., and M. Martinelli (eds), (1976), Avalanche Handbook, US Dept. Agriculture, Forest Service

Plate, E. (ed), (1982), Engineering Meteorology, Vol. 1, Elsevier

Powell, D. C., and J. R. Connell, (1980), "Definition of Gust Model Concepts and Review of Gust Models", Battelle Pacific Northwest Laboratory, PNL-3138

Ramsay, S. R., (1990), "Wake Resonance Mechanisms in Bluff Body Interactions", J. Wind Eng. and Ind. Aerodynamics, 36, 1125 - 1133.

Ramsdell, J. V., (1978), "Estimates of the Number of Large Amplitude Gusts", Battelle Pacific Northwest Laboratory, PNL-2508

Ramseier, R. O., and C. M. Keeler, (1966), "The Sintering Process in Snow", J. Glaciol., 45(6), 421 - 424.

Raupach, M. R., R. A. Antonia and S. Rajagoplan, (1991), "Rough-Wall Turbulent Boundary Layers", Appl. Mech. Rev., 44(1), 1 - 25.

Reid, S. J., (1983), "Design Winds for High Level Sites in New Zealand", J. Wind Eng. and Ind. Aerodynamics, 13, 77 - 86.

Reimer, (1980), "The Effect of Wind on Heat Transfer in Snow", Cold Regions Sci. and Tech., 3, 129 - 137.

Ribeiro J. L. D., and J. Blessmann, (1992), "Probability Distribution of Forces and Pressures on a Square Cylinder", J. Wind Eng. and Ind. Aerodynamics, 41-44, 813 - 824.

Rockwell, D., (1983), "Oscillations of Impinging Shear Layers", AIAA J., 21(5), 645 - 664.

Rockwell, D., and E. Naudascher, (1979), "Self-Sustained Oscillations of Impinging Free Shear Layers", Ann. Rev. Fluid Mech., 11, 67 - 94.

Rottman, J. W., and R. B. Smith, (1989), "A Laboratory Model of Severe Downslope Winds", Tellus, 41A, 401 - 415.

Rotunno, R., and P. K. Smolarkiewicz, (1991), "Further Results on Lee Vortices in Low-Froude-Number Flow", J. Atmos. Sci., (Notes and Correspondence), 48(19), 2204 - 2211.

Schmidt, R. A., (1982), "Vertical Profiles of Wind Speed, Snow Concentration, and Humidity in Blowing Snow", Boundary-Layer Meteorol., 23, 223 - 246.

Schols, J. L. J., (1984), "The Detection and Measurement of Turbulent Structures in the Atmospheric Surface Layer", Boundary-Layer Meteorol., 29, 39 - 58.

Schols, J. L. J., A. E. Jansen and J. G. Krom, (1985), "Characteristics of Turbulent Structures in the Unstable Atmospheric Boundary Layer", Boundary-Layer Meteorol., 33, 173 - 196.

Schols, J. L. J., and L. Wartena, (1986), "A Dynamical Description of Turbulent Structure in the Near Neutral Atmospheric Boundary Layer: The Role of Static Pressure Fluctuations", Boundary-Layer Meteorol., 34, 1 - 15.

Scotter, D. R., and P. A. C. Raats, (1969), "Dispersion of Water Vapour in Soil Due to Air Turbulence", Soil Sci., 108(3), 170 - 176.

Scotter, D. R., G. W. Thurtell and P. A. C. Raats, (1967), "Dispersion Resulting From Sinusoidal Gas Flows in Pourous Materials", Soil Sci., 104, 306 - 308.

Simpson, R. L., (1989), "Turbulent Boundary-Layer Separation", Ann. Rev. Fluid Mech., 21, 205 - 234.

Smedman, A., (1991), "Some Turbulence Characteristics in Stable Atmospheric Boundary Layer Flow", J. Atmos. Sci., 48(6), 856 - 868.

Smedman, A., and H. Bergström, (1984), "Flow Characteristics Above a Very Low and Gently Sloping Hill", Boundary-Layer Meteorol., 29, 21 - 37.

Smith, R. B., (1977), "The Steepening of Hydrostatic Mountain Waves", J. Atmos. Sci., 34, 1634 - 1654.

Smith, R. B., (1979), "The Influence of Mountains on the Atmosphere", in Advances in Geophysics, Vol. 21, Academic Press, 87 - 230.

Smith, R. B., Comment on, (1989), "Low Froude Number Flow Past Three-Dimensional Obstacles. Part I: Baroclinically Generated Lee Vortices", J. Atmos. Sci., 46(23), 3611 - 3613.

Smolarkiewicz, P. K., and R. Rotunno, (1989), "Low Froude Number Flow Past Three-Dimensional Obstacles. Part I: Baroclinically Generated Lee Vortices", J. Atmos. Sci., 46(8), 1154 - 1164.

Smolarkiewicz, P. K., and R. Rotunno, (1990), "Low Froude Number Flow Past Three-Dimensional Obstacles. Part II: Upwind Flow Reversal", J. Atmos. Sci., 47(12), 1498 - 1511.

Sogin, H. H., and R. I. Providence, (1958), "Sublimation From Disks to Air Streams Flowing Normal to Their Surfaces", ASME Transactions, 80, 61 - 69.

Sommerfeld, R. A., (1974), "Statistical Problems in Snow Mechanics", J. Glaciol., 13(67), 29 - 36.

Sommerfeld, R. A., (1983), "A Branch Grain Theory of Temperature Gradient Metamorphism in Snow", J. Geophys. Res., 88(C2), 1484 - 1494.

Sommerfeld, R. A., and T. L. Freeman, (1988), "Making Aritficial Snow for Laboratory Use", Rocky Mountain Forest and Range Experiment Station, USDA Forest Service, Research Note RM-486, 1 - 3.

Sparrow, E. M., and J. P. Kalejs, (1977), "Local Convective Transfer Coefficients in a Channel Downstream of a Partially Constricted Inlet", Int. J. Heat Mass Transfer, 20, 1241 - 1249.

Stull, R. B. (ed), (1988), An Introduction to Boundary Layer Meteorology, Kluwer

Sun, T. F., Z. F. Gu, D. X. He and L. L. Zhang, (1992), "Fluctuating Pressure on Two Circular Cylinders at High Reynolds Numbers", J. Wind Eng. and Ind. Aerodynamics, 41-44, 577 - 588.

Takeuchi, T., and M. Matsumoto, (1992), "Aerodynamic Response Characteristics of Rectangular Cylinders in Tandem Arrangement", J. Wind Eng. and Ind. Aerodynamics, 41-44, 565 - 575.

Tan, W. H., (1991), "Development of a Digital Wind Measuring System", BE Project Report (57), Mech. Eng. Dept., University of Canterbury

Taylor, G. I., (1938), "The Spectrum of Turbulence", Proc. Roy. Soc. London, A, 164, 476 - 490.

Taylor, P. A., P. J. Mason and E. F. Bradley, (1987), "Boundary-Layer Low Over Low Hills", Boundary-Layer Meteorol., 39, 107 - 132.

Thompson, R. S., M. S. Shipman and J. W. Rottman, (1991), "Moderately Stable Flow Over a Three-Dimensional Hill. A Comparison of Linear Theory with Laboratory Measurements", Tellus, 43A, 49 - 63.

Tieleman, H. W., (1992), "Wind Characteristics in the Surface Layer over Heterogeneous Terrain", J. Wind Eng. and Ind. Aerodynamics, 41-44, 329 - 340.

Tong, H. H. N., (1992), "Calibrating and Testing the Performance of Digital Vane and Gill Anemometers", BE Project Report (50), Mech. Eng., University of Canterbury

Vallance, A., and V. L. Doughtie (eds), (1951), Design of Machine Members, 3rd Ed., McGraw Hill

Van der Hoven, I., (1957), "Power Spectrum of Horizontal Wind Speed in the Frequency Range From 0.0007 to 900 Cycles per Hour", J. Meteorol., 14, 160 - 164.

Waldeck, J. L., (1986), "Effects of the Reference-Pressure System on the Dynamic Response of Pressure Transducers in Full-Scale Experiments", J. Wind Eng. and Ind. Aerodynamics, 23, 37 - 50.

Watanabe, Z., (1980), "Tensile Strain and Fracture of Snow", J. Glaciol., 26(94), 255 - 262.

Waterhouse, R. W., (1963), "On the Permeability of Snow in the Accumulation Zone of Polar Regions", in Ice and Snow Properties, Processes and Applications, W. D. Kinery (ed), The MIT Press, Cambridge, 576.

Waters, S., (1980), "Terrain Analysis and Hazard Assessment, Arthur's Pass National Park", MSc Thesis, Geography Dept., University of Canterbury

Wells, D. A., and R. P. Hoxey, (1980), "Measurement of Wind Loads on Full-Scale Glasshouses", J. Wind Eng. and Ind. Aerodynamics, 6, 139 - 167.

Willmarth, W. W., (1975), "Pressure Fluctuations Beneath Turbulent Boundary Layers", Ann. Rev. Fluid Mech., 13 - 38.

Wilson, D. J., G. Winkel and O. Neiman, (1979), "Reynolds Nomber Effects on Flow Recirculation Behind Two-Dimensional Obstacles in a Turbulent Boundary Layer", Proc. 5th Int. Conf. on Wind Engineering, Fort Collins, Colorado, USA, 965 - 974.

Wilson, P. B., (1985), "Behaviour of the Spinning Film Mass Transfer Coefficient", BE Project Report, Chem. Eng. Dept., University of Canterbury.

Wyngaard, J. C., (1981), "Cup, Propeller, Vane, and Sonic Anemometers in Turbulence Research", Ann. Rev. Fluid Mech., 13, 399 - 423.

Yosida, Z., (1955), "Physical Studies of Deposited Snow. I. Thermal Properties", Low Temp. Sci., Ser A(No. 7), 19 - 74.

Zangvil, A., (1981), "Some Aspects of the Interpretation of Spectra in Meteorology", Boundary-Layer Meteorol., 21, 39 - 46.

Zhang, H., and W. H. Melbourne, (1992), "Interference Between Two Circular Cylinders in Tandem in Turbulent Flow", J. Wind Eng. and Ind. Aerodynamics, 41-44, 589 - 600.

Zilker, D. P., and T. J. Hanratty, (1979), "Influence of the Amplitude of a Solid Wavy Wall on a Turbulent Flow. Part 2. Separated Flows", J. Fluid Mech., 90, 257 - 271.

Zilker, D. P., G. W. Cook and T. J. Hanratty, (1977), "Influence of the Amplitude of a Solid Wavy Wall on a Turbulent Flow. Part 1. Non-separated Flows", J. Fluid Mech., 82, 29 - 51.

Appendices

Table of Contents

List of Illustrations

Nomenclature

The definitions of DADiSP Worksheet functions are not included in this list.

A	column cross sectional area (m^2)
Bo_Δ	finite-difference form of the Biot number for heat dissipation
Bi_Δ^{pd}	finite-difference form of the Biot number for pressure dissipation
D	cone penetration depth (m)
$\overline{D}_{p2}$	mean particle diameter (m)
d	total snow pack depth (m)
d_b	bottom insulation thickness (mm)
d_t	top insulation thickness (mm)
F	applied force (N)
Fo_Δ	finite-difference form of the Fourier number for heat dissipation
Fo_Δ^{pd}	finite-difference form of the Fourier number for pressure dissipation
$f(z)$	initial temperature distribution (°C)
f_c	unconfined compressive strength (N/m^2)
h_{air}	convective heat transfer coefficient (W/m^2K)
h_c	convective heat transfer coefficient (W/m^2K)
K	permeability (m^2/Pas)
k_c	thermal conductivity (W/mK)
k_{ins}	insulation heat conductivity (W/mK)
k_{snow}	snow heat conductivity (W/mK)
l_n	the distance between nodes (m)
P_c	amplitude of pressure fluctuation (Pa)
$\overline{P}$	average ambient pressure (Pa)
p	pressure drop (Pa, Pa/m)
Δp	pressure drop across the leak (Pa)
Q_L	volumetric flow through the leak (m^3/s)
q	flowrate (l/s)
R	leak resistance (Pas/m^3), residual (W)
Re_b	bed Reynolds numbers
s	standard deviation
T	temperature, fluctuating temperature (°C, K)
T_A	cold laboratory (ambient) temperature (°C)
T_B	bottom plate temperature (°C)
T_c	amplitude of temperature fluctuation (°C)
T_I	initial temperature (°C)
T_T	top plate temperature (°C)

t	time (s)
V	voltage (V)
v	superficial velocity, instantaneous wind speed (m/s)
z	distance from the surface, height, vertical dimension (m)
α	thermal diffusivity (m^2/s)
ε	voidage
Φ_d	diameter of sphere having the same volume as the particle (m)
Φ_s	ratio of *surface area of a sphere of equal volume to the particle* to *surface area of the particle* (m^2/m^2)
μ	viscosity (Pas)
ρ	density ($kg/m^{3)}$
τ	period (s)

Appendix I
DADiSP Worksheet

DADiSP Worksheet is a data analysis and digital signal processing software package produced by DSP Development Corporation, Cambridge, USA for IBM and Compatibles 80286 upwards. This work utilizes version 2.01, 1991 on a DECpc 433 Workstation with 8 MB of Ram.

For this application DADiSP is used to produce the autocorrelation, and autospectral density functions of the wind speed and pressure fluctuations and the crosscorrelation function between the variables. It is also used in a similar application by Texas Tech field experiments (Levitan and Mehta, 1992a).

Theoretically DADiSP will handle files of any length as it 'pages' data to disk and only stores part of the large data file in memory at any one time (at the expense of processing speed). However occasional problems are encountered with DADiSP's Fast Fourier Transform functions, resulting in the error message "No Memory", if the file is not of length 2^a samples ($a = 1, 2, 3...$).

Although DADiSP had been used prior to this work by Tan (1991) and Tong (1992) they did not resolve many of the small idiosyncrasies in the software that renders their results meaningless.

This section describes the data processing in DADiSP and identifies such idiosyncrasies for future work. Fundamental knowledge of the software is assumed from this point, otherwise refer to the DADiSP Worksheet (1990). A flow chart of the following description is shown in figure I.1.

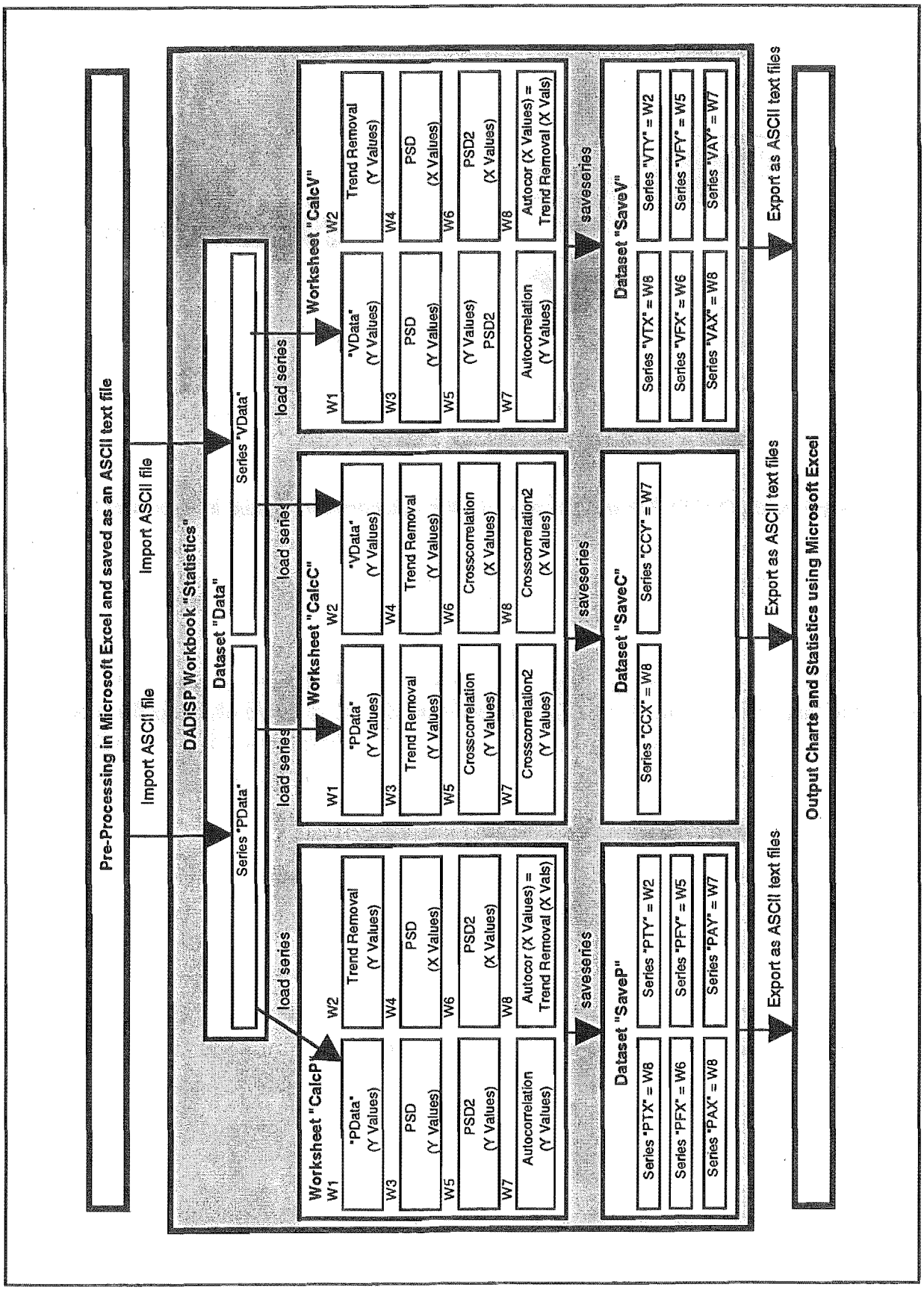

Figure I.1. Structural Flowchart for the Computations in DADiSP.

I.1. Importing Data from Microsoft Excel to DADiSP Worksheet

This step is required as DADiSP only works with internally defined files. The pre-processed sample records are saved as text files in Excel as two columns, Pressure Fluctuations (Pa) and Wind Speed Fluctuations (m/s). The time scale is eliminated as DADiSP recreates the time scale when the sample frequency is set to 2 Hz (in this case) in the Series Header.

The text file is then imported into DADiSP in ASCII format into two Series, the pressure data, "PData", and wind speed data, "VData".

I.2. Worksheets, Windows and Functions

Three Worksheets are used to process the data because of memory limitations doesn't allow the information required to be stored in one. A description of each Window in these Worksheets follows. Note that internal DADiSP functions used below are written in capitals.

I.3. Worksheet 'CalcP'

The worksheet 'CalcP' is used to evaluate the statistical properties of the pressure fluctuations.

W1 Window 1 has the yvalues of the pressure data loaded into it (as imported).

W2 Least Squares Polynomial Removal (yvalues).

=EXTRACT(W1,1,L)-POLYGRAPH(POLYFIT(W1,n),

GLINE(LENGTH(EXTRACT(w1,1,L)),$\frac{1}{\text{RATE(EXTRACT(w1,1,L))}}$,1,0))

where n=order of polynomial fit
n = 0 ≡ Mean Removal
n = 1 ≡ Linear Trend and Mean Removal
n = 2 ≡ Quadratic Trend and Mean Removal
L = length of series to be evaluated, often set at LENGTH(W1)

Fast Fourier Transform (FFT) functions work best in DADiSP if l= 2^a (a= 1, 2, 3...). DADiSP will evaluate FFT's for other series lengths but is much slower and execution occasionally halts with the error message "No Memory".

Note that moving average trend removal is done in Microsoft Excel as the moving average function MOVAVG(series,length) does not give the anticipated result.

W3 Autospectral Density Function (y values)

$$=PSD(W2)*\frac{RATE(PSD(W2))}{2}$$

where RATE(series) is the sampling frequency of the series. DADiSP's PSD function does not evaluate S(n) as expected and needs modification by the factor RATE(PSD(W2))/2. This is slightly different to Tan (1991) who used LENGTH(series)/2 which worked for his DVA data as it is related to those records sample lengths and frequency. It was incorrect to use the same factor for his Gill data as this was sampled at a different rate. Tong (1992) using Tan's information fell into the same trap.

W4 Autospectral Density Function (x values)

$$=GLINE(LENGTH(W3),\frac{1}{RATE(W3)},1,0)$$

This function gives the x axis values of the autospectral density function evaluated in W3. The DADiSP function XVALS(series) is not used here as it calculates the series with a constant relative error. As an example to illustrate this, if the relative errors is -1% in the first step calculated, then by the 100th step the calculated x axis value is one step out of phase with the actual value. The error calculated by DADiSP is about -0.05%, so over a 16,000 point series sampled at 2Hz it creates a phase shift error in the autocorrelation and crosscorrelation functions of about -2s at $\tau = 0$. The function defined above maintains that initial error as a absolute error through out the series.

W5 Dimensionless Autospectral Density Function (y values)

$$=\frac{EXTRACT(W3,2,LENGTH(W3)-1)*W6}{STDEV(W2)\text{^}2}$$

The EXTRACT function is used here to eliminate the initial zero value as this gives a calculation error when result is plotted on a Log_{10} scale.

W6 Dimensionless Autospectral Density Function (x values)

=EXTRACT(W4,2,LENGTH(W4)-1)

The EXTRACT function is used here as in W5, otherwise the x axis values do not change from W4.

W7 Autocorrelation Function (y values)

$$=\text{EXTRACT}(\frac{\text{FACOR(W2)}}{\text{STDEV(W2)}\hat{}2},1,\text{LENGTH(W2)})$$

FACOR(series) initially calculates the two sided circular autocorrelation function using the FFT technique. This is then presented as the one sided autocorrelation function.

W8 Least Squares Polynomial Removal and Autocorrelation Function (x values)

$$=\text{GLINE}(\text{LENGTH(W2)},\frac{1}{\text{RATE(W2)}},1,0)$$

As before this is used in place of XVALS(series).

I.4. Worksheet 'CalcV'

The worksheet 'CalcV' is used to evaluate the statistical properties of the wind speed fluctuations in the same manner as 'CalcP' does for the pressure fluctuations.

I.5. Worksheet 'CalcC'

The worksheet 'CalcC' is used to evaluate the correlation between the wind speed and pressure fluctuations.

Windows 1 and 3 contain the same information as windows 1 and 2 of 'CalcP' (data series and trend removal), and window 2 and 4 the same informations as 1 and 2 of 'CalcV'.

W5 Crosscorrelation Function (y values)

$$=\frac{\text{CROSSCOR(W3,W4)*2}}{\text{STDEV(W3)*STDEV(W4)}}$$

This calculates the two sided crosscorrelation function, but does not use FFT techniques. Note that this function has the limits of ±1.0, not ±0.5 as is usual with two sided functions. Hence, a comparative scale is made with the one sided autocorrelation function, whilst maintaining the option of seeing the wind speed fluctuations leading or lagging the pressure fluctuations.

W6 Crosscorrelation Function (x values)

$$=\text{GLINE}(\text{LENGTH(W5)},\frac{1}{\text{RATE(W5)}},1,0)$$

As before this is used in place of XVALS(series).

W7 Decimated Crosscorrelation Function (y values)

=DECIMATE(EXTRACT((W5,2,LENGTH(W5)-2),2,1)

W8 Decimated Crosscorrelation Function (x values)

$$=\text{DECIMATE}\left(W6 - \frac{\text{MAX}(W6)}{2},2,2\right)$$

As Microsoft Excel files are limited to 16384 rows these windows eliminate every 2nd point from the calculated crosscorrelation function series (up to 32768 points) at no significant loss of accuracy.

I.6. Exporting Data from DADiSP Worksheet to Microsoft Excel

Following the completion of calculations the appropriate series are saved from the Worksheets to Datasets and exported out of DADiSP as 14 single column ASCII text files. The appropriate pairs are joined in Microsoft Excel Spreadsheets to form 7 new data files for each original sample record. These are

Pressure Fluctuations

'PTX' and 'PTY'	Time domain series of the sample record with the applied mean and trend removal.
'PFX' and 'PFY'	Frequency domain series of the above as the dimensionless autospectral density function.
'PAX' and 'PAY'	One sided autocorrelation function of the above time domain series.

Wind Speed Fluctuations

'VTX' ... 'VAY'	as above

Pressure and Wind Speed Fluctuations

'CCX' and 'CCY'	Two sided crosscorrelation function of the above two time domain series.

As the print functions of DADiSP do not appear to work, all output is made through Microsoft Excel.

I.7. Automation of DADiSP Worksheet Computations

All DADiSP interaction is automated with the following command files which are written in a text editor and stored in the DADiSP Directory. For a full length sample record of 16384 samples DADiSP takes approximately three hours to complete the computations. This time is about doubled for near full length sample records, that is length $\neq 2^a$.

Command File "SaveP"

```
SAVESERIES(W2,"SaveP.1.TY",1) @CR        ! save TIME SERIES Y values
SAVESERIES(W8,"SaveP.1.TX",1) @CR        ! save TIME SERIES X values
SAVESERIES(W5,"SaveP.1.FY",1) @CR        ! save FREQUENCY SERIES Y values
SAVESERIES(W6,"SaveP.1.FX",1) @CR        ! save FREQUENCY SERIES X values
SAVESERIES(W7,"SaveP.1.AY",1) @CR        ! save AUTOCORRELATION Y values
SAVESERIES(W8,"SaveP.1.AX",1) @CR        ! save AUTOCORRELATION X values
@ESC @ESC U                              ! goto utilities
E SaveP.1 @CR TY @CR @CR PTY @CR         ! export series TY...AX from
E SaveP.1 @CR TX @CR @CR PTX @CR         ! dataset SaveP.1 and save
E SaveP.1 @CR FY @CR @CR PFY @CR         ! as PTY...PAX
E SaveP.1 @CR FX @CR @CR PFX @CR
E SaveP.1 @CR AY @CR @CR PAY @CR
E SaveP.1 @CR AX @CR @CR PAX @CR
D D SaveP.1 @CR Y @ESC                   ! delete dataset SaveP.1
@ESC W E @CNTL_HOME                      ! return to worksheet
```

Command File "SaveV"

```
SAVESERIES(W2,"SaveV.1.TY",1) @CR        ! save TIME SERIES Y values
SAVESERIES(W8,"SaveV.1.TX",1) @CR        ! save TIME SERIES X values
SAVESERIES(W5,"SaveV.1.FY",1) @CR        ! save FREQUENCY SERIES Y values
SAVESERIES(W6,"SaveV.1.FX",1) @CR        ! save FREQUENCY SERIES X values
SAVESERIES(W7,"SaveV.1.AY",1) @CR        ! save AUTOCORRELATION Y values
SAVESERIES(W8,"SaveV.1.AX",1) @CR        ! save AUTOCORRELATION X values
@ESC @ESC U                              ! goto utilities
E SaveV.1 @CR TY @CR @CR VTY @CR         ! export series TY...AX from
E SaveV.1 @CR TX @CR @CR VTX @CR         ! dataset SaveV.1 and save
E SaveV.1 @CR FY @CR @CR VFY @CR         ! as VTY...VAX
E SaveV.1 @CR FX @CR @CR VFX @CR
E SaveV.1 @CR AY @CR @CR VAY @CR
E SaveV.1 @CR AX @CR @CR VAX @CR
D D SaveV.1 @CR Y @ESC                   ! delete dataset SaveV.1
@ESC W E @CNTL_HOME                      ! return to worksheet
```

Command File "SaveC"

```
SAVESERIES(W7,"SaveC.1.CY",1) @CR"      ! save CROSSCORRELATION Y values
SAVESERIES(W8,"SaveC.1.CX",1) @CR"      ! save CROSSCORRELATION X values
@ESC @ESC U                             ! goto utilities
E SaveC.1 @CR CY @CR @CR CCY @CR        ! export series CY and CX from
E SaveC.1 @CR CX @CR @CR CCX @CR        ! dataset SaveC.1 and save
D D SaveC.1 @CR Y @ESC                  ! delete dataset SaveC.1
@ESC W E @CNTL_HOME                     ! return to worksheet
```

Command File "Process"

```
O Statistics @CR                        ! open labbook Statistics
U D D Data.1 @CR Y @ESC @ESC W          ! delete old dataset Data.1 and enter labbook
L CalcP @CR                             ! load worksheet CalcP
E @CNTL_HOME                            ! enter worksheet at W1
CALL("OPEN") @CR                        ! open and put input files into dataset Data.1
@POP("P1",-1,20,"Processing Pressure Data")
@F8 Data.1 @CR P @CR                    ! enter series Data.1.P into W1
CALL("SaveP") @CR                       ! export pressure results to DSP\ as P...
@ESC S CalcP @CR Y                      ! save worksheet CalcP
L CalcV @CR                             ! load worksheet CalcV
E @CNTL_HOME                            ! enter worksheet at W1
@POP("P2",-1,20,"Processing Velocity Data")
@F8 Data.1 @CR V @CR                    ! enter series Data.1.V into W1
CALL("SaveV") @CR"                      ! export velocity results to DSP\ as V...
@ESC S CalcV @CR Y                      ! save worksheet CalcV
L CalcC @CR                             ! load worksheet CalcC
E @CNTL_HOME @F3 @ESC                   ! enter worksheet at W1
@F8 Data.1 @CR P @CR                    ! enter series Data.1.P into W1
@POP("P5",-1,20,"Processing Cross Correlation")
@RT @F8 Data.1 @CR V @CR                ! enter series Data.1.V into W2
@CNTL_HOME CALL("SaveC") @CR            ! export crosscorr. results to DSP\ C...
@ESC S CalcC @CR Y                      ! save worksheet CalcC
```

Command File "Open"

```
@ESC @ESC U                          ! goto utilities
I @F2 C:\BELL\TRANSFER @CR           ! import from directory C:\BELL\TRANSFER
Data @CR                             ! import file Data
E @CR                                ! edit header
Data @CR                             ! dataset name Data
1 @CR                                ! version number 1
P @CR @CR @CR @CR @CR                ! series name P (pressure)
2 @CR @F2                            ! frequency 2 Hz and accept header values
F @DN @CR                            ! edit file
2 @CR                                ! 2 columns
1 @CR @F2                            ! select column 1 and accept file values
P                                    ! proceed to import
I Data @CR                           ! do the same for column 2
E @CR Data @CR 1 @CR V @CR @F2       ! edit header values (series name, V)
F @DN @CR 2 @CR 2 @CR @F2            ! edit file values
P                                    ! proceed to import
@ESC W E @CNTL_HOME                  ! return to worksheet
```

Appendix II
Wind Monitor

This instrument displays three wind parameters on a control box from wind speed and direction sensors which are mounted on a nearby six meter mast. The sensors are connected by a four core screened cable to prevent Kea damage. The instrument is powered from a 230V supply and has analog outputs for wind speed and direction.

II.1 Wind Direction

This is sensed by a vane made in the department which turns a high quality plastic 1KΩ potentiometer with 3.60VDC applied across it. The voltage picked off by the wiper is displayed on a Digital Volt Meter by the Wind Monitor. For the wind vane to indicate wind direction as points of a compass it is calibrated by aligning the pointer and wiper on the sensor itself with true north and 0.00 V respectively.

II.2 Wind Speed

This is sensed by a commercially supplied A100 Porton Anemometer which has a slotted disc and an optical switch in the head unit. This switch produces 5V pulses at the rate of 10pulses per meter of wind run. These pulses are led into the control unit and divided by 10 to give 1pulse per meter of wind run. The frequency of these pulses is measured against an R/C oscillator and displays the current wind speed in meters per second. This is averaged and updated each second.

II.3 Total Wind Run

This quantity is derived from the 1 meter pulses mentioned above. These are fed to a counter unit which sums them and displays the running total. A reset button resets this counter to zero. An Led flashing on each meter pulse indicates that the head signal is being received by the Wind Monitor.

II.4 Analog Outputs

There are two DC output voltages available at terminals on the rear of the instrument for connection to external devices. DIROUT gives 0to3.60VDC for the full 360° of the compass and RUNOUT gives a voltage of 0to1.7V for 0to44m/s of wind speed.

The electrical output for the anemometer is calibrated in a high speed recirculating wind tunnel in the University's Mechanical Engineering Department over the range 0to35m/s. For conversion of digital data the following third order polynomial fit is used to calculate the instantaneous wind speed v (m/s)

$$v = -4.53 + 7.36*V - 0.104*V^2 + 0.00799*V^3 \qquad \text{II.1}$$

where V is the output voltage. The error in this calibration is well below the anemometer accuracy.

To check for hysteresis the calibration is made for both increasing and decreasing wind speeds with no detectable change. Wind tunnel velocities are measured using a pitot tube attached to an Air Neotronics Micromanometer corrected for air density.

Appendix III
Blower Permeometer

III.1. Introduction

Early work by Waterhouse (1963) recognised that air permeability is a sensitive signatory to snow structure. Taking this further, Conway and Abrahamson (1984b) investigated air permeability as a textural indicator of snow and found it to be strongly dependent on its metamorphic state. Since then Buser and Good (1987) have studied the relationship between snow permeability and its connection to ice grain structure. For these reasons air permeability is used extensively throughout this thesis.

It is obvious that Conway and Abrahamson's ability to draw conclusions from their results is limited by the use of high flowrates, and inaccuracy (unsteadiness) of the flowrate measurement in their permeometer. However the convenience features of their second device, the Blower Air Permeometer, are retained in the permeometer developed for this experimental programme.

III.1.1. Background Theory

Darcy's Law is used to evaluate the permeability by defining the bed permeability, K (m^2/Pas) as

$$K = \frac{zv}{p} \qquad \text{III.1}$$

where z is the bed height, v the superficial velocity and p the pressure drop over the bed. The use of Darcy's law is limited to bed Reynolds numbers Re_b not exceeding some value of between 1 and 10 (Bear, 1972). The bed Reynolds number is defined by Fayed and Otten (1984) as

$$Re_b = \frac{\rho v \left(\Phi_s \Phi_d\right)}{\mu(1-\varepsilon)} \qquad \text{III.2}$$

where Φ_s is the ratio of *surface area of a sphere of equal volume to the particle* to *surface area of the particle*, Φ_d is the *diameter of sphere having the same volume as the particle*, ρ the fluid density, v the superficial velocity, μ the fluid viscosity and ε the bed voidage.

III.2. The Air Blower Permeometer

A permeometer similar to Conway and Abrahamson's second device was developed for use in the current work. The device is shown in detail in figure III.1. Plate III.1(a) shows a perspective of the unit and plate III.1(b) shows it in use in the field (prior to packing the baffles).

Like its predecessor, the new permeometer is constructed almost entirely of methylmethacrylate (perspex). The body is cut from Ø90 OD mm tubing and is 280 mm long. The upper 70 mm is dedicated to the sample, the remainder to supplying, stabilizing and measuring the air flow. The flow is still supplied by a fan and measured by an 8 mm orifice. Two key changes aimed at improving the instruments performance are

* A 9 V DC motor to drive the fan and a potentiometer to vary the power supplied to the motor, and hence the flowrate.
* The use of the Air Neotronics Digital Micromanometer described in section 3.7.2.1 to measure both flowrate and pressure drop across the sample.

These generally allow for much steadier measurements, and more specifically, enable repeatable measurements at the very low flowrates relevant to wind pumping (where the flow regime is laminar). Noise generated in the pressure signal by atmospheric turbulence (during windy conditions) can be the cause for limiting repeatability in the measurements.

The radial baffles above and below the fan were to minimise both the formation of vortexes and channelling of the flow. However, with a sample in place a markedly higher flowrate was measured with a hot wire anemometer around the rim compared to near the centre. After packing the baffle sections with 3 mm beads this difference became undetectable.

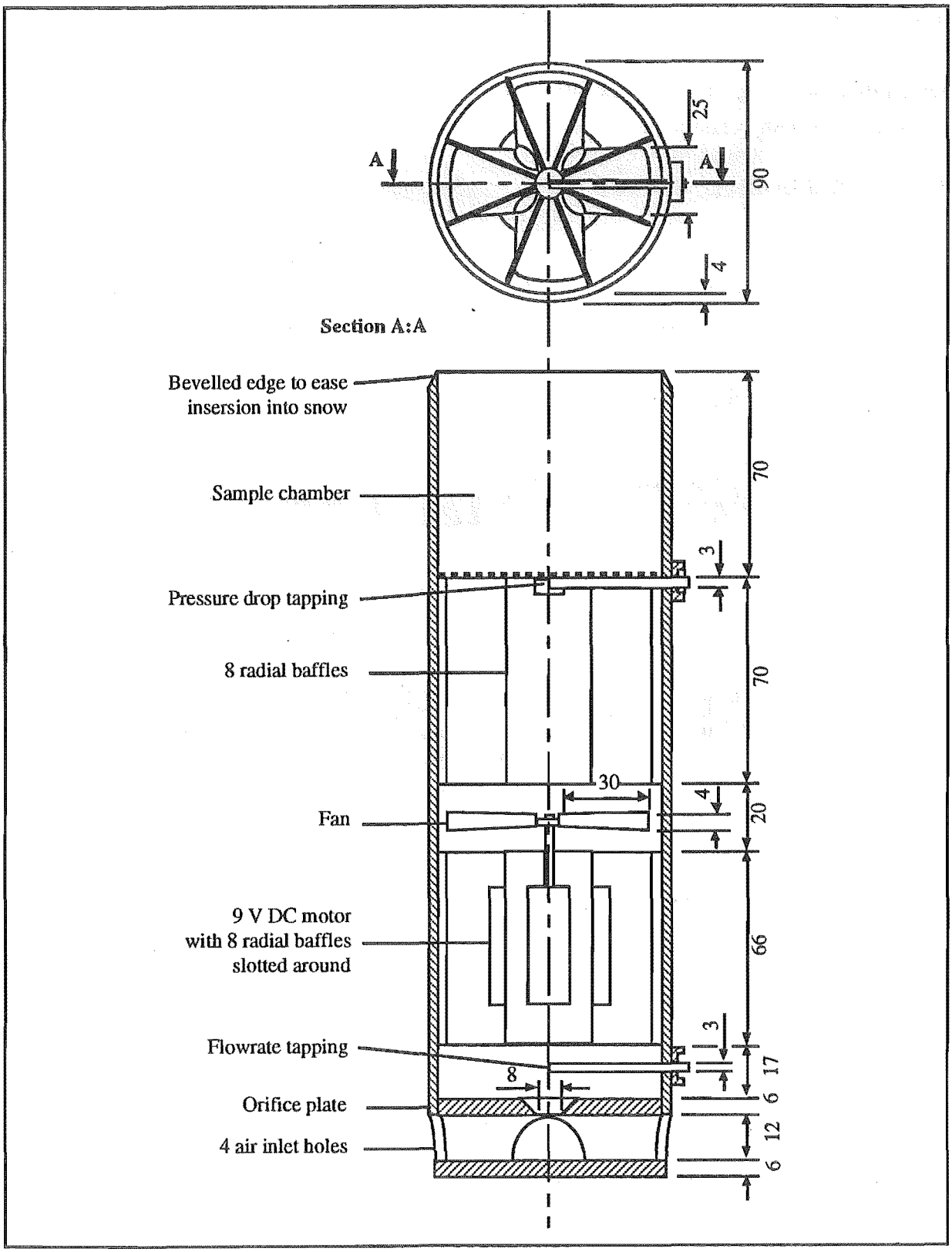

Figure III.1. Drawing of the Blower Permeometer. The baffle packing is not shown here, but can be seen in plate III.1(b). Scale 1:2. Dimensions in mm.

III.3. Calibration of the Orifice Plate

Two calibrations are performed; the first to recreate the flow regimes used by Conway and Abrahamson (1984b), and the second for direct use in this work.

III.3.1. Calibration Method

The required steady flow for calibration is produced by a stainless steel gasometer filled with water. The gasometer has a working volume of 50 l and is calibrated at 0.2545 l/mm of travel. A degree of unsteadiness in the flow, caused by friction through direct contact of the bell and bucket, and by viscous forces, is minimised by increasing both the weight on the bell and the bell balance weight. Figure III.2 shows a schematic of the experimental setup.

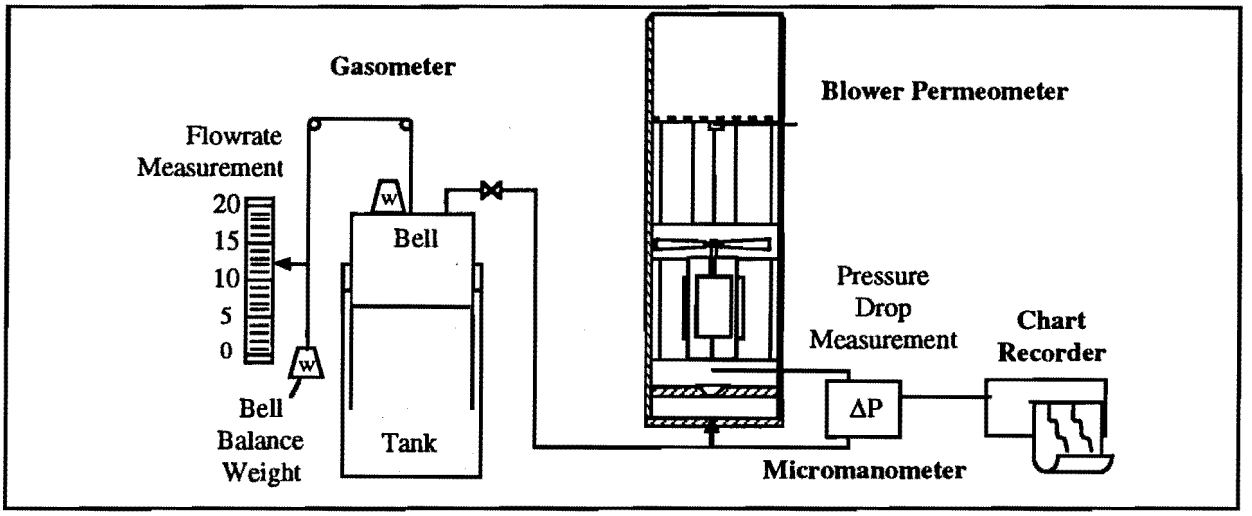

Figure III.2. Schematic of the Blower Permeometer Orifice Plate Calibration.

III.3.2. Calibration Results

Figure III.3 shows the calibration curve at the flow rates used by Conway and Abrahamson (1984b) for the new permeometer along with the calibration data for Conway and Abrahamson's blower permeometer (personal communication). As can be seen the modifications discussed above have significantly improved the instrument's accuracy. The curve fitted is a 5th order polynomial with a regression coefficient of 1.0.

$$q = 0.0463 + 0.0116p - 2.74\times10^{-4}p^2 + 4.41\times10^{-6}p^3 - 3.54\times10^{-8}p^4 + 1.09\times10^{-10}p^5 \qquad \text{III.3}$$

Figure III.4 shows the calibration data for the lower flowrates of more interest in wind pumping. The curve fitted is a 2nd order polynomial with a regression coefficient of 0.987.

$$q = 0.0161 + 0.0334p - 0.00567p^2 \qquad \text{III.4}$$

(a)

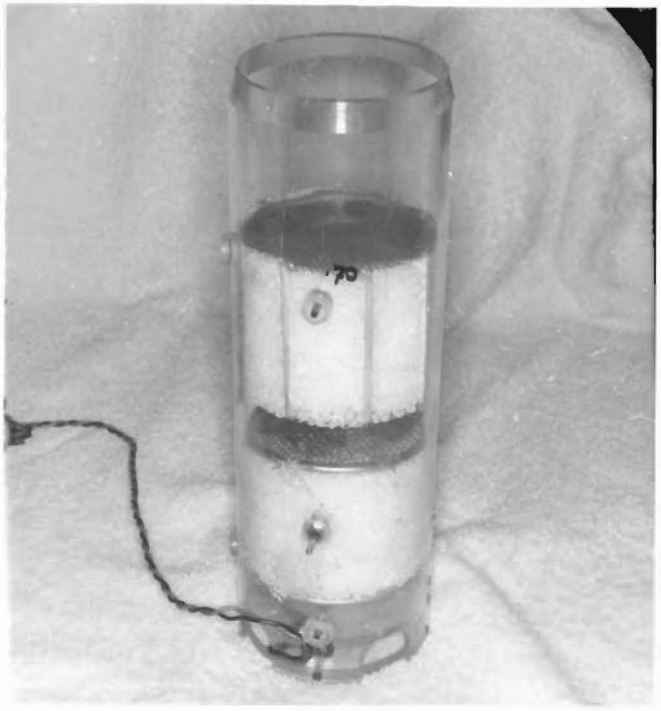

(b)

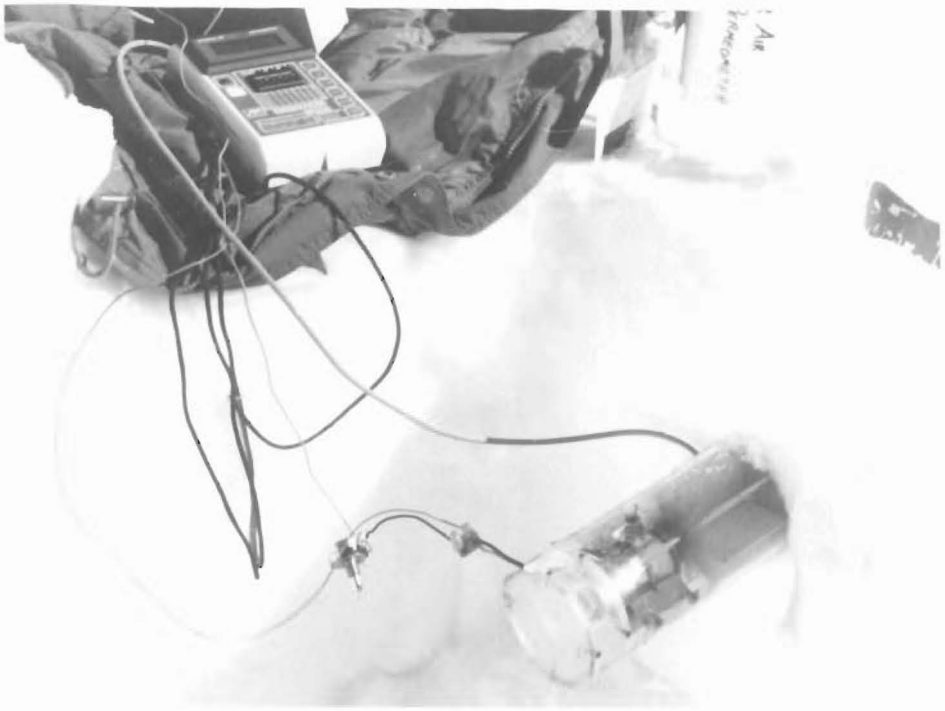

Plate III.1. The Blower Permeometer. (a) Perspective. (b) In the Field (prior to packing the baffles).

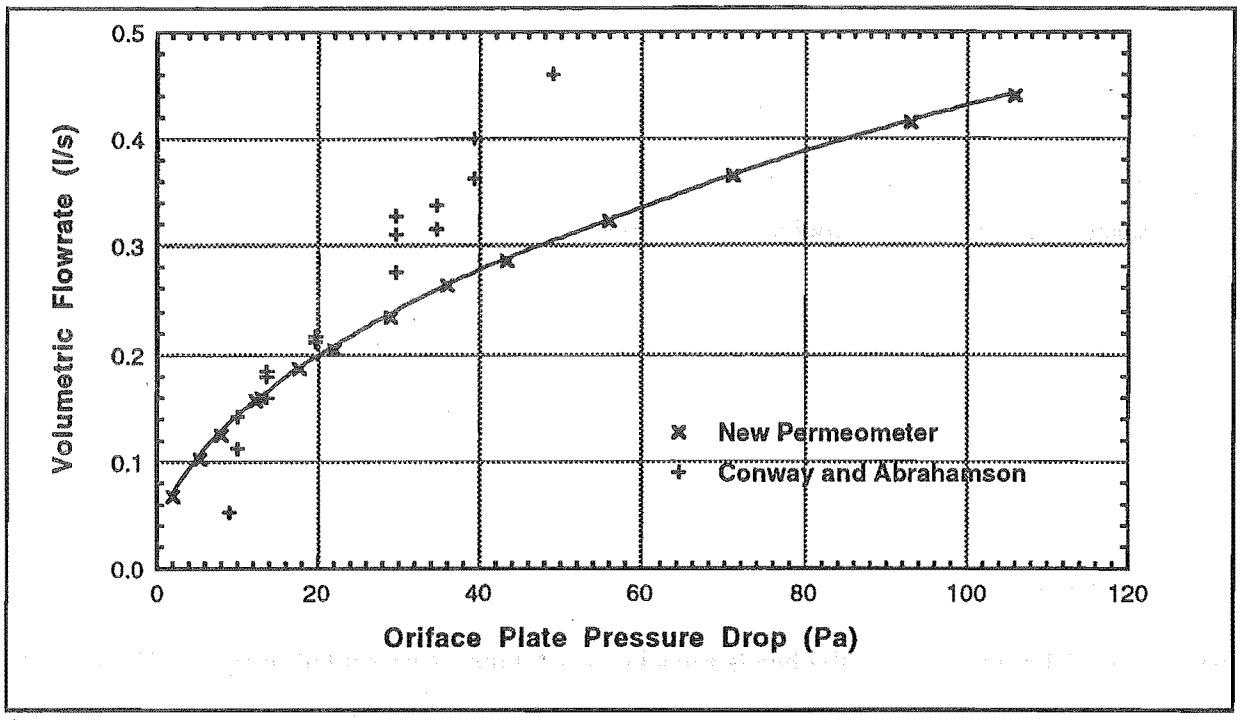

Figure III.3. High Flowrate Calibration Curves for the Orifice Plates in Both the New Blower Permeometer and the Blower Permeometer Used By Conway and Abrahamson (1984b). Note that the two orifice plates do not have the same dimensions. The Curve Fitted to the New Permeometer Data is a 5th Order Polynomial.

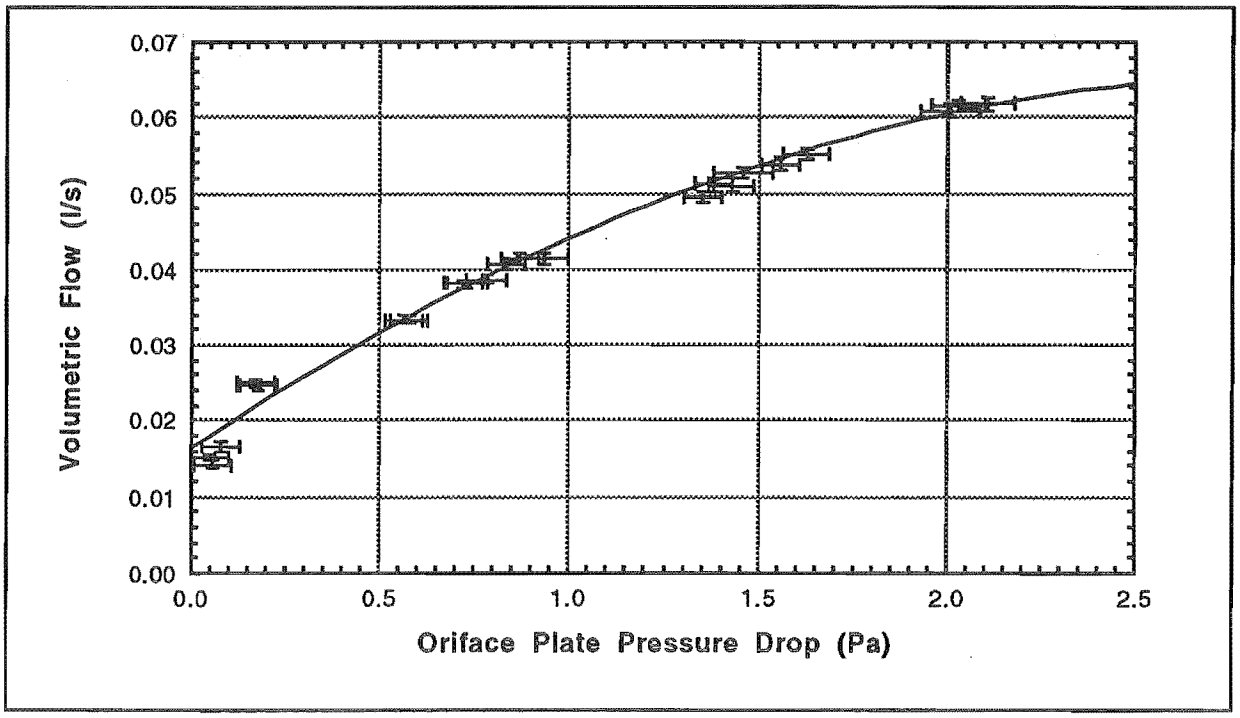

Figure III.4. Low Flowrate Calibration Data for the Orifice Plate in the New Blower Permeometer. The Fitted Curve is a Quadratic Polynomial.

Note that calibrations are presented with volumetric flow rather than superficial velocity because the sample cross sectional area changes with the permeometer's use.

III.4. Permeability Tests

No attempt is made to extend upon the results of Conway and Abrahamson (1984b) in this work. Instead the purpose is to be able to use some of their observed trends to compare with the permeability changes that coincide with the metamorphic changes during the cold laboratory experiments.

Several tests over the range in flowrates used by Conway and Abrahamson (to check on the effects of interstitial turbulence) and over the low velocity range are made. For convenience most of these tests are made with the plastic beads used in the column experiments (Chapter 3).

III.4.1. Plastic Beads

The results of three tests, with the beads repacked each time, is presented in figure III.5. The duplication at high flowrates (Trials A and B) is to check the consistency between packing techniques. Trial C (low flowrates only) is re-presented in figure III.6.

The bed Reynolds number range for the high flowrate trials of $3.3 > Re_b > 24.8$ indicates a degree of turbulent flow and some question over the validity of Darcy's law. This doubt is strengthened by the quadratic nature Trials A and B. The bed Reynolds number range for the low flowrate trial of $0.8 > Re_b > 8.3$ may also indicate a degree of turbulence. However, all the data points lie within the linear regression forced through the origin which strongly supports the applicability of Darcy's Law (see figure III.6).

From Fayed and Otten (1984) the Ergun equation (below) may be used to estimate the laminar and turbulent components of packed bed flow.

$$-p = v\left(\frac{A\mu(1-\varepsilon)^2}{\overline{D}_{p2}{}^2\varepsilon^3}\right) + v^2\left(\frac{B\rho(1-\varepsilon)}{\overline{D}_{p2}\varepsilon^3}\right) \qquad \text{III.5}$$

where p is the pressure drop per meter, v the superficial velocity, μ the viscosity, ε the voidage, ρ the density, $\overline{D}_{p2}$ the mean particle diameter and A = 180 and B = 2 are constants. This prediction for the pressure drop, also plotted in figures III.5 and III.6, appears to underestimate the measured values.

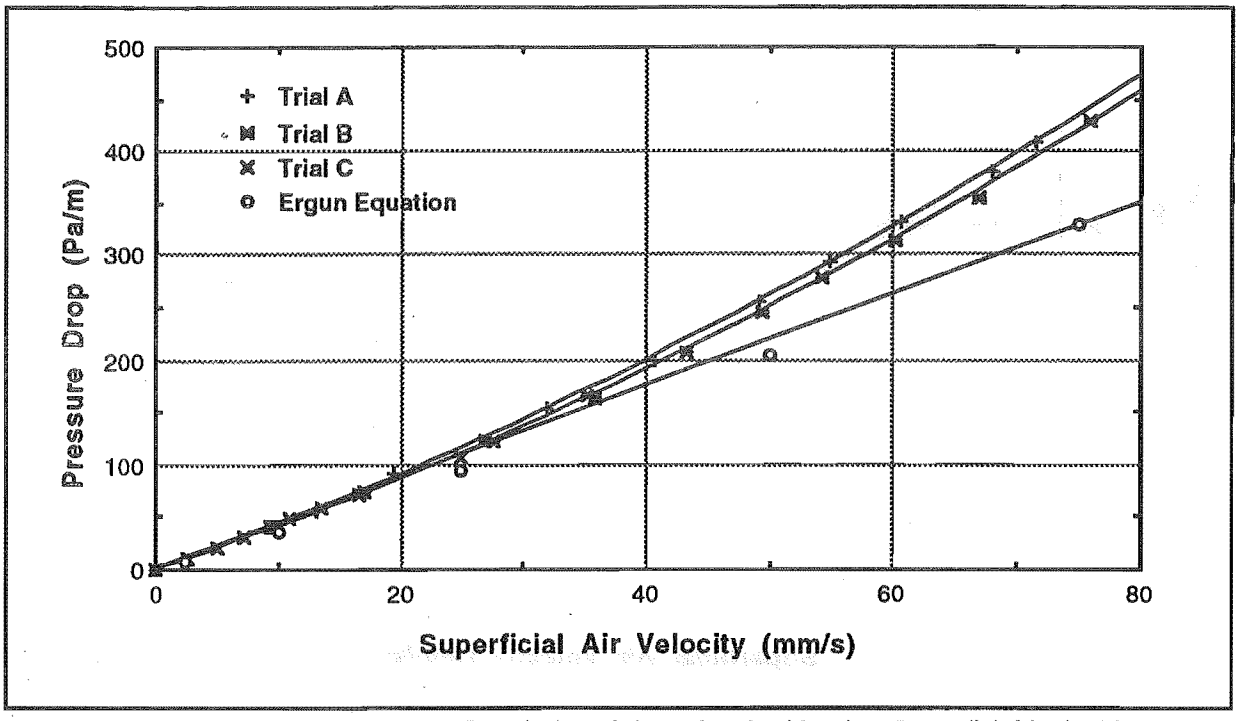

Figure III.5. Pressure Drop Across Plastic Bead Samples for Varying Superficial Velocities. The High Flowrate Trials (A and B) Have Quadratic Polynomials Fitted and the Low Flowrate Trial (C) a Linear Regression Fitted. Note that the Linear Regression is Not Fitted to the Ergun Equation Data.

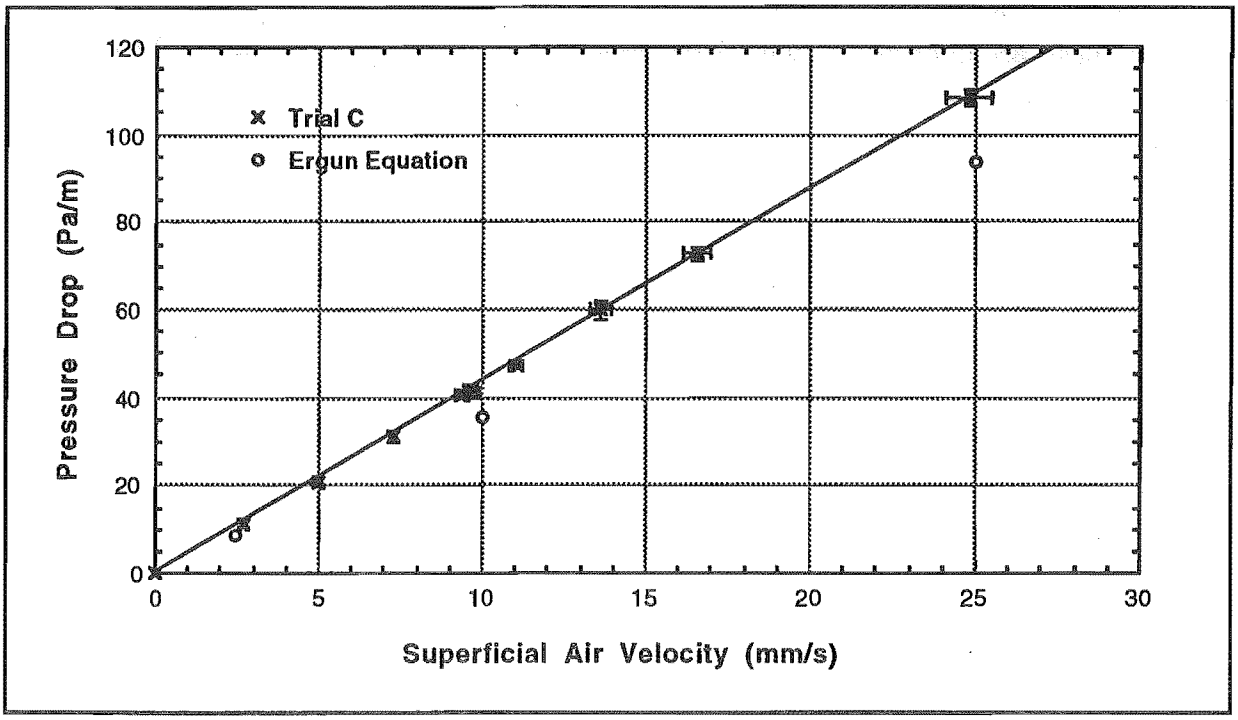

Figure III.6. Pressure Drop Across Plastic Bead Sample for Varying Low Superficial Velocities with a Linear Regression Fitted to the Experimental Data.

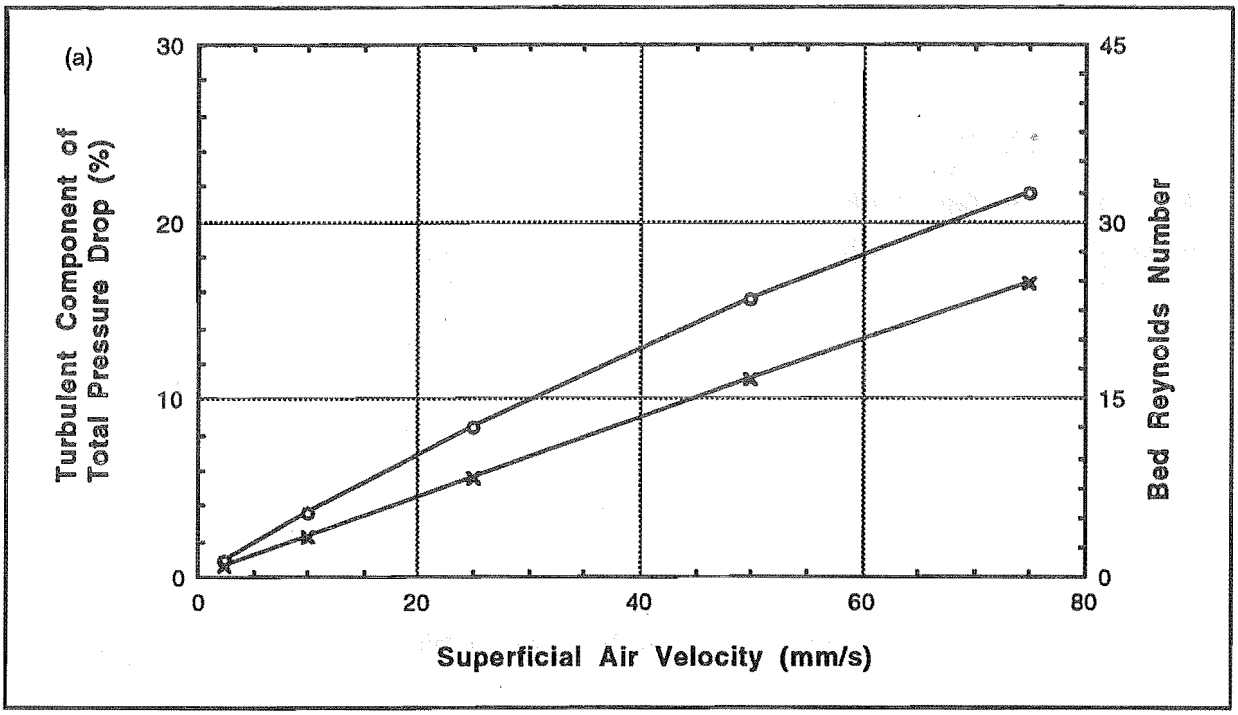

Figure III.7. Turbulent Component of the Ergun Equation and Bed Reynolds Number for Varying Superficial Velocities through a Bed of Plastic Beads.

Figure III.7 shows the turbulent component estimates plotted alongside bed Reynolds numbers over the range of flowrates. It can be seen from this that turbulence plays an important role in the plastic bead bed dynamics at superficial velocities much above v = 10 mm/s. However, the linearity of the low flowrate trial suggests that Darcy's law holds well up to a beds Reynolds number of $Re_b \approx 8$ (v = 25 mm/s).

Note the three repetitions at a superficial velocity of v = 9.5 mm/s indicate the accuracy of the measurement.

III.4.2. Snow Samples

To test the repeatability of the permeability measurement a number of trials were made at the same site. A consistent 20 cm thick snow layer, 25 cm from the surface, which consisted of 0.25 mm rounds at -2°C with a density of 250 kg/m^3 was chosen. All results lie within a standard deviation of 4% across the range of flowrates tested. This compares to 15% from the permeometer used by Conway and Abrahamson (1984b) who could not discern between instrument error or the snows intrinsic spatial variability as the source of error. It can be concluded that a large portion of their error was due to their instrument and therefore any statistically different permeability results in their work, due to orientation, site, snow structure, etc, must indeed be significantly different.

The results of two typical trials are presented in figure III.8 along with predictions from the Ergun equation. The bed Reynolds number range of $1.2 > Re_b > 4.0$ may also indicate a degree of turbulence, although the quadratic curves fitted are not as large in departure from linear compared to the plastic beads with the same superficial flowrates.

Figure III.9 shows the turbulent component estimates plotted along side bed Reynolds numbers over the range of flowrates. It can be seen that turbulence plays a much less important role in the snow sample for the same superficial velocities compared to the plastic beads (cf with figure III.7).

It can be concluded from this that if the assumption of laminar flow and the applicability of Darcy's law is good for the packed bed dynamics experiments, then it is likely the same assumptions can be applied to the snow pack and metamorphism experiments.

Note that, as snow is easily compressed, great care must be taken to push the permeometer in straight during sampling to avoid the production of channels down the walls.

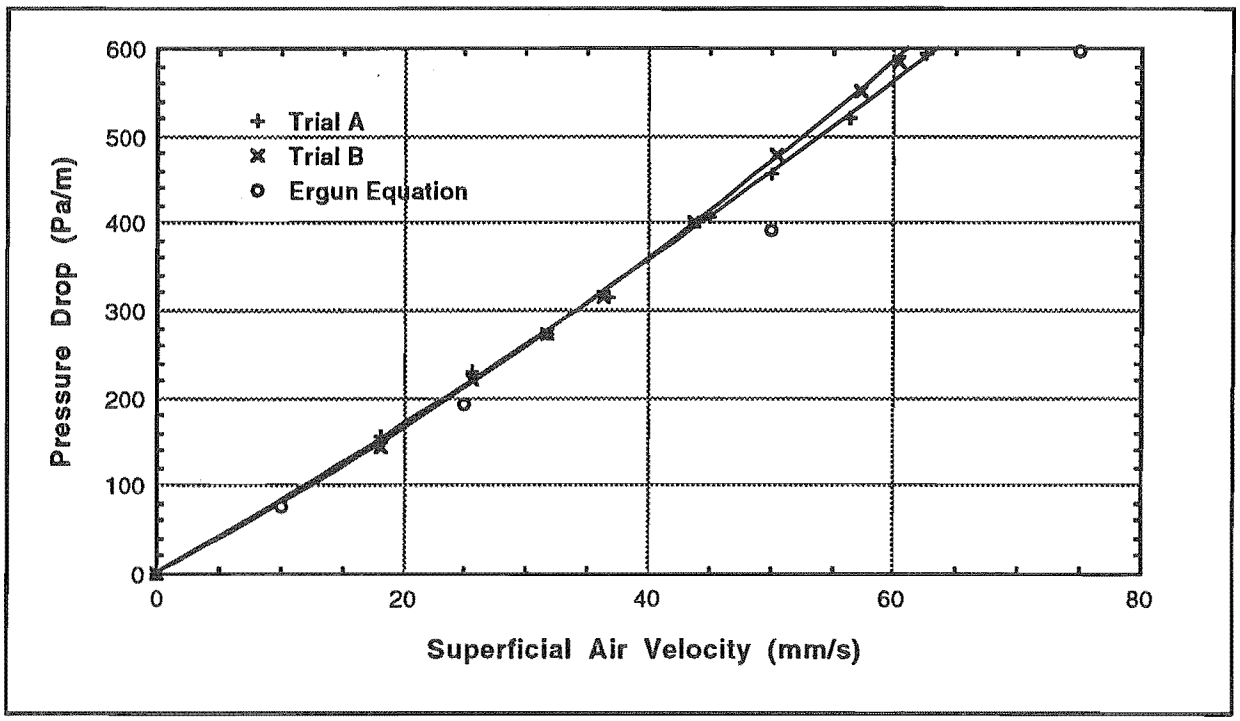

Figure III.8. Pressure Drop Across Snow Sample Varying High Superficial Velocities. Both Trials are Fitted with Quadratic Polynomials.

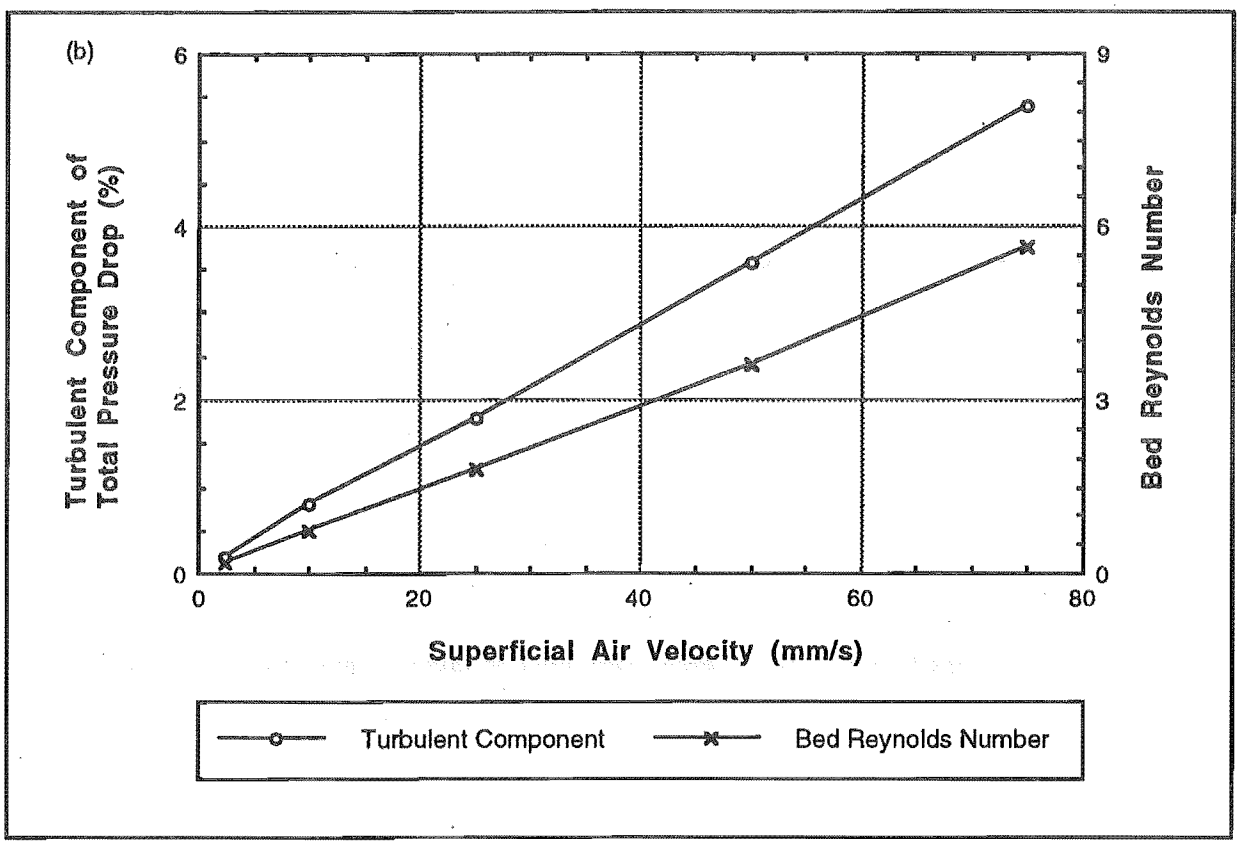

Figure III.9. Turbulent Component of the Ergun Equation and Bed Reynolds Number for Varying Superficial Velocities through a Snow Sample.

Appendix IV
Turbulence Sample Records

Tabulated data for the turbulence sample records.

IV.1. Normality Statistics

Runs	Length (min)	Wind Speed Skewness	Wind Speed Kurtosis	Probe Position	Probe Depth (m)	Pressure Skewness	Pressure Kurtosis
88 to 98	130.8	0.53	0.00	leeward	0.0	-0.05	-0.16
99 to 109	109.7	0.80	0.69	leeward	0.0	0.10	-0.16
125	27.3	0.80	0.69	leeward	0.0	-0.70	1.52
126	27.3	0.29	-0.46	leeward	0.0	0.08	0.97
127	27.3	0.14	-0.19	leeward	0.0	-0.72	1.84
128	27.3	0.13	-0.51	leeward	0.0	-0.50	0.26
129	27.3	0.54	-0.27	leeward	0.0	-0.34	0.48
110 to 120	130.8	0.33	-0.26	leeward	0.3	-0.12	0.23
14 to 16	41.1	0.18	0.01	ridge top	0.0	-0.09	-0.25
17 to 19	41.1	0.97	0.60	ridge top	0.0	-0.47	-0.05
130	27.3	0.56	-0.19	ridge top	0.0	0.49	-0.07
131	27.3	-0.06	-0.59	ridge top	0.0	-0.14	0.43
132	27.3	0.00	-0.61	ridge top	0.0	-0.39	0.80
133	27.3	0.06	-0.15	ridge top	0.0	-0.41	0.03
1 to 10	103.4	0.49	0.21	ridge top	0.5	-0.37	0.14
44 to 54	130.8	0.21	-0.50	ridge top	0.5	-0.31	0.09
33 to 43	136.5	0.71	0.82	ridge top	1.0	-0.92	1.86
61 to 65	68.3	0.62	0.27	windward	0.0	-0.89	1.37
66 to 76	130.7	0.00	-0.09	windward	0.5	0.50	-0.04
77 to 81	68.5	0.90	0.81	windward	0.5	0.19	-0.46
82 to 87	62.2	0.74	0.27	windward	0.5	-0.65	0.70
23 to 27	68.3	0.69	0.72	windward	1.0	0.00	-0.54
55 to 60	62.2	0.52	-0.01	ridge top	†	1.18	10.12
121 to 124	54.8	0.68	0.53	leeward	†	1.65	12.57

Table IV.1. Skewness and Kurtosis Normal Distribution Statistics for the Fluctuating Wind Speed and Pressure Records. Probe Depth † refers to a pressure probe configuration of two sub-surface probes separated by X = 4.5 m at the same snow pack depth of d = 0.5 m.

IV.2. Record Variance Statistics

Runs	Length (min)	Trend Removal	Wind Speed Fluctuations				Probe Position	Probe Depth (m)	Snow Pack Depth (m)	Pressure Fluctuations			
			Before Trend Removal		After Trend Removal					Before Trend Removal		After Trend Removal	
			Mean (m/s)	Standard Deviation (m/s)	Turbulent Intensity	Standard Deviation (m/s)				Standard Deviation (m/s)	RMS Pressure Coefficient	Standard Deviation (m/s)	RMS Pressure Coefficient
88 to 98	130.8	Moving Average	5.92	2.86	0.48	2.82	0.48	leeward	0.0	3.1	30.57	1.74	26.66	1.52
99 to 109	109.7	Moving Average	5.69	3.01	0.53	2.90	0.51	leeward	0.0	3.1	27.01	1.67	26.35	1.63
125	27.3	None	9.88	4.77	0.48	4.77	0.48	leeward	0.0	2.4	61.71	1.26	61.71	1.26
126	27.3	Linear	10.89	4.72	0.43	4.72	0.43	leeward	0.0	2.4	51.71	0.87	50.73	0.86
127	27.3	None	13.17	4.49	0.34	4.49	0.34	leeward	0.0	2.4	55.40	0.64	55.40	0.64
128	27.3	None	11.44	5.15	0.45	5.15	0.45	leeward	0.0	2.4	48.83	0.75	48.83	0.75
129	27.3	None	9.97	4.93	0.49	4.93	0.49	leeward	0.0	2.4	51.64	1.04	51.64	1.04
110 to 120	130.8	Moving Average	5.29	2.86	0.48	2.66	0.45	leeward	0.3	3.1	29.22	2.09	15.98	1.14
14 to 16	41.1	Quadratic	4.30	3.10	0.72	2.01	0.47	ridge top	0.0	2.8	25.72	2.78	19.7	2.13
17 to 19	41.1	None	3.93	2.47	0.63	2.47	0.63	ridge top	0.0	2.8	21.39	2.77	21.39	2.77
130	27.3	None	9.10	4.58	0.50	4.58	0.50	ridge top	0.0	2.5	59.99	1.45	59.99	1.45
131	27.3	None	12.75	4.66	0.37	4.66	0.37	ridge top	0.0	2.5	53.09	0.65	53.09	0.65
132	27.3	None	11.19	4.46	0.40	4.46	0.40	ridge top	0.0	2.5	44.62	0.71	44.62	0.71
133	27.3	None	12.44	3.33	0.27	3.33	0.27	ridge top	0.0	2.5	43.65	0.56	43.65	0.56
1 to 10	103.4	Moving Average	2.75	1.53	0.56	1.25	0.56	ridge top	0.5	2.4	18.05	4.77	6.16	1.63
44 to 54	130.8	Moving Average	4.59	2.28	0.50	2.90	0.44	ridge top	0.5	2.7	14.3	1.36	12.22	1.16
23 to 27	68.3	Quadratic	4.20	2.39	0.57	2.50	0.43	ridge top	1.0	2.7	20.13	2.28	13.61	1.54
33 to 43	136.5	Moving Average	5.00	2.36	0.47	1.84	0.37	ridge top	1.0	2.7	14.69	1.18	11.78	0.94
61 to 65	68.3	None	4.60	2.31	0.50	2.31	0.50	windward	0.0	1.6	28.54	2.7	28.54	2.7
66 to 76	130.7	Moving Average	5.31	2.66	0.50	2.18	0.53	windward	0.5	1.6	24.11	1.71	20.22	1.43
77 to 81	68.5	Linear	4.21	2.22	0.53	2.19	0.53	windward	0.5	1.6	22.4	2.53	18.21	2.05
82 to 87	62.2	Moving Average	5.25	2.76	0.53	2.50	0.53	windward	0.5	1.6	37.74	2.74	28.63	2.08
55 to 60	62.2	Moving Average	4.47	2.62	0.59	2.12	0.53	ridge top	†	2.7	2.41	0.24	2.53	0.25
121 to 124	54.8	Linear	3.91	1.95	0.50	1.76	0.45	leeward	†	2.9	1.77	0.23	1.75	0.23

Table IV.2. Means, Standard Deviations and Turbulence Intensities for the Fluctuating Wind Speed Records and Standard Deviations and RMS Pressure Coefficients for the Fluctuating Pressure Records Before and After Trend Removal. Probe Depth † refers to a pressure probe configuration of two sub-surface probes separated by X = 4.5 m at the same snow pack depth of d = 0.5 m.

IV.3. Gust Exceedance Statistics

Runs	Bandwidth (Hz)	Wind Speed (m/s)					Probe		Pressure (Pa)				
		2 to 0.4	...0.08	...0.016	...0.0032	...0.00064	Position	Depth (m)	2 to 0.4	...0.08	...0.016	...0.0032	...0.00064
88 to 98	σ	0.41	0.88	1.5	1.5	1.38	leeward	0.0	2.18	5.08	10.92	17.16	17.56
	gusts/hr	2216	561	115	28	6			2073	485	106	28	3
99 to 109	σ	0.40	0.91	1.50	1.70	1.08	leeward	0.0	2.25	5.47	10.93	18.08	13.13
	gusts/hr	2275	542	113	28	3			2044	488	104	23	5
110 to 120	σ	0.33	0.69	1.24	1.57	1.35	leeward	0.3	1.24	3.27	6.29	9.96	9.86
	gusts/hr	2279	575	116	26	5			1800	504	110	22	4
14 to 16	σ	0.3	0.57	1.01	1.2	0.47	ridge top	0.0	1.68	2.78	5.01	11.06	11.6
	gusts/hr	2093	553	123	20	0			2369	485	95	20	0
17 to 19	σ	0.23	0.53	0.96	1.77	0.63	ridge top	0.0	1.09	2.03	5.39	16.01	0.14
	gusts/hr	2188	564	98	19	0			2089	400	80	16	0
1 to 10	σ	0.13	0.33	0.54	0.8	0.56	ridge top	0.5	0.61	1.2	2.15	3.67	4.75
	gusts/hr	2573	647	148	33	4			2842	606	128	24	4
44 to 54	σ	0.23	0.5	0.81	1.19	1.38	ridge top	0.5	0.76	1.81	3.75	7.81	9.79
	gusts/hr	2235	570	116	22	4			2007	489	101	23	5
23 to 27	σ	0.28	0.58	0.97	0.97	0.95	ridge top	1.0	1.62	2.81	4.8	7.34	6.73
	gusts/hr	2298	575	132	26	4			2601	539	105	26	4
33 to 43	σ	0.23	0.49	0.91	0.92	1.02	ridge top	1.0	1.25	2.14	4.11	7.76	10.27
	gusts/hr	2269	571	114	21	3			2662	547	83	18	2
61 to 65	σ	0.29	0.69	1.22	1.3	0.87	windward	0.0	1.73	4.56	10.75	18.65	11.78
	gusts/hr	2230	531	127	26	4			2344	450	108	20	2
66 to 76	σ	0.3	0.64	1.14	1.45	0.78	windward	0.5	0.98	2.66	5.96	15.42	9.24
	gusts/hr	2244	564	110	27	4			1874	461	90	24	6
77 to 81	σ	0.27	0.69	1.15	1.35	0.78	windward	0.5	1.26	3.15	6.42	12.9	8.86
	gusts/hr	2144	554	110	32	4			1865	467	95	25	5
82 to 87	σ	0.79	0.81	1.27	1.56	1.43	windward	0.5	5.13	5.75	12.39	21.56	20.15
	gusts/hr	2918	740	150	36	8			3059	600	136	37	8
55 to 60	σ	0.3	0.63	1.05	1.24	1.12	ridge top	†	1.2	1.53	1.37	0.86	0.49
	gusts/hr	2924	743	167	36	6			3403	880	187	40	3
121 to 124	σ	0.25	0.6	0.99	1.05	0.36	leeward	†	0.73	1.1	0.79	0.48	0.21
	gusts/hr	2544	640	135	30	4			2501	578	120	27	4
Average	σ	0.32	0.64	1.08	1.3	0.95							
	gusts/hr	2324	584	123	27	4							

Table IV.3. Fluctuating Wind Speed and Pressure Gust Rates and Standard Deviation of Gust Magnitudes About the Record Mean for Each Bandwidth. Probe Depth † refers to a pressure probe configuration of two sub-surface probes separated by X = 4.5 m at the same snow pack depth of d = 0.5 m.

IV.4. Integral Length Scales

Runs	Record Length (min)	Wind Speed Eulerian (m)	Wind Speed Exponential (m)	Probe Position	Probe Depth (m)	Pressure Eulerian (m)	Pressure Exponential (m)
88 to 98	130.8	210	145	leeward	0.0	299	278
99 to 109	109.7	167	155	leeward	0.0	251	287
110 to 120	130.8	226	196	leeward	0.3	281	302
14 to 16	41.1	113	118	ridge top	0.0	402	355
17 to 19	41.1	196	214	ridge top	0.0	250	303
1 to 10	103.4	110	140	ridge top	0.5	174	220
44 to 54	130.8	240	269	ridge top	0.5	307	324
33 to 43	136.5	183	131	ridge top	1.0	189	215
61 to 65	68.3	117	116	windward	0.0	226	294
66 to 76	130.7	114	133	windward	0.5	258	308
77 to 81	68.5	86	105	windward	0.5	195	215
82 to 87	62.2	135	158	windward	0.5	245	278
23 to 27	68.3	249	176	windward	1.0	482	580
55 to 60	62.2	137	141	ridge top	†	22	11
121 to 124	54.8	60	68	leeward	†	11	8

Table IV.4. Eulerian and Exponential Integral Length Scales for the Fluctuating Wind Speed and Pressure Records. Probe Depth † refers to a pressure probe configuration of two sub-surface probes separated by X = 4.5 m at the same snow pack depth of d = 0.5 m.

Appendix V
Laboratory Snow

Artificial (laboratory) snow is used in the metamorphism experiments of Chapter 6. Numerous configurations and operating pressure were tried in the process of apparatus design. The apparatus and snow properties described below are for the two experimental runs for which the artificial snow was used.

V.1. Snow Making

The snow making concepts of Sommerfeld and Freeman (1988) are used in the snow making method here. Distilled water held in a 20 liter tank and pressurised with compressed air is sprayed downwards 0.8 m above a liquid nitrogen bath through a 0.02 mm straight nozzle. Upon hitting the liquid nitrogen surface the droplets freeze (approximately as ice spheres or grains) and cool to the liquid nitrogen temperature before sinking. The batch process is sized to give 20 liters of snow, sufficient to pack all five sample tubes. The snow making apparatus is illustrated schematically in figure V.1.

Finally the grains are dried, sieved and packed into the sample tubes. The spray process is done in a draft free laboratory with an ambient temperature of around 10 to 15°C. The sieving and packing processes are done in the cold laboratory at around -20°C.

Factors determining droplet size (and hence grain size) are predominantly nozzle type, operating (nozzle) pressure and flowrate. Fluid temperature, surface tension and viscosity play a minor part. In this process droplet size is coarsely controlled for the given nozzle with the tank pressure which in turn is controlled by the compressed air regulator. Fine control is gained with the needle valve which sets the nozzle pressure.

The droplets in the spray form spheres almost immediately on exit from the nozzle. The droplet density (in the air) decreases rapidly as they spread out and fall from the nozzle. This is important because a spray density which is too high when it hits the liquid nitrogen causes individual droplets to collided[1] and fuse during the freezing process.

[1]During the rather vigorous freezing process the droplets move around rapidly on the surface.

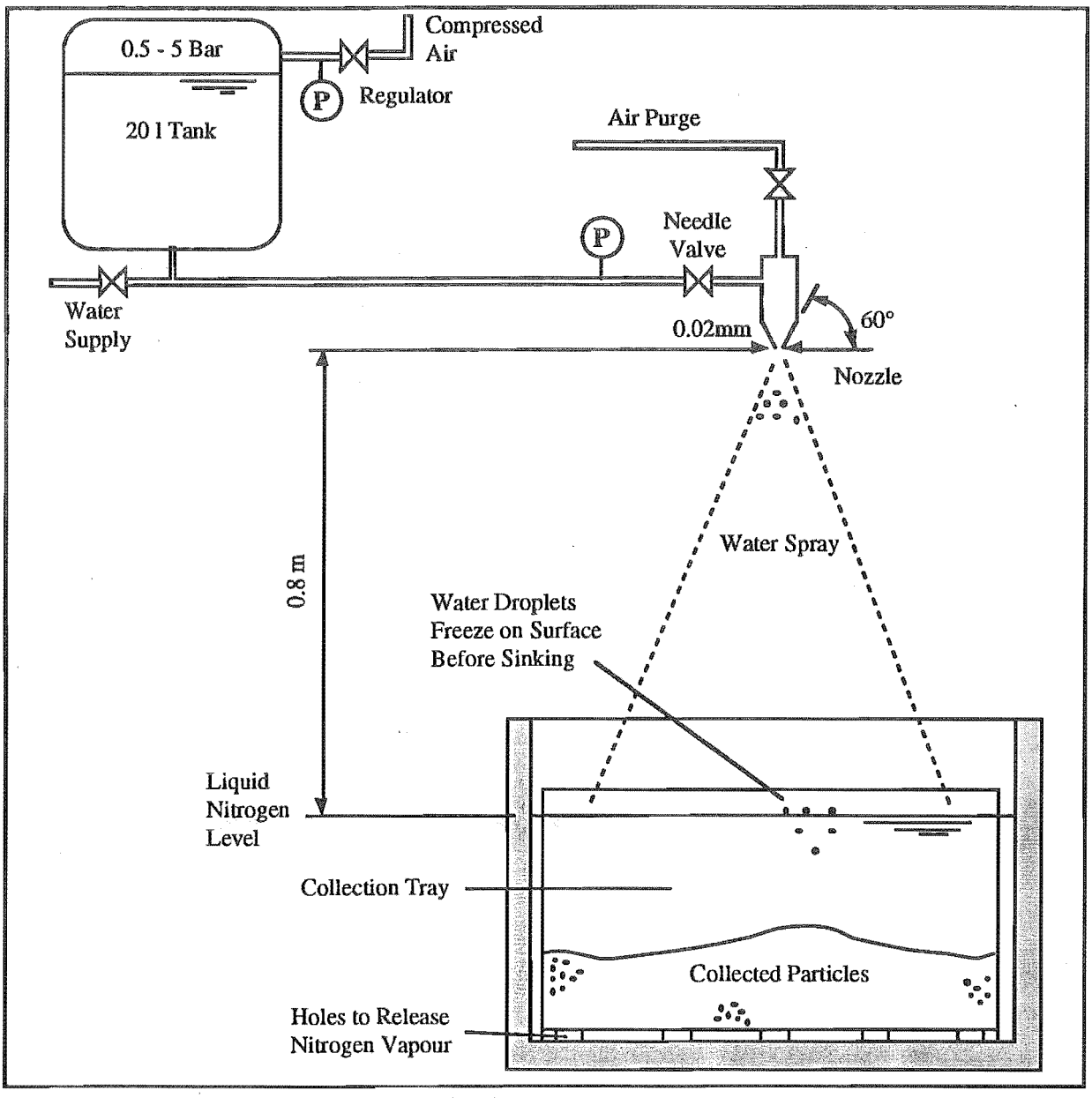

Figure V.1. Schematic of the Snow Making Apparatus.

The liquid nitrogen is held in a deep stainless steel tray measuring 400x400x400 mm internally and insulated with 50 mm of polystyrene foam on the walls and 100 mm on the bottom. Inside the liquid nitrogen tray sits a collection tray which serves two purposes:

1. The collected sample can be removed and the liquid nitrogen recycled. A wire mesh screen on the bottom of the collection tray allows the liquid nitrogen to drain out of the collected sample.
2. A 20 mm gap around the perimeter and underneath the collection tray minimises the fusing of freezing water droplets on the liquid nitrogen surface. Without the collection tray convection currents due to heat exchange through the walls of the liquid nitrogen tray rapidly push the surface droplets to the centre of the tray. This is illustrated in figure

V.2. Note that the liquid nitrogen level must be below the top of the collection tray for this to be effective.

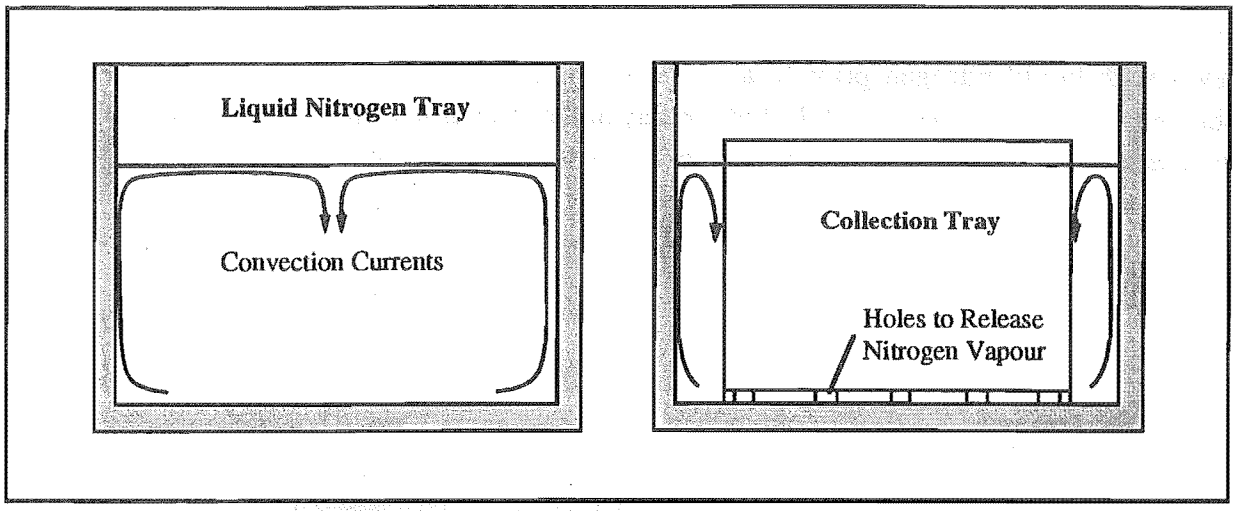

Figure V.2. Convection Currents in the Liquid Nitrogen Tray With and Without the Collection Tray.

V.2. Artificial Snow Properties

The snow making variables for the two runs in Chapter 6 in which laboratory snow is used are given below in table V.1 along with the resulting loaded sample densities and permeabilities. Sommerfeld and Freeman's (1988) snow density is very high compared to that of natural snow. The nozzle and snow making parameters used reflect the desire to have larger ice grains and lower density packed samples compared to Sommerfeld and Freeman.

	Run 2	Run 3
Flowrate (l/min[2])	0.0290	0.029
Tank Pressure (bar)	0.6	0.6
Nozzle Height (m)	0.8	0.8
Top Cut (μm) - discarded	710	710
Packed Sample Density (kg/m^3)	533	502
Packed Sample Permeability (m^2/Pas)	8.0×10^{-6}	8.8×10^{-6}

Table V.1. Snow Making Parameters Used for Runs 2 and 3 (Chapter 6) and Resulting Densities and Permeabilities of the Packed Samples.

V.2.1. Laboratory Snow Sample Size Distribution

The method developed for sieving a snow sample for determination of the sample size distribution at an ambient temperature of 15°C is illustrated in figure V.3.

---

[2]At this flowrate it takes approximately 8 hours to make sufficient snow to fill all five sample tubes.

At less than about -40°C the artificial snow behaves like a free flowing granular material for a reasonable period, long enough to sieve and pack the sample tubes. Above this it begins to agglomerate and become difficult to handle. Therefore a sample size distribution may be obtained if the snow is kept below -40°C. This is achieved by cooling a stack of standard sieves with liquid nitrogen prior to addition of the sample to the top (largest) sieve and vibrating. To keep the stack cool the bottom tray of the stack is half filled with liquid nitrogen. The stack is reasonably well sealed between sieves so the very cold evaporating nitrogen vapour passes up the stack and out the top.

The sieve stack is made up from a standard set of square mesh sieves (710, 500, 355, 250, 180, 125, 90, 63 and 45 μm). The sample is saturated with liquid nitrogen when added and sieving begun when the nitrogen has just finished boiling off. The sieve stack is secured to the bed of a Fritsch 03 502 vibrating bed set at full power and sieved for 10 minutes. The sieves are then separated and the contents of each cut weighed. Figure V.4 shows the results of two trials sampled for *run 2* (Chapter 6). Note that the top cut (710 μm) includes agglomerates of fused ice grains and is hence discarded.

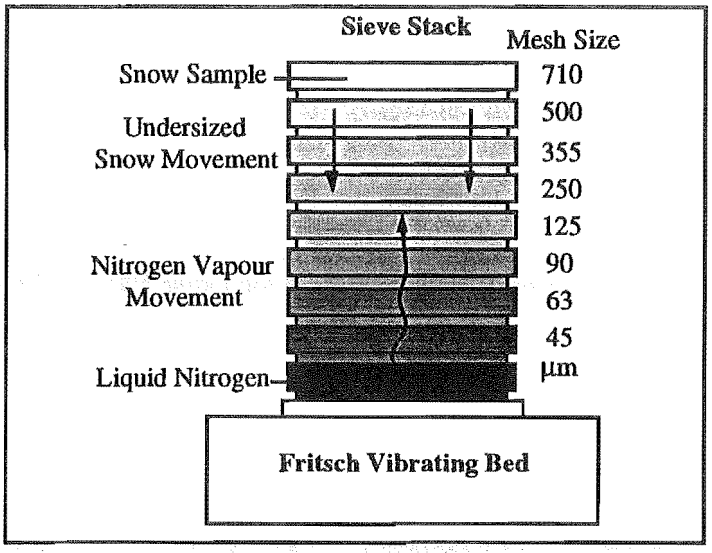

Figure V.3. Illustration of the Sample Size Distribution Sieving Method.

Figure V.4. Sample Size Distribution Results of Two Trials Sampled From the Laboratory Snow of Run 2 (Chapter 6).

Appendix VI
Hardness Test Rig

Ram penetration using a *Ramsonde* has long been used in conjunction with *in situ* standard snow profile observations (see Perla and Martinelli, 1976). The Ramsonde gives a full snow pack depth hardness profile from the snow surface (no pit is required) by successive hammering and penetration depth measurement of a cone on the end of a long rod. Whilst quick and easy to use the hardness is a function of the complex mechanism of penetration and difficulties are expected when attempts are made to relate the hardness to intrinsic snow properties (Perla, 1969). Perla (1969) reviews and assesses a drop cone penetrometer which uses the volume of indentation and drop height of the cone to measure hardness. It was thought that this would also have the same problems when comparing hardness to intrinsic snow properties. Adams and Brown (1982) used an Instron testing machine with a conical probe to measure laboratory snow strength profiles. They found the method gave a good indication of the relative strength of different layers. More recently, Dowd and Brown (1986) have developed a digital cone penetration resistograph for obtaining profiles of snow cover strength. This instrument measures the same information as the Ramsonde.

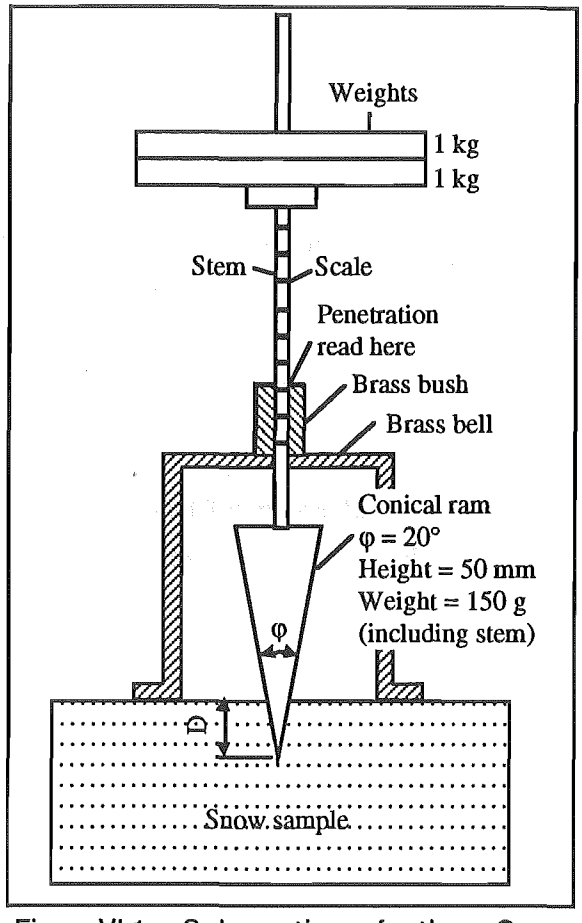

Figure VI.1. Schematic of the Cone Penetrometer.

A hardness test rig is developed for the wind pumping experiments in Chapter 6 along similar lines to Knight and Johnson's (1988) cone penetrometer. A schematic of the resulting *cone*

penetrometer[3] is shown in figure VI.1. Plate VI.1 shows the components of the ram penetrometer test rig and the test rig in use. Such cone penetration techniques are known in both soil mechanics and materials science although are not exploited in powder mechanics (Knight and Johnson, 1988).

In an investigation using their instrument Knight and Johnson find that reasonable correlation exists between cone penetrometer and shear cell data in determination of the unconfined compressive strength f_c, a strong vindication of this as a strength testing technique. No attempt is made to determine the absolute value of f_c but the following relation should be noted.

$$f_c \propto \frac{F}{D^2} \qquad \text{VI.1}$$

where F is the force applied and D is the cone penetration depth.

The key reason for the use of the cone penetrometer in this experimental study is that many more tests can be made on the same sample volume (compared to tensile and shear tests) provided the philosophy of partial cone penetration adopted by Knight and Johnson is used (rather than full insertion of the cone as used in soil mechanics and snow pack tests). It is also a very simple test to perform.

It is felt that the advantage of this (placed) cone penetrometer over Perla's (1969) drop cone penetrometer lies in the fact that the dropped cone must come to rest against a relatively strong portion of the sample (to halt its momentum), while the placed cone may come to rest against a weaker zone. In effect the drop cone is measuring the plastic energy dissipation, while the place cone measures the static force balance.

Test Procedure

It is the aim of this procedure to measure the static force balance. Therefore the cone must be place gently into the sample until it finds its equilibrium position. This normally takes about 2 s if shock loading is to be avoided.

Once the cone comes to rest in the sample the penetration depth (strain) D is read off the instrument. It was noted that a continued static load continues to deform the sample at a visible strain rate. Therefore, to minimise the viscoelastic component to D, the reading must be made as quickly as possible.

---

[3]The instrument developed for use in this work is referred to as a cone penetrometer, implying partial penetration of the cone, rather that a ram penetrometer. This will also avoid confusion with the Ramsonde used for in situ snow pack studies.

(a)

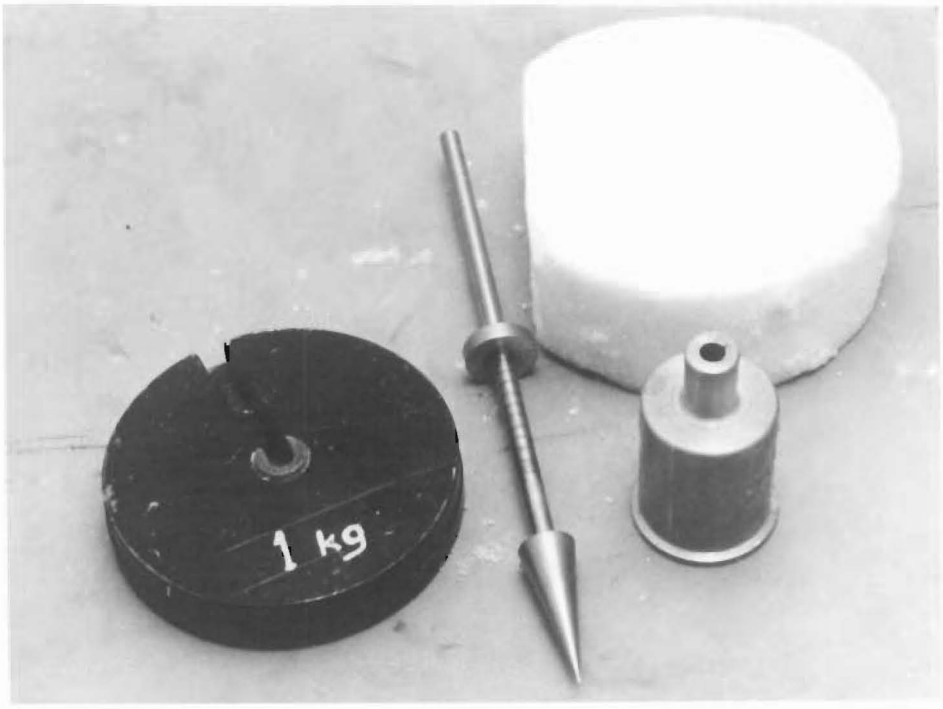

(b)

Plate VI.1. Cone Penetrometer: (a) Components of the Cone Penetrometer. (b) The Cone Penetrometer in Use.

Appendix VII
Tensile Test Rig

A tensile test rig similar to those used by Watanabe (1980) and Narita (1980) in scale and concept is developed for use in the wind pumping experiments (Chapter 6). It comprises of a rigid frame which applies a uniaxial tensile load to the shaped test sample frozen between two plates. A scale drawing of the rig developed is shown in figure VII.1. Plate VII.1 shows the test rig, a test sample and the rig in use.

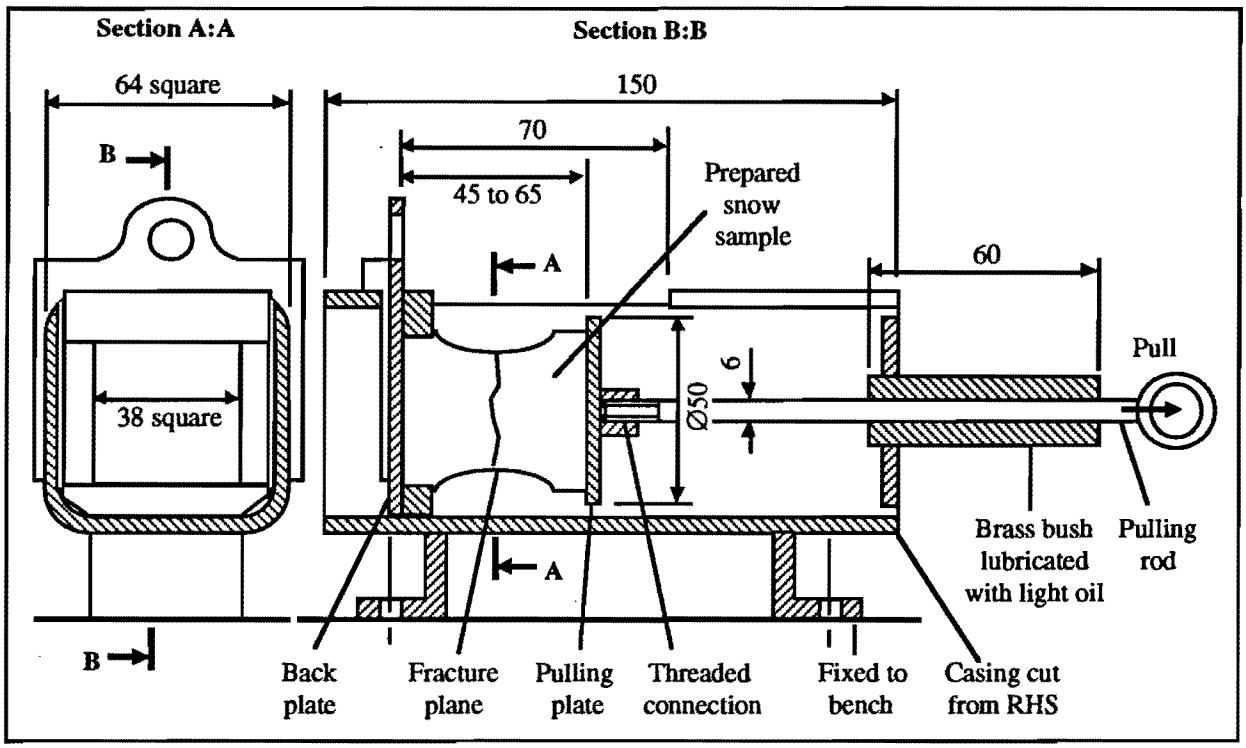

Figure VII.1. Drawing of the Tensile Test Rig. Scale 1:2. Dimensions in mm.

Watanabe (1980), Narita (1980) and Conway and Abrahamson (1984b) all freeze plates to the test samples to enable the load to be put on the snow. As with Narita the plates used here are not smooth, rather they are grooved to increase the sample plate contact area. Like Watanabe and Conway and Abrahamson (1984a). The diameter in the middle of the test samples is reduced with a large concave radius to eliminate localised stress concentrations, and failure at the test rig connections. This is illustrated in plate VII.1.

The load can be applied in two ways:

* Maximum recording pull spring balance.
* Lead shot addition to a bucket using the string and pulley arrangement illustrated in figure VIII.1.

Note that the load is applied so that a large enough strain rate results and brittle failure rather than ductile failure occurs (see for example Gubler, 1978, Narita, 1980 or de Montmollin, 1982).

Notes on the Test Sample Size

Test piece failure depends on the failure of its weakest link which the propagates through the remainder of the sample (see for example Sommerfeld, 1974). Consequently researchers have found that larger sample fracture planes give lower average strength results (see for example Perla, 1977, in shear tests).

This problem of spatial variability or the existence of *super weak zones* in the snow pack and their importance in slab avalanche formation is receiving increasing attention since their first measurement by Conway and Abrahamson (1984a) (see for example Conway and Abrahamson, 1988, and Föhn, 1988).

Test Procedure

1. The 40x40x60 mm test sample is cut from the assigned portion of the snow sample (see section 6.7.3).
2. One (40x40 mm) end of the test sample is pushed into the warmed (above 0°C) back plate and the joint allowed to freeze for around 1 minutes.
3. The sample and back plate are then slid into the casing groove and the warmed pulling plate (attacked to the pulling rod) pushed against the other (40x40 mm) end of the test sample[4] until it too freezes (around 1 minute).
4. The pulling rod is unscrewed from the pulling plate and the test sample and plates (now frozen together) removed and allowed to set firmly against the plates (about 15 minutes).
5. After this time the test sample is chamfered into the required tensile test piece shape.
6. Finally the sample (and plates) are reloaded into the test rig, the pulling rod screwed back into the pulling plate and the test sample loaded to failure.

---

[4]As the brass bush and the pulling rod have been set well in line this method minimises the bending stresses imposed on the sample during the test. If the prepared snow sample does not have perfectly flat or square ends the melting action (as the warmed plate is pressed onto the test piece) corrects this to align the sample.

(a)

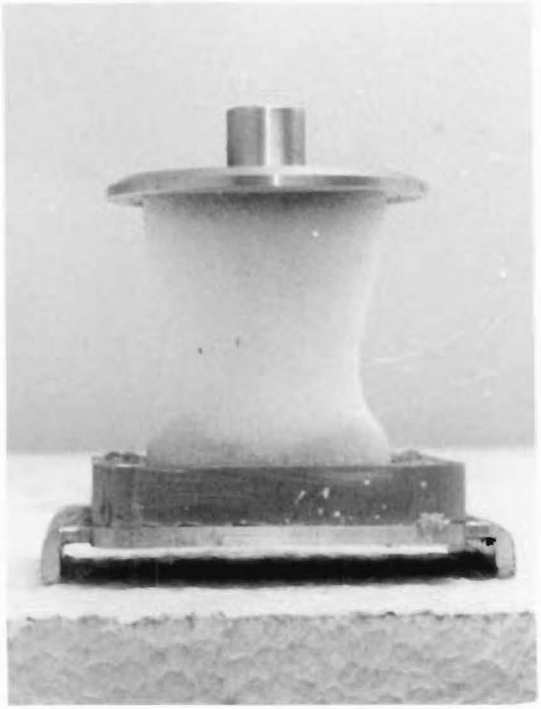

(b)

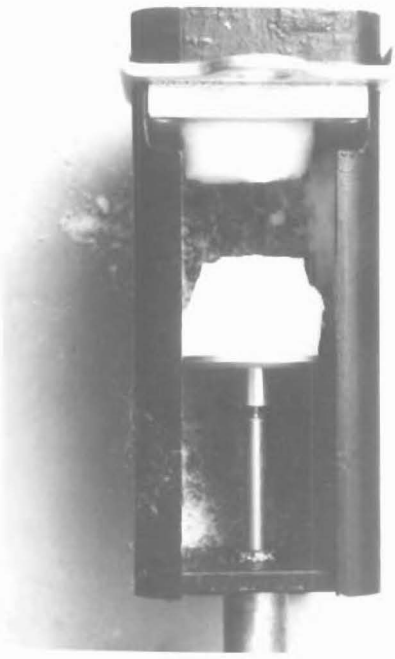

(c)

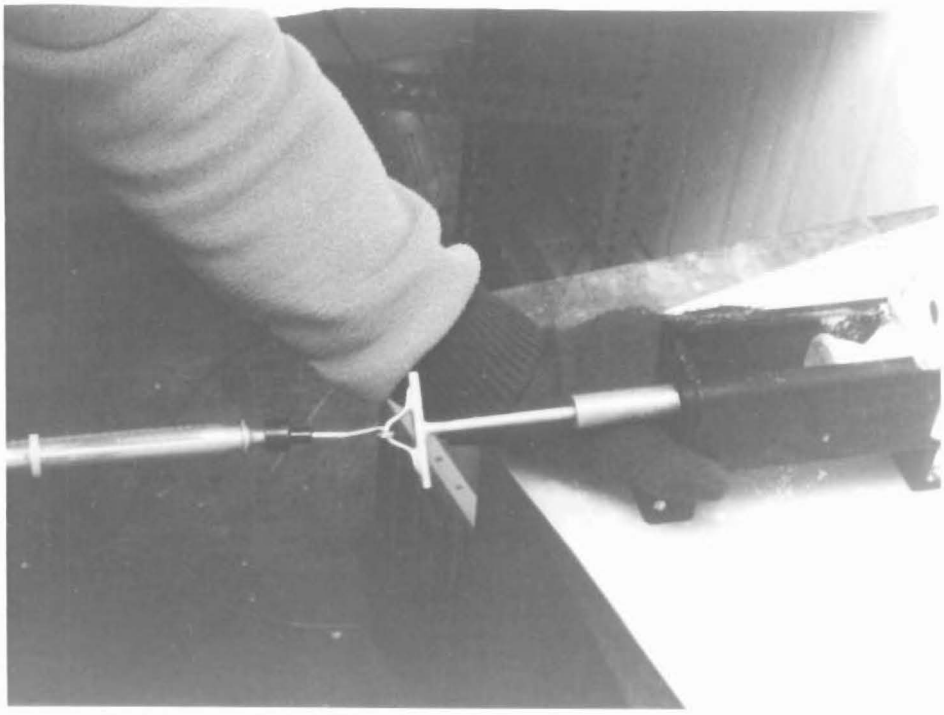

Plate VII.1. Tensile Test Rig: (a) Test Sample. (b) Test Rig. (c) Test Rig in Use.

Appendix VIII
Shear Test Rig

A shear test device is developed for use in the wind pumping experiments (Chapter 6). It comprises of a rigid lower block, which holds the test sample in place, and an upper shear block, which fits tightly over the top half of the test sample and rests against the lower block. The shearing load is applied by pulling the bottom of the upper shear block in the plane of the interface between the upper and lower blocks. A scale drawing of the rig developed is shown in figure VIII.1.

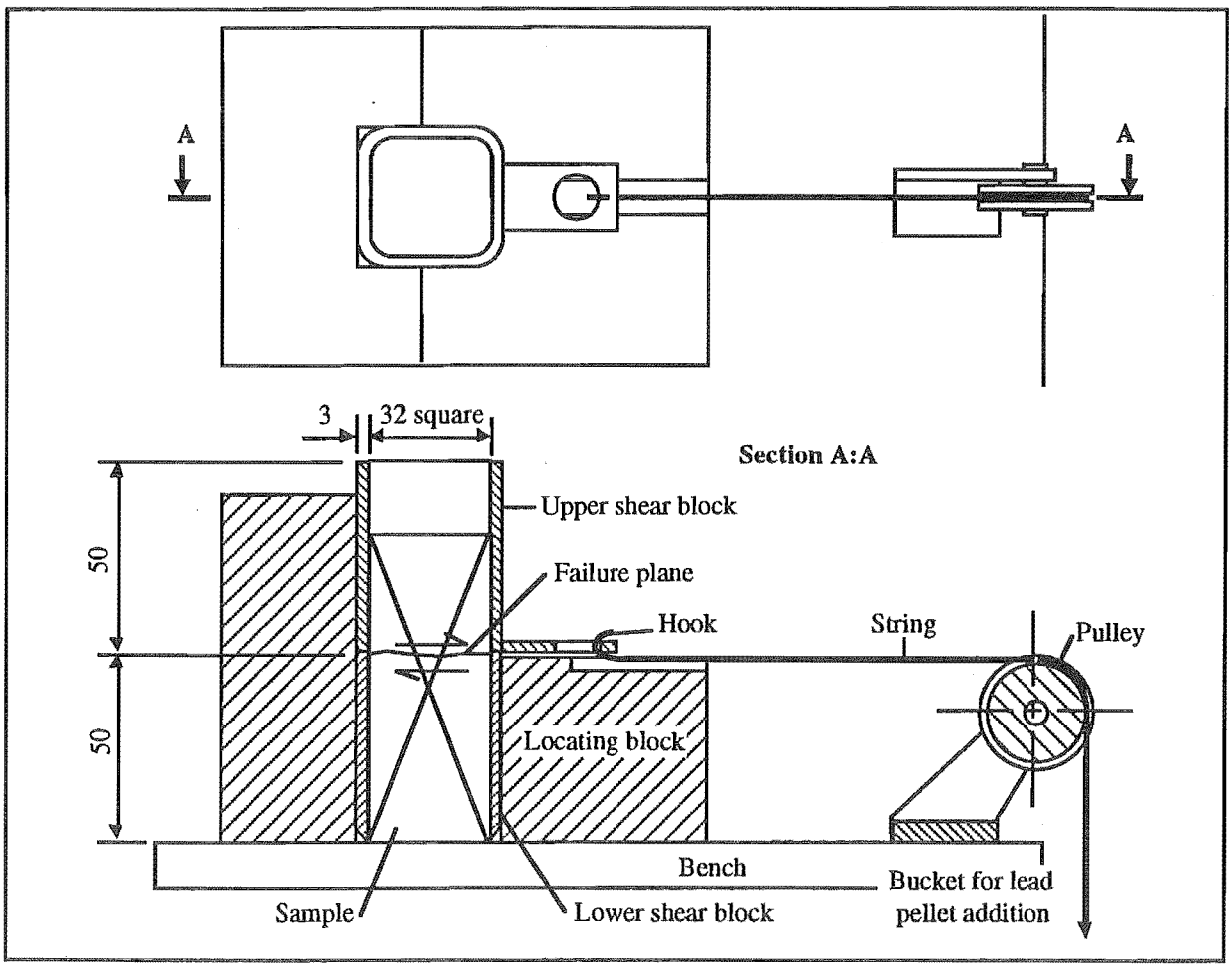

Figure VIII.1. Drawing of the Shear Test Rig. Scale 1:2, Dimensions in mm.

Whilst shear strengths are commonly measured in snow for slope stability analysis, they are usually made on planes of weakness or *weak layers*. Similarly the tensile strength of the

overlying cohesive slab are usually considered over that of the weak layer (see for example Conway and Abrahamson, 1984a). Consequently the measured shear strength is generally lower (up to an order of magnitude) than the tensile strength. The situation here is different in that there is no *weak layer* as such and the shear strength measurement is made in the cohesive snow (in the *slab* in conjunction with the discussion above).

The result of this is much higher shear strengths (about equal to the tensile strength) and a shear plane area much smaller than those in snow slope stability studies (about the same as tensile test failure plane area). The same notes on the test sample size applies for the shear test samples as for the tensile test samples (see Appendix VII).

The maximum indicating pull balance cannot be used to load the sample as in the tensile test due to the importance of the direction of pull. Instead the load is applied in a controlled direction by adding lead shot to a bucket using the string and pulley arrangement illustrated in figure VIII.1. Note that the load is applied so that a large enough strain rate results and brittle failure rather than ductile failure occurs (see for example Gubler, 1978, Narita, 1980 or de Montmollin, 1982).

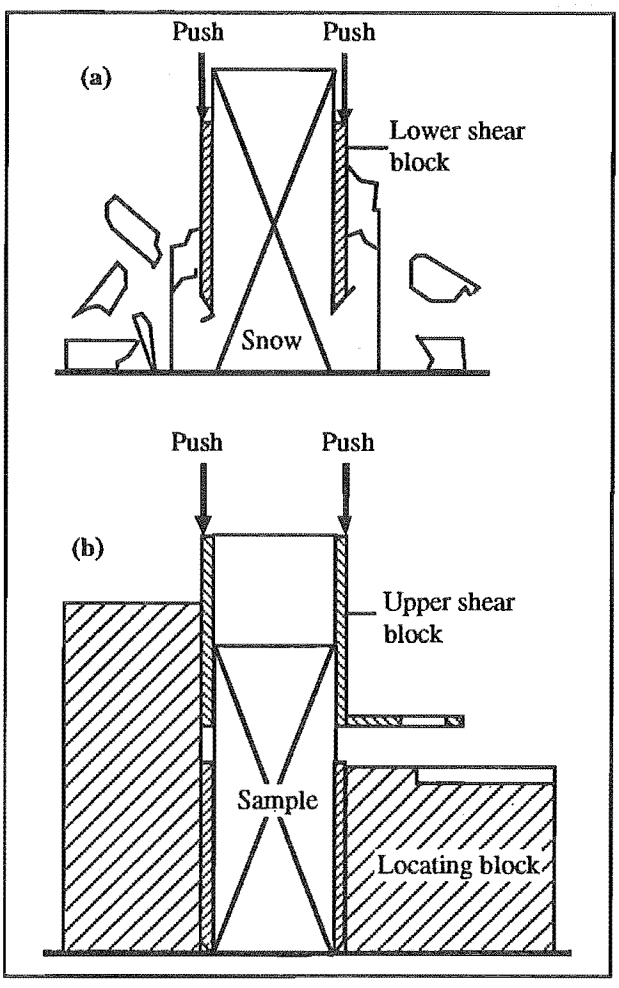

Figure VIII.2. Schematic of a Shear Sample Preparation: (a) Cutting the Shear Sample. (b) Fitting the Upper Shear Block.

Test Procedure

1. A 40x40x80 mm block is cut from the assigned portion of the snow sample (see section 6.7.3).
2. The exact size of the test sample is cut from this block as illustrated in figure VIII.2 (a).
3. The test sample and lower block are inserted into the locating block and the upper shear block fitted over the sample as illustrated in figure VIII.2 (b).
4. The bucket and string are attached to the upper shear block and shear force applied by loading the bucked with lead shot.

Appendix IX
Packed Bed Numerical Results

A comprehensive array of numerical experiments for the *infinite*, *finite-sealed* and *finite-free* lower boundary condition theories detailed in Chapter 4 are presented in this appendix.

It is shown in section 4.9.1.3 that the amplitude as a variable can be removed and results presented in reduced terms. For example, the pressure swing at depth z in the snow pack is reduced by the surface amplitude, so at the surface the reduced pressure swing is 1 Pa/Pa. Similarly the peak velocity and cyclic displacement at depth z are reduced to give units mm/sPa and mm/Pa respectively. All results are presented as functions of dimensionless depth z/d, where z is the distance from the surface, and d is the total snow pack depth.

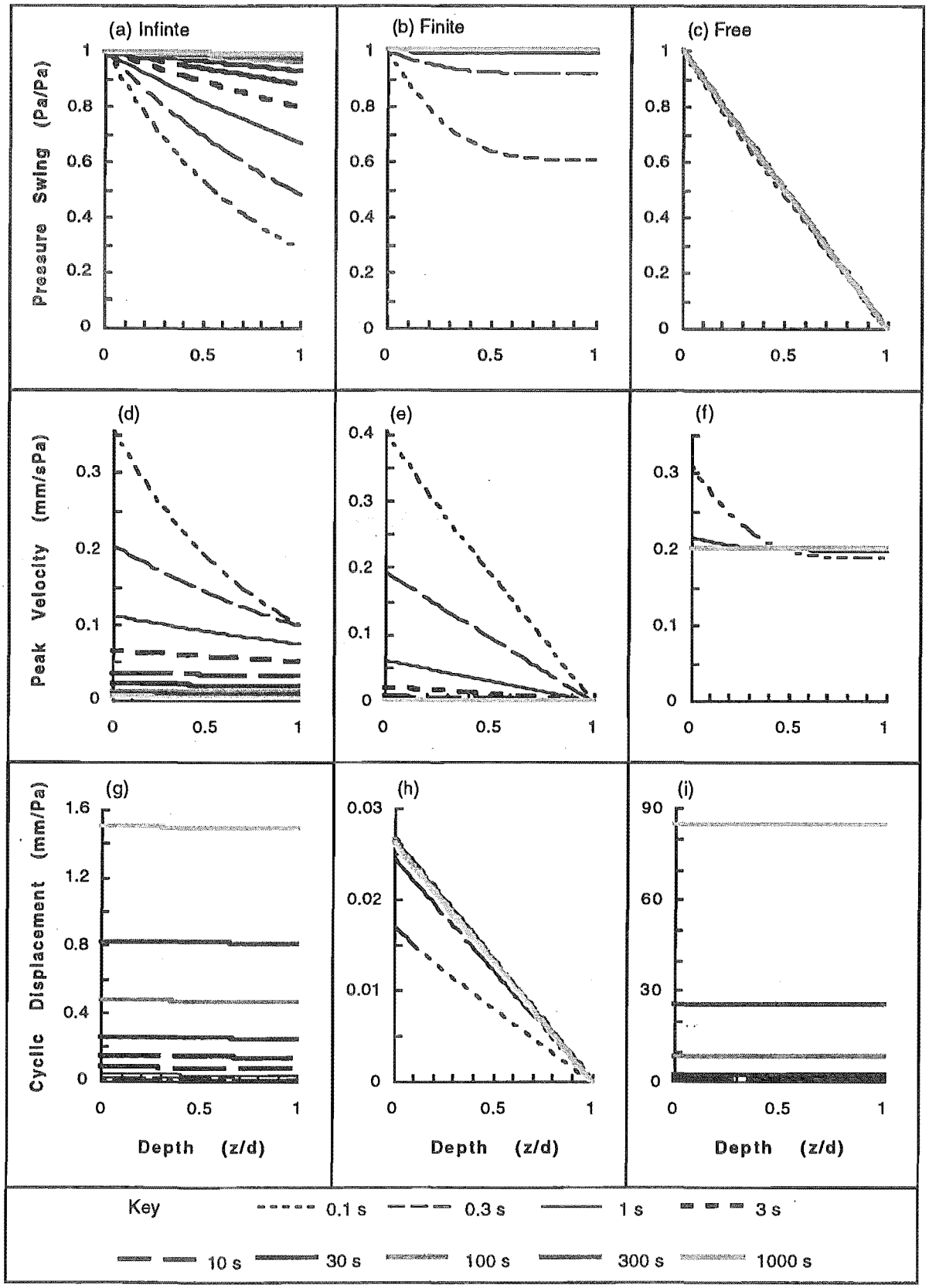

Figure IX.1. Depth Profiles of Pressure Swing, Peak Velocity and Cyclic Displacement (all reduced by the surface pressure swing) for Varying Period using *All Three Theories*. Total snow pack depth, permeability and voidage are $d = 1$ m, $K = 2 \times 10^{-4}$ m^2/Pas and $\varepsilon = 0.75$ respectively. The mean atmospheric pressure is $\overline{P} = 100{,}000$ Pa.

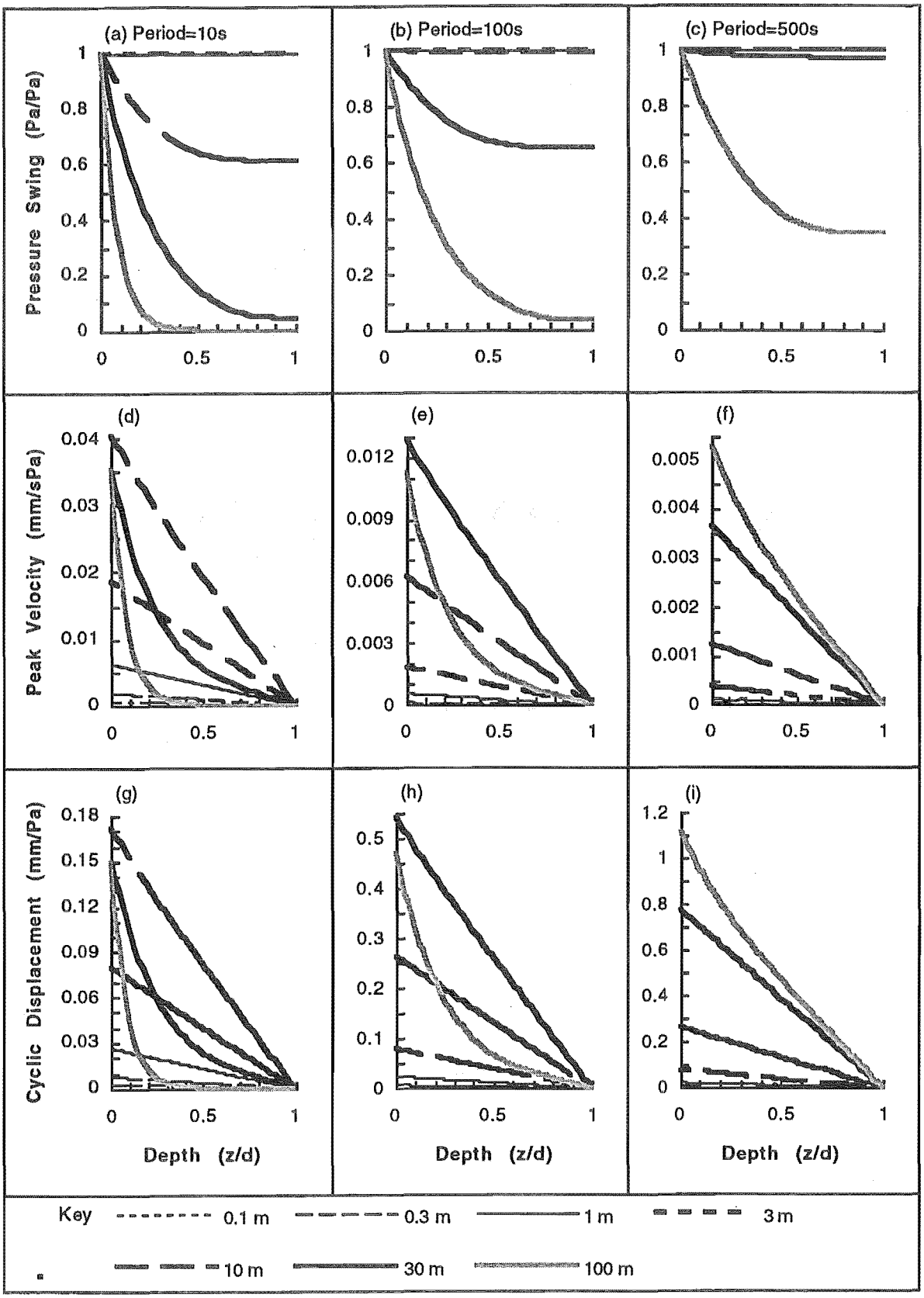

Figure IX.2. Depth Profiles of Pressure Swing, Peak Velocity and Cyclic Displacement (all reduced by the surface pressure swing) for Varying Total Snow Pack Depth and Period using the *Finite-Sealed Theory*. Snow pack permeability and voidage are $K = 2 \times 10^{-4}$ m^2/Pas and $\varepsilon = 0.75$ respectively and mean atmospheric pressure is $\overline{P} = 100{,}000$ Pa.

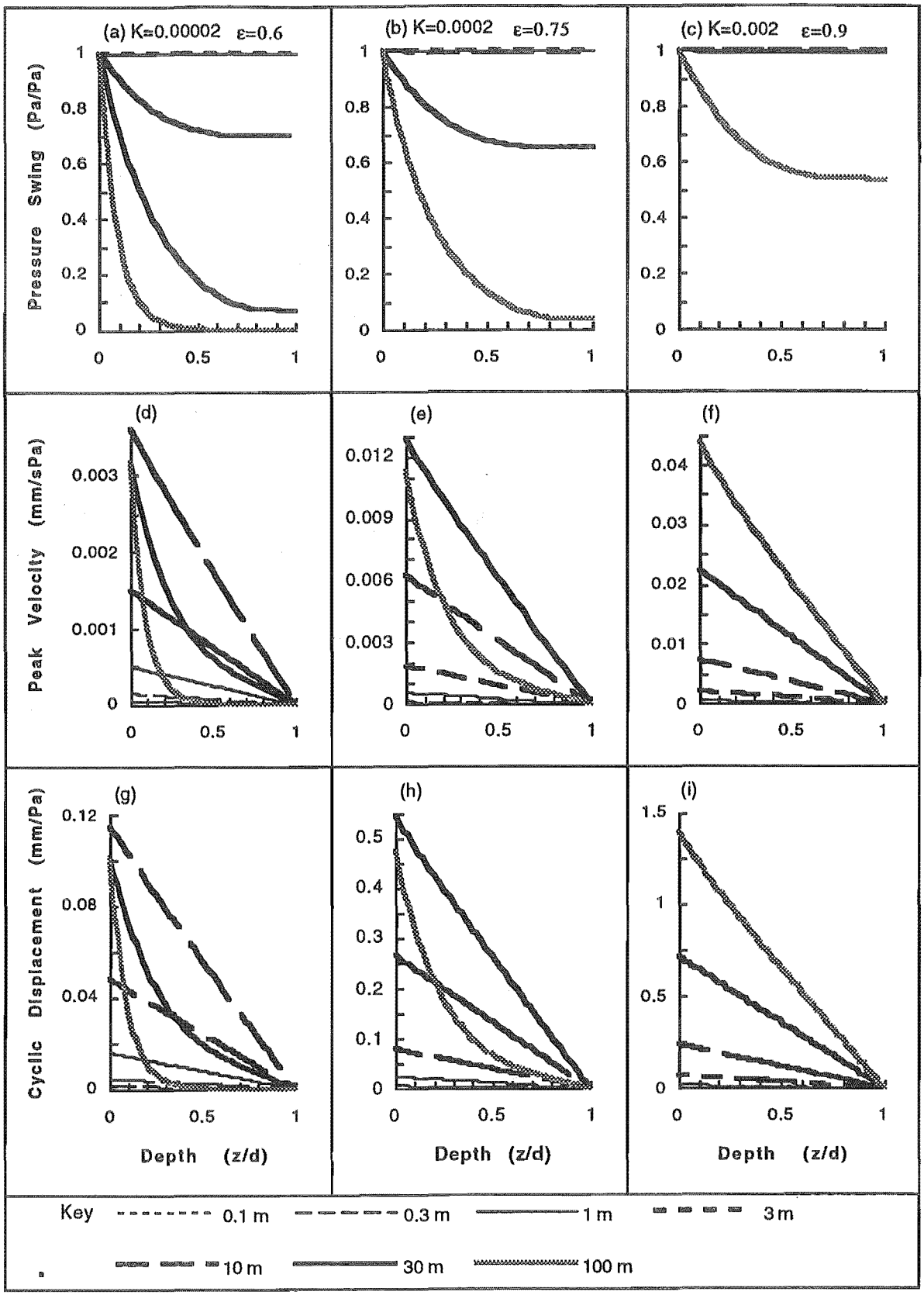

Figure IX.3. Depth Profiles of Pressure Swing, Peak Velocity and Cyclic Displacement (all reduced by the surface pressure swing) for Varying Total Snow Pack Depth, Permeability and Voidage using the *Finite-Sealed Bed Theory*. A period of $\tau = 100$ s and mean atmospheric pressure of $\overline{P} = 100{,}000$ Pa is used.

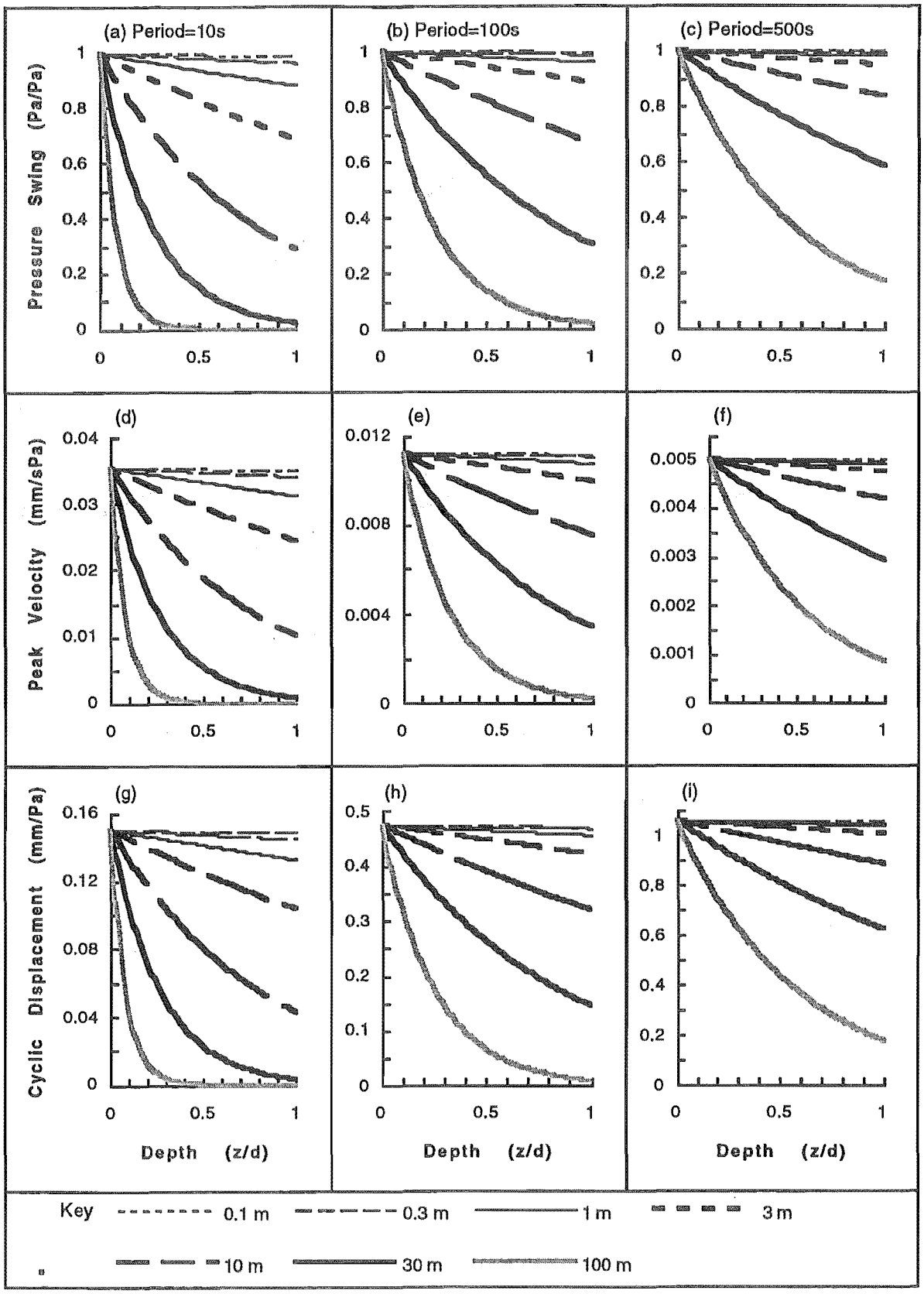

Figure IX.4. Depth Profiles of Pressure Swing, Peak Velocity and Cyclic Displacement (all reduced by the surface pressure swing) for Varying Total Snow Pack Depth and Period using the *Infinite Bed Theory*. The snow pack permeability and voidage are $K = 2 \times 10^{-4}$ m^2/Pas and $\varepsilon = 0.75$ respectively. The mean atmospheric pressure is $\overline{P} = 100{,}000$ Pa.

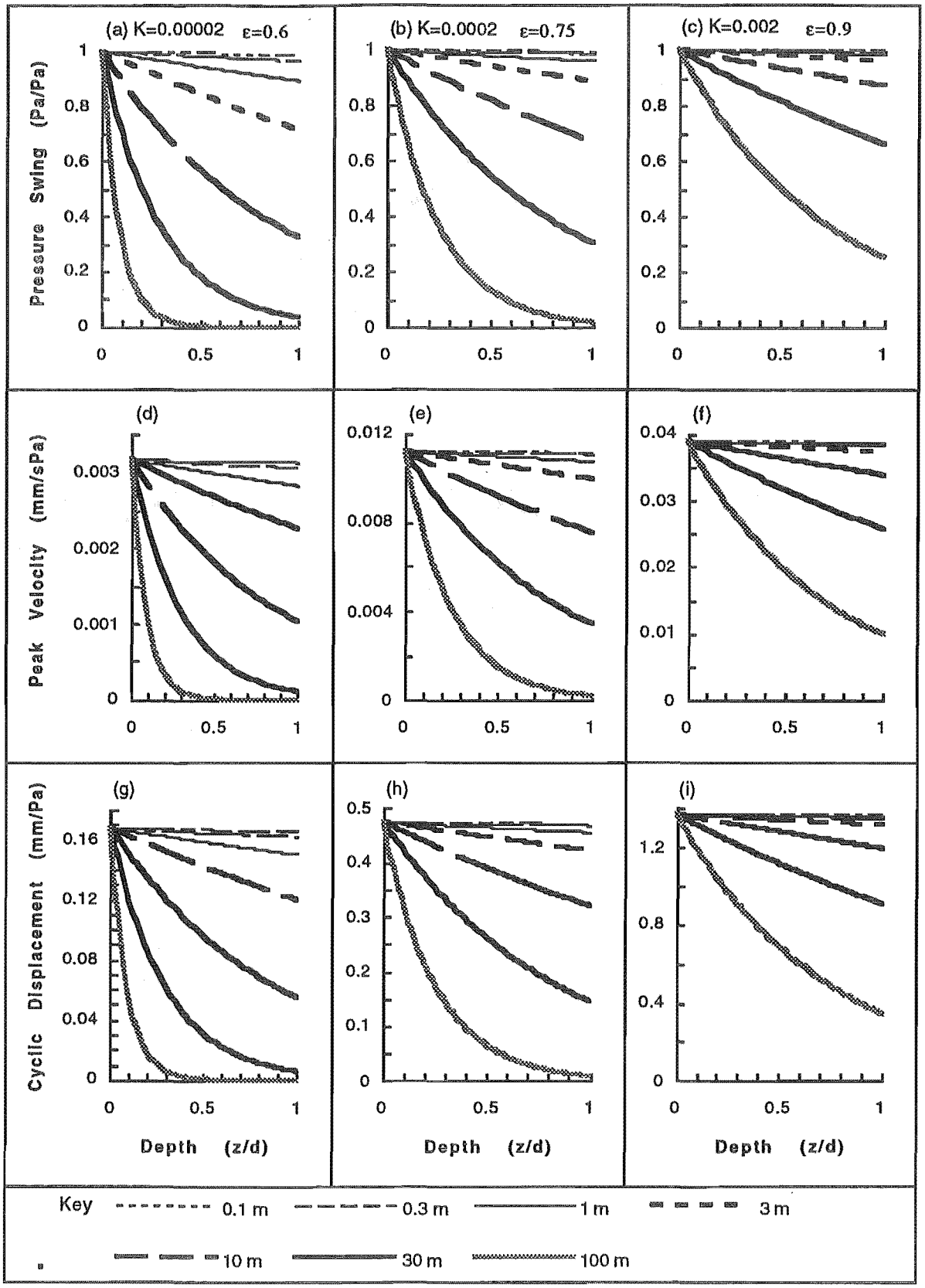

Figure IX.5. Depth Profiles of Pressure Swing, Peak Velocity and Cyclic Displacement (all reduced by the surface pressure swing) for Varying Total Snow Pack Depth, Permeability and Voidage using the *Infinite Bed Theory*. A period of τ = 100 s and mean atmospheric pressure of $\overline{P}$ = 100,000 Pa is used.

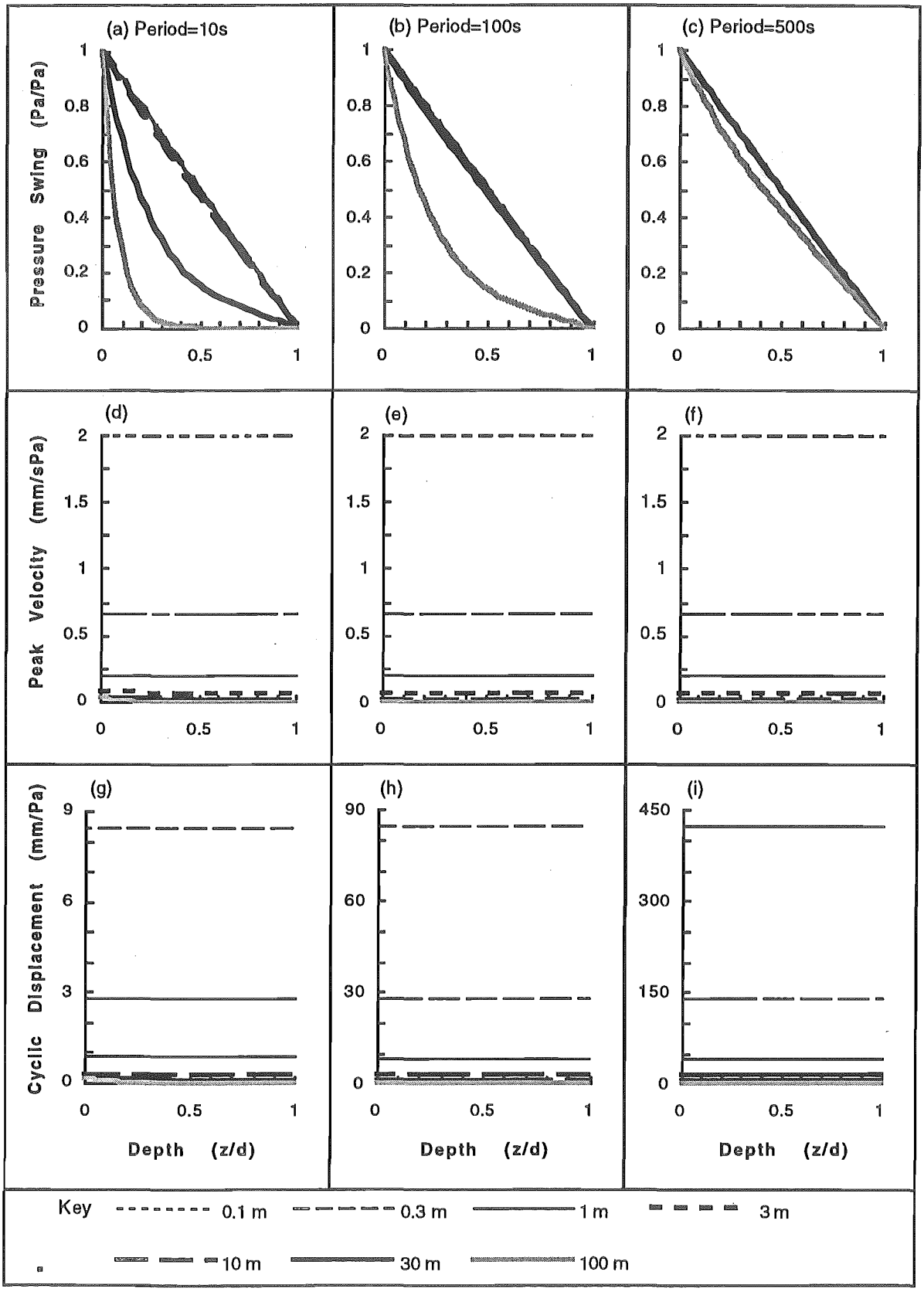

Figure IX.6. Depth Profiles of Pressure Swing, Peak Velocity and Cyclic Displacement (all reduced by the surface pressure swing) for Varying Total Snow Pack Depth and Period using the *Finite-Free Bed Theory*. Snow pack permeability and voidage are $K = 2 \times 10^{-4}$ m^2/Pas and $\varepsilon = 0.75$ respectively and mean atmospheric pressure is $\overline{P} = 100{,}000$ Pa.

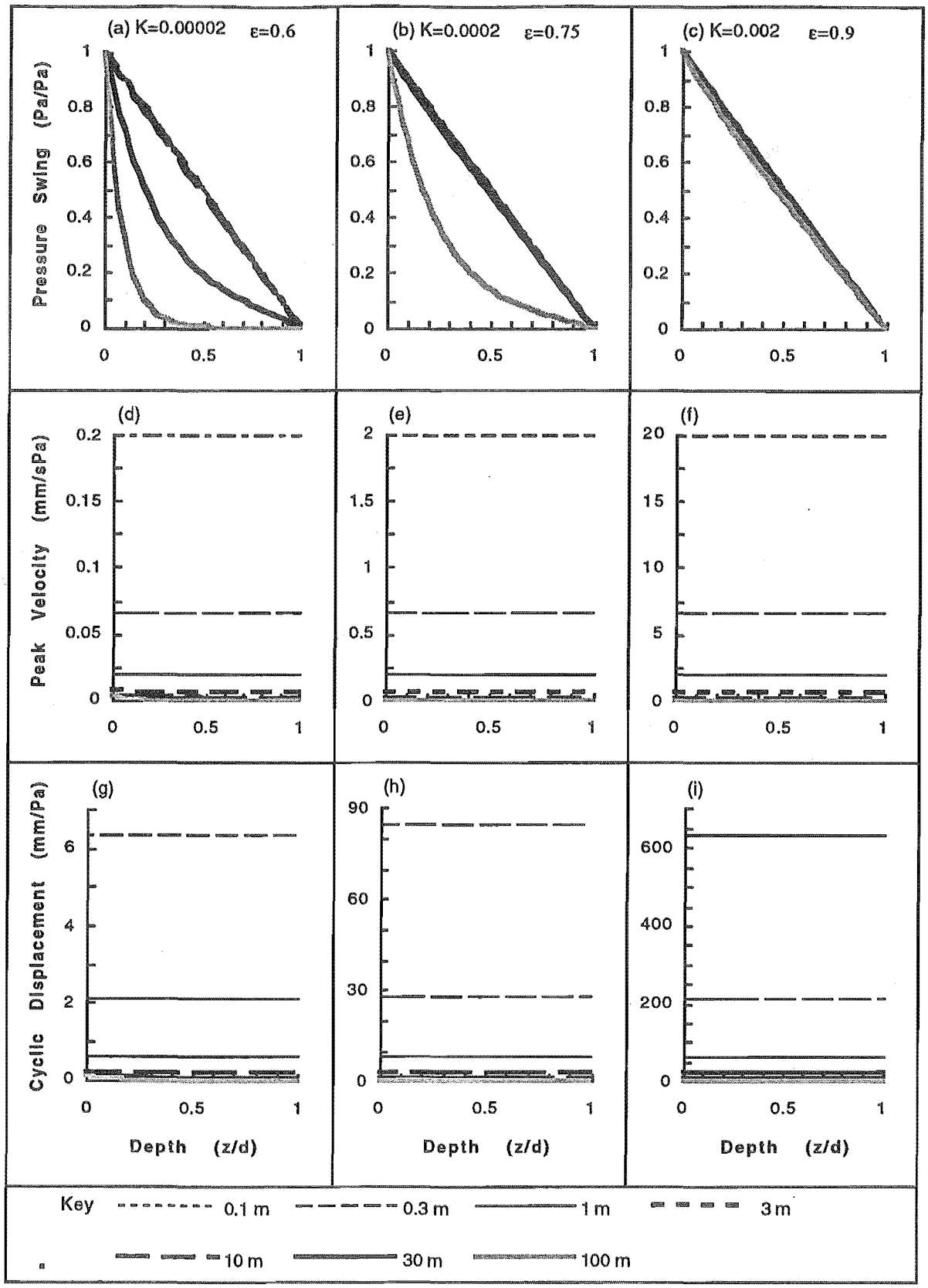

Figure IX.7. Depth Profiles of Pressure Swing, Peak Velocity and Cyclic Displacement (all reduced by the surface pressure swing) for Varying Total Snow Pack Depth, Permeability and Voidage using the *Infinite-Free Bed Theory*. A period of $\tau = 100$ s and mean atmospheric pressure of $\overline{P} = 100{,}000$ Pa is used.

Appendix X
Sample Apparatus Design Models

X.1. 3-Dimensional Steady State Design Model

Given the role of temperature gradients in snow metamorphism on both the macro and micro scales (Colbeck, 1987a) a three dimensional steady state conduction model has been developed to verify design decisions for the experiments in Chapter 6. Specifically the results of the model are aimed to give:

* Insulation thickness requirements around snow sample to give horizontal temperature gradients which are less than 1% of the vertical temperature gradients.
* The thickness of the top and bottom insulation to allow adequate control by plate heaters.
* Estimates of the top and bottom plate heater duties.

Relaxation techniques are used to solve the finite difference equations according to the algorithm in figure X.3. Such methods are well documented in heat transfer texts (see for example Janna, 1986).

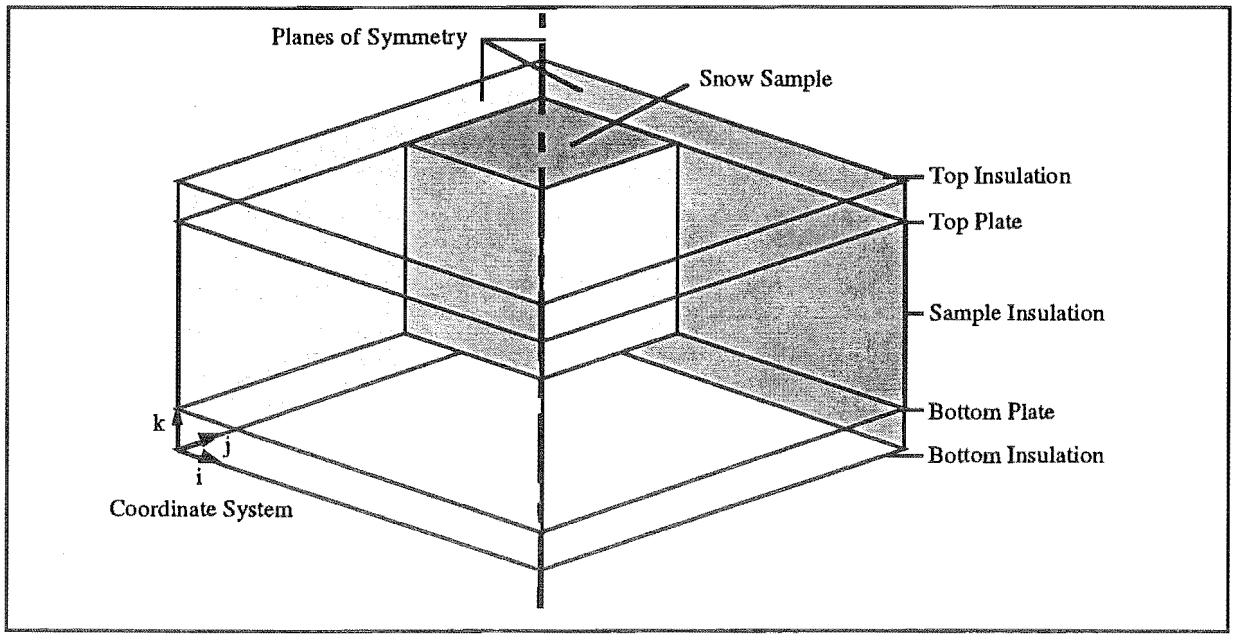

Figure X.1. Illustration of the 3-D Steady State Model Showing a Quarter of the Apparatus.

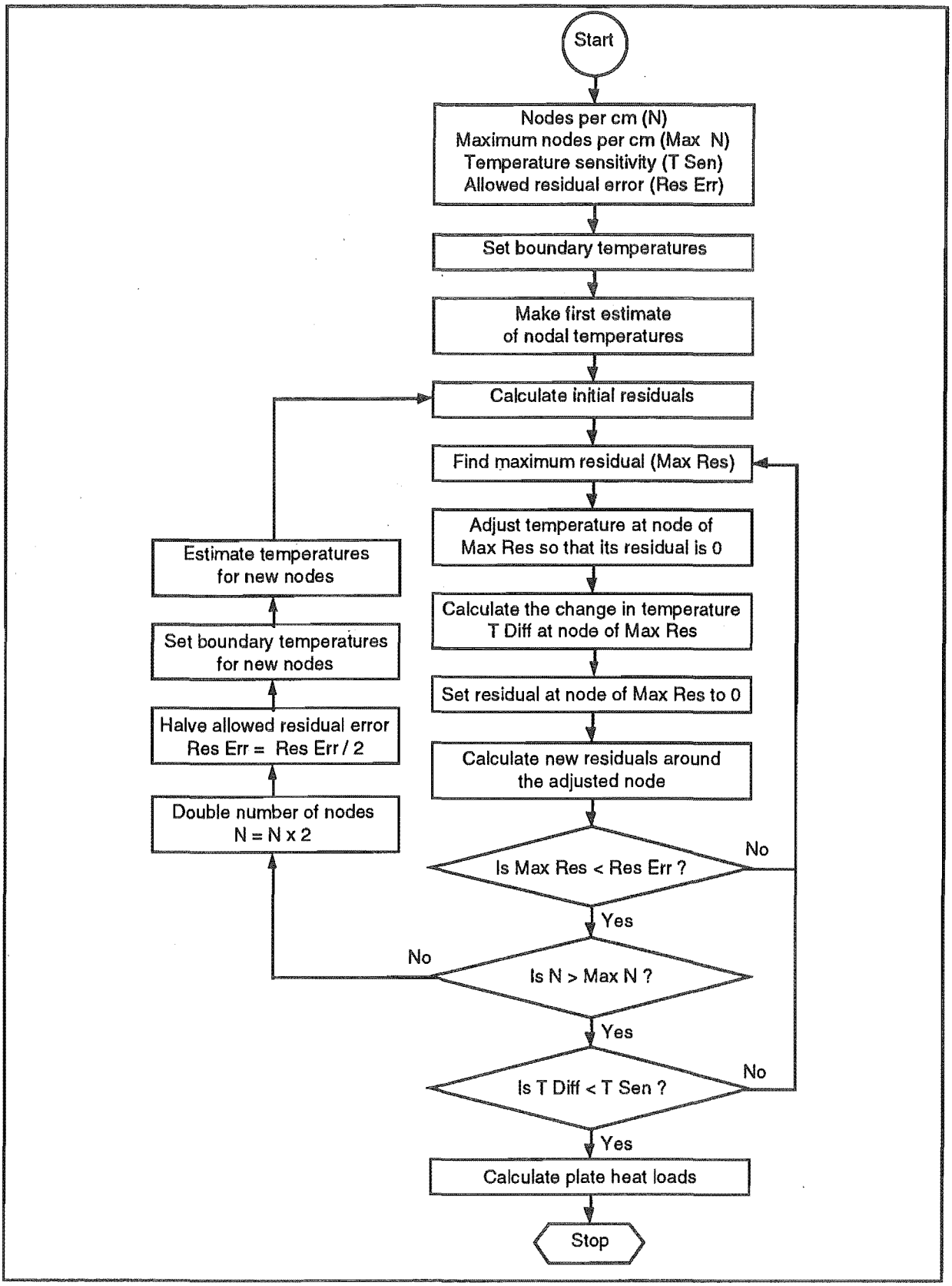

Figure X.2. Generalised Flow Diagram of the 3-D Steady State Model.

X.1.1. Model

The apparatus model illustrated in figure X.1 has four vertical planes of symmetry which are used to reduce the number of computations required. The unique one eighth portion of the apparatus is divided into nodes using the 3-D Cartesian coordinate system illustrated in figures X.1 and X.3.

X.1.2. Algorithm

After an initial guess is made at each nodal temperature relaxation techniques are used to progressively reduce all residuals to below an accepted limit (**Res Err**). To further increase computational efficiency a small initial number of nodes are used to improve the initial temperature guesses. Upon the reduction of the residuals below **Res Err** the intensity of nodes is doubled and the residuals again reduced to below **Res Err**.

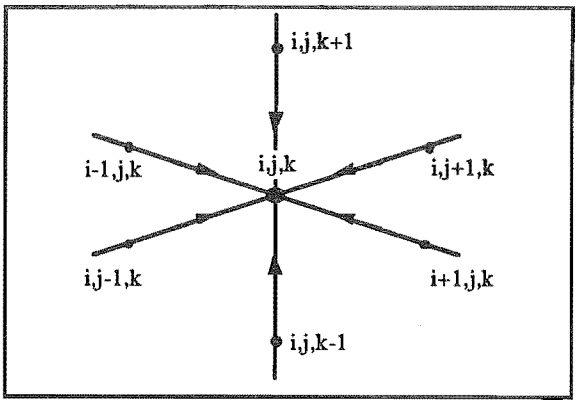

Figure X.3. Node Cartesian Coordinate System.

These steps are repeated until the model is divided up into the desired number of nodes. At this point, once all the residuals are reduced to below **Res Err**, the accuracy test is switched to temperature terms and the residual reduced further until the temperature difference (**T Diff**) at each nodal temperature adjustment is less than the desired limit (**T Sen**).

This algorithm, illustrated in figure X.2, is applied to the top (above the top plate), sample (between the plates) and bottom (below the bottom plate) sections individually.

Not shown in this algorithm is the iteration acceleration constant used to *overrelax* the residuals as another method to increase computational efficiency.

X.1.3. Equations

The temperature T at the node (i,j,k) due to the heat flow from surrounding nodes are calculated using the finite difference equation

$$T_{i,j,k} = \frac{(CT)_{i-1,j,k}+(CT)_{i+1,j,k}+(CT)_{i,j-1,k}+(CT)_{i,j+1,k}+(CT)_{i,j,k-1}+(CT)_{i,j,k+1}}{C_{i-1,j,k}+C_{i+1,j,k}+C_{i,j-1,k}+C_{i,j+1,k}+C_{i,j,k-1}+C_{i,j,k+1}} \qquad X.1$$

C is given by

$$C = \frac{k_{snow}}{l_n} \text{ or } \frac{k_{ins}}{l_n} \qquad \text{for a node within the snow or insulation} \qquad X.2$$

$$C = \frac{h_{air}}{l_n^2}$$ for a node on the apparatus surface X.3

$$C = \frac{k_{snow}+k_{ins}}{2l_n}$$ for a node on a snow / insulation interface X.4

where l_n is the distance between nodes, k_{snow} and k_{ins} are the thermal conductivities of the snow and the insulation respectively and h_{air} is the stagnant natural convection heat transfer coefficient of the laboratory air.

The residual R at the node (i,j,k) is given by

$$R_{i,j,k} = (CT)_{i-1,j,k}+(CT)_{i+1,j,k}+(CT)_{i,j-1,k}+(CT)_{i,j+1,k}+(CT)_{i,j,k-1}+(CT)_{i,j,k+1} - T_{i,j,k}[C_{i-1,j,k}+C_{i+1,j,k}+C_{i,j-1,k}+C_{i,j+1,k}+C_{i,j,k-1}+C_{i,j,k+1}]$$ X.5

X.1.4. Program

The algorithm is programmed in Vax-11 Fortran. The program listings are not included in this thesis.

X.1.5. Approximations, Assumptions and Limitations

The following approximations, assumptions and limitations are pertinent:

* Snow and insulation thermal conductivities and convective air heat transfer coefficient are all assumed constant throughout the model volume and with temperature.
* Stagnant vertical natural convection heat transfer coefficient (between the insulating foam and the cold laboratory air).
* Full sized top and bottom heating plates.
* Square sample column.
* Model dimensions which are factors of two for ease of node duplication.
* Memory limitations dictate a maximum sample depth and top, bottom and sample insulation thickness of 32 cm for 2 nodes/cm.

Unfortunately a simultaneous back up and hard disk failure caused the loss of the complied program. Considering the time estimated to debug the re-typed program and results gained by that point it was decided not to pursue this analysis any further. This eliminated the intended modifications to align the model to the chosen design (cylindrical sample tube and top and bottom plates which do not extend across the whole insulation area).

X.1.6. Numerical Results

Only one set of model results are presented here. They represent the closest physical parameters to those used in the experiment tested prior to loss of the executable program. The parameters in this example are as follows.

Model Variables

*	Sample depth	16 cm
*	Thickness of sample insulation	16 cm
*	Top and bottom insulation thickness	4 cm
*	Bottom plate temperature	-6.0°C
*	Top plate temperature	-1.0°C
*	Cold laboratory (ambient) temperature	-8.0°C
*	Insulation heat conductivity	0.04 W/mK
*	Snow heat conductivity[5]	0.4 W/mK
*	Convective heat transfer coefficient of air	30 W/m^2K

Numerical Variables

*	Initial number of nodes per centimeter	0.25 nodes/cm
*	Final number of nodes per centimeter	0.50 nodes/cm
*	Initial maximum residual (Res Err)	0.001 W
*	Final temperature sensitivity required	0.01°C
*	Iteration acceleration constant	1.3

X.1.6.1. Temperature Profiles

Temperature profile results are presented in two forms for one of the perpendicular axis of symmetry. Figure X.4 shows the form of the temperature distribution in the sample and blocks of insulating foam while figure X.5 presents the same results as a contour map for more accurate extraction of vertical temperature gradient information.

---

[5]The thermal conductivity of dry snow varies mainly according to density. The value used here of 0.4 W/mK (Akitaya, 1974) is for dense snow.

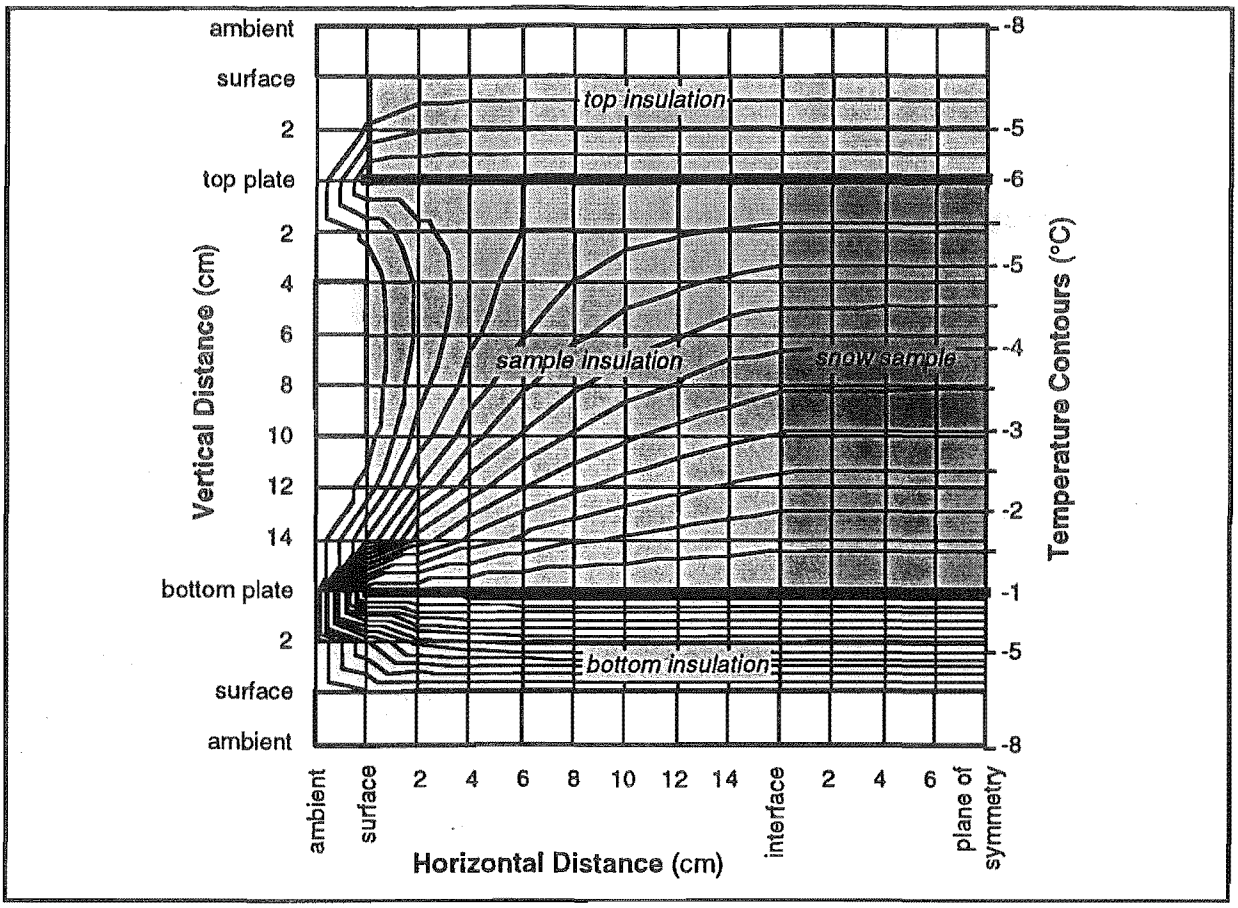

Figure X.4. Prediction of the Temperature Contours Within the Snow Sample and Insulation for a Slice Through One of the Perpendicular Planes of Symmetry in Figure X.1, using the 3-D Steady State Model.

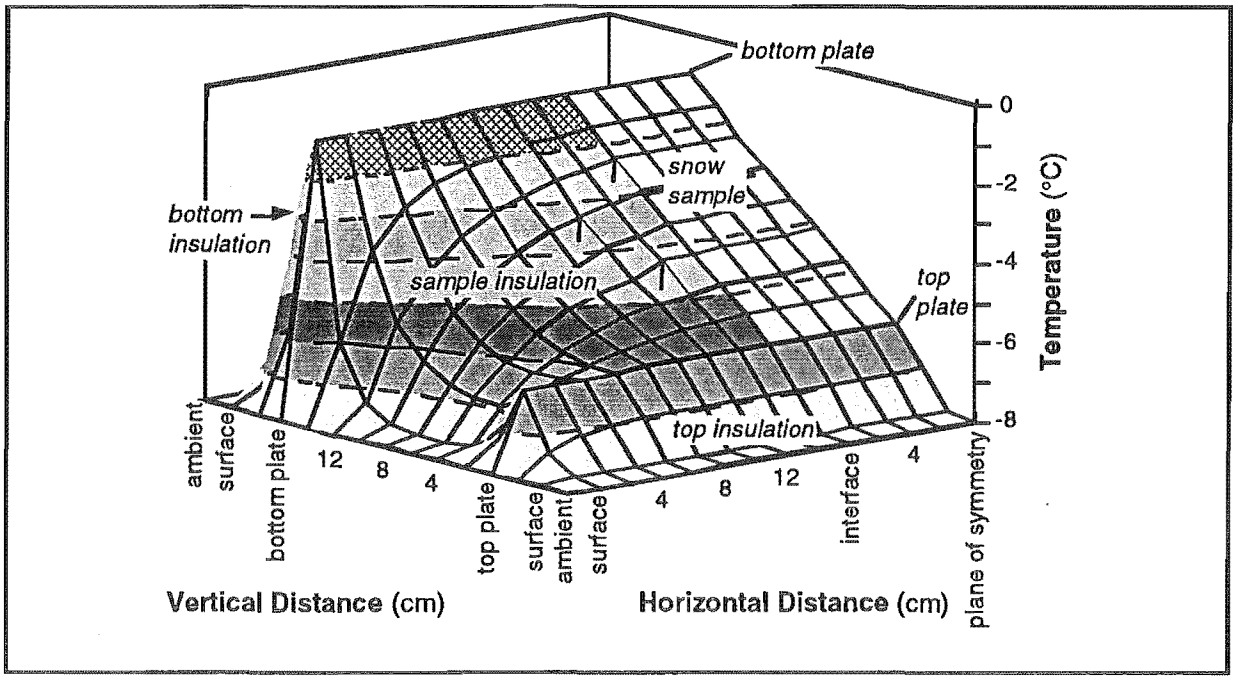

Figure X.5. Predicted Temperatures Within the Snow Sample and Insulation for a Slice Through One of the Perpendicular Planes of Symmetry in Figure X.1, using the 3-D Steady State Model.

X.1.6.2. Horizontal Temperature Gradients

Profiles of the horizontal temperature gradients for the snow sample and insulation and for the sample alone are shown in figures X.6 and X.7 respectively. The profiles are taken through one of the perpendicular planes of symmetry in figure X.1. From this and other profiles through the apparatus the maximum horizontal temperature gradient is 2% (0.31°C/m) of the vertical gradient imposed on the outer edges, and less than 1% for the inner 70% of the sample.

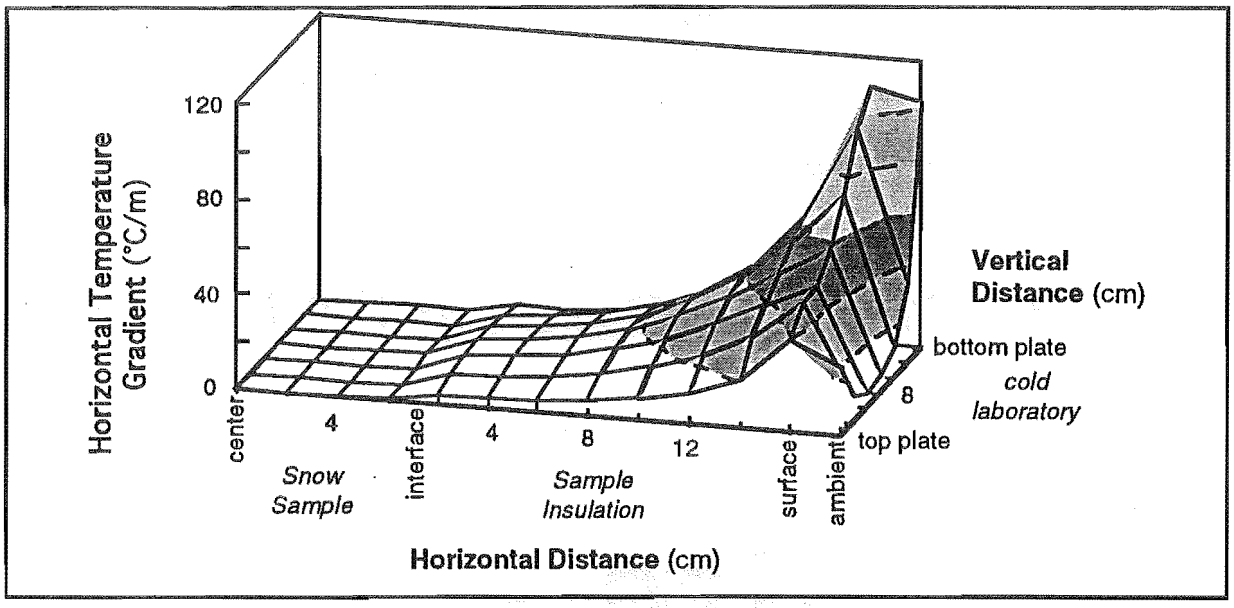

Figure X.6. Predicted Profile of the Horizontal Temperature Gradients for the Snow Sample and Insulation Taken Through One of the Perpendicular Planes of Symmetry (see Figure X.1) Using the 3-D Steady State Model.

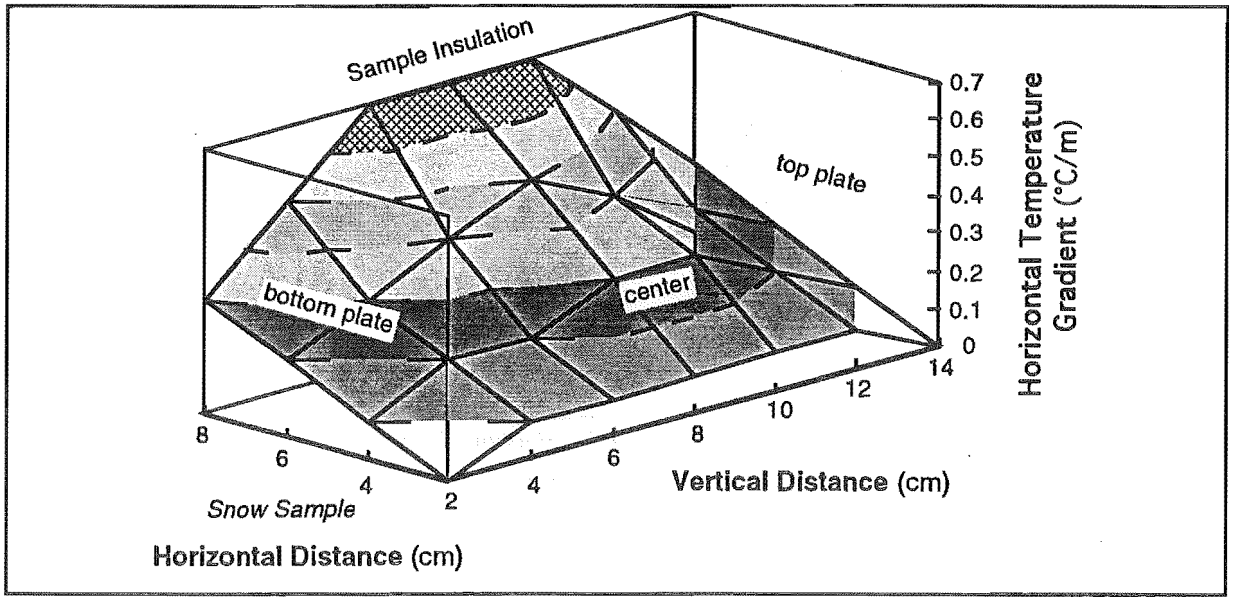

Figure X.7. Predicted Profile of the Horizontal Temperature Gradients for the Snow Sample Taken Through One of the Perpendicular Planes of Symmetry (see Figure X.1) Using the 3-D Steady State Model.

X.1.6.3. Plate Heat Loads

Figures X.8 and X.9 show maps of the bottom and top plate heat loads as predicted by the model for this configuration.

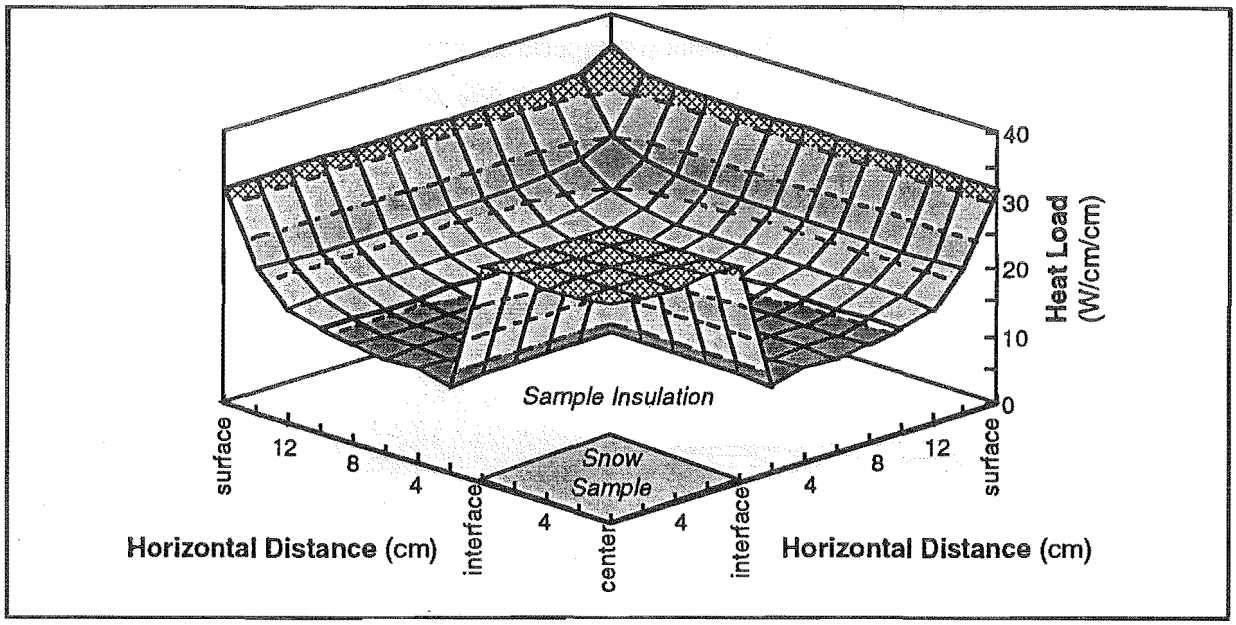

Figure X.8. Prediction of the Bottom Plate Heat Load Distribution From the 3-D Steady State Model.

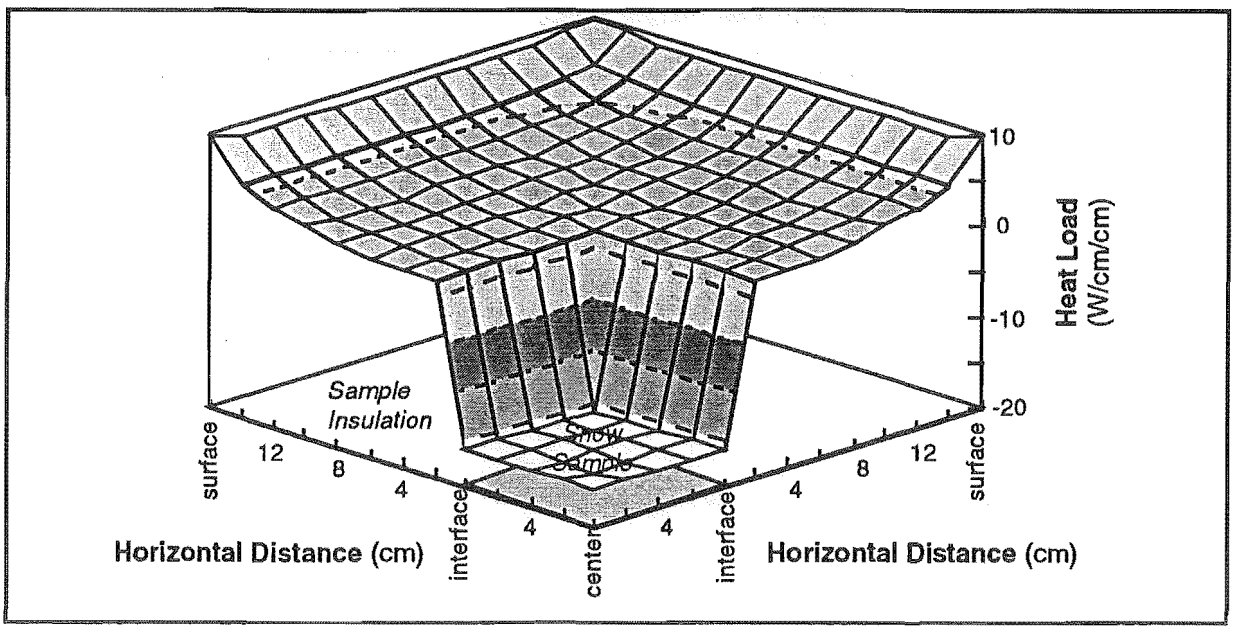

Figure X.9. Prediction of the Top Plate Heat Load Distribution From the 3-D Steady State Model. Note that the top insulation thickness is too large in this case as cooling is required over the snow sample.

Two points can be noted from these results other than the total heat loads used for plate design: Firstly, for the bottom plate, the higher thermal conductivity of snow (compared to that of polystyrene) puts a higher heat load onto the portion of the plate in contact with the sample (see

figure X.9). Secondly, for the top plate, the insulation thickness (50 mm) above the plate in this configuration is too large and results in a cooling requirement over the snow sample.

Total top and bottom plates loads in this case are 0.06 W and 0.69 W respectively.

X.1.6.4. Computational Requirements

This proved to be a heavy computational load on the Vax computer used - the result presented above required 24 million maximum residual checks and 12 hours to solve. This was for a relatively small problem, one sixteenth of the maximum nodes allowed. More detailed solutions required upwards of 600 million residual checks.

X.2. 1-Dimensional Steady State Design Model

A simple one dimensional steady state model was used to estimate the steady state heat load on the plates.

Unlike the three dimensional model the insulation and tube dimensions used for this model are those in the finalised experimental design. The lateral temperature gradients are assumed negligible so that the heat flows only in the vertical direction.

X.2.1. Model

The apparatus is split into two portions, the area over which the sample tube extends (figure X.10) and the area over which the sample insulation extends (figure X.11). The resulting steady state equations are solved analytically for the heat flow through the plates (giving the heating load).

Model Variables

*	Sample depth d	200 mm
*	Top and bottom insulation thickness d_t, d_b	0 to 50 mm
*	Bottom plate temperature T_B	-11.0°C
*	Top plate temperature T_T	-1.0°C
*	Cold laboratory (ambient) temperature T_A	-13.0°C
*	Insulation heat conductivity k_{ins}	0.04 W/mK
*	Snow heat conductivity k_{snow}	0.4 W/mK
*	Convective heat transfer coefficient h_{air}	30 W/m^{2}K

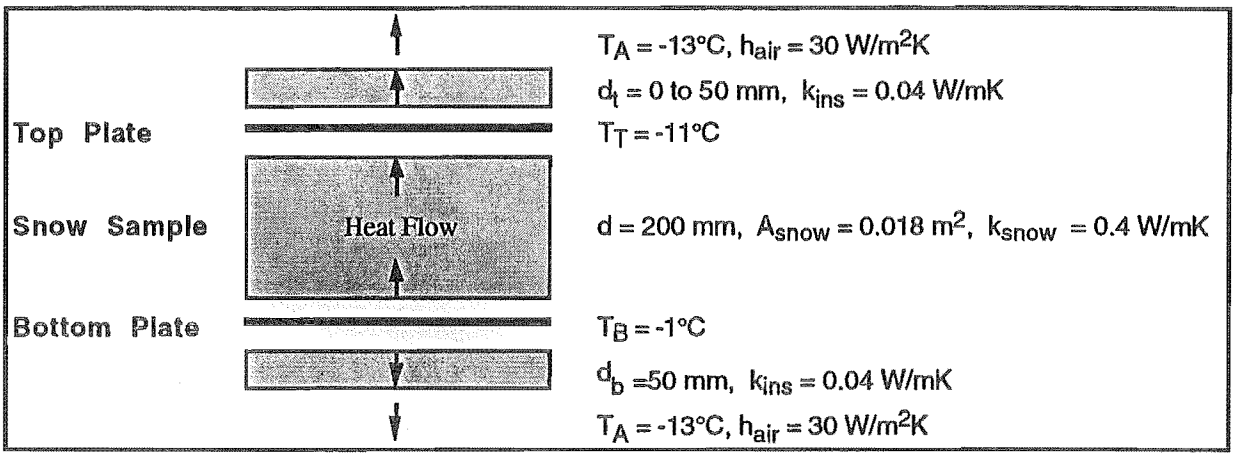

Figure X.10. Illustration of the 1-D Steady State Model Used for the Snow Sample Portion of the Sample Apparatus: High Temperature Gradient Case.

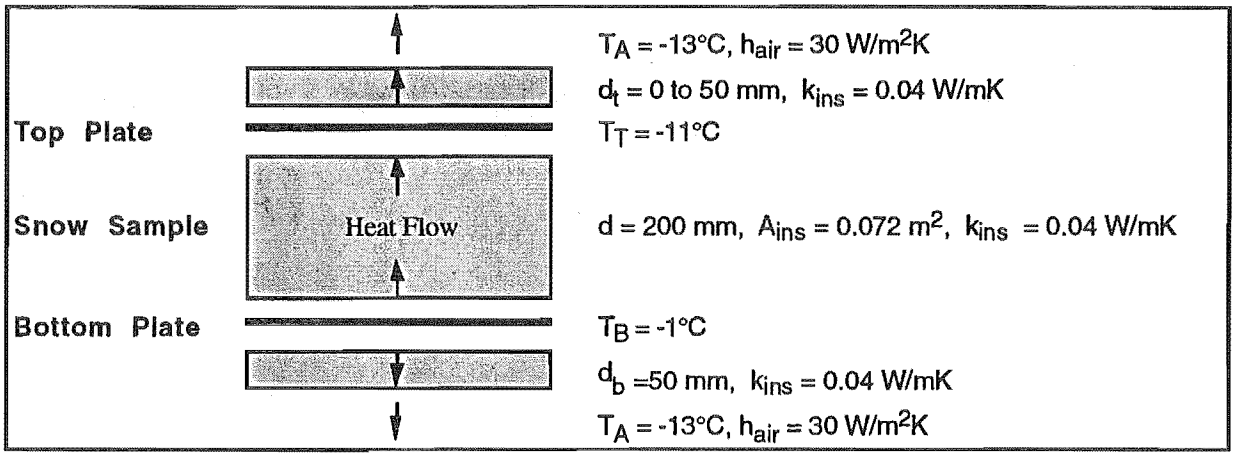

Figure X.11. Illustration of the 1-D Steady State Model Used for the Insulation Portion of the Sample Apparatus: High Temperature Gradient Case.

X.2.2. Analytical Results

The analytical results for the 1-D steady state model are summarised in table X.1. The temperature gradients imposed and consequently the heat loads are higher than the case documented in section X.1 (the 3-D model). 50 mm of insulation should be sufficient on the under side given the maximum plate output of around 3 W. Varying top insulation thicknesses are fitted according to the magnitude of the applied temperature gradient.

Insulation Thickness (mm)	Top Plate Load (W)	Bottom Plate Load (W)
0	0.82	-
3	0.12	-
25	-0.30	2.3
50	-0.33	1.5
100	-	1.0

Table X.1. Summary of Heat Loads for Varying Top and Bottom Insulation Thickness Using the 1-D Steady State Model. The applied temperature gradient is 30°C/m.

X.3. 1-Dimensional Unsteady State Design Model

A one dimensional unsteady state model is used to estimate the time the snow sample will take to reach a thermal steady state one it is loaded into the sample tubes, placed into the sample insulation and top and bottom plates fitted. Given the results from the 3-D steady state model (section X.1) the lateral temperature gradients are assumed to be negligible.

X.3.1. Model

Carslaw and Jaeger (1959) give the solution for the linear flow of heat between two parallel planes held at a constant temperature T_T and T_B with an initial temperature distribution in the slab ($0 < z < d$) given by the function f(z). Although the snow will not be loaded at a particularly consistent temperature (may be 5 or 10°C variation) a reasonable estimation of the time it will take for the sample to equilibriate with the plate temperatures is made using this solution with $f(z) = T_I$, a constant. This reduces Carslaw and Jaeger's solution to

$$T(z) = T_T + (T_B - T_T)\frac{z}{d} + \frac{2}{\pi}\sum_{n=1}^{\infty}\left(\frac{T_B\cos(n\pi) - T_T}{n}\sin\left(\frac{n\pi z}{d}\right)e^{-tkn^2\pi^2/\rho C_p d^2}\right)$$

$$+\frac{2T_I}{\pi}\sum_{n=1}^{\infty}\left(\frac{(1-\cos(n\pi))}{n}\sin\left(\frac{n\pi z}{d}\right)e^{-tkn^2\pi^2/\rho C_p d^2}\right) \qquad \text{X.6}$$

where d is the sample depth, T_T and T_B are the top and bottom plate temperatures respectively, f(z) is the initial sample temperature, z is the depth into sample from the top, k, ρ and C_p are the thermal conductivity,density, and heat capacity of the snow sample respectively and t is time.

Model Variables

*	Sample depth d	0.20 m
*	Bottom plate temperature T_B	-11.0°C
*	Top plate temperature T_B	-1.0°C
*	Snow heat conductivity k_{snow}	0.4 W/mK
*	Snow density ρ	300 kg/m^3
*	Snow heat capacity C_p	1330 J/kgK

Snow samples are loaded at a minimum temperature of $T_I = -40$°C. In figure X.12 displays approach to thermal steady state results for two loading temperatures $T_I = -4$°C and -40°C and two depths; $z/d = 0.25$ and $z/d = 0.50$. At time $t > 600$ s contributions to the solution of equation X.6 are negligible for $n > 20$.

X.3.1. Analytical Results

It takes 6 hours for the T_I = -4°C sample to reach steady state to within ±0.01°C and 9 hours for the T_I = -40°C sample to do the same. Consequently the sample temperatures should be brought to as close to the steady state temperature as possible before insulating.

As expected the central part of the sample takes longer to reach steady state than portions close to the plates.

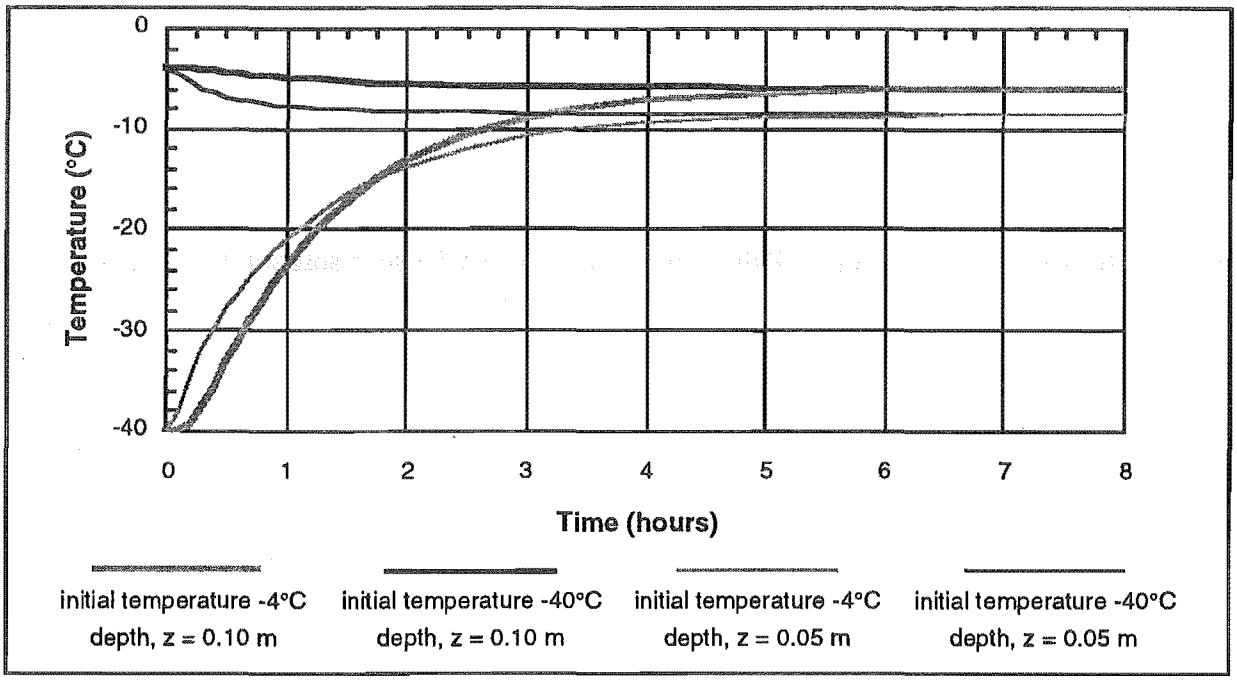

Figure X.12. Approach to Thermal Steady State for Sample Loading Temperatures of T_I = -4°C and -40°C and z/d = 0.25 and 0.50.

Appendix XI
Column Leakage

Given the larger than expected attenuation of the pressure signal found in the packed column experiments of Chapter 4, it is necessary to estimate the likely effects of a leak at the bottom of the column.

As this problem was discovered 18 months after the experiment had been dismantled, the full column could not be retested for leaks (a full test had been done prior to the experimental period). Limited tests are performed on the bottom end (z = d) fibreboard plate.

XI.1 The Finite-Leakage Model

The analytical solution to a leaking bottom boundary condition is difficult, so numerical methods are used to estimate the affect of the leakage on the pressure attenuation in the column. The unsteady state model developed is also used to confirm the time allowed for periodic steady state to establish itself upon switching the pump on.

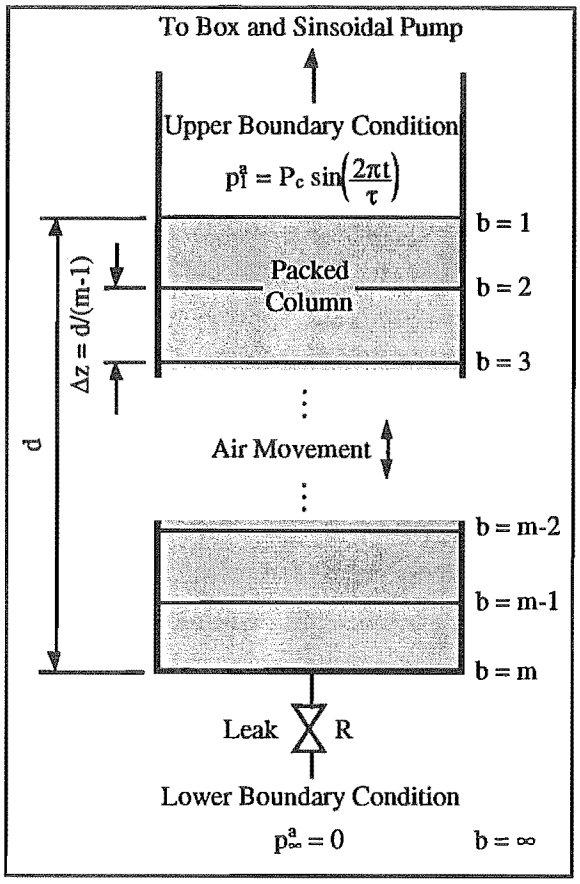

Figure XI.1. One Dimensional Unsteady State *Finite-Leakage Model* of the Pressure Dissipation Down a Packed Bed with a Forcing Sinusoid at the Top End and a Leak at the Bottom End.

In one dimension, the length of the column d is split into m nodes (denoted by the subscript b). At the upper surface node (b = 1) the pressure is given by the sinusoidal surface boundary condition. At the lower surface node (b = m) the pressure is determined by a combination of the surface pressure dissipation down the packed bed, and the leakage resistance characteristics at the bottom of the bed.

The distance Δz between each node is given by

$$\Delta z = \frac{d}{m-1} \qquad \text{XI.1}$$

There is a node ($b = \infty$) below the leakage to represent the ambient laboratory conditions. This model is illustrated in figure XI.1.

XI.1.1 Equations

Analogous equations, taken from numerical methods in heat transfer, are used to model the dissipation of the pressure fluctuations in the column.

XI.1.1.1 Heat Transfer Equations

A parallel model can be drawn for the heat transfer, case where a similar temperature forcing function exists on the upper surface, and a convective condition exists on the lower surface. Janna (1986) gives the following explicit formulation of the heat transfer equations obtained from a forward-difference scheme. The time t at which the node estimations are made is given by

$$t = a\Delta t \qquad \text{XI.2}$$

where the time interval between estimations Δt is given by equation XI.16. All nodes are evaluated for $a = 0, 1, 2\ldots$ until the desired periodic steady state solution is obtained.

For $\mathbf{b = 1}$, the top surface is the forcing sinusoid

$$T_1^a = T_c \sin\left(\frac{2\pi a \Delta t}{\tau}\right) \qquad \text{XI.3}$$

where T is fluctuating temperature, T_c is the amplitude of temperature fluctuation, t time and τ the period of fluctuation. For $\mathbf{2 \le b \le (m-1)}$, an internal heat conduction node

$$T_b^{a+1} = Fo_\Delta \left(T_{b+1}^a + T_{b-1}^a\right) + (1 - 2Fo_\Delta)\, T_b^a \qquad \text{XI.4}$$

where

$$Fo_\Delta = \frac{\alpha \Delta t}{(\Delta z)^2} \qquad \text{XI.5}$$

is a finite-difference form of the Fourier number and α the thermal diffusivity of the solid.

For **b = m**, the convecting surface node

$$T_m^{a+1} = 2Fo_\Delta \left(Bi_\Delta T_\infty^a + T_{m-1}^a\right) + \left(1 - 2Fo_\Delta - 2Bi_\Delta Fo_\Delta\right) T_m^a \qquad \text{XI.6}$$

where

$$Bi_\Delta = \frac{h_c \Delta z}{k_c} \qquad \text{XI.7}$$

is a finite-difference form of the Biot number, h_c is the outside convective heat transfer coefficient and k_c is the thermal conductivity of the material.

For **b = ∞**, the ambient condition

$$T_\infty^a = 0 \qquad \text{XI.8}$$

applies.

XI.1.1.2 Pressure Dissipation Analogy

The heat transfer equations are transposed directly to the pressure dissipation (pd) model. Assuming laminar flow exists through the leak, the leak can be characterised by

$$Q_L = \frac{\Delta p}{R} \qquad \text{XI.9}$$

where Q_L is the volumetric flow through the leak, Δp the pressure drop across the leak and R the leak resistance.

For **b = 1**, the top surface is the forcing sinusoid

$$p_1^a = P_c \sin\left(\frac{2\pi a \Delta t}{\tau}\right) \qquad \text{XI.10}$$

where p is fluctuating pressure and P_c is the amplitude of pressure fluctuation. For **2 ≤ b ≤ (m-1)**, an internal pressure node

$$p_b^{a+1} = Fo_\Delta^{pd} \left(p_{b+1}^a + p_{b-1}^a\right) + \left(1 - 2Fo_\Delta^{pd}\right) p_b^a \qquad \text{XI.11}$$

Assuming the ideal gas law, a finite-difference form of the Fourier number for the pressure dissipation is defined as

$$Fo_\Delta^{pd} = \frac{K\bar{P}\Delta t}{\varepsilon(\Delta z)^2} \qquad \text{XI.12}$$

where K is the permeability, $\bar{P}$ the (average) ambient pressure and ε voidage.

For $b = m$, the pressure at the leaking surface node is defined by

$$p_m^{a+1} = 2Fo_\Delta^{pd}\left(Bi_\Delta^{pd} p_\infty^a + p_{m-1}^a\right) + \left(1 - 2Fo_\Delta^{pd} - 2Bi_\Delta^{pd} Fo_\Delta^{pd}\right) p_m^a \qquad \text{XI.13}$$

A finite-difference form of the Biot number for the pressure dissipation is defined as

$$Bi_\Delta^{pd} = \frac{\Delta z}{RKA} \qquad \text{XI.14}$$

where A the column cross sectional area. For $b = \infty$, the ambient condition

$$p_\infty^a = 0 \qquad \text{XI.15}$$

applies.

The following condition is required for a stable solution to be obtained

$$2Fo_\Delta^{pd}\left(Bi_\Delta^{pd} + 1\right) \le 1 \qquad \text{XI.16}$$

This is used to determine Δt once the interval between nodes Δz has been selected, ie

$$\Delta t \le \frac{\varepsilon(\Delta z)^2}{2K\overline{P}\left(\frac{\Delta z}{RKA} + 1\right)} \qquad \text{XI.17}$$

The surface forcing function period also influences the choice of Δt. Sufficient accuracy is gained by ensuring

$$\Delta t \le \frac{\tau}{400} \qquad \text{XI.18}$$

The lesser of these two Δt's is used in the model.

Note that as R ' ∞ the solution should approach the *finite-sealed model*, and as R ' 0 it should approach the *finite-free model* (these models are described in section 4.5). These observations are used to tune the numerical variables (Δz and Δt) in the model.

XI.2 Results

XI.2.1 Leakage Tuning and Application

For each of the 25.1 and 2.0 m columns packed with plastic beads resistance R is fitted to the 3.185 s amplitude data by minimising the discrepancy between the finite-leakage model and experimental results. This R is then applied to the the other period amplitude data and the phase data for all periods.

The resistances found were $R = 3.9 \times 10^7$ and 4.5×10^7 Pas/m^3 for the 25.1 and 2 m columns respectively. The full results of this procedure are shown in figures 4.26 and 4.27.

From these figures little change can be seen in the fit of the finite-leakage model data for the various periods and column lengths. As the pressure gradient over an leak depends strongly on the period and column length, the results suggest that laminar flow existed in the leak, vindicating equation X.9.

XI.2.2 Bottom Plate Leakage Test

A 100 Pa pressure gradient was applied over the fibreboard bottom plate used in the experiments and the flow measured at 1.9×10^{-6} m^3/s. Using equation X.9 this gives a resistance $R = 5.3 \times 10^7$ Pas/m^3 which is very close to the above result.

XI.2.3 Approach to Periodic Steady State

An example of the calculated approach to periodic steady state (using the finite-leakage model) in a 25 m column packed with plastic beads is shown in figure XI.2 for period of 0.45 s. This represents the most difficult case (fast fluctuations and long column). For longer periods in the 25 m column, periodic steady state is reached in about the same time, but in fewer cycles. The time to periodic steady state for shorter columns are always less than for the 25 m column.

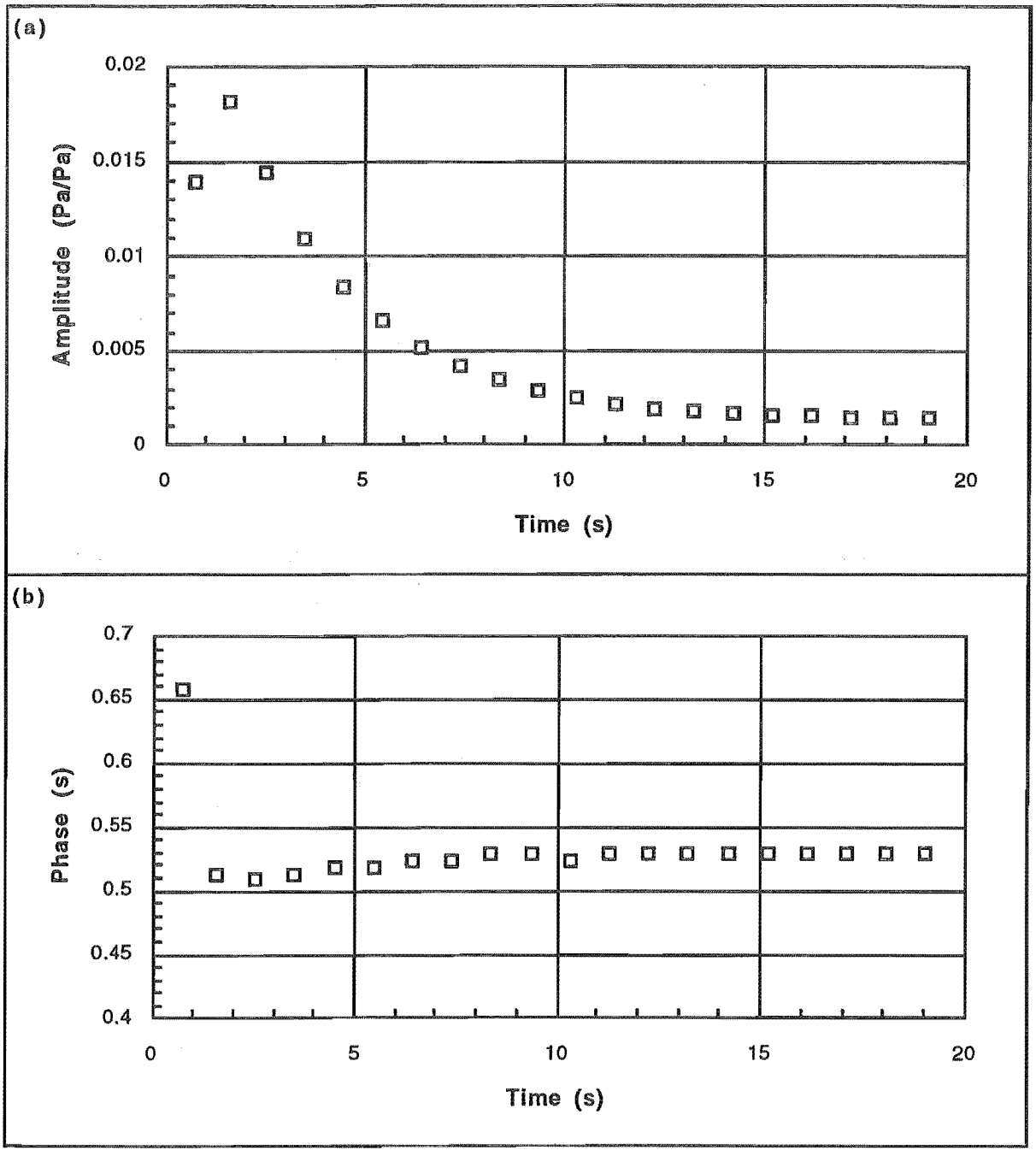

Figure XI.2. The Approach of Amplitude and Phase to Periodic Steady State Calculated from the Finite-Leakage Model for a Sinusoidal Period of $\tau = 0.45$ s in a $z = 25$ m Column Packed with Plastic Beads. The plotted points are the peaks of each period.

Appendix XII
Strength Testing Results

Sample Apparatus		Ram Weight of 2150 g			Ram Weight of 5150 g		
		Replications	Mean (mm)	s (mm)	Replications	Mean (mm)	s (mm)
A	upper	5	3.0	0.0	5	5.0	0.0
	centre	5	2.6	0.5	5	5.8	0.4
	lower	5	4.0	0.6	5	7.0	1.1
	all tests	15	3.2	0.7	15	5.9	1.1
B	all tests	17	2.9	1.1	14	5.1	1.3
C	upper	5	4.0	0.8	5	10	1.8
	centre	6	4.3	1.1	6	8.5	1.3
	lower	5	4.6	0.5	5	8.6	1.5
	all tests	16	4.4	0.9	16	9.0	1.6
D	upper	6	5.8	1.3	5	12	1.9
	centre	6	5.7	1.9	5	11	2.1
	lower	7	5.1	1.2	5	9.4	1.5
	all tests	19	5.5	1.5	15	10	2.1
E	upper	5	2.6	0.5	5	5.0	0.6
	centre	6	2.8	0.7	5	5.6	0.5
	lower	6	5.5	1.1	5	6.6	1.0
	all tests	17	3.7	1.6	15	5.7	1.0

Table XII.1. Ram Penetration Results for Run 3. s is the standard deviation of the replications made at each location. Figure 6.7.3 illustrates where in the sample *upper*, *centre* and *lower* refer to.

Sample Apparatus	Shear Strength ($x10^{-3}$ Pa)			Tensile Strength ($x10^{-3}$ Pa)		
	Replications	Mean	s	Replications	Mean	s
A	7	23	18	3	8	4
B	5	39	11	3	31	13
C	8	41	19	4	17	13
D	7	36	10	2	10	0
E	6	42	16	2	33	29

Table XII.2. Shear and Tensile Strength Results for Run 4. s is the standard deviation of the replications made in each sample.

Sample Apparatus	Shear Strength ($x10^{-3}$ Pa)			Tensile Strength ($x10^{-3}$ Pa)		
	Replications	Mean	s	Replications	Mean	s
B	4	11	3.6	4	11	5.6
C	5	16	12	4	15	14
D	5	13	6.7	3	17	9.7
E	4	25	12	3	20	7.6

Table XII.3. Shear and Tensile Strength Results for Run 5. s is the standard deviation of the replications made in each sample. Sample A was damaged during removal from the apparatus and could not analysed.

Sample Apparatus	Ram Weight of 150 g			Ram Weight of 650 g		
	Replications	Mean (mm)	s (mm)	Replications	Mean (mm)	s (mm)
A	19	9.2	1.6	18	16.8	1.5
B	22	5.9	1.1	22	12.4	2.5
C	27	9.1	1.7	22	17.8	2.6
D	25	8.0	1.7	25	16.9	1.9
E	25	7.0	1.9	25	16.2	1.9

Table XII.4. Ram Penetration Results for Run 6. s is the standard deviation of the replications made in each sample.